Mathematical models of filtration

Arkady Wey
Mansfield College
University of Oxford

A thesis submitted for the degree of
Doctor of Philosophy
Hilary 2023

To my siblings, Edie and Troy

I love you both so much. I owe you everything.
This is as much your achievement as it is mine.

Per angusta ad augusta, nunc ad meliora

Acknowledgements

My sincere thanks to the people who helped me think about this thesis...

To my supervisors, Prof. Chris Breward, Prof. Jon Chapman, and Prof. Ian Griffiths, for pushing me harder than I have ever been pushed before. Our work is something that I am truly proud of. Ian, you have been the best mentor I could hope for. Thank you for your help with my research, but even more so, for your guidance on personal matters. I am so grateful.

To our industrial collaborators, Dr. Uwe Beuscher and Dr. Vasu Venkateshwaran, at W.L. Gore & Associates, Inc., for introducing us to the physical problem, and keeping our research relevant outside of mathematics. Also, for the various trips to the USA, which have introduced me to so many friends for life.

To Dr. John Wilkinson and Dr. Edwina Yeo, for proofreading huge portions of this thesis. Thank you for helping to turn my drafts into something submittable.

To Tom Babb, Dr. Matthew Shirley, Dr. Kristian Kiradjiev, and Dr. Robert Timms, for their assistance with the ideas underpinning this work on more occasions than I can count. So much of this project has been a collaboration. I am so grateful to be able to call my colleagues my friends.

To Sophie Hurden and Amanda Guthland-Elmore. I am so sorry that you were unfortunate enough to be my InFoMM administrators. Sophie, I can only imagine how annoying it is dealing with my finances. Thank you. Amanda, thank you so much for taking me under your wing from day one.

To my fellow OCIAM graduates and friends, Dr. Amy K, Andrew A, Anna B, Brady M, Danny B, Dr. Eddy Y, Dr. Ellen L, Dr. Eva A, Georgia B, George B, Dr. Helen S, James H, Joe F, Joe R, Matt C, Dr. Matt S, Markus D, Dr. Michael N, Dr. Meredith E, Nick R, Ollie B, Phil W, Sophie A, Simon F, Tom B, and Torin F, for the mathematical and moral support. You will all do amazing things. I am so proud of us. Thanks for all the Najaars trips.

To my cohort, Dr. Alex P, Dr. Christoph H, Dr. Huining Y, Dr. Joel D, Dr. John F, Dr. Matt S, Dr. Meredith E, Dr. Nick B, Dr. Ollie B, Dr. Yu T, for surviving first year.

This research was funded by the Centre for Doctoral Training in Industrially Focused Mathematical Modelling (InFoMM) in the Mathematical Institute at University of Oxford. I would like to thank the Engineering and Physical Sciences Research Council (EPSRC) for my unique opportunity.

I would also like to thank the people who helped to stop me thinking about this thesis, for which I am at least as grateful...

To Edie, Troy, and Ellie, for picking me up whenever I'm down. And for the fun and the festivals, to MorgAn and Spike too. I could not have done it without you.

To The Cresidents. To Johnny Corrigan, for the COVID Sainsbury's runs. Thank you for always being right and for doing the bills. To George, because you're the only (other) person I know stupid enough to start a Breaking Bad marathon two weeks before submission. There's no one else I'd rather submit with (apart from maybe *our* sibli...). To Tom One, for the kebabs, and for being an all-round polite guest. To Sam, because you're the only person I know stupid enough to start a marathon. To Tom Two, for alerting us all to the dangers of PFAS. To Hattie and Liz, but mostly Adam, for finally getting us over the line on Thursday nights at the A and G. To Elise, for the extra bike by the washing machine. And, arguably most importantly, to Naymah, for the towel.

To The SDM(AI)C, Issy, Joe, Kris, Tom, and our silent participant, Seppe. Thanks for the 'office chat', Thursday NT-Coffees, and for generally cheering me up.

To the Mansfield lot who made the right decision by leaving in first year, Abi, Conor, and Lottie. Thanks for the wines and the cheeses, for the balls and the bops. Hanks has/will never been/be the same.

To Adam, Conor, Clarence, Lynn, and Tyler, for going to Hel(ston) and back with me.

To Julius and Pav, for inspiring me, teaching me thousands of new things about everything, and for the millions of calls in the COVID months.

To Benson, Conor, and all the other folks down at the CF. We had a few rough quarters, but I'm optimistic about the upcoming aforementioned off-site visit.

To the MtM boys, Aled, Dan, Eli, Nitin, and Tyler, for the holidays, the football, and the Feefs.

To The InBendtweeners, Mike, Kevin, Vinny, and Paige (and Morty, of course), for the amazing times away. I still root for The Timbers.

Lastly, thanks to my mum and dad. My experiences growing up have taught me to try anything and everything, to expect more, and to never give up.

Let's hope the remainder of this thesis is a better read than the last two pages...

Abstract

Filtration is the removal of particles from a fluid suspension by forcing it, either using a constant flow rate or pressure drop, through a porous material, which causes particles to become captured in the pores. Filtration using membranes is a well-studied industrial process with multiple important applications. Experimental observations of particle–pore interactions to gain insight into the filtration process are difficult and sometimes destructive. Some existing mathematical approaches either ignore important microscale information, such as the particle- and pore-size distribution or the connectivity of the pores, or are too computationally expensive for filter scale experiments. In this thesis we motivate, derive, solve, and discuss three novel models for particle filtration: (I) A size-structured model. In this work, the particle and pore sizes are treated as independent variables, which gives rise to a system of partial integro–differential equations within which the filter is treated as a macroscale continuum. We demonstrate that consideration of size structure allows for greater understanding of the filtration process; (II) A network model. Here, the filter is treated as a network composed of pores, which are modelled as edges, and junctions between pores, which are modelled as nodes. The connectivity of the network changes as particles deposit in pores. This gives rise to a system of ordinary algebraic–differential equations for variables defined at each pore and junction of the network. We show that this consideration of the structure of the microscale leads to physically intuitive behaviour of macroscale quantities, such as the flow rate and pressure; (III) A multiscale model. In this work, we extend the method of network homogenisation to apply to networks whose connectivity varies in time. We use this to derive a system of partial differential equations defined on the continuous macroscale geometry that is coupled, via its parameters, with variables that are defined on the discrete network that defines the microscale. We show that solutions of this multiscale model match those of the network model from (II) in a particular asymptotic limit, even though they are obtained at considerably reduced computational cost. These three models increase our understanding of the filtration process. The computational tractability of the models means that they are suitable candidates for filtration process optimisation tasks that involve repeated solution in future work.

Contents

Chapter 1

Introduction

We begin, in this chapter, by introducing the physical process of filtration, before reviewing the standard approaches to its mathematical modelling. We use these to motivate three novel models for filtration that will be derived, solved, and discussed in this thesis, and briefly outline each of these.

1.1 Filtration

First, in this section, we define our use of the term filtration, and motivate this thesis by explaining the social and economic importance of the process. We briefly summarise the filtration market and industry, and discuss the filtration processes for which this work is most relevant. Detailed explanation of filtration is beyond the scope of this study, so we direct the reader to a useful guide to filters and filtration by Sutherland *et al.*, [1], within which further explanation to most of the ideas discussed in this section can be found.

1.1.1 Definition

In this thesis, we define filtration to be the separation of solid particles from a fluid in which they are suspended, using a filter, which is a semi-permeable material that consists of a solid substance that is punctured with holes, which we call pores. In a paradigmatic filtration process, a diagram of which is shown in Figure 1.1, the feed is driven into the filter at the inlet, usually either by a constant pressure drop or flow rate. Fluid traverses the pores, and, as it does so, particles suspended within it are captured in pores in the filter. As a result, the filtrate, which is the fluid exiting the filter outlet, contains a lower concentration of particles than the feed.

Uses of filtration are vast and diverse, but can broadly be separated into applications that focus on:

- The removal of unwanted particles from a desired fluid. In this case, the particles retained in the filter are a waste product, and the filtrate is an end product;
- The recovery of desired particles from an unwanted fluid. In this case, the particles retained in the filter are the desired product, and the filtrate is waste.

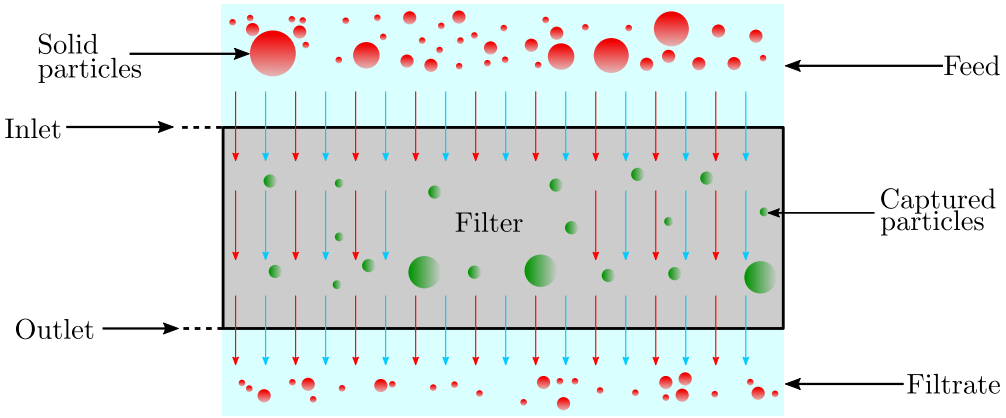

Figure 1.1: Diagram showing a paradigmatic filtration process.

1.1.2 Importance

Filtration is one of the most prevalent and important physical processes, and there are scarcely any human activities, domestic or commercial, that are not affected by it [2]. From tea bags [3] and coffee papers and presses [4], used to remove leaves and granules from water, to the drinking-water purifiers used to separate nitrates and dissolved solids in the kitchen [5, 6], to the dust collectors used to keep dirt particles entering vacuum cleaner motors [7], filters are common in the household. From the enormous processors in wastewater-treatment plants [8, 9], which use physical processes like sieving for size separation of pebbles on the centimetre scale, to the delicate nanofibres that use chemical properties like electrostatic adherence for bacteria and virus control in laboratories on the micrometre scale [10, 11], filters are equally common-place within industry. Filtration is also an important sub-step in many industrial processes where purification is not the primary focus, from the removal of debris from hydraulic fluids prior to use in machinery [12, 13], as a pre-process step, to the decontamination of vehicle and machinery exhaust-fumes [14, 15], as a post-process step.

In recent years, concerns over the global environment and the influence of humans upon it have grown. Scientists, politicians, and economists, are increasingly worried about three areas.

- Climate change [16]: There is more and more evidence [17, 18] to suggest that long-term shifts in temperature and weather patterns are due to increasingly polluted air [19], in part caused by growing energy consumption [20]. There is a need for solutions [21, 22] that minimise pollutant concentration in air and waste gasses emitted by industrial processes, and that minimise the energy consumed by these processes.

- Starvation and clean-water shortage [23, 24]: Despite the modest growth of the world economy [25], food and drink starvation has increased in recent years [26]. One reason is that pollutants from industry, such as chemicals and bacteria [27–29], find their way into waterways, and cause contamination that prevents water

from being safe for drinking, cooking, and cleaning. Solutions [30] that focus on decreasing the levels of harmful contaminants in water and other liquids are quickly becoming essential.

- Spread of pathogens [31]: The COVID-19 pandemic, which has been responsible for millions of deaths since 2019, has highlighted the importance of the filtration process in medicine, healthcare, and in society more generally. As the pandemic evolved, filtration processes and systems for mechanical ventilation, such as those used in intensive care and anaesthesia settings [32], became some of the most essential mechanisms for the protection of lives. Filters contained in face masks to shield the spread of infectious pathogens have become household items [33].

Air and water contamination, energy manufacture and consumption, and bacteria- and virus-spread prevention, then, are some of the biggest challenges humanity currently faces. Problems in these areas are largely due to human activity [34–38], and there is an urgent need to change the way life is conducted to help to eradicate these problems.

It is difficult to overstate the role that filtration, as a process and an industry, has to play [1]. As awareness increases, demand for filters with higher retention, that last longer, and are more energy efficient, increases. Laws [39] around minimisation of factory waste mean that filters need higher levels of particle retention, and to be able to process higher volumes of fluid before their disposal. Changes to policy [40] around energy-usage minimisation mean that filters need to be more energy efficient, so that this increased retention and high throughput occur in lower pressure drop or flow rate situations.

1.1.3 Utilisation

The uses of filtration are as vast as they are diverse. In 2007, it was estimated that the total market for filtration equipment was worth around $38 bn (USD), and was expanding at a rate comfortably in excess of that of the global economy [1]. As we see in Table 1.1, the market is dominated by solutions for domestic and institutional users, and applications in transport, which together account for almost 34% of the market. Water treatment, the production of bulk chemicals, and the manufacture of food and drinks account for another 28%, and filters for use in laboratories, hospitals, wider healthcare, and the pharmaceutical industry constitute a further 11%. Power generation and other applications make up the remaining 27%.

Segregating the market by the phase of fluid that is processed, important applications in gas filtration include the cleaning of air entering living and work spaces [41], protection from exhaust fumes emitted by machinery engines [15], and respirators and breathing apparatus [31].

Applications in liquid filtration include the production of potable water from ground and surface sources [42], refinement of ultrapure water for laboratory use [43], treatment of waste waters to prepare them for discharge [8], preparation of boiler feed water and the recycling of boiler condensate [44], processing of transformer oils [45],

End-user sector	Market share (%)
Domestic and institutional	17.9
Transport	15.9
Water treatment	10.3
Bulk chemicals	9.9
Food and drink	7.5
Pharmaceuticals and biochemicals	6.5
Power generation	6.3
Pulp and paper	5.1
Medicine and healthcare	4.8
Electricals	3.5
Other	12.3

Table 1.1: Table showing the proportions of the filtration market attributed to different end users [1].

cleaning of tool coolants and cutting fluids [46], and the cleaning of hydraulic-system fluids [12]. Altogether, filtration is an increasingly important physical process with a diverse set of uses.

1.1.4 Particles and the feed

Although some filtration regimes are used to control non-solid particles, such as liquid droplets that are well mixed or dissolved in the carrying fluid, we will focus our attention on solid particles suspended in a liquid or gas.

The most common way of partitioning the plethora of different solid particles is by their size. The mean particle size, and the distribution of sizes about this mean, has a major influence on the type of filter that is chosen for a retention-, throughput-, and energy-efficient solution. Particles in feeds range from pebbles that are at least centimetres in diameter to tiny dust particles and large molecules on the submicroscale (see Figure 1.2). Particles at the smaller end of this scale include viruses, tobacco smoke, and almost all combustion nuclei, while those at the larger end include stone particles, such as sand and limestone. The majority of filtration processes are concerned with the removal of particles that are fine enough to have stayed suspended in liquids or atmospheric air for long periods of time, and are less than 10μm, say. We will focus this study on these, since, as we will discuss shortly, we are most interested in filters that contain porous membranes with pore sizes distributed over the microscale.

Almost any fluid that contains a particle suspension could be considered as a candidate feed. In this thesis, we focus on fluids, like water, which are well modelled as a continuum with a given viscosity by traditional rules that govern the macroscopic and microscopic flow in porous media: Darcy's law and the Hagen–Poiseuille equation, respectively. That is, we are interested in fluids with a Reynolds number, Re, in the region $10^{-1} \leq \mathrm{Re} \leq 10^{3}$, say, which are not sufficiently viscous that edge effects cause substantial changes to the effective flow field, nor so inviscid that turbulence causes

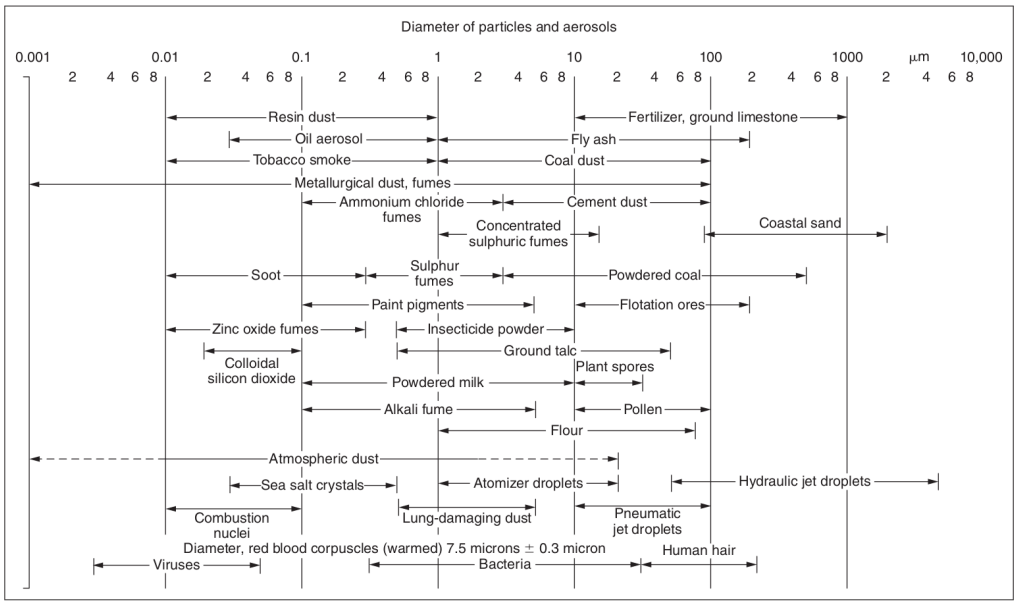

Figure 1.2: Diagram showing some types of particles commonly found in air, and their sizes [1].

significant changes on the microscale.

1.1.5 Pores and the filter

The variety of different filtration devices is enormous, and a full review is far beyond the scope of this introduction. It suffices to say that their properties, to a large extent, depend on the particles they are used for. In general, filters are characterised by the media that they are composed of and the arrangement of these media. Some common filtration media are: absorbent and adsorbent biological materials, and some papers and fabrics, for generally smaller particles; and woven wires and plate meshes for larger particles. Different configurations lead to different types of filter, such as strainers, bags, pleated membranes, screens, tipping pans, and rotary drums, to name just a few (see Figure 1.3).

In this thesis, we focus on membrane filters, which are thin, flexible, and semi-permeable sheets composed of polymers, modified cellulose products, or occasionally inorganic products, such as ceramics. Membrane filters are increasingly used to filter microscale and sub-microscale particles in many industrial sectors, including the chemical, petrochemical, and food and beverage processing industries, in pharmaceuticals and biotechnology, and especially in the treatment of water [1]. Some examples of membrane technologies and their main applications are shown in Figure 1.4.

Use of membrane filters began with so-called 'non-porous membranes', which are extremely thin films with pores of sizes around 0.1nm, used for the separation of water from other molecules via reverse osmosis. One disadvantage is that these sometimes operate at high transmembrane pressures ($3 \times 10^6 - 6 \times 10^6$ Pa) to obtain appropriate flow rates (at least $1 \times 10^{-3}\text{ms}^{-1}$, say). In recent years, polymers with slightly larger

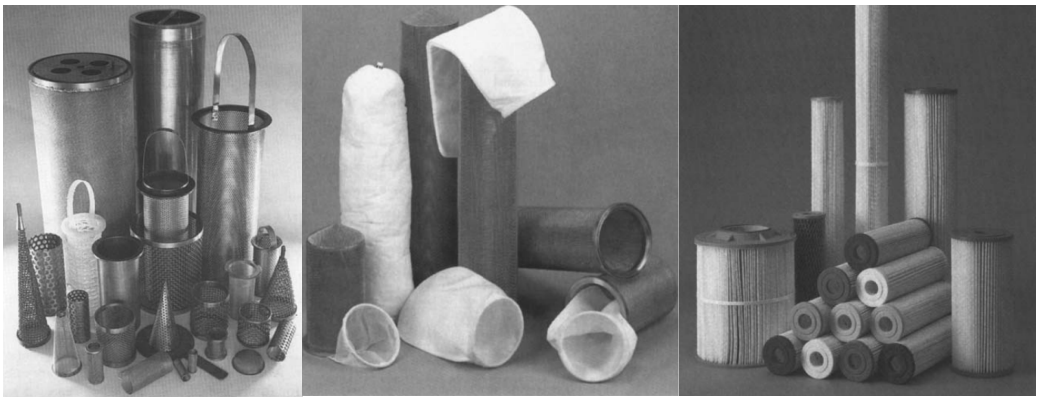

Figure 1.3: Photos showing (left to right) strainers, filter bags with their cartridges, and pleated membranes in their cartridges [1].

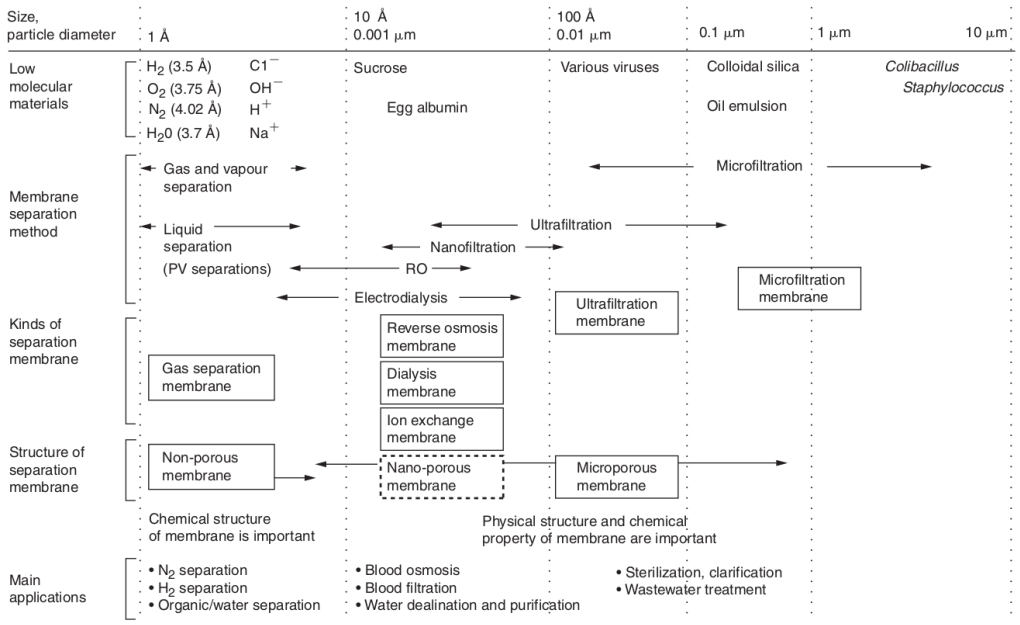

Figure 1.4: Diagram showing some membranes used for filtration, and their typical pore sizes [1].

mean pore sizes have been engineered, giving rise to the processes of nanofiltration, which needs correspondingly lower transmembrane pressures ($2 \times 10^6 - 4 \times 10^6$ Pa), ultrafiltration, which is used for the separation of large organic molecules, and colloidal solids, at pressures in the region of $5 \times 10^5 - 1 \times 10^6$ Pa, and microfiltration, operating at only a few times ambient pressure (3×10^5 Pa), while achieving fluxes around $1 \times 10^{-3} \mathrm{m}^3 \mathrm{s}^{-1}$. The lower pressure drops required for nanofiltration, ultrafiltration, and especially microfiltration, enable separation with relatively low energy demands while still providing a filtration capability that is suitable for many tasks.

We are particularly concerned with microfiltration membranes manufactured by

W. L. Gore & Associates, Inc (Gore), which are composed of a material called Expanded Polytetrafluoroethylene (ePTFE) (see [47] for a thorough description). Properties of ePTFE membranes, such as pore size distribution and average, depend, to a large extent, on the method used to manufacture them [48]. Several patents exist, and broadly involve the 'expansion' of PTFE, that is, the calendaring, drying, longitudinal stretching, and sintering of an extruded film of the original 'un-expanded' fluoropolymer (an organic molecule containing Fluorine atoms, PTFE in this case) [49]. On the macroscale (see Figure 1.5 (left)), ePTFE membranes are sheets that have a much larger length and width (around 1m, say) than depth (usually around 1mm, but sometimes as large as 1cm), which refers here to the direction of induced flow in a filtration process). On the microscale (see Figure 1.5 (right)), ePTFE membranes are composed of a mesh of millions of tiny hair-like fibres. This gives rise to a network of hollow tunnels between the fibres. These represent pores in the context of filtration. During filtration, particle-laden fluid is driven through the pore space between fibres, and some particles are captured on 'pore walls' (i.e., the fibres between pores). Repeated capture leads to the clogging of individual pores and thus, eventually, to the clogging of the filter. Typically, ePTFE membranes contain pores of sizes in the range 0.02μm to 40μm and are used in filters designed to filter suspensions containing particles of sizes in a similar range. In the most extreme case (i.e., where pores are around 0.01μm and the membrane is around 1cm thick), the ePTFE membranes contain around 1,000,000 pores in the depth direction. When ePTFE

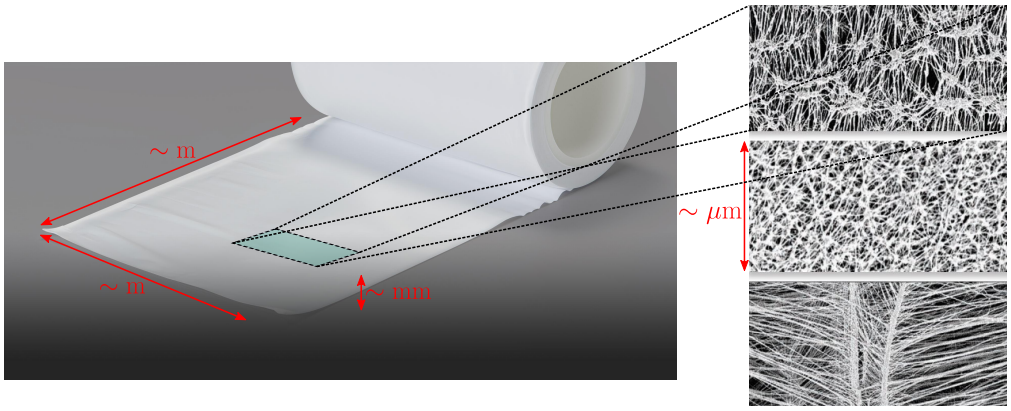

Figure 1.5: Diagram showing macroscale and microscale photographs of ePTFE [50].

membranes clog, this plastic must be cleaned or replaced, which is time-consuming and expensive, and has negative environmental impacts. Industrialists at Gore are interested in understanding the relationship between microscale and macroscale phenomena that lead to clogging, so that they can improve filtration performance in terms of retention, throughput, and energy consumption.

1.1.6 Particle capture and pore clogging

The mechanisms by which particle capture and pore clogging occur are not completely understood. In modelling literature (see [51], for example), particle capture and pore clogging are assumed to occur by any of four mechanisms, which are illustrated in Figure 1.6. These are:

- Blocking, where particles pass through larger pores but get stuck when they encounter small gaps;
- Deposition, where particles pass into larger pores and adhere to pore walls, due to electrostatic forces or chemical binding, causing pore constriction, for example;
- Partial surface blocking, where particles land on the surface of the membrane and partially cover a pore entrance;
- Caking, where particles build up on the surface of the membrane and form a porous layer through which the feed must permeate. This layer may evolve to have a distinct permeability from that of the actual membrane [52].

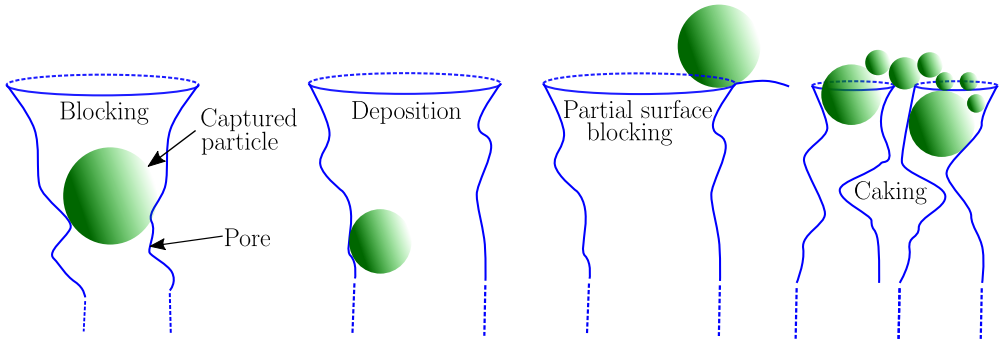

Figure 1.6: Diagram showing four particle capture and pore clogging mechanisms.

The relative prevalence of these clogging mechanisms depends on the membrane structure, feed composition, and the process conditions, and plays a part in determining the behaviour of filter properties, such as the flow rate [51]. In this thesis, we will focus our attention on blocking and deposition (as in [53], for example).

In summary, filtration is a socially and economically important process. We will focus this study on modelling microfiltration of particles of sizes around 10μm using pores of similar sizes in ePTFE, and pressure drops of around 3×10^5 Pa that achieve fluxes of around $1 \times 10^{-3}\text{m}^3\text{s}^{-1}$, say. We will assume that, as fluid traverses the filter, particles are captured in pores via blocking and deposition, which lead changes to the effective properties of the filter and eventually clogging.

1.2 Existing models for filtration

Industrialists and researchers have attempted to track and understand particle–pore interactions, and their effects, using many methods. One approach is to experimentally monitor particle build-up inside membranes. This is achieved through a variety of techniques, including: microscopy; laser censoring; reflectometry; spectroscopy; and 3-D imaging, to name just a few [54–64]. Experimental methods (see [65] for a review) provide useful data on almost every operational aspect of the filtration process. However, they are often difficult, can take a long time, and are usually expensive, due to the need for repetition. Some experiments also involve destruction, and subsequent disposal, of filtration membranes. This is problematic, since it leads to financial expense and has negative impacts on the environment (due to the lack of options for the safe disposal of fluoropolymers, and issues surrounding their recycling) [66], and can be prohibitive, since industrialists are interested in monitoring particle–pore interactions as filtration proceeds.

As early as 1935 [67], mathematical modelling of filtration was used as a cheaper and faster alternative to experimental techniques. Since then, a vast amount of research has been conducted, which can broadly be segregated into three categories: macroscale models; microscale models; and multiscale models.

1.2.1 Macroscale models

Macroscale models are descriptions of filter properties that mostly ignore the physical and chemical characteristics of the suspension and the membrane. In simple cases, the effects of microscale quantities, such as particle and pore size, are implicitly included in the value of a 'filter coefficient' that is predicted beforehand, as opposed to being calculated as part of the solution. One early example is that of Iwasaki *et al.* [68], who pose a simple model for the exponential decay of particle concentration in the flow as a function of filter depth. The filter coefficient plays the role of the decay rate, which was later fitted experimentally by Ison and Ives [69]. More complex macroscale models (see [70] for a review) usually take the form of systems of differential equations that describe the evolution of the fluid velocity, pressure, and particle concentration, as well as other variables, on a continuous domain. For example, Darcy's law, coupled with a continuity equation for the fluid velocity, is often used to describe the proportionality of the flow rate to the pressure gradient by the permeability. This is usually coupled to an advection equation that describes the transport of particles through the filter, often with additional diffusion or reaction terms that account for the global effects of particle–pore interactions. The permeability, as well as the diffusivity and reactivity (if they are included), are often viewed as other fitting parameters, to be improved by empirical measurement. These models are generally relatively computationally cheap to solve, but sometimes do not quantitatively agree with observations because they fail to model important microscale mechanisms, such as changes in the pore size distribution due to particle capture. Jegatheesan *et al.* provide a useful overview of some prominent research in [70], and we discuss a few models that are particularly relevant to this thesis in Chapter 2.

1.2.2 Microscale models

Microscale models, on the other hand, seek to resolve the mechanical and chemical interactions that cause particles to adhere to pores and decrease their fluid conductance. Prominent examples include computational fluid dynamics (CFD) simulations, which are used to solve highly complex flow equations through exact pore space geometry using finite element methods [71], and agent-based models, which track the position and behaviour of each particle or pore [72]. More recently, genetic programming techniques [73] and artificial neural network solvers (ANN) [74] have been applied to complicated membrane systems. Pore network models (PNMs) [75] are another prominent example, in which the microscale pore space is modelled as a network of nodes and edges whose connectivity and other statistical properties are representative of samples of real porous media. These usually consist of dynamical systems of algebraic or differential equations that describe the transport of particles through the network, and changes to the network structure due to particle interactions with the nodes and edges. Although microscale models can be highly accurate, they are usually computationally expensive to solve. This can render consideration of the entire filter geometry infeasible. We discuss network models in more detail in Chapter 6, and [75] provides a good overview of models that employ this framework.

1.2.3 Multiscale models

Multiscale models occupy the middle-ground between the two other approaches. Like macroscale models, these typically consist of differential equations, such as Darcy's law and advection–diffusion–reaction equations, which are defined on a continuum macroscale. Unlike macroscale models, however, the parameters of these equations are solved as part of the systems, and hold information about microscale interactions and geometry. Multiscale models provide computational feasibility near that of macroscale models, but are generally more accurate, due to explicit microscale dependence. Relevant recent work on multiscale models for porous media includes that of Bruna, Chapman, Dalwadi, Griffiths, Please, and Printsypar [76–83], among others. We discuss these at greater length in Chapter 10.

1.3 Three novel models for filtration

In this chapter, we have introduced the physical process of filtration, and summarised the existing approaches to mathematically modelling it. In the remaining chapters of this thesis, we will motivate, derive, solve, and discuss three novel models for filtration.

1.3.1 Macroscale model: A size-structured model for filtration

In Part I, we build and solve a continuum model for filtration on the macroscale geometry of the filter, which is novel because particle and pore sizes are treated as independent variables upon which parameters of the system depend.

To this end, in Chapter 2, we highlight the importance of the choice and continuous monitoring of the pore-size distribution as a means of controlling the sizes of particles in the filter and filtrate, and thus as a means of filtration-process control and optimisation. We discuss the need for a computationally tractable mathematical model in which particle and pore sizes are fully accounted for.

In Chapter 3, we derive a size-structured model for filtration by using ideas common in age-structured population models, where age is treated as an independent variable similar to space in more traditional population models. We arrive at a system of continuous partial integro–differential equations that govern the temporal and spatial evolution of the size distributions of particles and pores in the filter.

In Chapter 4, we solve this size-structured model in the cases where particles are mono-dispersed and pores are either mono-dispersed, bi-dispersed, or log-normally poly-dispersed. We find that our choice of modelling framework leads to equations that are soluble via explicit and asymptotic methods in certain physically relevant parameter regimes, and are solved via computationally tractable classical numerical methods in other regimes of interest. We find that knowledge of the evolution of the particle- and pore-size distributions leads to increased understanding of the behaviour of quantities of interest, such as the flow rate and pressure drop.

Finally, in Chapter 5, we conclude our discussion of the size-structured model by noting that our solutions agree with physical intuition, before highlighting the need for analysis of other industrially relevant operating regimes, such as poly-dispersed feeds. The computational feasibility of this model leads to its potential use in filtration-process optimisation tasks in future work.

1.3.2 Microscale model: A network model for filtration

In Part II, we build and solve a model for filtration in which the microscale structure of the filter is viewed as a network of pores, which we model as edges, and junctions at pore ends, which we model as nodes.

To this end, in Chapter 6, we note that recent developments in computational image analysis have led to algorithms that extract networks from high resolution characterisations of the microscale of porous membranes. In the resulting networks, void space is segregated into cylindrical edges, which are viewed as pores that carry flow, and spherical nodes, which are junctions at which the direction of particle flow may change. This gives rise to the potential for a model in which the microscale is represented as a network and the fluid as a continuum of particles, which accounts for particle capture that affects network structure.

In Chapter 7, we consider the flow of a fluid containing a continuum of particles through a network of pores and junctions. The particles can deposit on the inner walls with some adherence probability, which decreases the size of pores, causing a decrease in their fluid conductance. Continued deposition leads to removal of pores, which alters the connectivity of the network. We arrive at a system of ordinary algebraic–differential equations that govern the conductance, particle concentration, and pressure on a network whose connectivity is dynamic in time.

In Chapter 8, we solve the network model for filters with various pore-size distributions. We first focus on the case where the pore-size distribution is uni-modal, which gives rise to a network where all edges have the same conductance initially. Later, we explore the case where the pore sizes are distributed log-normally, and find solutions that qualitatively match the solutions for our size-structured model.

Lastly, in Chapter 9, we conclude that our network model allows us to specify an initial microscale structure and monitor temporal changes to this, and the effects of these changes on macroscale quantities of interest. However, although we are able to solve the model on portions of the filter, it is prohibitively expensive in cases where the network contains a number of pores comparable to that present in entire porous membranes. We look to our third model as a way of solving this problem.

1.3.3 Multiscale model: A multiscale model for filtration

In Part III, we build and solve a multiscale model for filtration in which the microscale membrane structure is treated as a network of pores and junctions, and the macroscale geometry is treated as a continuum of particles and pores.

In particular, in Chapter 10, we explore existing models that allow the simultaneous monitoring of changes to global and local properties of the membrane. We find that most models view the microscale as a continuous medium, in which it is not possible to incorporate network structure that we have already shown to model the microscale well. We conclude that there is a need for a framework for multiscale models, in which the microscale is treated as a dynamic network that represents the filter as a whole, while the macroscale is treated as a continuous medium.

In Chapter 11, we derive a new multiscale model for filtration, which is novel because the filter microscale is treated as a periodic network consisting of a repeating smaller network (which we call a cell), while systematic averaging leads to the emergence of a continuum system to represent the filter macroscale. To derive a network–continuum multiscale system from the discrete microscale problem, we extend an asymptotic method, called network homogenisation, to account for networks where the connectivity changes with time. The result is a system where partial differential equations defined on the continuous macroscale geometry are coupled with ordinary algebraic–differential equations defined on the discrete microscale network. Changes to the connectivity of the microscale due to deposition cause changes to the parameters of the macroscale system, and thus to macroscale quantities of interest, such as the flow rate and pressure.

In Chapter 12, we solve our multiscale model. Crucially, we find that the solution of our multiscale model matches that of our network model from Part II well in the asymptotic limit in which many cells constitute the network. This is significant as the cost of solution of the multiscale model is a function of the number of nodes within a cell, as opposed to the number of nodes in the entire network, meaning that simulation of the entire filter is now feasible. Furthermore, we explore the effect of microscale structure on macroscale quantities and show that the pore-size distribution and microscale connectivity are important in determining the permeability and adhesivity.

In Chapter 13, we conclude by noting that we have developed a framework for filtration that incorporates the entire structure of the microscale without the solution becoming prohibitively computationally expensive. Further work might involve further assessment of the effects of connectivity and pore-size distribution on the effective flow rate and particle concentration, or the inclusion of more complex physical and chemical laws on the microscale, which the framework permits.

Lastly, in Chapter 14, we conclude that we have developed three novel models for filtration and showed that these increase our understanding of the physical process. Importantly, solution of all three of our models is more computationally feasible than many existing models, which opens them up for the potential for the parameter sweeps and cost function descents necessary for filtration process optimisation in future work.

Part I

A size-structured model for filtration

Chapter 2

Introduction to the size-structured model

2.1 Particle and pore size in filtration

In industrial membrane filtration regimes, the size of the particles ranges from the nanoscale to the milliscale [1]:

- Particles on the nanoscale, 10^{-3}–$10^{-1}\mu$m, which are only detectable using electron microscopy, include virions (the complete, infective part of a virus) [84], tobacco smoke [85], soot [86], and many products of combustion [87];
- Microscale particles, of sizes in the range 10^{-1}–$10^{1}\mu$m, are only visible through microscopes and include bacteria [88], pigments [89], aerosols [90, 91], and blast-furnace dusts [92];
- On the milliscale, 10^{1}–$10^{3}\mu$m, examples of particles, some of which are visible to the naked eye, include pollen [93], and the dust from various types of industrial machinary [94].

A common goal in many industrial processes is to segregate particles based on their size [1]. Recently, for example, much attention has been paid to the development of filtration materials for protective face masks [95]. The aim is to prevent the passing of saliva droplets of typical sizes $1 - 10\mu$m from an infected person to an uninfected person [96], while simultaneously allowing the passage of particles prevalent in air, to prevent unsafe respiration [97]. Air purification devices (see [98] for a review), which have increased in popularity due to concerns about pollutant levels [99], provide another prominent example [41]. Some high-efficiency particulate absorbing (HEPA) filters are designed to remove tire matter, brake dust, and certain vehicle exhaust fumes from air. These particles are 2.5μm or less (around 100 times as thin as human hair).

The choice of the pore-size distribution, and the filtration process as a whole, depends to a large extent on the particle size [1]. Particles are often retained via blocking, using filters that contain pores in a similar size range, or via deposition,

using filters containing larger pores that are coated with agents that have some mutual adhesion property with the particles that are to be processed. For example:

- Nanoscale particles are often processed using membrane filters, active-carbon filters, and HEPA filters;
- Microscale particles are most commonly captured using methods such as electrostatic precipitation, wet scrubbing, and other fabric-dust filtration methods;
- Milliscale particles are usually retained using the most conventional filtration methods, which include sieving, venturi scrubbing, cyclonic separation, and filtration via paper and various fabric materials.

Recent research has increasingly focused on controlling the pore-size distribution in the filter as a means of controlling the sizes of particles that are retained [100–102]. For example, in so-called honeycomb-structured porous membranes, it is possible to control the size of the pores and even their spatial distribution with high accuracy [103, 104]. In general, the accuracy with which the pore-size distribution can be chosen varies depending on the material used to produce the filter. When control of the pore-size distribution is feasible, industrialists are generally interested in designing filters that contain pores with the distribution of sizes that maximises the throughput (total amount of fluid processed before the filter membrane is replaced) while ensuring that some minimum proportion of particles in the desired size is removed by the filter.

2.2 Existing size dependent models for filtration

Theoretical work on filtration is vast (see the reviews by Iritani [105] and Jegatheesan [70], for example), and yet, relative to the subject as a whole, models that explore the relationship between the particle- and pore-size distributions are sparse. In mathematical studies, filtration processes are frequently idealised by assuming that all particles in the feed fluid are one characteristic size (often the mean of a distribution that is obtained experimentally). This may be sufficient if the true distribution is tight, but seems cavalier in situations where particles are more widely poly-dispersed.

Indeed, there is experimental evidence to suggest that this simplification has a significant effect on solution behaviour. In [106], for example, Chang *et al.* explore mono-dispersed, bi-dispersed, and tri-dispersed feeds, and find that otherwise-equivalent regimes are more efficient when larger particles are present, since more large particles are retained per unit time than small ones. Thus the solutions exhibit different quantitative behaviour. One possible reason is that the dominant mechanism of particle capture varies with the particle-size distribution. In theory, if particles are larger than pores on average, then blocking is more prevalent than deposition, while if the opposite is true, then deposition is the more prominent capture mechanism, until pores become sufficiently clogged that blocking takes over.

In [107], Griffiths *et al.* suggest that the balance of blocking and deposition affects the behaviour of the flow rate as a function of the total volume of fluid processed.

As this volume increases, at first the flow rate decreases linearly, as pores are shrunk via deposition, but later it decreases super-linearly, as pores are removed completely via blocking. The transition from slower decrease to more rapid decrease occurs more quickly if particles are larger. The authors attribute this to the notion that more larger particles lead to pores blocking completely more often, so that a greater proportion of pores are no longer accessible for deposition sooner. This interplay between the two clogging mechanisms suggests that the relative sizes of particles and pores are important, and that the behaviour of solutions of models based on uni-modal size distributions may be misleading.

One early model that acknowledges the importance of the distribution of pore sizes is that of Kasottis *et al.* [108]. In this work, experiments determine the flux and retention of certain mono-dispersed suspensions in the presence of a poly-dispersed filter, and the authors derive a model to explain the results. The outcome is an equation for the number of pores present in the filter as a function of the flux and the retention of solid and spherical particles of a given size when the flow down an individual pore is governed by the Hagen–Poiseuille law (theoretically justified by Stokes in [109]). The immediate utility of the equation is to estimate the number of pores in the filter when the flux and retention are experimentally known. One could equally see the equation as a means of deducing the flow rate given a known initial pore distribution, since the number of pores appears as an integral over the pore-size distribution. Indeed, the authors go on to predict the proportions of particles that will be retained given particular pore distributions, assuming that retention is a result of 'geometric considerations only' (akin to blocking in our setup). That is, particles that are too large to fit through pores are always captured, but particles that are small enough to fit through pores are never retained (so that deposition does not occur), which is one limitation of the work.

Early models noting that attention should be paid to the entire distribution of particle sizes (as opposed to the mean or maximum) include that of Alon and Adin [110]. The model builds on an earlier one [111] by O'Melia and Ali, which itself builds on the seminal model developed by Kozeny, [112], and by Carman, [113, 114]. The result of Kozeny and Carman's original models is a proportionality law between the pressure drop across the filter and the flow rate, via the porosity of the filter and other intrinsic properties of the filter and fluid. In [111], O'Melia and Ali extended this model by accounting for particle size by adapting the equation to incorporate the mean diameter of the suspended particles. Alon and Adin's contribution was to suggest a rule for how the number of particles that have been retained depends on their size. The authors compared different models for retention as a function of size, and showed that a power law fitted their experimental data most accurately. They concluded that their size-dependent model produced better data fits than simply using the mean particle size, as in O'Melia and Ali's model, for example.

More recently, due to increasing computational resources, some attention has been paid to Lagrangian approaches to account for size, where particles and pores are tracked individually. One such work is that of Marrufo-Hernandez *et al.*, [72]. Here, the filter is modelled as a box containing a finite number of flat planes, stacked in parallel, which are permeated by circular holes, similarly to in [115]. This setting

is markedly different from more conventional models in which the filter is seen as a set of quenched spheres, for example, as in [116–118]. In Marrufo-Hernandez *et al.* [72], particles move subject to Brownian motion accompanied by a constant driving force, and collide with other particles and with pores, due to laws of motion on the microscale. The authors' presentation of the distributions of particle and pore sizes as functions of time and space mean that they are able to make detailed conclusions about the filtration process, such as the size structure of the filtrate, and the quantity of pores of a given size that remain in the filter at a given time. One limitation of the model is that the 'stacking' of a finite number of planes poses difficult modelling questions, such as how to choose the number of planes correctly, since the filters with which we are concerned do not really contain these planes. More fundamentally, although Lagrangian perspectives such as this offer a comprehensive description of filter behaviour, they are often limited by their significant computational expense. Marrufo-Hernandez *et al.* note that their simulations are based on the results obtained by using a batch of 500 particles, which is at least two orders of magnitude fewer than the number of particles in a typical filtration process.

In summary, the sizes of particles and pores are important in determining the key characteristics of filtration processes experimentally. Despite this, existing continuum models of filtration capture the large-scale observables of interest but do not fully account for poly-dispersed feeds and filters, and the simultaneous clogging mechanisms that occur due to the relationships between the particle- and pore-size distributions. On the other hand, some existing discrete models account for poly-dispersity more completely, but are usually computationally expensive. Therefore, a new, computationally tractable, modelling framework is needed, in which the poly-dispersity of particles and pores, and the associated clogging mechanisms, are accounted for.

2.3 A novel size-structured model for filtration

One candidate framework for describing the evolution of the size distributions of particles and pores is so-called 'age-structured' equations, which are common in population and disease models (see the book by Brauer *et al.*, [119], for an introduction to these). In simple population models, all members of the population are assumed to be interchangeable, and, in particular, behave independently of their age. However, in almost all physical populations, age is one of the most important defining characteristics, since different age groups often display different reproduction numbers and survival capacities [119]. The seminal work is that of McKendrick [120], who was the first to propose an 'age-structured' framework to account for populations' age dependency in mathematical models. Here, the key quantity is the density of individuals that are between the ages a and $a + \delta a$ (where δa is infinitesimally small), $\rho(t, a)$ say. Assuming that changes to this population density occur due to birth, growth, and death, assigning rates to these phenomena, and subsequently appealing to the conservation of the total number of individuals, one can derive continuous differential equations that describe the evolution of the population density, ρ. One such example is the McKendrick–von Foerster equation, which is a first-order linear

partial differential equation for the time- and age-dependent population density that was proposed by McKendrick and used by von Foerster to describe cell cycles [121]. In equations such as this, age and time are considered independently, and age is essentially treated as a space-like variable. One advantage of this approach is that the plethora of solution methods used for time and space dependent partial differential equations, such as asymptotic analysis, the method of characteristics, and various numerical schemes, are all applicable to find $\rho(t, a)$. Once this solution is obtained, secondary quantities of interest can be derived directly from it. For example, the total number of individuals in the population at time t is given by $P(t) = \int_0^\infty \rho(t, a)\,\mathrm{d}a$.

To derive a size-structured model for filtration, we will proceed by likening the variable 'size' in filtration processes to 'age' in population models. That is, we will treat size as a space-like variable, and seek distributions of particles and pores that depend on it.

Indeed, in Chapter 3, in Section 3.1 we will begin by assuming that any filter control volume contains a plane like the ones in [72], and propose that it consists of a continuous distribution of particles and pores of any size in the limit where the control volume is infinitesimally small. Assuming that these distributions are known, we will use them to derive secondary variables of interest, such as the particle and pore concentrations, and the local porosity and permeability of the filter. In analogy with the assumption of population conservation in McKendrick's framework, we will assume that fluid mass, particles, and pores are conserved, as well as a Hagen–Poiseuille law to link the velocity and pressure, and arrive at a system of partial integro–differential equations that describe the evolution of the particle and pore distributions, as well as the flow rate and local pressure. We will close this system by proposing initial and boundary conditions that model mono-dispersed, or log-normally-dispersed, particles and pores in industrial operational regimes, before, in Section 3.2, nondimensionalising to prepare the system for analysis and solution.

In Chapter 4, we will solve the dimensionless model under various assumptions. In Section 4.1, we will assume that particles and pores are both mono-dispersed, and explore the cases where particles are larger and smaller than pores. We will use these relatively simple scenarios to explore the dependence of the model on the various dimensionless parameter groups. In particular, we will examine the cases where particles are much smaller than the filter depth, and where the concentration of particles in the feed is very small relative to the concentration of pores in the filter. One advantage of our setup is that it allows us to circumvent awkward problems that appear in discrete models, such as choosing the 'correct number of planes' in [72], by instead choosing dimensionless parameters that are, perhaps, more physically motivated. In Section 4.2, we will increase the complexity of the problem by supposing that mono-dispersed particles are fed through pores that are log-normally-dispersed. We will first assume that the probability of deposition is zero, so that only blocking can occur. We will then explore the case where blocking and deposition occur simultaneously.

In Chapter 5, we will conclude by summarising and discussing potential avenues for future work.

Chapter 3

Derivation of the size-structured model

In this chapter, we develop a model for filtration in which particle and pore sizes are treated as independent variables. We begin by deriving a dimensional system of differential equations for the distributions of these sizes, pose industrially relevant boundary and initial conditions, and then scale the problem to arrive at a dimensionless system to be analysed and solved. Our focus is on building a model that demonstrates the utility of this size-structured framework for modelling filtration. Therefore, emphasis is placed on simplicity, to make solutions as intuitive as possible. For example, we suppose that the flow is driven only by advection (i.e., we do not consider diffusion, dispersion, or any other transport mechanisms), and that the solution depends only on depth (i.e., we ignore possible dependence on spatial variables transverse to the depth direction).

3.1 Dimensional model

We suppose that the filter membrane (see Figure 3.1 (Top-Left)) consists of a slab (see Figure 3.1 (Bottom-Left)) of solid material (see the grey areas) containing tunnels of pore space (see the white areas). This is located between $z = 0$, which we call the inlet, and $z = l$, which we call the outlet. We assume that a horizontal cross-section at a given depth (see the red line in Figure 3.1 (Top-Right)) contains solid material (see the solid parts of the line) perforated by circular pores (see the dashed parts of the red line in Figure 3.1 (Top-Right)), so that, if we look from above (see Figure 3.1 (Bottom-Right)) then we see a sheet of solid material containing circular pores with a distribution of sizes (i.e., radii).

Fluid, which contains solid spherical particles with various sizes (i.e., radii), is driven into the filter at the inlet. The particle-laden fluid flows through pores, which capture some of the particles (see Figure 3.2), causing pores to clog, decreasing their size. Fluid, containing any particles that have not been captured, exits the filter at the outlet.

In the next subsection, we define objects to model the pores in the filter and the

particles in the fluid.

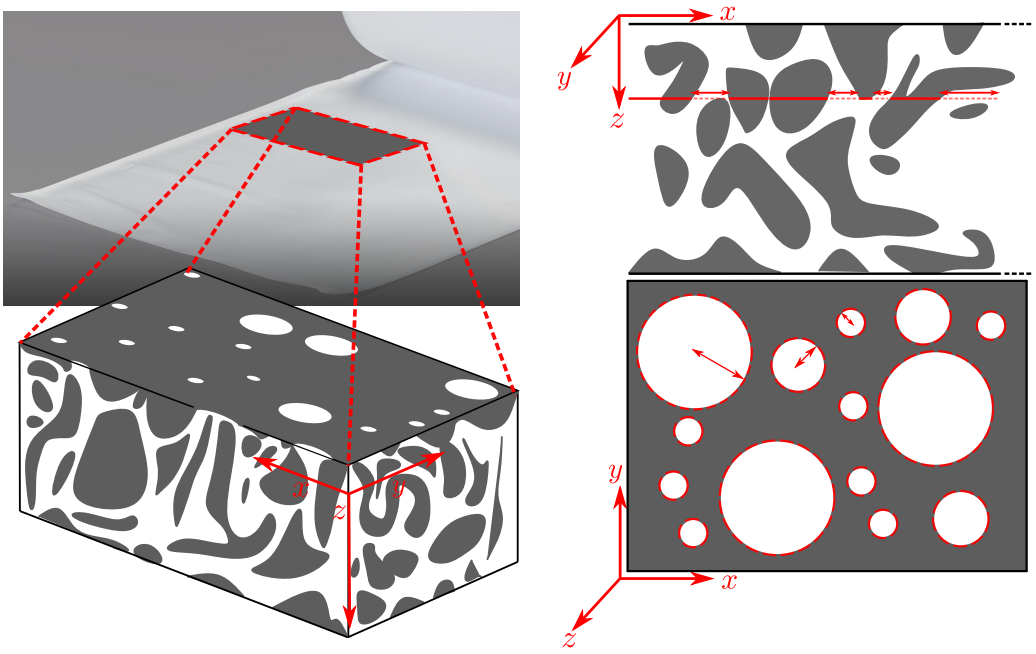

Figure 3.1: (Top–Left) Photograph of an ePTFE membrane on the macroscale. The membrane is much thinner than it is wide and long. (Bottom–Left) Diagram of an idealised membrane on the microscale. The membrane consists of solid space (grey) punctured by tunnels of pore space (white). (Top–Right) Side-view of the idealised membrane. Any depth (e.g., solid red line) consists of pores (dashed red lines) with a distribution of sizes (red arrows). (Bottom–Right) Top-view of the idealised membrane. Pores vary in radius but are circular, so that, from the top, we see circular pores with a distribution of radii (red arrows).

3.1.1 Particles and pores

We assume that the membrane is sufficiently homogeneous in the directions transverse to the depth (i.e., x and y, see Figure 3.1) that the solution does not depend on x or y. We define $\bar{r}(z)$ to be the mean pore-size in the cross-section in the control volume $z + \delta z$ located at z, and $\bar{r}^* = \bar{r}(l)$ to be the mean pore-size at the outlet. We introduce the pore-size distribution, $n(z, t, r)$, which is measured in number/m^3 so that $[n] = \mathrm{m}^{-3}$, where we will use $[x]$ to mean 'dimensions of x'. The distribution $n(z, t, r)\delta r$ is the number of pores with size in the range $(r, r + \delta r)$ per unit cross-sectional area at depth z and time t. It follows that the pore concentration, N, which is the number of pores of all sizes per unit filter area at depth z and time t is given by

$$N(z, t) = \int_0^\infty n(z, t, r)\,\mathrm{d}r, \tag{3.1}$$

which is measured in number/m^2, so that $[N] = \mathrm{m}^{-2}$.

We relate the local porosity, $\phi(z,t)$, which we define to be the fraction of the total cross-sectional area at z that is pore-space (which is dimensionless), to n using

$$\phi(z,t) = \int_0^\infty \pi r^2 n(z,t,r)\,\mathrm{d}r. \tag{3.2}$$

We define $\bar{a}^*$ to be the mean particle-size in the feed fluid. We introduce the particle-size distribution, $c(z,t,a)$, measured in number/m^4 with units $[c] = \mathrm{m}^{-4}$, such that $c(z,t,a)\delta a$ is the number of particles with size in the range $(a, a+\delta a)$ per unit filter volume at depth z and time t. Thus, the *filter* particle concentration, C, which is the number of particles of all sizes in the fluid *per unit filter volume* (i.e., pore space and solid space) at depth z and time t is

$$C(z,t) = \int_0^\infty c(z,t,a)\,\mathrm{d}a, \tag{3.3}$$

which is measured in number/m^3 so that $[C] = \mathrm{m}^{-3}$.

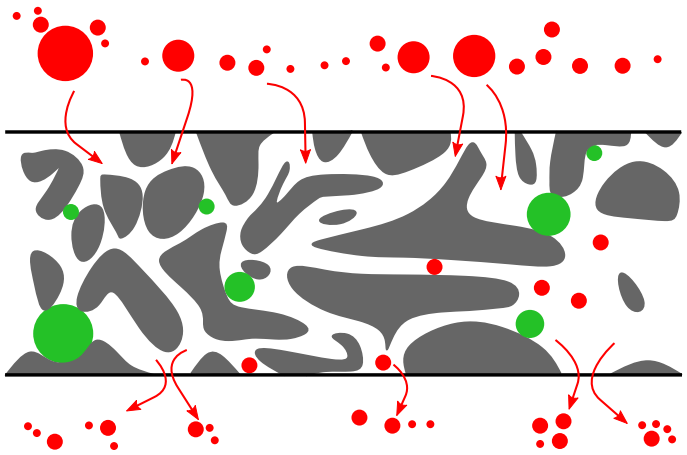

Figure 3.2: Diagram of a side-view of the filter as particle-laden fluid moves through it. Particle laden fluid enters the filter at the inlet. Some particles (green) adhere to pore walls, decreasing the sizes of the pores. Other particles (red) do not adhere to pore walls, and exit the filter at the outlet.

Lastly, we define the *void* particle concentration, C_V with $[C_\mathrm{V}] = \mathrm{m}^{-3}$, to be the number of particles of all sizes in the fluid *per unit void volume* (i.e., pore space and not solid space) at depth z and time t. Since the porosity, ϕ, represents the ratio of void volume to filter volume, we relate the void particle concentration to the filter particle concentration using

$$C_\mathrm{V}(z,t) = \frac{C(z,t)}{\phi(z,t)}. \tag{3.4}$$

Hence the void particle concentration, C_V, depends only on the filter particle concentration, C, and the porosity, ϕ. Therefore, in what follows, we will focus on writing

equations that describe the evolution of c and n, use these to determine C, N, and ϕ, and then infer C_{V} from C and ϕ. Note that we will usually refer to the filter particle concentration as the particle concentration (dropping the word filter). We will always refer to the void particle concentration in full. In the next subsection, we assume that fluid mass is conserved in order to derive equations that govern the pressure and velocity.

3.1.2 Conservation of fluid mass and Darcy's law

For simplicity, we assume that fluid is transported due to advection (and not, for example, diffusion). Therefore, to derive the equations that govern the fluid flow through the filter, we first consider a pore of size r and define $q(z,t,r)$ to be the volume of fluid passing through the pore per unit time, so that $[q] = \mathrm{m}^3\mathrm{s}^{-1}$. We assume that, at a given depth, the pores act like tubes connected in parallel and thus we relate this flux, q, to the fluid pressure, $p(z,t)$, using the Hagen–Poiseuille law [109],

$$q(z,t,r) = -\frac{\pi r^4}{8\mu}\frac{\partial p(z,t)}{\partial z}, \tag{3.5}$$

where μ is the dynamic viscosity of the fluid, with $[\mu] = \mathrm{Pa\,s}$.

The volumetric flow rate per unit cross-sectional area through *all* the pores of size r in the cross-section at depth z is $q(z,t,r)n(z,t,r)\delta r$. Therefore, multiplying (3.5) by the pore-size distribution $n(z,t,r)$ and integrating over r, we obtain the Darcy equation for the fluid velocity, $u(z,t) = \int_0^\infty qn\,\mathrm{d}r$, that is,

$$u(z,t) = -\frac{K(z,t)}{\mu}\frac{\partial p(z,t)}{\partial z}. \tag{3.6}$$

Here, $K(z,t)$ is the local permeability of the filter, given by

$$K(z,t) = \int_0^\infty \frac{\pi r^4}{8} n(z,t,r)\,\mathrm{d}r, \tag{3.7}$$

so that $[K] = \mathrm{m}^2$. This is a measure of the conductivity of the filter at depth z at time t.

We assume that the fluid is incompressible. As a consequence, in our one-dimensional setting, conservation of fluid mass implies that

$$u = U(t). \tag{3.8}$$

Substituting (3.8) into (3.6), and integrating with respect to the depth over the interval z to l, we find that (3.6) becomes

$$p(z,t) = p_{\mathrm{out}} + \mu U(t)\int_z^l \frac{1}{K(\zeta,t)}\,\mathrm{d}\zeta, \tag{3.9}$$

where $p_{\mathrm{out}} = p(l)$ is assumed to be a known constant outlet pressure. There are two industrially relevant regimes for the filter:

- the constant flow rate regime, in which U_c is a known constant, and (3.8) and (3.9) become

$$U(t) = U_\mathrm{c}, \quad p(z,t) = p_\mathrm{out} + \mu U_\mathrm{c} \int_z^l \frac{1}{K(\zeta,t)}\,\mathrm{d}\zeta, \tag{3.10}$$

- the constant pressure drop regime, where $p(0,t) = p_\mathrm{in}$ is a known constant, and (3.8) and (3.9) become

$$U(t) = \frac{\Delta p}{\mu \int_0^l \frac{1}{K(z,t)}\,\mathrm{d}z}, \quad p(z,t) = p_\mathrm{out} + \Delta p \frac{\int_z^l \frac{1}{K(\zeta,t)}\,\mathrm{d}\zeta}{\int_0^l \frac{1}{K(\zeta,t)}\,\mathrm{d}\zeta}, \tag{3.11}$$

  where $\Delta p = p_\mathrm{in} - p_\mathrm{out}$ is the known pressure drop across the entire filter.

We relate U to the void velocity, U_V with $[U_\mathrm{V}] = \mathrm{m\,s^{-1}}$, which is the rate at which fluid flows through the pores, using

$$U(t) = \phi(z,t) U_\mathrm{V}(z,t). \tag{3.12}$$

3.1.3 Conservation of particles and pores

Next, we derive partial differential equations that govern the evolution of the particle- and pore-size distributions, c and n, by appealing to conservation of particles and pores as particle capture, and the associated pore clogging, occur.

3.1.3.1 Particles

In order to derive the equation describing the evolution of the particle-size distribution, we consider a small control volume in the filter and appeal to conservation of particles. We assume that the advective flux of particles entering and leaving the control volume depends on the void velocity U_V, and that the rate of capture of particles of size a (by all pores in the control volume) is given by $\mathcal{C}(z,t,a)$. Shrinking the control volume to zero, the resulting equation for $c(z,t,a)$ reads

$$\frac{\partial c}{\partial t} + U \frac{\partial}{\partial z}\left(\frac{c}{\phi}\right) = -\mathcal{C}, \tag{3.13}$$

where $[\mathcal{C}] = \mathrm{m^{-4}s^{-1}}$.

3.1.3.2 Pores

To derive the governing equation for the pore-size distribution, we consider a cross-section through a control volume and assume that the number of pores of size r decreases when they become clogged, with rate $\mathcal{N}^-(z,t,r)$, and increases when larger pores become clogged and produce pores of size r, with rate $\mathcal{N}^+(z,t,r)$. Thus, we write

$$\frac{\partial n}{\partial t} = -\mathcal{N}^- + \mathcal{N}^+, \tag{3.14}$$

where $[\mathcal{N}^-], [\mathcal{N}^+] = \mathrm{m}^{-3}\mathrm{s}^{-1}$.

It remains to formulate relationships between the capture and clogging functions, $\mathcal{C}$, $\mathcal{N}^-$, and $\mathcal{N}^+$, and the variables U, ϕ, c, and n.

3.1.3.3 Particle capture and pore clogging

We focus our attention on the clogging mechanisms of blocking and deposition (see Figure 3.3), as defined in Chapter 2, and neglect partial surface blocking and caking. We treat the contribution of these two mechanisms separately, then combine them together to determine $\mathcal{C}$, $\mathcal{N}^-$, and $\mathcal{N}^+$.

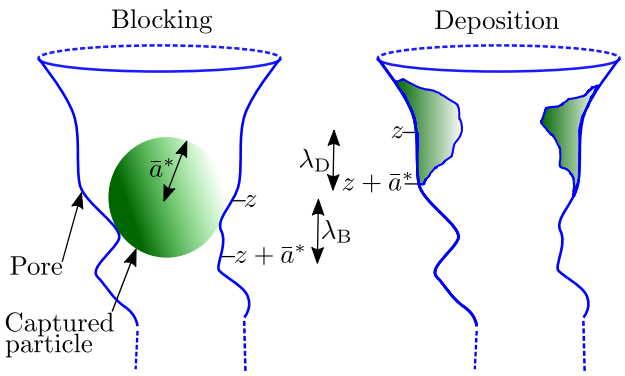

Figure 3.3: Diagram to illustrate blocking and deposition. The blocking and deposition lengths, λ_B and λ_D, are labelled.

We assume that particles are transported into pores by the *local* fluid flow. Thus, we assume that the local speed down pores of size r, $v(z,t,r)$ say, with units $[v] = \mathrm{s}^{-1}$, is proportional to the void velocity in these pores by the proportion of the local void area occupied by pores of size r, so that

$$v(z,t,r) = U_\mathrm{V}(z,t)\left(\frac{\pi r^2 n(z,t,r)}{\int_0^\infty \pi r^2 n(z,t,r)\,\mathrm{d}r}\right). \tag{3.15}$$

Rewriting (3.15) in terms of the Darcy velocity and the local porosity by recalling (3.2) and (3.12), it follows that the local-speed distribution is given by

$$v(z,t,r) = \frac{U(t)\pi r^2 n(z,t,r)}{\left(\phi(z,t)\right)^2}. \tag{3.16}$$

Blocking

We recall that pores become blocked when particles that are *larger* than pores are carried into the entrances of the pores by the local fluid flow.

When particles of size a block pores of size $r \leq a$, the number of pores of size r is reduced. This is accompanied by a corresponding reduction in the number of

particles of size a. We thus define

$$\mathcal{N}_{\mathrm{B}}^{-}(z,t,r) = v(z,t,r)\int_{r}^{\infty} c(z,t,a)\,\mathrm{d}a, \tag{3.17}$$

and

$$\mathcal{C}_{\mathrm{B}}(z,t,a) = \frac{1}{\lambda_{\mathrm{B}}}c(z,t,a)\int_{0}^{a} v(z,t,r)\,\mathrm{d}r, \tag{3.18}$$

where the subscript B indicates blocking. Here, λ_{B} (with $[\lambda_{\mathrm{B}}] = \mathrm{m}$) is the distance over which blocking occurs, which we assume to be $\mathcal{O}(\bar{a}^*)$ and call the blocking length (see Figure 3.3).

Deposition

We recall that deposition occurs when particles that are *smaller* than pores are carried into pores by the local fluid-flow and become captured.

We define ς_{D} to be the adherence, which is the probability of capture once a particle enters a pore, where the subscript D indicates deposition. In general, this might depend on time (e.g., since the probability of adhering to a 'clean' pore wall is likely to be different from the probability of adhering to a pore wall that already contains deposited particles), position (e.g., since the filter may be manufactured for larger adhesivity at some depths than others), and the sizes of the particle and pore (e.g., since a larger particle is more likely to move closer to a pore wall and thus more likely to stick), as well as any other variables or parameters of the system, or else an equation describing additional physical or chemical relationships between the particle and pore materials. To demonstrate a simple case, we assume that the adherence depends only on the size of the particle and pore, so that $\varsigma_{\mathrm{D}} = \varsigma_{\mathrm{D}}(a,r)$. Note that the adherence is dimensionless, and satisfies $0 \leq \varsigma_{\mathrm{D}} \leq 1$.

When particles of size a deposit in pores of size $r > a$, the number of pores of size r is reduced, and this is accompanied by a corresponding reduction in the number of particles of size a. We therefore define

$$\mathcal{N}_{\mathrm{D}}^{-}(z,t,r) = v(z,t,r)\int_{0}^{r} c(z,t,a)\varsigma_{\mathrm{D}}(a,r)\,\mathrm{d}a, \tag{3.19}$$

and

$$\mathcal{C}_{\mathrm{D}}(z,t,a) = \frac{1}{\lambda_{\mathrm{D}}}c(z,t,a)\int_{a}^{\infty} v(z,t,r)\varsigma_{\mathrm{D}}(a,r)\,\mathrm{d}r. \tag{3.20}$$

Here, λ_{D}, with $[\lambda_{\mathrm{D}}] = \mathrm{m}$, is a measure of the distance over which a particle is removed by sticking to the pore wall, which we assume to be $\mathcal{O}(\bar{a}^*)$ and call the deposition length (see Figure 3.3).

We suppose that deposition results in the transformation of pores of their original size to pores of a new size. We define τ_{D} to be the transformation, which is the probability that deposition of particles of size a in pores of size $r > a$ results in

pores of size $\rho < r$. Much like the adherence, in general this might depend on time, position, and the relative sizes of the particle and pore, or may be given by an equation that describes the physics and chemistry of the deposition mechanism. Again, for simplicity, we assume that this depends only on the sizes of the particle, the pore that the particle enters, and the pore that results from the deposition, so that $\tau_{\mathrm{D}}(a, r, \rho)$. Note that this is a probability density function over ρ for any a, r, so that $[\tau_{\mathrm{D}}] = \mathrm{m}^{-1}$, and it must be chosen to satisfy

$$\int_0^\infty \tau_{\mathrm{D}}(a, r, \rho)\,\mathrm{d}\rho = 1. \tag{3.21}$$

Thus, to account for the production of pores of size r due to deposition, we write

$$\mathcal{N}_{\mathrm{D}}^{+}(z, t, r) = \int_0^\infty v(z, t, \rho) \int_0^\rho c(z, t, a)\varsigma_{\mathrm{D}}(a, \rho)\tau_{\mathrm{D}}(a, \rho, r)\,\mathrm{d}a\,\mathrm{d}\rho. \tag{3.22}$$

Note that we have swapped r and ρ in τ_{D} (and v) since we are interested in the production of pores of size r from pores of size $\rho > r$ in (3.22).

To combine the effects of blocking and deposition, we write

$$\mathcal{C} = \mathcal{C}_{\mathrm{B}} + \mathcal{C}_{\mathrm{D}}, \quad \mathcal{N}^{+} = \mathcal{N}_{\mathrm{D}}^{+}, \quad \mathcal{N}^{-} = \mathcal{N}_{\mathrm{B}}^{-} + \mathcal{N}_{\mathrm{D}}^{-}. \tag{3.23}$$

3.1.4 Boundary and initial conditions

We assume that the concentration of particles in the feed, C_{in}^{*}, is known, and so we write

$$c(0, t, a) = C_{\mathrm{in}}^{*}\phi(0, t)d_c(a), \tag{3.24}$$

where ϕ accounts for the fact that all particles in the feed fluid enter void space when they enter the filter. Here, $d_c(a)$ is the distribution of particle sizes in the feed, which is normalised over a so that

$$\int_0^\infty d_c(a)\,\mathrm{d}a = 1. \tag{3.25}$$

Initially, we suppose that there are no particles in the filter, and that the pore distribution is given, but that it is not necessarily constant across the filter. Thus, we write

$$c(z, 0, a) = 0, \quad n(z, 0, r) = N_{\mathrm{init}}(z)d_n(z, r), \tag{3.26a,b}$$

where $N_{\mathrm{init}}(z)$ is the concentration of pores at depth z initially, and $d_n(z, r)$ is the distribution of their sizes, which is normalised over the pore size r so that

$$\int_0^\infty d_n(z, r)\,\mathrm{d}r = 1. \tag{3.27}$$

Experimentally, it is challenging to quantify $N_{\mathrm{init}}(z)$ directly, since characterisation of the internal filter structure requires filter destruction. Instead, we typically know the initial porosity of a cross-section, $\phi_{\mathrm{init}}(z)$, and infer $N_{\mathrm{init}}(z)$ using (3.2), so that

$$N_{\mathrm{init}}(z) = \frac{\phi_{\mathrm{init}}(z)}{\int_0^\infty \pi r^2 d_n(z, r)\,\mathrm{d}r}. \tag{3.28}$$

3.1.5 Operational regimes

It remains to specify the forms of the functions ϕ_{init}, d_c, d_n, ς_{D}, and τ_{D}, which depend on the industrial application of the filter. Here, we specify forms for these functions that represent operational regimes. We use these to demonstrate the solution of the model in the following chapter.

To simplify our analysis, we focus on cases in which the local porosity does not vary across the filter initially, so that

$$\phi_{\text{init}}(z) = \phi^*_{\text{init}}. \tag{3.29}$$

We assume that particles at the inlet are either mono-dispersed, of size $\bar{a}^*$, or log-normally dispersed, with mean size $\bar{a}^*$. It follows that either,

$$d_c(a) = \delta(a - \bar{a}^*), \quad \text{or,} \quad d_c(a) = \frac{1}{\sqrt{2\pi}\sigma_c a} e^{-\frac{\left(\log\left(\frac{a}{\bar{a}^*}\right) + \frac{\sigma_c^2}{2}\right)^2}{2\sigma_c^2}}, \tag{3.30a,b}$$

where σ_c is the dimensionless standard deviation of the normal distribution associated with (3.30b). We note that (3.30a) and (3.30b) both satisfy the constraint (3.25).

Similarly, we assume that, initially, pores in the filter are either mono-dispersed, and of size $\bar{r}^*$, or log-normally dispersed, with mean size $\bar{r}^*$, independently of depth, so that either

$$d_n(r) = \delta(r - \bar{r}^*), \quad \text{or} \quad d_n(r) = \frac{1}{\sqrt{2\pi}\sigma_n r} e^{-\frac{\left(\log\left(\frac{r}{\bar{r}^*}\right) + \frac{\sigma_n^2}{2}\right)^2}{2\sigma_n^2}}. \tag{3.31a,b}$$

Here σ_n is the dimensionless standard deviation of the normal distribution associated with (3.31b), and we note that (3.30a) and (3.30b) satisfy the constraint (3.27).

Furthermore, we assume that the probability that particles of size a are captured in pores of size $r > a$ is the same regardless of these sizes. As a result, the adherence is constant, so that

$$\varsigma_{\text{D}}(a, r) = \varsigma_{\text{D}}. \tag{3.32}$$

Lastly, we suppose that when particles of size a are captured in pores of size $\rho > a$, the resulting pore is always size $r = \rho - a$, so that

$$\tau_{\text{D}}(a, \rho, r) = \delta(r - (\rho - a)), \tag{3.33}$$

which satisfies (3.21). Note that, even the simplification that $\tau_{\text{D}} = \tau_{\text{D}}(a, r, \rho)$ allows for a huge number of possible forms for τ_{D}. Our choice in (3.33) corresponds to the simple case where deposition of a particle of size a in a pore of size ρ *always* results in a pore of size $r = \rho - a$. We might instead consider, for example, the case where $\mu_{\text{D}} = \rho - a$ is the mean resulting pore size and resulting pore sizes are distributed normally about this, so that $\tau(a, \rho, r)_{\text{D}} \sim \exp((\mu - r)/\sqrt{2}\sigma_{\text{D}})^2$. The standard deviation here, σ_{D}, may model, for example, the extent to which soft particles are deformed when deposition occurs, and the resulting variance in the possible resulting pore size. Any probability distribution (over ρ) is permitted, allowing for models that account, for example, for the 'spreading' of particle mass when deposition occurs.

3.1.6 Summary of the dimensional model

In summary, substituting the specific forms of the blocking and deposition functions, (3.17)–(3.22), into the clogging functions (3.23), and using these with the local speed distribution (3.16) in the particle and pore equations, (3.13)–(3.14), the equations that govern the size distributions of particles and pores read

$$\frac{\partial c}{\partial t} + U\frac{\partial}{\partial z}\left(\frac{c}{\phi}\right) = -\frac{\pi U}{\phi^2}c\left(\frac{1}{\lambda_{\mathrm{B}}}\int_0^a r^2 n\,\mathrm{d}r + \frac{1}{\lambda_{\mathrm{D}}}\int_a^\infty \varsigma_{\mathrm{D}} r^2 n\,\mathrm{d}r\right), \tag{3.34}$$

$$\begin{aligned}\frac{\partial n}{\partial t} = -\frac{\pi U}{\phi^2}\Bigg(& r^2 n\left(\int_r^\infty c\,\mathrm{d}a + \int_0^r \varsigma_{\mathrm{D}} c\,\mathrm{d}a\right) \\ &- \int_0^\infty \rho^2 n(z,t,\rho)\int_0^\rho \varsigma_{\mathrm{D}} c\tau_{\mathrm{D}}(a,\rho,r)\,\mathrm{d}a\,\mathrm{d}\rho\Bigg).\end{aligned} \tag{3.35}$$

Depending on the filtration regime, either

$$U(t) = U_{\mathrm{c}}, \quad p(z,t) = p_{\mathrm{out}} + \mu U_{\mathrm{c}}\int_z^l \frac{1}{K(\zeta,t)}\,\mathrm{d}\zeta, \tag{3.36}$$

or

$$U(t) = \frac{\Delta p}{\mu\int_0^l \frac{1}{K(z,t)}\,\mathrm{d}z}, \quad p(z,t) = p_{\mathrm{out}} + \Delta p\frac{\int_z^l \frac{1}{K(\zeta,t)}\,\mathrm{d}\zeta}{\int_0^l \frac{1}{K(\zeta,t)}\,\mathrm{d}\zeta}, \tag{3.37}$$

are the equations for the flow rate and the pressure, where

$$\phi(z,t) = \int_0^\infty \pi r^2 n(z,t,r)\,\mathrm{d}r, \quad K(z,t) = \int_0^\infty \frac{\pi r^4}{8} n(z,t,r)\,\mathrm{d}r \tag{3.38}$$

define the local porosity and permeability, respectively. The boundary condition at the inlet at the top of the filter is

$$c(0,t,a) = C_{\mathrm{in}}^* \phi(0,t) d_c(a), \tag{3.39}$$

and the initial conditions are

$$c(z,0,a) = 0, \quad n(z,0,r) = \frac{\phi_{\mathrm{init}}(z) d_n(z,r)}{\int_0^\infty \pi s^2 d_n(z,s)\,\mathrm{d}s}. \tag{3.40}$$

The equations (3.34)–(3.40) form a closed system for the six solution variables c, n, U, p, ϕ, K, subject to the specification of the five functions ϕ_{init}, d_c, d_n, ς_{D}, and τ_{D}, which depend on the choice of operational regime, and any numbers that parametrise these, for example the five parameters $\bar{r}^*, \bar{a}^*$, σ_c, σ_n, and ϕ_{init}, when these functions are chosen as in (3.30)–(3.33). The six parameters C_{in}^*, λ_{B}, λ_{D}, μ, l, and p_{out}, must also be specified, as well as either U_{c} or p_{in}, depending on whether a constant flow rate or pressure drop is applied in the filter.

3.2 Dimensionless model

Next, in this section, we nondimensionalise the size-structured model (3.34)–(3.40), summarise the resulting dimensionless system, and discuss the associated dimensionless parameter groups.

3.2.1 Nondimensionalisation

We begin by defining U^* to be the characteristic Darcy velocity (flux per unit cross-sectional area) of the fluid, and Δp^* to be the characteristic deviation of the pressure from the known pressure at the outlet, p_{out}. These depend on the operating regime:

- In the constant flow rate regime, we have

$$U^* = U_{\text{c}}, \quad \Delta p^* = \frac{8\mu U_{\text{c}} l}{\bar{r}^{*2}}; \tag{3.41}$$

- In the constant pressure drop regime, we have

$$U^* = \frac{\Delta p \bar{r}^{*2}}{\mu l}, \quad \Delta p^* = \Delta p. \tag{3.42}$$

Given these values, we nondimensionalise (3.34)–(3.40) using

$$z = l\tilde{z}, \quad a = \bar{r}^*\tilde{a}, \quad r = \bar{r}^*\tilde{r}, \quad U = U^*\tilde{U}, \quad p = p_{\text{out}} + \Delta p^*\tilde{p}, \quad t = \frac{l}{U^*}\tilde{t}, \tag{3.43}$$

$$n = \frac{1}{\pi\bar{r}^{*3}}\tilde{n}, \;\; c = \frac{C^*_{\text{in}}}{\bar{r}^*}\tilde{c}, \;\; d_n = \frac{1}{\bar{r}^*}\tilde{d}_n, \;\; d_c = \frac{1}{\bar{r}^*}\tilde{d}_c, \;\; \tau_{\text{D}} = \frac{1}{\bar{r}^*}\tilde{\tau}_{\text{D}}, \;\; K = \frac{\bar{r}^{*2}}{8}\tilde{K}, \tag{3.44}$$

where variables with tildes are dimensionless.

In (3.43) we see that the spatial variable is scaled so that the filter has unit length. The particle and pore sizes are scaled so that a pore of mean radius has unit size, and the particle size is measured relative to this. The timescale,

$$t^* = \frac{l}{U^*} \tag{3.45}$$

is the time that it takes for fluid to move through the filter.

In (3.44), we scale the pore-size distribution, n, and d_n, so that the initial distribution, defined in (3.40), is a probability density function that integrates to one. Similarly, we scale the particle-size distributions, c and d_c, so that the distribution at the inlet integrates to one, and for unit particle concentration in void space at the inlet. Furthermore, the transformation distribution, τ_{D}, is scaled so that it remains a probability density function that integrates to one, and we scale the local permeability K to balance terms in (3.38).

3.2.2 Summary of the dimensionless model

In dimensionless variables, dropping tildes, the size-structured model, (3.34)–(3.40), becomes

$$\frac{\partial c}{\partial t} + U\frac{\partial}{\partial z}\left(\frac{c}{\phi}\right) = -\frac{U}{\phi^2}c\left(\Lambda_{\mathrm{B}}\int_0^a r^2 n\,\mathrm{d}r + \Lambda_{\mathrm{D}}\int_a^\infty \varsigma_{\mathrm{D}} r^2 n\,\mathrm{d}r\right), \tag{3.46}$$

$$\begin{aligned}\frac{\partial n}{\partial t} = -\Gamma\frac{U}{\phi^2}\Bigg(& r^2 n\left(\int_r^\infty c\,\mathrm{d}a + \int_0^r \varsigma_{\mathrm{D}} c\,\mathrm{d}a\right) \\ &- \int_0^\infty \rho^2 n(z,t,\rho)\int_0^\rho \varsigma_{\mathrm{D}} c\tau_{\mathrm{D}}(a,\rho,r)\,\mathrm{d}a\,\mathrm{d}\rho\Bigg),\end{aligned} \tag{3.47}$$

where, either

$$U(t) = 1, \quad p(z,t) = \int_z^1 \frac{1}{K(\zeta,t)}\,\mathrm{d}\zeta, \tag{3.48}$$

or

$$U(t) = \frac{1}{\int_0^1 \frac{1}{K(z,t)}\,\mathrm{d}z}, \quad p(z,t) = \frac{\int_z^1 \frac{1}{K(\zeta,t)}\,\mathrm{d}\zeta}{\int_0^1 \frac{1}{K(\zeta,t)}\,\mathrm{d}\zeta}, \tag{3.49}$$

define the flow rate and the pressure, depending on the filtration regime, and the local porosity and permeability are given by

$$\phi(z,t) = \int_0^\infty r^2 n(z,t,r)\,\mathrm{d}r, \quad K(z,t) = \int_0^\infty r^4 n(z,t,r)\,\mathrm{d}r \tag{3.50}$$

respectively. The boundary condition at the inlet at the top of the filter is

$$c(0,t,a) = \phi(0,t)d_c(a), \tag{3.51}$$

and the initial conditions are

$$c(z,0,a) = 0, \quad n(z,0,r) = \frac{\phi_{\mathrm{init}}(z)d_n(z,r)}{\int_0^\infty s^2 d_n(z,s)\,\mathrm{d}s}. \tag{3.52a,b}$$

The dimensionless analogues of the functions that specify the operational regime, given in (3.29)–(3.33), are

$$d_c(a) = \delta(a-A), \quad \text{or} \quad d_c(a) = \frac{1}{\sqrt{2\pi}\sigma_c a}e^{-\frac{\left(\log\left(\frac{a}{A}\right)+\frac{\sigma_c^2}{2}\right)^2}{2\sigma_c^2}}, \tag{3.53a,b}$$

so that particles are either all size A or this is their mean size, and

$$d_n(r) = \delta(r-1), \quad \text{or} \quad d_n(r) = \frac{1}{\sqrt{2\pi}\sigma_n r}e^{-\frac{\left(\log(r)+\frac{\sigma_n^2}{2}\right)^2}{2\sigma_n^2}}, \tag{3.54a,b}$$

so that, similarly, pores are either all size 1 or this is their mean size. Also, we have

$$\phi_{\text{init}}(z) = \phi^*_{\text{init}}, \quad \varsigma_{\text{D}}(a, r) = \varsigma_{\text{D}}, \quad \tau_{\text{D}}(a, \rho, r) = \delta(r - (\rho - a)). \tag{3.55a,b,c}$$

The equations (3.46)–(3.52) form a closed system for the six dimensionless variables c, n, U, p, ϕ, K, subject to the specification of the operational regime via the five dimensionless functions d_c, d_n, ϕ_{init}, ς_{D}, τ_{D}. Equations (3.53)–(3.55) are the examples that we will use for these, which are parametrised by the four dimensionless numbers:

- the size ratio,

$$A = \frac{\bar{a}^*}{\bar{r}^*}, \tag{3.56}$$

  which is the particle size if they are mono-dispersed, as in (3.53a), or the mean particle-size if they are log-normally dispersed, as in (3.53b) (since $\exp(\mu + \sigma_c^2/2) = A$, where $\mu = \log(A) - \sigma_c^2/2$ is the mean of the normal distribution associated with the log-normal distribution (3.53b));

- the particle- and pore-size distribution widths, σ_c, σ_n. These are the standard deviations of the normal distributions associated with the log-normal distributions (3.53b) and (3.54b);

- the initial porosity, ϕ^*_{init}, which specifies the ratio of pore space to impermeable-material space in the filter at all depths initially.

The system is parametrised by three other dimensionless numbers that result from the specification of the dimensional parameters. These are:

- the blocking-length ratio,

$$\Lambda_{\text{B}} = \frac{l}{\lambda_{\text{B}}}, \tag{3.57}$$

  which is the ratio of the filter length to the blocking length;

- the deposition-length ratio,

$$\Lambda_{\text{D}} = \frac{l}{\lambda_{\text{D}}}, \tag{3.58}$$

  which is the ratio of the filter length to the deposition length;

- the concentration ratio,

$$\Gamma = \frac{C^*_{\text{in}} l/\bar{r}^*}{1/\pi \bar{r}^{*3}}, \tag{3.59}$$

  which is the ratio of the characteristic concentrations of particles and pores.

In practice, we suppose that there are at least as many pores as particles per unit area in filters, and that filters are much thicker than both the blocking and deposition lengths. Thus, we anticipate that $\Gamma \ll 1$ (or at most that $\Gamma = \mathcal{O}(1)$), and that $\Lambda_{\text{B}} \gg 1$ and $\Lambda_{\text{D}} \gg 1$.

Chapter 4

Solutions of the size-structured model

In this chapter, we explore solutions of the dimensionless size-structured model, (3.46)–(3.59), in various operational regimes. In Section 4.1, we briefly discuss our method of solution. Then, in Section 4.2, we consider the case where feed particle sizes are mono-dispersed, and pore sizes are mono-dispersed initially, and remain mono-dispersed or bi-dispersed for all time. In Section 4.3, we focus on the case where the particles are still of a single size, but the pore sizes are initially log-normally poly-dispersed.

4.1 Solution methodology

In general, the size-structured model, (3.46)–(3.59), is a hyperbolic system of partial integro–differential equations. At most, solution variables depend on the single spatial variable, z, the time variable, t, and the size variables, a and r, which behave much like additional spatial variables. The system is thus a four-dimensional problem. In the following sections, we will demonstrate that the system can be solved explicitly or asymptotically in various parameter regimes. For general parameter regimes, however, we must appeal to computational methods for solution.

We use the method of lines. That is, we use the method of finite differences to discretise the space and size variables, and then use an initial value problem solver (`SciPy.solve_ivp()` in `Python`) to solve the resulting system of ordinary differential equations (in the time variable). For simplicity, we use a first-order upwind scheme to discretise the spatial variable, and the trapezium rule to discretise the integrals in the size variables. We note that higher order schemes, such as Lax-Wendroff, are available, and would lead to faster solution convergence. In our chosen setup, we find that 500 spatial points, and 100 particle and pore size points are enough for convergence.

The advective term in the advection–reaction equation contains the ratio U/ϕ. As a result, the difference between discrete time points needed, δt say, depends on the desired final state of the solution. To see this, note that we must satisfy the CFL condition, and, therefore, we must ensure that δt is small enough to allow for U/ϕ to get large when ϕ becomes small near the inlet when the filter is almost

completely clogged (i.e., near the end of simulation). In practice, we find that $\delta t/\delta z < \phi(0,T)/\phi(0,0)$ is sufficient (since U decreases as a function of time), where δz is the difference between spatial points and T is the terminal time. For example, we simulate the case where the terminal inlet porosity is around 10% of the initial inlet porosity, $\phi(0,T) \approx 0.1\phi(0,0)$, and so $\delta t \approx 0.1\delta z$ is sufficient, and we choose 5000 temporal points (for 500 spatial points).

4.2 Mono-dispersed particles and mono-dispersed or bi-dispersed pores

In this section, we assume that the particles entering the filter at the inlet are all size A (which, from (3.53), is constant and not to be confused with the variable a), and the pores are all size 1 initially. If $A \geq 1$ then all particles are larger than all pores, and we expect blocking to occur when a particle enters a pore, while if $A < 1$ then all particles are smaller than pores, and we expect deposition to occur (with probability ς_{D}) when a particle enters a pore. We choose (3.53a) as the distribution of particle-sizes at the inlet, so that the boundary condition, (3.51), becomes

$$c(0,t,a) = \phi(0,t)\delta(a-A). \tag{4.1}$$

Further, we choose (3.54a) as the initial pore-size distribution, so that the initial conditions, (3.52), become

$$c(z,0,a) = 0, \quad n(z,0,r) = \phi^*_{\mathrm{init}}\delta(r-1). \tag{4.2a,b}$$

Thus we solve the system (3.46)–(3.59) subject to the boundary and initial conditions (4.1), (4.2). We consider first the case $A \geq 1$ (when only blocking, and not deposition, occurs), look for explicit asymptotic solutions in the cases $\Gamma \ll 1$ (i.e., where the particle concentration is much smaller than the pore concentration) and $\Lambda_{\mathrm{B}} \gg 1$ (i.e., where the filter length is much larger than the length over which blocking occurs), and compare these with a numerical solution. We then consider the case $A < 1$ in which blocking and deposition both occur, which gives rise to a second pore size, so that the pores become bi-dispersed.

4.2.1 Blocking and no deposition

We choose $A \geq 1$, since we first want to consider the simple case in which the pore sizes are mono-dispersed for all time. This choice allows us to pose the ansatz

$$c(z,t,a) = \delta(a-A)C(z,t), \quad n(z,t,r) = \delta(r-1)N(z,t). \tag{4.3}$$

Using this ansatz, (3.46) and (3.47) become

$$\frac{\partial C}{\partial t} + U\frac{\partial}{\partial z}\left(\frac{C}{N}\right) = -\Lambda_{\mathrm{B}}U\frac{C}{N}, \tag{4.4}$$

$$\frac{\partial N}{\partial t} = -\Gamma U\frac{C}{N}. \tag{4.5}$$

In the constant flow rate case it follows from (3.48) that the Darcy velocity and pressure are given by

$$U = 1, \quad p(z,t) = \int_z^1 \frac{1}{N(\zeta,t)}\,\mathrm{d}\zeta, \tag{4.6}$$

while in the constant pressure drop case it follows from (3.49) that these are given by

$$U(t) = \frac{1}{\int_0^1 \frac{1}{N(z,t)}\,\mathrm{d}z}, \quad p(z,t) = \frac{\int_z^1 \frac{1}{N(\zeta,t)}\,\mathrm{d}\zeta,}{\int_0^1 \frac{1}{N(\zeta,t)}\,\mathrm{d}\zeta}, \tag{4.7}$$

since, for mono-dispersed pores, the local porosity and permeability, given by (3.50), become

$$\phi(z,t) = N(z,t), \quad K(z,t) = N(z,t), \tag{4.8}$$

respectively. The boundary condition, (3.51), becomes

$$C(0,t) = N(0,t), \tag{4.9}$$

and the initial conditions, (3.52), become

$$C(z,0) = 0, \quad N(z,0) = 1. \tag{4.10}$$

In the following subsections we will consider solutions of this system (4.4)–(4.10).

4.2.1.1 The case $\Gamma \ll 1$ (with $\Gamma\Lambda_\mathrm{B} \ll 1$): A characteristic solution

In this subsection, we first suppose that the concentration of particles to be removed from the feed fluid is small compared to the concentration of pores in the filter, so that $\Gamma \ll 1$.

We seek a solution in the form of an asymptotic expansion in the small parameter, Γ, given by

$$C = C^{(0)} + \Gamma C^{(1)} + \mathcal{O}(\Gamma^2), \quad N = N^{(0)} + \Gamma N^{(1)} + \mathcal{O}(\Gamma^2). \tag{4.11}$$

Noting that

$$\frac{C}{N} = \frac{C^{(0)}}{N^{(0)}} + \Gamma\left(\frac{C^{(1)}}{N^{(0)}} - \frac{C^{(0)}N^{(1)}}{(N^{(0)})^2}\right) + \mathcal{O}(\Gamma^2), \tag{4.12}$$

we find that (4.4) and (4.5) become

$$\frac{\partial C^{(0)}}{\partial t} + U^{(0)}\frac{\partial}{\partial z}\left(\frac{C^{(0)}}{N^{(0)}}\right) = -U^{(0)}\Lambda_\mathrm{B}\frac{C^{(0)}}{N^{(0)}} + \mathcal{O}(\Gamma\Lambda_\mathrm{B}), \tag{4.13}$$

$$\frac{\partial N^{(0)}}{\partial t} = -\Gamma U^{(0)}\frac{C^{(0)}}{N^{(0)}} + \mathcal{O}(\Gamma^2). \tag{4.14}$$

We find, assuming that $\mathcal{O}(\Gamma)$ terms are small enough to be neglected, that the leading-order pore concentration is independent of time,

$$N^{(0)}(z,t) = 1, \tag{4.15}$$

and that the velocity and pressure are given by

$$U^{(0)}(t) = 1, \quad p^{(0)}(z,t) = 1 - z, \tag{4.16}$$

in both the constant flow rate and pressure drop cases, since the local porosity and permeability are both constant at leading order when $N^{(0)}$ is constant, and given by

$$\phi^{(0)}(z,t) = 1, \quad K^{(0)}(z,t) = 1. \tag{4.17}$$

Meanwhile, assuming that $\mathcal{O}(\Gamma\Lambda_{\mathrm{B}})$ terms are small enough to be neglected, the leading-order particle concentration satisfies

$$\frac{\partial C^{(0)}}{\partial t} + \frac{\partial C^{(0)}}{\partial z} = -\Lambda_{\mathrm{B}} C^{(0)}, \tag{4.18}$$

subject to the boundary and initial conditions

$$C^{(0)}(0,t) = 1, \quad C^{(0)}(z,0) = 0, \tag{4.19}$$

which we solve explicitly using the method of characteristics. Indeed, the characteristic curves of (4.18), parametrised by the time-like characteristic coordinate, τ, satisfy the characteristic equations

$$\frac{\mathrm{d}t}{\mathrm{d}\tau} = 1, \quad \frac{\mathrm{d}z}{\mathrm{d}\tau} = 1, \quad \frac{\mathrm{d}C^{(0)}}{\mathrm{d}\tau} = -\Lambda_{\mathrm{B}} C^{(0)}, \tag{4.20}$$

which must be solved with initial data, at $\tau = 0$, parametrised by s and given by

$$t(s) = t_0(s), \quad z(s) = z_0(s), \quad C^{(0)}(s) = C_0^{(0)}(s). \tag{4.21}$$

The general solutions to (4.20) and (4.21) are

$$t(s,\tau) = \tau + t_0(s), \quad z(s,\tau) = \tau + z_0(s), \quad C^{(0)}(s,\tau) = C_0^{(0)}(s) e^{-\Lambda_{\mathrm{B}}\tau}. \tag{4.22}$$

Eliminating τ between the first two solutions in (4.22), we find that the characteristic projections are straight lines with unit gradient, given by

$$t = z + (t_0(s) - z_0(s)). \tag{4.23}$$

We note that the characteristic projection through $t = z = 0$, that is, the line $z = t$, splits the domain into characteristic projections emanating from the $t = 0$ axis, and those emanating from the $z = 0$ axis, as shown in Figure 4.1. After $t = 1$, there is no influence of the initial condition on the solution. We specify the initial data on $t = 0$,

$$t_0(s) = 0, \quad z_0(s) = s, \quad C_0^{(0)}(s) = 0, \quad \text{for} \quad 0 \leq s \leq 1, \tag{4.24}$$

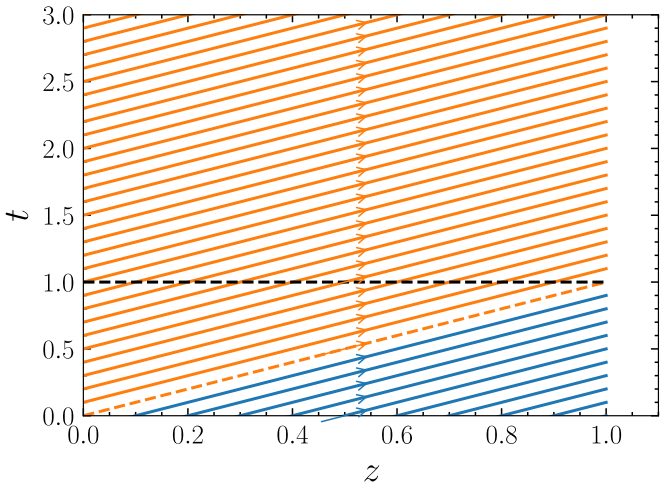

Figure 4.1: Graph showing the characteristic projections, (4.23), of the equation for the particle concentration at leading order in Γ, (4.18). Blue lines propagate information from the initial condition, orange lines propagate information from the boundary condition. The black line shows the last time at which the solution depends on information from the initial condition.

and find, using (4.22), that the solution is

$$C^{(0)}(z,t) = 0 \quad \text{for} \quad t < z \leq 1, \quad 0 \leq z \leq 1. \tag{4.25}$$

Meanwhile, the boundary data on $z = 0$ can be parametrised as

$$t_0(s) = s, \quad z_0(s) = 0, \quad C_0^{(0)}(s) = 1, \quad \text{for} \quad s \geq 0, \tag{4.26}$$

so that, from (4.22), the solution is

$$C^{(0)}(z,t) = e^{-\Lambda_B z} \quad \text{for} \quad 0 \leq z \leq t, \quad 0 \leq z \leq 1. \tag{4.27}$$

Altogether, we have that

$$C^{(0)}(z,t) = \begin{cases} e^{-\Lambda_B z} & 0 \leq z \leq t, \\ 0 & t < z \leq 1, \end{cases} \tag{4.28}$$

for $0 \leq z \leq 1$.

We plot the leading-order particle concentration, $C^{(0)}$ given by (4.28), as a function of depth for various times for two values of Λ_B, in Figure 4.2. For both values of Λ_B, we see that, as time increases, particles travel as a wave from the inlet, but are almost all captured via blocking in the first 10% of the filter. Ahead of the wave front, the concentration of particles is zero because particles have not reached here yet. Behind the wave front, particles are captured over a layer near the inlet. The capture layer has thickness $\mathcal{O}(\Lambda_B^{-1})$. For example, comparing Figure 4.2(a) with Figure 4.2(b), we see that when the value of Λ_B is doubled, the thickness of the layer is halved. Note that, since the porosity is given by the pore concentration, and this is constant via (4.15), the void concentration, C_V, is equal to the concentration, C, in this case.

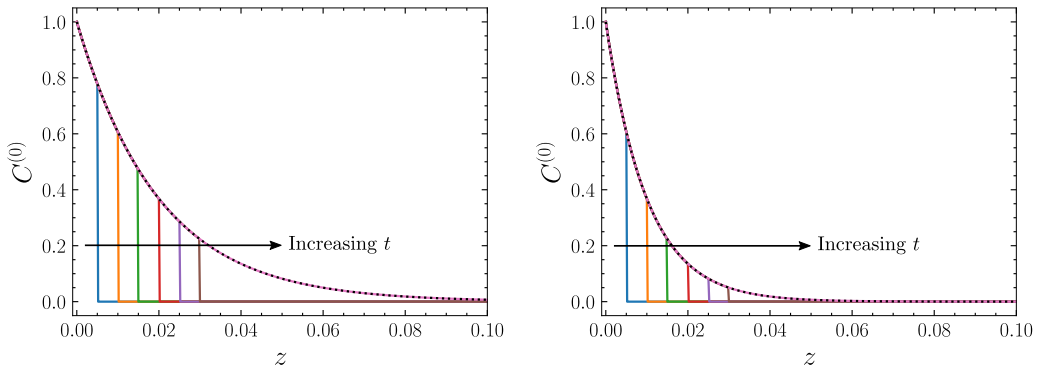

(a) (b)

Figure 4.2: Graphs showing how the particle concentration at leading-order in $\Gamma \ll 1$, $C^{(0)}$, varies with depth, z, for various times, t. The values of t are 0.005 (blue), 0.010 (orange), 0.015 (green), 0.020 (red), 0.025 (purple), 0.030 (brown), 1 (pink). Later t values are identical to the pink curve. The arrows show the direction of increasing time. The value of $e^{-\Lambda_B z}$ is plotted with a black dotted line to aid the eye. Note that only the depths $0 \leq z \leq 0.1$ are shown. (a) The case $\Lambda_B = 50$. (b) The case $\Lambda_B = 100$.

4.2.1.2 The case $\Lambda_B \gg 1$ (with $\Gamma\Lambda_B^{-1} \ll 1$)

An asymptotic solution In this subsection, we suppose that the filter is much longer than the length over which a particle is captured when a pore is blocked, so that $\Lambda_B \gg 1$. We seek a solution in the form of an asymptotic expansion in the small parameter, Λ_B^{-1}, given by

$$C = C^{(0)} + \Lambda_B^{-1} C^{(1)} + \mathcal{O}(\Lambda_B^{-2}), \quad N = N^{(0)} + \Lambda_B^{-1} N^{(1)} + \mathcal{O}(\Lambda_B^{-2}). \tag{4.29}$$

Noting that

$$\frac{C}{N} = \frac{C^{(0)}}{N^{(0)}} + \Lambda_B^{-1}\left(\frac{C^{(1)}}{N^{(0)}} - \frac{C^{(0)}N^{(1)}}{(N^{(0)})^2}\right) + \mathcal{O}(\Lambda_B^{-2}), \tag{4.30}$$

we find that (4.4) and (4.5) become

$$\frac{\partial C^{(0)}}{\partial t} + U^{(0)}\frac{\partial}{\partial z}\left(\frac{C^{(0)}}{N^{(0)}}\right) = -\Lambda_B U^{(0)}\frac{C^{(0)}}{N^{(0)}} - U^{(0)}\left(\frac{C^{(1)}}{N^{(0)}} - \frac{C^{(0)}N^{(1)}}{(N^{(0)})^2}\right) + \mathcal{O}\left(\Lambda_B^{-1}\right), \tag{4.31}$$

$$\frac{\partial N^{(0)}}{\partial t} = -\Gamma U^{(0)}\frac{C^{(0)}}{N^{(0)}} + \mathcal{O}\left(\Gamma\Lambda_B^{-1}\right). \tag{4.32}$$

We find, assuming that $\mathcal{O}(\Lambda_B)$ terms are large enough that $\mathcal{O}(1)$ (and thus $\mathcal{O}(\Lambda_B^{-1})$) terms can be neglected, that the leading order particle concentration is given by

$$C^{(0)}(z,t) = 0, \tag{4.33}$$

and so it follows from (4.32), assuming that $\mathcal{O}(\Gamma\Lambda_{\mathrm{B}}^{-1})$ terms are small enough to be neglected, that

$$N^{(0)}(z,t) = 1. \tag{4.34}$$

Solutions (4.33) and (4.34) imply that there are no particles in the filter and that the pore concentration remains at its initial value. These solutions do not match the boundary condition (4.9), however, since particles must enter the filter at the inlet, so the concentration cannot be zero everywhere.

With this in mind, we seek an inner solution that matches the boundary condition in a layer of thickness $\mathcal{O}(\Lambda_{\mathrm{B}}^{-1})$ inside the filter near the inlet. We define the short spatial coordinate $\zeta = \Lambda_{\mathrm{B}} z$, and find that, in the boundary layer, the leading-order problem becomes

$$\frac{\partial}{\partial\zeta}\left(\frac{C_{\mathrm{bl}}^{(0)}}{N_{\mathrm{bl}}^{(0)}}\right) = -\frac{C_{\mathrm{bl}}^{(0)}}{N_{\mathrm{bl}}^{(0)}}, \tag{4.35}$$

$$\frac{\partial N_{\mathrm{bl}}^{(0)}}{\partial t} = -\Gamma U_{\mathrm{bl}}^{(0)} \frac{C_{\mathrm{bl}}^{(0)}}{N_{\mathrm{bl}}^{(0)}}, \tag{4.36}$$

where the subscript, bl, signifies the solution in the boundary layer. Equation (4.35) has the solution

$$C_{\mathrm{bl}}^{(0)} = N_{\mathrm{bl}}^{(0)} e^{-\zeta}, \tag{4.37}$$

where $N_{\mathrm{bl}}^{(0)}$ depends on the form of the velocity, $U_{\mathrm{bl}}^{(0)}$, and therefore the operating regime, through (4.36). Thus, we will consider the constant flow rate and pressure drop regimes separately.

Before proceeding, we note that (4.37) does not satisfy the initial conditions, (4.10), and deduce that the boundary-layer particle and pore concentrations satisfy a different problem at early times. Indeed, defining a short temporal coordinate $\tau = \Lambda_{\mathrm{B}} t$, we find that, at early times, the leading-order problem is

$$\frac{\partial C_{\mathrm{bl;et}}^{(0)}}{\partial\tau} + U_{\mathrm{bl;et}}^{(0)} \frac{\partial}{\partial\zeta}\left(\frac{C_{\mathrm{bl;et}}^{(0)}}{N_{\mathrm{bl;et}}^{(0)}}\right) = -U_{\mathrm{bl;et}}^{(0)} \frac{C_{\mathrm{bl;et}}^{(0)}}{N_{\mathrm{bl;et}}^{(0)}}, \tag{4.38}$$

$$\frac{\partial N_{\mathrm{bl;et}}^{(0)}}{\partial\tau} = 0, \tag{4.39}$$

where the subscript, bl;et, signifies the boundary-layer solution at early times. Equation (4.39) is trivially satisfied by

$$N_{\mathrm{bl;et}}^{(0)}(z,t) = 1, \tag{4.40}$$

and so we find that the particle concentration satisfies

$$\frac{\partial C_{\mathrm{bl;et}}^{(0)}}{\partial\tau} + \frac{\partial C_{\mathrm{bl;et}}^{(0)}}{\partial\zeta} = -C_{\mathrm{bl;et}}^{(0)}, \tag{4.41}$$

which, returning to the original coordinate system, has the solution

$$C^{(0)}_{bl;et}(z,t) = \begin{cases} e^{-\Lambda_B z} & 0 \le z \le t, \\ 0 & t < z \le \Lambda_B^{-1}, \end{cases} \tag{4.42}$$

for $0 \le z \le \Lambda_B^{-1}$. The early time boundary layer solution, given by (4.40) and (4.42), satisfies the initial conditions, (4.10) (as well as the boundary condition, (4.9)). We now return to the boundary-layer problem at later times. Note that, since the porosity is equal to the pore concentration which is constant via (4.40), the void concentration, $C^{(0)}_{\text{V bl;et}}$, is also equal to the function given by (4.42).

Constant flow rate

After the early times discussed above, in the constant flow rate regime, we have $U^{(0)} = 1$ from (4.6), and so (4.36) has the solution

$$N^{(0)}_{\text{bl}} = 1 - \Gamma t e^{-\zeta}. \tag{4.43}$$

Therefore, in the original spatial coordinate, the inner solution reads

$$C^{(0)}_{\text{bl}}(z,t) = (1 - \Gamma t e^{-\Lambda_B z}) e^{-\Lambda_B z}, \quad N^{(0)}_{\text{bl}}(z,t) = 1 - \Gamma t e^{-\Lambda_B z}, \tag{4.44}$$

which matches the outer solution (4.33), (4.34), and the condition at the inlet boundary, (4.9).

Note, using (4.36), that, the boundary-layer void concentration satisfies

$$\frac{\partial}{\partial \zeta}\left(C^{(0)}_{\text{V bl}}\right) = -C^{(0)}_{\text{V bl}}, \tag{4.45}$$

so that

$$C^{(0)}_{\text{V bl}}(z,t) = e^{-\Lambda_B z}. \tag{4.46}$$

As expected, particles are all removed from the fluid near the inlet, and so the fluid concentration drops exponentially as a function of depth (see Figure 4.3).

We plot the boundary-layer particle and pore concentrations at leading order in Λ_B^{-1}, $C^{(0)}_{\text{bl}}$ and $N^{(0)}_{\text{bl}}$ respectively, given by (4.44), as functions of depth, z, for various times, t, in Figure 4.3. As in the $\Gamma \ll 1$ case (see Figure 4.2), changes in the solutions occur in a layer near the inlet. Particles never reach the region outside of this layer, so the pore concentration maintains its initial condition here. The length of this layer is $\mathcal{O}(\Lambda_B^{-1})$.

Inside the layer we see that, as particles enter the filter, they are captured inside the pores. This capture causes pores to become blocked, which in turn decreases the pore concentration in the layer (unlike in the $\Gamma \ll 1$ case, or in the early time solution).

Pore decrease is fastest at the inlet, since pores here see the most particles per unit time. The particle concentration also decreases fastest at the inlet because the

concentration of particles driven into the filter decreases at the same rate as the pore concentration, to maintain a constant incoming void particle concentration, which is the enforced condition at the boundary. At $t = \Gamma^{-1}$ ($t = 1$ in this example), all inlet pores are blocked so particles no longer enter the filter.

Note that the filter particle concentration, unlike the void particle concentration (which decreases exponentially in space, see the dashed black line in Figure 4.3(a)), is not spatially monotonic at larger times (see the red and purple lines in Figure 4.3(a))). To see why, note that, as time increases at any particular depth, the void particle concentration remains constant (since new particles enter via the inlet and replace those that have been captured), but the pore concentration (see Figure 4.3(b))), and therefore the porosity, decreases (since particles block pores). Since the filter particle concentration is equal to the product of the void particle concentration and the porosity (via (3.4)), the filter particle concentration decreases in time, fastest near the inlet (where most pores are blocked per unit time). Far from the inlet, the filter particle concentration approaches the void particle concentration because there are not enough particles in the fluid to block pores and alter the pore concentration, so that the porosity is constant.

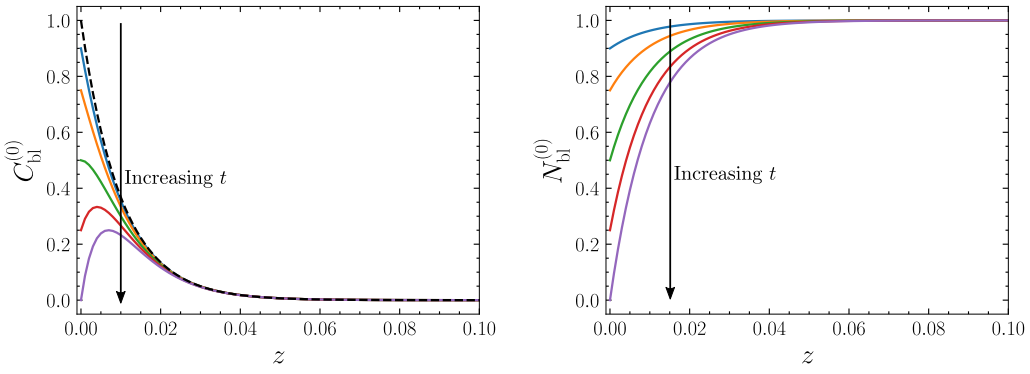

(a) (b)

Figure 4.3: Graphs showing how the particle concentration and pore concentration at leading order in $\Lambda_{\mathrm{B}}^{-1}$ in the boundary layer near the inlet, $C_{\mathrm{bl}}^{(0)}$ and $N_{\mathrm{bl}}^{(0)}$, respectively, vary with depth, z, for various t. The parameters are $\Lambda_{\mathrm{B}} = 100$, $\Gamma = 1$. The values of t are 0.10 (blue), 0.25 (orange), 0.50 (green), 0.75 (red), 1.00 (purple). The arrows show the direction of increasing time. Note that only the depths $0 \leq z \leq 0.1$ are shown. (a) The particle concentration, $C_{\mathrm{bl}}^{(0)}$. The void concentration, $C_{\mathrm{V\,bl}}^{(0)}$ is shown with a dashed black line. (b) The pore concentration, $N_{\mathrm{bl}}^{(0)}$.

Constant pressure drop

In the constant pressure drop regime, we have

$$U_{\mathrm{bl}}^{(0)}(t) = \frac{1}{\int_0^1 \frac{1}{N_{\mathrm{bl}}^{(0)}(z,t)}\,\mathrm{d}z} \tag{4.47}$$

from (4.7), and so, in the original spatial coordinate, (4.36) becomes

$$\frac{\partial N_{\mathrm{bl}}^{(0)}}{\partial t} = -\frac{\Gamma e^{-\Lambda_{\mathrm{B}} z}}{\int_0^1 \frac{1}{N_{\mathrm{bl}}^{(0)}}\,\mathrm{d}z}, \tag{4.48}$$

where we have used the inner solution, (4.37), for the particle concentration, $C_{\mathrm{bl}}^{(0)}$.

Thus (in analogy with the constant flow rate solution (4.44)) the pore concentration is given by

$$N_{\mathrm{bl}}^{(0)}(z,t) = 1 - \gamma(t) e^{-\Lambda_{\mathrm{B}} z}, \tag{4.49}$$

where γ satisfies

$$\frac{\mathrm{d}\gamma}{\mathrm{d}t} = \frac{\Gamma}{\int_0^1 \frac{1}{1-\gamma(t)e^{-\Lambda_{\mathrm{B}} z}}\,\mathrm{d}z}, \tag{4.50}$$

and, calculating the integral, we find that (4.50) simplifies to

$$\frac{\mathrm{d}\gamma}{\mathrm{d}t} = \frac{\Gamma \Lambda_{\mathrm{B}}}{\log\left(\frac{e^{\Lambda_{\mathrm{B}}} - \gamma(t)}{1-\gamma(t)}\right)}, \tag{4.51}$$

which is separable. Integrating (4.51), we find that

$$\Lambda_{\mathrm{B}}\gamma(t) + \Big(1-\gamma(t)\Big)\log\Big(1-\gamma(t)\Big) - e^{\Lambda_{\mathrm{B}}}\Big(1-e^{-\Lambda_{\mathrm{B}}}\gamma(t)\Big)\log\Big(1-e^{-\Lambda_{\mathrm{B}}}\gamma(t)\Big) = \Gamma\Lambda_{\mathrm{B}} t, \tag{4.52}$$

so that

$$\gamma(t) = \Gamma t + \mathcal{O}(\Lambda_{\mathrm{B}}^{-1}) \quad \text{for} \quad 0 < t < \frac{1}{\Gamma}. \tag{4.53}$$

Thus $\gamma(t) \to \Gamma t$ in the limit $\Lambda_{\mathrm{B}} \to \infty$ at times until the filtration process ceases (at $t = 1/\Gamma$, because this is when pores at the inlet are all blocked). As such, as in the constant flow rate regime, Γ fully determines the gradient of γ (for $\Lambda_{\mathrm{B}} \gg 1$). The implication is that, as expected, the relative concentrations of particles and pores dictate the rate of blocking.

Thus, in the constant pressure drop regime, the inner solution reads

$$C_{\mathrm{bl}}^{(0)}(z,t) = (1-\gamma(t)e^{-\Lambda_{\mathrm{B}} z})e^{-\Lambda_{\mathrm{B}} z}, \quad N_{\mathrm{bl}}^{(0)}(z,t) = 1 - \gamma(t)e^{-\Lambda_{\mathrm{B}} z}, \tag{4.54}$$

where γ satisfies (4.53). This matches the outer solution (4.33), (4.34), and the condition at the inlet boundary, (4.9). Physically, the constant pressure drop solution, (4.54), matches the constant flow rate solution, (4.44), because, in the former, changes to the flow rate are restricted to the layer over which pores block. This has $\mathcal{O}(\Lambda_{\mathrm{B}}^{-1})$ thickness, and we thus expect an $\mathcal{O}(\Lambda_{\mathrm{B}}^{-1})$ flow rate change that is negligible for $\Lambda_{\mathrm{B}} \gg 1$. Note that the void particle concentration solution also approaches that in the steady, constant flow rate case, (4.46).

4.2.1.3 The cases $\Gamma \ll 1$ and $\Lambda_B \gg 1$: A numerical solution

We use numerical methods to solve the system (4.4)–(4.10) for more general values of Γ and Λ_B. In this subsection, we solve numerically for $\Gamma \ll 1$ or $\Gamma = \mathcal{O}(1)$ with $\Lambda_B \gg 1$ and compare the solutions with the asymptotic ones we have already found. We use the constant flow rate case since we know the constant pressure drop solution behaves similarly for large enough Λ_B.

For general values of Γ and Λ_B, (4.4)–(4.10) is difficult to solve explicitly, since (4.4) is an advection–reaction equation that is coupled to (4.5). We solve the system using a finite-difference scheme that is first order in time and space. Since the system is hyperbolic, we use upwinding [122] in the appropriate direction, so that the known information at the inlet boundary is propagated downstream. We plot the solutions in Figures 4.4 and 4.5.

The case $\Gamma \ll 1$: Comparison with the characteristic solution in

We find that the numerical solution agrees well with the explicit solution in the case $\Gamma \ll 1$. To demonstrate this, in Figure 4.4, we plot the numerical solution for the particle concentration, C as a function of depth, z, at various times, t, and compare it to the explicit asymptotic solution at leading order in $\Gamma \ll 1$, from (4.28).

At later times, the explicit solution is an exponentially decaying curve over a layer of length $\mathcal{O}(\Lambda_B^{-1})$. The numerical solution agrees well with the explicit solution, even for a relatively small number of spatial points. For example, in Figure 4.4(a) we see that 400 spatial points is enough to match the solutions almost exactly, even though changes occur over the first 10% of the filter.

At earlier times, the explicit solution takes the form of a wave that travels through the layer of length $\mathcal{O}(\Lambda_B^{-1})$. We must discretise more finely in the spatial coordinate so that the numerical solution resolves the sharp steps in the explicit solution. As such, a finer discretisation in the temporal coordinate is also required, to ensure that the Courant–Friedrichs–Lewy (CFL) condition [122] is satisfied, for convergence of the scheme. In Figure 4.4(b), for example, we see that 1000 spatial points leads to reasonable agreement, and, in particular, correctly captures the wave speed.

The case $\Lambda_B \gg 1$: Comparison with asymptotic solution

The numerical solution also agrees well with the explicit solution in the case $\Lambda_B \gg 1$. To demonstrate this, in Figure 4.5, we plot the numerical solution for the particle and pore concentrations in the case $\Lambda_B = 100$ and compare this to the boundary layer solution at leading order in $\Lambda_B^{-1} \ll 1$, $C_{\mathrm{bl}}^{(0)}$ and $N_{\mathrm{bl}}^{(0)}$, from (4.37).

We see, as expected, that changes to the numerical solution are restricted to a boundary layer of length $\mathcal{O}(\Lambda_B^{-1})$ near the inlet. Around 400 spatial points are enough for good agreement with the asymptotic solution (with $\Lambda_B = 100$). The agreement with 1000 spatial points (see Figure 4.5) is excellent. The number of time points needed depends on the maximum time at which the solution is to be solved. As time increases, the local porosity near the inlet decreases, which causes the void velocity to increase. Since this velocity drives changes to the particle concentration profile,

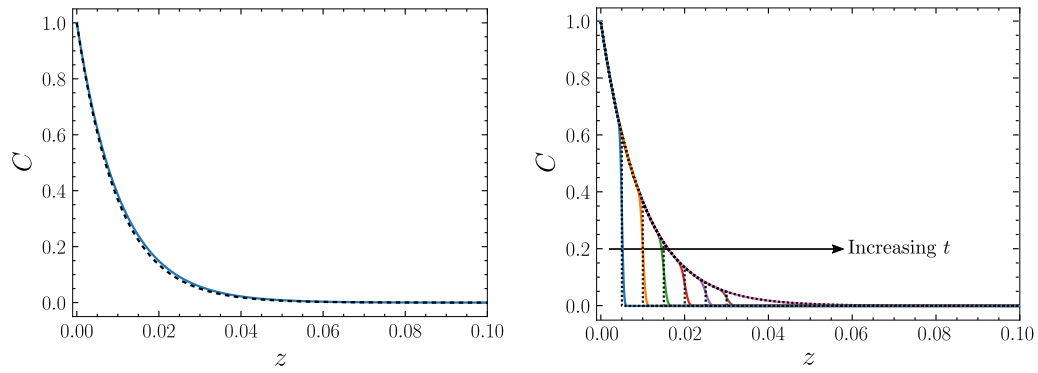

(a) (b)

Figure 4.4: Graphs showing how the particle concentration, C, varies with depth, z, for various times, t. The parameters are $\Lambda_B = 100$, $\Gamma = 0.01$, $A = 2$. The numerical solution is shown with solid lines. The solution at leading order in $\Gamma \ll 1$ is shown in dotted black lines. (a) The later time solution at time $t = 1$ using 400 spatial points. (b) The earlier time solution at various times, t, using 1000 spatial points. The values of t are 0.005 (blue), 0.01 (orange), 0.015 (green), 0.02 (red), 0.025 (purple), 0.03 (brown), 0.1 (pink).

small time steps (perhaps $\mathcal{O}(10)$ times as small as the spatial steps) are needed at times near the block time, to ensure convergence.

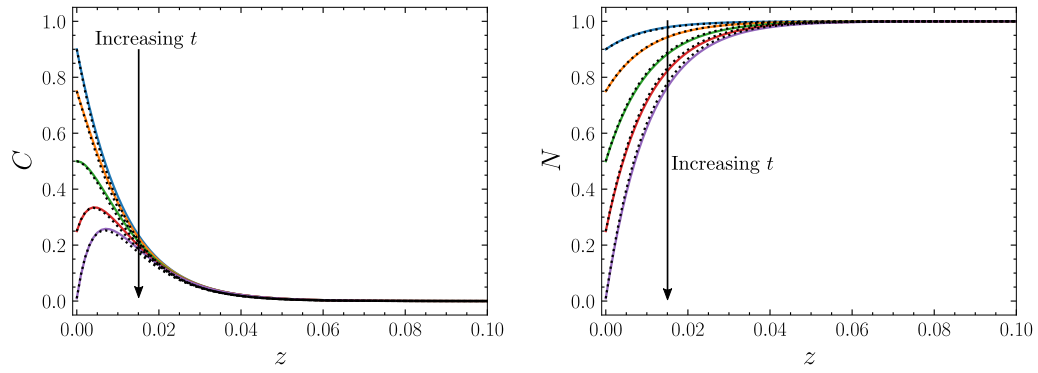

(a) (b)

Figure 4.5: Graphs showing how the particle concentration and pore concentration, C and N, vary with depth, z, for various times, t. The parameters are $\Lambda_B = 100$, $\Gamma = 1$, $A = 2$. The numerical solutions are shown with solid coloured lines. The spatial domain is discretised using 1000 points. The corresponding solutions at leading order in Λ_B^{-1} in the boundary layer near the inlet, $C_{bl}^{(0)}$ and $N_{bl}^{(0)}$, are shown in black dotted lines. The values of t are 0.1 (blue), 0.25 (orange), 0.5 (green), 0.75 (red), 1 (purple). The arrows show the direction of increasing time. Note that only the depths $0 \leq z \leq 0.1$ are shown. (a) The particle concentration, C. (b) The pore concentration, $N_{bl}^{(0)}$.

Thus, in the cases $\Gamma \ll 1$ and $\Lambda_B \gg 1$, we have found explicit solutions that accurately approximate the numerical solution but are cheaper computationally. These are useful for tasks that involve repeated solution, such as parameter sweeps. To demonstrate this, we now use the explicit formulae to show how the solution varies as we vary Γ (with $\Lambda_B \gg 1$) and Λ_B (with $\Gamma \ll 1$).

Behaviour as Γ varies

Firstly, we solve the mono-dispersed system, (4.4)–(4.10), for fixed Λ_B and various values of Γ. We plot the particle and pore concentrations, C and N, as functions of depth, z, for various values of Γ at $t = 1$ in Figure 4.6. As t increases, Γ decreases, and vice versa, from (4.44). Therefore, we see that increasing Γ accelerates the rate of evolution of the solution, effectively decreasing the timescale, and decreasing the blocking time, $T \approx \Gamma^{-1}$.

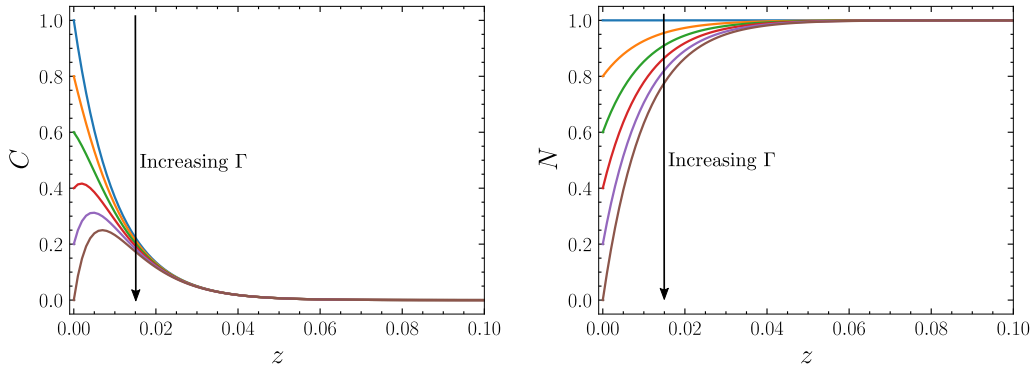

(a) (b)

Figure 4.6: Graphs showing how the particle concentration and pore concentration, C and N, respectively, vary with depth, z, for various Γ. The parameters are $\Lambda_B = 100$, $A = 2$, and the solutions are plotted at time $t = 1$. The values of Γ are 0.0 (blue), 0.2 (orange), 0.4 (green), 0.6 (red), 0.8 (purple). 1.0 (brown). The arrows show the direction of increasing Γ. Note that only the depths $0 \leq z \leq 0.1$ are shown. (a) The particle concentration, C. (b) The pore concentration, N.

As such, the case $\Gamma \gg 1$ corresponds to $T \ll 1$. This represents the case where a huge number of particles are fed into the filter at once and block the pores on the surface almost instantaneously. For example, when $\Gamma = 10$ there are 10 times as many particles as there are pores, and we see that $T = 0.1$, so that the filter is blocked after fluid has passed through the top 10% of its length. On the other hand, when $\Gamma \ll 1$, it follows that $T \gg 1$. This case models the situation where few particles enter the filter at once, and the filter is useful for much longer. For example, we see that, when there are 100 times as many pores as there are particles entering per unit time, so that $\Gamma = 0.01$, we have $T = 100$, and the filter is useful until fluid has traversed its entire length 100 times. As expected then, the ratio Γ^{-1} characterises the useful

lifetime of the filter, at least in the present case, where all the particles are larger than all the pores.

Behaviour as Λ_B varies

Secondly, we solve the mono-dispersed system, (4.4)–(4.10), for fixed Γ and various values of Λ_B. In Figure 4.7 we plot the concentrations of particle and pores, C and N, as functions of depth, z, for various values of Λ_B. We plot the solutions at $t = 1$, and, since $\Gamma = 1$, we have that $T = 1$, so these plots show the solutions when the filtration process ceases. In Figure 4.7(a) we see that particles have penetrated to a depth within the filter that decreases as Λ_B increases, as expected. In Figure 4.7(b) we see that pores have been blocked over a layer of corresponding length. We conclude that, as the filter length increases compared to the blocking length, more of the filter is wasted.

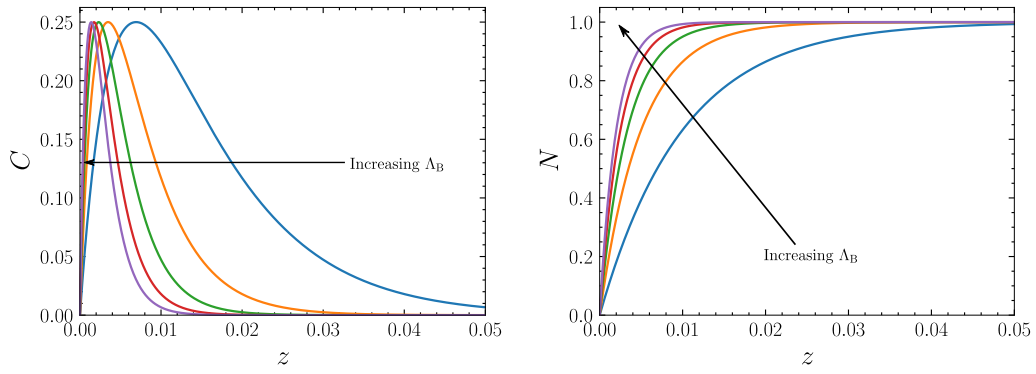

(a) (b)

Figure 4.7: Graphs showing how the particle concentration and pore concentration, C and N, respectively, vary with depth, z, for various Λ_B. The parameters are $\Gamma = 1$, $A = 2$, and the solutions are plotted at time $t = 1$. The values of Λ_B are 1 (blue), 10 (orange), 100 (green), 1000 (red), The arrows show the direction of increasing Λ_B. (a) The particle concentration, C. (b) The pore concentration, N.

To calculate the effective length, l_{eff}, the length of the filter that has been used for particle capture, we define a desired threshold filtrate fluid particle concentration, C_{eff} say, below which the concentration at $z = 1$ must remain. Given C_{eff}, we say that l_{eff} is the distance from the inlet that is required to reduce the void concentration to C_{eff}. In Figure 4.8(a), for example, we plot the void concentration, C_V, as a function of depth, z, at $t = 1$, for various values of Λ_B. We see how, given an example threshold concentration, $C_{\text{eff}} = 0.1$ here, we read off values of l_{eff}. We see that, for a given C_{eff}, increasing Λ_B decreases the value of l_{eff}.

To understand this quantitatively, we recall that, for large Λ_B, at leading order in Λ_B^{-1}, the void concentration is given by (4.46). It follows that

$$l_{\text{eff}} = -\frac{\log(C_{\text{eff}})}{\Lambda_B}. \tag{4.55}$$

We plot l_{eff} as a function of C_{eff} for various values of Λ_{B} in Figure 4.8(b). As expected, the length, l_{eff}, of filter needed to reduce the concentration to an acceptable level, C_{eff}, decreases as C_{eff} increases. In other words, a smaller proportion of the filter is needed if the filtration task is less stringent. l_{eff} decreases as Λ_{B} increases, which implies, as expected, that less of the filter is used when particles are smaller in comparison to the filter as a whole. One implication is that, in this idealistic regime, where there is one particle size and pore size, if the filter is long compared to the particle size, a very stringent concentration constraint (i.e., $C_{\text{eff}} \ll 1$) can be obtained at no extra cost, as the filtration process will use more pores but take the same amount of time to run to completion.

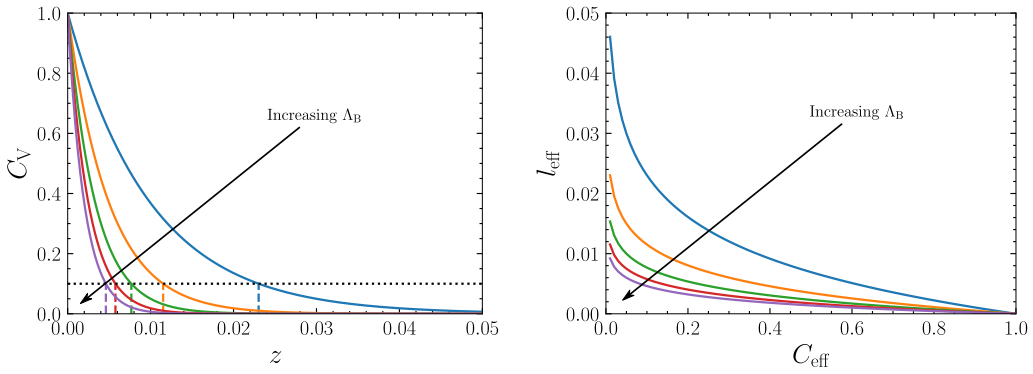

(a) (b)

Figure 4.8: (a) Graph showing how the particle concentration, C, varies with depth, z, at $t = 1$ for $\Gamma = 1$. for two values of Λ_{B}. The values of Λ_{B} are 10 (orange), 100 (green), The arrow shows the direction of increasing Λ_{B}. An example efficient concentration threshold, C_{eff}, is plotted with a dotted black line. The lengths of the corresponding capture layers are extrapolated in correspondingly coloured dashed lines. (b) Graph showing how the capture-layer length, l_{eff}, varies with Λ_{B}, for various efficient concentrations, C_{eff}. The values for C_{eff} are 0.01 (blue), 0.05 (orange), 0.1 (green), 0.2 (red). The arrow shows the direction of increasing C_{eff}.

4.2.2 Blocking and deposition

We now consider the case where particles are smaller than pores. As before, pores are all size 1 initially, and we choose $A < 1$.

We choose the sticking probability $\varsigma_{\text{D}} = 0.1$, so that particles deposit in pores that are larger than them 10% of the times that they pass through them. We choose the transformation distribution $\tau_{\text{D}}(a, \rho, r) = \delta(r - (\rho - a))$, so that pores of size ρ are transformed to pores of size r by particles of size $a < \rho$. It follows that particles of size A can deposit in pores of size 1, and, when they do so, these pores are transformed to pores of size $R = 1 - A$. We assume that $A \geq 1/2$, so that the new pores of size R are blocked by particles of size A. This special case is the simplest scenario within which to observe blocking and deposition in the same filter, since it follows

that the pore-size distribution remains (at most) bi-dispersed for all time, permitting the ansatz

$$c(z,t,a) = \delta(a-A)C(z,t),\ n(z,t,r) = N_R(z,t)\delta(r-R) + N_1(z,t)\delta(r-1), \quad (4.56)$$

where N_R and N_1 are the concentrations of pores of sizes R and 1 respectively.

Using this ansatz, (3.46) and (3.47) become

$$\frac{\partial C}{\partial t} + \frac{\partial}{\partial z}\left(\frac{UC}{R^2N_R + N_1}\right) = -\frac{UC}{(R^2N_R+N_1)^2}\left(\Lambda_{\mathrm{B}}R^2N_R + \Lambda_{\mathrm{D}}\varsigma_{\mathrm{D}}N_1\right), \quad (4.57)$$

$$\frac{\partial N_R}{\partial t} = -\frac{\Gamma UC}{(R^2N_R+N_1)^2}\left(R^2N_R - \varsigma_{\mathrm{D}}N_1\right), \quad (4.58)$$

$$\frac{\partial N_1}{\partial t} = -\frac{\Gamma UC}{(R^2N_R+N_1)^2}\varsigma_{\mathrm{D}}N_1. \quad (4.59)$$

In the constant flow rate case it follows from (3.48) that the velocity and pressure are given by

$$U = 1, \quad p(z,t) = \int_z^1 \frac{1}{R^4N_R(\zeta,t) + N_1(\zeta,t)}\,\mathrm{d}\zeta, \quad (4.60)$$

while in the constant pressure drop case it follows from (3.49) that these are given by

$$U(t) = \frac{1}{\int_0^1 \frac{1}{R^4N_R(z,t)+N_1(z,t)}\,\mathrm{d}z}, \quad p(z,t) = \frac{\int_z^1 \frac{1}{R^4N_R(\zeta,t)+N_1(\zeta,t)}\,\mathrm{d}\zeta}{\int_0^1 \frac{1}{R^4N_R(\zeta,t)+N_1(\zeta,t)}\,\mathrm{d}\zeta}, \quad (4.61)$$

since, for bi-dispersed pores, the local porosity and permeability, defined in (3.50), are given by

$$\phi(z,t) = R^2N_R(z,t) + N_1(z,t), \quad K(z,t) = R^4N_R(z,t) + N_1(z,t), \quad (4.62)$$

respectively. The boundary and initial conditions, (3.51) and (3.52), become

$$C(0,t) = R^2N_R(0,t) + N_1(0,t), \quad (4.63)$$

and

$$C(z,0) = 0, \quad N_R(z,0) = 0, \quad N_1(z,0) = 1, \quad (4.64)$$

since the pore sizes are mono-dispersed initially. In the remainder of this subsection, we will numerically solve this system, (4.57)–(4.64), and analyse the solutions.

4.2.2.1 The case $\Gamma = \mathcal{O}(1)$, $\Lambda_{\mathrm{B}} \gg 1$, and $\Lambda_{\mathrm{D}} \gg 1$: A numerical solution

For general values of Γ, Λ_{B}, and Λ_{D}, we solve the blocking and deposition system, (4.57)–(4.64), similarly to the system in the case where there is no deposition, (4.4)–(4.10). The particle concentration equation, (4.57), is now coupled to a reaction equation, (4.58) and (4.59), for the concentration of pores of each size, but, from a numerical-methods perspective, this does not pose any new challenges. We now discuss the numerical solutions in the case $\Gamma = \mathcal{O}(1)$, $\Lambda_{\mathrm{B}} \gg 1$, and $\Lambda_{\mathrm{D}} \gg 1$.

Particle concentration and porosity

We plot the solutions for the particle concentration, C, and the porosity, $\phi = N_1 + R^2 N_R$, as functions of depth, z, at early times, in Figure 4.9. We see that the behaviour is qualitatively similar to the early-time behaviour of the system in the blocking only regime, from before. Particles travel as a wave through a layer at the top of the filter, and, as they do so, they are removed so that the concentration follows a curve of exponential decay behind the wave front. We choose $\Lambda_B = 200$, which is twice as large as $\Lambda_B = 100$ before. This has the effect of decreasing the length of the layer over which particles are captured due to blocking. However, $\Lambda_D = 100$ and $\varsigma_D = 0.1$, so that $\Lambda_D \varsigma_D = 10$ is ten times as small as $\Lambda_B = 100$ before. This has the effect of increasing the length over which particles are captured. The net effect is that particles are captured over a longer length in the present parameter regime. In general, particles are captured via a mixture of blocking and deposition, and the length of the capture layer is determined by $\max\{\Lambda_B^{-1}, (\Lambda_D \varsigma_D)^{-1}\}$.

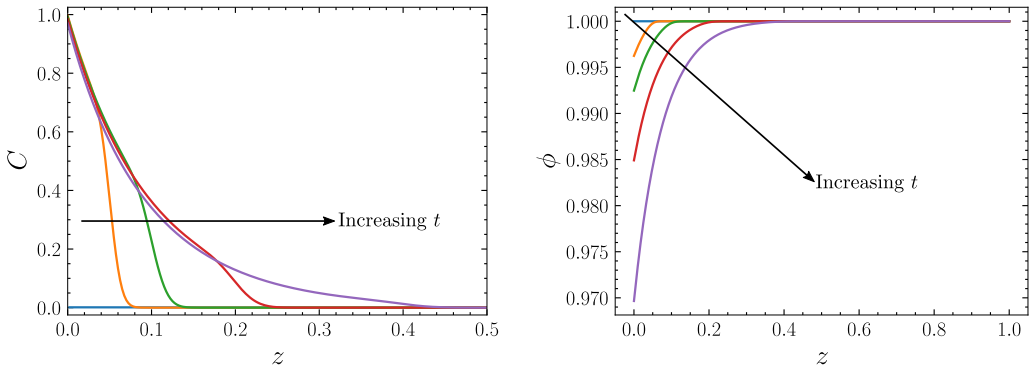

(a) (b)

Figure 4.9: Graphs showing how the particle concentration and local porosity, C and ϕ, vary with depth, z, for various times, t. The parameters are $\Lambda_B = 200$, $\Lambda_D = 100$, $\Gamma = 1$, $A = 0.5$, $\varsigma_D = 0.1$. The values of t are 0 (blue), 0.005 (orange), 0.01 (green), 0.02 (red), 0.04 (purple). The arrows show the direction of increasing time. Note that only the depths $0 \leq z \leq 0.5$ are shown. (a) The particle concentration, C. (b) The local porosity, ϕ.

Next, in Figure 4.10, we plot the particle concentration and the local porosity as functions of depth at later times. We see that the solutions are qualitatively similar to those in the blocking regime. In Figure 4.10(b) we see that the decrease in the porosity is fastest at the inlet, where there are the most particles. However, this time, the porosity at the inlet decreases to zero over a longer timescale than in the blocking regime. This is because, in this example, deposition is ten times less likely to occur than blocking in the previous case (since $\varsigma_D = 0.1$), so that removal of all inlet pores takes around a factor of $\varsigma_D^{-1} = 10$ times as long so that all inlet pores become clogged around $t = 10$ here (as opposed to around $t = 1$ before).

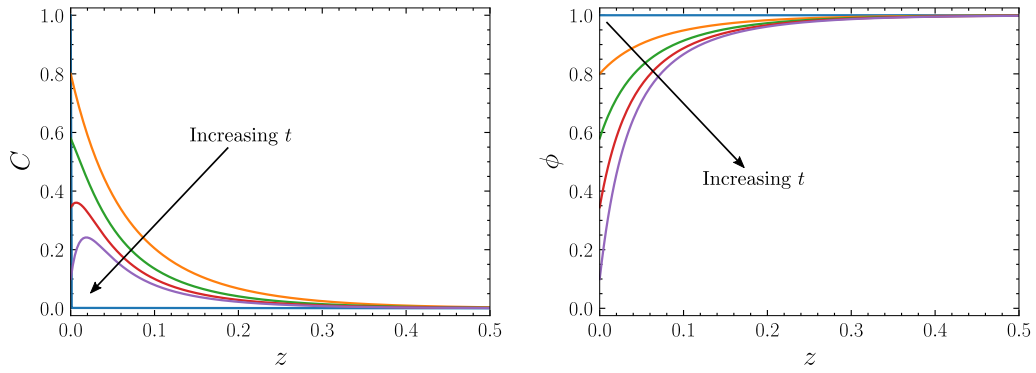

(a) (b)

Figure 4.10: Graphs showing how the particle concentration and local porosity, C and ϕ, vary with depth, z, for various times, t. The parameters are $\Lambda_B = 200$, $\Lambda_D = 100$, $\Gamma = 1$, $A = 0.5$, $\varsigma_D = 0.1$. The values of t are 0 (blue), 2.5 (orange), 5 (green), 7.5 (red), 10 (purple). The arrows show the direction of increasing time. Note that only the depths $0 \leq z \leq 0.5$ are shown. (a) The particle concentration, C. (b) The local porosity, ϕ.

Pore concentration and permeability

We plot the local permeability, and the concentrations of large and small pores, as functions of depth, for various times, in Figure 4.11. We focus on the concentration of large pores first, which we show in Figure 4.11(a). We see that large pores (solid lines) are removed via deposition (only) over the deposition layer. We see that the permeability (dashed lines) is almost identical to the concentration of large pores, since the correction to the permeability due to smaller pores in (4.62) is $R^4 N_R \approx 0.06 N_R$.

We now turn our attention to the concentration of small pores, which is plotted in Figure 4.11(b). We notice that these are removed due to a complex combination of deposition and blocking. To see this, we first note that, at earlier times, the concentration of small pores increases over the entire deposition layer. This is because, early on, large pores are transformed into small pores as particles (that are smaller than the large pores) deposit in them. Small pores are being blocked by the particles (which are larger than the small pores) at the same time as they are being produced by deposition in the large pores. This deviation is more extreme closer to the inlet, because there are the most particles available to block the small pores. Blocking happens in a shorter layer than deposition because $\Lambda_B^{-1} > (\Lambda_D \varsigma_D)^{-1}$, so particles never reach the small pores further down the filter to remove them. At later times, we see that the concentration of small pores begins to decrease near the inlet. This is because blocking is 10 times as likely to occur as deposition (since $\varsigma_D = 0.1$). As a result, when there are enough small pores, the rate at which they are removed due to blocking exceeds the rate at which they are produced due to deposition. Note that this is despite the fact that more particles flow through large pores per unit time. This

example demonstrates the complicated interplay between blocking and deposition in filters with more complicated size distributions.

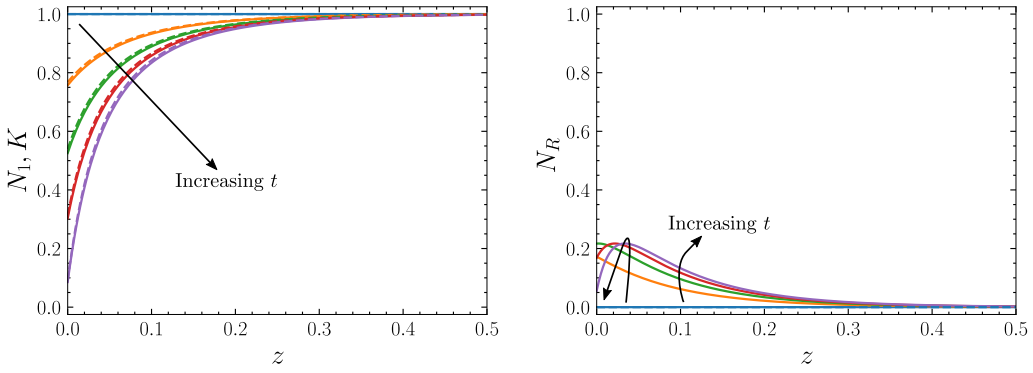

(a) (b)

Figure 4.11: Graphs showing how the local permeability, K, and the concentrations of the larger and smaller pores, N_1 and N_R, vary with depth, z, for various times, t. The parameters are $\Lambda_B = 200$, $\Lambda_D = 100$, $\Gamma = 1$, $A = 0.5$, $\varsigma_D = 0.1$. The values of t are 0 (blue), 2.5 (orange), 5 (green), 7.5 (red), 10 (purple). The arrows show the direction of increasing time. Note that only the depths $0 \leq z \leq 0.5$ are shown. (a) The concentration of the larger pores, N_1 (solid lines). The local permeability, K (dashed lines). (b) The concentration of the smaller pores, N_R.

Behaviour as ς_D varies

We now assess the effect of varying the sticking probability, ς_D. We solve the system (4.57)–(4.64) for fixed Γ, Λ_B, and Λ_D, with various values of ς_D. We note that parameter sweeps, such as this, are significantly more computationally expensive than in the blocking regime, since before we were equipped with explicit asymptotic solutions.

In Figure 4.12 we plot the particle concentration and local porosity as functions of depth, z, at time $t = 10$, for various values of ς_D. Firstly, we see that as ς_D increases, the length of the layer over which particle capture and pore removal occurs decreases. For example, when $\varsigma_D = 0.02$ (blue line), deposition occurs over the entire filter. Particles only deposit in pores that are larger (than the particles) 2% of the time, so the layer over which deposition occurs has length $\mathcal{O}((\Lambda_D\varsigma_D)^{-1}) = \mathcal{O}(1)$. Some particles pass all the way to the end of the filter without being captured, and so the concentration of particles that remain at the outlet is around 0.025. On the other hand, when the probability of deposition is 10%, so that $\varsigma_D = 0.1$, the deposition layer is length $\mathcal{O}((\Lambda_D\varsigma_D)^{-1}) = \mathcal{O}(10^{-1})$ and almost all particles are captured by the time they have traversed the first 10% of the filter. The concentration is negligible at the outlet. Secondly, we see that the rate at which pores are removed at the inlet increases as ς_D increases. Thus, for larger ς_D, the filtration process runs for much less time, even though the concentration of particles present at the outlet is not substantially different. One important implication is that, if it is possible to control the sticking

probability, ς_D, then it could be chosen so that the capture layer is longer, increasing the proportion of pores that are used for particle capture, thus extending the useful lifetime of the filter.

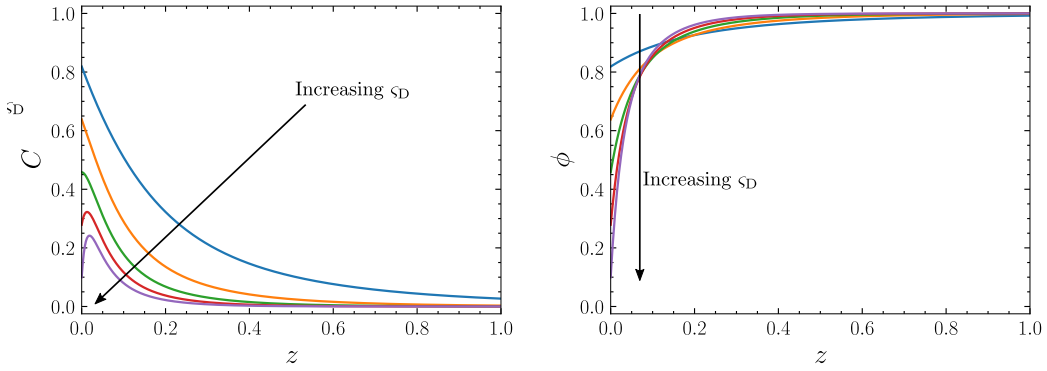

(a) (b)

Figure 4.12: Graphs showing how the particle concentration and local porosity, C and ϕ, vary with depth, z, for various values of deposition probability, ς_D. The parameters are $\Lambda_B = 200$, $\Lambda_D = 100$, $\Gamma = 1$, $A = 0.5$, and the solutions are plotted at time $t = 10$. The values of ς_D are 0.02 (blue), 0.04 (orange), 0.06 (green), 0.08 (red), 0.1 (purple). The arrows show the direction of increasing ς_D (and therefore increasing $\Lambda_D\varsigma_D$). (a) The particle concentration, C. (b) The local porosity, ϕ.

In this section, we have explored the case where particles and pores are both one size initially. When the particles are larger than the pores, only blocking is possible, and we used this case to explore the effect of changing Γ and Λ_B. When the particles are smaller than the pores, blocking and deposition are both possible (when A is chosen appropriately), and we used this case to explore the effect of changing ς_D. In the next section, we turn our attention to more complex cases, in which the pores in the filter are poly-dispersed.

4.3 Mono-dispersed particles and poly-dispersed pores

In this section, we assume that particles entering the filter at the inlet all have size A, so that particles are mono-dispersed everywhere at all times,

$$c(z, t, a) = \delta(a - A)C(z, t). \tag{4.65}$$

We suppose that pores in the filter have log-normally dispersed sizes, with mean size 1. It follows that the boundary condition, (3.51), becomes

$$C(0, t) = \phi(0, t), \tag{4.66}$$

as in the previous section, while the initial conditions, (3.52), become

$$C(z,0) = 0, \quad n(z,0,r) = n_{\text{init}}(r), \tag{4.67a,b}$$

where we define

$$n_{\text{init}}(r) = \frac{\phi^*_{\text{init}} e^{-\sigma_n^2}}{\sqrt{2\pi}\sigma_n r} e^{-\frac{\left(\log(r)+\frac{\sigma_n^2}{2}\right)^2}{2\sigma_n^2}}, \tag{4.68}$$

since we calculate that the denominator in (3.52b) satisfies

$$\frac{1}{\sqrt{2\pi}\sigma_n}\int_0^\infty r e^{-\frac{\left(\log(r)+\frac{\sigma_n^2}{2}\right)^2}{2\sigma_n^2}}\,\mathrm{d}r = e^{\sigma_n^2}. \tag{4.69}$$

In this section, we solve the size-structured model (3.46)–(3.59) subject to the boundary and initial conditions (4.66) and (4.67). In Subsection 4.3.1 we consider the case where $\varsigma_{\text{D}} = 0$ in which only blocking is possible. In Subsection 4.3.2, we then consider the case $\varsigma_{\text{D}} = 0.001$, so that deposition occurs with 0.1% of the probability that blocking does.

4.3.1 Blocking and no deposition

We first consider the system (3.46)–(3.59) subject to the boundary and initial conditions for mono-dispersed particles and log-normally poly-dispersed pores, (4.66) and (4.67), in the case of zero adherence, $\varsigma_{\text{D}} = 0$. We find a numerical solution for general Λ_{B} and then use the intuition gained from this solution to reduce the system to a more simple one when $\Lambda_{\text{B}} \gg 1$.

The equations for the particle- and pore-size distributions, (3.46) and (3.46), become

$$\frac{\partial C}{\partial t} + \frac{\partial}{\partial z}\left(\frac{C}{\phi}\right) = -\frac{\Lambda_{\text{B}} C}{\phi^2}\int_0^A r^2 n\,\mathrm{d}r, \tag{4.70}$$

$$\frac{\partial n}{\partial t} = \frac{\Gamma C}{\phi^2} r^2 n H(A-r), \tag{4.71}$$

where H is the Heaviside function. The velocity and pressure are given by either (3.48) or (3.49). In (4.71) we see that the distribution of pores of size $r > A$ is constant and remains at the initial distribution. We therefore write the porosity and permeability, (3.50), explicitly in terms of pores that are larger and smaller than the particles,

$$\phi = \varphi + \varphi_{[r>A]}, \quad K = \kappa + \kappa_{[r>A]}, \tag{4.72}$$

where

$$\varphi(z,t) = \int_0^A r^2 n(z,t,r)\,\mathrm{d}r, \quad \varphi_{[r>A]} = \int_A^\infty r^2 n_{\text{init}}\,\mathrm{d}r, \tag{4.73}$$

$$\kappa(z,t) = \int_0^A r^4 n(z,t,r)\,\mathrm{d}r, \quad \kappa_{[r>A]} = \int_A^\infty r^4 n_{\text{init}}\,\mathrm{d}r. \tag{4.74}$$

We call the unknown variables, φ and κ, the small-pore porosity and permeability. Note that $\varphi_{[r>A]}$ and $\kappa_{[r>A]}$, which we call the large-pore porosity and permeability, are fully specified by the initial conditions, and, indeed, we calculate that

$$\varphi_{[r>A]} = \frac{\phi^*_{\text{init}}}{2}(1 + \text{erf}(f(A)), \tag{4.75}$$

$$\kappa_{[r>A]} = \frac{\phi^*_{\text{init}} e^{5\sigma_n^2}}{2}(1 + \text{erf}(g(A)), \tag{4.76}$$

where we define

$$f(A) = \frac{3\sigma_n^2 - 2\log(A)}{2\sqrt{2}\sigma_n}, \quad g(A) = \frac{7\sigma_n^2 - 2\log(A)}{2\sqrt{2}\sigma_n}. \tag{4.77}$$

In the remainder of this subsection we solve (4.70)–(4.72) with either (3.48) or (3.49) subject to the boundary and initial conditions (4.66) and (4.67).

4.3.1.1 The case $\Gamma = \mathcal{O}(1)$ and $\Lambda_{\mathrm{B}} \gg 1$: A numerical solution

For general values of Γ and Λ_{B}, the equation for the particle concentration, (4.70), is a partial integro–differential advection–reaction equation that is coupled to a reaction equation, (4.71), which describes changes to the pore-size distribution. Note that (4.71) does not contain an integral because there is no deposition and particles are all one size. These two equations, together with those for the porosity and permeability, (4.72), and either (3.48) or (3.49), subject to the boundary and initial conditions, (4.66) and (4.67), are similar to those in the case where the pore sizes are monodispersed, save for the integral on the right-hand side of (4.70). We therefore solve them using a similar numerical scheme, this time using the trapezium rule with 100 pore size points to evaluate the integral. That is, we use a first-order upwinding finite-difference scheme and discretise using 400 spatial points, and $N_t > 400$ temporal points (where the choice of N_t depends on how close to block time, T, and therefore how close to a local porosity of zero at the inlet, we will run), noting that we must choose time steps sufficiently small compared to space steps to satisfy the Courant–Friedrichs–Lewy (CFL) condition. We present the solution for $\Lambda_{\mathrm{B}} \gg 1$ and $\Gamma = \mathcal{O}(1)$ in the constant flow rate regime, and so choose (3.48), rather than (3.49), to specify the velocity and the pressure.

Particle concentration and local porosity

In Figure 4.13, we demonstrate how the particle concentration, C, and the local porosity, ϕ, vary with depth, z, at various times, t. In Figure 4.13(a), we see that, at early times, particles block pores at the inlet, which decreases the porosity and thus the concentration. Particles begin to travel through the filter, but are removed over a layer of thickness $\mathcal{O}(\Lambda_{\mathrm{B}}^{-1})$. In Figure 4.13(b) we see that, as time continues to increase, this early time behaviour settles into a regime in which particles begin to traverse the filter as a wave. No particles have reached the region in front of the wave, so the concentration is zero and the porosity retains its initial value. Behind

the wave, all pores that are smaller than the particles have been blocked. Since no pores larger than the particles can be clogged (because there is no deposition), after the wave has passed, the porosity retains some constant value that is dictated by the proportion of pores that are larger than the particles. Behind the wave, the particle concentration matches the inlet concentration, since the fluid carries all particles that enter the filter through the larger pores unobstructed. The concentration and local porosity transition between their two values within a layer of thickness $\mathcal{O}(\Lambda_B^{-1})$, which is thin when particles are small compared to the depth of the filter.

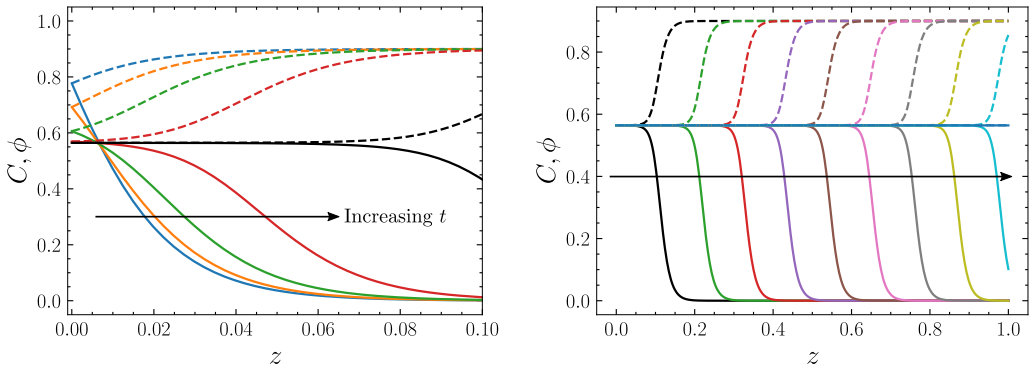

(a) (b)

Figure 4.13: Graphs showing how the particle concentration, C (solid lines), and local porosity, ϕ (dashed lines), vary with the depth, z, at various times, t. The parameters are $\Lambda_B = 200$, $\Gamma = 1$, $A = 1$, $\sigma_n = 0.2$, $\phi^*_{\text{init}} = 0.9$. The arrows show the direction of increasing time. (a) The earlier-time solutions, C, ϕ. The values of t are 0.5 (blue), 1.0 (orange), 2.0 (green), 4.0 (red), 10.0 (black). (b) The later-time solutions, C, ϕ. The values of t are 10 (black), 20 (green), 30 (red), 40 (purple), 50 (brown), 60 (pink), 70 (grey), 80 (olive), 90 (cyan), 100 (blue). The dotted black lines show the explicit solution.

Local porosity and local permeability

In Figure 4.14 we show how the local porosity and permeability, ϕ and K, vary with depth, z, at various times. In Figure 4.14(a) we see, as expected, that the value that the porosity is reduced to after the particle wave has passed is the large-pore porosity, $\varphi_{[r>A]} < \phi^*_{\text{init}}$, which is the proportion of total pore area that is attributed to pores that are larger than the particles. In Figure 4.14(b), we see that the local permeability behaves similarly to the local porosity. It transitions from its initial value to the large-pore permeability, $\kappa_{[r>A]}$, over the thin blocking layer. The permeability drop is less extreme than the porosity drop, since K is a factor of r^2 different from ϕ, so unaffected larger pores are weighted more heavily.

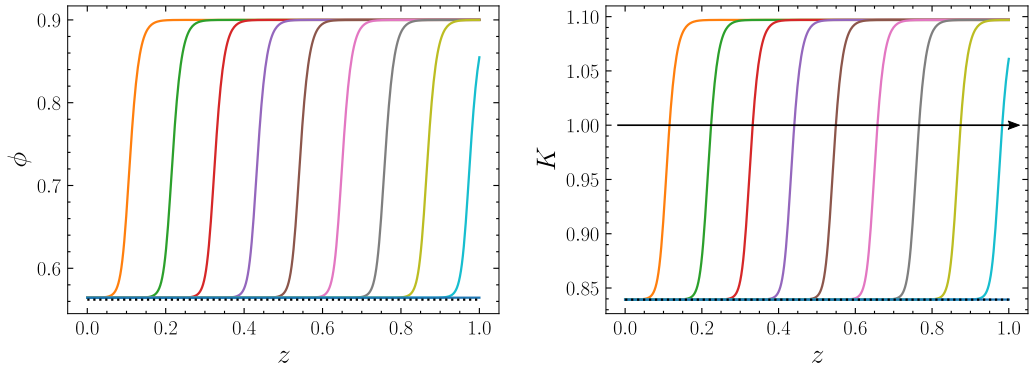

(a) (b)

Figure 4.14: Graphs showing how the local porosity (left) and permeability (right), ϕ and K, vary with the depth, z, at various times, t. The parameters are $\Lambda_{\mathrm{B}} = 200$, $\Gamma = 1$, $A = 1$, $\sigma_n = 0.2$, $\phi^*_{\mathrm{init}} = 0.9$. The values of t are 10 (orange), 20 (green), 30 (red), 40 (purple), 50 (brown), 60 (pink), 70 (grey), 80 (olive), 90 (cyan), 100 (blue). The arrows show the direction of increasing time. (a) The local porosity, ϕ. The value of the large-pore porosity, $\varphi_{[r>A]}$, is plotted in a black dotted line. (a) The local permeability, K. The value of the large-pore permeability, $\kappa_{[r>A]}$, is plotted in a black dotted line.

Global porosity and global permeability

We define the global porosity and global permeability to be

$$\bar{\phi}(t) = \int_0^1 \phi(z,t)\,\mathrm{d}z, \quad \bar{K}(t) = \int_0^1 K(z,t)\,\mathrm{d}z. \tag{4.78}$$

These are distinct from the local porosity and permeability, and we interpret them to be (depth-independent) measures of the 'total' porosity and permeability (i.e., of the entire filter). In Figure 4.15 we demonstrate how these vary with time, t. We see that these decrease linearly from their initial values, which are dictated by the initial distribution of pore-sizes, to lower values at some critical time, $t \approx 90$. After $t \approx 90$, these global measures of pore space remain constant for all time. We see that the values that the global porosity and permeability are reduced to are $\varphi_{[r>A]}$ and $\kappa_{[r>A]}$ respectively. The critical time, $t \approx 90$ here, is the time at which the particle wave reaches the filter outlet. Before this, pores are being blocked at the wave-front, and the local porosity and permeability are being reduced, which contributes to the constant reduction of their integrals. After this, there are no longer any smaller pores to be blocked at any depth, and the filter is no longer useful, so further changes to the global porosity and permeability do not occur.

Pressure and pore-size distribution

In Figure 4.16(a) we plot the local pressure as a function of depth at various times. We see that, initially, the pressure gradient is uniform. At later times, we observe

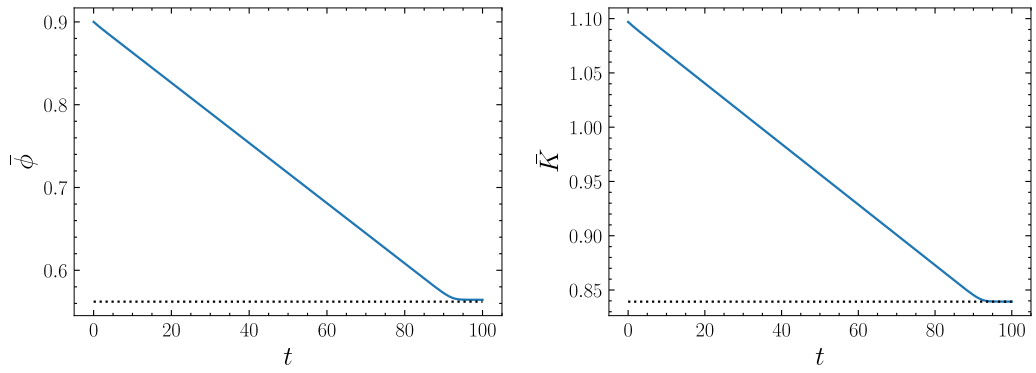

(a) (b)

Figure 4.15: Graphs showing how the global porosity and permeability, $\bar{\phi}$ and $\bar{K}$, vary with time, t. The parameters are $\Lambda_{\mathrm{B}} = 200$, $\Gamma = 1$, $A = 1$, $\sigma_n = 0.2$, $\phi^*_{\mathrm{init}} = 0.9$. (a) The global porosity, $\bar{\phi}$. The value of the large-pore porosity, $\varphi_{[r>A]}$, is plotted in a black dotted line. (b) The global permeability, $\bar{K}$. The value of the large-pore permeability, $\kappa_{[r>A]}$, is plotted in a black dotted line.

how changes to the local permeability impact the pressure. As the local permeability decreases at a given depth, the pressure here increases so that the pressure drop over the entire filter increases. At the critical time, $t \approx 90$ in this case, the value of $p(0,t)$, which is the filter pressure drop (i.e., the pressure drop across the entire filter), reaches $1/\kappa_{[r>A]}$, after which there are no further changes to the pressure. In practice, in constant flow rate regimes, operators monitor the filter pressure drop and ensure that this does not exceed some threshold, at which point the process must be halted due to external operational constraints. We see that, in the present case where there is no deposition, it is relatively simple to construct a pore-size distribution for which the threshold value is not exceeded during the useful lifetime of the filter, by choosing a pore-size distribution for which enough pores are larger than the particles, so that $\kappa_{[r>A]}$ is not too small and thus $p(0,t)$ is not too large.

In Figure 4.16(b) we show the distribution of pore sizes halfway down the filter (i.e., at $z = 0.5$), for various times. The times are chosen so that we capture the changes that occur to the distribution when the particle wave passes through this region of the filter. We see that the pore distribution is split into two critical regions: pores that are larger than the particles, and those that are smaller. The distribution of pores that are larger than the particles never changes, because particles pass through these pores without blocking them. However, as time increases, the number of pores of any particular size smaller than the particles decreases to zero. We see that the decrease happens faster for larger pores because there is more flow through these and so more particles are transported through them per unit time. However, there are more of these pores to block, so the number of pores of all sizes (smaller than particles) are eventually reduced to zero at around the same time, $t \approx 49$ here. have not reached them. After this time, there are no further changes to the distribution, since particles now flow unobstructed through the larger pores.

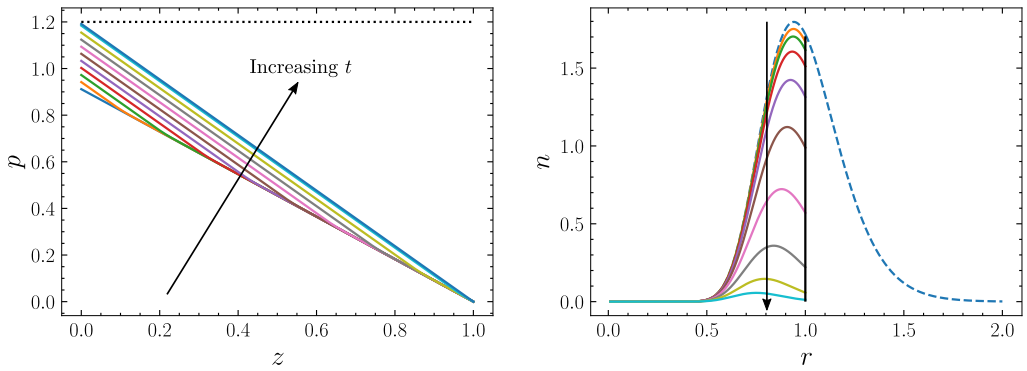

(a) (b)

Figure 4.16: Graphs showing how the pore-size distribution (left) and local pressure (right), n and p, vary with the pore size, r, and depth, z, respectively, at various times t. The parameters are $\Lambda_{\mathrm{B}} = 200$, $\Gamma = 1$, $A = 1$, $\sigma_n = 0.2$, $\phi^*_{\mathrm{init}} = 0.9$. The arrows show the direction of increasing time. (a) The local pressure, p, as a function of depth, z, at various times. The values of t are 0 (blue), 10 (orange), 20 (green), 30 (red), 40 (purple), 50 (brown), 60 (pink), 70 (grey), 80 (olive), 90 (cyan), 100 (blue). The value of the inverse large-pore permeability, $\kappa^{-1}_{[r>A]}$, is plotted in a black dotted line. (b) The pore-size distribution, n, as a function of the pore size, r, at various times, t. The initial condition is shown in a dashed line. The mean particle-size, A, is plotted in a solid black line. The values of t are 0 (blue), 41 (orange), 42 (green), 43 (red), 44 (purple), 45 (brown), 46 (pink), 47 (grey), 48 (olive), 49 (cyan).

4.3.1.2 The case $\Lambda_{\mathrm{B}} \gg 1$ (with $\Gamma = \mathcal{O}(1)$): An earlier time characteristic solution and a later time asymptotic solution

We use a similar asymptotic method to the case where pore sizes were mono-dispersed, and so seek an explicit solution at leading order in $\Lambda_{\mathrm{B}}^{-1} \ll 1$. Using the numerical solution as a guide, we expect the particle concentration to behave like a travelling wave.

Earlier times: A characteristic solution

We begin by considering the solution at early times. We scale the time and depth variables, defining $\hat{t} = \Lambda_{\mathrm{B}} t$ and $\hat{z} = \Lambda_{\mathrm{B}} z$. In these new coordinates, (4.70) and (4.71) become

$$\frac{\partial C}{\partial \hat{t}} + \frac{\partial}{\partial \hat{z}}\left(\frac{C}{\phi}\right) = -\frac{C}{\phi^2}\varphi \tag{4.79}$$

$$\frac{\partial n}{\partial \hat{t}} = -\frac{1}{\Lambda_{\mathrm{B}}}\frac{\Gamma C}{\phi^2} r^2 n H(A - r), \tag{4.80}$$

and the boundary and initial conditions, (4.66) and (4.67), become

$$C(0, \hat{t}) = \phi(0, \hat{t}), \tag{4.81}$$

and

$$C(\hat{z},0)=0, \quad n(\hat{z},0,r)=n_{\text{init}}(r), \tag{4.82}$$

where

$$n_{\text{init}}(r)=\frac{\phi^*_{\text{init}}e^{-\sigma_n^2}}{\sqrt{2\pi}\sigma_n r}e^{-\frac{\left(\log(r)+\frac{\sigma_n^2}{2}\right)^2}{2\sigma_n^2}}. \tag{4.83}$$

At leading order in $\Lambda_{\text{B}}^{-1} \ll 1$, (4.79) and (4.80) become

$$\frac{\partial C^{(0)}}{\partial \hat{t}}+\frac{\partial}{\partial \hat{z}}\left(\frac{C^{(0)}}{\phi^{(0)}}\right)=-\frac{C^{(0)}}{(\phi^{(0)})^2}\varphi^{(0)} \tag{4.84}$$

$$\frac{\partial n^{(0)}}{\partial \hat{t}}=0. \tag{4.85}$$

Using (4.85), we immediately see that the leading-order pore density is given by $n^{(0)}=n_{\text{init}}$ for all time. Since $n^{(0)}$ is constant, we solve the leading-order particle concentration equation, (4.84), by the method of characteristics similarly to before, and find, in the original coordinates, that

$$C^{(0)}(z,t)=\begin{cases}0 & z<t/\phi^*_{\text{init}},\\ \phi^*_{\text{init}}e^{-\frac{\Lambda_{\text{B}}z}{2}(1+\text{erf}(f(A)))} & z>t/\phi^*_{\text{init}},\end{cases} \tag{4.86}$$

where we recall, from (4.77), that

$$f(A)=\frac{3\sigma_n^2-2\log(A)}{2\sqrt{2}\sigma_n}. \tag{4.87}$$

Similarly to the mono-dispersed case, at early times, particles travel as a steep wave over a thin layer near the inlet, and display behaviour similar to the early-time numerical solution that we showed in Figure 4.13(a). Behind the wave, the particle concentration exponentially decreases with depth, and in front of the wave, there are no particles, since they have not reached these depths at times this early. This time, the gradient of the concentration profile depends on the particle size, A, as well as the blocking parameter Λ_{B}, since A determines the proportion of pores that block particles, and thus the rate at which particles are captured.

Later times: An asymptotic solution

At later times, we seek a solution that matches the behaviour of the later-time numerical solution shown in Figure 4.13(b). We seek a travelling wave solution and so re-write the problem in a frame that is moving with the wave. In front of the wave, we assume that $C=0$ and that $\phi=\phi^*_{\text{init}}$. Behind the wave, we assume that $C=\varphi_{[r>A]}=\phi$.

Using this intuition, we change to coordinates that are fixed in the frame of the wave, and so define $\zeta = \Lambda_{\mathrm{B}} z - Vt$, $\tau = t$. Equations (4.70) and (4.71) become

$$\frac{\partial C}{\partial \tau} - V\frac{\partial C}{\partial \zeta} + \Lambda_{\mathrm{B}}\frac{\partial}{\partial \zeta}\left(\frac{C}{\phi}\right) = -\frac{\Lambda_{\mathrm{B}} C}{\phi^2}\varphi, \tag{4.88}$$

$$\frac{\partial n}{\partial \tau} - V\frac{\partial n}{\partial \zeta} = \frac{\Gamma C}{\phi^2} r^2 n H(A - r). \tag{4.89}$$

We seek steady (in this frame) asymptotic solutions in the small parameter, $\Lambda_{\mathrm{B}}^{-1} \ll 1$, of the form

$$X(\zeta, \tau) = X^{(0)}(\zeta, \tau) + \frac{1}{\Lambda_{\mathrm{B}}} X^{(1)}(\zeta, \tau) + \mathcal{O}\left(\frac{1}{\Lambda_{\mathrm{B}}^2}\right). \tag{4.90}$$

At leading order, we see that (4.88) and (4.89) imply that

$$\frac{\partial C^{(0)}}{\partial \zeta}\left(\frac{C^{(0)}}{\phi^{(0)}}\right) = -\frac{C^{(0)}}{(\phi^{(0)})^2}\varphi^{(0)}, \tag{4.91}$$

$$V\frac{\partial n^{(0)}}{\partial \zeta} = \frac{\Gamma C^{(0)}}{(\phi^{(0)})^2} r^2 n^{(0)} H(A - r), \tag{4.92}$$

which satisfy the conditions

$$C^{(0)} \to \varphi_{[r>A]}, \quad n^{(0)} \to 0 \quad (\text{for} \quad (r > A) \quad \text{as} \quad \zeta \to -\infty, \tag{4.93}$$

$$C^{(0)} \to 0, \qquad n^{(0)} \to n_{\mathrm{init}} \qquad\qquad \text{as} \quad \zeta \to \infty, \tag{4.94}$$

Note that (4.93) implies that $\varphi^{(0)} \to 0$ as $\zeta \to -\infty$ so that $\phi^{(0)} \to \varphi_{[r>A]}$.

To solve the leading-order system, (4.91) and (4.92) with (4.93) and (4.94), we begin by integrating (4.92) with respect to r from 0 to A. We find, dropping leading-order notation, that

$$V\frac{\partial N_{[r<A]}}{\partial \zeta} = \frac{\Gamma C \varphi}{\phi^2}, \tag{4.95}$$

where we define

$$N_{[r<A]}(z, t) = \int_0^A n(z, t, r)\,\mathrm{d}r \tag{4.96}$$

to be the small-pore concentration, which is the concentration of pores that are smaller than the particles. Combining (4.95) with (4.91) we find that

$$V\frac{\partial N_{[r<A]}}{\partial \zeta} = -\Gamma\frac{\partial}{\partial \zeta}\left(\frac{C}{\phi}\right). \tag{4.97}$$

Integrating (4.97) with respect to some temporary variable $\tilde{\zeta}$ from ζ to ∞, and using the boundary condition as $\zeta \to \infty$, (4.94), we find that

$$V(N_{[r<A]\mathrm{init}} - N_{[r<A]}) = \frac{\Gamma C}{\phi}, \tag{4.98}$$

where

$$N_{[r<A]\text{init}} = \int_0^A n_{\text{init}}(r)\,\mathrm{d}r \tag{4.99}$$

is the known initial concentration of pores that are smaller than the particles. Applying the boundary condition as $\zeta \to -\infty$, (4.93), to (4.99), and noting that $\phi \to \varphi_{[r>A]}$ as $\zeta \to -\infty$, we find that we must choose

$$V = \frac{\Gamma}{N_{[r<A]\text{init}}}. \tag{4.100}$$

Thus, the speed of the wave is given by $\Gamma/\Lambda_{\mathrm{B}} N_{[r<A]\text{init}}$. Substituting (4.100) into (4.98) and returning to leading-order notation, we find that the leading-order particle concentration is given by

$$C^{(0)} = \phi\left(1 - \frac{N_{[r<A]}}{N_{[r<A]\text{init}}}\right). \tag{4.101}$$

Furthermore, substituting this solution into the equation for the leading-order pore-size distribution, (4.92), we conclude that

$$\frac{\partial n^{(0)}}{\partial \zeta} = (N_{[r<A]\text{init}} - N_{[r<A]})\frac{r^2 n}{\phi} H(A-r), \tag{4.102}$$

with

$$n^{(0)} \to n_{\text{init}} \quad \text{as} \quad \zeta \to \infty. \tag{4.103}$$

Although (4.102) with (4.103) is not straightforward enough to solve explicitly, we note that it is a reaction equation that is no longer coupled to the hyperbolic advection–reaction equation, and is therefore considerably more simple to solve numerically than the original problem. Thus, (4.102) subject to (4.103), together with (4.101), provide a leading-order solution in the case $\Lambda_{\mathrm{B}}^{-1} \ll 1$. We plot this solution in Figure 4.13 and observe good agreement with the numerical solution.

4.3.2 Blocking and deposition

In this subsection, we assume that $\varsigma_{\mathrm{D}} \neq 0$ and solve the size-structured model (3.46)–(3.59) subject to the boundary and initial conditions for mono dispersed particles and log-normally poly-dispersed pores, (4.66) and (4.67), in the case where blocking and deposition both occur. We find an explicit solution at leading order in $\Gamma \ll 1$, and a numerical solution for $\Gamma = \mathcal{O}(1)$.

4.3.2.1 The case $\Gamma \ll 1$ (with $\Lambda_{\mathrm{B}} \gg 1$ and $\Lambda_{\mathrm{D}} \gg 1$): A characteristic solution

We first suppose that the concentration of particles to be removed from the mono-dispersed feed fluid is very small compared to the concentration of log-normally dispersed pores in the filter, and so consider the system (3.46)–(3.59) subject to the boundary and initial conditions (4.66) and (4.67) in the case $\Gamma \ll 1$.

We seek a solution of the form of an asymptotic expansion in the small parameter, Γ, given by

$$X = X^{(0)} + \Gamma X^{(1)} + \mathcal{O}(\Gamma^2), \tag{4.104}$$

where X is any of the solution variables, C, N, U, p, ϕ, K. At leading order, we find that (3.46)–(3.59) become

$$\frac{\partial C^{(0)}}{\partial t} + U^{(0)} \frac{\partial}{\partial z}\left(\frac{C^{(0)}}{\phi^{(0)}}\right) = -U^{(0)} \frac{F(A)}{\phi^{(0)}} C^{(0)} \tag{4.105}$$

$$\frac{\partial n^{(0)}}{\partial t} = 0, \tag{4.106}$$

where we define

$$F(A) = \frac{\Lambda_{\mathrm{B}} \int_0^A r^2 d_n(r)\,\mathrm{d}r + \Lambda_{\mathrm{D}} \varsigma_{\mathrm{D}} \int_A^\infty r^2 d_n(r)\,\mathrm{d}r}{\int_0^\infty r^2 d_n(r)\,\mathrm{d}r}, \tag{4.107}$$

and either

$$U^{(0)}(t) = 1, \quad p^{(0)}(z,t) = \int_z^1 \frac{1}{K^{(0)}(\zeta,t)}\,\mathrm{d}\zeta, \tag{4.108}$$

or

$$U^{(0)}(t) = \frac{1}{\int_0^1 \frac{1}{K^{(0)}(z,t)}\,\mathrm{d}z}, \quad p^{(0)}(z,t) = \frac{\int_z^1 \frac{1}{K^{(0)}(\zeta,t)}\,\mathrm{d}\zeta}{\int_0^1 \frac{1}{K^{(0)}(\zeta,t)}\,\mathrm{d}\zeta}, \tag{4.109}$$

for

$$\phi^{(0)}(z,t) = \int_0^\infty r^2 n^{(0)}(z,t,r)\,\mathrm{d}r, \quad K^{(0)}(z,t) = \int_0^\infty r^4 n^{(0)}(z,t,r)\,\mathrm{d}r. \tag{4.110}$$

The boundary and initial conditions, (4.66) and (4.67), become

$$C^{(0)}(0,t) = \phi^{(0)}(0,t), \tag{4.111}$$

and

$$C^{(0)}(z,0) = 0, \quad n^{(0)}(z,0,r) = n_{\mathrm{init}}(r), \tag{4.112a,b}$$

for $n_{\mathrm{init}}(r)$ defined in (4.68).

We see from (4.106) that $n^{(0)}$ keeps its initial value, n_{init}, and it follows that $\phi^{(0)}$, and $U^{(0)}$, $p^{(0)}$, and $K^{(0)}$ keep their initial values, ϕ^*_{init}, and U_{init}, p_{init} and K_{init} say, too. The latter three solutions are given by substituting the constant solution $n^{(0)} = n_{\mathrm{init}}$ into either (4.108) or (4.109), and (4.110). Thus, it remains to solve

$$\frac{\partial C^{(0)}}{\partial t} + \frac{U_{\mathrm{init}}}{\phi^*_{\mathrm{init}}} \frac{\partial C^{(0)}}{\partial z} = -\frac{U_{\mathrm{init}}}{\phi^*_{\mathrm{init}}} F(A) C^{(0)}, \tag{4.113}$$

subject to (4.111) and (4.112a).

We proceed via the method of characteristics similarly to in Section 4.2.2, and find the explicit solution

$$C^{(0)}(z,t) = \begin{cases} (\phi^*_{\text{init}}/U_{\text{init}})e^{-F(A)z} & z \leq t(U_{\text{init}}/\phi^*_{\text{init}}), \\ 0 & z > t(U_{\text{init}}/\phi^*_{\text{init}}), \end{cases} \tag{4.114}$$

for $0 \leq z \leq 1$. We calculate that

$$F(A) = \frac{1}{2}\left(\Lambda_{\text{B}}\left(1 - \text{erf}\Big(f(A)\Big)\right) + \Lambda_{\text{D}}\varsigma_{\text{D}}\left(1 + \text{erf}\Big(f(A)\Big)\right)\right) \tag{4.115}$$

where erf is the error function, and

$$f(A) = \frac{3\sigma_n^2 - 2\log(A)}{2\sqrt{2}\sigma_n}, \tag{4.116}$$

from (4.77). We plot $F(A)$ in Figure 4.17, for various σ_n. We see that if $A \gg 1$ then, since $\text{erf}(f(A)) \approx -1$, $F(A) \approx \Lambda_{\text{B}}$. Meanwhile, if $A \ll 1$ then, since $\text{erf}(f(A)) \approx 1$, $F(A) \approx \Lambda_{\text{D}}$. As σ_n decreases, the transition region of A between these two limiting cases becomes thinner.

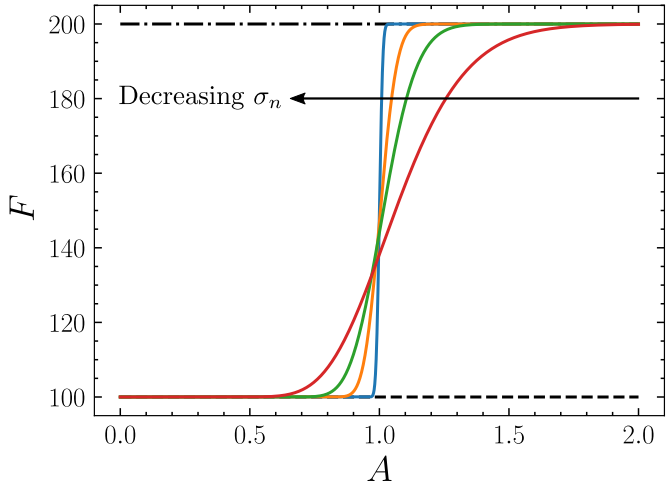

Figure 4.17: Graph showing how the function F varies with the particle size, A, at various σ_n. The parameters are $\Lambda_{\text{B}} = 200$, $\Lambda_{\text{D}} = 100$, $\Gamma = 1$, $U_{\text{init}} = 1$, and $\phi^*_{\text{init}} = 1$. The values of σ_n are 0.01 (blue), 0.05 (orange), 0.1 (green), 0.2 (red). The limiting cases $A \gg 1$, $F(A) = \Lambda_{\text{B}}$ (dash-dotted), and $A \ll 1$, $F(A) = \Lambda_{\text{D}}$ (dashed), are plotted in black.

Particle concentration and capture-layer length

We plot the explicit leading-order asymptotic solution, $C^{(0)}(z,t)$, given by (4.114), in Figure 4.18(a). We see that the particle concentration decreases exponentially over a

layer near the inlet of the filter. We see that the gradient of the concentration profile increases as the particle size increases, so that the length of the layer over which particles are captured decreases. This is because $\Lambda_D < \Lambda_B$ in this example. Indeed, if particles are very large, and thus larger than all pores, then the solution (4.114) matches the solution for mono-dispersed particle- and pore-sizes, since $F(A) = \Lambda_B$ for $A \gg 1$. In this case, particle capture occurs only via blocking very close to the filter inlet. As the particle size decreases, particle capture occurs via both blocking and deposition in a layer that is fatter than the blocking layer (since $\Lambda_D < \Lambda_B$). As the particle size decreases more, eventually all pores are larger than the particles. Now particle capture occurs only via deposition, which occurs over a still-fatter layer, the thickness of which is dictated by the value of Λ_D.

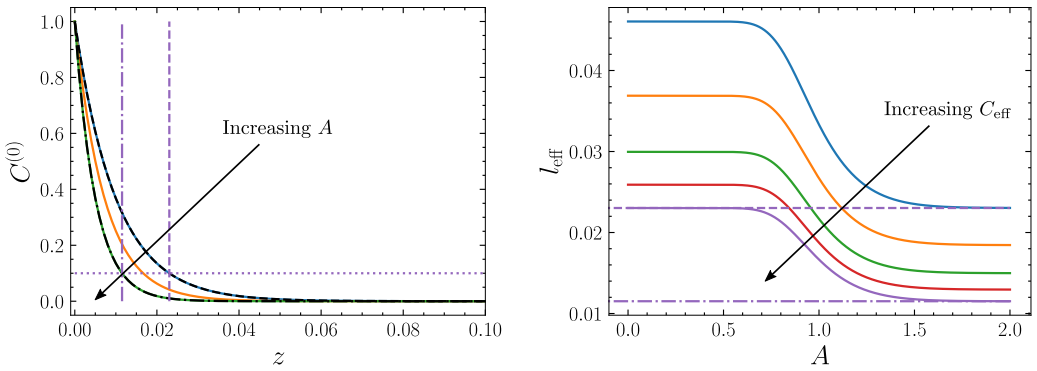

(a) (b)

Figure 4.18: Graphs showing how the leading-order particle concentration, $C^{(0)}$, varies with depth, z, and how the capture-layer length, l_{eff}, varies with the particle size, A. The parameters are $\Lambda_B = 200$, $\Lambda_D = 100$, $\Gamma = 1$, $U_{\text{init}} = 1$, $\phi^*_{\text{init}} = 1$, and $\varsigma_D = 1$. (a) The concentration, $C^{(0)}$, as a function of depth, z, at time $t = 0.1$ for various A. The values of A are 0 (blue), 1 (orange), 2 (green). The limiting cases when $A \gg 1$, $F(A) = \Lambda_B$ (dash-dotted) and when $A \ll 1$, $F(A) = \Lambda_D$ (dashed), are plotted in black. The efficient concentration $C_{\text{eff}} = 0.1$ is shown a horizontal dotted purple line, with the capture-layer lengths in the cases $F(A) = \Lambda_B$ (dash-dotted) and $F(A) = \Lambda_D$ (dashed) extrapolated in vertical purple lines. (b) The capture-layer length, l_{eff}, as a function of the particle size, A, for various efficient concentrations, C_{eff}. The values of C_{eff} are 0.010 (blue), 0.025 (orange), 0.050 (green), 0.075 (red), 0.100 (purple). The cases $F(A) = \Lambda_B$ (dash-dotted) and $F(A) = \Lambda_D$ (dashed) are extrapolated in horizontal purple lines.

We calculate the length of the capture layer, l_{eff}, by imposing a required concentration at the inlet, C_{eff} say, to which the inlet concentration must be reduced by the time particles exit the filter for the filtration regime to be considered effective. Using (4.114), we see that this length is given by

$$l_{\text{eff}} = \frac{1}{F(A)} \log\left(\frac{\phi^*_{\text{init}}/U_{\text{init}}}{C_{\text{eff}}}\right). \tag{4.117}$$

We plot the capture-layer length, l_{eff}, as a function of the particle size, A, for various efficient concentrations, C_{eff}, in Figure 4.18(b), and demonstrate how we read off a value for the capture-layer length given a required efficient concentration, 0.1 for example. We see that, for any choice of efficient concentration, the capture-layer length decreases from some lower limiting-value to an upper limiting-value over a transition region of A. For small enough particles, capture occurs via deposition only, over a layer of length $l_{\text{eff}} = \Lambda_{\text{D}}^{-1} \log((\phi^*_{\text{init}}/U_{\text{init}})/C_{\text{eff}})$. For large enough particles, capture occurs via blocking only, over a layer of length $\Lambda_{\text{B}}^{-1} = \log((\phi^*_{\text{init}}/U_{\text{init}})/C_{\text{eff}})$, which is smaller than the deposition layer since $\Lambda_{\text{B}} > \Lambda_{\text{D}}$. For other particle sizes, capture occurs via blocking and deposition and the capture-layer length lies between these two extremes, so that $\Lambda_{\text{B}}^{-1} \log((\phi^*_{\text{init}}/U_{\text{init}})/C_{\text{eff}}) \leq l_{\text{eff}} \leq \Lambda_{\text{D}}^{-1} \log((\phi^*_{\text{init}}/U_{\text{init}})/C_{\text{eff}})$. The exact value of l_{eff} depends on the relative densities of pores that are smaller and larger than the particles.

4.3.2.2 The case $\Gamma = \mathcal{O}(1)$, $\Lambda_{\mathbf{B}} \gg 1$, and $\Lambda_{\mathbf{D}} \gg 1$: A numerical solution

We now suppose that the concentration of particles to be removed from the monodispersed feed fluid is comparable to the concentration of log-normally dispersed pores in the filter, and so $\Gamma = \mathcal{O}(1)$. Thus, we solve the system (3.46)–(3.59) subject to the boundary and initial conditions (4.66) and (4.67) in the case $\Lambda_{\text{B}} \gg 1$, $\Lambda_{\text{D}} \gg 1$, and $\Gamma = \mathcal{O}(1)$.

The equation for the particle concentration, (4.70), is a partial integro–differential advection–reaction equation, as it was for the case $\varsigma_{\text{D}} = 0$. However, since $\varsigma_{\text{D}} \neq 0$, (4.71) becomes an integro–differential reaction equation. The integral appears because now particles can deposit in larger pores and transform them to smaller pores. These equations, with (4.72) and either (3.48) or (3.49) subject to the boundary and initial conditions, (4.66) and (4.67), are of a similar form to that in the case where there was no deposition, despite the extra integral. We discretise the extra integral using the trapezium rule, and solve via a similar numerical scheme as before. Again, we present the solution for the constant flow rate regime, and so choose (3.48), rather than (3.49), to specify the velocity and the pressure.

Particle concentration and local porosity

In Figure 4.19, we demonstrate how the particle concentration, C, and the local porosity, ϕ, vary with depth, z, at various times, t. The first thing we notice is that there are two regions of time, $10 \leq t \leq 90$ and $90 < t \leq 300$, within which we observe distinct dynamics. In Figure 4.19(a) we see that, in the earlier time region, $10 \leq t \leq 90$, particles traverse the filter as a wave. As they do so, the amplitude of the wave decreases. In the second time region, $90 < t \leq 300$, the particle concentration (at any depth) decreases in time with a spatial gradient that is almost uniform. Correspondingly, in Figure 4.19(b) we see that, in the first time region, the porosity decreases in a wave across the filter, and decreases linearly with time in the second time-region, maintaining a constant depth-wise gradient.

Firstly, consider the waves in the first time-region. Similarly to the case of no

deposition, in front of the wave we see that there are no particles and the porosity retains its initial value. Behind the wave, smaller pores have all been blocked by the particles, as before. This time, however, since $\varsigma_D \neq 0$, some larger pores have decreased in size due to deposition. As a result, the porosity drops slightly below the small-pore porosity, $\varphi_{[r>A]}$, which we observed in the no-deposition case. Correspondingly, the concentration of particles drops below the value observed in the no-deposition scenario, as some particles are also captured in larger pores due to deposition. The length of the capture-layer, within which the concentration decreases as the waves progresses, is still $\mathcal{O}(\Lambda_B^{-1})$.

Secondly, consider the linear decrease in the second time region. At a critical time similar to that in the blocking regime, $t \approx 90$ here, the particle wave reaches the outlet, which means that all original smaller pores have been blocked. After this, pore clogging occurs mostly due to deposition, although blocking still occurs in the smaller pores that have been transformed from larger pores by deposition. Although $\Lambda_D \gg 1$, so that particles are much smaller than the filter, $\varsigma_D \ll 1$, so that the probability that particles are captured via deposition is small. It follows that the length over which deposition occurs is $\mathcal{O}((\Lambda_D \varsigma_D)^{-1})$ ($\mathcal{O}(10)$ here), which is much longer than the length of the layer over which blocking occurs, $\mathcal{O}(\Lambda_B^{-1})$ ($\mathcal{O}(10^{-2})$ here). Hence, we observe a slow decrease in the particle concentration over the entire length of the filter, as particles deposit in the larger pores that were not blocked in the first time region.

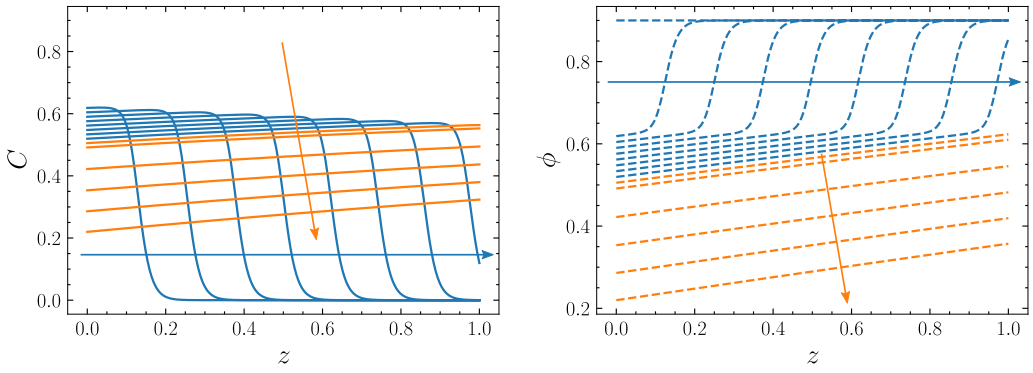

(a) (b)

Figure 4.19: Graphs showing how the particle concentration (solid lines) and local porosity (dashed lines), C and ϕ, vary with the depth, z, at various times, t. The parameters are $\Lambda_B = 200$, $\Lambda_D = 100$, $\Gamma = 1$, $A = 1$, $\sigma_n = 0.2$, $\phi^*_{\text{init}} = 0.9$, $\varsigma_D = 0.001$. The times, t, at which the wave travels through the filter are shown in blue. The values of t shown in blue are $10, 20, \ldots, 70, 80$. The blue arrow shows the direction of increasing t for these values. The times after the wave has travelled through the filter are shown in orange. The values of t shown in orange are $90, 100, 150, 200, 250, 300$. The orange arrow shows the direction of increasing t for these values. (a) The particle concentration, C. (b) The local porosity, ϕ.

Local permeability and local pressure

In Figure 4.20(a) we plot the local permeability, K, and the local pressure, p, as functions of depth, z, at various times. In Figure 4.20(a) we see that the behaviour of the local permeability is similar to that of the local porosity. At earlier times, it decreases in a wave that traverses the filter. Unlike in the no-deposition case, the permeability decreases below $\kappa_{[r>A]}$, since particles continue to deposit in larger pores after all smaller pores have been blocked. In Figure 4.20(b), we demonstrate how the local pressure, p, varies with depth, z, at various times. As in the no-deposition case from before, initially, we see that the local pressure drop is uniform. In the first time region, the decrease to the local permeability at each depth causes an increase to the local pressure at a rate that is determined by the rate at which the permeability is decreased by blocking. At times near the end of the first time region, $t \approx 90$, we see that the pressure at the inlet begins to exceed the value we observed in the no-deposition case, $1/\kappa_{[r>A]}$. The local permeability has decreased below $\kappa_{[r>A]}$ at depths behind the wave due to the deposition of particles in larger pores. After the critical time, the pressure drop at the inlet required to maintain the constant flow rate continues to increase, at a rate that is determined by the rate of decrease of the permeability due to deposition. When deposition is possible, the filter pressure drop continues to increase until all pores are removed, regardless of the choice of the initial pore-size distribution.

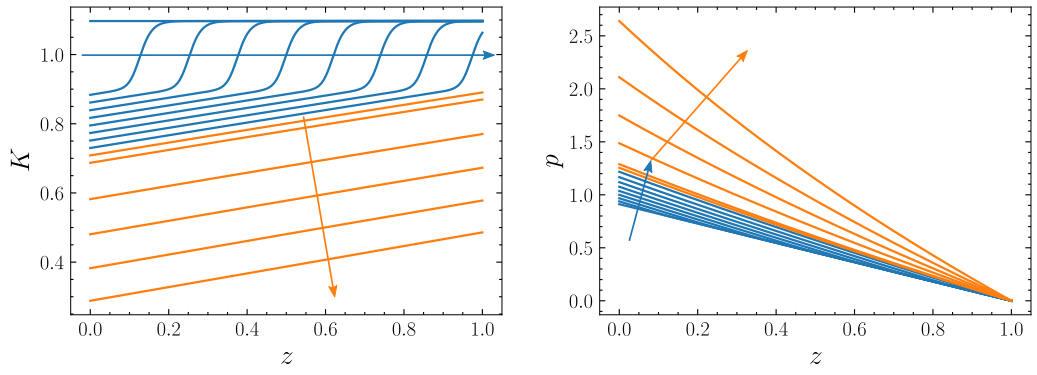

(a) (b)

Figure 4.20: Graphs showing how the local permeability, K, and local pressure, p, vary with the depth, z, at various times, t. The parameters are $\Lambda_B = 200$, $\Lambda_D = 100$, $\Gamma = 1$, $A = 1$, $\sigma_n = 0.2$, $\phi^*_{\text{init}} = 0.9$, $\varsigma_D = 0.001$. The times, t, at which the wave travels through the filter are shown in blue. The values of t shown in blue are $10, 20, \ldots, 70, 80$. The blue arrow shows the direction of increasing t for these values. The times after the wave has travelled through the filter are shown in orange. The values of t shown in orange are $90, 100, 150, 200, 250, 300$. The orange arrow shows the direction of increasing t for these values. (a) The local permeability, K. (b) The local pressure, p.

Global porosity and global permeability

In Figure 4.21 we demonstrate how the global porosity, $\bar{\phi}$, and global permeability, $\bar{K}$, vary with time, t. These variables are also split into two time regions. In the earlier one, they decrease linearly until the critical time, $t \approx 90$. The gradient is similar to that in the no-deposition case, since the majority of the clogging is caused by blocking (since this occurs with unit probability), but is steeper, since deposition also occurs behind the waves. As a result, the variables reach values below the previously observed critical values, $\varphi_{[r>A]}$ and $\kappa_{[r>A]}$, by the time that particles have reached the outlet for the first time. After this time, $t \approx 90$, unlike in the blocking regime, the global porosity and permeability continue to decrease. This is still due to a combination of blocking and deposition, but the rate is slower, because most smaller pores have already been blocked and the majority of clogging is deposition in larger pores. The difference in the rates is determined by $\varsigma_{\mathrm{D}} = 0.001$, so that deposition only occurs around 0.1% of the time that blocking does. Filtration processes are usually halted when the ratio of the global permeability as a proportion of the initial global permeability drops below some threshold. We use a value of around 0.35 here. As we have discussed, this ratio dictates the inlet pressure required to maintain a constant flux, which must not exceed some maximum value due to external operational constraints such as energy usage or safety precautions. However, once the wave has traversed the filter, the filtrate is more likely to contain too many particles, because fewer are removed from the fluid due to blocking.

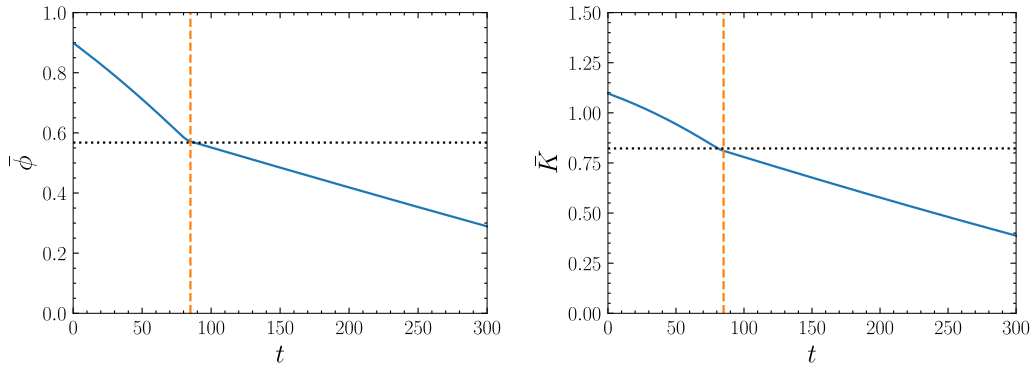

(a) (b)

Figure 4.21: Graphs showing how the global porosity, $\bar{\phi}$, and global permeability, $\bar{K}$, vary with time, t. The parameters are $\Lambda_{\mathrm{B}} = 200$, $\Lambda_{\mathrm{D}} = 100$, $\Gamma = 1$, $A = 1$, $\sigma_n = 0.2$, $\phi^*_{\mathrm{init}} = 0.9$, $\varsigma_{\mathrm{D}} = 0.001$. The values of the large-pore porosity, $\varphi_{[r>A]}$, and large-pore permeability, $\kappa_{[r>A]}$, are plotted in black dotted lines. The times at which corners in the solutions occur are extrapolated in orange dashed lines. (a) The global porosity, $\bar{\phi}$. (b) The global permeability, $\bar{K}$.

Pore-size distribution

We plot the inlet pore distribution, $n(0,t,r)$, as a function of the pore size, r, for various times, t, in Figure 4.22. Earlier times are displayed in Figure 4.22(a), while later times are shown in Figure 4.22(b).

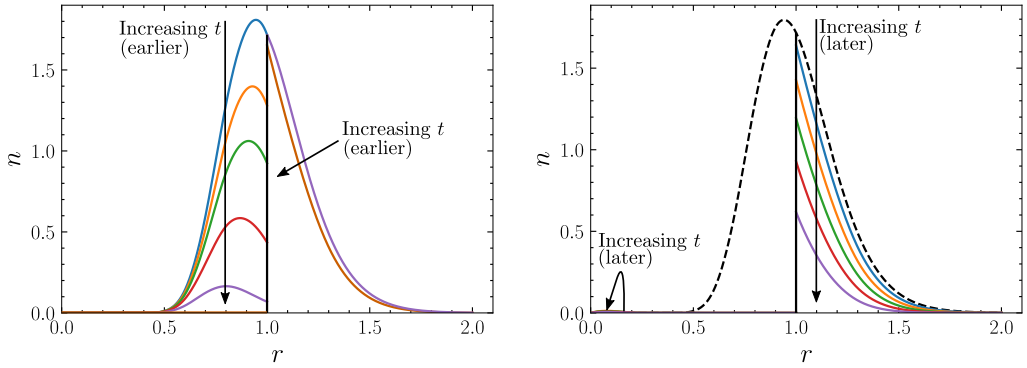

(a) (b)

Figure 4.22: Graphs showing how the pore-size distribution at the inlet, $n(0,t,r)$, varies with the pore size, r, for various times, t. The parameters are $\Lambda_B = 200$, $\Lambda_D = 100$, $\Gamma = 1$, $A = 1$, $\sigma_n = 0.2$, $\phi^*_{\text{init}} = 0.9$, $\varsigma_D = 0.001$. The arrows show the directions of increasing time. The particle size, $A = 1$, is highlighted with a solid black line. (a) The solution at earlier times. The values of t are 0.00 (blue), 0.25 (orange), 0.50 (green), 1.00 (red), 2.00 (purple), 50 (brown). (b) The solution at later times. The values of t are 50 (blue), 100 (orange), 150 (green), 200 (red), 250 (purple). The initial pore-size distribution is plotted in a dashed black line.

Firstly, we focus on the solution at earlier times. In Figure 4.22(a) we see that, initially (blue line), the pore sizes are distributed log-normally, as prescribed. At non-zero times, we see that the solution behaviour is split into the two regions, $r \leq A$ and $r > A$. In the first region, we see that the distribution of the smaller pores rapidly drops towards zero, and has almost reached zero by $t = 2$ (purple line). Particles enter the filter at the inlet and immediately block pores that are smaller than the particles. This happens whenever particles flow to smaller pores, and happens over a short length, so smaller pores are lost rapidly. In the second region, we see that the distribution evolves much more slowly. Particles enter large pores at the inlet and deposit in them. But this only happens 0.1% of the time that blocking does, and happens over a longer length scale (since $\Lambda_D < \Lambda_B$), so deposition does not make a visible difference to the distribution of larger pores until later times.

Secondly, turning our attention to the solution at later times, in Figure 4.22(b) we see that the solution is still split into the behaviour of pores that are larger and smaller than the particles. At later times, all the small pores have been removed at the inlet, due to the blocking that took placed at earlier times. We see that larger pores are still being removed due to deposition. This happens much more slowly than by blocking (noting that the difference in times here is 50 as opposed to $\mathcal{O}(1)$ in the

early time plot). We see that deposition in the large pores leads to the production of small pores. At times around 100 (orange line), the rate at which small pores are produced due to deposition exceeds than the rate at which small pores are removed due to blocking. Even though deposition happens with lower probability, it happens more often, since particles are more likely to flow to large pores, and by late times, there are more large pores than small pores to flow to. However, by times around 150 (green line), the number of large pores has decreased. The rate of removal of the smallest pores outweighs their production again, and the distribution of small pores returns to values near zero.

Thus, we have explored the blocking only, and combined blocking and deposition cases. When there is no adherence between particles and pores, so that deposition does not occur, particles are removed from the fluid in a wave that traverses the filter, and particle capture terminates when this wave first reaches the outlet, since there are no more small pores to block the particles. When deposition can occur, particles are still removed in a wave over roughly the same time interval. However, filtration continues after the wave reaches the outlet for the first time, because deposition continues to remove larger pores and create smaller ones that are blocked. The filtration process is less efficient in this second time interval, because the majority of particle capture occurs due to deposition, which occurs less frequently than blocking.

Chapter 5

Conclusions for the size-structured model

In summary, in Part I, in Chapters 2–4 we have motivated, derived, and solved a novel size-structured model for filtration. Our model will be useful for increasing our understanding of the filtration process, and for filter optimisation, and there are several extensions to be considered in future work.

5.1 Summary

5.1.1 Motivation for the model

In Chapter 2, we introduced size-structured modelling in the context of filtration. In particular, in Section 2.1, we highlighted the importance of the sizes of particles and pores in industrial filtration processes and explained that knowledge of the particle size is often key to choosing the distribution of pore sizes in the filter. Tracking both distributions is crucial for evaluation and optimisation of the process.

In Section 2.2, we explored existing mathematical models of filtration that account for size. Broadly, we found that continuum models are computationally tractable but do not fully account for particle- and pore-size distributions, or the interplay between the two. On the other hand, discrete models that discuss size structure are often computationally expensive, since the states of each particle and pore are usually tracked individually.

In Section 2.3, we noted that there is a need for a computationally tractable model of filtration that more completely accounts for size structure. We discussed ideas used in age-structured models for population, and concluded that this is a candidate framework.

5.1.2 Derivation of the model

In Chapter 3, we used ideas from age-structured population models to derive a size-structured model for filtration, within which the sizes of particles and pores are treated

as independent variables. In Section 3.1, we modelled the feed fluid and filter as continua of particles and pores, and defined distributions of these. Other quantities of interest, such as the particle and pore concentrations, and the local porosity and permeability of the filter, were derived as variables that depend on these distributions. We included two mechanisms by which particles are captured in pores: blocking (when particles are too large to traverse pores) and deposition (when particles are small enough to traverse pores but stick to pore walls as they do so), and built our model around conservation equations for fluid, particles, and pores. The result of this section is a system of continuous partial integro–differential equations that consist of:

- An advection–reaction equation for the particle distribution that describes the movement of particles through pores due to a constant flow rate or a constant pressure drop, and the reduction of the distribution of particles in the fluid due to blocking and deposition in pores;
- A reaction equation for the pore distribution that describes the decrease of the pore distribution due to the capture of particles by either blocking or deposition, and the increase of the distribution of smaller pores due to deposition of particles in larger pores;
- A fluid-mass conservation equation and Darcy's equation, which together govern the flow rate and local pressure in the fluid.

In Section 3.2, we nondimensionalised the model and found that there are four dimensionless parameter groups of interest: Λ_B (the ratio of the filter length to the blocked-particle length); Λ_D (the ratio of the filter length to the deposited-particle length); ς_D (the probability that deposition of particles in smaller pores occurs); and Γ (the ratio of the concentrations of particle and pores). Furthermore, parameters such as the mean particle size, A, and the pore size variance parameter, σ_n, dictate the particle- and pore-size distributions of the specific operational regime.

5.1.3 Solution of the model

In Chapter 4, we found explicit, asymptotic, and numerical solutions for the dimensionless model in various regimes. In Section 4.2, we focused on the case where the feed and filter are both mono-dispersed. We considered the scenario where the pores are smaller than the particles, so that only blocking occurs. We discussed the case in which there is an excess of pores in the filter compared to the number of particles in the feed, $\Gamma \ll 1$, and the case where the filter is very long compared to the size of a particle, $\Lambda_B \gg 1$. In both cases, we found explicit leading-order asymptotic solutions that agree well with numerical solutions in the appropriate limits. Broadly, we found that, when particles are larger than pores, particles are captured in a layer very close to the inlet. The thickness of the capture layer is $\mathcal{O}(\Lambda_B^{-1})$. One consequence is that, when all particles are larger than the pores, only a small proportion of the filter membrane is used to obtain a required particle removal and the vast majority of the filter membrane is wasted. Increasing Γ, we found, understandably, that as the particle concentration increases, the filter clogs more quickly.

In Section 4.3, we turned our attention to the case where particles are all one size, but the distribution of pore sizes is log-normal. Firstly, we once again considered the case where only blocking occurs. We found that this situation gives rise to a wave of particles that gradually traverses the entire filter. Upstream of the wave front, particles have blocked all pores that are smaller than the particles, and the concentration is dictated by the number of particles that occupy pores that are larger than the particles. Downstream of the wave front, there are no particles, since they were all removed further upstream. In the travelling capture layer, which is of thickness $\mathcal{O}(\Lambda_{\mathrm{B}}^{-1})$, particles block any smaller pores that still remain, and so the particle concentration transitions from its upstream value to its downstream value. Pores that are larger than the particles keep their original distribution, since they are unaffected by particles that are smaller than them when deposition occurs with zero probability. We found an explicit formula for the speed of the travelling wave that depends on the characteristic ratio of the concentrations of particles in the feed and pores in the filter, Γ, the characteristic length over which blocking occurs, $\Lambda_{\mathrm{B}}^{-1}$, and the initial concentration of pores that are smaller than the particles, $N_{[r<A]\mathrm{init}}$.

Secondly, we considered the case where blocking and deposition both occur. In the limit where there are many more pores than particles, $\Gamma \ll 1$, we found an explicit leading-order asymptotic solution and used this to show that particles are captured over a layer at the top of the filter, the thickness of which decreases as the particle size increases, at least when the characteristic blocking length is shorter than the characteristic deposition length, so that $\Lambda_{\mathrm{B}}^{-1} < (\Lambda_{\mathrm{D}}\varsigma_{\mathrm{D}})^{-1}$ (due to particles spreading when they deposit, or a small sticking probability, $\varsigma_{\mathrm{D}} \ll 1$, for example). In the limit $\Gamma \ll 1$, we saw that most pores in the filter are not used to capture particles. We then explored the case $\Gamma = \mathcal{O}(1)$. We solved the system numerically and showed that, as in the case of no deposition, a particle wave travels through the filter. This time, however, the particles that are left in larger pores upstream of the wave continue to deposit within them, which causes further reduction to the distribution of large pores long after the wave front has passed. The decrease is most severe at the inlet, where particles have had the most chance to deposit. Depending on the required retention threshold, it could be argued that the useful lifetime of the filter is much longer when deposition can occur as opposed to when it cannot (consistent with observations in [123], for example). When it can occur, particle capture continues long after the wave has reached the outlet for the first time, until all pores have been removed. However, at later times, far fewer particles are captured per unit time, so that the fluid exiting the filter is likely to contain many particles.

5.2 Further work

There are several natural extensions to our work, which we will discuss in this section.

5.2.1 Poly-dispersed particles and poly-dispersed pores

In this thesis, we limited our analysis to the cases where either the feed and filter are mono-dispersed, or the feed is mono-dispersed and the filter is poly-dispersed. However, one of the advantages of this model is that it is a simple framework within which to analyse the case where the feed and filter are both poly-dispersed, a case that industrialists are interested in, to assess the size distribution in the filtrate, for example. In Section 3.1 we wrote down the condition at the inlet in the case where particles are log-normally distributed, and our future work would include solving the model in this case.

5.2.2 Depth-dependent initial pore-size distributions

We focused our analysis on the case where the initial distribution of pore sizes is independent of depth. It would be interesting to introduce depth dependence, via, for example, a depth dependent mean pore size parameter, $\bar{r}^*(z)$, a depth dependent pore size variance parameter, $\sigma_n(z)$, or a depth dependent initial porosity function, $\phi^*_{\text{init}}(z)$. In the case where particles are mono-dispersed and pores are poly-dispersed, we found that, once the wave has passed, a gradient in the particle concentration and porosity is established, because deposition, and subsequent blocking, occur more often at the top of the filter than at the bottom. If we stipulated that, on average, pores increased in size towards the top of the filter (as in [124] or [125], for example), then deposition would have less effect on the porosity, per occurrence, at the top of the filter than at the bottom. By tailoring the pore size gradient, it might therefore be possible to establish a regime in which the porosity decreases uniformly across the filter. This would be favourable as it would mean that the lifetime of the filter would be extended, since it would take longer to reduce the porosity near the inlet (and further down the filter) to zero. Whether this proposed lifetime extension is useful depends on the adherence between particles and pores. If this is large enough (close to one), then significant retention continues after the particle wave has traversed the filter.

5.2.3 Deposition transformation and sticking probability

In our simulations, we chose simple forms for the deposition transformation distribution and for the sticking probability. We supposed that, after deposition, the reduction in pore size was always exactly the particle size, and that the adherence between particles and pores is a constant that is independent of their sizes. Further work would include solving the model using more realistic forms for these two functions, motivated by physical intuition, experimental evidence, or detailed mathematical modelling of the physics and chemistry on the microscale. Choosing a depth-dependent sticking probability, for example, may provide an industrially relevant alternative to depth-grading the initial pore-size distribution. That is, if the probability of sticking is small (or even zero) near the inlet, but increases towards the outlet, then for a well-chosen pore-size distribution, we would expect a greater number of pores to be used

for particle retention than in the scenario where the sticking probability is depth independent.

5.2.4 Additional particle and pore interactions

Our model provides a framework for filtration modelling, upon which many additional features could be added. We did not discuss particle–particle interactions, for example, but it would be relatively simple to include additional terms to describe, say, particle coagulation, by modelling this as the sticking together of small particles to form larger particles. Additionally, our current model does not account for 'caking', which is the build-up of particles on the surface of the filter to form a layer through which the feed must permeate. Extending our model to account for this behaviour would make it more versatile, and would be another feasible addition, since our framework captures the evolution of the pore distribution, so that the prediction of the onset of caking (when the pores at the surface of the filter become small enough for particle build-up on the surface to begin) would be relatively straightforward.

5.2.5 Optimisation and experimental data

Since repeated solution of our model is computationally feasible, it lends itself to optimisation problems, but we did not focus on these in this thesis. It would be relatively simple, for example, to construct an experiment where a performance metric is returned for each value of a given parameter, which is incrementally changed. The result would be the performance metric, such as the proportion of particles retained, or the useful lifetime of the filter, say, as a function of the parameter, which would be useful for improvement of the filtration regime. Lastly, in future work, it would also be interesting to compare our results to experimental data. This would allow use to verify our solution, and to find exact physically relevant parameter regimes.

In Part I we have developed a mathematical framework for filtration in which the filter and feed are continua of pores and particles, with their sizes accounted for. In future, the model will be useful to increase our understanding of filtration processes and to enhance filter performance. In Part II, we will turn our attention to an alternative framework for filtration, in which the filter membrane is considered as a network of pores.

Part II

A network model for filtration

Chapter 6

Introduction to the network model

6.1 Networks in filtration

In Chapter 1, we introduced expanded polytetrafluoroethylene (ePTFE) as a filtration membrane material of interest, and explained that the microscale consists of a mesh or fibres. This gives rise to a complex network of pore space between them, through which particle-laden fluid is transported. Intuitively, the exact geometry of the pore space has a significant influence on the effective properties of the filter. For example, if the space between fibres is larger, then more fluid is advected through it per unit time, causing a larger effective permeability. If the space is smaller, then particles are close to fibres more often, so we might expect larger effective adhesivity (i.e., the overall 'stickiness' of the filter that quantifies its ability to capture particles).

Due to this link between microscale geometry and macroscale behaviour, much attention has been paid to the accurate determination of microscale structure (see [75] for a useful review, and [64, 126–130] for some general examples). One significant experimental complication is the evolution of the microscale structure that occurs during filtration. Mechanical, chemical, and electrostatic interactions between particles and fibres (that act as pore walls) cause adherence between them. This leads to deposition of particles on pore walls, and thus changes to the size and shape of pores as filtration occurs. These structural changes are difficult to capture empirically because observations of the process are usually invasive and may even involve destruction of the filter membrane itself.

One alternative approach is to mathematically model these changes to the microscale by representing it as a directed and weighted network of nodes and edges and then posing governing equations on this geometry (see [131–133], for example). In this context, node and edge weights usually represent pore size, and deposition is modelled as a decrease in the concentration of particles in the fluid that is accompanied by changes to these weights, and thus the connectivity of the network. Unsurprisingly, to a large extent, the success of this strategy depends on the degree to with which the initial network represents the initial microscale of the membrane [75].

The network representation process, by which a network is obtained, is therefore

critical. It usually consists of two steps, which are illustrated in Figure 6.1. First, methods that are broadly referred to as experimental characterisation are used to produce high resolution images of the microscale. Second, so-called network construction algorithms are used to transform these images into a network of nodes and edges that together represent pore space.

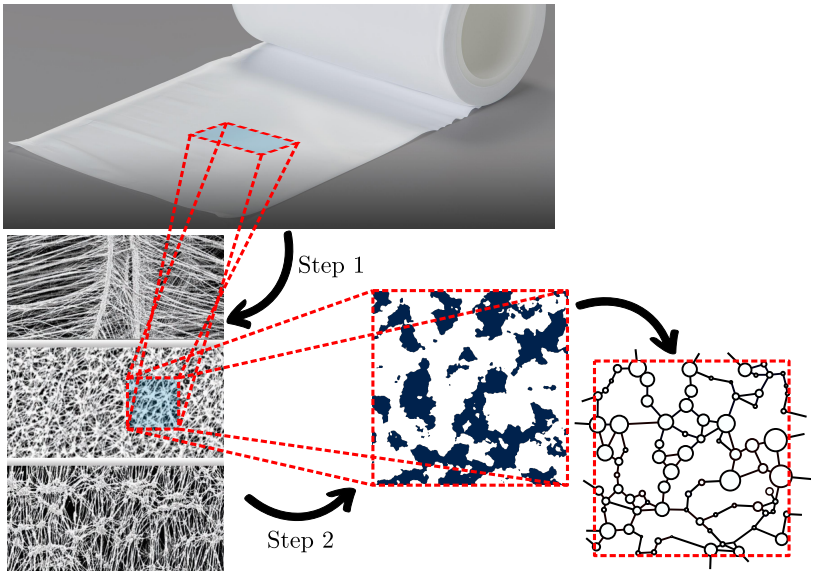

Figure 6.1: An illustration of network representation, which is the systematic extraction of a network from the microscale of filtration membranes such as ePTFE. Step 1 is experimental characterisation, in which high resolution images of the microscale are obtained. Step 2 is network extraction, in which the microscale is algorithmically segregated into solid space and pore space, before the pore space is further separated into nodes and edges that form a network.

The choice of characterisation strategy depends heavily on the filtration material. Some common methods include: X-ray computed microtomography (micro-CT) [134, 135]; Focused ion beams (FIB) and Scanning electron microscopy (SEM) [64, 136–139]; Nuclear magnetic resonance (NMR) [140, 141]; and Mercury intrusion porosimetry (MIP) [142–144]. Characterisation using gas adsorption techniques [145] can also be useful, since the adsorption behaviour of porous materials is a function primarily of their microstructure [75]. In most characterisation methods, a trade-off is established between representation and resolution. The portion of the microscale selected must be large enough to permit good representation of the filter as a whole, whilst still being small enough to permit a resolution that is sufficient for algorithmic post-processing.

The choice of network construction algorithm depends to a large extent on the characterisation method employed, and on the type of image that this produces. Some examples are: Direct mapping [146]; Medial axis algorithms [147–150]; and Grain-based models [151–155]. One alternative approach is to use statistical reconstruction methods, which obtain larger networks that have the same statistical properties as characterisations of smaller portions of the membrane [156–159]. For example, images of small membrane samples are analysed for the average coordination number (the

number of other nodes that are connected by edges to each node on average) and pore-size distribution, and then a larger network with identical statistical properties is constructed, sometimes with more regular or periodic structure [75].

Over the past few decades, network representation has received considerable attention, and both experimental characterisation and network construction have become substantial subject areas in their own right. They are, however, far too broad and diverse for complete examination here. It suffices to note that, in general, the output of the these two processes in series is a network of nodes and edges, the connectivity and size distribution of which are known, and preserve or at least statistically represent the topology of the microscale pore space of the filtration medium.

6.2 Existing network models for filtration

Equation systems defined on network geometries are often referred to as pore network models (PNMs). These describe the transport and deposition of particles that occurs in nodes or edges, or both. The first PNM was constructed by Fatt in 1956 [160]. It exploits the analogy between the microscale of porous media and electrical resistor networks. Fluid flow plays a similar role as electrical current, and the fluid conductance of edges is analogous to the inverse resistance of resistors, so that conservative laws for fluid mass can be written as Kirchoff's law [161, 162]. Much of the notation in PNMs is borrowed from percolation theory, as are several of the central ideas. For example, in [163], Grimmett studies the effect of the coordination number of some simple networks with regular structure on the effective properties of one-phase fluid flow. PNMs have rapidly grown in sophistication [75], and have since been extended to study the properties of irregular networks and two- and three-phase flow through them, as well as a variety of different physical processes [164–168].

In many studies, the notion that the connectivity and size distribution of edges (usually modelled as cylinders with specified initial radius) and nodes (often modelled as spheres of given initial size) affect transport coefficients is central [151, 169, 170]. It has been shown that microscale structure impacts important industrial indicators of filter performance. In [107], for example, Griffiths *et al.* find that increasing the complexity of random edge connectivity increases the tortuosity of the filter, which substantially improves its particle removal efficiency. Meanwhile, in [124], Sanaei *et al.* find that even incorporating simple symmetric branching structure allows for the study of the effect of pore size gradients on clogging patterns and thus filter performance.

Generally, PNMs that model the fluid suspension as a continuum and the filter medium as a network are useful for models of the mesoscale of membranes. Systems with tens or hundreds of nodes and edges can be used to represent sections of porous media that are too large for simulations that track each particle to be computationally feasible. On the other hand, PNMs can be more accurate than PDE systems that usually involve Darcy flow coupled with advection–reaction equations, since these typically ignore microscale geometry that is still important at this scale.

6.3 A novel network model for filtration

Broadly, our ultimate aim in Part II is to present a relatively simple PNM, with the goal of incorporating this into a multiscale framework in Part III. As such, in Part II, the objective is not to provide detailed analysis of a complex network model that fully accounts for the intricacies of the phenomena that occur on the microscale of the membrane as filtration occurs. Instead, we will derive a relatively straightforward network model and illustrate intuitive solutions in one particular operating regime.

To this end, in Chapter 7, we will derive a novel network model for filtration. In Section 7.1, we will begin by supposing that a particle-laden fluid continuum is driven through a network of edges, which model pores, and nodes, which model junctions between them. We will then consider the conservation of fluid mass, particle mass, and pore volume, to derive a governing system. We will suppose that edges are cylinders, and will account for deposition by supposing that particles adhere to the inner walls of these cylinders with some adherence probability, which causes changes to their cross-sectional area and thus their conductance. We will suppose that the initial structure of the network results from the representation methods outlined in Section 6.1, and thus that it is statistically representative of a filtration membrane. Consequently, the pore size distribution, and thus edge conductances and node volumes, as well as the connectivity of the network, are all known initially. The result is a dimensional system of ordinary algebraic–differential equations on a directed and weighted network whose weights and connectivity change with time. To demonstrate solution of this system, we will establish suitable initial and boundary conditions for closure that represent a toy operating regime that is simple enough for intuitive interpretation. In Section 7.2, we will nondimensionalise this system, introduce dimensionless parameter groups, and prepare it for solution and analysis.

In Chapter 8, we will briefly discuss solutions of this network model. In Section 8.1, we will begin by discussing our numerical strategy. Emphasis is placed on the computational cost of solution, which, as we have discussed, allows for simulation of tens or hundreds of nodes and edges. With this in mind, in Section 8.2, we describe the numerical solutions of the system on a relatively small network. We consider a four-regular network containing nodes and edges of equal volume and conductance, which corresponds to a membrane with mono-dispersed pore sizes and an average coordination number of four. We will show examples of how macroscale properties, such as average particle concentration, effective conductivity, average flow rate, and filter pressure drop, can be derived from the microscale variables that solve the network model. We will then explore their changes as functions of the system parameters, which correspond to the adherence probability in the pores and to the average size of particles in the suspension. Consequently, we will find that these parameters affect properties of industrial interest, such as the efficiency (the proportion of particles that are retained in the filter) and total throughput (the total quantity of fluid that is processed before termination of the filtration regime). Solution of the model on random networks with log-normally distributed pore sizes and thus edge conductances is saved for Part III, Section 12.2.

Chapter 7

Derivation of the network model

In this chapter, we develop a model for filtration in which the filter is treated as a network of edges, which model pores, and nodes, which model the junctions between them. We begin by deriving a dimensional system of algebraic–differential equations for the concentration of particles, the conductance of pores, and the pressure. We pose industrially relevant boundary and initial conditions, and then scale the problem to arrive at a dimensionless system to be analysed and solved.

7.1 Dimensional model

We consider a filter membrane that is composed of a network that is embedded in D-dimensional space, where $D \in \{1, 2, 3\}$, as illustrated in Figure 7.1. The filter is located between $\boldsymbol{x} = \boldsymbol{0}$ and $\boldsymbol{x} = \boldsymbol{l}$, so that the m^{th} component of $\boldsymbol{l}$, l^m, is the length of the network in the m direction. The network consists of a series of pores, which we model as edges, that are connected to one another at junctions, which we model as nodes.

A particle-laden fluid is driven through the filter in the x^1 direction. The fluid enters the filter at the inlet, which is located at $x^1 = 0$, and passes through the pores via the junctions until it reaches the outlet, which is located at $x^1 = l^1$. As the fluid traverses the filter, particles in the fluid deposit on the inner walls of the pores due to a mutual adherence between the particles and pores. This deposition decreases the cross-sectional area of the pores (see Figure 7.1), which decreases their fluid conductance. Eventually, pores are removed completely, which causes a change in the connectivity of the network within the filter. In the next subsection, we define objects to track the pores in the filter and the particles in the feed fluid.

7.1.1 Particles and pores

We track pores by defining $G_{ij}(T)$ to be the conductance of pore ij at time T, so that $[G_{ij}] = \mathrm{m}^D\mathrm{s}^{-1}\mathrm{Pa}^{-1}$ (recall from Chapter 3 that we use $[x]$ to mean 'the dimensions of x'). Defining $P_i(T)$ to be the pressure in junction i at time T, so that $[P_i] = \mathrm{Pa}$,

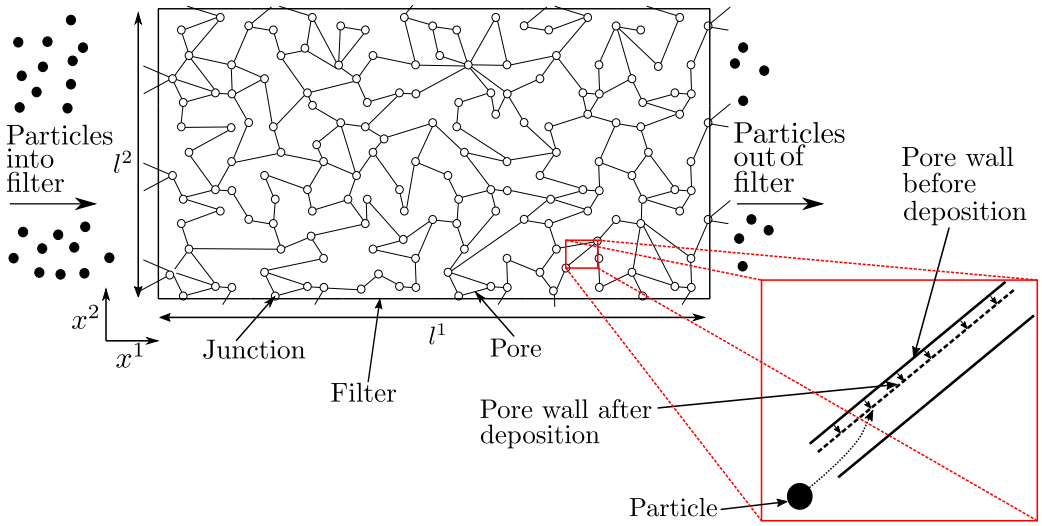

Figure 7.1: A diagram showing a two-dimensional filter that is composed of a network of pores, which are visualised as edges, and junctions, which are visualised as nodes. Particles in the flow enter through edges crossing the left boundary and exit through those crossing the right boundary after traversing the network. Particles deposit in pores, and their volume is spread uniformly across the pore walls, which decreases the cross-sectional area of the pores.

we write

$$Q_{ij} = G_{ij}\,(P_i - P_j)\,. \tag{7.1}$$

Here, $Q_{ij}(T)$ is the volumetric flux through pore ij at time T, which is the volume of fluid that is transported from junction i to junction j along pore ij per unit time, so that $[Q_{ij}] = \mathrm{m}^D\mathrm{s}^{-1}$.

To track particles, we first define $V_i(T)$ to be the volume of junction i, so that $[V_i] = \mathrm{m}^D$. Next, we define $C_i(T)$ to be the concentration of particles in junction i, which is the number of particles per unit volume of void space (i.e., node volume plus edge volume) in junction i at time T, so that $[C_i] = \mathrm{m}^{-D}$. For simplicity, we consider the case where the filter and void particle concentrations (discussed in Part I), are equal: the total node volume, V_N, represents junctions that make up the bulk of pore space; the total edge volume, V_E, represents small conductive pore space regions between junctions; and the total fibre volume, V_F, represents tiny fibres that make up the solid space external to the network. We choose $V_\mathrm{E}, V_\mathrm{F} \ll V_\mathrm{N}$, and note that, since the porosity (i.e., the ratio of pore space to filter space) is given by $\phi = (V_\mathrm{N} + V_\mathrm{E})/(V_\mathrm{N} + V_\mathrm{E} + V_\mathrm{F})$, it follows that $\phi \approx 1$ (the porosity of ePTFE can exceed 95% [49]). Since void and filter particle concentrations differ only by a factor of ϕ (see (3.4), for example), it follows that they are approximately equivalent in this simple setting. We note that it follows that $V_i(T)C_i(T)$ is the number of particles in node i at time T, a property that we will use to derive an equation to describe the evolution of the particle concentration in the following sections.

7.1.2 Conservation of fluid

We assume that fluid is conserved in each junction. That is, the mass of fluid that enters junction i from pores that are connected to it is equal to the mass that exits junction i to other connected pores. It follows that

$$\sum_{j=1}^{N_\mathrm{f}} Q_{ij} = 0, \tag{7.2}$$

where we define N_f to be the number of junctions in the filter. Note that $Q_{ij} = 0$ if there is no pore connecting junctions i and j.

7.1.3 Conservation of particles

We assume that particles are conserved at each junction. We suppose that, as particles move into junction i from junction j (provided that there is a pore ji between these two junctions), some proportion, $0 \leq A_{ji}(T) \leq 1$ say, of the particles are deposited in pore ji. Since the total number of particles is conserved, the number of particles that arrive in junction i from pore ji in the infinitesimal time-step $T + \delta T$ is equal to the number of particles that leave junction j to the pore ji in this time step minus the number of particles that deposit inside the pore during the time step. Accounting for the possibility that each junction i is connected to more than one pore ji, and taking the limit $\delta t \to 0$, it follows that

$$\frac{\partial (V_i C_i)}{\partial T} = \sum_{j=1}^{N_\mathrm{f}} \Big((1 - A_{ji}) Q_{ji} C_j H(P_j - P_i) - Q_{ij} C_i H(P_i - P_j) \Big). \tag{7.3}$$

We call $A_{ji}(T)$ (which is equal to $A_{ij}(T)$) the adherence of pore ji at time T, with $[A_{ji}] = 1$. This is the fraction of particles in junction j that deposit in pore ji when they are transported to junction i, and therefore represents the 'stickiness' between pore ji and the particles. If $A_{ji} = 0$, for example, then no particles stick inside pore ji, and all particles that leave junction j arrive in junction i, while if $A_{ji} = 1$ then all of these particles get stuck in pore ji before they arrive in junction i, and contribute to the decrease of the cross-sectional area of the pore. Meanwhile, H denotes the Heaviside function,

$$H(P_i - P_j) = \begin{cases} 1 & P_i - P_j > 0, \\ 0 & P_j - P_i < 0. \end{cases} \tag{7.4}$$

In (7.3), we consider particle conservation at junction i. H ensures that only deposition in pores ji upstream of junction i (i.e., those that connect it to junctions j for which $P_j > P_i$) is accounted for in this conservation law, to avoid double counting deposition. Specification of $H(0)$ is not necessary, provided that the imposed filter pressure difference is unidirectional for all time. In this case, for any connected junctions i and j, G_{ij} decreases monotonically (due to deposition, via (7.9)) but never

reaches zero, and so the inequality $P_i > P_j$ is preserved (via (7.2)) for all time. Therefore, if pore ij conducts fluid from junction i to junction j initially, then it does so for all time. We restrict our study to unidirectional filter pressure differences (see (7.27)). In Chapter 11, we will see that this permits asymptotic expansion of H as a continuous function, away from the discontinuity at $P_i = P_j$.

7.1.4 Conservation of pores

We assume that pore volume is conserved so that when particles deposit within a pore, the volume of the pore decreases. As in the particle-conservation equation, (7.3), we suppose that deposition occurs at a rate that is proportional (by a factor of the adherence) to the number of particles that enter the pore per unit time. Assuming that particles deposit uniformly along the length of a pore (see Figure 7.1), conservation of pore volume implies that the decrease in the cross-sectional area of a pore in the infinitesimal time-step $T + \delta T$ is equal to the cross-sectional area occupied by particles that flow into the pore and stick to it in that time step. Taking the limit $\delta T \to 0$, it follows that

$$\frac{\partial(\pi R_{ij}^2)}{\partial T} = -SA_{ij}C_{ij}|Q_{ij}|, \tag{7.5}$$

where R_{ij} is the radius of edge ij, so that $[R_{ij}] = \mathrm{m}$. Here, C_{ij}, which we interpret as the concentration of particles in pore ij, is the same as the particle concentration in the junction upstream of the pore, so that

$$C_{ij} = \begin{cases} C_i & P_i > P_j, \\ C_j & P_i \leq P_j. \end{cases} \tag{7.6}$$

The edge-independent constant (for simplicity) of proportionality, $S \geq 0$, with $[S] = \mathrm{m}^{D-1}$, is the particle-size parameter, which represents the cross-sectional area (volume per unit length) that the particles that deposit in the pore occupy. The case $S = 0$ corresponds to absorption, in which particles deposited in pore ij do not alter its cross-sectional area, so that the structure of the network is static. The filter is unaffected by particle retention, and never becomes clogged. We will not discuss this case further. The case $S < 0$ corresponds to pore expansion due to erosion effects, which is also out of scope for the present work. The case of interest is $S > 0$. In this scenario, deposition decreases the cross-sectional area of pore ij, and the size of S determines the extent of this effect.

We suppose that flow in pores is laminar, so that it satisfies the Hagen–Poiseuille equation (see [109], for example), which is given by

$$P_i - P_j = \frac{8\mu L_{ij} Q_{ij}}{\pi R_{ij}^4}, \tag{7.7}$$

where L_{ij} is the length of pore ij, so that $[L_{ij}] = \mathrm{m}$, and μ is the dynamic viscosity of the fluid, with $[\mu] = \mathrm{Pa\,s}$. Using the definition of the pore flux, (7.1), with the

Hagen–Poiseuille equation, (7.7), it follows that the conductance is related to the cross-sectional area via

$$G_{ij} = \frac{\pi R_{ij}^4}{8\mu L_{ij}}. \tag{7.8}$$

Using (7.8) to substitute the cross-sectional area for the conductance in the pore-area conservation equation, (7.5), we arrive at the conductance equation,

$$\frac{\partial G_{ij}}{\partial T} = -\frac{2S}{(8\pi\mu)^{\frac{1}{2}} L_{ij}^{\frac{1}{2}}} A_{ij} C_{ij} G_{ij}^{\frac{3}{2}} |P_i - P_j|. \tag{7.9}$$

In the next subsection we define boundary conditions for the governing equations, (7.1)–(7.6).

7.1.5 Boundary and initial conditions

To define the boundary of the filter, we introduce 'in' and 'out' nodes, which are two nodes that are external to the network in the direction of the flow (see Figure 7.2). We refer to these nodes with two further indices: in and out. We call nodes that are connected to the in and out nodes 'inlet' and 'outlet' nodes, respectively. We impose zero adherence on the edges that connect the inlet and outlet nodes to the in and out nodes so that their conductances remain constant. These are not pores, but rather external edges necessary to conduct fluid in and out of the filter. These represent the inlet and outlet boundaries of the filter. We define the external edges to the outermost nodes on the sides of the network that are parallel to the flow as the other boundaries of the filter, and suppose that solution variables are periodic across these.

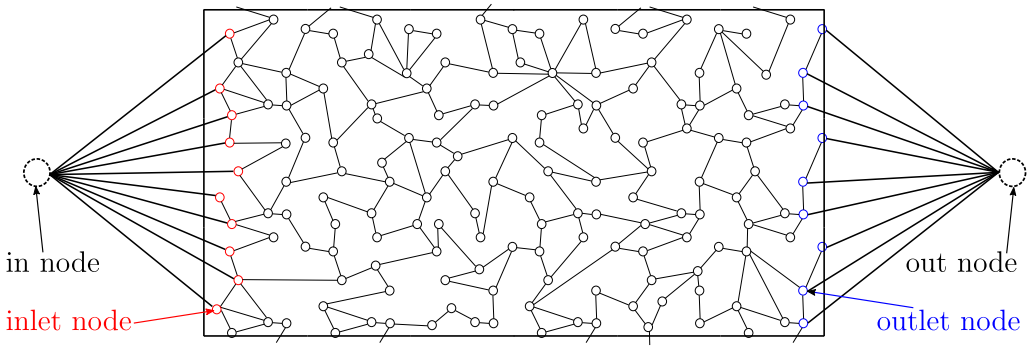

Figure 7.2: A diagram showing a network embedded in two dimensions, connected to in and out nodes, which are external. Inlet and outlet nodes are coloured red and blue, respectively.

We assume that the fluid flow is driven by a known pressure drop from the inlet to the outlet. We suppose that the pressure at the inlet and outlet are given by $p_{\text{in}}(T)$

and $p_{\text{out}}(T)$ respectively, and thus write

$$P_{\text{in}}(T) = p_{\text{in}}(T), \quad P_{\text{out}}(T) = p_{\text{out}}(T), \tag{7.10a,b}$$

for $T \geq 0$. Additionally, the concentration of particles in the feed fluid, $c_{\text{in}}(T)$ say, is known, and we write

$$C_{\text{in}}(T) = c_{\text{in}}(T), \tag{7.11}$$

for $T \geq 0$.

Initially, we suppose that there are no particles in the filter, so that

$$C_i(0) = 0, \tag{7.12}$$

for $i \in \{1, \ldots, N_{\text{f}}, \text{out}\}$. Note here that $i \neq \text{in}$, since $C_i(0) = c_{\text{in}}$ for $i = \text{in}$ (from the boundary condition (7.11)). Furthermore, we suppose that the initial pore-size distribution is given, from which the initial pore conductance values can be deduced. Thus, we write

$$G_{ij}(0) = G_{ij}^0, \tag{7.13}$$

for $i, j \in \{1, \ldots, N_{\text{f}}, \text{in}, \text{out}\}$, where G_{ij}^0 is the known initial-conductance of pore ij.

7.1.6 Operational regime

The forms of the functions L_{ij}, A_{ij}, V_i, p_{in}, p_{out}, and c_{in}, and the values of the parameters G_{ij}^0, depend on the industrial application of the filter. In this subsection, we specify these in order to demonstrate the solution of the model in the following chapter.

We suppose that deposition in a pore does not affect its length, and so we write

$$L_{ij} = L_{ij}^0, \tag{7.14}$$

where L_{ij}^0 is the constant initial-length of pore ij, which is drawn from a known distribution, $\mathcal{L}$ say, with mean $\bar{L}$. We write $L_{ij}^0 \sim \mathcal{L}(\bar{L})$ to mean that L_{ij}^0 is drawn from the distribution $\mathcal{L}$ that is specified by the parameter $\bar{L}$, with known probability density function (PDF), ℓ, say. It remains to specify a particular distribution, $\mathcal{L}$ (and therefore an associated PDF, ℓ), which depends on the structure of the network. To simplify, we will consider the case where the network is four-regular, which means that each junction is connected to exactly four pores, in a repeating lattice, as in Figure 7.3. In this case, it follows that all pores are the same length, $\bar{L}$, so that

$$\ell(L_{ij}^0) = \delta(L_{ij}^0 - \bar{L}), \tag{7.15}$$

where δ is the PDF for the Dirac-delta distribution.

For simplicity, we assume that deposition does not occur in junctions and write

$$V_i = V_i^0, \tag{7.16}$$

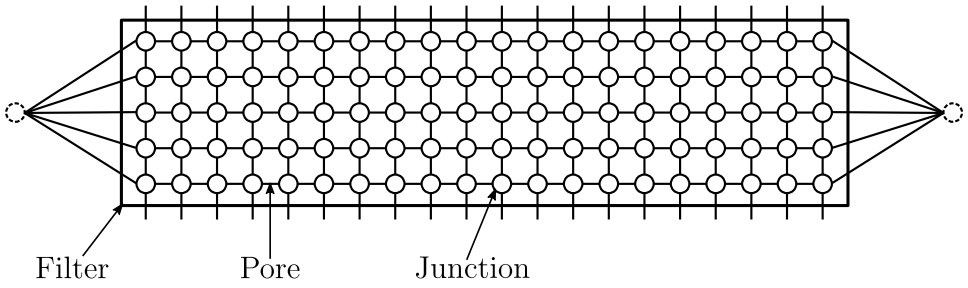

Figure 7.3: A diagram showing a two-dimensional filter represented as a four-regular network.

for some known initial junction-volumes, V_i^0 with $[V_i^0] = \mathrm{m}^D$, so that $V_i^0 \sim \mathcal{V}$ with the PDF $\mathscr{v}$. We will focus on the simplest case, in which all junctions have the same volume, $\bar{V}$ say, so that

$$\mathscr{v}(V_i^0) = \delta(V_i^0 - \bar{V}). \tag{7.17}$$

To further simplify our analysis, we assume that the adherence of a pore is independent of other variables, such as the pore size, and is therefore constant, so that

$$A_{ij} = A_{ij}^0, \tag{7.18}$$

for $0 \leq A_{ij}^0 \leq 1$ with $[A_{ij}^0] = 1$, so that $A_{ij}^0 \sim \mathcal{A}$ with the PDF $\mathscr{a}$. Furthermore, we assume that all pores in the filter have the same adherence, and write

$$\mathscr{a}(A_{ij}^0) = \delta(A_{ij}^0 - \bar{A}). \tag{7.19}$$

We assume that the pressures at the inlet and outlet are known constants, and so we write

$$p_{\mathrm{in}}(T) = p_{\mathrm{in}}^*, \quad p_{\mathrm{out}}(T) = p_{\mathrm{out}}^*, \tag{7.20}$$

where $[p_{\mathrm{in}}^*] = [p_{\mathrm{out}}^*] = \mathrm{Pa\,s}$.

Furthermore, we suppose that the concentration of particles in the feed fluid is also constant and known, so that

$$c_{\mathrm{in}}(T) = c_{\mathrm{in}}^*, \tag{7.21}$$

for $[c_{\mathrm{in}}^*] = \mathrm{m}^{-D}$.

Finally, we assume that the distribution of pore sizes, R_{ij}^0, is known initially. Since the initial length distribution is also known (see (7.15)), it follows (noting, from (7.8), that the conductance is completely specified by the pore radius and length) that we are given the initial pore conductance distribution, $\mathcal{G}$, with PDF $\mathscr{g}$, say. We consider the cases where, initially, the pore radii, and thus the pore conductances,

are either mono-dispersed, with conductance $\bar{G}$, or log-normally dispersed, with mean conductance $\bar{G}$. That is, either

$$g(G_{ij}^0) = \delta(G_{ij}^0 - \bar{G}), \quad \text{or} \quad g(G_{ij}^0) = \frac{1}{\sqrt{2\pi}\sigma_G G_{ij}^0} \exp\left(-\frac{\left(\log\left(\frac{G_{ij}^0}{\bar{G}}\right) + \frac{\sigma_G^2}{2}\right)^2}{2\sigma_G^2} \right). \tag{7.22a,b}$$

In the latter case, $G_{ij}^0 \sim \mathcal{G}(\mu_G, \sigma_G)$ where $\mathcal{G} = \text{Lognormal}$, and the mean and standard deviation of the associated normal distribution are the dimensionless numbers $\mu_G = \log(\bar{G}) - \sigma_G^2/2$ and σ_G, so that $\log(G_{ij}^0) \sim \text{Normal}(\mu_G, \sigma_G)$. It follows that the expected initial pore conductance is $\mathbb{E}[G_{ij}^0] = \exp(\mu_G + \sigma_G^2/2) = \bar{G}$, as required.

7.1.7 Summary of the dimensional model

In summary, using the specific forms of the operational-regime dependent functions and parameters, (7.14)–(7.22), the equations for the conservation of fluid, particles, and pores, (7.2), (7.3), and (7.9), respectively, read

$$\sum_{j=1}^{N_\text{f}} Q_{ij} = 0, \tag{7.23}$$

$$\bar{V}\frac{\partial C_i}{\partial T} = \sum_{j=1}^{N_\text{f}} \Big((1-\bar{A}) Q_{ji} C_j H(P_j - P_i) - Q_{ij} C_i H(P_i - P_j) \Big), \tag{7.24}$$

$$\frac{\partial G_{ij}}{\partial T} = -\frac{2SA}{(8\pi\mu\bar{L})^{\frac{1}{2}}} C_{ij} G_{ij}^{\frac{3}{2}} |P_i - P_j|, \tag{7.25}$$

respectively, where the flux down each pore is related to the pressure drop and conductance of the pore via

$$Q_{ij} = G_{ij}\left(P_i - P_j\right). \tag{7.26}$$

The boundary conditions are

$$P_\text{in}(T) = p_\text{in}^*, \quad P_\text{out}(T) = p_\text{out}^*, \tag{7.27a,b}$$

and

$$C_\text{in}(T) = c_\text{in}^*, \tag{7.28}$$

for $T \geq 0$, and the initial conditions are

$$C_i(0) = 0, \tag{7.29}$$

for $i \in \{1, \ldots, N_\text{f}, \text{out}\}$, and

$$G_{ij}(0) = G_{ij}^0, \tag{7.30}$$

for $i, j \in \{1, \ldots, N_\mathrm{f}, \mathrm{in}, \mathrm{out}\}$, which are drawn from the distribution $\mathcal{G}$ with a PDF of either

$$g(G_{ij}^0) = \delta(G_{ij}^0 - \bar{G}), \quad \text{or} \quad g(G_{ij}^0) = \frac{1}{\sqrt{2\pi}\sigma_G G_{ij}^0} \exp\left(-\frac{\left(\log\left(\frac{G_{ij}^0}{\bar{G}} \right) + \frac{\sigma_G^2}{2} \right)^2}{2\sigma_G^2} \right). \tag{7.31a,b}$$

The equations (7.23)–(7.31) form a closed system for the solution variables Q_{ij}, C_i, P_i, and G_{ij}, subject to the specification of the dimensional parameters $\bar{L}$, $\bar{V}$, $\bar{A}$, S, μ, p_in^*, p_out^*, and c_in^*, along with any other parameters that are needed to specify the probability density functions for the initial conductance distribution from which G_{ij}^0 are drawn, $\mathcal{G}$, such as σ_G in (7.31). Note that our network model is independent of node positions. The structure (in terms of connectivity) of the network enters the system through the pore conductances, G_{ij}. In the next section, we will nondimensionalise the dimensional network model (7.23)–(7.31).

7.2 Dimensionless model

In this section, we scale the variables of the dimensional network model, (7.23)–(7.31), to arrive at a dimensionless model to be analysed and solved in the subsequent chapter.

7.2.1 Nondimensionalisation

We begin by introducing two dimensionless parameters that make it easy to compare networks that contain different numbers of nodes (and to make our multiscale analysis in Part III simple). We suppose that the network consists of cells, as illustrated in Figure 7.4. We define N^m to be the number of cells, which are length $L^m = l^m/N^m$, in the m direction, and define N to be the mean number of nodes within each cell. We use these to define the two scaling parameters,

$$\delta = \frac{1}{\sqrt[D]{N}}, \quad \varepsilon = \frac{1}{N^1}. \tag{7.32}$$

Interpreting these, we see that ε^{-1} is the number of cells in a row in the flow direction (direction 1) since ε is the ratio of the cell length to the network length, $\varepsilon = L^1/l^1$ (see the cells boxed in blue in Figure 7.4). Meanwhile, δ^{-1} is the average number of pores in one cell in a row of nodes in the flow direction (see the pores highlighted and circled in green in Figure 7.4). It follows that $(\delta\varepsilon)^{-1}$ is the average number of pores in a row of nodes that leads from the inlet to the outlet, and is therefore the average number of pores that fluid flows through in order to traverse the filter (see the pores highlighted and circled in orange in Figure 7.4). Note that we expect $\delta\varepsilon \ll 1$ to represent a physically relevant filtration regime, since this corresponds to the case where many pores constitute the membrane.

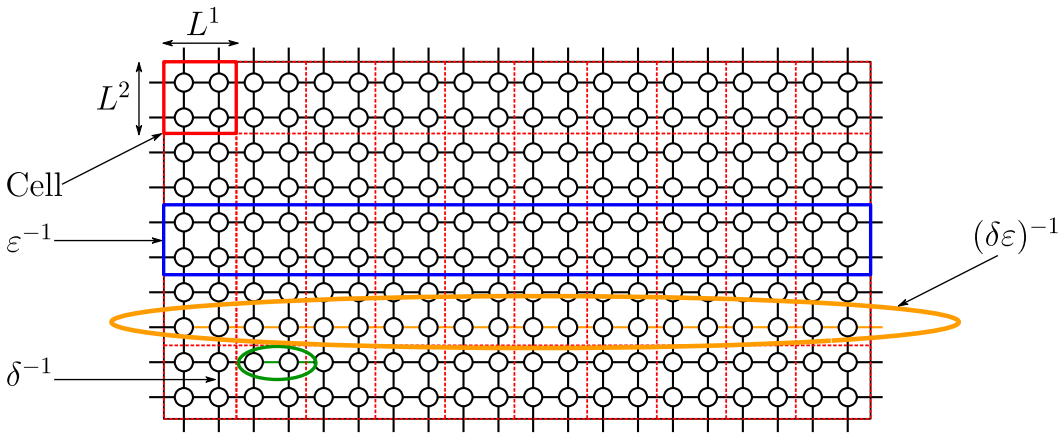

Figure 7.4: A diagram showing a two-dimensional filter represented as a four-regular network. Cells are shown with dashed red lines, and one cell is boxed in red. A row of cells is boxed in blue. A row of pores within a cell are highlighted and circled in green. A row of pores within the network are highlighted and circled in orange. In this example: $N^1 = 10$, since each row of cells contains 10 cells; $N^2 = 5$, since each column of cells contains 5 cells; $N = 4$, since each cell contains 4 nodes; $\delta = 1/2$, since $D = 2$ and $N = 4$; $\varepsilon = 1/10$, since $N^1 = 10$; $(\delta\varepsilon)^{-1} = 20$ since each row of pores contains 20 pores, so that fluid traverses 20 pores as it traverses the filter.

Given these scaling parameters, we define dimensionless variables (denoted by tilde) by

$$L_{ij} = \bar{L}\tilde{L}_{ij}, \quad V_i = \bar{V}\tilde{V}_i, \quad P_i = (p_{\text{in}} - p_{\text{out}})\tilde{P}_i + p_{\text{out}}, \quad C_i = c_{\text{in}}\tilde{C}_i, \tag{7.33}$$

$$Q_{ij} = \bar{G}(p_{\text{in}} - p_{\text{out}})\tilde{Q}_{ij} \quad G_{ij} = \frac{\bar{G}}{\varepsilon}\tilde{G}_{ij}, \quad T = \frac{\bar{V}}{\delta^2\varepsilon\bar{G}(p_{\text{in}} - p_{\text{out}})}\tilde{T}. \tag{7.34}$$

We see that the scalings in (7.33) imply unit pore-lengths and node-volumes,

$$\tilde{L}^0_{ij} = 1, \quad \tilde{V}^0_i = 1, \tag{7.35}$$

and unit concentration in the feed fluid. The pressure is scaled for unit pressure drop across the entire network.

In (7.34) we have scaled the remaining variables so that networks with different numbers of nodes in each cell, N, and different numbers of cells in the network, N^m, can be compared simply. To see this, we first note that fluid traverses $\mathcal{O}((\delta\varepsilon)^{-1})$ pores in order to traverse the network. Therefore, the pressure drop in any pore ij, $(P_i - P_j)$, is $\mathcal{O}((p_{\text{in}} - p_{\text{out}})\delta\varepsilon))$. However, in (7.33), the pore pressure drop is scaled with the network pressure drop, $p_{\text{in}} - p_{\text{out}}$. Thus, scaling the pore conductance with ε, as in (7.34), it follows that the flux through each pore is $\mathcal{O}(\delta\bar{G}(p_{\text{in}} - p_{\text{out}}))$, using (7.26). As a consequence, the time it takes for fluid to traverse a single pore is $\mathcal{O}(T_{\text{p}})$, where

$$T_{\text{p}} = \frac{\bar{V}}{\delta\bar{G}(p_{\text{in}} - p_{\text{out}})}. \tag{7.36}$$

Since the fluid traverses $\mathcal{O}((\delta\varepsilon)^{-1})$ pores to traverse the filter (see Figure 7.4), it follows that the time it takes for fluid to travel from the inlet to the outlet is $\mathcal{O}(T_{\mathrm{f}})$, where

$$T_{\mathrm{f}} = \frac{\bar{V}}{\delta^2 \varepsilon \bar{G}(p_{\mathrm{in}} - p_{\mathrm{out}})}. \tag{7.37}$$

Therefore, in our dimensionless variables, which are given by (7.33) and (7.34), we expect to have to wait $\mathcal{O}(1)$ time units for fluid to traverse the filter, regardless of the number of nodes it contains (both in terms of the number of cells, and the number of nodes within each cell). We summarise our dimensionless network model in the following subsection.

7.2.2 Summary of the dimensionless model

In summary, in dimensionless variables, with tildes dropped for ease of notation, the equations for the conservation of fluid, particles, and pores, are

$$\sum_{j=1}^{N_{\mathrm{f}}} Q_{ij} = 0, \tag{7.38}$$

$$\frac{\partial C_i}{\partial T} = \frac{1}{\delta^2 \varepsilon} \sum_{j=1}^{N_{\mathrm{f}}} \Big((1 - \alpha\delta\varepsilon) Q_{ji} C_j H(P_j - P_i) - Q_{ij} C_i H(P_i - P_j) \Big), \tag{7.39}$$

$$\frac{\partial G_{ij}}{\partial T} = -\frac{\alpha\beta}{\delta\varepsilon} C_{ij} G_{ij}^{\frac{3}{2}} |P_i - P_j|, \tag{7.40}$$

where the flux down each pore is related to the pressure drop and conductance of the pore via

$$Q_{ij} = \frac{G_{ij}}{\varepsilon} (P_i - P_j). \tag{7.41}$$

The boundary conditions are

$$P_{\mathrm{in}}(T) = 1, \quad P_{\mathrm{out}}(T) = 0, \tag{7.42a,b}$$

and

$$C_{\mathrm{in}}(T) = 1, \tag{7.43}$$

for $T \geq 0$, and the initial conditions are

$$C_i(0) = 0, \tag{7.44}$$

for $i \in \{1, \ldots, N_{\mathrm{f}}, \mathrm{out}\}$, and

$$G_{ij}(0) = G_{ij}^0 \tag{7.45}$$

for $i, j \in \{1, \ldots, N_\mathrm{f}, \mathrm{in}, \mathrm{out}\}$.

The dimensionless parameters are

$$\alpha = \frac{\bar{A}}{\delta\varepsilon}, \quad \beta = \frac{2S\bar{V}c_\mathrm{in}\varepsilon^{\frac{1}{2}}}{(8\pi\mu\bar{L}\bar{G})^{\frac{1}{2}}}, \quad \delta = \frac{1}{\sqrt[D]{N}}, \quad \varepsilon = \frac{1}{N^1} \tag{7.46}$$

We see that α is the effective adherence, that is, the mean adherence scaled by the number of pores in an average path from the inlet to the outlet. Note that the factor $\delta\varepsilon$ in α ensures that when $\alpha = \mathcal{O}(1)$ there is $\mathcal{O}(1)$ removal of particles by the time that they reach the outlet (as we will show in Section 8.2). Also, β is the effective particle size, that is, a ratio of the size of the average number of particles entering a pore to the average cross-sectional area of a pore. Note that, the factor $\varepsilon^{1/2}$ in β ensures that when $\alpha = \mathcal{O}(1)$ and $\beta = \mathcal{O}(1)$ there is an $\mathcal{O}(1)$ reduction in the conductance of pores near the inlet by the time that fluid reaches the outlet (again, we will demonstrate this point in Section 8.2). Note that we expect $\alpha = \mathcal{O}(1)$ and $\beta \ll 1$ to represent a physically relevant filtration regime, where the aim is to remove a large proportion of the incoming particles without greatly decreasing the effective conductance of the filter. The dimensionless analogies of the example PDFs of the initial conductance distribution, $\mathcal{G}$, are

$$g(G_{ij}^0) = \delta(G_{ij}^0 - 1), \quad \text{or} \quad g(G_{ij}^0) = \frac{1}{\sqrt{2\pi}\sigma_G G_{ij}^0} \exp\left(-\frac{\left(\log(G_{ij}^0) + \frac{\sigma_G^2}{2}\right)^2}{2\sigma_G^2} \right). \tag{7.47a,b}$$

Note that, in the dimensionless setting, $\mu_G = -\sigma_G^2/2$ so that the expectation of the initial conductances is $\mathbb{E}[G_{ij}^0] = \exp(\mu_G + \sigma_G^2/2) = 1$, as we expected, since, in (7.34), we scaled the conductance distribution for unit mean.

The equations (7.38)–(7.45) form a closed system for the dimensionless variables Q_{ij}, C_i, P_i, and G_{ij}, subject to the specification of the dimensionless parameters α, β, δ, and ε, which are defined in terms of the dimensional parameters in (7.46), and any further dimensionless parameters, for example σ_G in (7.47), that are needed to specify the initial conductance distribution, $\mathcal{G}$.

In this chapter, we have derived a novel model for filtration, (7.38)–(7.47), within which the filter is treated as a dynamically structured network of pores and junctions. The feed is modelled as a continuum of particles, that deposit smoothly on pore walls and so cause changes to the connectivity of the network and thus to the fluid-conductivity of the filter. In the next chapter, we will solve this model in the cases where the pore sizes are mono-dispersed.

Chapter 8

Solutions of the network model

In this chapter, we will describe our method of solution, before defining some quantities of interest that depend on the solution of the model. We will then solve the dimensionless network model, (7.38)–(7.47), in the case where the initial pore conductances are given by (7.47a), so that edges in the network all have the same conductance initially. This corresponds to the scenario where pore sizes are initially mono-dispersed.

8.1 Solution methodology

The network model, (7.38)–(7.47), is a system of linear ordinary algebraic–differential equations. Several computational tools exist for such problems, such as `CasADi`, [171], in `Python`. To gain an intuitive understanding of the system, we demonstrate a method to implement it explicitly from first principles (we have verified our results using `CasADi`). Later, in Section 12.1, we will use this to explain why the multiscale model that we discuss in Part III is computationally advantageous. Given initial conductances, we eliminate the pore fluxes, Q_{ij}, by substituting the relationship between the pore flux and the pore conductance and junction pressure, (7.41), into the fluid-conservation equation, (7.38), so that

$$\sum_{j=1}^{N_\mathrm{f}} \Big(G_{ij} - \delta_{ij} \sum_{k=1}^{N_\mathrm{f}} G_{ik} \Big) P_j = 0, \tag{8.1}$$

where δ_{ij} are elements of the Kronecker-delta matrix, $\boldsymbol{\delta}$. At $T = 0$, we solve (8.1) (given initial conductances) to find the initial pressure, $P_i(0)$, at each junction. At $T_k > 0$ (where T_k is the k^{th} discrete time-point), we use a first-order explicit scheme to discretise the particle-conservation equation, (7.39), and the pore-conductance conservation equation, (7.40). That is, we update the particle concentrations, $C_i(T_k)$, and pore conductances, $G_{ij}(T_k)$, by using the particle concentrations, $C_i(T_{k-1})$, pore conductances, $G_{ij}(T_{k-1})$, and junction pressures, $P(T_{k-1})$, at the previous time-point, T_{k-1}. We then update the node pressures, $P(T_k)$ by solving (8.1) using the pore conductances at the current time step, $G_{ij}(T_k)$.

At each time point, then, we solve a linear system that depends on the number of nodes in the network, N_f, via the number of nodes in each cell, N, and the number of cells in the network, N^1 and N^2, and the connectivity of the network, since this dictates the number of edges. For example, a two-dimensional four-regular network contains $\mathcal{O}(N^1N^2(N)^2)$ edges, since there are $(2(N)^2-2N)$ in each cell, and there are N^1N^2 cells in the network. It follows that, in the most expensive case (where matrix sparsity due to local connectivity is not exploited), we solve $N_\mathrm{e} = \mathcal{O}(N^1N^2(N)^2)$ equations in order to find the pressure and concentration in all nodes, and the conductance of all pores. We note that this is prohibitively large in cases where there are many nodes in the cell, so that $N \gg 1$, and many cells in the network, so that $N^1N^2 \gg 1$ ($N = \mathcal{O}(10^2)$ and $N^1, N^2 = \mathcal{O}(10)$, say, so that $N_\mathrm{e} = \mathcal{O}(10^6)$), since solution of a linear system of size N_e requires $\mathcal{O}(N_\mathrm{e}^2)$ operations.

8.2 Non-random networks: Mono-dispersed pores

In this section, we define some properties that depend on the solution of the model that we will use to analyse it. We then consider the solution of the network model, (7.38)–(7.47), in the scenario where pores are mono-dispersed initially, in which case the initial pore conductances are given by (7.47a). We first discuss the simplest case, in which the adherence is zero, $\alpha = 0$, so that no deposition can occur. We then discuss a non-zero adherence case, $\alpha = 0.2$ for example, which demonstrates a particular case in which deposition can occur. After this, we explore the effect that changing the parameters α, β, δ, and ε, has on the solutions of (7.38)–(7.47).

8.2.1 Macroscale properties

In filtration applications, industrialists are most interested in certain macroscopic properties of the filter, and how these vary with filter depth and time. In the present case, where the network is mono-dispersed and four-regular, we do not expect variables to vary in the x^2 direction, which is transverse to the direction of flow. As such, we define macroscale quantities to represent the particle concentration, pore conductance, junction pressure, and fluid flow rate, which are depth and time dependent, and which are averaged over the transverse direction. Since the present network is two-dimensional and four-regular, this calculation is straightforward, because junctions form 'columns' (in the x^2 direction) at each depth (see Figure 7.4), and we simply average the solution variables down these columns. That is, calling $x^1 = X_j$ the depth of the junctions that are in column j (where j varies between 1 and $(\delta\varepsilon)^{-1}$), we define

$$\bar{C}(X_j, t) = \frac{\delta}{N^2} \sum_{j=1}^{N^2/\delta} C_j(t), \tag{8.2}$$

$$\bar{P}(X_j, t) = \frac{\delta}{N^2} \sum_{j=1}^{N^2/\delta} P_j(t). \tag{8.3}$$

We call these the average particle concentrations and junction pressures, which are averaged over the flow-transverse direction, since N^2/δ is the number of nodes in each junction column. Similarly, defining $x^1 = X_{ij}$ to be the depth of the centre of each flow-parallel pore, ij, and averaging down each column of pores, we obtain the average pore conductances,

$$\bar{G}(X_{ij}, t) = \frac{\delta}{N^2} \sum_{j=1}^{N^2/\delta} G_{ij}(t). \tag{8.4}$$

This is the conductance in pores that are parallel to the flow, averaged over the flow-transverse direction. Lastly, we define the average flow rate through the filter. Since fluid mass is conserved in each node, this is equal to the rate of flow of fluid into the filter. It follows that

$$U(t) = \frac{\delta}{N^2} \sum_{j=1}^{N^2/\delta} \frac{1}{\delta\varepsilon} G_{\mathrm{in}j}(P_{\mathrm{in}} - P_j), \tag{8.5}$$

where we have summed the volumetric flow through all the edges that lead into the filter, and divided by N^2/δ, which is the total number of these. In the following section, we will solve the network model numerically, and find: the average particle concentration, $\bar{C}$, given by (8.2); the average junction pressure, $\bar{P}$, given by (8.3); the average pore conductance, $\bar{G}$, given by (8.4); the average flow rate, U, given by (8.5). We will use these to analyse the effective behaviour of the filter, and how this depends upon the dimensionless parameters, α, β, δ, and ε. In what follows, we explore various parameter regimes (rather than the physically relevant filtration regime already discussed: $\alpha = \mathcal{O}(1)$, $\beta \ll 1$, $\delta\varepsilon \ll 1$) to demonstrate the key properties of the network model.

8.2.2 No deposition

To gain an intuitive understanding of the model, we first consider the simple case of zero adherence, $\alpha = 0$, so that deposition cannot occur. In Section 8.2.6, we will use this case to analyse the effects of varying δ and ε. First, in Figure 8.1, we display the behaviour of the four average macroscale quantities, $\bar{C}$, $\bar{P}$, $\bar{G}$, and U, which are defined in (8.2)–(8.5), in the no-deposition scenario.

Observing Figure 8.1(a), the first thing we notice is that particles, unimpeded by pores, travel in the wave of fluid that traverses the filter, which reaches the outlet in $\mathcal{O}(1)$ time. Far upstream of the wave front, at any particular time, the particle concentration matches the concentration in the fluid entering the filter at the inlet, since the junctions and pores that make up the void space in the filter here are completely filled with particle-laden fluid. On the other hand, fluid has not had time to reach the area far downstream of the wave front, and so the particle concentration is zero here. Between these two areas, we observe a transition region, within which the particle concentration decreases smoothly from the inlet value to zero.

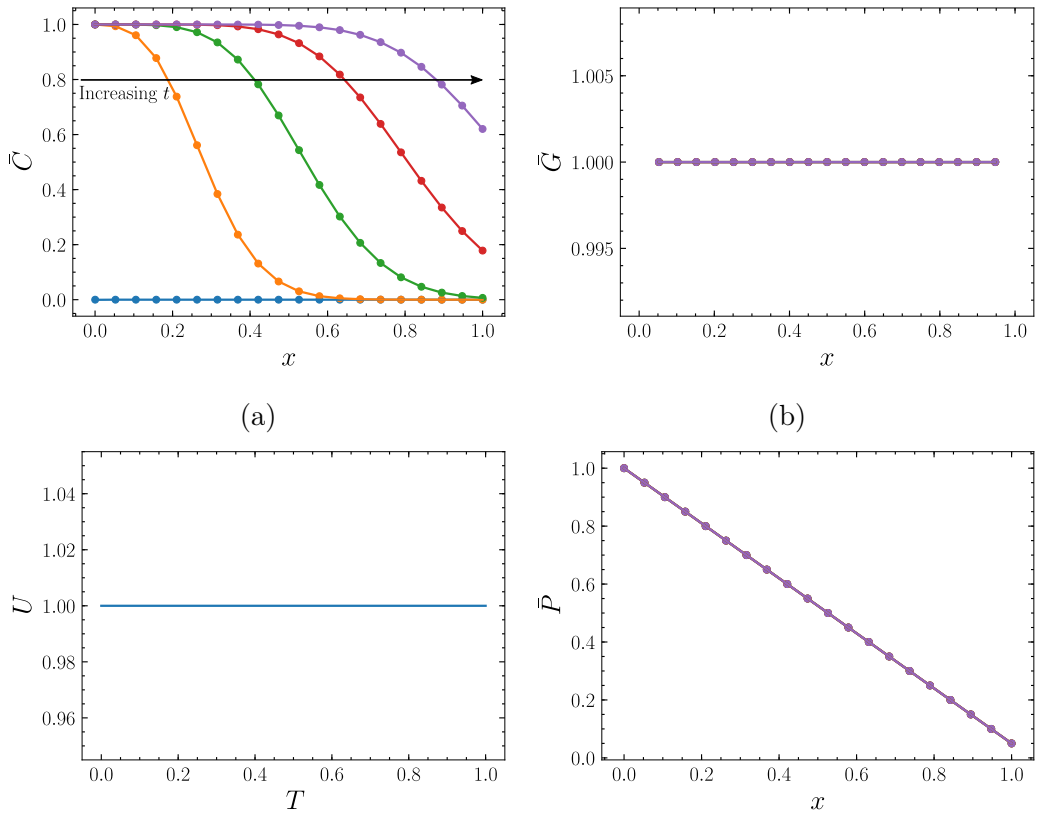

Figure 8.1: Graphs showing how the average particle concentration, $\bar{C}$, pore conductance, $\bar{G}$, flow rate, U, and junction pressure, $\bar{P}$, vary with depth, x and time, T. The parameters are $N = 4$, $N^1 = 10$, $N^2 = 2$, $\alpha = 0$, $\beta = 1$, $\delta = 0.5$, $\varepsilon = 0.1$. Coloured dots show the exact value of the quantity at the depths at which it is evaluated. Correspondingly coloured lines show a spline interpolation of the quantity between evaluation points. In plots where depth is shown on the independent-variable axis, the values of T are 0 (blue), 0.25 (orange), 0.5 (green), 0.75 (red), 1 (purple), and the arrow shows the direction of increasing time. (a) The average particle concentration, $\bar{C}$, as a function of depth, x, at various times, T. (b) The average pore conductance, $\bar{G}$, as a function of depth, x, at various times, T. Since the solution is the same for all times, only the time $T = 1$ is visible. (c) The average flow rate, U, as a function of time, T. (d) The average junction pressure, $\bar{P}$, as a function of depth, x, at various times, T. Since the solution is the same for all times, only the time $T = 1$ is visible.

Since particles cannot stick to pore walls, deposition never occurs, and so the cross-sectional area of the pores, and thus their conductance, is unchanged as particles traverse them. As a result, in Figure 8.1(b), we observe unit average-conductance within the entire filter, for all time, so that the permeability of the filter is unaltered. It follows that the flow rate of the fluid is unchanged, and thus, in Figure 8.1(c), we observe unit average flow rate for all time.

Since the network is four-regular, and pore sizes are mono-dispersed initially, the

pressure drop in the flow-transverse pores is exactly zero. This implies that there is no flow in the transverse direction. As a result, changes in junction pressure occur purely to changes to the conductance of flow-parallel pores. Since these conductances are constant (see Figure 8.1(b)), in Figure 8.1(d), we see that the junction pressure decreases linearly with depth in flow-parallel pores, so that a unit pressure drop is maintained for all time across the filter.

In summary, in the no-deposition scenario, the fluid travels with unit flow rate for all time, and the average junction pressures set up a linearly decreasing profile with depth, so that a unit pressure drop across the entire filter depth is preserved for all time. In the following subsection, we discuss the non-zero adherence case, $\alpha \neq 0$, so that deposition can occur. This leads to changes to the conductances of pores, and thus the flow rate and pressure.

8.2.3 Deposition

We now discuss the case of non-zero adherence, $\alpha \neq 0$, so that particles do deposit within pores. To demonstrate, we consider the case $\alpha = 0.2$, which, as we will show, corresponds to a decrease in concentration of around 20% over the length of the filter. As we will see, the behaviour of the solution is markedly different at earlier times, ($T < 1$), and later times, ($T > 1$), and we display these cases separately, in Figures 8.2 and 8.3, respectively.

8.2.3.1 Earlier times

We demonstrate the behaviour of the macroscale quantities at earlier times in Figure 8.2. In Figure 8.2(a), we see that, as in the case where particles do not deposit in pores (see Figure 8.1), particles travel through the filter in a wave. This time, as they do so, particles are captured in pores via deposition, so that their concentration decreases smoothly with depth.

As deposition occurs, particles stick to the inner walls of pores, which reduces their cross-sectional area. As we see in Figure 8.2(b), this causes a decrease in pore conductance as time passes. Conductance decrease is fastest in pores nearer the inlet, since there are more particles in the fluid that have the chance to adhere to the pores, and particles have been traversing these pores for longer. For example, by the time particles reach the outlet for the first time (in $\mathcal{O}(1)$ time), the conductance in pores near the inlet has decreased by around 20%, while in pores near the outlet, the conductance has dropped by less than 5%.

As deposition occurs, the drop in the conductance of pores causes a drop in the permeability of the filter, and thus a decrease in the average flow rate of the fluid traversing the filter. This drop is slight, since particles have not had time to decrease the conductances of pores by much yet, which is why particles still reach the outlet in $\mathcal{O}(1)$ time. In Figure 8.2(c), we see that the drop in the flow rate is concave. At first, for $0 \leq T < 0.25$ say, the rate of decrease of the flow rate is small, because only the pores near the top of the filter have been reached by fluid, and so it is only possible for particles to deposit in these. The overall conductance of the filter has

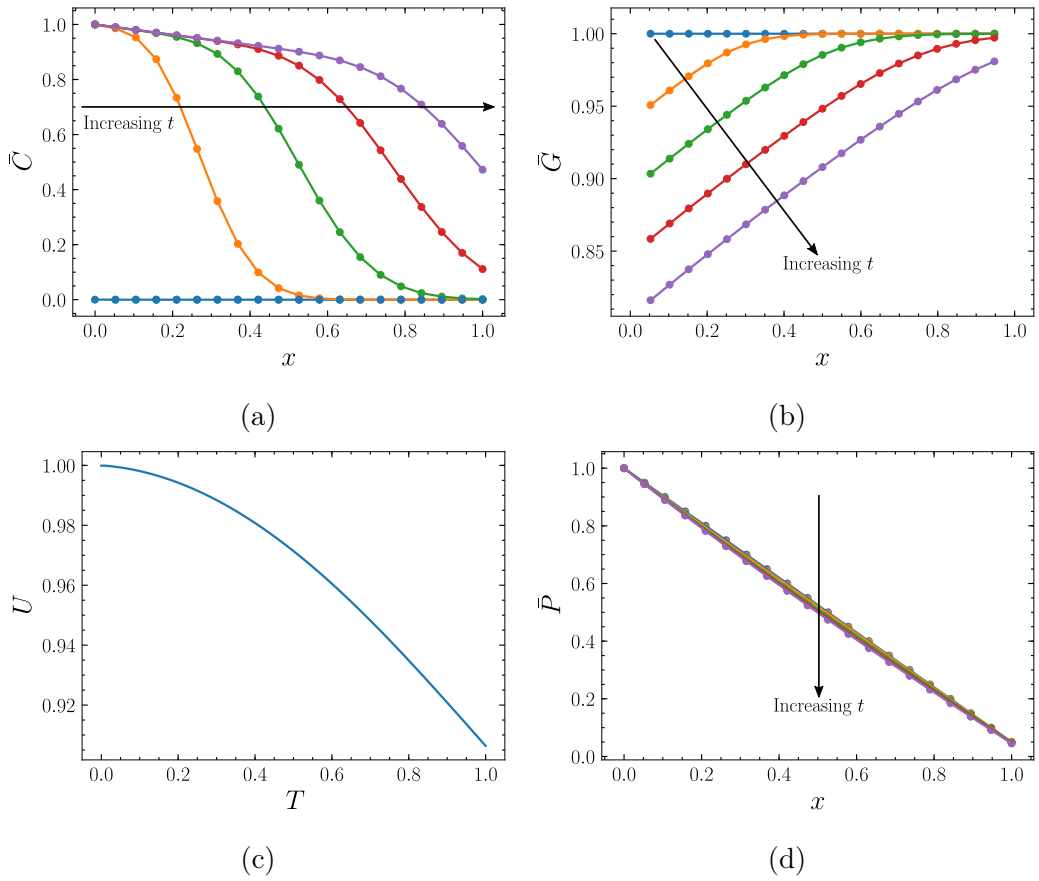

Figure 8.2: Graphs showing how the average particle concentration, $\bar{C}$, pore conductance, $\bar{G}$, flow rate, U, and junction pressure, $\bar{P}$, vary with depth, x, and time, T. The parameters are $N = 4$, $N^1 = 10$, $N^2 = 2$, $\alpha = 0.2$, $\beta = 1$, $\delta = 0.5$, $\varepsilon = 0.1$. Coloured dots show the exact value of the quantity at the depths at which it is evaluated. Correspondingly coloured lines show a spline interpolation of the quantity between evaluation points. In plots where depth is shown on the independent-variable axis, the values of T are 0 (blue), 0.25 (orange), 0.5 (green), 0.75 (red), 1 (purple), and the arrow shows the direction of increasing time. (a) The average particle concentration, $\bar{C}$, as a function of depth, x, at various times, T. (b) The average pore conductance, $\bar{G}$, as a function of depth, x, at various times, T. (c) The average flow rate, U, as a function of time, T. (d) The average junction pressure, $\bar{P}$, as a function of depth, x, at various times, T.

barely been altered. Later, for $0.25 \leq T \leq 1$, say, we see that the flow rate decrease is faster. In this time interval, fluid has reached more pores in the filter, and particles are decreasing the size of many pores at once, so that the overall conductance of the filter is being decreased more rapidly. Despite this, the flow rate has only dropped by around 5% by $T = 1$, because the cross-sectional area of most pores away from the inlet remain similar to their initial values.

As a result, the filter still maintains a pressure–depth profile that is almost linear. Indeed, in Figure 8.2(d), we see that changes to the pore conductances have not

altered the average junction pressure substantially by $T = 1$ (hence the blue line cannot be detected behind the purple line, similar to that in the graph in the no-deposition case, 8.1(d)). At earlier times, then, pores have begun to clog, but the decrease in their cross-sectional area has not yet caused substantial changes to the pressure field that drives the fluid through the filter.

8.2.3.2 Later times

To see how this situation develops, we plot the macroscale quantities at later times in Figure 8.3. In Figure 8.3(a), the first thing we notice is that the average-concentration profile is identical at all non-zero times that we display. We see that particles have reached the outlet and that, now, the concentration of particles in the flow decreases almost linearly with depth, so that, at the outlet, the particle concentration has dropped by around 1/5 (which is exactly the value of α that we use in this example).

To understand the form of the average particle concentration–depth profile, we first note that fluid loses a proportion, $\alpha\delta\varepsilon$, of particles as it traverses each pore, ij. Labelling a row of junctions that lead from the inlet to the outlet (see the row of pores highlighted in orange in Figure 7.4, for example) with indices $1, \ldots, (\delta\varepsilon)^{-1}$ (since there are $(\delta\varepsilon)^{-1}$ such junctions), it follows that the concentrations in junction i and junction $i+1$ satisfy $C_{i+1} = (1-\alpha\delta\varepsilon)C_i$. Writing the concentration in junction i as a function of the inlet concentration, we see that $C_i = (1-\alpha\delta\varepsilon)^i C_{\text{in}}$, and so we define

$$\tilde{C}(x) = (1-\alpha\delta\varepsilon)^{x/\delta\varepsilon}. \tag{8.6}$$

This represents the expected average-concentration that we observe on the macroscale, so that we expect $\tilde{C} \approx C$. As such, we call $\tilde{C}$ the approximate concentration. In Figure 8.3(a) we see (comparing the dashed black line with the purple line) that this approximation is exact in a mono-dispersed four-regular network, since deposition only occurs in pores that are parallel to the direction of the flow (the 1 direction, here). This is because there is no pressure gradient in the transverse direction to drive particles through the flow-transverse pores. When the network is mono-dispersed and four-regular, then, $\tilde{C}$ provides the average particle concentration at any time that is large enough for particles to have traversed the filter, without the need for numerical solution of the network system.

In industrial applications, experimentalists are often interested in the efficiency of the filter. We assume that the efficiency is given by the proportion of the total particles that enter the filter that do not exit it, and, since we have nondimensionalised for unit inlet concentration, we write

$$\eta(T) = 1 - C(1,T). \tag{8.7}$$

Since (8.6) provides an approximation for the particle concentration, we define

$$\tilde{\eta} = 1 - \tilde{C}(1) = 1 - (1-\alpha\delta\varepsilon)^{1/\delta\varepsilon}, \tag{8.8}$$

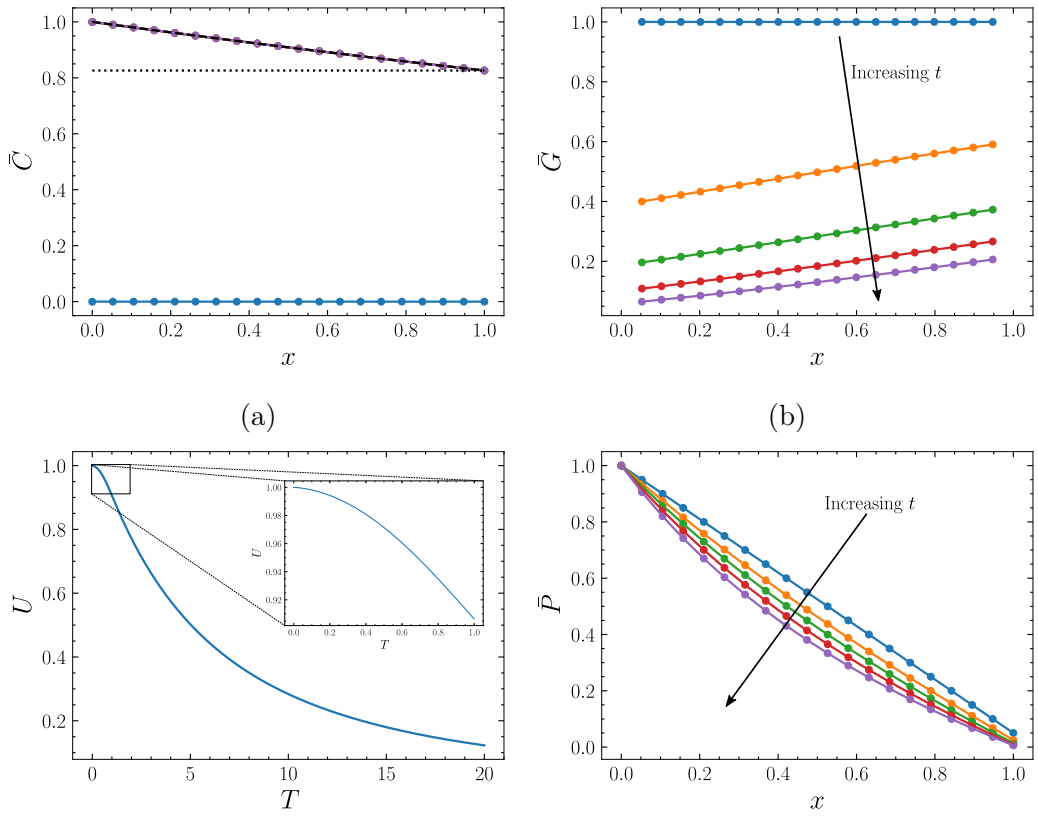

Figure 8.3: Graphs showing how the average particle concentration, $\bar{C}$, pore conductance, $\bar{G}$, flow rate, U, and junction pressure, $\bar{P}$, vary with depth, x, and time, T. The parameters are $N = 4$, $N^1 = 10$, $N^2 = 2$, $\alpha = 0.2$, $\beta = 1$, $\delta = 0.5$, $\varepsilon = 0.1$. Coloured dots show the exact value of the quantity at the depths at which it is evaluated. Correspondingly coloured lines show a spline interpolation of the quantity between evaluation points. In plots where depth is shown on the independent-variable axis, the values of T are 0 (blue), 5 (orange), 10 (green), 15 (red), 20 (purple), and the arrow shows the direction of increasing time. (a) The average particle concentration, $\bar{C}$, as a function of depth, x, at various times, T. Since the concentration profile is the same for all times and $T > 0$ that are shown, only the times $T = 0$ (blue) and $T = 20$ (purple) are visible. The dashed black line shows the approximate concentration, $\tilde{C}(x^1)$. The dotted black line shows the extrapolation of the outlet concentration, $\tilde{C}(1)$. (b) The average pore conductance, $\bar{G}$, as a function of depth, x, at various times, T. (c) The average flow rate, U, as a function of time, T. The solution at earlier times, $0 \leq T \leq 1$, is shown in an expanded box. (d) The average junction pressure, $\bar{P}$, as a function of depth, x, at various times, T.

which we call the approximate efficiency, since we expect that $\tilde{\eta} \approx \eta$. Indeed, since $\tilde{C} = \bar{C}$ for T large enough for particles to have traversed the filter, in the case of a mono-dispersed four-regular network, it follows that $\tilde{\eta} = \eta$, so that we have found an explicit formula for the efficiency for large enough T. In (8.8) we see that this formula

depends on the adherence, that is, the proportion of particles that are expected to be lost in a particular pore, through α, and on $(\delta\varepsilon)^{-1}$, which is the approximate number of pores that fluid traverses to travel from the inlet to the outlet. In the present example, we have that $\alpha = 0.2$, $\delta = 0.5$, and $\varepsilon = 0.1$, and, using (8.6), we calculate that $\tilde{C}(1) \approx 0.82$ (see the dotted black line in Figure 8.3(a)), so that, using (8.8), it follows that $\eta = \tilde{\eta} \approx 0.2$, which means that the filter is around 20% efficient. Note that $\alpha = 0.2$, which corresponds to 20% adherence in each pore (scaled by $(\delta\varepsilon)^{-1}$). Thus we see that the order of α dictates the order of the efficiency.

Returning to our analysis of the solution at later times, shown in Figure 8.3, we next discuss the average pore conductance, a plot of which is shown in Figure 8.3(b). We see (comparing with the solution at earlier times, shown in Figure 8.2(b)), that the conductance of pores continues to decrease as time increases. Pores near the inlet still have the smallest conductance, since more particles flow through them per unit time. However, as time increases, the gradient of the average pore conductance–depth profile decreases, because the rate of decrease of pore conductance is smaller in pores with less conductance, since they have less cross-sectional area and thus surface area to adhere to, and fewer particles are conducted through them per unit time.

As conductance decreases, the average flow rate through the filter continues to decrease, as we see in Figure 8.3(c). After the earlier times, at which the flow rate decreases rapidly (see Figure 8.2(c)), the flow rate decreases more slowly, which corresponds to the decrease in the rate of deposition in pores. The concave behaviour of the flow rate at earlier times ($0 \leq T < 1$) (see the zoomed region in Figure 8.3(c)) is replaced with convex behaviour at later times ($1 \leq T \leq 20$), after fluid has reached the outlet for the first time. By times $T > 10$ (green line), for example, the pores near the inlet have less than 20% of their original conductance (see Figure 8.3(b)), and so they are almost completely clogged. As a result, we see that fluid flows through the filter at less than 20% of its initial rate. This would be problematic from an industrial perspective, since it means that particles are being processed 80% more slowly than they were originally. In industrial applications, filtration processes are often halted when the flow rate drops below some minimum-required threshold, U_{c} say, and industrialists are interested in the amount of fluid that has been processed when this first occurs, which is called the total throughput, τ, say. We will discuss these two quantities more in the next subsections.

Comparing the average junction pressure–depth profile at later times, in Figure 8.3(d), with that at earlier times (see Figure 8.2(d)), we see that the substantial drop in the average pore conductance (see Figure 8.3(b)) results in much larger changes to the junction pressures than before. As time increases, the pressure in each node drops away from its initial value towards the pressure in the outlet, which is zero. As a result, the average junction pressure–depth profile becomes convex, since the pressure drops fastest in nodes that are far from the inlet and the outlet, because pressures outside of the filter are fixed.

To explain the behaviour in the deposition and no-deposition cases further, in the following three subsections we analyse the behaviour of the solutions as functions of the parameters, α, β, δ and ε, respectively.

8.2.4 Dependence on α: Retention efficiency

We first explore the effects of varying the adherence parameter, α. We will find that the behaviour of the solutions is different for smaller values, $1 < \alpha < \mathcal{O}(1)$ (we examine the region $0 \leq \alpha \leq 1$), and larger values, $\alpha = \mathcal{O}((\delta\varepsilon)^{-1})$ (we examine the region $0.25(\delta\varepsilon)^{-1} \leq \alpha \leq (\delta\varepsilon)^{-1}$), and so we will treat these cases separately.

8.2.4.1 Smaller α values

We first plot the four key macroscale quantities in Figure 8.4 for equally spaced values of α, in $0 \leq \alpha \leq 1$.

Firstly, in Figure 8.4(a), we see that, as α increases, the negative gradient of the average particle concentration–depth profile increases. For larger values of α, a larger proportion of particles stick to each pore, which means that there are fewer particles in the fluid by the time it exits the filter.

Secondly, we plot the average pore conductance in Figure 8.4(b). We see that, for smaller α values, particles are less likely to stick in pores, and so the fluid that reaches the region near the outlet still contains a large concentration of particles (see Figure 8.4(a)) transported from the inlet. Consequently, deposition occurs here, decreasing pore conductance. As α increases, particles are increasingly likely to be removed in pores nearer to the inlet, and so fewer particles reach the region near the outlet (since they have all been removed further up the filter), As a result, the pore conductance hardly decreases here. Altogether, near the outlet, the pore conductance decreases as α increases for small α, but begins to increase again for larger values.

Thirdly, in Figure 8.4(c), we see that the α increase that caused the faster pore conductance decrease results in a more rapidly decreasing average flow rate. That is, the average flow rate decreases as α increases. Correspondingly, in Figure 8.4(d), we see that the junction pressures are driven towards zero faster for larger values of α.

In the previous subsections, we concluded that α controls the proportion of particles that are retained in the filter, and, as such, it dictates the filter efficiency. To formalise this dependency, we plot the efficiency, η, and the approximate efficiency, $\tilde{\eta}$, as functions of α, in Figure 8.5. In Figure 8.5(a), we notice that the efficiency of the filter increases as α increases. As we saw in Figure 8.4(a), as α increases, more particles are removed in each pore, which means that, by the time fluid reaches the outlet, it contains fewer particles when α is larger. As a result, for example, the choice $\alpha = 0.2$ leads to an efficiency of less than 20%, while $\alpha = 1$ leads to an efficiency of around 60%. We see (comparing the dashed black line with the blue line) that, for the present choice of network, the approximate efficiency matches the efficiency exactly.

The accuracy of the approximate efficiency allows us to calculate the efficiency for values of α for which we have not solved the system numerically. Indeed, in Figure 8.5(b), we extrapolate the approximate-efficiency curve and use it to read off the efficiency for various new values of α. We see that the efficiency rapidly increases for $0 \leq \alpha \leq 3$, so that the filter is more than 95% efficient for $\alpha > 3$ (dashed red line). For $\alpha = 4$, the filter is around 99% efficient (dashed purple line), and so almost all

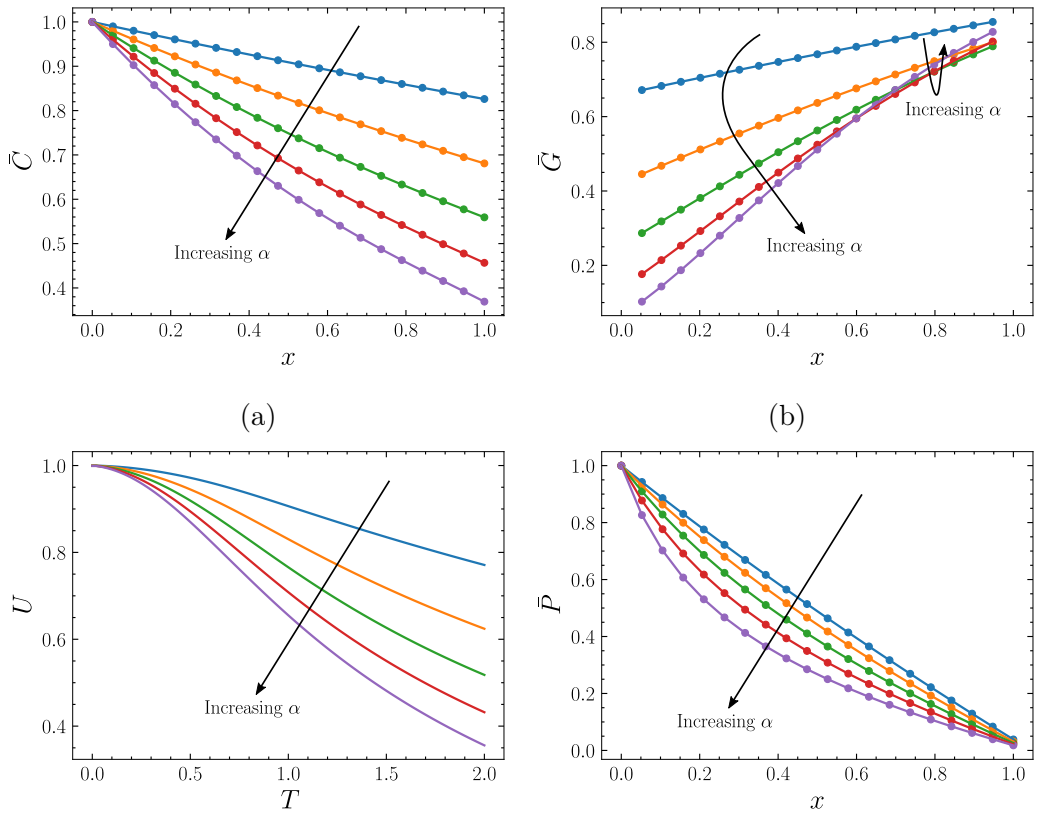

Figure 8.4: Graphs showing how the average particle concentration, $\bar{C}$, pore conductance, $\bar{G}$, flow rate, U, and junction pressure, $\bar{P}$, vary with depth, x, and time, T, at various values of α. The parameters are $N = 4$, $N^1 = 10$, $N^2 = 2$, $\beta = 1$, $\delta = 0.5$, $\varepsilon = 0.1$. Coloured dots show the exact value of the quantity at the depths at which it is evaluated. Correspondingly coloured lines show a spline interpolation of the quantity between evaluation points. The values of α are 0.2 (blue), 0.4 (orange), 0.6 (green), 0.8 (red), 1 (purple), and the arrow shows the direction of increasing α. (a) The average particle concentration, $\bar{C}$, as a function of depth, x, at time $T = 2$. (b) The average pore conductance, $\bar{G}$, as a function of depth, x, at time $T = 2$. (c) The average flow rate, U, as a function of time, T. (d) The average junction pressure, $\bar{P}$, as a function of depth, x, at time $T = 2$.

particles are retained in the filter. The efficiency can never exceed one (dotted black line), since it indicates proportional retention, and so the efficiency asymptotically approaches its maximum value for even larger values of α. In an industrial application, Figure 8.5(b) could be used to read off a required value of α necessary to achieve some required efficiency value.

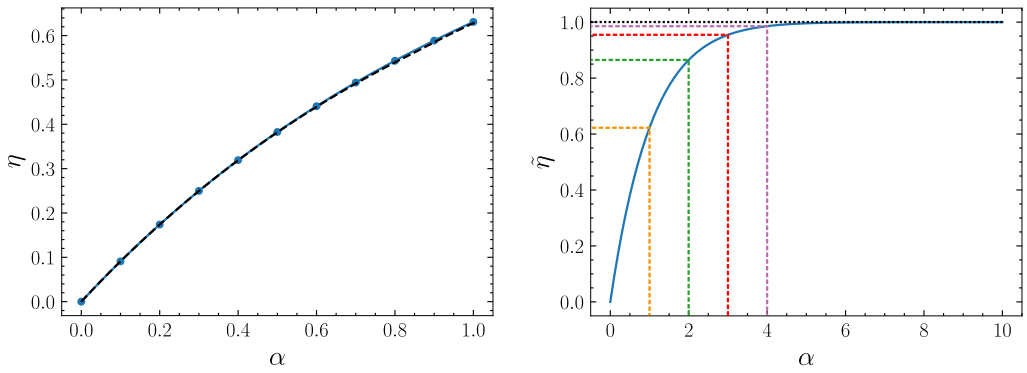

(a) (b)

Figure 8.5: Graphs showing how the efficiency, η, and approximate efficiency, $\tilde{\eta}$, vary with α. The parameters are $N = 4$, $N^1 = 10$, $N^2 = 2$, $\beta = 1$, $\delta = 0.5$, $\varepsilon = 0.1$. (a) The efficiency, η, as a function of α. Blue dots show the numerical solution at values of α equal to $0, 0.2, 0.4, 0.6, 0.8, 1$. The blue line shows a spline interpolation between these values. The dashed black line shows the approximate efficiency, $\tilde{\eta}$, as a function of α. (b) The average efficiency, $\tilde{\eta}$, as a function of α. The dotted black line shows the asymptote, which is 1. The dashed coloured lines show extrapolations of the approximate efficiency for α values of 1 (orange), 2 (green), 3 (red), 4 (purple).

8.2.4.2 Larger α values

We analyse the behaviour of the solution for larger values of α, in the range $0.25(\delta\varepsilon)^{-1} \leq \alpha \leq (\delta\varepsilon)^{-1}$ say, using Figure 8.6. We see that filters with α values that are $\mathcal{O}((\delta\varepsilon)^{-1})$ are 100% efficient: all particles that are suspended in the feed fluid are captured in pores within the filter.

Indeed, in Figure 8.4(a) we see that, for these large values of α, particles are all captured in a layer that extends from the inlet. The thickness of this capture layer is $\mathcal{O}(\alpha^{-1})$, so that it becomes thinner for increasing values of α. When $\alpha = (\delta\varepsilon^{-1}$ (purple line), we see that particles are captured over a layer that has length $\delta\varepsilon$. This extreme corresponds to the case where pores retain 100% of the particles in the fluid that enters them, so that all particles suspended in a given volume of fluid are captured within the first pore that this volume enters. As a result, we see that particles are captured within an extremely thin layer at the top of the filter (similarly to the blocking regime in Part I).

Once fluid reaches depths outside the capture layer, it does not contain any particles. It traverses the remainder of the filter without affecting the conductances of the pores that it enters until the conductances of pores at the inlet reach zero, at which time the filter effectively ceases to conduct fluid. Correspondingly, in Figure 8.4(b), we see that, for large values of α, only the conductances of pores near the inlet are altered.

We observe, in Figure 8.4(c), that, for large α values, the average flow rate rapidly drops towards zero at times $0 \leq T < 1$, at which fluid has not even reached the outlet

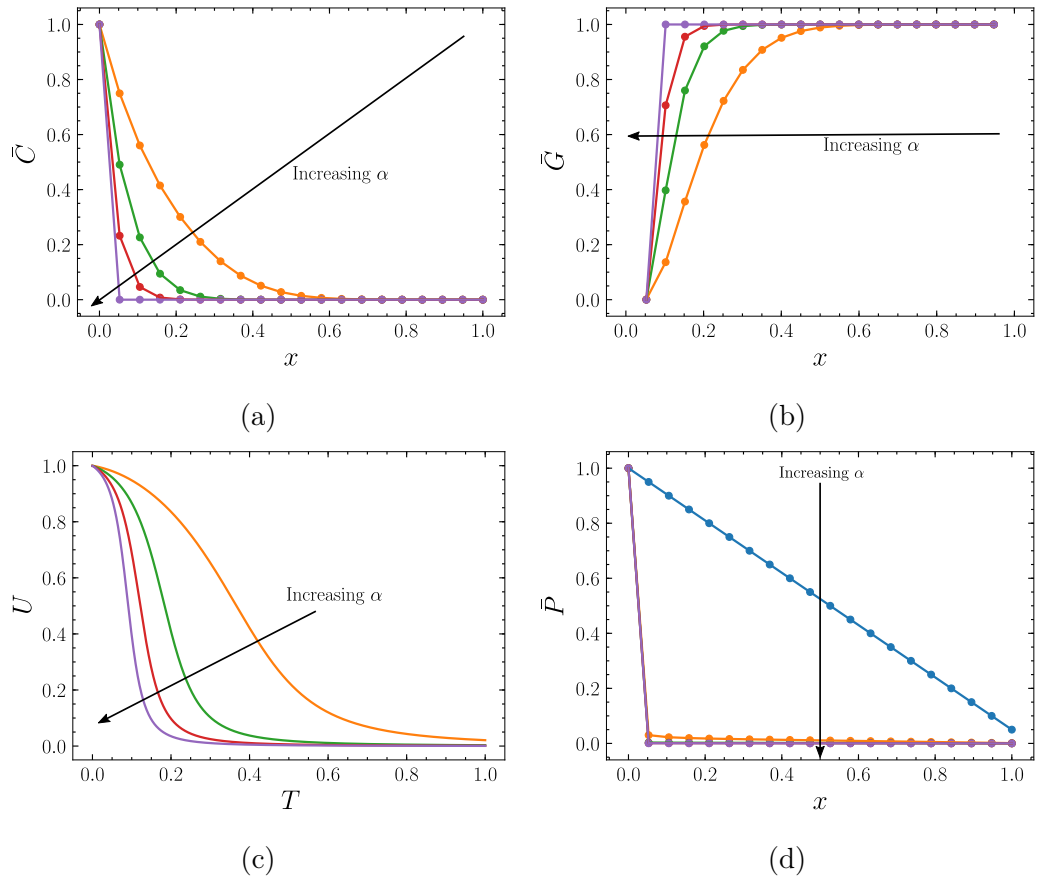

Figure 8.6: Graphs showing how the average particle concentration, $\bar{C}$, pore conductance, $\bar{G}$, flow rate, U, and junction pressure, $\bar{P}$, vary with depth, x, and time, T, at various values of α. The parameters are $N = 4$, $N^1 = 10$, $N^2 = 2$, $\beta = 1$, $\delta = 0.5$, $\varepsilon = 0.1$. Coloured dots show the exact value of the quantity at the depths at which it is evaluated. Correspondingly coloured lines show a spline interpolation of the quantity between evaluation points. The values of α are $0.25(\delta\varepsilon^{-1}$ (orange), $0.5(\delta\varepsilon^{-1}$ (green), $0.75(\delta\varepsilon^{-1}$ (red), $(\delta\varepsilon^{-1}$ (purple), and the arrow shows the direction of increasing α. (a) The average particle concentration, $\bar{C}$, as a function of depth, x, at time $T = 1$. (b) The average pore conductance, $\bar{G}$, as a function of depth, x, at time $T = 1$. (c) The average flow rate, U, as a function of time, T. (d) The average junction pressure, $\bar{P}$, as a function of depth, x, at time $T = 1$. The blue dots and line show the solution at $\alpha = 0$, and are included to aid the eye.

for the first time, since the pores near the inlet become clogged very quickly. The average flow rate–time profiles are strictly concave while the flow rate is large enough for reasonable operation (that is, flow rates exceeding 20% of the initial rate, say). By $T = 1$, the filter is effectively clogged for all the values of α that we consider here. Correspondingly, in Figure 8.4(d) we see that the pressure in all internal junctions rapidly drops to zero by $T = 1$.

Altogether, in this subsection, we have shown that the parameter α controls the 'stickiness' of the pores, and thus the proportion of particles that are retained in each

pore. As a result, the value of α dictates the efficiency of the filter. As α increases, a greater proportion of particles are captured near the inlet of the filter. As a result, pores close to the inlet clog more quickly, and the flow rate and pressure drop more rapidly. In the next subsection, we explore the dependence of the solution on the parameter β.

8.2.5 Dependence on β: Total throughput

In this subsection, we discuss the dependence of the solution on the particle size parameter, β. We will find that the behaviour of the solutions is different for smaller β values, say $\beta = \mathcal{O}(10^{-1})$ (we examine the region $0 \leq \beta \leq 0.1$), and larger β values, say $\beta = \mathcal{O}(1)$ (we examine the region $1 \leq \beta \leq 5$, and we will treat these two cases separately.

8.2.5.1 Smaller β values

We begin by plotting the four key macroscale quantities for equally spaced values of β in the range $0 \leq \beta \leq 0.1$, in Figure 8.7.

Firstly, in Figure 8.7(a), we see that, once fluid has reached the outlet for the first time, the average particle concentration–depth profile is constant, and is given exactly by the approximate concentration, $\tilde{C}$ (dashed black line). We find that this profile is independent of the choice of β, since pores retain a quantity of particles that is given by α, δ, and ε, but not β (see the definition of $\tilde{C}$, (8.6)). As a result, the proportion of the incoming particles that are present at the outlet, and thus the efficiency, η, are constants with respect to β.

Secondly, we note that, as β increases, the average pore conductance decreases, as we show in Figure 8.7(b). This is because larger values of β correspond to a greater particle size, which means that deposition causes a faster decrease in the cross-sectional area of pores, and thus their conductance. The gradient of the average pore conductance–depth profile is also independent of β, since changes in β affect all pores equally.

Correspondingly, larger values of β result in more rapidly decreasing average flow rates (see Figure 8.7(c)) and average junction pressures (see Figure 8.7(d)). For $\beta = 0.02$ (blue lines), for example, we see that by $T = 100$, when fluid has traversed the filter 100 times, fluid still flows at almost 40% of its initial rate. For $\beta = 0.1$ (purple lines), however, the flow rate drop-off is much more rapid, and by $T = 100$ we see that the flow rate is almost zero, so that the filter is unusable, since pores at the inlet have infinitesimal conductance (see Figure 8.7(b)).

As we have discussed, in practice, industrial applications are halted when the average flow rate drops below some threshold, U_{c}, say, at which the cost associated with the increased process time (due to lower flow rate) outweighs the cost of the cleaning or replacement of the filter membrane. For a given flow rate threshold, U_{c}, industrialists are interested in predicting the total throughput, θ say, which is the number of times that fluid traverses the filter before the flow rate threshold is subceeded. In constant flow rate regimes, this is exactly the terminal time, τ say,

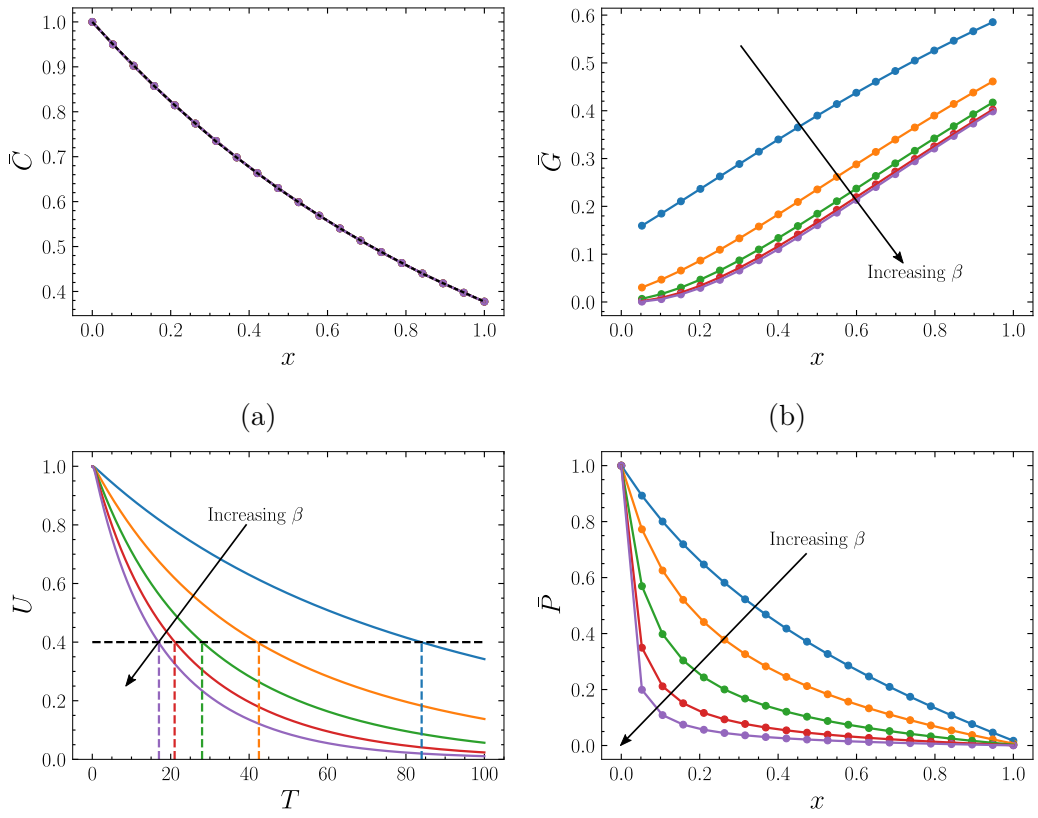

Figure 8.7: Graphs showing how the average particle concentration, $\bar{C}$, pore conductance, $\bar{G}$, flow rate, U, and junction pressure, $\bar{P}$, vary with depth, x, and time, T, at various values of β. The parameters are $N = 4$, $N^1 = 10$, $N^2 = 2$, $\alpha = 1$, $\delta = 0.5$, $\varepsilon = 0.1$. Coloured dots show the exact value of the quantity at the depths at which it is evaluated. Correspondingly coloured lines show a spline interpolation of the quantity between evaluation points. The values of β are 0.02 (blue), 0.04 (orange), 0.06 (green), 0.08 (red), 0.1 (purple), and the arrow shows the direction of increasing β. (a) The average particle concentration, $\bar{C}$, as a function of depth, x, at time $T = 100$. The dashed black line shows the approximate concentration, $\tilde{C}$, as a function of depth. Since the average particle concentration is identical for all values of β considered, only the solution for $\beta = 0.1$ (purple line) is visible. (b) The average pore conductance, $\bar{G}$, as a function of depth, x, at time $T = 100$. (c) The average flow rate, U, as a function of time, T. The dashed coloured lines show extrapolations of the total throughput, τ, for a given flow rate threshold, $U_c = 0.4$ (dashed black line), for the various values of β. (d) The average junction pressure, $\bar{P}$, as a function of depth, x, at time $T = 100$.

which is the associated time to reach the threshold, so that

$$\theta = \tau. \tag{8.9}$$

In constant pressure drop regimes, the total throughput is related to the terminal

time via

$$\theta = \int_0^{\tau} U(T)\,\mathrm{d}T. \tag{8.10}$$

In either scenario, the terminal time, which is

$$\tau \quad \text{such that} \quad U(T) < U_{\mathrm{c}} \quad \text{for} \quad T > \tau, \tag{8.11}$$

since the average flow rate is always monotonically decreasing in this model, is the key quantity. In Figure 8.7(c), we demonstrate how, given an average flow rate threshold, U_{c} (40%, for example), we read off the terminal time, τ. When $\beta = 0.02$ (dashed blue lines), for example, $U_{\mathrm{c}} = 0.4$ yields $\tau \approx 84$. As β increases (dashed blue lines to dashed purple lines), we see that τ, decreases. For $\beta = 0.1$ (dashed purple lines), the same flow rate threshold yields a terminal time of just $\tau \approx 17$. The physical interpretation is that, as the size of the particles increases, filters are able to maintain a given efficiency for less time before they become clogged.

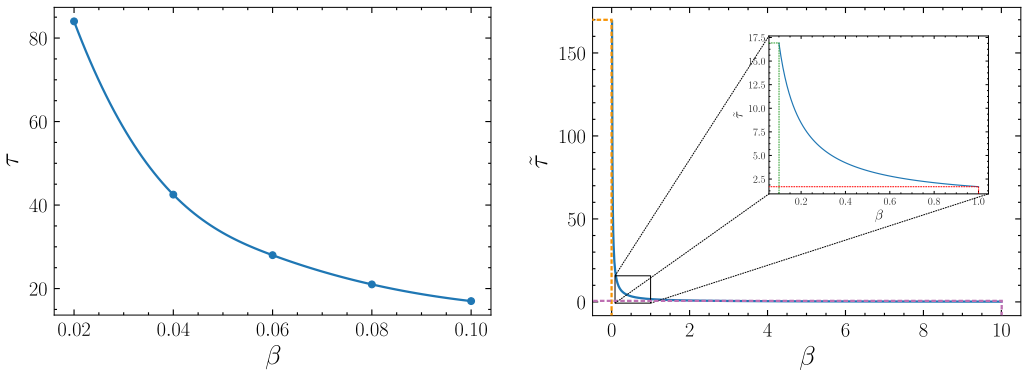

(a) (b)

Figure 8.8: Graphs showing how the terminal time, τ, and the approximate terminal time, $\tilde{\tau}$, vary with β, for a given flow rate threshold, 0.4. The parameters are $N = 4$, $N^1 = 10$, $N^2 = 2$, $\alpha = 1$, $\delta = 0.5$, $\varepsilon = 0.1$. (a) The terminal time, τ, as a function of β. Blue dots show the numerical solution at β values of $0.02, 0.04, 0.06, 0.08, 0.1$. The blue line shows the function $1.69\beta^{-1}$, found using a log-log plot, which we call the approximate terminal time, $\tilde{\tau}$. (b) The average terminal time, $\tilde{\tau}$, as a function of β. The dashed coloured lines show extrapolations of the approximate terminal time for β values of 0.01 (orange), 0.1 (green), 1 (red), 10 (purple).

Indeed, in Figure 8.8(a), we plot the terminal time for the small values of β shown in Figure 8.7. Using a log-log plot to fit a curve (blue line) to our numerical results (blue dots), we find that this decreases like β^{-1}. That is, we define the approximate terminal time to be

$$\tilde{\tau} = 1.69\beta^{-1}, \tag{8.12}$$

(for $\alpha = 1$, note that this is α dependent) which matches the terminal time almost exactly for $0.02 \leq \beta \leq 0.1$, so that $\tilde{\tau} \approx \tau$.

This finding means that we are able to approximate the terminal time that corresponds to values of β for which we have not solved the network model numerically. As such, in Figure 8.8(b), we show how, extrapolating the approximate terminal time, $\tilde{\tau}$, we are able to approximate times at which filtration terminates for large and infinitesimal β values, without appealing to further numerical simulations. We see, for example, that for $\beta = 0.01$ (dashed orange line), we expect that $\tilde{\tau} \approx 170$, while for $\beta = 10$ (dashed purple line), $\tau \ll 1$, and filtration terminates almost immediately.

8.2.5.2 Larger β values

To understand why the terminal time is so small for large values of β, we solve the system numerically for β values in the region $1 \leq \beta \leq 5$, and plot the solution in Figure 8.9. Comparing Figure 8.9 with Figure 8.7, we see that the behaviour of the solution is markedly different when $\beta = \mathcal{O}(1)$ as opposed to when $\beta = \mathcal{O}(10^{-1})$.

In particular, we see, in Figure 8.9(a), that particles are all captured within a layer near the inlet, the thickness of which decreases as β increases. For $\beta = 1$, the average particle concentration–depth profile (see blue line in Figure 8.9(a)) matches that in the $\beta = 0.1$ case (see purple line in Figure 8.7(a)). However, for $\beta = 5$ (purple line in Figure 8.9(a)), all particles are captured in approximately the first 50% of the filter.

To interpret this, we note that β is dictated by the size of particles in the fluid. When particles are larger, it takes less time to reduce the flow rate to negligible values, after which only minor changes to the average particle concentration can occur. If particles are large enough, then pores at the inlet become clogged before fluid has traversed the filter and reached the outlet. In Figure 8.9(b), we see that, correspondingly to the particle concentration plot, when $\beta = 5$ (purple line), only the pores in the first 50% of the filter have been affected by deposition. One physical implication is that, when particles are large, clogging occurs near the inlet, and much of the filter is unused when the membrane is disposed of, due to a flow rate decrease.

In Figure 8.9(c), we demonstrate how we read off terminal times, τ, for given flow rate thresholds, U_c (40% here), for larger values of β. Comparing the present case, with β values that are $\mathcal{O}(1)$ (Figure 8.9(c)), with the previous case, in which β values are $\mathcal{O}(10^{-1})$ (see Figure 8.7(c)), we observe that, as we predicted using the approximate terminal time curve in Figure 8.8(b), the terminal times are much smaller in the present case.

In summary, in this subsection we have shown that the parameter β controls the size of the particles, and thus the change in pore cross-sectional area, and therefore conductance, that occurs due to deposition. As a result, the value of β dictates the terminal time, τ, and thus the total throughput, θ. As β increases, deposition causes greater decrease in conductance, so that pore clogging occurs more rapidly. Consequently, the filter clogs over a shorter time, which means that the total throughput is smaller. In the next subsection, we explore the dependence of the solution on the parameters δ and ε.

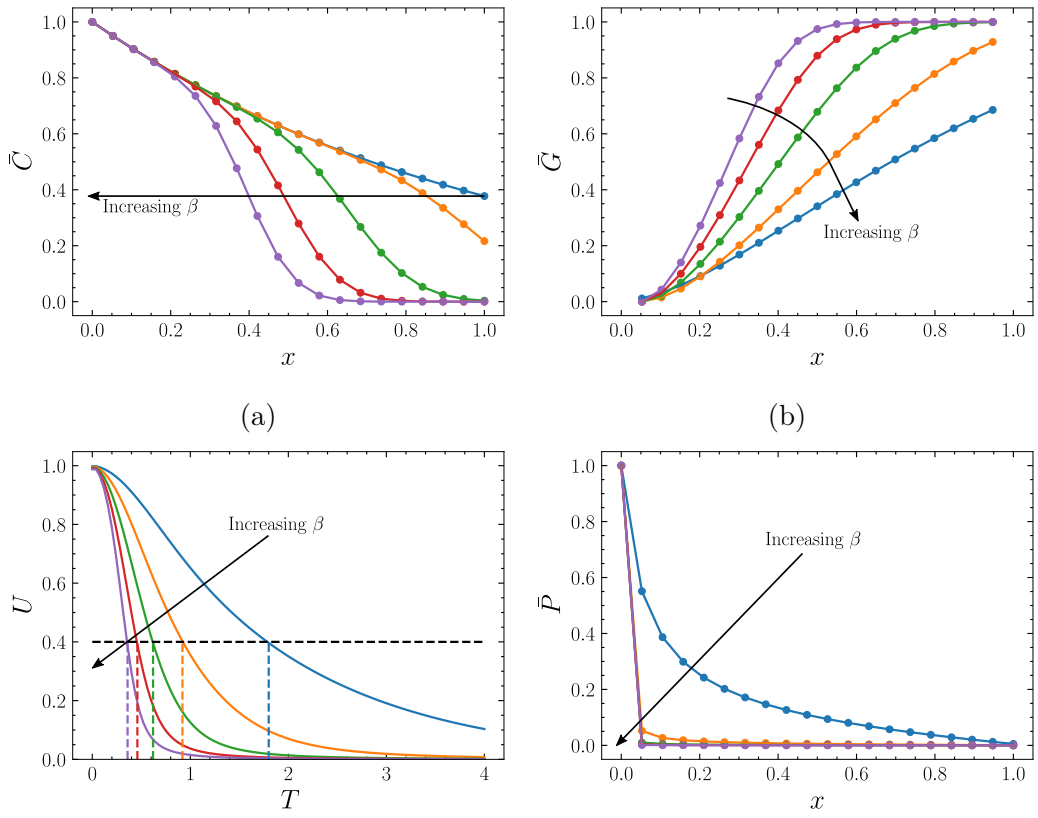

Figure 8.9: Graphs showing how the average particle concentration, $\bar{C}$, pore conductance, $\bar{G}$, flow rate, U, and junction pressure, $\bar{P}$, vary with depth, x, and time, T, at various values of β. The parameters are $N = 4$, $N^1 = 10$, $N^2 = 2$, $\alpha = 1$, $\delta = 0.5$, $\varepsilon = 0.1$. Coloured dots show the exact value of the quantity at the depths at which it is evaluated. Correspondingly coloured lines show a spline interpolation of the quantity between evaluation points. The values of β are 1 (blue), 2 (orange), 3 (green), 4 (red), 5 (purple), and the arrows show the direction of increasing β. (a) The average particle concentration, $\bar{C}$, as a function of depth, x, at time $T = 4$. (b) The average pore conductance, $\bar{G}$, as a function of depth, x, at time $T = 4$. (c) The average flow rate, U, as a function of time, T. The dashed coloured lines show extrapolations of the total throughput, τ, for a given flow rate threshold, $U_c = 0.4$, for the various values of β. (d) The average junction pressure, $\bar{P}$, as a function of depth, x.

8.2.6 Dependence on δ and ε: Discretisation

Lastly, in this subsection, we assess the effect of changing the scaling parameters, δ and ε, on the solution. It is easiest to see the effect of sweeping these two parameters if we set $\alpha = 0$, which we have shown to correspond to the no deposition scenario.

We plot the average particle concentration as a function of depth in Figure 8.10, and show the solution for various values of δ (with ε fixed) and ε (with δ fixed) in Figures 8.10(a) and 8.10(b), respectively. We recall that particles traverse the filter

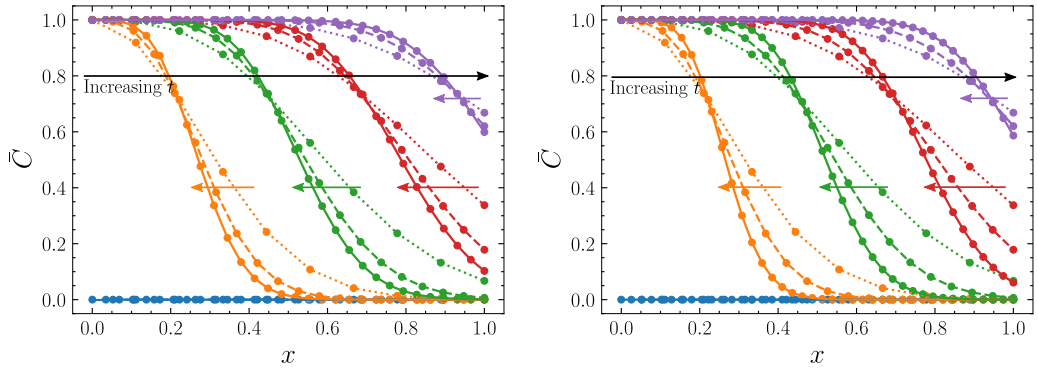

(a) (b)

Figure 8.10: Graphs showing how the average particle concentration, $\bar{C}$, varies with depth, x, at various values of time, T, and δ (a), and ε (b). The parameters are $N = 4$, $N^1 = 10$, $N^2 = 2$, $\alpha = 0$, $\beta = 1$. The values of T are 0.00 (blue), 0.25 (orange), 0.50 (green), 0.75 (red), 1.00 (purple). The black arrows show the direction of increasing time. The coloured arrows show the direction of decreasing δ (a) and ε (b) at the correspondingly coloured times. (a) The solution at various values of δ for $\varepsilon = 0.1$. The values of δ are 1 (dotted), 0.5 (dashed), 0.33 (solid). (b) The solution at various values of ε for $\delta = 0.5$. The values of δ are 0.5 (dotted), 0.1 (dashed), 0.05 (solid).

in a wave. Comparing Figures 8.10(a) and 8.10(b) we see that decreasing the values of δ and ε independently has similar effects on the solution. As δ and ε decrease, the transition region of the wave decreases in size. Physically, for smaller values of δ and ε, there are more junctions and pores in the filter, and so these are packed more closely to one-another. As a result, junctions fill with particles more quickly, which increases the sharpness of the wave front, thus decreasing the dispersion of particles.

One alternative interpretation is to view the network as a microscale discretisation of the macroscale. On the microscale, solution variables are tracked at nodes or pores, which are located at discrete points. On the macroscale, these solution variables are used to calculate 'average' quantities that, when the underlying solution variables are interpolated, vary in continuous space. In this setting, δ and ε dictate the 'closeness' of the points at which microscale solution variables are evaluated, and thus the 'fineness' of the discretisation of the average macroscale quantities. It follows that decreasing δ and ε has the effect of decreasing the numerical diffusion in the system, and thus of improving the quality of the discretisation, and the accuracy of the average macroscale quantities. This corresponds to increasing the number of nodes in a cell, or increasing the number of cells in the network. We showed at the beginning of this chapter, though, that increasing these numbers can be problematic, as it can lead to computationally infeasibly large linear systems to solve. In the following part, we will formalise the view that the network model is a discretisation of the macroscale, by developing an asymptotic method. We will thus develop a more rigorous method for deriving the average particle concentration, pore conductance, junction pressure,

and flow rate. Furthermore, we will show that the quality of these averages increases as ε and δ decrease, and that this decrease can be achieved without increasing the computational complexity of the system.

Chapter 9

Conclusions for the network model

In summary, in Part II, Chapters 6–8, we motivated, derived, and solved a novel network model for filtration. Our model serves as an introduction to the uses of pore network models (PNMs) in filtration, and there are several extensions to be explored as further work.

9.1 Summary

9.1.1 Motivation for the model

In Chapter 6, we began by introducing networks of nodes and edges as useful representations of the microscale of filtration media. In particular, in Section 6.1, we summarised recent research that produces network representations of filtration membranes by creating high quality characterisations and then analysing these algorithmically. The end result is a network whose size (and thus conductance) distribution and connectivity statistically match that of membrane pore space.

In Section 6.2, we discussed existing PNMs. These are typically systems of differential equations that use the pore space network as an underlying geometry. In general, these are computationally cheap enough to model 'mesoscopic' (i.e., areas containing hundreds or thousands of pores) properties. However, due to the complexity of pore space, and the resulting number of nodes and edges in the network, PNMs are too expensive to solve for macroscopic properties across the entire membrane, such as the effective permeability and adhesivity of the filter.

With computational constraints in mind, in Section 6.3, we motivated a novel network model for filtration. The aim was to derive and solve a simple system on a network that we supposed to be statistically representative of a membrane, which accounts for the particle deposition that causes dynamic connectivity in the network.

9.1.2 Derivation of the model

In Chapter 7, we derived a network model. Indeed, in Section 7.1, we began by assuming that the filter consists of a network of pores and junctions, modelled as cylinders

and spheres with known initial size distributions. The feed fluid is a continuum of particles that is forced through the network via a constant pressure drop. Particles adhere to, and so deposit on, the inner walls of pores, which causes a decrease in their cross-sectional area, and thus their conductance. This causes changes to the network connectivity. We assumed that fluid and particle mass, and pore volume, are conserved quantities, and arrived at a system of ordinary algebraic–differential equations on a dynamic network that consist of:

- A fluid mass conservation equation, which takes the form of a linear algebraic equation for the pressure in junctions as a function of the conductance of pores;
- An ordinary differential equation for the number of particles in each junction that describes the flux of particles in and out of the junction through connected pores, and the loss of particles in the flow as they deposit in pores;
- An ordinary differential equation for the conductance of each pore, which describes the decrease in conductance due to uniform deposition of particle volume along the pore walls caused by an adherence probability between particles and pores.

In Section 7.2, we nondimensionalised the model, and found four dimensionless parameter groups of interest: α (the adherence parameter); β (the particle size parameter); δ (the inverse of the number of pores in a cell); and ε (the inverse of the number of cells in the network).

9.1.3 Solution of the model

In Chapter 8, we found numerical solutions of the dimensionless network model. To this end, in Section 8.1, we began by proposing a suitable numerical scheme, involving solution of a linear problem the size of the number of nodes in the network. This is problematic because networks corresponding to entire membranes can contain $\mathcal{O}(10^4)$ or more pores, and thus nodes and edges, rendering solution computationally challenging.

Nevertheless, network models are useful for simulating smaller subsections of membranes. To demonstrate this, in Section 8.2, we solved our network model for a four-regular network containing $\mathcal{O}(10^2)$ nodes. For simplicity, we focused on the case where the network characterises a mono-dispersed filter. As a result, pore conductances are all equal initially, and need not be sampled as part of the solution scheme. We derived macroscale quantities: particle concentration; pressure; conductivity; and flow rate, by straightforwardly averaging the microscale solution variables, and explored how these vary with time and with the system parameters.

We began by discussing the simplest scenario, in which $\alpha = 0$ so that deposition does not occur. In this case, we found, as in Part I, that particles traverse the filter in a wave, with constant unit average conductance across the entire filter. The flow rate and local pressure are unchanged, since pore sizes are unaffected by the particles in the flow.

We then discussed the case $\alpha \neq 0$, so that deposition does occur. We found that the behaviour of the solution splits into two distinct time regions: before and after the fluid has reached the outlet for the first time. Before, particles travel as a wave. However, as they traverse the filter, some proportion, which is dictated by α, stick to pores, so that the particle concentration decreases in the region behind the wavefront. The deposition of particles in pores causes them to constrict, which decreases their conductance, more rapidly near the inlet, since there are the most particles in the flow here that are available for deposition. Because the conductance distribution is no longer uniform across the filter, the flow rate decreases concavely, which decreases the local pressure. Once fluid has reached the outlet for the first time, a constant particle concentration profile is maintained, since the deposition probability is constant. The conductance continues to decrease across the filter, but the rate of decrease slows, since there is less pore surface area available for deposition. As such, changes to velocity occur less rapidly, and decrease becomes convex.

We analysed this behaviour as functions of the system parameters. Firstly, we found that increasing α corresponds to increasing the adherence of each pore. Consequently, we found that α dictates the particle retention efficiency: If α is larger, then more particles are removed from the flow by each pore, so the total removal across the whole filter increases, and thus it is more efficient.

Secondly, we found that increasing β has the effect of increasing the size of particles in the suspension. Thus, as β increases, the rate at which the volume, and thus the conductance, of each pore decreases is accelerated. Consequently, we found that β dictates the total throughout of the filter: If β is larger, then particles cause a faster decrease in the conductance of each pore, so the flow rate of fluid through the filter drops below some critical threshold more rapidly, so that the total throughput decreases.

Lastly, we explored the effects of decreasing δ and ε, and thus increasing the numbers of nodes and edges in the network. We found that these had a similar effect on the solution. As δ and ε decrease, nodes and edges pack more tightly, so that the quality of the resolution of the macroscale quantities improves. This motivates the interpretation of the network model as a discretisation of the macroscale filter, but presents a numerical challenge: As the number of nodes and edges in the network increases, the approximation of effective properties improves, but solution becomes increasingly computationally expensive.

9.2 Further work

Further work might generally revolve around more detailed consideration of microscale structure and interactions. This could include closer attention to mechanisms involved in deposition, or consideration of particle size, to account for blocking, as in Part I. Porosity gradients could be explored using spatially dependent initial conductance distributions, for example. We outline some other extensions in this section.

9.2.1 Network connectivity

We focused on the simplest two-dimensional structure: a four-regular network. More complex connectivity could be simulated with little additional effort, using, for example, the plethora of existing construction algorithms for networks with random connectivity.

9.2.2 Initial conductance distributions and poly-dispersed pores

We considered initial edge conductances drawn from a Dirac delta distribution, which corresponds to mono-dispersed pore sizes. More accurate capture of microscale structural variation might focus on obtaining a distribution from which edge conductances are sampled, corresponding to poly-dispersed pore sizes (log-normally, for example, as in Subsection 7.1.6). Consideration of random initialisations would require repeated simulation, introducing additional computational expense.

9.2.3 Network representation and experimental data

Examination of real porous media samples would be another interesting extension. This might involve the coupling of our numerical scheme with an algorithm to derive a network from an actual microscale representation. One approach would inspect high resolution images for exact network extraction. Another would employ data on the statistical properties of real samples to infer the average coordination number corresponding to a particular material and thus parametrise the algorithm used to generate the network connectivity or else the distribution of initial conductances.

9.2.4 Multiscale models

Although these extensions would be interesting, they emphasise the key problem with our model, and with network models in general. More accurate representations of the microscale result in larger networks, which require increased computational resources to solve. An alternative direction for future study, then, is to focus on the development of models that offer the accuracy of network models but are more computationally efficient. To this end, in Part III, we introduce multiscale models as a candidate framework, and explore a particular example. In Part II, we averaged microscale variables in the most straightforward way to obtain macroscale properties. We will suggest 'network homogenisation' as a method for the systematic averaging of network quantities to obtain effective ones. We will find that the computational complexity of the effective model depends on the size of a statistically representative cell that contains far fewer nodes than the network as a whole. Yet, solutions of the cheaper effective model still agree with solutions of the more expensive network model in an asymptotic limit. Because of the computational benefit of our multiscale model, we will use it, rather than our network model, to explore the effects of the microscale on the macroscale properties, including some questions concerning connectivity and conductance distribution that we raised earlier in this section.

Part III

A multiscale model for filtration

Chapter 10

Introduction to the multiscale model

10.1 Multiple scales in filtration

Filtration is an inherently multiscale process because particle and pore interactions that occur on the microscale affect macroscale filter properties [83]. In Part I, we found that the size distributions of particles and pores dictate the mechanisms by which particles being captured affects the pore size, which further influences the rate of capture, and thus determines the effective properties of the filter, such as the shape of the flow rate profile. In Part II, we established that the geometry of the microscale helps to determine macroscale properties of industrial interest, such as the particle removal efficiency and process termination time. In special cases, either microscopic or macroscopic effects may dominate, so that operation properties are well predicted by independent microscale or macroscale simulations. Generally, however, microscale and macroscale effects are strongly coupled in filtration media, and consideration of multiple scales is required.

In some ePTFE filters, for example, pore sizes can range from around 0.02μm to 15μm [48]. Although individual sheets of ePTFE are relatively thin, perhaps millimetres deep, it is quite common to stack these or combine them in some other way, so that the effective thickness is significantly larger. As a consequence, process properties of industrial interest that depend on the entire depth, such as the proportion of the incoming particles that are retained across the membrane, are the result of processes that occur over an area of around a centimetre squared, say, which can contain as many as 1.4 billion pores [48].

This poses significant challenges in models that involve detailed resolution of the microscale or agent-based approaches that track the behaviour of individual particles. Non-specialist computers struggle with the memory demands of solvers that seek to solve pore network models (PNMs) like the one in Part II when the number of nodes and edges, which represent individual pores, exceeds the order of thousands. The problem worsens when industrialists are interested in obtaining optimal filter configurations, requiring repeated solution of models for cost function descents and parameter sweeps. PNMs alone, then, are insufficient for at least some aspects of filtration modelling, and there is a need for alternative mathematical approaches.

10.2 Existing multiscale models for filtration

Multiscale models are a useful tool for deriving the macroscopic behaviour of systems that contain microscale information [172]. Classical examples include the derivation of: Darcy's law [172, 173]; the Navier–Stokes equations with various boundary conditions [174]; and advection–diffusion in porous media [175]. Homogenisation, the method by which effective equations are derived from microscale dynamics, is an active area of research for filtration applications due to the inherent multiscale nature of many filtration membranes (see Chapter 6). Indeed, recent work includes [77], in which Dalwadi *et al.* homogenise the problem of flow through a filter with a near periodic microstructure coupled with particle transport owing to advection, diffusion, and filter adsorption, and use the resulting computationally efficient macroscale equations to investigate why porosity gradients (imposed on the microscale, by varying the pore size) can improve filter efficiency. In [76], Bruna *et al.* consider the problem of diffusion in a porous medium containing a collection of impenetrable spheres and find the corresponding effective diffusion coefficient using two different methods. Meanwhile, in [82], Printsypar *et al.* investigate how the microstructure of a porous medium influences overall filtration performance, by combining a homogenisation approach with an algorithm that accounts for the agglomeration of fibres when they grow until they touch each other, due to particle deposition.

In these examples, the microscale consists of circles of given initial radii that represent fibres in the filter medium and thus obstructions to the suspension. This is a typical approach, adopted by many authors. In [78], for example, Dalwadi *et al.* propose a similar setup and use the resulting homogenised model to predict the onset of filter clogging. This work typifies the homogenisation method, and we use it to outline the process used to average the problem of particle-laden flow through a filter.

Dalwadi *et al.*, [78], begin with the equations for Stoke's flow coupled to an advection–diffusion equation that governs the evolution of the particle concentration. Deposition is imposed via a partially absorbing Robin boundary condition that results in growth of the fibres via a volume conservation law. The contaminants are small compared to the obstacles, and so particle–particle interactions are unimportant. The authors proceed with homogenisation by introducing a 'microscale' spatial variable that varies more quickly and, crucially, independently, of the 'macroscale' one. The microscale coordinate is later removed again by introducing periodicity in this variable via repetition of a representative cell, which is a small area of the microscale. Intra-cell variation is accounted for with the microscale variable, while inter-cell variation is accounted for with the macroscale variable. Then, expanding the velocity, pressure, particle concentration, as well as any other dependent variables, in terms of the small parameter that separates the cell size from the filter size, the authors obtain effective equations, which govern the evolution of homogenised variables that have been averaged over the cell and are thus independent of the microscale variable at the asymptotic order of interest. The parameters of these resulting equations depend on the microscale information (the size of the obstacles in this case) via a cell

problem, which, in this example, links the effective permeability to the obstacle radius via an integral equation. It follows that solution of this system allows the authors to obtain the effective permeability, and thus other effective properties of the filter, without losing all the information gained from having knowledge of the microscale, unlike purely macroscale models, which ignore microscale structure entirely.

In this example, as well as many others, the microscale geometry is a continuum that is referenced by a continuous spatial variable. However, in studies of porous media (as we discussed in Part II), it is common to simplify by approximating the microscale pore space with a network, with a discrete set of locations at which system variables, such as the particle concentration and fluid conductance, are measured (nodes and edges, respectively). This approximation has led to the derivation of multiscale systems in which the microscale is discrete (i.e., a network). The main advantage of homogenising a network over homogenising the exact geometry is the reduction in computational complexity, since in a network there are a finite number of spatial points to consider. Firstly, this allows for the study of a larger physical area. Secondly, this permits rapid repetition of solution, so that effective parameter *distributions* may be obtained from systems with a stochastic element (like the one considered in Part II, since the initial conditions are drawn from a distribution). This Monte Carlo approach is infeasible when the microscale is fully resolved, like in the finite element method, for example. We generally refer to the process of obtaining effective equations on the macroscale continuum from network representations of the microscale as 'network homogenisation'.

Much of the literature on network homogenisation involves the study of the emergence of continuum diffusion from discrete particle jumps on an underlying lattice. The traditional approach, which is reviewed in [176] in the context of the evolution of Brownian particles in disordered environments, uses generating functions and lattice Green functions (see also [177]). The first step is usually to split the spatial variable into one that gives the position in the cell and a second that references the position of the cell (see [178, 179]). Since the probabilities of particle state transitions do not vary from one cell to another, the traditional process continues by taking a discrete Fourier transform with respect to the second index.

In recent work, by Chapman *et al.* [79, 80], however, a slightly different methodology is followed, which more closely corresponds to the standard continuous homogenisation method (in [78], for example). In the first of these, [79], Chapman *et al.* begin by introducing a node index in the representative cell, which is $\varepsilon \ll 1$ times as small as the network as a whole. This index plays the role of the usual continuous microscale spatial variable. That is, the dependent variable of interest, the probability of finding a particle at node i at the continuous macroscale position $\boldsymbol{x}$, in this case, is a function of i and $\boldsymbol{x}$ independently. Carrying out a Taylor expansion about the point $\boldsymbol{x}$, and assuming an asymptotic form for the solution as usual, the authors obtain a master equation for the probability, which is now explicitly independent of the microscale index (and thus averaged over the cell) at leading order. Solutions of the master equation agree with solutions of the underlying dynamics in the asymptotic limit $\varepsilon \to 0$. Only the parameters of the homogenised system, the effective diffusion coefficient in this case, depend on the microscale (the transition probabilities, here).

As in the continuous case, this dependence occurs via a cell problem. In the discrete scenario, this takes the form of a linear matrix equation, which returns the 'cell solution' as a function of the transition probabilities.

In the second piece, [80], Chapman *et al.* use a generally similar method. This time, though, the microscale contains a continuum fluid rather than particles that transition discretely. As such, fluid moves through the microscale due to mass conservation laws, as opposed to transition probabilities. That is, the authors homogenise the problem of incompressible flow through a network with specified initial edge conductances and node volumes. The microscale setup is thus identical to that in Part II, except for the absence of particles in the flow. As a result, deposition does not occur, and the network's structure is static. Via a similar method as that in [79], Chapman *et al.* [80] arrive at an effective system defined on the continuum macroscale geometry that consists of a continuity equation and the Darcy equation, which relates the macroscale flow rate to the pressure gradient via the effective permeability. The permeability depends on the conductances of the network edges via the cell solution. The computational complexity of the cell problem is a function of the number of nodes in the cell, which is considerably less than that in the entire network. This allows the authors to obtain a distribution for the effective permeability given only statistical information about the network, as opposed to the exact conductance of every edge, via repeated solution of the cell problem. In this way, Chapman *et al.* [80] examine the influence of the microscale structure, in terms of both the connectivity and the distribution of random conductances, upon the effective properties of the network.

10.3 A novel multiscale model for filtration

In the remainder of Part III, we will extend the work in [80] by homogenising the flow *and deposition* of a *particle-laden* fluid through a *dynamic* network representation of the filter microscale, that is, the network model discussed in Part II.

In Chapter 11, we will derive the multiscale model corresponding to the network model in Part II. We will begin, in Section 11.1, by posing the network model on a periodic network that consists of repeated translation of a representative cell, and introducing the necessary notation, similar to that used in [80]. The result is a dimensionless periodic network model to be homogenised, with initial conditions corresponding to Dirac-delta distributed of log-normally distributed initial pore conductances. In Section 11.2, we outline the process of network homogenisation. In Section 11.3, we then carry out homogenisation of our model. We first focus on the quasi-one-dimensional case, in which a network with nodes that are not necessarily connected to their spatially nearest neighbours is embedded in a single macroscopic dimension. Then, in Section 11.4, we consider the case where a network with arbitrary (though still periodic) connectivity is embedded in a continuum of arbitrary dimension. We will see that this case is conceptually similar, although notationally more complex. Proof of the algebraic results that underpin our findings are also more challenging. Sections 11.3 and 11.4 proceed relatively similarly to the derivation in [80]. The process is extended, however, by the need to homogenise the equation for

the conservation of mass of particles, and the corresponding equation for the conservation of the volume of pores. As such, we will find that the problem deviates from that in [80] in so much as that the pore conductances, and the cell solutions from which they are derived, are functions of time, so that the structure of the underlying network is dynamic. Darcy's law, which is parametrised by a function of the microscale that represents the effective permeability, is identical to that derived in [80]. In our model, this is coupled to an advection–reaction equation for the particle concentration, which is parametrised by a second microscale-dependent function, which we call the adhesivity, since it represents the effective ability of the filter to capture particles via adhesion based deposition, and thus the reactivity in the macroscale system.

In Chapter 12, we will explore solutions of our multiscale model. We will begin, in Section 12.1, by discussing a numerical scheme for solution of a reduction of the model that still contains its interesting properties. We will find that even the most straightforward solution method is less computationally complex than solution of the corresponding network model. Furthermore, we will suggest a pre-calculation step that further decreases computation time substantially. In Section 12.2, we will exhibit solutions of the multiscale model on various four-regular networks, to demonstrate the case where the underlying structure is indeed exactly periodic, as is assumed in the homogenisation process. Firstly, we will consider non-random edge conductances, which corresponds to the case where pore sizes are initially mono-dispersed. We will find that, despite vast improvements in computational complexity, the solution of the multiscale model agrees with that of the network model in the asymptotic limit where many small cells constitute the network. Secondly, we will consider log-normally random edge conductances, which corresponds to poly-dispersed initial pore sizes, and show that a general run of the multiscale model will agree qualitatively but not quantitatively with the underlying network solution, due to different random initialisations. As such, in Section 12.3, we demonstrate the results of repeated calculation of the effective parameters on four regular networks, as well as those with more complex connectivity. We will show that the *statistics* of the multiscale solution do agree with that of the microscale solution in the asymptotic limit, provided that the repeated cell is statiscally *represantative* of the network as a whole. In particular, in [80], Chapman *et al.* derive the sampled distribution of the effective permeability and show that its average represents the effective flow dynamics provided that the cell contains enough nodes and has approximately the correct coordination number. We find good agreement, and extend these conclusions to the effective adhesivity, thus showing that multiscale models derived from *dynamic* network models are a valid approach for the prediction of the effective properties of filters in which particles deposit due to adhesion between particles and pores on the microscale (that is perhaps not even periodic).

Chapter 11

Derivation of the multiscale model

In this chapter, we derive a multiscale model for filtration in which the microscale and macroscale geometry are accounted for simultaneously. We begin by deriving a system of ordinary algebraic–differential equations on the microscale, which we model as a spatially periodic network of pores and junctions. We then develop an asymptotic method, called network homogenisation, to average this system. Carrying out this method on the periodic-network model, we arrive at a system of partial differential equations on the macroscale, which is modelled as a continuum of porous material. The parameters of this continuous system, which model the permeability and adhesivity of the membrane, depend on the dynamically varying conductances of the pores in the underlying network, so that the macroscale dynamics are coupled with the behaviour of microscale.

11.1 Microscale model

We begin by modelling the microscale of the filter as a periodic network. We first derive a dimensional system of equations that is similar to the non-periodic network model in Part II, but accounts for simplifications that arise from the periodicity of the network. We then nondimensionalise this model, scaling to account for the assumption that the network contains many cells in the direction of dominant flow.

11.1.1 Dimensional model

As in Part II, we consider the pressure driven flow of a particle-laden fluid through a filter that is modelled as a network of pores and junctions. Particles in the flow deposit on pore walls due to a mutual adhesivity between the particles and pores, which decreases their cross-sectional area and thus their conductance, so that the structure of the network is dynamic. Here, unlike in Part II (see the non-periodic network illustrated in Figure 7.1), the filter is spatially periodic, so that the network is constructed by repeated translation of a cell in D-dimensional space, where $D \in \{1, 2, 3\}$, as illustrated in Figure 11.1.

The basic setup is the same as that in the dimensional network model from Part II,

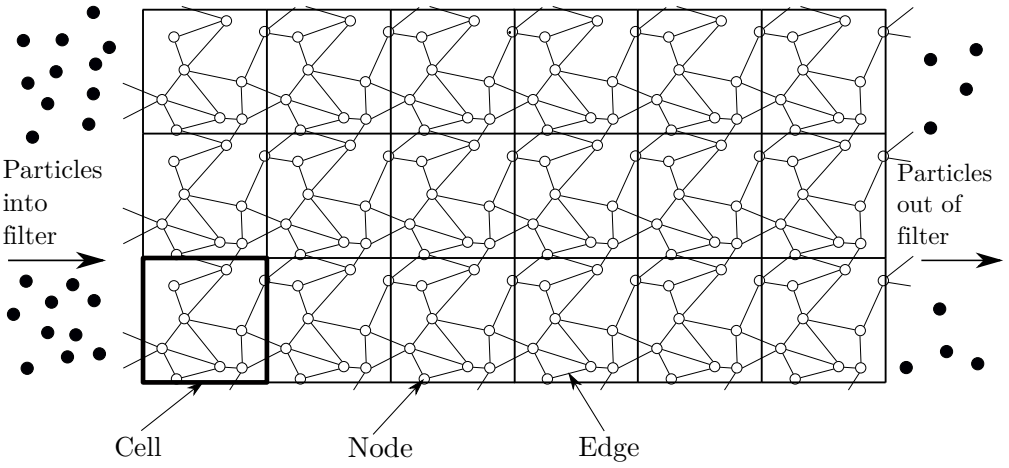

Figure 11.1: A diagram of a two-dimensional filter composed of a periodic network formed from a cell that is repeated vertically and horizontally. Particles in the flow enter through edges crossing the left boundary and exit through those crossing the right boundary, after traversing the network.

(7.23)–(7.31). We call ε the ratio of the cell length to the filter length, so that ε^{-1} cells constitute the filter depth (see Figure 11.1). When the network is non-periodic, pores and junctions are referenced by indices i and j that vary between 1 and the number of junctions in the filter, N_{f}, say. Here, however, we account for the periodicity of the network by introducing one further index called the cell reference, $\boldsymbol{r} = (r^1, \ldots, r^D)^\top$, which is a vector that describes the position of a cell containing one junction relative to the cell containing another. We use i, j, and $\boldsymbol{r}$, together, to index a pore, so that, for example, $G_{ij}^{\boldsymbol{r}}$ is the conductance of the pore between junction i in one cell and junction j in a cell at position $\boldsymbol{r}$ relative to the first one. In a two-dimensional network, therefore, $G_{1\,2}^{(1,0)^\top}$ denotes the conductance of the pore connecting junction 1 in one cell to junction 2 in the cell directly to the right of the first cell. This convention is illustrated in Figure 11.2. The indices i and j now vary between 1 and the number of junctions in the cell, N, say. Junctions in one cell are connected to junctions in another cell up to K cells away, and so the set of possible values of each r^m is $\mathcal{R} = \{-K, \ldots, -1, 0, 1, \ldots, K\}$, so that the set of possible $\boldsymbol{r}$ is $\boldsymbol{\mathcal{R}} = \mathcal{R}^D$. For example, when $K = 1$, junctions in a cell are connected to junctions in the same cell or its nearest-neighbouring cells, and $\mathcal{R} = \{-1, 0, 1\}$ so that $\boldsymbol{\mathcal{R}} = \{-1, 0, 1\}^D$ (see Figure 11.2 (Top)). When $K = 2$, pores cross up-to two cell boundaries, and $\mathcal{R} = \{-2, -1, 0, 1, 2\}$ so that $\boldsymbol{\mathcal{R}} = \{-2, -1, 0, 1, 2\}^D$ (see Figure 11.2 (Bottom)). The symmetric structure of $\mathcal{R}$ follows by noting that if r^m is an element of $\mathcal{R}$, then so too is $-r^m$. This is because, for any i, j, and $\boldsymbol{r}$, we have $G_{ij}^{\boldsymbol{r}} = G_{ji}^{-\boldsymbol{r}}$, by periodicity of the network (see Figure 11.2). Note that non-planar networks, like the ones in Figure 11.2, are permitted.

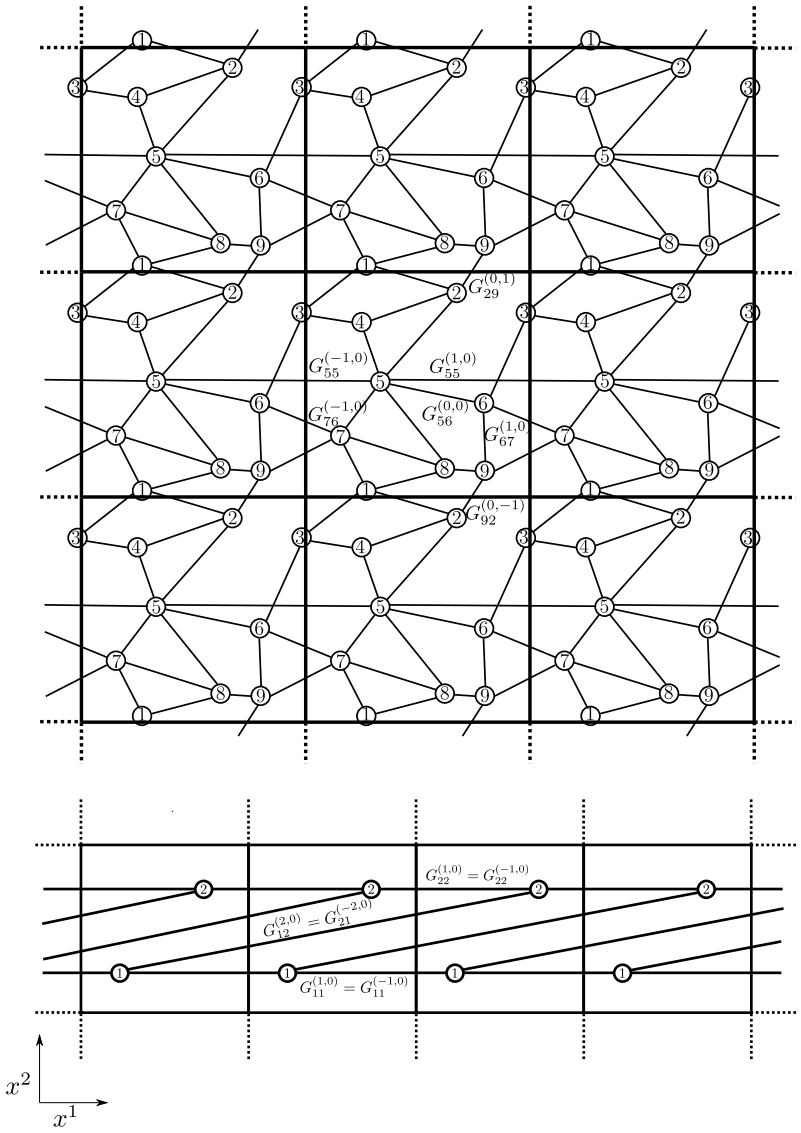

Figure 11.2: Diagrams of sections of two periodic networks that are embedded in two-dimensional space. The conductances of some pores are labelled to illustrate the use of the lower indices, i and j, and the upper index, $\boldsymbol{r}$, to index the pore between junction i in one cell and junction j in a second cell at position $\boldsymbol{r}$ relative to the first. (Top) A cell of $N = 9$ junctions repeated nine times. Junctions in one cell are connected to junctions in cells up to one cell away. It follows that r^1 and r^2 are drawn from the set $\mathcal{R} = \{-1, 0, 1\}$, so that $\boldsymbol{r}$ is drawn from $\boldsymbol{\mathcal{R}} = \{-1, 0, 1\}^2$. (Bottom) A cell of $N = 2$ junctions repeated four times. Junctions in one cell are connected to junctions in cells up to two cells away. It follows that r^1 and r^2 are drawn from the set $\mathcal{R} = \{-2, -1, 0, 1, 2\}$, so that $\boldsymbol{r}$ is drawn from $\boldsymbol{\mathcal{R}} = \{-2, -1, 0, 1, 2\}^2$.

Proceeding similarly to Part II, we arrive at a dimensional network model similar to (7.23)–(7.31). Accounting for the periodicity of the network, the equations for the conservation of fluid, particles, and pores, (7.23), (7.24), and (7.25), become

$$\sum_{j=1}^{N}\sum_{\boldsymbol{r}\in\boldsymbol{\mathcal{R}}} Q_{ij}^{\boldsymbol{r}} = 0, \tag{11.1}$$

$$\bar{V}\frac{\partial C_i}{\partial T} = \sum_{j=1}^{N}\sum_{\boldsymbol{r}\in\boldsymbol{\mathcal{R}}} \Big((1-\bar{A})Q_{ji}^{-\boldsymbol{r}}C_j H(Q_{ji}^{-\boldsymbol{r}}) - Q_{ij}^{\boldsymbol{r}}C_i H(Q_{ij}^{\boldsymbol{r}})\Big), \tag{11.2}$$

$$\frac{\partial G_{ij}^{\boldsymbol{r}}}{\partial T} = -\frac{2S\bar{A}}{(8\pi\mu\bar{L})^{\frac{1}{2}}} C_{ij}^{\boldsymbol{r}}(G_{ij}^{\boldsymbol{r}})^{\frac{3}{2}}|P_i - P_j|, \tag{11.3}$$

respectively, where the flux down each pore is related to the pressure drop and conductance of the pore via

$$Q_{ij}^{\boldsymbol{r}} = G_{ij}^{\boldsymbol{r}}\left(P_i - P_j\right). \tag{11.4}$$

Note that, in the summations here, lower indices, i and j, vary from 1 to the number of junctions in the repeating cell, N. Sums over the upper index, $\boldsymbol{r}$, are over all possible cell references in the set $\boldsymbol{\mathcal{R}} = \{-K, \ldots -1, 0, 1 \ldots, K\}$, the size of which depends on K.

As in Part II, we enforce a constant pressure drop across the filter, and a constant particle concentration at the inlet, so that the boundary conditions are

$$P_{\text{in}}(T) = p_{\text{in}}^*, \quad P_{\text{out}}(T) = p_{\text{out}}^*, \tag{11.5a,b}$$

and

$$C_{\text{in}}(T) = c_{\text{in}}^*, \tag{11.6}$$

for $T \geq 0$. There are no particles in the filter initially, and initial pore radii, and therefore pore conductances, are drawn from the distribution $\mathcal{G}$, which we assume is either a Dirac-delta distribution, or a log-normal distribution, to exemplify solutions of the model. Thus the initial conditions are

$$C_i(0) = 0, \tag{11.7}$$

for $i \in \{1, \ldots, N, \text{out}\}$, and

$$G_{ij}^{\boldsymbol{r}}(0) = G_{ij}^{\boldsymbol{r}0}, \tag{11.8}$$

for $i, j \in \{1, \ldots, N, \text{in}, \text{out}\}$, where the probability density function (PDF) of $\mathcal{G}$ is either

$$g(G_{ij}^{\boldsymbol{r}0}) = \delta(G_{ij}^{\boldsymbol{r}0} - \bar{G}), \quad \text{or} \quad g(G_{ij}^{\boldsymbol{r}0}) = \frac{1}{\sqrt{2\pi}\sigma_G G_{ij}^{\boldsymbol{r}0}} \exp\left(-\frac{\left(\log\left(\frac{G_{ij}^{\boldsymbol{r}0}}{\bar{G}}\right) + \frac{\sigma_G^2}{2}\right)^2}{2\sigma_G^2}\right). \tag{11.9a,b}$$

The equations (11.1)–(11.9) form a closed system for the solution variables, $Q_{ij}^{\boldsymbol{r}}$, C_i, P_i, and $G_{ij}^{\boldsymbol{r}}$, on a periodic network, subject to the specification of the dimensional parameters, $\bar{L}$, $\bar{V}$, $\bar{A}$, S, μ, p_{in}^*, p_{out}^*, and c_{in}^*, along with any other parameters that are needed to specify the probability density functions for the initial conductance distribution from which $G_{ij}^{\boldsymbol{r}0}$ are drawn, $\mathcal{G}$, such as $\bar{G}$ and σ_G in (11.9). As in the non-periodic case, this network model is independent of node positions. The periodic connectivity of the network enters the system through the pore conductances, $G_{ij}^{\boldsymbol{r}}$. In the next section we will nondimensionalise the dimensional network model (11.1)–(11.9).

11.1.2 Dimensionless model

In the subsequent sections of this chapter, we will focus on deriving a macroscale system from our microscale model, (11.1)–(11.9). To this end, we will take a network containing a fixed number of junctions in each cell (so that δ from Part II is fixed) and consider the case in which the network contains many infinitesimally small cells, which corresponds to the asymptotic limit $\varepsilon \to 0$. The aim of our nondimensionalisation is to arrive at a scaled system for which this analysis is simple. We therefore scale periodic variables so that

$$L_{ij}^{\boldsymbol{r}} = \bar{L}\tilde{L}_{ij}^{\boldsymbol{r}}, \quad V_i = \bar{V}\tilde{V}_i, \quad P_i = (p_{\text{in}} - p_{\text{out}})\tilde{P}_i + p_{\text{out}}, \quad C_i = c_{\text{in}}\tilde{C}_i, \tag{11.10}$$

$$Q_{ij}^{\boldsymbol{r}} = \bar{G}(p_{\text{in}} - p_{\text{out}})\tilde{Q}_{ij}^{\boldsymbol{r}} \quad G_{ij}^{\boldsymbol{r}} = \frac{\bar{G}}{\varepsilon}\tilde{G}_{ij}^{\boldsymbol{r}}, \quad T = \frac{\varepsilon\bar{V}}{\bar{G}(p_{\text{in}} - p_{\text{out}})}\tilde{T}. \tag{11.11}$$

Similarly to our scaling of the non-periodic variables in (7.33) and (7.34), the scalings in (11.10) mean that pores and junctions all have unit length and volume initially, respectively, the feed has unit particle concentration, and the filter has a unit pressure drop enforced across it. We will find (see (11.76)), that the timescale in (11.11),

$$T_{\text{c}} = \frac{\varepsilon\bar{V}}{\bar{G}(p_{\text{in}} - p_{\text{out}})}, \tag{11.12}$$

is the average time it takes fluid to cross a cell.

In dimensionless variables, dropping tildes, the equations for the conservation of fluid, particles, and pores, are

$$\sum_{j=1}^{N}\sum_{\boldsymbol{r}\in\boldsymbol{\mathcal{R}}} Q_{ij}^{\boldsymbol{r}} = 0, \tag{11.13}$$

$$\frac{\partial C_i}{\partial T} = \sum_{j=1}^{N}\sum_{\boldsymbol{r}\in\boldsymbol{\mathcal{R}}}\Big((1-\alpha\varepsilon)Q_{ji}^{-\boldsymbol{r}}C_jH(Q_{ji}^{-\boldsymbol{r}}) - Q_{ij}^{\boldsymbol{r}}C_iH(Q_{ij}^{\boldsymbol{r}})\Big), \tag{11.14}$$

$$\frac{\partial G_{ij}^{\boldsymbol{r}}}{\partial T} = -\alpha\beta C_{ij}^{\boldsymbol{r}}(G_{ij}^{\boldsymbol{r}})^{\frac{3}{2}}|P_i - P_j|, \tag{11.15}$$

where the flux down each pore is related to the pressure drop and conductance of the pore via

$$Q_{ij}^{\boldsymbol{r}} = \frac{G_{ij}^{\boldsymbol{r}}}{\varepsilon}\left(P_i - P_j\right). \tag{11.16}$$

The boundary conditions are

$$P_{\text{in}}(T) = 1, \quad P_{\text{out}}(T) = 0, \tag{11.17a,b}$$

and

$$C_{\text{in}}(T) = 1, \tag{11.18}$$

for $T \geq 0$, and the initial conditions are

$$C_i(0) = 0, \tag{11.19}$$

for $i \in \{1, \ldots, N, \text{out}\}$, and

$$G_{ij}^{\boldsymbol{r}}(0) = G_{ij}^{\boldsymbol{r}0}, \tag{11.20}$$

for $i, j \in \{1, \ldots, N, \text{in}, \text{out}\}$. This time, the dimensionless parameters, in terms of the dimensional ones, are

$$\alpha = \frac{\bar{A}}{\varepsilon}, \quad \beta = \frac{2S\bar{V}c_{\text{in}}\varepsilon^{\frac{3}{2}}}{(8\pi\mu\bar{L}\bar{G})^{\frac{1}{2}}}, \quad \varepsilon = \frac{1}{N^1}. \tag{11.21}$$

We will find (see Section 11.3), that the factor of ε^{-1} in α ensures that particle deposition occurs at $\mathcal{O}(\varepsilon)$ in each cell, which results in $\mathcal{O}(1)$ removal over the filter for $\alpha = \mathcal{O}(1)$. Similarly, the extra factor of ε in β ensures $\mathcal{O}(1)$ conductance variation for $\alpha = \mathcal{O}(1)$ and $\beta = \mathcal{O}(1)$. The dimensionless initial pore conductances, $G_{ij}^{\boldsymbol{r}0}$, are drawn from the initial conductance distribution, $\mathcal{G}$, which has a pdf that is either given by

$$g(G_{ij}^{\boldsymbol{r}0}) = \delta(G_{ij}^{\boldsymbol{r}0} - 1), \quad \text{or} \quad g(G_{ij}^{\boldsymbol{r}0}) = \frac{1}{\sqrt{2\pi}\sigma_G G_{ij}^{\boldsymbol{r}0}} \exp\left(-\frac{\left(\log(G_{ij}^{\boldsymbol{r}0}) + \frac{\sigma_G^2}{2}\right)^2}{2\sigma_G^2}\right), \tag{11.22a,b}$$

so that, either pores have unit conductance initially, or their conductances are distributed log-normally about a unit mean.

The equations (11.13)–(11.20) form a closed system for the dimensionless periodic-variables $Q_{ij}^{\boldsymbol{r}}$, C_i, P_i, and $G_{ij}^{\boldsymbol{r}}$, given the dimensionless parameters α, β, and ε. These are defined in terms of the dimensional parameters in (7.46), and any further dimensionless parameters, for example σ_G in (11.22), that are needed to specify the initial conductance distribution, $\mathcal{G}$, from which the initial pore conductances, $G_{ij}^{\boldsymbol{r}0}$, are drawn.

In this section, we have extended the non-periodic network model that we derived in Part II, (7.38)–(7.45), to a periodic-network model, (11.13)–(11.20). In the remainder of this chapter, we will develop an asymptotic method to systematically homogenise the system, and use this method to derive an effective system that is defined on the macroscale and microscale geometry of the filter simultaneously.

11.2 Network homogenisation methodology

We are interested in the case where the ratio of the cell length to the network length, ε defined in (11.21), is small, $\varepsilon \ll 1$, so that many cells constitute the network in the dominant direction of the flow. In this scenario, there are two scales in our model, which are separated by ε. The microscale is the scale of each cell, while the macroscale is the scale of the entire network. In the limit $\varepsilon \to 0$, we will derive a continuous approximation of the discrete periodic-network model, (11.13)–(11.20), by using the following steps:

Step 1. Evaluate all microscale-dependent variables, by which we mean variables indexed by i, j, and $\boldsymbol{r}$, relative to a common, continuous point, and assume that these variables depend on the macroscopic continuous spatial coordinate and the microscale index *independently*.

Step 2. Carry out a Taylor-series expansion of each of these variables about the common point in terms of the small parameter, ε.

Step 3. Assume an asymptotic expansion in terms of the small parameter, ε, as the ansatz for each variable for which the solution is sought.

Step 4. Solve the resulting master equation at each asymptotic order. Higher-order problems may need to be considered to close lower order problems, to specify the macroscale solution variable.

We call this process network homogenisation, which is a variation of the usual method of multiple scales, in which the microscale consists of discrete spatial points.

To carry out network homogenisation, therefore, we must define discrete spatial points at which the solution variables of the microscale model, (11.13)–(11.20), $Q_{ij}^{\boldsymbol{r}}$, C_i, P_i, and $G_{ij}^{\boldsymbol{r}}$, are defined. To this end, we define $\boldsymbol{X}_i$ so that εX_i^m is the component of the position of junction i in the x^m direction relative to some fixed point $\boldsymbol{x}$. It follows that $\boldsymbol{x}+\varepsilon\boldsymbol{X}_i$ is the position of junction i in the continuous macroscopic spatial variable. We exemplify this convention in Figure 11.3. Since the network is periodic, it follows that junction j in the cell at position $\boldsymbol{r}$ relative to the cell containing i is located at the point $\boldsymbol{x} + \varepsilon(\boldsymbol{X}_j + \boldsymbol{r} \circ \boldsymbol{l})$, where $\circ$ denotes the Hadamard product ($\boldsymbol{r} \circ \boldsymbol{l} = (r^1 l^1, \ldots, r^D l^D)^\top$), and $\boldsymbol{l}$ is a vector containing the dimensions of the filter, so that l^m is the length of the filter in the x^m direction (see Figure 11.3). It remains to specify the points, $\varepsilon\boldsymbol{X}_{ij}^{\boldsymbol{r}}$, say, at which pores are defined (relative to $\boldsymbol{x}$). We choose the midpoint between nodes i and j, which we call $\varepsilon\boldsymbol{M}_{ij}^{\boldsymbol{r}}$, so that $\varepsilon M_{ij}^{\boldsymbol{r}m}$ is the component of this midpoint in direction x^m, as illustrated in Figure 11.4.

$$M_{ij}^{\boldsymbol{r}m} = \frac{X_j^m + r^m l^m + X_i^m}{2}. \tag{11.23}$$

To demonstrate network homogenisation, we define the fixed point $\boldsymbol{x}$ to be the left-bottom corner of a particular cell, which we will call the reference cell, and consider Steps 1–4 in the context of three example quantities:

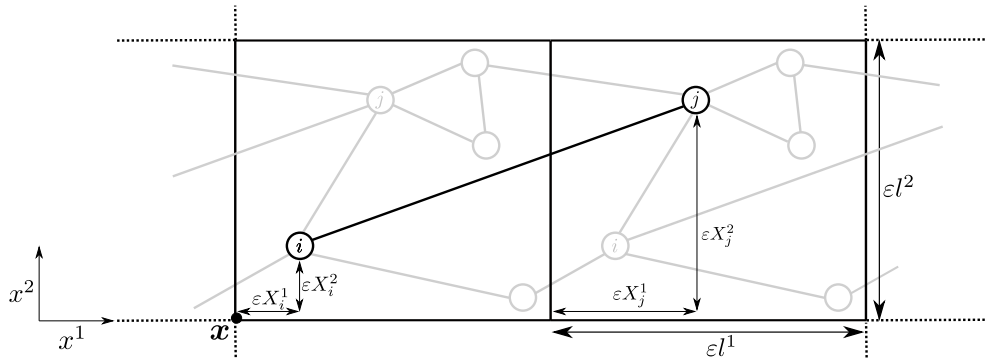

Figure 11.3: A diagram of a section of a two-dimensional filter with two cells shown. The point $\boldsymbol{x}$, the lengths of the cell boundaries, and the distances between nodes i and j and the cell boundaries are labelled. Lower indices reference nodes and edges, while upper indices refer to dimensional directions.

Quantity 1. The pressure at junction i, P_i, in the reference cell (e.g., see i in the left cell in Figure 11.4).

Quantity 2. The pressure at junction j, P_j, which is in a cell at position $\boldsymbol{r}$ relative to the reference cell (e.g., see j in the cell at position $\boldsymbol{r} = (1, 0)^\top$ (i.e., right) relative to the cell that contains i, in Figure 11.4).

Quantity 3. The conductance of pore $ij\boldsymbol{r}$, $G_{ij}^{\boldsymbol{r}}$ (i.e., the pore that connects junction i to junction j in the cell at position $\boldsymbol{r}$ relative to the cell containing junction i, see Figure 11.4).

Quantities 1–3, and the positions at which they are defined in the example case, $D = 2$ and $\boldsymbol{r} = (1, 0)$, are illustrated in Figure 11.4.

11.2.1 Step 1: Independent spatial variables

In Step 1, we define Quantities 1–3 with respect to their microscale and macroscale variables independently:

- For Quantity 1, we write

$$P_i = P_i(\boldsymbol{x} + \varepsilon \boldsymbol{X}_i), \tag{11.24}$$

  which depends on both the macroscopic spatial coordinate, $\boldsymbol{x}$, and the microscopic index, i, independently;

- For Quantity 2, we write

$$P_j = P_j\Big(\boldsymbol{x} + \varepsilon(\boldsymbol{X}_j + \boldsymbol{r} \circ \boldsymbol{l})\Big). \tag{11.25}$$

  Note (see Figure 11.4) that j is shifted by $\varepsilon \boldsymbol{r} \circ \boldsymbol{l}$, since junction j is in a cell at position $\boldsymbol{r}$ relative to the reference cell in which junction i is found;

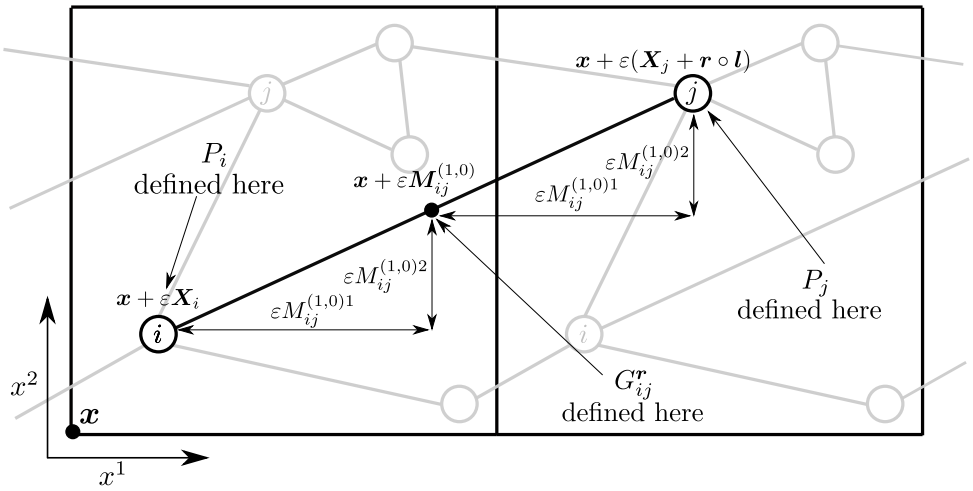

Figure 11.4: A diagram of two adjacent two-dimensional cells. The position $\boldsymbol{x}$ in the reference cell, and the positions of the node i in the reference cell, node j in the right-neighbouring cell, and the midpoint between these nodes are labelled above the points. Since node i is in the reference cell, the edge to j in the right-neighbouring cell, which is highlighted, is referenced by $\boldsymbol{r} = (1, 0)^\top$.

- For Quantity 3, we write

$$G_{ij}^{\boldsymbol{r}} = G_{ij}^{\boldsymbol{r}}(\boldsymbol{x} + \varepsilon \boldsymbol{M}_{ij}^{\boldsymbol{r}}). \tag{11.26}$$

  Note that, although the pore midpoint, $\boldsymbol{M}_{ij}^{\boldsymbol{r}}$ (defined in (11.23)), is the natural choice for $\boldsymbol{X}_{ij}^{\boldsymbol{r}}$, we will find that the process of network homogenisation is independent of this choice provided that $X_{ji}^{-\boldsymbol{r}m} = X_{ij}^{\boldsymbol{r}m}$ for each m, which ensures that a quantity defined on an edge, such as the flux, $Q_{ij}^{\boldsymbol{r}}$, is defined at the same point regardless of the direction of its flow.

11.2.2 Step 2: Taylor expansion

The position at which each variable is defined is important for Step 2, since it is crucial to carry out Taylor expansion about the common point $\boldsymbol{x}$. For example:

- Expanding Quantity 1 gives

$$P_i(\boldsymbol{x} + \varepsilon \boldsymbol{X}_i) = P_i(\boldsymbol{x}) + \varepsilon \sum_{m=1}^{D} X_i^m \frac{\partial P_i}{\partial x^m}(\boldsymbol{x}) + \frac{\varepsilon^2}{2} \sum_{m=1}^{D} \sum_{n=1}^{D} X_i^m X_i^n \frac{\partial^2 P_i}{\partial x^m \partial x^n}(\boldsymbol{x}); \tag{11.27}$$

- Expanding Quantity 2 gives

$$P_j\Big(\boldsymbol{x}+\varepsilon(\boldsymbol{X}_j+\boldsymbol{r}\circ\boldsymbol{l})\Big)=P_j(\boldsymbol{x})+\varepsilon\sum_{m=1}^{D}(X_j^m+r^m l^m)\frac{\partial P_j}{\partial x^m}(\boldsymbol{x})+ \frac{\varepsilon^2}{2}\sum_{m=1}^{D}\sum_{n=1}^{D}(X_j^m+r^m l^m)(X_j^n+r^n l^n)\frac{\partial^2 P_j}{\partial x^m\partial x^n}(\boldsymbol{x}); \tag{11.28}$$

- Expanding Quantity 3 gives

$$G_{ij}^{\boldsymbol{r}}\Big(\boldsymbol{x}+\varepsilon\boldsymbol{M}_{ij}^{\boldsymbol{r}}\Big)=G_{ij}^{\boldsymbol{r}}(\boldsymbol{x})+\varepsilon\sum_{m=1}^{D}M_{ij}^{\boldsymbol{r}m}\frac{\partial G_{ij}^{\boldsymbol{r}}}{\partial x^m}(\boldsymbol{x})+ \frac{\varepsilon^2}{2}\sum_{m=1}^{D}\sum_{n=1}^{D}M_{ij}^{\boldsymbol{r}m}M_{ij}^{\boldsymbol{r}n}\frac{\partial^2 G_{ij}^{\boldsymbol{r}}}{\partial x^m\partial x^n}(\boldsymbol{x}). \tag{11.29}$$

11.2.3 Step 3: Asymptotic expansion

Step 3 involves assuming asymptotic forms for solutions, and, for example:

- For Quantity 1, we write

$$P_i(\boldsymbol{x})=P_i^{(0)}(\boldsymbol{x})+\varepsilon P_i^{(1)}(\boldsymbol{x})+\varepsilon^2 P_i^{(2)}(\boldsymbol{x})+\mathcal{O}(\varepsilon^3); \tag{11.30}$$

- For Quantity 2, we write

$$P_j(\boldsymbol{x})=P_j^{(0)}(\boldsymbol{x})+\varepsilon P_j^{(1)}(\boldsymbol{x})+\varepsilon^2 P_j^{(2)}(\boldsymbol{x})+\mathcal{O}(\varepsilon^3); \tag{11.31}$$

- For Quantity 3, we write

$$G_{ij}^{\boldsymbol{r}}(\boldsymbol{x})=G_{ij}^{\boldsymbol{r}(0)}(\boldsymbol{x})+\varepsilon G_{ij}^{\boldsymbol{r}(1)}(\boldsymbol{x})+\varepsilon^2 G_{ij}^{\boldsymbol{r}(2)}(\boldsymbol{x})+\mathcal{O}(\varepsilon^3). \tag{11.32}$$

11.2.4 Step 4: Asymptotic solution

In Step 4 we will find some leading-order asymptotic solutions, such as that for the pressure, $P_i^{(0)}$, that are independent of the microscale index and are thus given by functions that depend only on the continuous macroscopic spatial variable. Other leading-order variables, such as the conductance, $G_{ij}^{\boldsymbol{r}}$, depend on the microscale and macroscale simultaneously. That is, for example:

- For Quantity 1, we will find that $P_i^{(0)}(\boldsymbol{x},t)=p^{(0)}(\boldsymbol{x},t)$ for any junction in the reference cell, $i\in\{1,\ldots,N\}$;

- For Quantity 2, we will find that $P_j^{(0)}(\boldsymbol{x},t)=p^{(0)}(\boldsymbol{x},t)$ for any junction in the neighbouring cell, $j\in\{1,\ldots,N\}$;

- For Quantity 3, we will find that $G^{\boldsymbol{r}}_{ij}(\boldsymbol{x},t) = G^{\boldsymbol{r}(0)}_{ij}(\boldsymbol{x},t)$ for any pore in the cells, $i,j \in \{1,\ldots,N\}$ and $\boldsymbol{r} \in \boldsymbol{\mathcal{R}}$.

Analysing higher-order equations, we will obtain a system for the explicitly microscale-independent variables, such as $p^{(0)}$. The parameters of this system will depend on microscale-dependent variables, such as $G^{\boldsymbol{r}(0)}_{ij}$. In this way, the evolution of the solution variables will depend on both the continuously varying macroscale spatial-variable, $\boldsymbol{x}$, and the discretely varying microscale indices, i,j, and $\boldsymbol{r}$, as we illustrate in Figure 11.5.

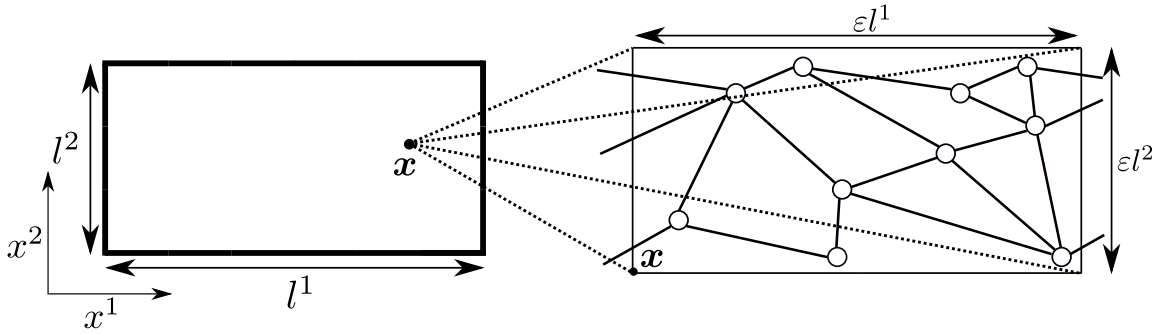

Figure 11.5: A diagram to illustrate a filter in the limit $\varepsilon \to 0$. Explicitly, macroscale variables are independent of the microscale structure. However, the parameters of the system that determine these macroscale variables depend on the structure of an infinitesimal cell defined at any continuous point $\boldsymbol{x}$.

In this section, we have summarised the process of network homogenisation. In the remainder of this chapter, we will carry out Steps 1–4 of network homogenisation to systematically average our periodic-network model, (11.13)–(11.22). We will first consider the case where the network is embedded in one-dimensional space, to exemplify a simple version of the process, before demonstrating the D-dimensional scenario, which is similar, but more notationally complex.

11.3 Multiscale model in one dimension

In this section, we begin by considering the quasi-one-dimensional case, in which non-spatially-adjacent nodes may be connected in a network that is embedded in one-dimensional space (see Figure 11.6 for an example). This case exemplifies the network homogenisation process while still affording significant notational simplification, since all vectors, such as the cell position, $\boldsymbol{x}$, the junction position, $\boldsymbol{X}_i$, and the reference, $\boldsymbol{r}$, are replaced by scalars, so that we drop the directional upper index, m, in the obvious way. In the remainder of this section, we will homogenise the fluid, particle, and pore conservation equations, (11.13)–(11.15), and systematically find a macroscale flow rate.

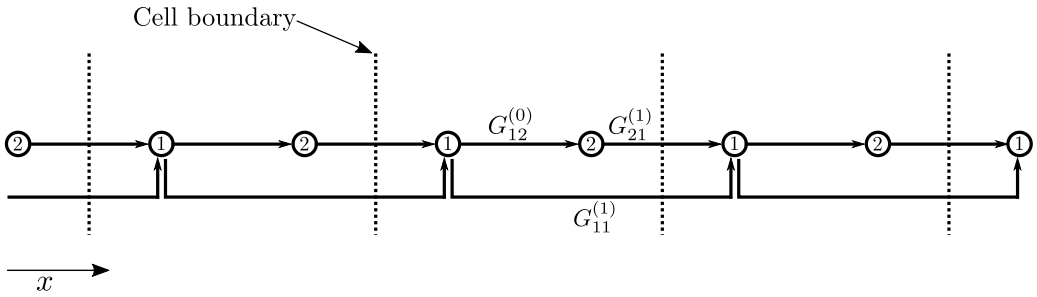

Figure 11.6: A diagram of a section of a periodic network composed of a cell containing $N = 2$ nodes that is repeated three times. The conductance on some edges is labelled. The network is quasi-one-dimensional since nodes are organised spatially in one dimension, but non-spatially-adjacent nodes are connected. For example, an edge exists between node 1 in one cell and node 1 in the cell to the right, but these two nodes are not spatially adjacent, since node 2 lies between them in the same plane.

11.3.1 Conservation of fluid

We first homogenise the microscale equation for conservation of fluid, (11.13). Writing this in terms of the junction pressure and pore conductance, using (11.16), gives

$$\sum_{j=1}^{N}\sum_{r\in\mathcal{R}} G_{ij}^r(P_j - P_i) = 0. \tag{11.33}$$

Carrying out Step 1 by evaluating G_{ij}^r, P_i, and P_j at x, which we choose to be the left-most point in the reference cell, and further Step 2, a Taylor expansion of the pressure and conductance about x, we find that (11.33) becomes

$$\begin{aligned}\sum_{j=1}^{N}\sum_{r\in\mathcal{R}} &\left\{G_{ij}^r\Big(P_j - P_i\Big)\right\} + \varepsilon\left\{\frac{\partial G_{ij}^r}{\partial x}M_{ij}^r(P_j - P_i) + G_{ij}^r\Big((X_j + rl)\frac{\partial P_j}{\partial x} - X_i\frac{\partial P_i}{\partial x}\Big)\right\}\\ &+ \varepsilon^2\left\{\frac{1}{2}\frac{\partial^2 G_{ij}^r}{\partial x^2}(M_{ij}^r)^2(P_j - P_i) + \frac{\partial G_{ij}^r}{\partial x}M_{ij}^r\Big((X_j + rl)\frac{\partial P_j}{\partial x} - X_i\frac{\partial P_i}{\partial x}\Big)\right.\\ &\left.+ \frac{G_{ij}^r}{2}\left((X_j + rl)^2\frac{\partial^2 P_j}{\partial x^2} - X_i^2\frac{\partial^2 P_i}{\partial x^2}\right)\right\} + \mathcal{O}(\varepsilon^3) = 0.\end{aligned} \tag{11.34}$$

Here, and throughout, we use { and } to group terms of the same asymptotic order. We next carry out Step 3 by substituting the asymptotic forms for the pressure and conductance, (11.30) and (11.32), into (11.34) to obtain

$$\begin{aligned}\boldsymbol{A}^{(0)}\boldsymbol{P}^{(0)} + \varepsilon&\left\{\boldsymbol{A}^{(0)}\boldsymbol{P}^{(1)} + \boldsymbol{A}^{(1)}\boldsymbol{P}^{(0)} + \boldsymbol{D}^{(0)}\boldsymbol{P}^{(0)} + \boldsymbol{B}^{(0)}\frac{\partial \boldsymbol{P}^{(0)}}{\partial x}\right\} + \varepsilon^2\left\{\boldsymbol{A}^{(0)}\boldsymbol{P}^{(2)} + \right.\\ &\boldsymbol{A}^{(1)}\boldsymbol{P}^{(1)} + \boldsymbol{D}^{(0)}\boldsymbol{P}^{(1)} + \boldsymbol{B}^{(0)}\frac{\partial \boldsymbol{P}^{(1)}}{\partial x} + \boldsymbol{A}^{(2)}\boldsymbol{P}^{(0)} + \boldsymbol{D}^{(1)}\boldsymbol{P}^{(0)} + \boldsymbol{B}^{(1)}\frac{\partial \boldsymbol{P}^{(0)}}{\partial x} + \\ &\left.\boldsymbol{F}^{(0)}\boldsymbol{P}^{(0)} + \boldsymbol{E}^{(0)}\frac{\partial \boldsymbol{P}^{(0)}}{\partial x} + \boldsymbol{C}^{(0)}\frac{\partial^2 \boldsymbol{P}^{(0)}}{\partial x^2}\right\} + \mathcal{O}(\varepsilon^3) = \boldsymbol{0},\end{aligned} \tag{11.35}$$

which is the master equation for fluid conservation that we seek to solve. Here, $\boldsymbol{P}^{(s)}$ is a vector of length N in the junction index that contains the $\mathcal{O}(\varepsilon^s)$ pressure solutions, so that

$$\boldsymbol{P}^{(s)} = \begin{pmatrix} P_1^{(s)} \\ \vdots \\ P_N^{(s)} \end{pmatrix}, \tag{11.36}$$

and $\boldsymbol{A}, \boldsymbol{B}, \boldsymbol{C}, \boldsymbol{D}, \boldsymbol{E}$, and $\boldsymbol{F}$, are matrices of shape (N, N) in the junction index, the entries of which are given by

$$A_{ij}^{(s)} = \sum_{r\in\mathcal{R}} \left(G_{ij}^{r(s)} - \delta_{ij} \sum_{k=1}^{N} G_{ik}^{r(s)} \right), \tag{11.37}$$

$$B_{ij}^{(s)} = \sum_{r\in\mathcal{R}} \left(G_{ij}^{r(s)}(X_j + rl) - \delta_{ij} X_i \sum_{k=1}^{N} G_{ik}^{r(s)} \right), \tag{11.38}$$

$$C_{ij}^{(s)} = \frac{1}{2} \sum_{r\in\mathcal{R}} \left(G_{ij}^{r(s)}(X_j + rl)^2 - \delta_{ij} X_i^2 \sum_{k=1}^{N} G_{ik}^{r(s)} \right), \tag{11.39}$$

$$D_{ij}^{(s)} = \sum_{r\in\mathcal{R}} \left(\frac{\partial G_{ij}^{r(s)}}{\partial x} M_{ij}^{r} - \delta_{ij} \sum_{k=1}^{N} \frac{\partial G_{ik}^{r(s)}}{\partial x} M_{ik}^{r} \right), \tag{11.40}$$

$$E_{ij}^{(s)} = \sum_{r\in\mathcal{R}} \left(\frac{\partial G_{ij}^{r(s)}}{\partial x} M_{ij}^{r}(X_j + rl) - \delta_{ij} X_i \sum_{k=1}^{N} \frac{\partial G_{ik}^{r(s)}}{\partial x} M_{ik}^{r} \right), \tag{11.41}$$

$$F_{ij}^{(s)} = \frac{1}{2} \sum_{r\in\mathcal{R}} \left(\frac{\partial^2 G_{ij}^{r(s)}}{\partial x^2} (M_{ij}^{r})^2 - \delta_{ij} \sum_{k=1}^{N} \frac{\partial^2 G_{ik}^{r(s)}}{\partial x^2} (M_{ik}^{r})^2 \right). \tag{11.42}$$

To solve the master equation, (11.35), it is useful to note (see Appendix A.1.1 for proofs of (11.43a)–(11.44b)) that

$$\boldsymbol{A}^{(s)}\mathbf{1} = \mathbf{0}, \quad \mathbf{1}^\top \boldsymbol{B}^{(s)}\mathbf{1} = \mathbf{0}, \quad \boldsymbol{D}^{(s)}\mathbf{1} = \mathbf{0}, \quad \boldsymbol{F}^{(s)}\mathbf{1} = \mathbf{0}, \tag{11.43a–d}$$

and that

$$\mathbf{1}^\top \boldsymbol{D}^{(s)} = \frac{\partial}{\partial x}\Big(\mathbf{1}^\top \boldsymbol{B}^{(s)}\Big), \quad \mathbf{1}^\top \boldsymbol{E}^{(s)}\mathbf{1} = \frac{\partial}{\partial x}\Big(\mathbf{1}^\top \boldsymbol{C}^{(s)}\mathbf{1}\Big), \tag{11.44a,b}$$

where $\mathbf{1} = (1, \ldots, 1)^\top$ and $\mathbf{0} = (0, \ldots, 0)^\top$ are both vectors of length N. Note additionally that, since $\boldsymbol{A}^{(s)\top}$ is symmetric, such that

$$\boldsymbol{A}^{(s)\top} = \boldsymbol{A}^{(s)}, \tag{11.45}$$

it follows from (11.43a) that

$$\mathbf{1}^\top \boldsymbol{A}^{(s)} = \mathbf{0}^\top. \tag{11.46}$$

We use these results extensively in Step 4.

Indeed, proceeding with Step 4, at leading order in the master equation, (11.35), we have that

$$\boldsymbol{A}^{(0)}\boldsymbol{P}^{(0)} = \boldsymbol{0}, \tag{11.47}$$

and, using the identity (11.43a), it follows that

$$\boldsymbol{P}^{(0)} = p^{(0)}(x,t)\boldsymbol{1}, \tag{11.48}$$

where $p^{(0)}(x,t)$ is the leading-order macroscale pressure solution to be found. We have discovered that the leading-order pressure at any junction i is independent of i, which means that pressures at junctions in the same cell are identical at leading order. One consequence is that the leading-order intra-cell pressure difference between any two junctions is zero, so that there is no flux through the pore at leading order (using (11.16)),

$$P_j^{(0)} - P_i^{(0)} = 0. \tag{11.49}$$

It remains to find $p^{(0)}$ by seeking a solvability condition at higher order. Thus, continuing Step 4 by considering first-order terms in the master equation, (11.35), substituting the leading-order pressure solution, (11.48), into (11.35), and using the identities (11.43a) and (11.43c), we find that

$$\boldsymbol{A}^{(0)}\boldsymbol{P}^{(1)} + \boldsymbol{B}^{(0)}\boldsymbol{1}\frac{\partial p^{(0)}}{\partial x} = \boldsymbol{0}. \tag{11.50}$$

Searching for a solvability condition, we pre-multiply both sides of (11.50) by $\boldsymbol{1}^\top$, but, using (11.43b), we see that the resulting equation is satisfied for any $p^{(0)}$. We must, therefore, proceed to even higher order problems to determine the leading-order solution, $p^{(0)}$. Before this, we note that (11.50) has the solution

$$\boldsymbol{P}^{(1)} = f(x,t)\boldsymbol{1} + \frac{\partial p^{(0)}}{\partial x}\boldsymbol{W}, \tag{11.51}$$

where $f(x,t)$ is an arbitrary (see (11.75)) microscale-independent function, and $\boldsymbol{W}$ is a vector of length N that satisfies

$$\boldsymbol{A}^{(0)}\boldsymbol{W} = -\boldsymbol{B}^{(0)}\boldsymbol{1}. \tag{11.52}$$

Unlike the leading-order pressure, then, the first-order pressure, given by (11.51), is microscale dependent, via $\boldsymbol{W}$. We refer to (11.52) as the cell problem, since its solution, $\boldsymbol{W}$, which we call the cell solution, determines the dependence of the pressure at a continuous spatial point on the structure of the cell located at this point (in the limit $\varepsilon \to 0$, see Figure 11.5) and thus on the microscale network, via the conductances that define $\boldsymbol{A}^{(0)}$ and $\boldsymbol{B}^{(0)}$ (defined in (11.37) and (11.38)). Since the first term in the

right-hand side of (11.51) is microscale-independent, the first-order pressure difference is given by

$$P_j^{(1)} - P_i^{(1)} = (W_j - W_i)\frac{\partial p^{(0)}}{\partial x}, \tag{11.53}$$

which is of interest since this pressure difference determines the pore flux, via (11.16).

At second order, by substituting the leading- and first-order solutions, (11.48) and (11.51), into the master equation, (11.35), and using the identities (11.43a,c,d), we find that

$$\begin{aligned}\boldsymbol{A}^{(0)}\boldsymbol{P}^{(2)} + \boldsymbol{A}^{(1)}\frac{\partial p^{(0)}}{\partial x}\boldsymbol{W} + \boldsymbol{D}^{(0)}\frac{\partial p^{(0)}}{\partial x}\boldsymbol{W} + \boldsymbol{B}^{(0)}\frac{\partial}{\partial x}\Big(f\mathbf{1} + \frac{\partial p^{(0)}}{\partial x}\boldsymbol{W}\Big) + \\ \boldsymbol{B}^{(1)}\mathbf{1}\frac{\partial p}{\partial x} + \boldsymbol{E}^{(0)}\mathbf{1}\frac{\partial p^{(0)}}{\partial x} + \boldsymbol{C}^{(0)}\mathbf{1}\frac{\partial^2 p^{(0)}}{\partial x^2} = \mathbf{0}.\end{aligned} \tag{11.54}$$

Seeking a solvability condition once more, we pre-multiply both sides of (11.54) by $\mathbf{1}^\top$, and use the identity (11.46) to eliminate $\boldsymbol{P}^{(2)}$. Using the identity (11.43b) to simplify, we obtain

$$\mathbf{1}^\top\boldsymbol{D}^{(0)}\frac{\partial p^{(0)}}{\partial x}\boldsymbol{W} + \mathbf{1}^\top\boldsymbol{B}^{(0)}\frac{\partial}{\partial x}\Big(\frac{\partial p^{(0)}}{\partial x}\boldsymbol{W}\Big) + \mathbf{1}^\top\boldsymbol{E}^{(0)}\mathbf{1}\frac{\partial p^{(0)}}{\partial x} + \mathbf{1}^\top\boldsymbol{C}^{(0)}\mathbf{1}\frac{\partial^2 p^{(0)}}{\partial x^2} = 0. \tag{11.55}$$

Furthermore, using the identities in (11.44) and the product rule to write $\boldsymbol{D}^{(0)}$ and $\boldsymbol{E}^{(0)}$ in terms of $\boldsymbol{B}^{(0)}$ and $\boldsymbol{C}^{(0)}$, we simplify (11.55), and arrive at

$$\frac{\partial}{\partial x}\Big(\sigma^{(0)}\frac{\partial p^{(0)}}{\partial x}\Big) = 0, \tag{11.56}$$

where $\sigma^{(0)}$ is the scalar defined by

$$\sigma^{(0)} = \frac{1}{l}\Big(\mathbf{1}^\top\boldsymbol{B}^{(0)}\boldsymbol{W} + \mathbf{1}^\top\boldsymbol{C}^{(0)}\mathbf{1}\Big). \tag{11.57}$$

Equation (11.56) is the solvability condition for the leading-order pressure solution, $p^{(0)}$, that we seek, and thus (11.56) is the homogenised version of the equation for conservation of fluid, (11.13). We see that we have arrived at an equation, which governs the evolution of the leading-order pressure, $p^{(0)}$, over continuous macroscale space, x, which is explicitly independent of the microscale. Instead, microscale structure enters the system via the parameter of the equation, $\sigma^{(0)}$, which depends explicitly on the structure of the underlying network via $\boldsymbol{W}$, $\boldsymbol{B}^{(0)}$, $\boldsymbol{C}^{(0)}$, which are defined in terms of the pore conductances, $G_{ij}^{r(0)}$, subject to the cell problem, (11.52), and the definitions in (11.38) and (11.39), respectively.

11.3.2 Darcy's law

Next, our aim is to relate the leading-order macroscale pressure solution, $p^{(0)}$, to a flow rate. To this end, we define the Darcy velocity to be

$$u = \frac{1}{2}\sum_{i=1}^{N}\sum_{j=1}^{N}\sum_{r\in\mathcal{R}} rQ_{ij}^r. \tag{11.58}$$

To see why (11.58) is indeed the net flux per unit area through a cell, first notice that terms containing $r = 0$ correspond to flow through edges with no inter-cell connectivity, and so do not contribute to the sum. The terms containing $r = 1$ correspond to flow out of a cell through edges connected to the cell directly to the right of it, and, since $Q^r_{ij} = -Q^r_{ji}$, the terms containing $r = -1$ correspond to flow into a cell through edges connected to the cell directly to the left. Therefore, averaging these two contributing flows (by dividing by two) gives the flux through the cell. Now consider terms containing $r = 2$, which, we recall, describes the case in which a node in one cell is connected by an edge to a cell two steps to the right. In such a case, two copies of the edge will pass through the right-hand boundary of the reference cell (see Figure 11.7), and hence Q^r_{ij} must be counted twice. Similarly, for longer-range connections, multiplying by r ensures that Q^r_{ij} is counted the correct number of times (see Appendix A.3 for proof).

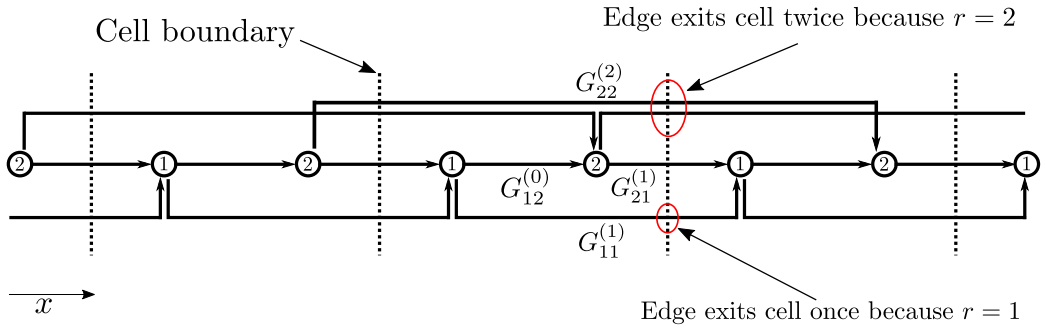

Figure 11.7: A diagram of a periodic network composed of a cell of $N = 2$ nodes repeated three times. The conductance of some pores is labelled. The pore with conductance $G^{(1)}_{11}$ connects junction 1 in one cell junction 1 in the next cell to the right, since $r = 1$. Only one instance of this pore exits the first cell, and so flow through this pore need only be counted once. On the other hand, the pore with conductance $G^{(2)}_{22}$ connects junction 2 in one cell to junction 2 in the cell two cells to the right, since $r = 2$. Two instances of this pore exit the first cell, and so flow through this pore must be counted twice.

To homogenise the Darcy velocity, (11.58), we will begin by homogenising the pore flux, Q^r_{ij}. To this end, following Steps 1–3 of network homogenisation, that is, writing the pore flux in terms of the pore pressure drop and conductance using (11.16), carrying out a Taylor expansion of the pressure and conductance about x, and substituting in an asymptotic expansion for the conductance, given by (11.32), we find that

$$Q^r_{ij} = -\Bigg(\Big\{G^{r(0)}_{ij}\Big(P_j - P_i\Big)\Big\} + \varepsilon\Big\{G^{r(1)}_{ij}\Big(P_j - P_i\Big) + G^{r(0)}_{ij}\Big((X_j + rl)\frac{\partial P_j}{\partial x} - X_i\frac{\partial P_i}{\partial x}\Big) + \frac{\partial G^{r(0)}_{ij}}{\partial x}M^r_{ij}\Big(P_j - P_i\Big)\Big\} + \mathcal{O}(\varepsilon^2)\Bigg). \tag{11.59}$$

Furthermore, using the leading- and first-order asymptotic pressure solutions, (11.48) and (11.51), and noting the cancellation of terms by using the leading- and first-order pressure differences, (11.49) and (11.53), we find that

$$Q_{ij}^r = G_{ij}^{r(0)} \Delta_{ij}^r \frac{\partial p^{(0)}}{\partial x} + \mathcal{O}(\varepsilon). \tag{11.60}$$

The leading-order microscale flux is therefore given by

$$Q_{ij}^{r(0)} = G_{ij}^{r(0)} \Delta_{ij}^r \frac{\partial p^{(0)}}{\partial x}, \tag{11.61}$$

where

$$\Delta_{ij}^r = W_i + X_i - (W_j + X_j + rl), \tag{11.62}$$

which, we note, satisfies

$$\Delta_{ji}^{-r} = -\Delta_{ij}^r. \tag{11.63}$$

Equation (11.61) tells us that Δ_{ij}^r is the pressure difference (per unit pressure gradient) in pore ijr. Equation (11.58) implies that this dictates the effective contribution of the pressure difference in pore ijr to the overall macroscale flow rate, u.

It follows that elements of the cell solution W_i, have dimensions of length (pressure divided by pressure gradient). Therefore, we interpret these as the 'corrections' to the position of each junction i necessary to obtain the imposed 'correct' pressure gradient on the macroscale. These 'corrected' positions (as opposed to the actual positions, X_i) are dictated by pore conductances, $G_{ij}^{r(0)}$, via solution of the cell problem, (11.52).

We find (see Appendix A.1.3 for proof) that the macroscale solution of the model is independent of the positions of the junctions, X_i. We expect this, since the microscale model, (11.13)–(11.20), is only dependent on the network structure via the conductances of the pores. Choosing $X_i = 0$ for all $i \in \{1, \ldots, N\}$, we see that

$$\Delta_{ij}^r = W_i - (W_j + rl). \tag{11.64}$$

Substituting the homogenised microscale flux, (11.60), into the Darcy-velocity definition, (11.58), we find that the homogenised Darcy velocity is

$$u = \frac{1}{2} \sum_{i=1}^{N} \sum_{j=1}^{N} \sum_{r \in \mathcal{R}} r G_{ij}^{r(0)} \Delta_{ij}^r \frac{\partial p^{(0)}}{\partial x} + \mathcal{O}(\varepsilon), \tag{11.65}$$

so that the leading-order Darcy velocity is given by

$$u^{(0)} = \frac{1}{2} \sum_{i=1}^{N} \sum_{j=1}^{N} \sum_{r \in \mathcal{R}} r G_{ij}^{r(0)} \Delta_{ij}^r \frac{\partial p^{(0)}}{\partial x}. \tag{11.66}$$

Re-writing (11.66), therefore, we find that the leading-order Darcy velocity satisfies

$$u^{(0)} = -k^{(0)}\frac{\partial p^{(0)}}{\partial x}, \tag{11.67}$$

where, using (11.63),

$$k^{(0)} = \frac{1}{2}\sum_{i=1}^{N}\sum_{j=1}^{N}\sum_{r\in\mathcal{R}} rG_{ij}^{r(0)}\Delta_{ji}^{-r}. \tag{11.68}$$

It turns out (see the proof in Appendix A.1.3) that $\sigma^{(0)} = k^{(0)}$, and, using this identity in (11.56), we find that the leading-order Darcy velocity is divergence-free, so that

$$\frac{\partial u^{(0)}}{\partial x} = 0. \tag{11.69}$$

Carrying out network homogenisation on the microscale equation for conservation of fluid, (11.13), and the pore flux definition, (11.16), we have shown that the leading-order flow rate and pressure, $u^{(0)}$ and $p^{(0)}$, satisfy the Darcy equation, (11.67), and the expected macroscale equation for fluid conservation, (11.69). Therefore, (11.58) is indeed the correct definition for the flow rate, u. Inspecting (11.67), it follows that $k^{(0)}$ is the leading-order permeability of the filter, which depends on the microscale via (11.68).

11.3.3 Conservation of particles

We next homogenise the microscale equation for the conservation of particles, (11.14). Writing this in terms of the junction pressure and pore conductance, using (11.16), gives

$$\begin{aligned}\frac{\partial C_i}{\partial T} = \frac{1}{\varepsilon}\Bigg\{ \sum_{j=1}^{N}\sum_{r\in\mathcal{R}} \Big(&G_{ji}^{-r}(P_j - P_i)C_j H(G_{ji}^{-r}(P_j - P_i)) - \\ &G_{ij}^{r}(P_i - P_j)C_i H(G_{ij}^{r}(P_i - P_j))\Big)\Bigg\} \\ &- \sum_{j=1}^{N}\sum_{r\in\mathcal{R}} \alpha G_{ji}^{-r}(P_j - P_i)C_j H(G_{ji}^{-r}(P_j - P_i)).\end{aligned} \tag{11.70}$$

We begin by noting that the Heaviside function, H, can be homogenised (since the pressure difference in a pore never reaches zero, as discussed in Section 7.1) first and carried through the rest of the process. Specifically, we carry out Steps 1–3 on the term $H(G_{ij}^{r}(P_i - P_j))$, and find that

$$H(Q_{ij}^{r}) = H\left(G_{ij}^{r(0)}(P_i - P_j) + \varepsilon G_{ij}^{r(0)}\left\{X_i\frac{\partial P_i}{\partial x} - (X_j + rl)\frac{\partial P_j}{\partial x}\right\} + \mathcal{O}(\varepsilon^2)\right) \tag{11.71}$$

$$= H\left(\varepsilon\left\{G_{ij}^{r(0)}\Delta_{ij}^{r}\frac{\partial p^{(0)}}{\partial x}\right\} + \mathcal{O}(\varepsilon^2)\right), \tag{11.72}$$

where we have used the leading- and first-order pressure solutions, (11.48) and (11.51), respectively. We therefore define

$$H_{ij}^{r(0)} = H\Big(\Delta_{ij}^{r}\frac{\partial p^{(0)}}{\partial x}\Big), \tag{11.73}$$

which satisfies

$$H_{ij}^{r(0)} + H_{ji}^{-r(0)} = 1. \tag{11.74}$$

In (11.73), note that $H_{ij}^{r(0)}$ is only non-zero when Δ_{ij}^{r} is negative, or equivalently, when Δ_{ji}^{-r} is positive, using (11.63). Recalling our interpretation of Δ_{ij}^{r}, this means that $H_{ij}^{r(0)}$ indicates pores ijr along which particles move from junction i to junction j. From (11.74), it follows that $H_{ji}^{-r(0)}$ indicates the pores ijr along which particles flow from junction j to junction i, which are the pores along which deposition occurs. Thus $H_{ji}^{-r(0)}$ is the leading-order equivalent of H.

We now carry out Steps 1–3 of the network homogenisation process on the remaining terms in the particle conservation equation, (11.70). Using the leading- and first-order pressure solutions, (11.48) and (11.51), and noting the cancellation of terms that contain the leading-order pressure difference, (11.49), and the cancellation of terms involving the function f via the first-order pressure difference, (11.53), we arrive at

$$\begin{aligned}
&\frac{\partial}{\partial T}\Big(C_i^{(0)} + \varepsilon\Big\{C_i^{(1)} + X_i\frac{\partial C_i^{(0)}}{\partial x}\Big\} + \varepsilon^2\Big\{C_i^{(2)} + X_i\frac{\partial C_i^{(1)}}{\partial x} + \frac{1}{2}X_i^2\frac{\partial^2 C_i^{(0)}}{\partial x\partial x}\Big\}\Big) = \\
&\quad\sum_{j=1}^{N}\sum_{r\in\mathcal{R}}\Big\{G_{ij}^{r(0)}\Delta_{ji}^{-r}\frac{\partial p^{(0)}}{\partial x}(C_j^{(0)}H_{ji}^{-r(0)} + C_i^{(0)}H_{ij}^{r(0)})\Big\} + \\
&\qquad\varepsilon\Big\{G_{ij}^{r(0)}\Delta_{ji}^{-r}\frac{\partial p^{(0)}}{\partial x}(C_j^{(1)}H_{ji}^{-r(0)} + C_i^{(1)}H_{ij}^{r(0)}) + \\
&\qquad G_{ij}^{r(0)}\Delta_{ji}^{-r}\frac{\partial p^{(0)}}{\partial x}\Big((X_j + rl)\frac{\partial C_j^{(0)}}{\partial x}H_{ji}^{-r(0)} + X_i\frac{\partial C_i^{(0)}}{\partial x}H_{ij}^{r(0)}\Big) + \\
&\qquad\Big(G_{ij}^{r(0)}\Big(P_j^{(2)} - P_i^{(2)}\Big) + G_{ij}^{r(1)}\Delta_{ji}^{-r}\frac{\partial p^{(0)}}{\partial x} + \\
&\qquad G_{ij}^{r(0)}\Big((X_j + rl)\frac{\partial}{\partial x}\Big(f + W_j\frac{\partial p^{(0)}}{\partial x}\Big) - X_i\frac{\partial}{\partial x}\Big(f + W_i\frac{\partial p^{(0)}}{\partial x}\Big)\Big) + \\
&\qquad\frac{G_{ij}^{r(0)}}{2}\Big((X_j + rl)^2 - X_i^2\Big)\frac{\partial^2 p^{(0)}}{\partial x^2} + \\
&\qquad\frac{\partial G_{ij}^{r(0)}}{\partial x}M_{ij}^{r}\Delta_{ji}^{-r}\frac{\partial p^{(0)}}{\partial x}\Big)(C_j^{(0)}H_{ji}^{-r(0)} + C_i^{(0)}H_{ij}^{r(0)}) - \\
&\qquad\alpha G_{ij}^{r(0)}\Delta_{ji}^{-r}\frac{\partial p^{(0)}}{\partial x}C_j^{(0)}H_{ji}^{-r(0)}\Big\} + \mathcal{O}(\varepsilon^2).
\end{aligned} \tag{11.75}$$

This is the master equation for the conservation of particles that we seek to solve.

We now carry out Step 4 to solve the master equation. At leading order in (11.75) we see that

$$\mathbf{1} \circ \frac{\partial \boldsymbol{C}^{(0)}}{\partial T} = \boldsymbol{S}^{(0)} \boldsymbol{C}^{(0)} \frac{\partial p^{(0)}}{\partial x}, \tag{11.76}$$

where, recall that $\circ$ denotes the Hadamard product (and we use it here to remember that the unit sum of the volumes of nodes in the cell appears on the left of this equation, which we use to interpret the parameter ϕ in (11.90)), and $\boldsymbol{S}^{(0)}$ is a matrix of shape (N, N) with elements

$$S_{ij}^{(0)} = \sum_{r \in \mathcal{R}} \Big(G_{ij}^{r(0)} \Delta_{ji}^{-r} H_{ji}^{-r(0)} - \delta_{ij} \sum_{k=1}^{N} G_{ik}^{r(0)} \Delta_{ik}^{r} H_{ik}^{r(0)} \Big). \tag{11.77}$$

We identify the terms inside the sums in $\boldsymbol{S}^{(0)}$ as the pore fluxes (per unit pressure gradient) into (since $G_{ij}^{r(0)} \Delta_{ji}^{-r}$ is multiplied by $H_{ji}^{-r(0)}$), and out of (since $G_{ik}^{r(0)} \Delta_{ik}^{r}$ is multiplied by $H_{ik}^{r(0)}$) junction i. We note (see the proof in Appendix A.1.4) that $\boldsymbol{S}^{(0)}$ satisfies

$$\boldsymbol{S}^{(0)} \mathbf{1} = \mathbf{0} = \mathbf{1}^{\top} \boldsymbol{S}^{(0)}, \tag{11.78}$$

which means that the total mass of particles in the fluid inside the cell is conserved. This is to be expected, because there is no intra-cell deposition, since adherence is an $\mathcal{O}(\varepsilon)$ phenomenon. We will find that one implication of this conservation is that $\boldsymbol{S}^{(0)}$ does not appear on longer timescales, on which inter-cell evolution occurs. Despite this, $\boldsymbol{S}^{(0)}$ controls the evolution of the microscale-dependent concentration in (11.76), and the timescale, T_{c} (see (11.12)), is the one over which the concentration settles down to one that is the same for all junctions in the cell.

Since we are primarily interested in macroscale concentration changes, and thus inter-cell variation, we define a longer time variable, $t = \varepsilon T$. Substituting this into the master equation, (11.75), a leading-order balance yields

$$\mathbf{0} = \boldsymbol{S}^{(0)} \boldsymbol{C}^{(0)} \frac{\partial p^{(0)}}{\partial x}. \tag{11.79}$$

Using the first equation of the identities in (11.78), it follows that

$$\boldsymbol{C}^{(0)} = c^{(0)}(x, t) \mathbf{1}, \tag{11.80}$$

where $c^{(0)}(x, t)$ is the leading-order concentration solution that we seek. We see that this is independent of the junction index, i, so that it is microscale independent. The new longer timescale,

$$T_{\mathrm{n}} = \frac{T_{\mathrm{c}}}{\varepsilon} = \frac{\bar{V}}{\bar{G}(p_{\mathrm{in}}^{*} - p_{\mathrm{in}}^{*})}, \tag{11.81}$$

is the one associated with evolution of the particle concentration on the network as a whole.

Proceeding to second order to close the problem by finding an equation that governs $c^{(0)}$, by substituting the leading-order solution for the concentration, given by (11.80), into the master equation, (11.75), and noting that $H_{ij}^{r(0)}$ disappears from terms containing $c^{(0)}$ by using the Heaviside-function identity, (11.74), we find that

$$\begin{aligned}\frac{\partial c^{(0)}}{\partial t}\mathbf{1} =& \boldsymbol{S}^{(0)}\boldsymbol{C}^{(1)}\frac{\partial p^{(0)}}{\partial x} + \boldsymbol{K}^{(0)}\mathbf{1}\frac{\partial p^{(0)}}{\partial x}\frac{\partial c^{(0)}}{\partial x} - \boldsymbol{J}^{(0)}\mathbf{1}\frac{\partial p^{(0)}}{\partial x}c^{(0)} + \\ &\left(\boldsymbol{A}^{(0)}\boldsymbol{P}^{(2)} + \boldsymbol{A}^{(1)}\boldsymbol{W}\frac{\partial p^{(0)}}{\partial x} + \boldsymbol{B}^{(1)}\mathbf{1}\frac{\partial p^{(0)}}{\partial x} + \boldsymbol{B}^{(0)}\frac{\partial}{\partial x}\Big(f\mathbf{1} + \right. \\ &\left.\frac{\partial p^{(0)}}{\partial x}\boldsymbol{W}\Big) + \boldsymbol{C}^{(0)}\mathbf{1}\frac{\partial^2 p^{(0)}}{\partial x^2} + \boldsymbol{D}^{(0)}\boldsymbol{W}\frac{\partial p^{(0)}}{\partial x} + \boldsymbol{E}^{(0)}\mathbf{1}\frac{\partial p^{(0)}}{\partial x}\right)c^{(0)}\end{aligned} \tag{11.82}$$

where $\boldsymbol{K}^{(0)}$ is the matrix of shape (N, N) with elements

$$K_{ij}^{(0)} = \sum_{r\in\mathcal{R}}\left(G_{ij}^{r(0)}\Delta_{ji}^{-r}\Big((X_j + rl)H_{ji}^{-r(0)} + X_i H_{ij}^{r(0)}\Big)\right), \tag{11.83}$$

and $\boldsymbol{J}^{(0)}$ is another matrix of shape (N, N) with elements

$$J_{ij}^{(0)} = \sum_{r\in\mathcal{R}}\Big(\alpha G_{ij}^{r(0)}\Delta_{ji}^{-r}H_{ji}^{-r(0)}\Big). \tag{11.84}$$

We identify the term inside the sum in $K_{ij}^{(0)}$ as the microscale contribution to the homogenised flux (noting the presence of $G_{ij}^{r(0)}\Delta_{ji}^{-r}$) and so we expect $\boldsymbol{K}^{(0)}$ to be a quantity related to macroscale advection. Meanwhile, we identify the term inside the sum in $J_{ij}^{(0)}$ as the microscale component of the homogenised flux multiplied by the adherence (noting the presence of α) in pores conducting particles into junction i (noting the presence of $H_{ji}^{-r(0)}$), and so we expect to find that $\boldsymbol{J}^{(0)}$ corresponds to deposition in the macroscale equation.

Using the second-order fluid conservation equation, (11.54), we find that the sum of all but the first three terms on the right-hand side of (11.82) is equal to zero, and so, pre-multiplying (11.82) by $\mathbf{1}^\top$ gives

$$\frac{\partial c^{(0)}}{\partial t} = \frac{\mathbf{1}^\top\boldsymbol{K}^{(0)}\mathbf{1}}{\mathbf{1}^\top\mathbf{1}}\frac{\partial p^{(0)}}{\partial x}\frac{\partial c^{(0)}}{\partial x} - \frac{\mathbf{1}^\top\boldsymbol{J}^{(0)}\mathbf{1}}{\mathbf{1}^\top\mathbf{1}}\frac{\partial p^{(0)}}{\partial x}c^{(0)}, \tag{11.85}$$

where we have used the second equation in the identities given by (11.78). This is the governing equation that determines the leading-order particle concentration, $c^{(0)}$, and thus closes the problem.

To interpret (11.85), we first note (see Appendix A.1.5 for proof) that $\boldsymbol{K}^{(0)}$ is proportional to the leading-order permeability, such that

$$\mathbf{1}^\top\boldsymbol{K}^{(0)}\mathbf{1} = lk^{(0)} = l\sigma^{(0)}, \tag{11.86}$$

so that $\boldsymbol{K}^{(0)}$ is indeed an advective term, since it is proportional to the macroscale conductivity of the network. Similarly, we define

$$j^{(0)} = -\frac{\mathbf{1}^\top\boldsymbol{J}^{(0)}\mathbf{1}}{l} = -\frac{1}{l}\sum_{i=1}^{N}\sum_{j=1}^{N}\sum_{r\in\mathcal{R}}\alpha G_{ij}^{r(0)}\Delta_{ji}^{-r}H_{ji}^{-r(0)}, \tag{11.87}$$

which is a positive scalar quantity (since Δ_{ji}^{-r} is negative on the relevant pores). We call $j^{(0)}$ the adhesivity, since it represents the macroscale result of pore adherence on the microscale in the same way that the permeability, $k^{(0)}$, represents the macroscale result of pore conductance on the microscale. To interpret (11.85) further, we define

$$v = \mathbf{1}^\top \mathbf{1} = N, \tag{11.88}$$

which is the total volume of all junctions in the cell. Using the proportionality of $\boldsymbol{K}^{(0)}$ and $k^{(0)}$, (11.86), and of $\boldsymbol{J}^{(0)}$ and $j^{(0)}$, (11.87), and the definition of junction volume, v in (11.88), we re-write (11.85) in terms of the leading-order permeability and adhesivity, which gives

$$\frac{\partial c^{(0)}}{\partial t} = \frac{l}{v}\Big(k^{(0)}\frac{\partial p^{(0)}}{\partial x}\Big)\frac{\partial c^{(0)}}{\partial x} + \frac{l}{v}\Big(j^{(0)}\frac{\partial p^{(0)}}{\partial x}\Big)\, c^{(0)}. \tag{11.89}$$

Furthermore, we identify

$$\phi = \frac{v}{l}, \tag{11.90}$$

as the junction porosity, which is a constant, since it is the scaled ratio of the total volume of junctions, within which deposition does not occur, to the cell volume. Therefore, defining

$$\psi^{(0)} = -j^{(0)}\frac{\partial p^{(0)}}{\partial x}, \tag{11.91}$$

which we call the reactivity, and using Darcy's law, (11.67), to relate the permeability to the Darcy velocity, $u^{(0)}$, we arrive at

$$\frac{\partial c^{(0)}}{\partial t} + \frac{\partial}{\partial x}\Big(\frac{u^{(0)}}{\phi}c^{(0)}\Big) = -\frac{\psi^{(0)}}{\phi}c^{(0)}, \tag{11.92}$$

where we have used the macroscale equation for conservation of fluid, (11.69), to write the macroscale equation for the conservation of particles, (11.89), in conservative form.

We have found that the particle concentration, $c^{(0)}$, varies on the continuous macroscale subject to an advection–reaction equation, (11.92). Particles are advected through the filter by the pore velocity, $u^{(0)}\phi^{-1}$, which is related to the pressure, $p^{(0)}$, and the permeability, $k^{(0)}$, which is the effective conductance of the filter, using the Darcy equation (11.67). As they do so, particles deposit inside the filter at a rate determined by the reactivity, $\psi^{(0)}\phi^{-1}$, which is related to the pressure, $p^{(0)}$, and the adhesivity, $j^{(0)}$, which is the effective adherence of the filter, using the reaction equation, (11.91). The permeability and the adhesivity are related to the conductance of pores in the network, $G_{ij}^{r(0)}$, via (11.68) and (11.87), respectively, and thus the macroscale particle concentration depends upon the dynamic structure of the microscale.

11.3.4 Conservation of pores

Lastly, we homogenise the equation for the conservation of pores, (11.15),

$$\frac{\partial G_{ij}^r}{\partial T} = -\alpha\beta C_{ij}^r (G_{ij}^r)^{\frac{3}{2}} |P_i - P_j|. \tag{11.93}$$

Carrying out Steps 1–3 of network homogenisation on the remaining terms in (11.93), using the leading- and first-order pressure solutions, (11.48) and (11.51), and the leading-order particle concentration, (11.80), and noting the cancellation of the leading-order pressure difference, (11.49), we find that

$$\frac{\partial G_{ij}^{r(0)}}{\partial T} = -\varepsilon \left\{ \alpha\beta c^{(0)} (G_{ij}^{r(0)})^{\frac{3}{2}} \left| \Delta_{ij}^r \frac{\partial p^{(0)}}{\partial x} \right| \right\} + \mathcal{O}(\varepsilon^2). \tag{11.94}$$

A leading-order balance in (11.94) implies that

$$\frac{\partial G_{ij}^{r(0)}}{\partial T} = 0. \tag{11.95}$$

We have found that the conductances of pores do not change over the shorter timescale, T_c (see (11.12)), which is unsurprising, since we showed (see (11.76)) that deposition occurs over a longer timescale. Scaling onto the longer timescale over which particle deposition occurs, T_n (see (11.81)), and recalling that $t = \varepsilon T$, we find that

$$\frac{\partial G_{ij}^{r(0)}}{\partial t} = -\alpha\beta c^{(0)} (G_{ij}^{r(0)})^{\frac{3}{2}} \left| \Delta_{ij}^r \frac{\partial p^{(0)}}{\partial x} \right| + \mathcal{O}(\varepsilon). \tag{11.96}$$

This time, balancing terms at leading order, we find that

$$\frac{\partial \boldsymbol{G}^{(0)}}{\partial t} = -\alpha\beta \boldsymbol{R}^{(0)} \left| \frac{\partial p^{(0)}}{\partial x} \right| c^{(0)}, \tag{11.97}$$

where $\boldsymbol{G}^{(0)}$ and $\boldsymbol{R}^{(0)}$ are tensors of shape $(N, N, 2K+1)$ (recalling from Section 11.1 that K dictates the size of the set $\mathcal{R}$) with elements

$$G_{ij}^r = G_{ij}^{r(0)}, \quad R_{ij}^r = (G_{ij}^{r(0)})^{\frac{3}{2}} |\Delta_{ji}^{-r}|. \tag{11.98}$$

We have found that the evolution of the conductances of pores within the cell depend on the microscale structure, via the elements of $\boldsymbol{R}^{(0)}$, and on the evolution of the macroscale concentration and pressure gradient, $c^{(0)}$ and $\partial p^{(0)}/\partial x$, respectively.

11.3.5 Summary

In summary, we homogenise the microscale model, (11.13)–(11.22), and find a multiscale model. In particular, homogenising the microscale equations for the conservation of fluid, particles, and pores, (11.13)–(11.15), we find, dropping leading-order notation, that their macroscale equivalents are

$$\frac{\partial u}{\partial x} = 0, \quad \frac{\partial c}{\partial t} + \frac{\partial}{\partial x}\left(\frac{uc}{\phi}\right) = -\frac{\psi}{\phi} c, \quad \frac{\partial G_{ij}^r}{\partial t} = -\alpha\beta (G_{ij}^r)^{\frac{3}{2}} |\Delta_{ji}^{-r}| \left| \frac{\partial p}{\partial x} \right| c, \tag{11.99a,b,c}$$

respectively, where $\phi = N/l$ is the constant junction porosity, which represents the proportion of void space in the filter that is attributed to junctions. Homogenising the microscale flux, (11.16), we find that the Darcy velocity, u, is related to the permeability, k, and the pressure, p, by the Darcy equation, and that the reactivity, ψ, is related to the adhesivity, j, and the pressure by the reactivity equation, which are respectively given by

$$u = -k\frac{\partial p}{\partial x}, \quad \psi = -j\frac{\partial p}{\partial x}. \tag{11.100a,b}$$

The permeability and adhesivity, k and j, which are the parameters of this system, are related to the pore conductances, G_{ij}^r, by the equations

$$k = \frac{1}{2}\sum_{i=1}^{N}\sum_{j=1}^{N}\sum_{r\in\mathcal{R}} rG_{ij}^r\Delta_{ji}^{-r}, \quad j = -\frac{1}{l}\sum_{i=1}^{N}\sum_{j=1}^{N}\sum_{r\in\mathcal{R}} \alpha G_{ij}^r\Delta_{ji}^{-r}H_{ji}^{-r}. \tag{11.101a,b}$$

Here, the pore pressure drop is

$$\Delta_{ij}^r = W_i - (W_j + rl), \tag{11.102}$$

where the cell solution, W_i, is an effective junction position that dictates the contribution of the pressure drop to the solution evolution on the macroscale, via the permeability and adhesivity in (11.101). The cell solution is given by solving the linear cell problem,

$$\sum_{j=1}^{N}\sum_{r\in\mathcal{R}}\left(G_{ij}^{r(s)} - \delta_{ij}\sum_{k=1}^{N}G_{ik}^{r(s)}\right)W_j = \sum_{j=1}^{N}\sum_{r\in\mathcal{R}}\left(G_{ij}^{r(s)}rl\right) \tag{11.103}$$

where we have chosen the position of junction i to be $X_i = 0$ for simplicity, since this does not affect the solution.

Homogenising the microscale boundary conditions, (11.17) and (11.18), we find that we are given the pressure at the inlet and outlet,

$$p(0,t) = 1, \quad p(l,t) = 0, \tag{11.104a,b}$$

and the concentration at the inlet,

$$c(0,t) = 1, \tag{11.105}$$

for $t \geq 0$. Homogenising the microscale initial conditions, (11.19) and (11.20), we find that there are no particles in the filter initially,

$$c(x,0) = 0, \tag{11.106}$$

and that the initial pore conductances are drawn from a known distribution, so that

$$G_{ij}^r(x,0) = G_{ij}^{r0}(x) \tag{11.107}$$

for $i,j \in \{1,\ldots,N,\text{in},\text{out}\}$. Note that the initial conductances, $G_{ij}^{r0}(x)$, may vary with the spatial variable, x, which permits, for example, enforcement of slowly varying conductance distributions due to macroscale porosity gradients.

11.4 Multiscale model in D dimensions

We now present the D-dimensional formulation of the homogenisation of the periodic-network model, (11.13)–(11.15), where $D \in \{1, 2, 3\}$. In this setting, the spatial vectors defined in Section 11.1, such as $\boldsymbol{x}, \boldsymbol{X}_i$, and $\boldsymbol{r}$, are D-dimensional, and we describe dynamics on networks such as that illustrated in Figure 11.8, as well as Figures 11.1–11.4. We will find that the D-dimensional derivation is similar to the quasi-one-dimensional case presented in Section 11.3, and we will therefore find D-dimensional analogies to the one-dimensional objects already defined.

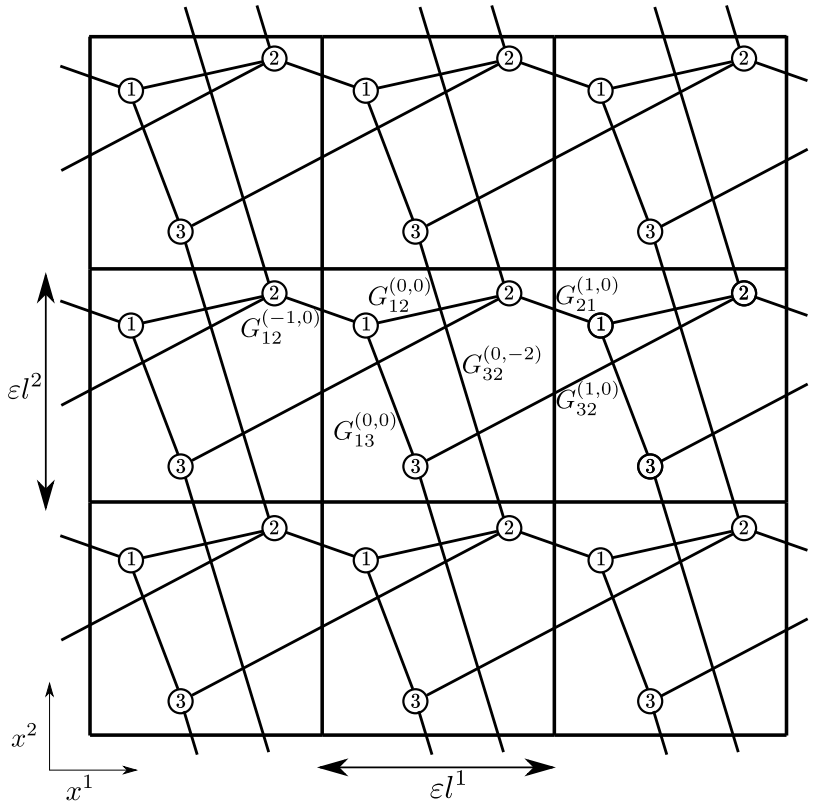

Figure 11.8: A diagram of a periodic network embedded in two-dimensional space. There are $N = 3$ nodes in the cell and this is repeated nine times. The conductance on some edges is labelled.

11.4.1 Conservation of fluid

As before, we begin by homogenising the microscale equation for the conservation of fluid mass, (11.13). As such, using the definition of the pore flux, (11.16), to write (11.13) in terms of the junction pressure, P_i, and pore conductance, $G_{ij}^{\boldsymbol{r}}$, and then following Steps 1–3 by evaluating the pressure and conductance at $\boldsymbol{x}$, which we define to be the left-bottom corner of the reference cell, carrying out a Taylor expansion

of the pressure and conductance about $\boldsymbol{x}$, and assuming asymptotic forms for these quantities, (11.30) and (11.32), we find that

$$\begin{aligned}
&\boldsymbol{A}^{(0)}\boldsymbol{P}^{(0)} + \varepsilon\Bigg\{\boldsymbol{A}^{(0)}\boldsymbol{P}^{(1)} + \boldsymbol{A}^{(1)}\boldsymbol{P}^{(0)} + \sum_{m=1}^{D}\boldsymbol{D}^{m(0)}\boldsymbol{P}^{(0)} + \sum_{m=1}^{D}\boldsymbol{B}^{m(0)}\frac{\partial \boldsymbol{P}^{(0)}}{\partial x^m}\Bigg\} + \\
&\quad \varepsilon^2\Bigg\{\boldsymbol{A}^{(0)}\boldsymbol{P}^{(2)} + \boldsymbol{A}^{(1)}\boldsymbol{P}^{(1)} + \sum_{m=1}^{D}\boldsymbol{D}^{m(0)}\boldsymbol{P}^{(1)} + \sum_{m=1}^{D}\boldsymbol{B}^{m(0)}\frac{\partial \boldsymbol{P}^{(1)}}{\partial x^m} + \boldsymbol{A}^{(2)}\boldsymbol{P}^{(0)} + \\
&\qquad \sum_{m=1}^{D}\boldsymbol{D}^{m(1)}\boldsymbol{P}^{(0)} + \sum_{m=1}^{D}\boldsymbol{B}^{m(1)}\frac{\partial \boldsymbol{P}^{(0)}}{\partial x^m} + \sum_{m=1}^{D}\sum_{n=1}^{D}\boldsymbol{F}^{mn(0)}\boldsymbol{P}^{(0)} + \\
&\qquad\quad \sum_{m=1}^{D}\sum_{n=1}^{D}\boldsymbol{E}^{mn(0)}\frac{\partial \boldsymbol{P}^{(0)}}{\partial x^n} + \sum_{m=1}^{D}\sum_{n=1}^{D}\boldsymbol{C}^{mn(0)}\frac{\partial^2 \boldsymbol{P}^{(0)}}{\partial x^m \partial x^n}\Bigg\} + \mathcal{O}(\varepsilon^3) = \boldsymbol{0}, \qquad (11.108)
\end{aligned}$$

which is the master equation for the conservation of fluid that we seek. This is the D-dimensional equivalent of (11.35), where upper indices now denote the spatial direction, so that $m, n \in \{1, \dots, D\}$. As before, $\boldsymbol{P}^{(s)} = (P_1^{(s)}, \dots, P_N^{(s)})^\top$ is the vector of $\mathcal{O}(\varepsilon^{(s)})$ pressure solutions in the lower indices, which is length N. This time, $\boldsymbol{A}^{(s)}$, $\boldsymbol{B}^{(s)}$, $\boldsymbol{C}^{(s)}$, $\boldsymbol{D}^{(s)}$, $\boldsymbol{E}^{(s)}$, and $\boldsymbol{F}^{(s)}$, are defined by the elements

$$A_{ij}^{(s)} = \sum_{\boldsymbol{r}\in\mathcal{R}}\left(G_{ij}^{\boldsymbol{r}(s)} - \delta_{ij}\sum_{k=1}^{N}G_{ik}^{\boldsymbol{r}(s)}\right), \qquad (11.109)$$

$$B_{ij}^{m(s)} = \sum_{\boldsymbol{r}\in\mathcal{R}}\left(G_{ij}^{\boldsymbol{r}(s)}(X_j^m + r^m l^m) - \delta_{ij}X_i^m\sum_{k=1}^{N}G_{ik}^{\boldsymbol{r}(s)}\right), \qquad (11.110)$$

$$C_{ij}^{mn(s)} = \frac{1}{2}\sum_{\boldsymbol{r}\in\mathcal{R}}\left(G_{ij}^{\boldsymbol{r}(s)}(X_j^m + r^m l^m)(X_j^n + r^n l^n) - \delta_{ij}X_i^m X_i^n\sum_{k=1}^{N}G_{ik}^{\boldsymbol{r}(s)}\right), \qquad (11.111)$$

$$D_{ij}^{m(s)} = \sum_{\boldsymbol{r}\in\mathcal{R}}\left(\frac{\partial G_{ij}^{\boldsymbol{r}(s)}}{\partial x^m}M_{ij}^{\boldsymbol{r}m} - \delta_{ij}\sum_{k=1}^{N}\frac{\partial G_{ik}^{\boldsymbol{r}(s)}}{\partial x^m}M_{ik}^{\boldsymbol{r}m}\right), \qquad (11.112)$$

$$E_{ij}^{mn(s)} = \sum_{\boldsymbol{r}\in\mathcal{R}}\left(\frac{\partial G_{ij}^{\boldsymbol{r}(s)}}{\partial x^m}M_{ij}^{\boldsymbol{r}m}(X_j^n + r^n l^n) - \delta_{ij}X_i^n\sum_{k=1}^{N}\frac{\partial G_{ik}^{\boldsymbol{r}(s)}}{\partial x^m}M_{ik}^{\boldsymbol{r}m}\right) \qquad (11.113)$$

$$F_{ij}^{mn(s)} = \frac{1}{2}\sum_{\boldsymbol{r}\in\mathcal{R}}\left(\frac{\partial^2 G_{ij}^{\boldsymbol{r}(s)}}{\partial x^m \partial x^n}M_{ij}^{\boldsymbol{r}m}M_{ij}^{\boldsymbol{r}n} - \delta_{ij}\sum_{k=1}^{N}\frac{\partial^2 G_{ik}^{\boldsymbol{r}(s)}}{\partial x^m \partial x^n}M_{ik}^{\boldsymbol{r}m}M_{ik}^{\boldsymbol{r}n}\right). \qquad (11.114)$$

These are tensors that are lower indexed by junction indices, i and j, and upper spatial indices, m and n. Comparing these tensors with the matrices defined in (11.37)–(11.42), we see that $\boldsymbol{A}^{(s)}$ is a matrix of shape (N, N) with no spatial indices, and is identical to that defined before, (11.37). The other objects have gained spatial indices. It is simple to verify that when $m = 1$, the 3-tensors of shape (N, N, D) with a single spatial index, $\boldsymbol{B}^{(s)}$ and $\boldsymbol{D}^{(s)}$, are equal to their one-dimensional versions defined in (11.38) and (11.40), and when $m = 1, n = 1$, the 4-tensors of shape (N, N, D, D)

with two spatial indices, $\boldsymbol{C}^{(s)}$, $\boldsymbol{E}^{(s)}$, $\boldsymbol{F}^{(s)}$, defined in (11.39), (11.41), and (11.42), are equal to their one-dimensional versions. We therefore interpret diagonal elements (in the spatial indices) of these new tensors as their one-dimensional counterparts, and so only off-diagonal elements are new. The implication is that the D-dimensional master equation, (11.108), contains cross-derivative terms that the one-dimensional equivalent, (11.35), does not. In analogy with (11.43)–(11.46), it can be shown (see Appendix A.2.1 for proof) that these new tensors satisfy

$$\boldsymbol{A}^{(s)}\mathbf{1} = \mathbf{0}, \quad \mathbf{1}^\top \boldsymbol{B}^{m(s)}\mathbf{1} = \mathbf{0}, \quad \boldsymbol{D}^{m(s)}\mathbf{1} = \mathbf{0}, \quad \boldsymbol{F}^{mn(s)}\mathbf{1} = \mathbf{0}, \tag{11.115a–d}$$

and

$$\mathbf{1}^\top \boldsymbol{D}^{m(s)} = \frac{\partial}{\partial x^m}\Big(\mathbf{1}^\top \boldsymbol{B}^{m(s)}\Big), \tag{11.116}$$

$$\mathbf{1}^\top \boldsymbol{E}^{mn(s)}\mathbf{1} = \frac{\partial}{\partial x^m}\Big(\mathbf{1}^\top \boldsymbol{C}^{mn(s)}\mathbf{1}\Big) + \frac{1}{2}\sum_{i=1}^{N}\sum_{j=1}^{N}\sum_{\boldsymbol{r}\in\boldsymbol{\mathcal{R}}} \frac{\partial G_{ij}^{\boldsymbol{r}(s)}}{\partial x^m}(r^n l^n X_i^m - r^m l^m X_i^n), \tag{11.117}$$

for each spatial index m and n, where $\mathbf{1} = (1, \ldots, 1)^\top$ and $\mathbf{0} = (0, \ldots, 0)^\top$ are vectors of length N in the junction index, as before. Comparing (11.117) to (11.44), we see (in Appendix A.126) that off-diagonal elements of these new identities now make non-zero contributions, which, as we will see, is one source of complication in the D-dimensional derivation in comparison to the quasi-one-dimensional equivalent. Note that $\boldsymbol{A}^{(s)}$ is still symmetric in the junction indices, and so $\mathbf{1}^\top$ is still a left zero-eigenvector, so that (11.45) and (11.46) are unchanged.

We now solve the master equation for fluid conservation, (11.108). Balancing leading-order terms, we find that

$$\boldsymbol{A}^{(0)}\boldsymbol{P}^{(0)} = \mathbf{0}, \tag{11.118}$$

as before, which has the solution

$$\boldsymbol{P}^{(0)} = p^{(0)}(\boldsymbol{x}, t)\mathbf{1}. \tag{11.119}$$

Here, as usual, $p^{(0)}(\boldsymbol{x}, t)$ is the leading-order macroscale pressure solution to be found. As in the one-dimensional case (see (11.48)), the leading-order pressure solution is independent of the microscale, so that the leading-order intra-cell pressure difference is zero,

$$P_j^{(0)} - P_i^{(0)} = 0. \tag{11.120}$$

We pre-multiply both sides of (11.118) by $\mathbf{1}^\top$ and see that the resulting equation is satisfied by any $p^{(0)}$, so we must proceed to the next order in ε for a solvability condition.

At first order, substituting the leading-order pressure solution, (11.119), into the master equation, (11.108), and using the identities (11.115a) and (11.115c) to simplify, we find that

$$\boldsymbol{A}^{(0)}\boldsymbol{P}^{(1)} + \sum_{m=1}^{D} \boldsymbol{B}^{m(0)}\mathbf{1}\frac{\partial p^{(0)}}{\partial x^m} = \mathbf{0}. \tag{11.121}$$

This has the solution

$$\boldsymbol{P}^{(1)} = f(\boldsymbol{x}, t)\mathbf{1} + \sum_{m=1}^{D} \frac{\partial p^{(0)}}{\partial x^m}\boldsymbol{W}^m, \tag{11.122}$$

where $f(\boldsymbol{x}, t)$ is an arbitrary microscale-independent function, and $\boldsymbol{W}^m$ satisfies

$$\boldsymbol{A}^{(0)}\boldsymbol{W}^m = -\boldsymbol{B}^{m(0)}\mathbf{1}, \tag{11.123}$$

for each $m \in \{1, \ldots, D\}$. Comparing the first-order pressure solution, (11.122), to its one-dimensional equivalent, (11.51), we see that the D-dimensional version is a sum of the one-dimensional solutions, as we would expect. Meanwhile, comparing the D-dimensional cell problem, (11.123), to the one-dimensional one, (11.52), we see that the cell solution, $\boldsymbol{W}$, is now a matrix of shape (N, D). As such, D independent linear problems of size N must now be solved to find its elements, W_i^m. From (11.122), we see that each vector of length N of the cell solution, $\boldsymbol{W}^m$, contributes to the first-order pressure in the corresponding direction, x^m. Using (11.110), we see that the first-order pressure difference is non-zero, and is given by

$$P_j^{(1)} - P_i^{(1)} = \sum_{m=1}^{D} G_{ij}^{\boldsymbol{r}(0)}(W_j^m - W_i^m)\frac{\partial p^{(0)}}{\partial x^m}, \tag{11.124}$$

which remains independent of f. As before, the first-order pressure difference, (11.124), determines the flux down the corresponding pore, and this depends on the macroscale pressure gradient, $\partial p^{(0)}/\partial x^m$. Pre-multiplying both sides of the first order problem, (11.121), by $\mathbf{1}^\top$ and using (11.115b), we see that the resulting equation holds for any $p^{(0)}$, and we must therefore consider higher-order equations to find a solvability condition.

Proceeding to second order, by substituting the leading- and first-order pressure solutions, (11.119) and (11.122), into the master equation, (11.108), and using (11.115a), (11.115c), and (11.115d) to simplify, we see that

$$\begin{aligned}
&\boldsymbol{A}^{(0)}\boldsymbol{P}^{(2)} + \boldsymbol{A}^{(1)}\sum_{m=1}^{D}\frac{\partial p^{(0)}}{\partial x^m}\boldsymbol{W}^m + \sum_{m=1}^{D}\boldsymbol{D}^{m(0)}\sum_{n=1}^{D}\frac{\partial p^{(0)}}{\partial x^n}\boldsymbol{W}^n + \\
&\sum_{m=1}^{D}\boldsymbol{B}^{m(0)}\frac{\partial}{\partial x^m}\Big(f\mathbf{1} + \sum_{n=1}^{D}\frac{\partial p^{(0)}}{\partial x^n}\boldsymbol{W}^n\Big) + \sum_{m=1}^{D}\boldsymbol{B}^{m(1)}\mathbf{1}\frac{\partial p^{(0)}}{\partial x^m} + \\
&\sum_{m=1}^{D}\sum_{n=1}^{D}\boldsymbol{E}^{mn(0)}\mathbf{1}\frac{\partial p^{(0)}}{\partial x^n} + \sum_{m=1}^{D}\sum_{n=1}^{D}\boldsymbol{C}^{mn(0)}\mathbf{1}\frac{\partial^2 p^{(0)}}{\partial x^m \partial x^n} = \mathbf{0},
\end{aligned} \tag{11.125}$$

which is the D-dimensional equivalent of the one-dimensional second-order conservation of fluid problem, (11.54). Searching for a solvability condition by pre-multiplying (11.125) by $\mathbf{1}^\top$ and using the identity (11.46) to eliminate the second-order pressure, $\boldsymbol{P}^{(2)}$, we find that

$$\begin{aligned}\mathbf{1}^\top \boldsymbol{A}^{(1)} \sum_{m=1}^{D} \frac{\partial p^{(0)}}{\partial x^m} \boldsymbol{W}^m + \mathbf{1}^\top \sum_{m=1}^{D} \boldsymbol{D}^{m(0)} \sum_{n=1}^{D} \frac{\partial p^{(0)}}{\partial x^n} \boldsymbol{W}^n + \\ \mathbf{1}^\top \sum_{m=1}^{D} \boldsymbol{B}^{m(0)} \frac{\partial}{\partial x^m} \Big(f\mathbf{1} + \sum_{n=1}^{D} \frac{\partial p^{(0)}}{\partial x^n} \boldsymbol{W}^n \Big) + \mathbf{1}^\top \sum_{m=1}^{D} \boldsymbol{B}^{m(1)} \mathbf{1} \frac{\partial p^{(0)}}{\partial x^m} + \\ \mathbf{1}^\top \sum_{m=1}^{D} \sum_{n=1}^{D} \boldsymbol{E}^{mn(0)} \mathbf{1} \frac{\partial p^{(0)}}{\partial x^n} + \mathbf{1}^\top \sum_{m=1}^{D} \sum_{n=1}^{D} \boldsymbol{C}^{mn(0)} \mathbf{1} \frac{\partial^2 p^{(0)}}{\partial x^m \partial x^n} = 0. \end{aligned} \tag{11.126}$$

Using the identities (11.115a) and (11.115b), and further (11.116) and (11.117) to simplify, before using the product rule to write the result in terms of $\boldsymbol{B}^{m(0)}$ and $\boldsymbol{C}^{mn(0)}$, we get

$$\begin{aligned}\sum_{m=1}^{D} \frac{\partial}{\partial x^m} \Bigg(\sum_{n=1}^{D} \Big(\frac{1}{2} \mathbf{1}^\top \boldsymbol{B}^{m(0)} \boldsymbol{W}^n + \frac{1}{2} \mathbf{1}^\top \boldsymbol{B}^{n(0)} \boldsymbol{W}^m + \mathbf{1}^\top \boldsymbol{C}^{mn(0)} \mathbf{1} \Big) \Bigg) \frac{\partial p^{(0)}}{\partial x^n} + \\ \frac{1}{2} \sum_{m=1}^{D} \frac{\partial}{\partial x^m} \Bigg(\sum_{n=1}^{D} \Bigg(\sum_{i=1}^{N} \sum_{j=1}^{N} \sum_{\boldsymbol{r} \in \boldsymbol{\mathcal{R}}} \Big(G_{ij}^{\boldsymbol{r}(0)} (r^n l^n X_i^m - r^m l^m X_i^n) + \\ \mathbf{1}^\top \boldsymbol{B}^{m(0)} \boldsymbol{W}^n - \mathbf{1}^\top \boldsymbol{B}^{n(0)} \boldsymbol{W}^m \Big) \frac{\partial p^{(0)}}{\partial x^n} \Bigg) \Bigg) = 0. \end{aligned} \tag{11.127}$$

Since the last term in (11.127) is equal to zero (see Appendix A.2.3), we arrive at

$$\boldsymbol{\nabla} \cdot \Big(\boldsymbol{\sigma}^{(0)} \boldsymbol{\nabla} p^{(0)} \Big) = 0, \tag{11.128}$$

where $\boldsymbol{\sigma}^{(0)}$ is the symmetric matrix, with shape (D, D), defined by

$$\sigma^{mn(0)} = \frac{1}{\prod_{a=1}^{D} l^a} \Big(\frac{1}{2} \mathbf{1}^\top \boldsymbol{B}^{m(0)} \boldsymbol{W}^n + \frac{1}{2} \mathbf{1}^\top \boldsymbol{B}^{n(0)} \boldsymbol{W}^m + \mathbf{1}^\top \boldsymbol{C}^{mn(0)} \mathbf{1} \Big). \tag{11.129}$$

The macroscale fluid conservation equation, (11.128), is the D-dimensional equivalent of (11.56), which we have shown to be the macroscale Darcy equation. The parameter of the equation, $\boldsymbol{\sigma}^{(0)}$ defined in (11.129), which is a symmetric matrix of shape (D, D), is the D-dimensional analogy to the scalar $\sigma^{(0)}$ in (11.57). This dictates the dependence of the macroscale pressure on the microscale, since it depends on the pore conductance, $G_{ij}^{\boldsymbol{r}(0)}$, via the tensors $\boldsymbol{B}^{(0)}$ and $\boldsymbol{C}^{(0)}$, which are defined in (11.110) and (11.112), respectively, and the cell solution matrix, $\boldsymbol{W}$, which is the solution of the cell problem, (11.123). We see that the diagonal elements of $\boldsymbol{\sigma}^{(0)}$ are equal to $\sigma^{(0)}$. In the one-dimensional setting, we found that $\sigma^{(0)}$ was equal to the scalar permeability, $k^{(0)}$, and similarly, here we will find (see Appendix A.2.4) that $\boldsymbol{\sigma}^{(0)}$ is the permeability matrix. As such, $\sigma^{mn(0)}$ is the permeability in the x^n direction through the surface that is normal to the x^m direction.

11.4.2 Darcy's law

We now construct a D-dimensional macroscale flow rate from microscale fluxes, similar to (11.58), in order to find the velocity that results from the macroscale pressure, $p^{(0)}$. To this end, we introduce the D-dimensional Darcy velocity vector, $\boldsymbol{u}$, where the component in the x^m direction is

$$u^m = \frac{l^m}{2\prod_n l^n} \sum_{i=1}^{N} \sum_{j=1}^{N} \sum_{\boldsymbol{r}\in\boldsymbol{\mathcal{R}}} r^m Q_{ij}^{\boldsymbol{r}}. \tag{11.130}$$

for $m \in \{1, \ldots, D\}$. Note the division by the cross-sectional area of the surface that is normal to the x^m direction, $\prod_{n\neq m} l^n$, so that, analogously with the one-dimensional Darcy velocity, (11.58), (11.130) is the $\mathcal{O}(1)$ flux of fluid per unit cross-sectional area through a cell in the x^m direction.

As before, we homogenise the Darcy velocity, (11.130), by writing the microscale flux, $Q_{ij}^{\boldsymbol{r}}$, in terms of the pressure and conductance, using (11.16), and following Steps 1–3. Using the D-dimensional pressure solutions, (11.119) and (11.122), and noting the cancellations due to the leading- and first-order pressure differences, (11.120) and (11.124), we find that the leading-order flux is

$$Q_{ij}^{\boldsymbol{r}(0)} = \sum_{n=1}^{D} G_{ij}^{\boldsymbol{r}(0)} \Delta_{ij}^{r^n} \frac{\partial p^{(0)}}{\partial x^n}, \tag{11.131}$$

where

$$\Delta_{ij}^{r^m} = W_i^m + X_i^m - (W_j^m + X_j^m + r^m l^m), \tag{11.132}$$

which satisfies

$$\Delta_{ji}^{-r^m} = -\Delta_{ij}^{r^m}. \tag{11.133}$$

Here, (11.131)–(11.133) are analogous is with (11.61)–(11.63). We see that (11.132) defines the elements of a D-dimensional pressure drop, $\boldsymbol{\Delta}$, which is a 4-tensor with shape $(N, N, 2K+1, D)$, where we recall that K determines the number of references, r, in their set, $\mathcal{R}$. From (11.131), we see that each element, $\Delta_{ij}^{r^m}$, is the leading-order component of the pressure difference across the pore between junction i and the junction j in the cell at reference r in direction x^m, per unit pressure gradient. This dictates the contribution that the r^m component of the pressure drop in pore ij makes to the macroscale pressure gradient across the cell as a whole. Similarly to before, we interpret the cell solution element, W_i^m, as the component of the pressure (per unit pressure gradient) at junction i in the x^m direction that is required to induce the pressure gradient, $\partial p^{(0)}/\partial x^m$. It follows (see Appendix A.2.4), as in the one-dimensional formulation, that the problem is independent of junction positions, so that, choosing $X_i^m = 0$, (11.132) may be simplified to

$$\Delta_{ij}^{r^m} = W_i^m - (W_j^m + r^m l^m). \tag{11.134}$$

Substituting the homogenised leading-order flux, (11.131), into the Darcy velocity, (11.130), we find that

$$u^m = \frac{l^m}{2\prod_{a=1}^{D} l^a} \sum_{i=1}^{N} \sum_{j=1}^{N} \sum_{\boldsymbol{r}\in\boldsymbol{\mathcal{R}}} \sum_{n=1}^{D} r^m G_{ij}^{\boldsymbol{r}(0)} \Delta_{ij}^{r^n} \frac{\partial p^{(0)}}{\partial x^n} + \mathcal{O}(\varepsilon), \tag{11.135}$$

in analogy with (11.65). Note that elements of $\Delta_{ij}^{r^n}$ are summed with the corresponding elements of $G_{ij}^{(r^1,\ldots,r^n,\ldots,r^D)^\top}$. Therefore, writing (11.135) in vector form, it follows that the leading-order Darcy velocity satisfies the D-dimensional version of Darcy's law. That is, we find that

$$\boldsymbol{u}^{(0)} = -\boldsymbol{k}^{(0)} \boldsymbol{\nabla} p^{(0)}, \tag{11.136}$$

where, this time, $\boldsymbol{k}^{(0)}$ is a symmetric matrix of shape (D, D), with elements

$$k^{mn(0)} = \frac{l^m}{2\prod_n l^n} \sum_{i=1}^{N} \sum_{j=1}^{N} \sum_{\boldsymbol{r}\in\boldsymbol{\mathcal{R}}} r^m G_{ij}^{\boldsymbol{r}(0)} \Delta_{ji}^{-r^n}. \tag{11.137}$$

This matrix is analogous with the permeability scalar defined in (11.68). We find that $\boldsymbol{k}^{(0)} = \boldsymbol{\sigma}^{(0)}$ (see Appendix A.2.4), and, using this identity in the governing equation for the macroscale pressure, (11.128), we find that the leading-order Darcy velocity, $\boldsymbol{u}^{(0)}$, is divergence-free, so that

$$\boldsymbol{\nabla} \cdot \boldsymbol{u}^{(0)} = 0, \tag{11.138}$$

in analogy with the one-dimensional fluid conservation equation, (11.69). Inspecting (11.136), we identify $\boldsymbol{k}^{(0)}$ as the leading-order permeability matrix. As such, each element, $k^{mn(0)}$, is the permeability in the x^n direction through a cross-section that is normal to the x^m direction.

11.4.3 Conservation of particles

Next, we homogenise the equation for the conservation of particles on the microscale, (11.14), which we re-write, substituting the pore flux for the pressure and conductance using (11.16), as

$$\begin{aligned} \frac{\partial C_i}{\partial T} = \frac{1}{\varepsilon} \Bigg\{ \sum_{j=1}^{N} \sum_{\boldsymbol{r}\in\boldsymbol{\mathcal{R}}} \Big(& G_{ji}^{-\boldsymbol{r}} (P_j - P_i) C_j H(G_{ji}^{-\boldsymbol{r}} (P_j - P_i)) - \\ & G_{ij}^{\boldsymbol{r}} (P_i - P_j) C_i H(G_{ij}^{\boldsymbol{r}} (P_i - P_j)) \Big) \Bigg\} \\ & - \sum_{j=1}^{N} \sum_{\boldsymbol{r}\in\boldsymbol{\mathcal{R}}} \alpha G_{ji}^{-\boldsymbol{r}} (P_j - P_i) C_j H(G_{ji}^{-\boldsymbol{r}} (P_j - P_i)). \end{aligned} \tag{11.139}$$

As before, we begin by noting that the Heaviside function can be homogenised first and carried through the rest of the process without interacting with the other terms of (11.139). Specifically, we carry out Steps 1–3 on the term $H(Q_{ij}^{\boldsymbol{r}})$ and find that

$$H(Q_{ij}^{\boldsymbol{r}}) = H\bigg(G_{ij}^{\boldsymbol{r}}(P_i - P_j) + \varepsilon\bigg\{\sum_{m=1}^{D} G_{ij}^{\boldsymbol{r}}\bigg(X_i^m \frac{\partial P_i}{\partial x^m} - (X_j^m + r^m l^m)\frac{\partial P_j}{\partial x^m}\bigg)\bigg\} + \mathcal{O}(\varepsilon^2)\bigg) \tag{11.140}$$

$$= H\bigg(\varepsilon\bigg\{\sum_{m=1}^{D} G_{ij}^{\boldsymbol{r}}\Delta_{ij}^{r^m}\frac{\partial p^{(0)}}{\partial x^m}\bigg\} + \mathcal{O}(\varepsilon^2)\bigg), \tag{11.141}$$

which is equivalent to (11.72). The first equality is obtained by writing the flux in terms of the conductance and pressure using (11.16), followed by a Taylor expansion of the pressure and conductance about $\boldsymbol{x}$. The second equality is a substitution of the asymptotic expansion for pressure, (11.30), and use of the leading- and first-order pressure solutions, (11.119) and (11.122). We therefore define

$$H_{ij}^{\boldsymbol{r}(0)} = H\bigg(G_{ij}^{\boldsymbol{r}}\sum_{m=1}^{D}\Delta_{ij}^{r^m}\frac{\partial p^{(0)}}{\partial x^m}\bigg), \tag{11.142}$$

in analogy with (11.73), and note that this satisfies

$$H_{ij}^{\boldsymbol{r}(0)} + H_{ji}^{-\boldsymbol{r}(0)} = 1, \tag{11.143}$$

which is the D-dimensional equivalent of (11.74). As before, we will find that this homogenised Heaviside function, (11.142), disappears from all terms except the one containing the adherence parameter, α, which we expect, since we require it to indicate the pores $ij\boldsymbol{r}$ that carry fluid into i, since it is within these pores that deposition occurs in the underlying network.

We then carry out Steps 1–3 on the rest of the particle conservation equation, (11.139), similarly as in the one-dimensional case. We apply a Taylor expansion and an asymptotic expansion to the particle concentration, the conductance, and the pressure, about $\boldsymbol{x}$. Using the leading- and first-order pressure solutions, (11.119) and (11.122), and noting the cancellation of terms that contain the leading-order pressure difference, (11.120), and the cancellation of terms involving the function f (which ensures that f is arbitrary in (11.122)) via the first-order pressure difference,

(11.124), we arrive at

$$\frac{\partial}{\partial T}\Big(C_i^{(0)}+\varepsilon\Big\{C_i^{(1)}+\sum_{m=1}^{D}X_i^m\frac{\partial C_i^{(0)}}{\partial x}\Big\}+\varepsilon^2\Big\{C_i^{(2)}+ \sum_{m=1}^{D}X_i^m\frac{\partial C_i^{(1)}}{\partial x}+\frac{1}{2}\sum_{m=1}^{D}\sum_{n=1}^{D}X_i^mX_i^n\frac{\partial^2 C_i^{(0)}}{\partial x^m\partial x^n}\Big\}\Big)=$$
$$\sum_{j=1}^{N}\sum_{\boldsymbol{r}\in\boldsymbol{\mathcal{R}}}\Big\{G_{ij}^{\boldsymbol{r}(0)}\sum_{m=1}^{D}\Delta_{ji}^{-r^m}\frac{\partial p^{(0)}}{\partial x^m}(C_j^{(0)}H_{ji}^{-\boldsymbol{r}(0)}+C_i^{(0)}H_{ij}^{\boldsymbol{r}(0)})\Big\}+$$
$$\varepsilon\Big\{G_{ij}^{\boldsymbol{r}(0)}\sum_{m=1}^{D}\Delta_{ji}^{-r^m}\frac{\partial p^{(0)}}{\partial x^m}(C_j^{(1)}H_{ji}^{-\boldsymbol{r}(0)}+C_i^{(1)}H_{ij}^{\boldsymbol{r}(0)})+$$
$$G_{ij}^{\boldsymbol{r}(0)}\sum_{m=1}^{D}\Delta_{ji}^{-r^m}\frac{\partial p^{(0)}}{\partial x^m}\Big(\sum_{n=1}^{D}(X_j^n+r^nl^n)\frac{\partial C_j^{(0)}}{\partial x^n}H_{ji}^{-\boldsymbol{r}(0)}+$$
$$\sum_{n=1}^{D}X_i^n\frac{\partial C_i^{(0)}}{\partial x^n}H_{ij}^{\boldsymbol{r}(0)}\Big)+\Big(G_{ij}^{\boldsymbol{r}(0)}\Big(P_j^{(2)}-P_i^{(2)}\Big)+G_{ij}^{\boldsymbol{r}(1)}\sum_{m=1}^{D}\Delta_{ji}^{-r^m}\frac{\partial p^{(0)}}{\partial x^m}+$$
$$G_{ij}^{\boldsymbol{r}(0)}\Big(\sum_{m=1}^{D}(X_j^m+r^ml^m)\frac{\partial}{\partial x^m}\Big(f+\sum_{n=1}^{D}W_j^n\frac{\partial p^{(0)}}{\partial x^n}\Big)-\sum_{m=1}^{D}X_i^m\frac{\partial}{\partial x^m}\Big(f+$$
$$\sum_{n=1}^{D}W_i^n\frac{\partial p^{(0)}}{\partial x^n}\Big)\Big)+\frac{G_{ij}^{\boldsymbol{r}(0)}}{2}\Big(\sum_{m=1}^{D}\sum_{n=1}^{D}(X_j^m+r^ml^m)(X_j^n+r^nl^n)-$$
$$\sum_{m=1}^{D}\sum_{n=1}^{D}X_i^mX_i^n\Big)\frac{\partial^2 p^{(0)}}{\partial x^m\partial x^n}+\sum_{m=1}^{D}\frac{\partial G_{ij}^{\boldsymbol{r}(0)}}{\partial x^m}M_{ij}^{\boldsymbol{r}m}\sum_{n=1}^{D}\Delta_{ji}^{-r^n}\frac{\partial p^{(0)}}{\partial x^n}\Big)(C_j^{(0)}H_{ji}^{-\boldsymbol{r}(0)}+$$
$$C_i^{(0)}H_{ij}^{\boldsymbol{r}(0)})-G_{ij}^{\boldsymbol{r}(0)}\sum_{m=1}^{D}\Delta_{ji}^{-r^m}\frac{\partial p^{(0)}}{\partial x^m}C_j^{(0)}H_{ji}^{-\boldsymbol{r}(0)}A_{ji}^{-\boldsymbol{r}(0)}\Big\}+\mathcal{O}(\varepsilon^2), \tag{11.144}$$

which is the D-dimensional master equation for the conservation of particles. This has a similar form as its one-dimensional equivalent, (11.75). For example, the deposition term appears at first order in ε because there is no pressure difference at leading order.

To simplify the master equation, we continue by carrying out Step 4. Similarly to in (11.75), a leading-order balance in the D-dimensional the master equation, (11.144), yields

$$\mathbf{1}\circ\frac{\partial\boldsymbol{C}^{(0)}}{\partial T}=\sum_{m=1}^{D}\boldsymbol{S}^{m(0)}\boldsymbol{C}^{(0)}\frac{\partial p^{(0)}}{\partial x^m}. \tag{11.145}$$

In analogy with (11.76), here, $\mathbf{1}=(1,\ldots,1)^\top$ and $\boldsymbol{C}=(C_1,\ldots,C_N)^\top$ are the vectors of length N that contain the junction volumes and concentrations, and $\boldsymbol{S}^{(0)}$ is a 3-tensor with shape (N,N,D) that is the analogy of the matrix defined in (11.77), with

elements

$$S_{ij}^{m(0)} = \sum_{\boldsymbol{r}\in\mathcal{R}} \left(G_{ij}^{\boldsymbol{r}(0)} \Delta_{ji}^{-r^m} H_{ji}^{-\boldsymbol{r}(0)} - \delta_{ij} \sum_{k=1}^{N} G_{ik}^{\boldsymbol{r}(0)} \Delta_{ik}^{r^m} H_{ik}^{\boldsymbol{r}(0)} \right). \tag{11.146}$$

In Appendix A.2.5, we show that each matrix in this tensor, $\boldsymbol{S}^{m(0)}$, has the same form as the equivalent one-dimensional form, (11.77), and so satisfies

$$\boldsymbol{S}^{m(0)}\mathbf{1} = \mathbf{0} = \mathbf{1}^\top \boldsymbol{S}^{m(0)}. \tag{11.147}$$

As before, on this shorter timescale, T_c defined in (11.12), we see that (11.145) implies that particles flow in and out of the cell without depositing, so that the net particle flux is zero, from (11.147). Therefore, (11.145) describes the behaviour of the microscale-dependent particle concentration before it settles down to the microscale-independent solution that we seek.

Rescaling time onto a longer timescale, T_n defined in (11.81), and recalling that $t = \varepsilon T$, at leading order we find that

$$\mathbf{0} = \sum_{m=1}^{D} \boldsymbol{S}^{m(0)} \boldsymbol{C}^{(0)} \frac{\partial p^{(0)}}{\partial x^m}. \tag{11.148}$$

Therefore, using the first identity in (11.147), it follows that

$$\boldsymbol{C}^{(0)} = c^{(0)}(\boldsymbol{x}, t)\mathbf{1}, \tag{11.149}$$

which is equivalent to (11.80). As usual, $c^{(0)}(\boldsymbol{x}, t)$ denotes the microscale-independent leading-order concentration solution to be found.

Proceeding to first order to look for an equation that determines $c^{(0)}$, by substituting this leading-order solution, (11.149), into the master equation, (11.144), and noting that $H_{ij}^{\boldsymbol{r}(0)}$ disappears from terms containing $c^{(0)}$ (using the identity (11.143)), we find that

$$\begin{aligned}
\mathbf{1}\frac{\partial c^{(0)}}{\partial t} = &\sum_{m=1}^{D} \boldsymbol{S}^{m(0)} \boldsymbol{C}^{(1)} \frac{\partial p^{(0)}}{\partial x^m} + \sum_{m=1}^{D}\sum_{n=1}^{D} \boldsymbol{K}^{mn(0)} \mathbf{1} \frac{\partial p^{(0)}}{\partial x^m}\frac{\partial c^{(0)}}{\partial x^n} - \\
&\sum_{m=1}^{D} \boldsymbol{J}^{m(0)} \mathbf{1} \frac{\partial p^{(0)}}{\partial x^m} c^{(0)} + \Bigg(\boldsymbol{A}^{(0)} \boldsymbol{P}^{(2)} + \boldsymbol{A}^{(1)} \sum_{m=1}^{D} \boldsymbol{W}^m \frac{\partial p^{(0)}}{\partial x^m} + \sum_{m=1}^{D} \boldsymbol{B}^{m(1)} \mathbf{1} \frac{\partial p^{(0)}}{\partial x^m} + \\
&\sum_{m=1}^{D} \boldsymbol{B}^{m(0)} \frac{\partial}{\partial x^m} \Big(f\mathbf{1} + \sum_{n=1}^{D} \frac{\partial p^{(0)}}{\partial x^n} \boldsymbol{W}^n \Big) + \sum_{m=1}^{D}\sum_{n=1}^{D} \boldsymbol{C}^{mn(0)} \mathbf{1} \frac{\partial^2 p^{(0)}}{\partial x^m \partial x^n} + \\
&\sum_{m=1}^{D} \boldsymbol{D}^{m(0)} \sum_{n=1}^{D} \boldsymbol{W}^n \frac{\partial p^{(0)}}{\partial x^n} + \sum_{m=1}^{D}\sum_{n=1}^{D} \boldsymbol{E}^{mn(0)} \mathbf{1} \frac{\partial p^{(0)}}{\partial x^n} \Bigg) c^{(0)},
\end{aligned} \tag{11.150}$$

where $\boldsymbol{K}^{mn(0)}$ is the mn element of a 4-tensor of shape (N, N, D, D), which is equivalent to the matrix $\boldsymbol{K}^{(0)}$ from the one-dimensional case, (11.83), and is defined by

$$K_{ij}^{mn(0)} = \sum_{\boldsymbol{r}\in\mathcal{R}} \left(G_{ij}^{\boldsymbol{r}(0)} \Delta_{ji}^{-r^m} \left((X_j^n + r^n l^n) H_{ji}^{-\boldsymbol{r}(0)} + X_i^n H_{ij}^{\boldsymbol{r}(0)} \right) \right), \tag{11.151}$$

while $\boldsymbol{J}^{m(0)}$ is the m element of a 3-tensor of shape (N, N, D), which is equivalent to the matrix $\boldsymbol{J}^{(0)}$ from before, (11.84), and is defined by

$$J_{ij}^{m(0)} = \sum_{\boldsymbol{r}\in\boldsymbol{\mathcal{R}}} \left(\alpha G_{ij}^{\boldsymbol{r}(0)} \Delta_{ji}^{-r^m} H_{ji}^{-\boldsymbol{r}(0)} \right). \tag{11.152}$$

Using the second-order equation that results from the problem for conservation of mass, (11.125), we find that the sum of all but the first three terms on the right-hand side of (11.150) is equal to zero, and so, pre-multiplying (11.150) by $\mathbf{1}^\top$ gives

$$\frac{\partial c^{(0)}}{\partial t} = \sum_{m=1}^{D}\sum_{n=1}^{D} \frac{\mathbf{1}^\top \boldsymbol{K}^{mn(0)} \mathbf{1}}{\mathbf{1}^\top \mathbf{1}} \frac{\partial p^{(0)}}{\partial x^m} \frac{\partial c^{(0)}}{\partial x^n} - \sum_{m=1}^{D} \frac{\mathbf{1}^\top \boldsymbol{J}^{m(0)} \mathbf{1}}{\mathbf{1}^\top \mathbf{1}} \frac{\partial p^{(0)}}{\partial x^m} c^{(0)}, \tag{11.153}$$

where we have used the second equality in the identity (11.147). Therefore, as in the one-dimensional case, the macroscale evolution of the leading-order particle concentration is governed by an advection–reaction equation.

Comparing the definition of $\boldsymbol{K}^{mn(0)}$, (11.151), to its one-dimensional counterpart, $\boldsymbol{K}^{(0)}$ in (11.83), we expect $\boldsymbol{K}^{mn(0)}$ to be a matrix related to advective terms in the x^n direction on the surface that is normal to the x^m direction, on the macroscale. Indeed, it follows (see Appendix A.2.6 for proof) that

$$\mathbf{1}^\top \boldsymbol{K}^{mn(0)} \mathbf{1} = \prod_{a=1}^{D} l^a k^{mn(0)} = \prod_{a=1}^{D} l^a \sigma^{mn(0)}, \tag{11.154}$$

so that this tensor is proportional to the permeability matrix, $\boldsymbol{k}^{(0)}$ of shape (D, D), which corresponds to the effective conductance of the filter. Similarly, comparing the definition of $\boldsymbol{J}^{m(0)}$, (11.152), to its one-dimensional counterpart, $\boldsymbol{J}^{(0)}$, (11.84), we expect $\boldsymbol{J}^{m(0)}$ to be a matrix related to reactive terms in the x^m direction on the macroscale. Accordingly, we define

$$j^{m(0)} = -\frac{\mathbf{1}^\top \boldsymbol{J}^{m(0)} \mathbf{1}}{\prod_{n=1}^{D} l^n} = -\frac{1}{\prod_{n=1}^{D} l^n} \sum_{i=1}^{N}\sum_{j=1}^{N}\sum_{\boldsymbol{r}\in\boldsymbol{\mathcal{R}}} \alpha G_{ij}^{\boldsymbol{r}(0)} \Delta_{ji}^{-r^m} H_{ji}^{-\boldsymbol{r}(0)}. \tag{11.155}$$

We call $\boldsymbol{j}^{(0)}$ the adhesivity vector, which is of length D, since we expect it to correspond to the effective adherence of the filter.

To illustrate this, in analogy with the one-dimensional case, we define

$$v = \mathbf{1}^\top \mathbf{1} = N, \tag{11.156}$$

which is the total volume of the junctions in a cell. Using the relationships between $\boldsymbol{K}^{mn(0)}$ and $k^{mn(0)}$, (11.154), and between $\boldsymbol{J}^{m(0)}$ and $j^{m(0)}$, (11.155), we re-write the macroscale concentration equation, (11.153), as

$$\frac{\partial c^{(0)}}{\partial t} = \frac{\prod_{m=1}^{D} l^m}{v} (\boldsymbol{k}^{(0)} \cdot \boldsymbol{\nabla} p^{(0)}) \cdot \boldsymbol{\nabla} c^{(0)} + \frac{\prod_{m=1}^{D} l^m}{v} (\boldsymbol{j}^{(0)} \cdot \boldsymbol{\nabla} p^{(0)})\, c^{(0)}. \tag{11.157}$$

Identifying

$$\phi = \frac{v}{\prod_{m=1}^{D} l^m} \tag{11.158}$$

as the D-dimensional junction porosity, which is the constant proportion of total filter space occupied by junctions, defining the reactivity,

$$\psi^{(0)} = -\boldsymbol{j}^{(0)} \cdot \boldsymbol{\nabla} p^{(0)}, \tag{11.159}$$

and using this equation along with Darcy's law, (11.136), we arrive at

$$\frac{\partial c^{(0)}}{\partial t} + \boldsymbol{\nabla} \cdot \frac{\boldsymbol{u}^{(0)}}{\phi} c^{(0)} = -\frac{\psi^{(0)}}{\phi} c^{(0)}. \tag{11.160}$$

In D dimensions, we have found that the particle concentration, $c^{(0)}$, varies on the continuous macroscale subject to an advection–reaction equation, (11.160). That is, particles are advected through the filter by the pore velocity, $\boldsymbol{u}^{(0)}\phi^{-1}$, which is related to the pressure, $p^{(0)}$, and the permeability, $\boldsymbol{k}^{(0)}$, via the Darcy equation (11.136). As they do so, particles deposit in the filter at a rate determined by the reactivity, $\psi^{(0)}\phi^{-1}$, which is related to the pressure, $p^{(0)}$, and the adhesivity, via the reaction equation, (11.159). The permeability and the adhesivity are related to the conductance of pores in the network, $G_{ij}^{\boldsymbol{r}(0)}$, via (11.137) and (11.87), respectively, and thus the macroscale particle concentration depends upon the dynamic structure of the microscale. The analogy is thus with the one-dimensional advection–reaction equation, (11.92), and the interpretation is similar. However, we must now discretise macroscale space in D dimensions to find macroscale variables, and solve D linear cell problems, (11.123), to determine microscale variables. This, of course, is more computationally expensive than discretising in one dimension and solving one linear problem, to solve in the one-dimensional formulation.

11.4.4 Conservation of pores

Lastly, we homogenise the equation for the conservation of pores, (11.15),

$$\frac{\partial G_{ij}^{\boldsymbol{r}}}{\partial T} = -\alpha\beta C_{ij}^{\boldsymbol{r}} (G_{ij}^{\boldsymbol{r}})^{\frac{3}{2}} |P_i - P_j|. \tag{11.161}$$

Carrying out Steps 1–3 of network homogenisation on (11.161), we find that

$$\frac{\partial G_{ij}^{\boldsymbol{r}(0)}}{\partial T} = -\varepsilon \left\{ \alpha\beta c^{(0)} (G_{ij}^{\boldsymbol{r}(0)})^{\frac{3}{2}} \sum_{n=1}^{D} \left| \Delta_{ji}^{-r^n} \frac{\partial p^{(0)}}{\partial x^n} \right| \right\} + \mathcal{O}(\varepsilon^2). \tag{11.162}$$

A leading-order balance in (11.162) implies that

$$\frac{\partial G_{ij}^{\boldsymbol{r}(0)}}{\partial T} = 0. \tag{11.163}$$

We have found that the conductances of pores do not change over this timescale, T_{c} (see (11.12)), which is unsurprising, since we showed (see (11.145)) that deposition does not occur this quickly. Scaling onto the timescale over which particle deposition does occur, T_{n} (see (11.81)), and recalling that $t = \varepsilon T$, we find that

$$\frac{\partial G_{ij}^{\boldsymbol{r}(0)}}{\partial t} = -\alpha\beta c^{(0)} (G_{ij}^{\boldsymbol{r}(0)})^{\frac{3}{2}} \sum_{n=1}^{D} \left| \Delta_{ji}^{-r^n} \frac{\partial p^{(0)}}{\partial x^n} \right| + \mathcal{O}(\varepsilon). \tag{11.164}$$

Balancing terms at leading order, we find that

$$\frac{\partial \boldsymbol{G}^{(0)}}{\partial t} = -\alpha\beta \boldsymbol{R}^{(0)} \left| \frac{\partial p^{(0)}}{\partial x} \right| c^{(0)}. \tag{11.165}$$

The analogy here is with (11.97). This time, however, $\boldsymbol{G}^{(0)}$ and $\boldsymbol{R}^{(0)}$ are 4-tensors of shape (N, N, K, D) (recalling from Section 11.1 that $K \times D$ dictates the size of the set $\boldsymbol{\mathcal{R}}$), with elements

$$G_{ij}^{\boldsymbol{r}(0)} = G_{ij}^{\boldsymbol{r}(0)}, \quad R_{ij}^{\boldsymbol{r}(0)} = (G_{ij}^{\boldsymbol{r}(0)})^{\frac{3}{2}} \sum_{n=1}^{D} |\Delta_{ji}^{-r^n}|. \tag{11.166}$$

As in (11.97), (11.165) implies that the evolution of the conductances of pores within the cell depend on the microscale structure, via the elements of $\boldsymbol{R}^{(0)}$, and on the evolution of the macroscale concentration and pressure gradient, $c^{(0)}$ and $\partial p^{(0)}/\partial x$, respectively.

11.4.5 Summary

In summary, we homogenise the microscale model, (11.13)–(11.22) in D dimensions, and find the corresponding multiscale model. In particular, this time, homogenising the microscale equations for the conservation of fluid, particles, and pores, (11.13)–(11.15), we find, dropping leading-order notation, that their macroscale equivalents are

$$\boldsymbol{\nabla} \cdot \boldsymbol{u} = 0, \tag{11.167}$$

$$\frac{\partial c}{\partial t} + \boldsymbol{\nabla} \cdot \frac{\boldsymbol{u}}{\phi} c = -\frac{\psi}{\phi} c, \tag{11.168}$$

$$\frac{\partial G_{ij}^{\boldsymbol{r}}}{\partial t} = -\alpha\beta c (G_{ij}^{\boldsymbol{r}})^{\frac{3}{2}} \sum_{n=1}^{D} |\Delta_{ji}^{-r^n}| \left| \frac{\partial p}{\partial x^n} \right|, \tag{11.169}$$

respectively, where $\phi = N / \prod_{m=1}^{D} l^m$ is the constant junction porosity, which represents the proportion of void space in the filter that is attributed to junctions. Homogenising the microscale flux, (11.16), we find that the Darcy velocity vector, $\boldsymbol{u}$, is related to the permeability matrix, $\boldsymbol{k}$, and the pressure, p, by the Darcy equation, and that the reactivity, ψ, is related to the adhesivity vector, $\boldsymbol{j}$, and the pressure by the reactivity equation, which are respectively given by

$$\boldsymbol{u} = -\boldsymbol{k} \boldsymbol{\nabla} p, \quad \psi = -\boldsymbol{j} \cdot \boldsymbol{\nabla} p. \tag{11.170a,b}$$

The permeability and adhesivity, $\boldsymbol{k}$ and $\boldsymbol{j}$, which are the parameters of this system, are related to the pore conductances, $G_{ij}^{\boldsymbol{r}}$, by the equations

$$k^{mn} = \frac{l^m}{2\prod_{a=1}^{D} l^a} \sum_{i=1}^{N} \sum_{j=1}^{N} \sum_{\boldsymbol{r}\in\boldsymbol{\mathcal{R}}} r^m G_{ij}^{\boldsymbol{r}} \Delta_{ji}^{-r^n}, \tag{11.171}$$

$$j^m = -\frac{1}{\prod_{n=1}^{D} l^n} \sum_{i=1}^{N} \sum_{j=1}^{N} \sum_{\boldsymbol{r}\in\boldsymbol{\mathcal{R}}} \alpha G_{ij}^{\boldsymbol{r}} \Delta_{ji}^{-r^m} H_{ji}^{-\boldsymbol{r}}. \tag{11.172}$$

Here, the pore pressure drop is defined by

$$\Delta_{ij}^{r^m} = W_i^m - (W_j^m + r^m l^m), \tag{11.173}$$

where the cell solution, W_i^m, is the component of the effective junction position in the x^m direction, which dictates the contribution of the component of the pressure drop in pore $ij\boldsymbol{r}$ in direction x^m to the solution evolution on the macroscale, via the permeability and adhesivity, (11.171) and (11.172). The cell solution is given by solving the linear cell problem,

$$\sum_{j=1}^{N} \sum_{\boldsymbol{r}\in\boldsymbol{\mathcal{R}}} \left(G_{ij}^{\boldsymbol{r}} - \delta_{ij} \sum_{k=1}^{N} G_{ik}^{\boldsymbol{r}} \right) W_j^m = \sum_{j=1}^{N} \sum_{\boldsymbol{r}\in\boldsymbol{\mathcal{R}}} G_{ij}^{\boldsymbol{r}} r^m l^m, \tag{11.174}$$

where we have chosen all components of the position of junction i to be $X_i^m = 0$ for simplicity, since this does not affect the solution.

Homogenising the microscale boundary conditions, (11.17) and (11.18), we find that we are given the pressure at the inlet and outlet,

$$p(0,t) = 1, \quad p(l^1,t) = 0, \tag{11.175a,b}$$

and the concentration at the inlet,

$$c(0,t) = 1, \tag{11.176}$$

for $t \geq 0$. Homogenising the microscale initial conditions, (11.19) and (11.20), we find that there are no particles in the filter initially,

$$c(\boldsymbol{x},0) = 0, \tag{11.177}$$

and that the initial pore conductances are drawn from a known distribution, so that

$$G_{ij}^{\boldsymbol{r}}(\boldsymbol{x},0) = G_{ij}^{\boldsymbol{r}0}(\boldsymbol{x}) \tag{11.178}$$

for $i,j \in \{1,\ldots,N,\text{in},\text{out}\}$. Note that the initial conductances, $G_{ij}^{\boldsymbol{r}0}(\boldsymbol{x})$, now vary with the spatial vector, $\boldsymbol{x}$, so that initial macroscale porosity gradients in any direction are permitted. We seek solutions of this multiscale model in the next chapter.

Chapter 12

Solutions of the multiscale model

In this chapter, we solve the dimensionless multiscale model, (11.167)–(11.178). In Section 12.1, we begin by describing our solution methodology. We reduce the problem to a simple and yet physically relevant case, and describe the resulting numerical system to be solved, highlighting various ways in which its computational cost can be decreased. In Section 12.2, we then solve the system on periodic networks. Firstly, we use the initial conductance distribution (7.47a), in which the network conductances are non-random, which describes the physical scenario of mono-dispersed pore radii and thus conductances. We find that solutions of the multiscale model can be made arbitrarily close to solutions of the microscale model by increasing the number of repeated cells in the periodic network. Secondly, we use (7.47b) for the initial conductance distribution. In this case, the conductances of pores are random, which describes poly-dispersed pore sizes. We find that any single simulation of the multiscale model does not match that of the microscale model in general (although their averages do agree), due to the randomness of the network. This motivates us, in Section 12.3, to discuss the distributions of the solutions that arise from repeated Monte Carlo simulations of the multiscale problem, to account for the randomness of the initial conditions. We focus on calculation of the parameters of the system, the permeability and adhesivity, since these dictate the dependence of the effective solution on the microscale. We explain why our system could also be used to approximate the solution of dynamical systems defined on non-periodic networks.

12.1 Solution methodology

We begin by reducing the multiscale system to a simpler case that we will use to demonstrate the solution method. We discuss a numerical scheme, and show that significant reduction in the computational complexity of this is possible if microscale dependent parameters are 'pre-calculated' outside the time-dependent scheme.

12.1.1 Model reduction

To demonstrate the solution of the multiscale model, (11.167)–(11.178), we simplify by considering the case where the permeability and adhesivity, $\boldsymbol{k}$ and $\boldsymbol{j}$, do not vary in the directions that are transverse to the pressure gradient and therefore the flow, x^2 and x^3, so that

$$\frac{\partial \boldsymbol{k}}{\partial x^2} = \frac{\partial \boldsymbol{k}}{\partial x^3} = \boldsymbol{0}, \quad \frac{\partial \boldsymbol{j}}{\partial x^2} = \frac{\partial \boldsymbol{j}}{\partial x^3} = \boldsymbol{0}. \tag{12.1}$$

Furthermore, we assume periodicity of all the dependent variables, $\boldsymbol{c}$, $G^{\boldsymbol{r}}_{ij}$, $\boldsymbol{u}$, p, ψ, $\boldsymbol{k}$, $\boldsymbol{j}$, $\boldsymbol{W}$, across the transverse boundaries, $x^2 = 0$, $x^2 = l^2$ and $x^3 = 0$, $x^3 = l^3$. We then seek spatially univariate solutions that are independent of the transverse directions, so that

$$\frac{\partial c}{\partial x^2} = \frac{\partial c}{\partial x^3} = 0, \quad \frac{\partial G^{\boldsymbol{r}}_{ij}}{\partial x^2} = \frac{\partial G^{\boldsymbol{r}}_{ij}}{\partial x^3} = 0, \quad \frac{\partial \boldsymbol{u}}{\partial x^2} = \frac{\partial \boldsymbol{u}}{\partial x^3} = \boldsymbol{0}, \quad \frac{\partial p}{\partial x^2} = \frac{\partial p}{\partial x^3} = 0. \tag{12.2}$$

Under these assumptions, we omit the third dimension, x^3, since we expect the dependence of the solution on the two transverse directions to be identical.

Combining the fluid conservation equation, (11.167), with the particle conservation equation, (11.168), which is the advection–reaction equation that governs the evolution of the particle concentration, c, we find that

$$\frac{\partial c}{\partial t} + \frac{u^1}{\phi}\frac{\partial c}{\partial x^1} = -\frac{\psi}{\phi}c. \tag{12.3}$$

The pore conservation equation, (11.169), which governs the evolution of the conductances of pores, becomes

$$\frac{\partial G^{\boldsymbol{r}}_{ij}}{\partial t} = -\alpha\beta c (G^{\boldsymbol{r}}_{ij})^{\frac{3}{2}} |\Delta_{ji}^{-r^1}| \Big| \frac{\partial p}{\partial x^1} \Big|. \tag{12.4}$$

The Darcy equation, (11.170a), which relates the pressure, p, to the Darcy velocity vector, $\boldsymbol{u}$, via the permeability matrix, $\boldsymbol{k}$, becomes

$$u^1 = -k^{11}\frac{\partial p}{\partial x^1}, \quad u^2 = -k^{21}\frac{\partial p}{\partial x^1}. \tag{12.5a,b}$$

The reactivity equation, (11.170b), which relates the pressure to the reactivity, ψ, via the adhesivity, $\boldsymbol{j}$, becomes

$$\psi = -j^1\frac{\partial p}{\partial x^1}. \tag{12.6}$$

Using the definitions of the permeability and adhesivity, (11.171) and (11.172) (recalling that the permeability and adhesivity are independent of junction positions, from Appendix A.2.4), we find that the elements that remain in the system are given

by

$$k^{11} = \frac{l^1}{2\prod_{m=1}^{D} l^m} \sum_{i=1}^{N} \sum_{j=1}^{N} \sum_{\boldsymbol{r}\in\boldsymbol{\mathcal{R}}} r^1 G_{ij}^{\boldsymbol{r}} (W_j^1 + r^1 l^1 - W_i^1), \tag{12.7}$$

$$k^{21} = \frac{l^2}{2\prod_{m=1}^{D} l^m} \sum_{i=1}^{N} \sum_{j=1}^{N} \sum_{\boldsymbol{r}\in\boldsymbol{\mathcal{R}}} r^2 G_{ij}^{\boldsymbol{r}} (W_j^1 + r^1 l^1 - W_i^1), \tag{12.8}$$

$$j^1 = -\frac{1}{\prod_{m=1}^{D} l^m} \sum_{i=1}^{N} \sum_{j=1}^{N} \sum_{\boldsymbol{r}\in\boldsymbol{\mathcal{R}}} \alpha G_{ij}^{\boldsymbol{r}} (W_j^1 + r^1 l^1 - W_i^1) H_{ji}^{-\boldsymbol{r}}, \tag{12.9}$$

where we have used the relevant elements of the pore pressure drop from (11.173),

$$\Delta_{ij}^{r^1} = W_i^1 - (W_j^1 + r^1 l^1). \tag{12.10}$$

The cell problem, (11.174), simplifies to

$$\sum_{j=1}^{N} \sum_{\boldsymbol{r}\in\boldsymbol{\mathcal{R}}} \Big(G_{ij}^{\boldsymbol{r}} - \delta_{ij} \sum_{k=1}^{N} G_{ik}^{\boldsymbol{r}} \Big) W_j^1 = -\sum_{j=1}^{N} \sum_{\boldsymbol{r}\in\boldsymbol{\mathcal{R}}} G_{ij}^{\boldsymbol{r}} r^1 l^1, \tag{12.11}$$

which is one linear problem of size N. Its solution defines the elements of the cell solution matrix, W_i^1. As in (11.175)–(11.178), we assume a constant pressure drop in the flow direction, x^1, and a constant concentration of particles at the inlet, so that

$$p(0,t) = 1, \quad p(l^1,t) = 0, \tag{12.12a,b}$$

and

$$c(0,t) = 1, \tag{12.13}$$

for $t \geq 0$. We assume that there are no particles in the filter initially,

$$c(x^1,0) = 0, \tag{12.14}$$

and that the initial pore conductances are drawn from a known distribution, $\mathcal{G}$, so that

$$G_{ij}^{\boldsymbol{r}}(x^1,0) = G_{ij}^{\boldsymbol{r}0}(x^1) \tag{12.15}$$

for $i,j \in \{1,\ldots,N,\text{in},\text{out}\}$. As in Part II (see (7.47)), we assume that $\mathcal{G}$ is either the Dirac-delta distribution, or the log-normal distribution, so that the probability density function, g, of $\mathcal{G}$ is either

$$g(G_{ij}^{\boldsymbol{r}0}) = \delta(G_{ij}^{\boldsymbol{r}0} - 1), \quad \text{or} \quad g(G_{ij}^{\boldsymbol{r}0}) = \frac{1}{\sqrt{2\pi}\sigma_G G_{ij}^{\boldsymbol{r}0}} \exp\left(-\frac{\Big(\log(G_{ij}^{\boldsymbol{r}0}) + \frac{\sigma_G^2}{2}\Big)^2}{2\sigma_G^2} \right), \tag{12.16a,b}$$

at any position x^1. Comparing the reduced system, (12.3)–(12.16), with the full system, (11.167)–(11.178), we note that the assumption of spatially univariate effective parameters and solutions affords a significant reduction in mathematical complexity. These assumptions are not especially physically restrictive, however: although we derived a model that is general enough to model scenarios that involve heterogeneity in the transverse directions, in filtration processes that are driven by unidirectional pressure drops we do not usually expect large transverse variation in filter properties such as permeability. In the remainder of this section, we outline the process of solution of the reduced system, (12.3)–(12.16).

12.1.2 Solution without parameter pre-calculation

To solve the reduced system, (12.3)–(12.16), we begin by noting that

$$u^1 = \frac{1}{\int_0^1 \frac{1}{k^{11}}\,\mathrm{d}x^1}, \quad u^2 = \frac{1}{\int_0^1 \frac{1}{k^{21}}\,\mathrm{d}x^1}, \tag{12.17a,b}$$

and that

$$\psi = \frac{1}{\int_0^1 \frac{1}{j^1}\,\mathrm{d}x^1}. \tag{12.18}$$

Here, we have eliminated the pressure gradient from the Darcy equation, (12.5), and from the reactivity equation, (12.6), using the conditions on the pressure at the boundaries, (12.12).

We proceed by using a first-order upwind scheme in space and a first-order scheme in time to discretise the reduced system, using the discrete indices $\xi \in \{1, \ldots, X\}$ and $\tau \in \{1, \ldots, T\}$ to denote discrete space and time. At each spatial point, ξ, and at each temporal point, τ, we assume that there is a cell containing N junctions (see Figure). At $t = 0$, which corresponds to $\tau = 1$, we are given the concentration and conductances for all space points, $c[\xi, 1] = 0$ and $G^{\boldsymbol{r}}_{ij}[\xi, 1] = G^{\boldsymbol{r}0}_{ij}$, from (12.14) and (12.15). At $x = 0$, which corresponds to $\xi = 1$, we are given the concentration for all time points, $c[1, \tau] = 1$, from (12.13).

To solve numerically at the time point τ, we substitute the known conductance on each pore in the cell, $G^{\boldsymbol{r}}_{ij}[\xi, \tau]$, into the cell problem, (12.11), and solve the resulting linear problem to determine the N cell solution elements, $W_i[\xi, \tau]$. Next, we substitute these cell solution elements into the permeability and adhesivity definitions, (12.7) and (12.9), to find the current permeability and adhesivity elements, $k^{11}[\xi, \tau]$, $k^{21}[\xi, \tau]$, and $j^1[\xi, \tau]$. Next, we substitute these into the modified Darcy equations, (12.17), and the reactivity equation, (12.18). We use the trapezium rule to discretise the integrals in these equations, and solve these to find the velocity and reactivity, $u^1[\tau]$, $u^2[\tau]$, and $\psi[\tau]$. We then find the pressure gradient, $(\partial p/\partial x^1)[\xi, \tau]$ by substituting the known reactivity, $\psi[\xi, \tau]$, and adhesivity, $j^1[\xi, \tau]$, into the reactivity equation, (12.6).

Next, we use the particle and pore conservation equations, (12.3) and (12.4), to calculate the particle concentration and pore conductances at the current spatial point, ξ, at the next time point, $\tau + 1$. Substituting the current concentration at

the previous spatial point, $c[\xi-1,\tau]$, the current concentration at the current spatial point, $c[\xi,\tau]$, the flow rate and reactivity at the current time point, $u^1[\tau]$ and $\psi[\tau]$, and the porosity, $\phi = N/\prod_m^D l^m$ into the discretised version of (12.3), we obtain the new concentration, $c[\xi,\tau+1]$. Lastly, we substitute $c[\xi,\tau+1]$, $G^{\boldsymbol{r}}_{ij}[\xi,\tau]$, $W_i[\xi,\tau]$, and $(\partial p/\partial x^1)[\xi,\tau]$ into the discretised version of (12.4) to calculate the new conductances, $G^{\boldsymbol{r}}_{ij}[\xi,\tau+1]$. Since the initial concentration and conductances, $c[\xi,1]$ and $G^{\boldsymbol{r}}_{ij}[\xi,1]$, are given, this method determines the discrete solution variables for all $\xi \in \{1,\dots,X\}$ and $\tau \in \{1,\dots,T\}$.

At each spatial point, ξ, and time point, τ, we solve a linear problem to obtain $(N)^2 \times (2K+1)^D + N + 8$ values, so that the overall cost (since $K = \mathcal{O}(1)$ and $D = \mathcal{O}(1)$) of solution with no pre-calculation is $C_{\mathrm{NPC}} = \mathcal{O}(T(XN^2)^L)$, where $\mathcal{O}(S^L)$ for $2 < L < 3$ is the number of operations involved in the solution of a linear system for S variables. In Section 8.1, we showed that the cost of solving the network model is $C_{\mathrm{NM}} = \mathcal{O}((N^1N^2(N)^2)^L)$, where we recall that N^1 and N^2 are the numbers of cells in the network in the x^1 and x^2 directions. In many physical membranes, we might expect to see as many as 10^6 junctions in the flow direction, so that $N^1 = \mathcal{O}(10^5)$ for $N = \mathcal{O}(10)$, for example. This means that the solution of the network model that describes the entire membrane is computationally infeasible. Crucially, the cost of solution of the multiscale model only depends on the size of one cell within the network. This is useful, since later in this chapter, we will show that $N = \mathcal{O}(10)$ in the multiscale model is sufficient for representation of the network as a whole. Next, we will show that much of the computational cost of solution is avoidable, by 'pre-calculating' $G^{\boldsymbol{r}}_{ij}$ and W^m_i, and thus the parameters of the macroscale model, $\boldsymbol{k}$ and $\boldsymbol{j}$, before the solution of the time-dependent linear problem that we outlined above.

12.1.3 Solution with parameter pre-calculation

As we discussed, the main source of computational cost in the solution of the multiscale model emerges from the need to find the conductances of the $\mathcal{O}(N^2)$ pores in the cell at each time and space step, and the desire is to derive a numerical scheme for which this is unnecessary. To this end, we begin by defining

$$f(x^1,t) = \int_0^t c(x^1,s)\left|\frac{\partial p}{\partial x^1}(x^1,s)\right| \mathrm{d}s. \tag{12.19}$$

We interpret this as the mass concentration flux of particles, since in dimensional terms we find that $[f] = \mathrm{kgm^{-3}s^{-1}}$.

Crucially, we note that the mass flux, f, satisfies the relation

$$\frac{\partial f}{\partial t} = c(x^1,t)\left|\frac{\partial p}{\partial x^1}(x^1,t)\right|. \tag{12.20}$$

Using (12.20), it follows that the pore conductances satisfy

$$\frac{\partial G^{\boldsymbol{r}}_{ij}}{\partial t} = \frac{\partial G^{\boldsymbol{r}}_{ij}}{\partial f}\frac{\partial f}{\partial t} = \frac{\partial G^{\boldsymbol{r}}_{ij}}{\partial f}c(x^1,t)\left|\frac{\partial p}{\partial x^1}(x^1,t)\right|. \tag{12.21}$$

Substituting the right hand side of (12.21) into the pore conservation equation, (12.4), we find that

$$\frac{\partial G_{ij}^{\boldsymbol{r}}}{\partial f} = -\alpha\beta(G_{ij}^{\boldsymbol{r}})^{\frac{3}{2}}|W_j^1 + r^1 l^1 - W_i^1|. \tag{12.22}$$

We have removed the explicit time dependence from the pore conservation equation, and we now view the pore conductances and the cell solutions as explicit functions of the mass flux, f, $G_{ij}^{\boldsymbol{r}}(f)$ and $W_i^1(f)$.

To see why this is useful, we note that the modified pore conservation equation, (12.22), with the initial conductance condition, (12.15), together with the cell problem, (12.11), now defines an ordinary algebraic–differential initial value problem for the pore conductances and the cell solutions that can be solved independently of the rest of the explicitly time-dependent macroscale problem. We begin by defining points at which the mass flux is discretised, $\varphi \in \{1, \ldots, F\}$, say, and note that, at $\varphi = 1$, the conductances $G_{ij}^{\boldsymbol{r}}[1] = G_{ij}^{\boldsymbol{r}0}$ are given, so that the cell solutions, $W_i^1[1]$, are given by solution of the cell problem, (12.11). We then use a first-order scheme for explicit discretisation of the modified pore conservation equation (12.22), with $G_{ij}^{\boldsymbol{r}}[1]$ and $W_i^1[1]$, to compute the pore conductances at the next mass flux value, $G_{ij}^{\boldsymbol{r}}[2]$. In general, for $\varphi > 1$, we use the current pore conductances, $G_{ij}^{\boldsymbol{r}}[\varphi]$, in the cell problem, (12.11), to obtain the current cell solutions, $W_i^1[\varphi]$. We use the current conductances and cell solutions in (12.7) and (12.9) to calculate the current permeability and adhesivity, $k^{11}[\xi, \tau]$ and $j^1[\xi, \tau]$. We then use these current conductances and cell solutions to calculate the next pore conductances, $G_{ij}^{\boldsymbol{r}}[\varphi + 1]$. In this way, we pre-calculate a discretisation of the functions $G_{ij}^{\boldsymbol{r}}(f)$ and $W_i^1(f)$ and therefore $k^{11}(f)$ and $j^1(f)$ using $C_{\mathrm{PC}} = \mathcal{O}(F(N^2)^L)$ computations.

To solve the multiscale model, we then solve a smaller linear system and interpolate this function. In particular, similarly to before, at each space point, ξ, and at each time point, τ, we are given the current concentration, $c[\xi, \tau]$ (due to solution of a forward system at the previous time step), and the previous pressure gradient, $(\partial p/\partial x^1)[\xi, \tau - 1]$. We begin by discretising the definition of f, (12.20), and using $c[\xi, \tau]$ and $(\partial p/\partial x^1)[\xi, \tau - 1]$ to obtain $f[\xi, \tau]$. We then interpolate the functions $k^{11}[\varphi]$ and $j^1[\varphi]$, using that $\varphi \approx f$ for suitably large F ($\mathcal{O}(10^2)$, say), which gives $k^{11}[\xi, \tau]$, $k^{21}[\xi, \tau]$, and $j^1[\xi, \tau]$. The scheme now proceeds as before. That is, we use (12.17) and (12.18) to obtain $u^1[\tau]$, $u^2[\tau]$, and $\psi[\tau]$, and then find $(\partial p/\partial x^1)[\xi, \tau]$ by substituting $\psi[\xi, \tau]$ and $j^1[\xi, \tau]$ into (12.6). The next concentration value, $c[\xi, \tau + 1]$, is then found by substituting these values into a first-order discretisation of the particle conservation equation, (12.3), without needing to solve the pore conservation equation, (12.4).

The cost of solution of the multiscale system with pre-calculation, C_{WPC}, is the cost of the pre-calculation plus the cost of solution of the time-dependent problem, so that $C_{\mathrm{WPC}} = \mathcal{O}(F(N^2)^L) + \mathcal{O}(T(X)^L) < \mathcal{O}(T(XN^2)^L) < \mathcal{O}((N^1N^2(N)^2)^L)$. That is, the cost of solution of the multiscale problem with pre-calculation is cheaper than that with no pre-calculation, which is cheaper than the infeasible network problem: $C_{\mathrm{WPC}} < C_{\mathrm{NPC}} < C_{\mathrm{NM}}$. The main cost of the solution has shifted to the pre-calculation step, $C_{\mathrm{PC}} = \mathcal{O}(F(N^2)^L)$, and we will show that this need not be large, since $N =$

$\mathcal{O}(10)$ is sufficient for most applications. Since the N^2 term associated with parameter calculation has been removed from the time-dependent scheme, the number of spatial and temporal points, X and T, can be chosen, as usual, to be suitably large as to accurately numerically discretise the continuous macroscale system, to satisfy the Courant–Friedrichs–Lewy (CFL) condition [122] for advective systems, for example. In the next section, we will use the numerical scheme with parameter pre-calculation (WPC) to demonstrate the solution of the macroscale model.

12.2 Periodic networks

In this section, to demonstrate the solution of the reduced multiscale model, (12.3)–(12.16), we consider a microscale given by a four-regular network. To simplify our analysis, we will consider the case where each cell is composed of four nodes. A diagram of the repeating cell is shown in Figure 12.1. We will first assume that the initial conductances of the pores in this cell are given by (12.16a). This case models the scenario where the pore-size distribution is mono-dispersed initially, which corresponds to a non-random network structure that need not be sampled. We will then assume that the initial conductances are given by (12.16b), which models log-normally poly-dispersed initial pore sizes. In this case, the network structure is random, and each initialisation of the problem gives rise to a cell with a different set of conductances. Throughout, we will consider the case where $\alpha = 1$ and $\beta = 1$. In Part II, we showed that this corresponds to $\mathcal{O}(1)$ particle removal and $\mathcal{O}(1)$ reduction by the time that fluid has traversed the filter once. We use the numerical solution scheme discussed in Section 12.1. That is, we pre-calculate the permeability and adhesivity parameters of (12.3)–(12.16), k^{11} and j^1, as functions of the mass concentration flux, f, which acts as a time-like variable. We then interpolate these functions to find the parameters at each position and time.

12.2.1 Non-random networks: Mono-dispersed pores

We begin by considering the case where the initial pore conductances are given by (12.16a), so that all pores have unit conductance initially.

12.2.1.1 Conductance and pressure drop

In Figure 12.2, we show the pore conductances, $G_{ij}^{\boldsymbol{r}}$, and the pore pressure drops in the direction of the flow, $\Delta_{ij}^{r^1}$, as functions of the mass concentration flux, f. In Figure 12.2(a), we see (dotted black line) that the conductance of pores that are perpendicular to the flow (see the orange and red edges in Figure 12.1) does not change with f. Observing Figure 12.2(b), we see that this is because the pressure drop on these pores (orange line) is zero. There is no pressure difference across these pores, so that they do not contribute to the macroscale pressure gradient that drives the flow. On the other hand, returning to Figure 12.2(a), we see (solid coloured lines) that the conductance of the pores that are parallel to the flow (see the green and blue

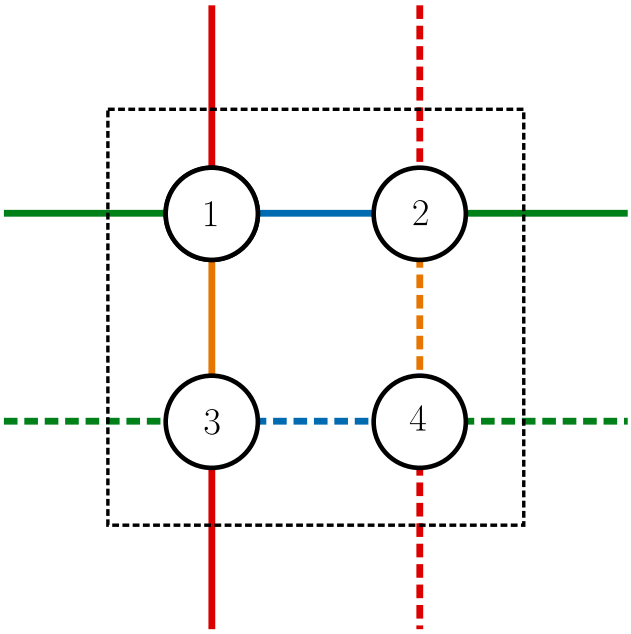

Figure 12.1: A Diagram showing one cell of a four-regular network. Each node is labelled with an index. Intra-cell edges that are parallel to the flow direction are coloured blue. Intra-cell edges that are perpendicular to the flow direction are coloured orange. Inter-cell edges that are parallel to the flow direction are coloured green. Inter-cell edges that are perpendicular to the flow direction are coloured red.

edges in Figure 12.1) decreases as f increases. To explain this, we begin by noting, from Figure 12.2(b), that these pores have unit pressure drop, so that they contribute equally to the macroscale pressure gradient for any f value. Since the pore deltas are constant, we find that the pore conservation equation, (12.22), has an explicit solution, which is given by

$$G_{ij}^{\boldsymbol{r}}(f) = \frac{4}{(\alpha\beta f + 2)^2}, \tag{12.23}$$

which we plot in Figure 12.2(a) (dashed black line). We observe that, as F increases, so that discretisation of f in our numerical scheme, φ, becomes finer, the numerical solution (coloured lines) approaches this explicit solution, and that F need not be too large ($F = \mathcal{O}(10^2)$) before we find good agreement.

12.2.1.2 Permeability and adhesivity

In Figure 12.3, we demonstrate the variation of the permeability and adhesivity, k^{11} and j^1, with the mass concentration flux, f, and position, x^1. In Figure 12.3(a), we see the permeability and adhesivity curves that result from our calculation of the pore conductances (above). We see that these are identical. Checking the definitions of these parameters, (12.7) and (12.9), we see that this is because $\alpha = 1$, and because pore conductances are all the same initially and decrease at the same rate,

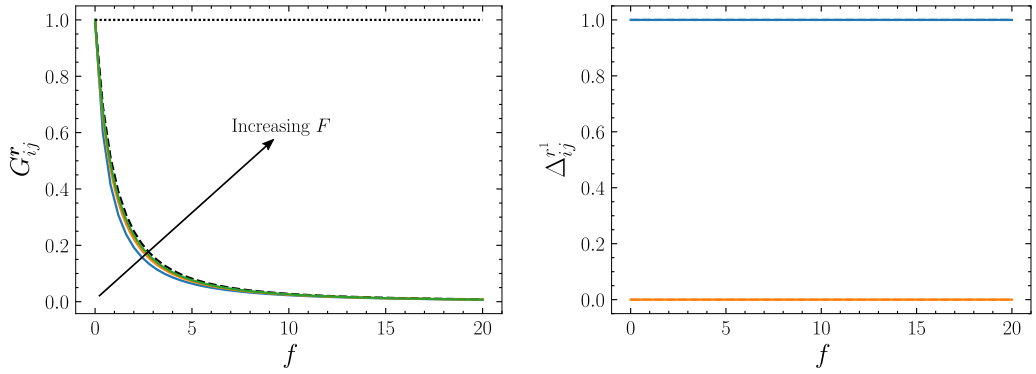

(a) (b)

Figure 12.2: Graphs showing how the pore conductance, $G_{ij}^{\boldsymbol{r}}$, and the pore pressure drop in the x^1 direction, $\Delta_{ij}^{r^1}$, vary with the mass concentration flux, f. The parameters are $N = 4$, $\alpha = 1$, $\beta = 1$. (a) The pore conductance, $G_{ij}^{\boldsymbol{r}}$, as a function of the mass concentration flux, f. The dotted black line shows the explicit solution on pores that are perpendicular to the x^1 direction (see the orange and red pores in Figure 12.1) The dashed black line shows the explicit solution on pores that are parallel to the x^1 direction (see the blue and green pores in Figure 12.1). The solid coloured lines show numerical solutions for various values of F. The values of F are 50 (blue), 100 (orange), 200 (green), and the arrow shows the direction of increasing F. (b) The x^1 component of the pore pressure drop, $\Delta_{ij}^{r^1}$, as a function of the mass concentration flux, f. The blue line shows the solution for pores that are parallel to the x^1 direction (see the blue and green pores in Figure 12.1). For example, the pore $i = 1, j = 2, \boldsymbol{r} = (0, 0)^\top$ (solid blue), for which $\Delta_{12}^{r^1=0} = 1$, or the pore $i = 2, j = 1, \boldsymbol{r} = (1, 0)^\top$ (solid green), for which $\Delta_{21}^{r^1=1} = 1$. The orange line shows the solution for pores that are perpendicular to the x^1 direction (see the orange and red pores in Figure 12.1). For example, the pore $i = 1, j = 3, \boldsymbol{r} = (0, 0)^\top$ (solid orange), for which $\Delta_{13}^{r^1=0} = 0$, or the pore $i = 3, j = 1, \boldsymbol{r} = (0, -1)^\top$ (solid red), for which $\Delta_{21}^{r^1=0} = 0$.

from (12.23). We demonstrate (dashed black line) how we read off values for the permeability and adhesivity given a discrete approximation of these parameters as functions of f by using an interpolation, which is the strategy that we use in our numerical scheme. Figure 12.3(b), we illustrate (dashed black line) how, given a mass concentration flux, our numerical scheme obtains a value for the position at a given time. Then, in Figures 12.3(c) and 12.3(d), we demonstrate how the permeability and adhesivity are constructed as functions of position and time. We see that these decrease as time increases, as we expect (see Part II). This decrease is faster at positions closer to the inlet, since pores here conduct more particles per unit time, and thus experience more deposition per unit time.

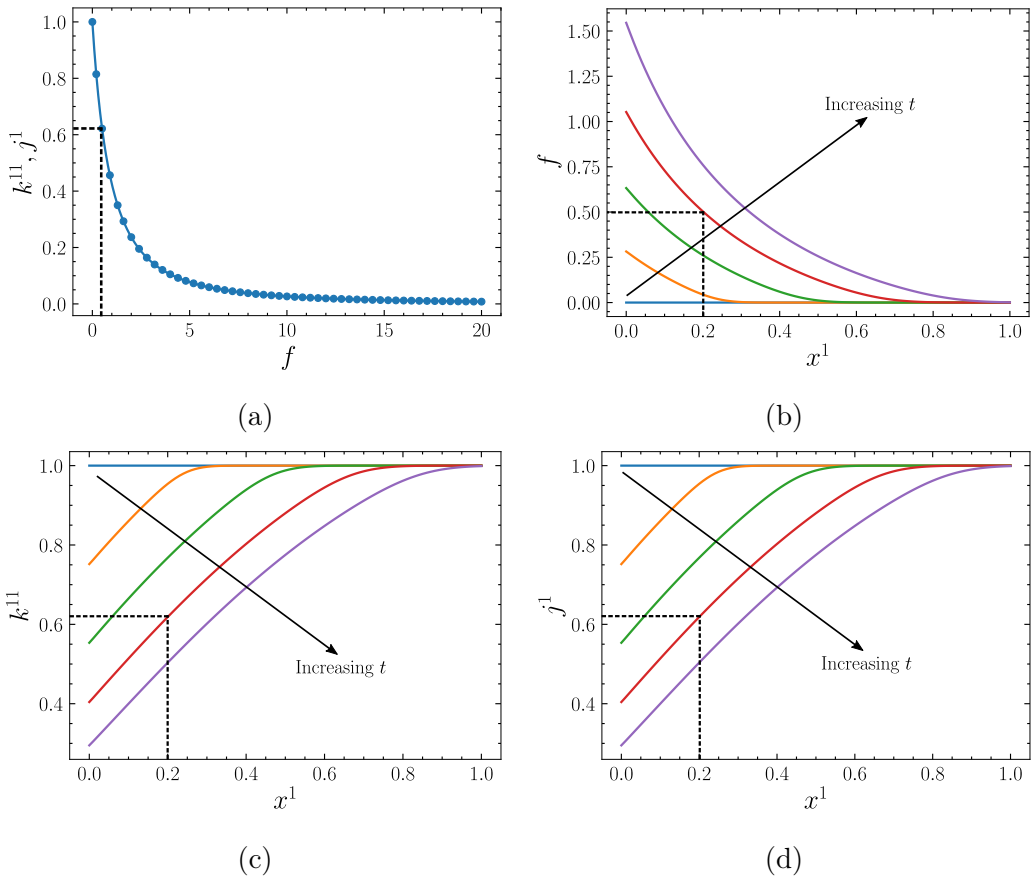

Figure 12.3: Graphs showing how the permeability, k^{11}, and adhesivity, j^1, vary with the mass concentration flux, f, and position, x^1, at various times, t. The parameters are $N = 4$, $\alpha = 1$, $\beta = 1$. The values of t are 0 (blue), 0.25 (orange), 0.5 (green), 0.75 (red), 1 (purple). The arrows show the direction of increasing time. (a) The permeability, k^{11}, and adhesivity, j^1, as functions of f. These are the same for a mono-dispersed network. The blue dots show the numerical solution at discrete values of f, φ. The blue line shows an interpolation of this numerical solution. The dashed black line shows an extrapolation at $f = 0.5$ (which corresponds to position $x^1 \approx 0.2$ at time $t = 0.75$) to determine the permeability and adhesivity, $k^{11}(f \approx 0.5) \approx 0.625$, $j^1(f \approx 0.5) \approx 0.625$. (b) The mass concentration flux, f, as a function of position, x^1, at various times, t. The dashed black line shows an extrapolation at position $x^1 = 0.2$ and time $t = 0.75$ to determine the mass concentration flux here, $f(x^1 = 0.2, t = 0.75) \approx 0.5$. (c) The permeability, k^{11}, as a function of position, x^1, at various times, t. The dashed black line shows an extrapolation at $x^1 = 0.2$ and $t = 0.75$ to confirm that $k^{11}(x^1 = 0.2, t = 0.75) \approx 0.625$. (d) The adhesivity, j^1, as a function of position, x^1, at various times, t. The dashed black line shows an extrapolation at $x^1 = 0.2$ and $t = 0.75$ to confirm that $j^1(x^1 = 0.2, t = 0.75) \approx 0.625$.

12.2.1.3 Concentration and conductance

Using Figure 12.4, we compare the concentration and permeability (effective conductance) from the multiscale solution (left plots in the figure) with the effective

concentration and conductance from the microscale solution (see (8.2) and (8.4) from Part II) (right plots in the figure). We plot the network solution for decreasing values (reading down the figure) of ε, so that we increase the number of cells in the network. We see that, when $\varepsilon = \mathcal{O}(10^{-1})$, the fit is modest. The network solution is dispersive because pores and junctions are further apart, and the multiscale solution does not capture this behaviour. As ε decreases, the microscale solution becomes less dispersive, since junctions and pores are packed more tightly. As a result, the accuracy of the fit of the multiscale solution to the microscale solution improves. This is impressive since, as discussed in Part II, concentration solutions of the network model are travelling waves that consist of step functions that vary rapidly in space.

12.2.1.4 Velocity and reactivity

We plot the velocity of the flow and reactivity of the filter in Figure 12.5. Comparing Figure 12.5(a) with Figure 12.5(b), the first thing we spot is that these are identical for a mono-dispersed filter (for $\alpha = 1$). This is because, as we have shown, the permeability and adhesivity are identical in this case. As time increases, these functions decrease monotonically. As filtration proceeds, the filter becomes less permeable because more particles have deposited in pores, which has decreased the conductance of each pore, which decreases the flow rate. As deposition occurs, pores become smaller, which means that pore walls have less surface area for particles to adhere to, which decreases the reactivity (i.e., the ability of the filter to capture particles). In Figure 12.5(a), we see that (when $\varepsilon = 0.025$) the agreement of the macroscale Darcy velocity with the average velocity in the network solution (see (8.5)) is good. Notice that when the filter is monodispersed, the reactivity is uniform across the filter, which is not the case in poly-dispersed filters. We will discuss such filters in the second part of this section.

12.2.2 Random networks: Poly-dispersed pores

We will now explore the case where the initial pore conductances are given by (12.16b), so that they are drawn randomly from a log-normal distribution. In this case, each initialisation of the underlying network gives rise to a different, independent and identically distributed set of pore conductances.

12.2.2.1 Conductance and pressure drop

We present the solutions for the pore conductances and pore pressure drops as functions of the mass concentration flux in Figure 12.6 (compare this with the solutions for a mono-dispersed filter in Figure 12.2). Observing Figure 12.6(a), we begin by noting that poly-dispersed solutions (coloured lines) are more complicated than monodispersed solutions (black lines). We see that the conductances of pores that are parallel (blue and green lines) and perpendicular (orange and red lines) to the direction of the macroscale pressure gradient behave differently from each other. The conductance of parallel pores decreases more rapidly than that of perpendicular pores. In

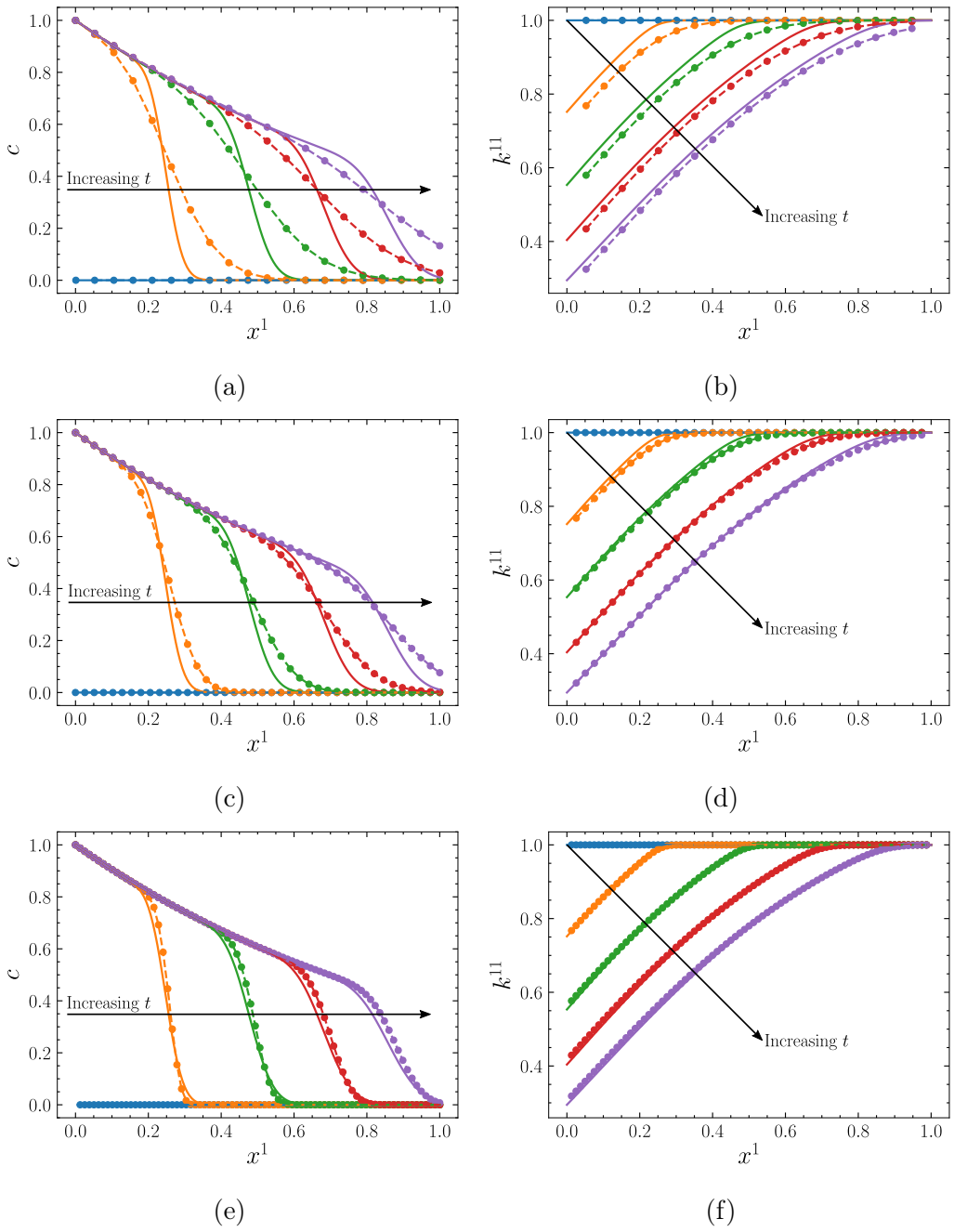

Figure 12.4: Graphs showing how the homogenised and average network (left) concentrations, c and $\bar{C}$, and (right) conductances, k^{11} and $\bar{G}$, vary with position, x^1, at various times, t. The parameters are $N = 4$, $\alpha = 1$, $\beta = 1$. The values of t are 0 (blue), 0.25 (blue), 0.5 (green), 0.75 (red), 1 (purple). Dots show the average network quantities, interpolated with correspondingly coloured dashed lines. Solid lines of the same colours show the effective quantities. (a) and (b) The case $N^1 = 10$, so that $\varepsilon = 0.1$ (see (7.32) in Part II). (c) and (d) $N^1 = 20$, $\varepsilon = 0.05$. (e) and (f) $N^1 = 40$, $\varepsilon = 0.025$.

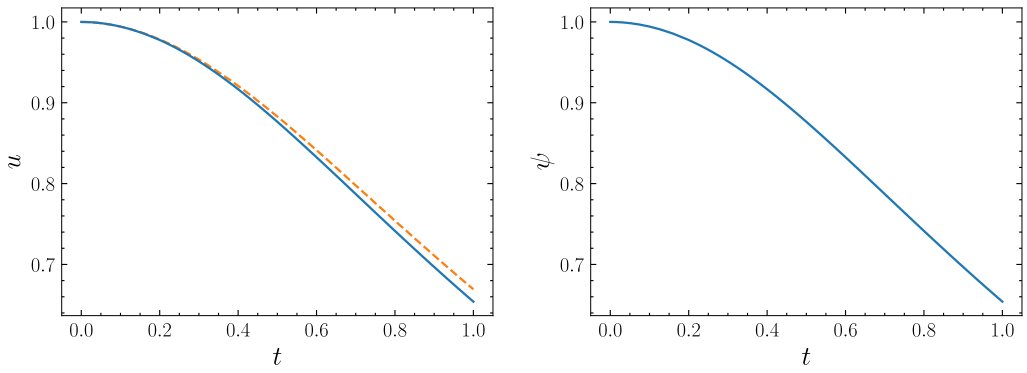

(a) (b)

Figure 12.5: Graphs showing how the velocity, u, and reactivity, ψ, vary with time t. The parameters are $N = 4$, $\alpha = 1$, $\beta = 1$, $\varepsilon = 0.025$. (b) The Darcy velocity, u, as a function of time, t. The solid blue line shows the macroscale solution. The dashed orange line shows the average of the microscale solution (see (8.5) in Part II). (b) The reactivity, ψ, as a function of time, t.

Figure 12.6(b), we see that this is because parallel pores have much larger pressure drops than perpendicular pores, which means that particles are driven through parallel pores more rapidly so that more particles deposit inside them per unit time. We see that the parallel and perpendicular pressure deltas are distributed about the corresponding pressure drop values in the mono-dispersed case. It follows that the expected pressure drops in pores that are parallel and perpendicular to the flow direction are $\mathbb{E}[\Delta_{ij}^{r^1}] = 1$ and $\mathbb{E}[\Delta_{ij}^{r^1}] = 0$, respectively. As filtration proceeds, deposition causes the pressure drops on flow-parallel pores (dashed and solid blue lines) to converge to one another. This causes the pressure drops in flow-perpendicular pores to approach zero. The result is that, regardless of the initial conductances, as time proceeds, the behaviour of the random network approaches that of the mono-dispersed network, in which there is no microscale flow in pores that are perpendicular to the macroscale pressure gradient.

12.2.2.2 Permeability and adhesivity

In Figure 12.7 we plot the permeability and adhesivity as functions of position and the mass concentration flux (compare with the mono-dispersed case in Figure 12.3). We illustrate (dashed black lines) how, using the numerical scheme discussed in Section 12.1, we are able to construct permeability and adhesivity functions that depend on position and time from discrete representations of these parameters as a function of the mass concentration flux. We see that when the filter is poly-dispersed, the permeability and adhesivity are no longer equal, as they were in the mono-dispersed case. For example, in Figure 12.7(a), the permeability drops below the mono-dispersed value and the adhesivity consistently lies above it. That is, particles are driven through the filter less rapidly (than in the mono-dispersed case), because the filter is

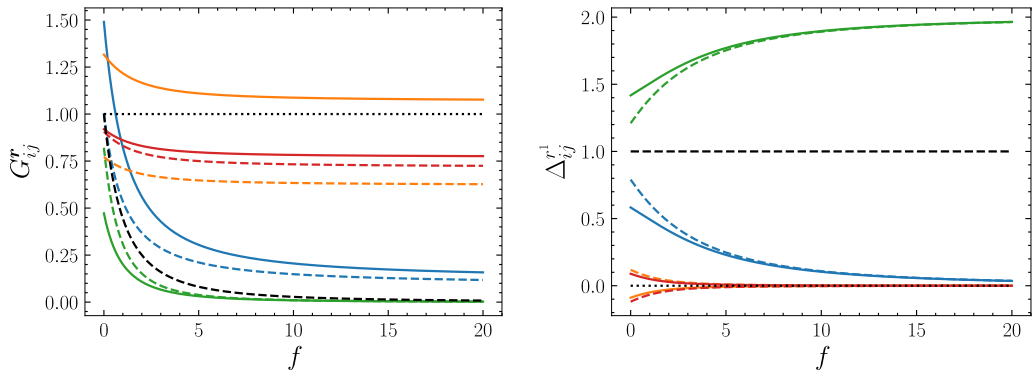

(a) (b)

Figure 12.6: Graphs showing how the pore conductance, $G^{\boldsymbol{r}}_{ij}$, and pore pressure drop in the x^1 direction, $\Delta^{r^1}_{ij}$, vary with the mass concentration flux, f. The parameters are $N = 4$, $\alpha = 1$, $\beta = 1$. Each coloured line corresponds (with colour and dashing) to an edge in the cell shown in Figure 12.1. Each black line shows the solution in the non-random network case (see Figure 12.2) for comparison. That is, the dashed black line shows the solution on pores that are parallel to the x^1 direction for a non-random network (the blue and green edges in Figure 12.1). The dotted black line shows the solution on pores that are perpendicular to the x^1 direction for a non-random network (the orange and red pores in Figure 12.1). (a) The pore conductance, $G^{\boldsymbol{r}}_{ij}$, as a function of the mass concentration flux, f. (b) The x^1 component of the pore pressure drop, $\Delta^{r^1}_{ij}$, as a function of the mass concentration flux, f.

more adhesive.

12.2.2.3 Concentration and conductance

Next, in Figure 12.8, we display a comparison between the macroscale and microscale solutions for the concentration (left) and conductance (right) (compare with the mono-dispersed case in Figure 12.4) given random initial pore conductances. In Figure 12.8(a), we see that the qualitative behaviour of the two concentration solutions agrees. Similarly, in Figure 12.8(b), we see that the permeability behaves qualitatively like the average of the microscale conductances that result from the log-normally distributed initial values. Note that we have used *different* (random) initial pore conductances for the microscale and multiscale simulations, which fully explains differences in the quantitative behaviour of the two solutions (even in the limit $\varepsilon \to 0$). When the same initial conductances are used, we find, as expected, that the microscale and multiscale solutions agree quantitatively, as in the mono-dispersed case. Instead, in the poly-dispersed case, we expect the *statistics* (such as the mean and standard deviation) of the distributions of the microscale and multiscale solutions to agree in the limit $\varepsilon \to 0$ (when the initial pore conductances are chosen randomly). We explore this hypothesis in the next section.

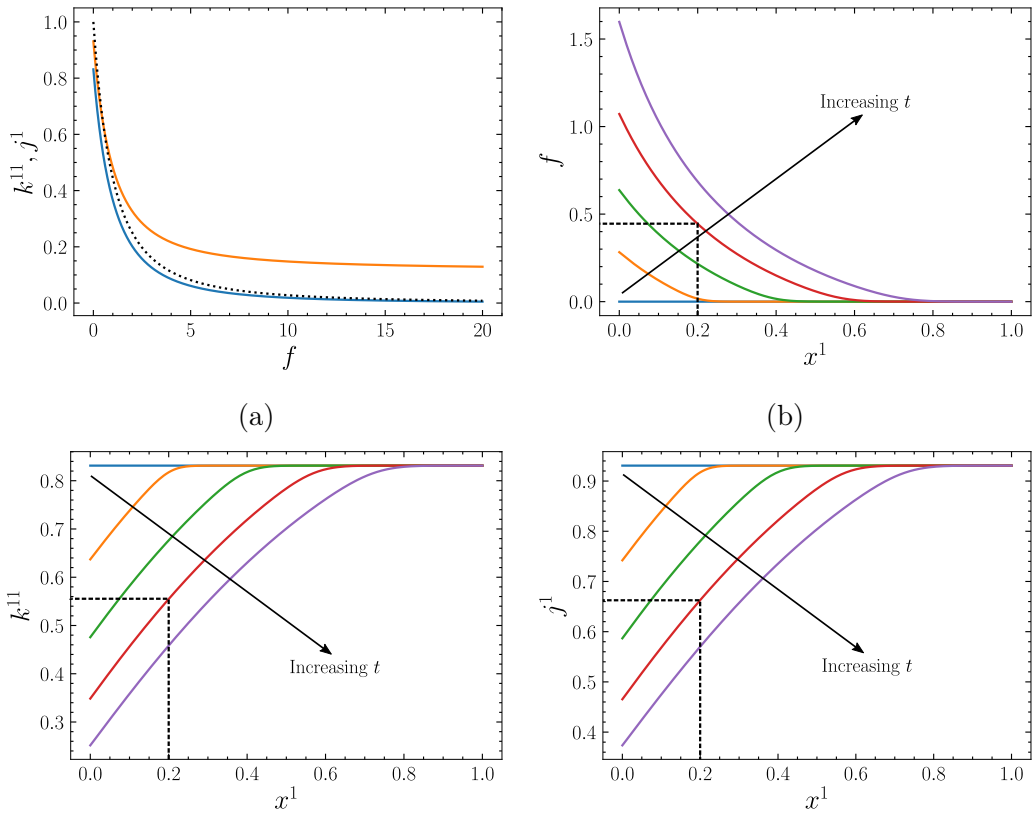

Figure 12.7: Graphs showing how the permeability, k^{11}, and adhesivity, j^1, vary with the mass concentration flux, f, and position, x^1, at various times, t. The parameters are $N = 4$, $\alpha = 1$, $\beta = 1$. The values of t are 0 (blue), 0.25 (orange), 0.5 (green), 0.75 (red), 1 (purple). The arrows show the direction of increasing time. (a) The permeability (blue), k^{11}, and adhesivity (orange), j^1, as functions of f. The black dotted line shows the solution in the non-random network case, for comparison. (b) The mass concentration flux, f, as a function of position, x^1, at various times, t. The dashed black line shows an evaluation at position $x^1 = 0.2$ and time $t = 0.75$ to determine the mass concentration flux here, $f(x^1 = 0.2, t = 0.75) \approx 0.45$. (c) The permeability, k^{11}, as a function of position, x^1, at various times, t. The dashed black line shows an evaluation at $x^1 = 0.2$ and $t = 0.75$ to confirm that $k^{11}(x^1 = 0.2, t = 0.75) \approx 0.56$. (d) The adhesivity, j^1, as a function of position, x^1, at various times, t. The dashed black line shows an evaluation at $x^1 = 0.2$ and $t = 0.75$ to confirm that $j^1(x^1 = 0.2, t = 0.75) \approx 0.66$.

12.2.2.4 Velocity and reactivity

Before we explore the statistics of the multiscale solution, we present the velocity and adhesivity in Figure 12.9 (compare this with the mono-dispersed case in Figure 12.5). In Figure 12.9(a), we see, as expected, that the poly-dispersed and mono-dispersed solutions exhibit the same qualitative behaviour (but not quantitative behaviour,

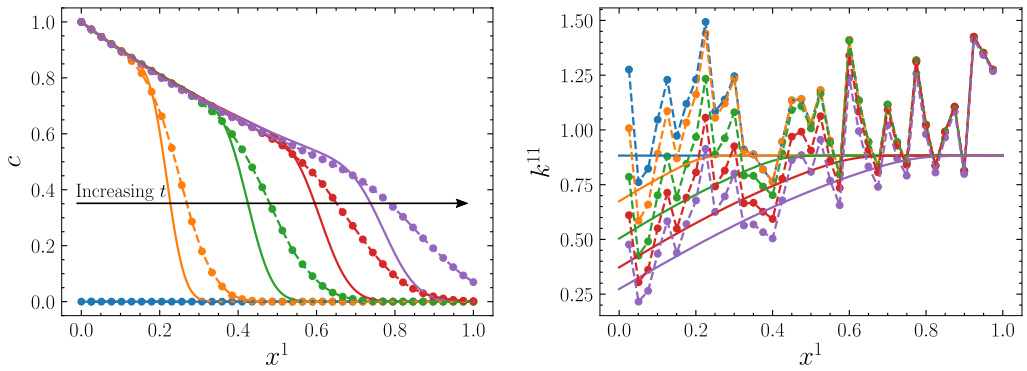

(a) (b)

Figure 12.8: Graphs showing how the macroscale and microscale (left) concentrations, c and $\bar{C}$ (see (8.2) in Part II), and (right) conductances (see (8.4)), k^{11} and $\bar{G}$, vary with position, x^1, at various times, t. The parameters are $N = 4$, $\alpha = 1$, $\beta = 1$, $\varepsilon = 0.1$. The values of t are 0 (blue), 0.25 (blue), 0.5 (green), 0.75 (red), 1 (purple). Dots show the average network quantities, interpolated with correspondingly coloured dashed lines. Correspondingly coloured solid lines show the effective quantities. The arrows show the direction of increasing time. (b) The macroscale and microscale concentrations, c and $\bar{C}$, as functions of position, x^1, at various times, t. (a) The macroscale and microscale conductances, $G^{\boldsymbol{r}}_{ij}$ and $\bar{G}$, as functions of position, x^1, at various times, t.

even for small ε, due to differences in initial conductances). In Figure 12.9(b), we see that, unlike in the mono-dispersed case (see Figure 12.5(b)), the reactivity is not uniform across the filter. Instead, it is largest near the inlet, and decreases with depth. It is proportional to the ratio of the adhesivity and the permeability, and so, at the inlet, the reactivity increases before decreasing again, because the decrease of the permeability is significantly faster than that of the adhesivity here at early times (see Figures 12.7(a), 12.7(c), and 12.7(d)). That is, the filter captures more particles nearer the inlet, so that by the time fluid reaches pores further down the filter, there are fewer particles in the suspension to be caught. As time increases, the reactivity decreases, since smaller pores can capture fewer particles, due to their decreased surface area.

In this section, we have demonstrated the solution of distinct initialisations of the multiscale model, (12.3)–(12.16), and shown that solutions match those of the underlying periodic network in the limit $\varepsilon \to 0$ (when the initial conductances used are the same between the two models). In the next section, we will view the solutions of the multiscale model as distributions that result from realisations of many distinct realisations of the initial random network. We will see how sampling the resulting permeability and adhesivity distributions may lead to approximation of microscale solutions on networks that are non-periodic.

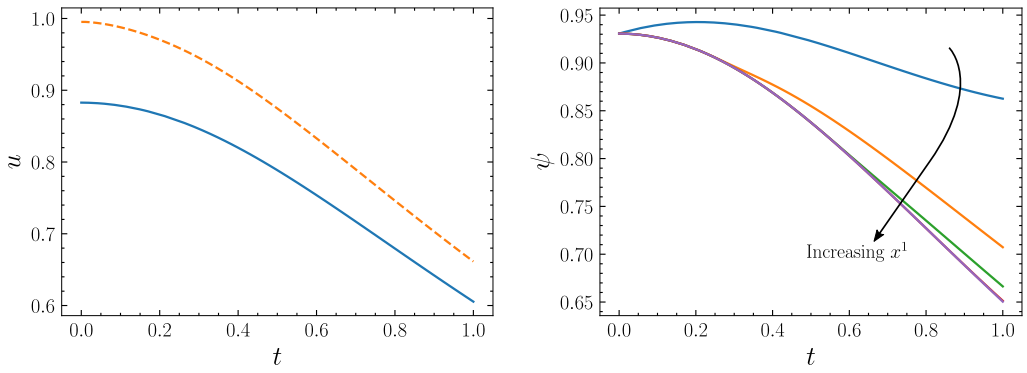

(a) (b)

Figure 12.9: Graphs showing how the velocity, u, and reactivity, ψ, vary with time t. The parameters are $N = 4$, $\alpha = 1$, $\beta = 1$. (b) The Darcy velocity, u, as a function of time, t. The solid blue line shows the macroscale solution. The dashed orange line shows the average of the microscale solution (see (8.5) in Part II). (b) The reactivity, ψ, as a function of time, t.

12.3 Non-periodic networks

In the previous sections, we showed that the behaviour of the solution of the effective system matches the behaviour of the solution of the periodic network system from which it is derived, in the limit $\varepsilon \to 0$ (see Step 2 in Figure 12.10 for an illustration). The hope, however, is that the solution of the effective system also matches the solution of a system defined on a non-periodic network, which we interpret here as a single cell of size $N \to \infty$. To achieve this, the repeating cell used for homogenisation must be chosen carefully so that it is *representative* of the non-periodic network, by which we mean that the statistical properties of the conductances, and the degree of connectivity of the nodes and edges, which together dictate the structure of the cell, must match those of the entire non-periodic network (see Step 1 in Figure 12.10). This intuition motivates the question: how should the repeating cell of size N be chosen so that the solution of the resulting effective system matches that of a corresponding system defined on a non-periodic network of size $N \to \infty$?

To answer this question, we will assess the statistical properties of the distributions of the effective parameters, k^{11} and j^1, as functions of the statistical properties of the distributions of conductances, $G_{ij}^{\mathbf{r}}$, in the cell. Note, from the formulae (12.7) and (12.9), that the permeability and adhesivity are both nonlinear with respect to the conductances, since the cell solutions, W_i^m, upon which the effective parameters also depend, are solutions of the cell problem, (12.11), which is itself a function of the edge conductances. This complex dependence of k^{11} and j^1 upon $G_{ij}^{\mathbf{r}}$ via W_i^m implies that, even for a network with i.i.d. (independent and identically distributed) edge conductances, the expectations of the permeability and adhesivity are not necessarily the same as the permeability and adhesivity of the network with all edge conductances equal to the mean edge conductance, $\bar{G}$, which we will refer to as the mean network.

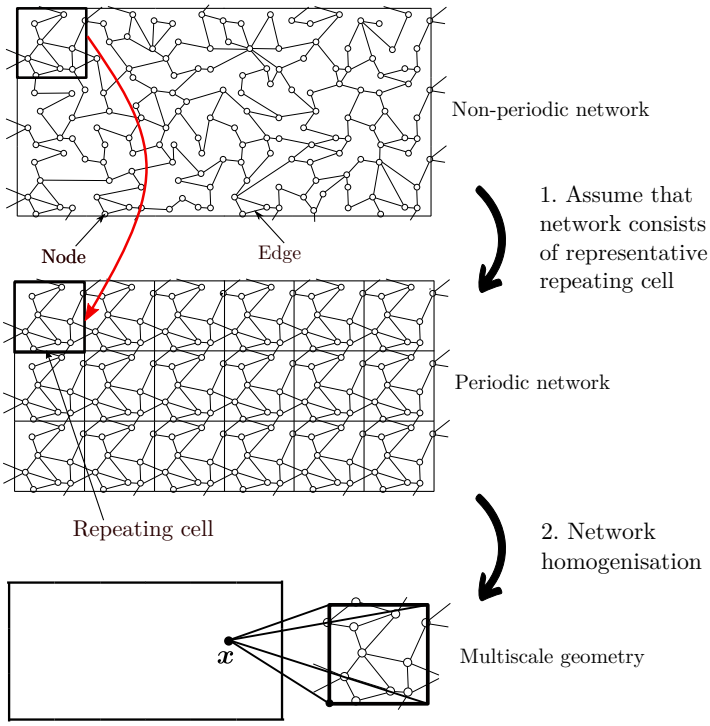

Figure 12.10: A diagram to illustrate the derivation of a multiscale effective system from one defined on a non-periodic network. Step 1 is the construction of a periodic network by repeating a cell that has properties that are representative of the non-periodic network. Step 2 is the derivation of an effective system from a system defined on a network, which was detailed in the previous chapter.

We focus our analysis on two properties of the cell: size and structure. We vary these independently of each other (see Figure 12.11 for an illustration). For each structure, and for each size, N, we define a probability distribution, $\mathcal{G}$, from which initial conductances, $G_{ij}^{\boldsymbol{r}0}$, are drawn. We then carry out the process of parameter pre-calculation outlined in Section (12.1) many times to find the resulting distributions for the parameters. That is, we sample $\mathcal{G}$ to specify a particular set of $G_{ij}^{\boldsymbol{r}0}$ in the cell, and solve the cell problem, (12.11), to find the set of corresponding cell solutions, W_i^m. We then use (12.7) and (12.9) to calculate k^{11} and j^1 for these conductance values. Since the initial conductances are sampled at random, we repeat this process $S \gg 1$ times. This process results in discretisations of the probability distributions for the permeability and adhesivity, $\mathcal{K}$ and $\mathcal{J}$, say, which depend on the distribution of the initial conductances, $\mathcal{G}$. For each structure, we vary N and thus observe how $\mathcal{K}$ and $\mathcal{J}$ vary with the cell size, N. We find the expected values of the parameters, $\mathbb{E}[k^{11}]$ and $\mathbb{E}[j^1]$, and their standard deviations $\mathbb{S}[k^{11}]$ and $\mathbb{S}[j^1]$, by sampling $\mathcal{K}$ and $\mathcal{J}$, and compare these four statistics across the different structures.

We begin by considering a four-regular structure, which, we recall, is a cell where each node connects to exactly four other nodes, to form a regular grid in two dimen-

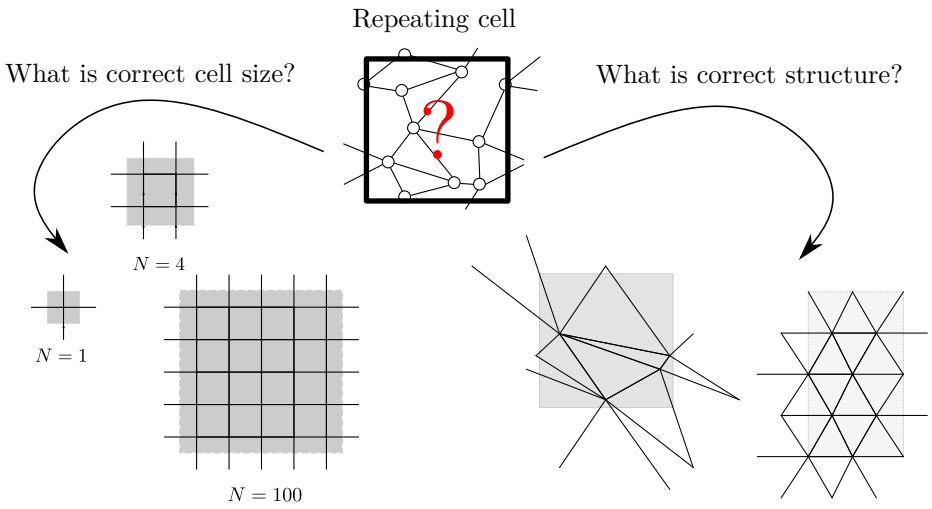

Figure 12.11: A diagram to illustrate the selection of a repeating cell for a periodic network that is representative of a non-periodic network. The left arrow illustrates the choice of the cell size, N. All cells on the left have the same structure, but have different sizes. The right arrow illustrates the choice of the cell structure. Both cells on the right have the same size and a average degree of six, but different connectivity.

sions. However, networks in porous media usually have a larger average degree (the average number of other nodes to which each node connects) [75]. This motivates our study of a *six-regular* structure, which is a cell where each node connects to exactly six other nodes. The physical networks that motivate this work are irregular in the sense that the size of the neighbourhood of each node varies [75]. This motivates our analysis of a *six-irregular* cell, which has an average degree of six, although some nodes connect to fewer than six nodes, while others connect to more.

We will keep two properties of all three structures consistent. Firstly, by scaling the cell dimensions, l^1 and l^2, if necessary, we will ensure that the node density,

$$\varrho = \frac{N}{l^1 l^2}, \tag{12.24}$$

which is the number of nodes divided by the area of the cell, is unity. Secondly, noting that

$$\hat{R}^{\boldsymbol{r}}_{ij} = \frac{1}{\hat{G}^{\boldsymbol{r}}_{ij}}, \tag{12.25}$$

where $\hat{G}^{\boldsymbol{r}}_{ij}$ and $\hat{R}^{\boldsymbol{r}}_{ij}$ are the conductance and resistance of pore $ij\boldsymbol{r}$ per unit length, we will ensure, by scaling $G^{\boldsymbol{r}0}_{ij}$ if necessary, that the mean of $\mathcal{G}$ is consistent, so that the mean pore resistance per unit length is the same in all structures. These two controls ensure that the experiment results are comparable.

12.3.1 Blocking

To demonstrate the generality of our framework, we will carry out this analysis using an alternative model for particle–pore interactions, and the resulting changes to the connectivity of the network. We assume that each pore becomes clogged instantaneously at the first time at which the concentration within it exceeds some threshold. At this time, the conductance of the pore is instantaneously reduced to zero and the particles that clogged the pore are removed from the flow. The analogy is with the 'blocking' mechanism discussed in the size-structured model in Part I, where pore radii are instantaneously reduced to zero after interactions with large particles.

Conductance and adherence

To model blocking in the present framework, we define

$$c^{\max}(\boldsymbol{x},t) = \max_{s\leq t}(c(\boldsymbol{x},s)), \tag{12.26}$$

which is the maximum concentration observed at point $\boldsymbol{x}$ up to time t. We then assume the conductance model

$$G_{ij}^{\boldsymbol{r}}(\boldsymbol{x},t) = G_{ij}^{\boldsymbol{r}0}\Big(1 - H(t - T_{ij}^{\boldsymbol{r},\text{block}})\Big) \tag{12.27}$$

$$= \begin{cases} G_{ij}^{\boldsymbol{r}0} & c^{\max}(\boldsymbol{x},t) \leq \alpha G_{ij}^{\boldsymbol{r}0}, \\ 0 & c^{\max}(\boldsymbol{x},t) > \alpha G_{ij}^{\boldsymbol{r}0}, \end{cases} \tag{12.28}$$

and the associated adherence model

$$A_{ij}^{\boldsymbol{r}}(\boldsymbol{x},t) = \begin{cases} 1 & c^{\max}(\boldsymbol{x},t) = \alpha G_{ij}^{\boldsymbol{r}0}, \\ 0 & c^{\max}(\boldsymbol{x},t) \neq \alpha G_{ij}^{\boldsymbol{r}0}. \end{cases} \tag{12.29}$$

We recall that $G_{ij}^{\boldsymbol{r}0}$ is the initial conductance, and define $T_{ij}^{\boldsymbol{r},\text{block}}$ to be the block time, at which the maximum concentration exceeds the threshold in pore $ij\boldsymbol{r}$, when the condition $c^{\max} > \alpha G_{ij}^{\boldsymbol{r}0}$ is first satisfied. We replace the pore conservation equation that corresponds to deposition, (12.4), with (12.27). This time, we pre-calculate the pore conductances, and thus the permeability and adhesivity, by replacing (12.22) with (12.28) to find $G_{ij}^{\boldsymbol{r}}(c^{\max})$ (rather than $G_{ij}^{\boldsymbol{r}}(f)$). The adherence is no longer constant (compare with α in (11.21)), and instead depends on the indices of the pore, $ij\boldsymbol{r}$, the position of the pore, $\boldsymbol{x}$, and time, t.

To gain an intuition for this modified multiscale model, in which blocking occurs instead of deposition, consider the point $\boldsymbol{x}$ at time t, which contains a cell in the limit $\varepsilon \to 0$. Before $T_{ij}^{\boldsymbol{r},\text{block}}$, the concentration of particles in the flow in pore $ij\boldsymbol{r}$ has not exceeded the threshold, so the pore conducts all particles through it. At the block time, $T_{ij}^{\boldsymbol{r},\text{block}}$, the maximum concentration, $c^{\max}$, defined in (12.26), first exceeds the threshold, and the adherence of pore $ij\boldsymbol{r}$, $A_{ij}^{\boldsymbol{r}}$, becomes non-zero according to (12.29). This leads to an instantaneous non-zero adhesivity, j^1, according to (12.9), which in-turn causes an instantaneous non-zero reactivity, ψ, according to (12.6). This results

in the instantaneous removal of free particles from the system, since the reaction term in the advection–reaction equation, (12.3), becomes non-zero. At the same time, the conductance of this pore, $G_{ij}^{\boldsymbol{r}}$, switches from its initial value to zero, and remains there for the duration of the process, according to (12.28). The linear cell problem, (12.11), depends on the pore conductances, $G_{ij}^{\boldsymbol{r}}$. Consequently, this instantaneous change in conductance causes an instantaneous change in its solution, the cell solution W_i^m, which, in turn, causes changes to the permeability, k^{11}, according to (12.7), and to the adhesivity, j^1, according to (12.9). Changes to the permeability then affect the velocity of the flow, given by u^1 and u^2, due to (12.5). Consequently, the rate of the transport of particles is altered, since the x^1-directional velocity, u^1, appears in the advective term of the advection–reaction equation, (12.3). Since, in the limit $\varepsilon \to 0$, the spatial point $\boldsymbol{x}$ contains the entire cell, changes to the conductance and adherence of all edges $ij\boldsymbol{r}$ occur here at the same time.

Threshold parameter

The threshold concentration above which a pore blocks is dictated by α in (12.28) and (12.29). This parameter contains information about the size or coagulation of particles, for example. As an illustrative case, we set α so that α^{-1} is the mean, $\bar{G}$, of the distribution from which initial edge conductances are drawn,

$$\alpha = \frac{1}{\bar{G}}. \tag{12.30}$$

To see why this is a useful test case, we substitute (12.30) into the conductance and adherence models, (12.28) and (12.29). We find that these imply that pore $ij\boldsymbol{r}$ at position $\boldsymbol{x}$ remains conductive at time t if the initial conductance of the pore, $G_{ij}^{\boldsymbol{r}0}$, satisfies $G_{ij}^{\boldsymbol{r}0} \geq c^{\max}(\boldsymbol{x},t)\bar{G}$, but blocks if $G_{ij}^{\boldsymbol{r}0} < c^{\max}(\boldsymbol{x},t)\bar{G}$. So the probability of the event $E_{ij}^{\boldsymbol{r}}(\boldsymbol{x},t)$, which we define to be 'pore $ij\boldsymbol{r}$ in the cell at position $\boldsymbol{x}$ blocks at time t', is the probability that $G_{ij}^{\boldsymbol{r}0}$ lies to the left of the scaled mean, $c^{\max}(\boldsymbol{x},t)\bar{G}$. That is,

$$\mathbb{P}[E_{ij}^{\boldsymbol{r}}(\boldsymbol{x},t)] = \mathrm{cdf}(c^{\max}(\boldsymbol{x},t)\bar{G}), \tag{12.31}$$

where $\mathrm{cdf}(G_{ij}^{\boldsymbol{r}0} = g)$ is the cumulative density function of the initial conductance distribution, $\mathcal{G}$, at any value g, which returns the integral of the probability density function (PDF) (which we recall from (12.16) is denoted by g) to the left of g.

Examples of the PDF and CDF of $\mathcal{G}$ = Log-normal are shown in Figure 12.12, with values of $c^{\max}(\boldsymbol{x},t)\bar{G}$ shown with dashed lines. In Figure 12.12(a), we see, for example, that if $G_{ij}^{\boldsymbol{r}0}$ lies to the left of the dashed blue line, then pore $ij\boldsymbol{r}$ blocks when a maximum concentration value of $c^{\max} = 1$ is observed. Using Figure 12.12(b), we find the intersection of $\bar{G}$ with the CDF, shown in a solid blue line, to find that the corresponding probability in the case $c^{\max}$ (dotted blue line), for example, is around 0.56. Physically, if the point $\boldsymbol{x}$ has received the maximum concentration of particles, any pore with a conductance less than the mean blocks. On the other hand, for $c^{\max} = 0$, in 12.12(a) we see that the probability that pore $ij\boldsymbol{r}$ blocks is the probability that $G_{ij}^{\boldsymbol{r}0}$ lies to the left of the dashed orange line, which is at zero. Using Figure 12.12(b), we find the intersection of this line with the CDF and

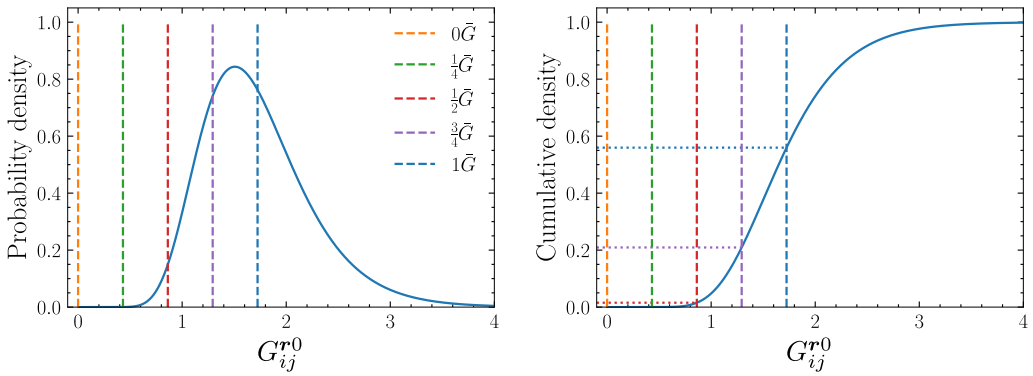

(a) (b)

Figure 12.12: Graphs showing how the PDF and CDF of the initial conductance distribution, $\mathcal{G}$, vary with $G_{ij}^{\boldsymbol{r}0}$. The value of the scaled mean, $c^{\max}\bar{G}$, is shown in dashed coloured lines for $c^{\max} \in \{0, 1/4, 1/2, 3/4, 1\}$. (a) The pdf of $\mathcal{G}$. (b) The CDF of $\mathcal{G}$. The cumulative densities corresponding to the various scaled means are extrapolated using correspondingly coloured dotted lines.

find that the corresponding probability (dotted orange line) is zero. Physically, if the point $\boldsymbol{x}$ has not received any particles, then no pores here block. Note that the maximum concentration to have reached the point $\boldsymbol{x}$ at time t is bounded by these two cases, $0 \leq c^{\max}(\boldsymbol{x}, t) \leq 1$, and further that we will always consider initial conductance distributions that have $\text{cdf}(\bar{G}) \approx 1/2$. Therefore, since the number of blocked pores in a cell is approximately equal to the number of total pores multiplied by the probability of each pore blocking, it follows that the choice $\alpha^{-1} = \bar{G}$ in (12.30) ensures that, in a cell with E edges initially, the number of pores that are blocked will range from zero, when no particles have passed through it, to $\text{cdf}(\bar{G})E \approx E/2$, when the concentration of particles is as large as possible.

12.3.2 Four-regular structure

To illustrate our method, we begin by considering a four-regular structure, so that the degree of each node is four. An example of some cells with four-regular structure containing various numbers of nodes, N, are shown in Figure 12.13.

To satisfy the constraint of unit node-density, we choose $l^1 = l^2 = \sqrt{N}$ for a given N. This scales the area of the cell, $l^1 l^2$, so that $\varrho = 1$ in (12.24), which ensures spatial invariance between cells with different N (see Figure 12.13).

We draw i.i.d. initial edge conductances from a log-normal distribution, $\mathcal{G}$, so that $G_{ij}^{\boldsymbol{r}0} \sim \text{logNorm}(\mu, \sigma^2)$. We choose the parameters of $\mathcal{G}$ to simplify comparison with a related study by Chapman *et al.*, [80], and so set the mean of the normal distribution associated with $\mathcal{G}$ to be $\mu = 0.5$. We are interested in the dependence of $\mathcal{K}$ and $\mathcal{J}$ on the variance of $\mathcal{G}$, and thus present scenarios where the standard deviation of the associated normal distribution is either $\sigma = 0.03 = \sigma_{\text{N}}$ or $\sigma = 0.3 = \sigma_{\text{W}}$. The first value corresponds to the scenario where $\mathcal{G}$ is narrow (N) around its mean, and the

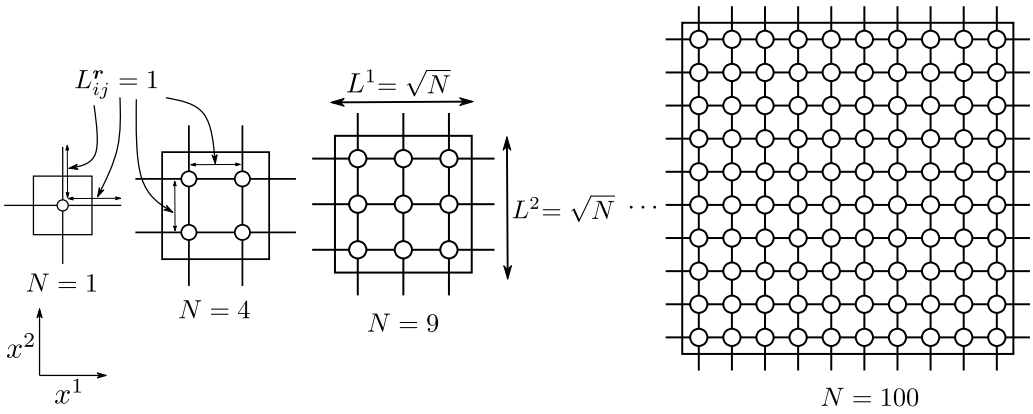

Figure 12.13: A diagram of cells of various sizes, N, with four-regular structure. The cell dimensions, l^1 and l^2, are set to be $\sqrt{N}$ so that the node density, ϱ, satisfies $\varrho = 1$ in all cells. Consequently, the length of each pore $ij\boldsymbol{r}$ is $L^{\boldsymbol{r}}_{ij} = 1$. We arbitrarily choose the x^1 direction to be from left to right. Thus, horizontal edges in this diagram are parallel to the pressure gradient, and thus the flow. We call these flow-parallel edges. Vertical edges are transverse to the pressure gradient, and we call these flow-transverse edges.

second corresponds to a wider (W) case. We plot the PDF and CDF for the cases $G^{\boldsymbol{r}0}_{ij} \sim \mathcal{G}(0.5, 0.3^2)$ and $G^{\boldsymbol{r}0}_{ij} \sim \mathcal{G}(0.5, 0.03^2)$ in Figure 12.14. Here, and throughout, results for the narrower and wider underlying distributions are shown on the left and right respectively.

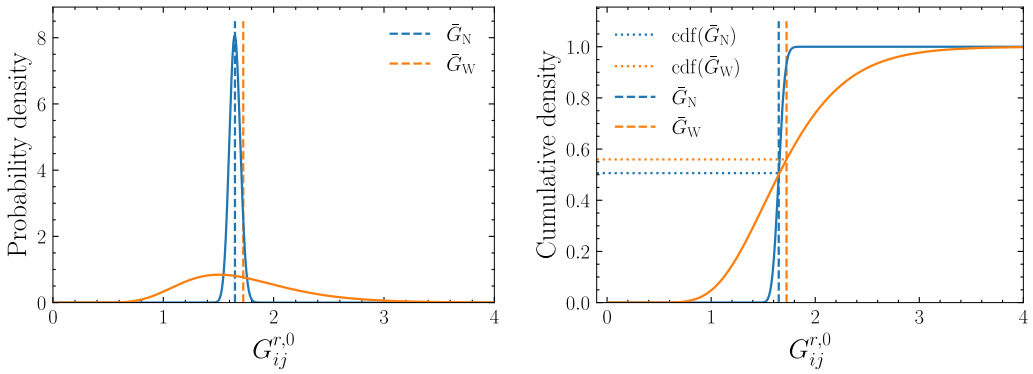

(a) (b)

Figure 12.14: Graphs showing the PDF and CDF of the initial conductance distribution, $\mathcal{G}$. The narrower case is shown in blue. The wider case is shown in orange. The mean initial conductances, $\bar{G}_{\mathrm{W}}$ and $\bar{G}_{\mathrm{N}}$, are shown with correspondingly coloured dashed lines. (a) The pdf, g, as a function of the initial conductance, $G^{\boldsymbol{r}0}_{ij}$. (b) The CDF as a function of the initial conductance, $G^{\boldsymbol{r}0}_{ij}$. The cumulative densities of the means, $\mathrm{cdf}(\bar{G}_{\mathrm{N}})$ and $\mathrm{cdf}(\bar{G}_{\mathrm{W}})$ are extrapolated in correspondingly coloured dotted lines.

The mean of the log-normal distribution from which initial conductances are drawn is $\exp(\mu + \sigma^2/2) = \bar{G}$, so that $\bar{G} \approx 1.72461 = \bar{G}_{\mathrm{N}}$ in the narrower case, and $\bar{G} \approx 1.64946 = \bar{G}_{\mathrm{W}}$ in the wider one (see Figure 12.14). Note, from Figure 12.14(b), that $\mathrm{cdf}(\bar{G}_{\mathrm{W}}) > \mathrm{cdf}(\bar{G}_{\mathrm{N}}) \approx 1/2$, which will have consequences for our analysis of the effective adhesivity, j^1. Also note that, since all edges have unit length, the mean resistance per unit length of edges in this structure is $\bar{G}^{-1}$. We will preserve this quantity in the other structures that we study. We present the case $c^{\max} = 1$, so that we display the permeability and adhesivity distributions, $\mathcal{K}$ and $\mathcal{J}$, when the cell contains the largest-feasible concentration. Note that the qualitative behaviour is similar for any $0 \leq c^{\max} < 1$.

12.3.2.1 Permeability

For a cell with $N = 1$ (see Figure 12.13 for an illustration), the permeability formula, (12.7), simplifies to

$$k^{11}_{N=1} = \frac{1}{2l^2} \sum_{r^1 \in \mathcal{R}} \sum_{r^2 \in \mathcal{R}} (r^1)^2 l^1 G_{11}^{(r^1, r^2)^\top}, \tag{12.32}$$

where $\mathcal{R} = \{-1, 0, 1\}$. Since $r^1 = 0$ on flow-transverse pores (see Figure 12.13), only the conductances of flow-parallel pores, $G_{11}^{(\pm 1,0)^\top}$, contribute to the permeability in (12.32). The two flow-parallel pores, $(1, 1, (1, 0)^\top)$ and $(1, 1, (-1, 0)^\top)$, are identical by periodicity, and so $G_{11}^{(1,0)^\top} = G_{11}^{(-1,0)^\top}$. It follows that there is only one unique value of $G_{ij}^{\boldsymbol{r}0}$, and therefore that the distribution, $\mathcal{K}$, of the permeability, k^{11}, is identical to the distribution, $\mathcal{G}$, of the initial conductances, $G_{ij}^{\boldsymbol{r}0}$. Indeed, in Figure 12.15, we plot samples of $\mathcal{K}_{N=1}$ and the PDF of $\mathcal{G}$ and see that these match (up to randomness caused by sampling). We see that one consequence is that, when $N = 1$, the expected permeability, $\mathbb{E}[k^{11}]$, of the four-regular network is exactly equal to the permeability of the mean network, $\bar{k}_4$ say, which is equal to $\bar{G}$ (see the orange and green dashed lines in Figure 12.15). Note, more generally, that regardless of structure and size of the cell, inter-cell pores that are transverse to the flow (those given by $(i, j, \boldsymbol{r} = (0, \pm 1)^\top)$ in the $N = 1$ cell) do not contribute to the flow-directional permeability, k^{11} in (12.7), since $r^1 = 0$ for these pores.

We plot samples of the permeability distribution, and their statistics, for several other N, in the cases $\sigma = 0.03$ (left) and $\sigma = 0.3$ (right), in Figure 12.16. Since we have used the parameters $\mu = 0.5$ and $\sigma = 0.3$ to specify $\mathcal{G}$ and thus $\mathcal{K}$ in Figures 12.16(b) and 12.16(d), it is simple to verify that our results agree well (up to the randomness caused by sampling) with those presented in [80] (Figure 3). This helps validate our method and thus the rest of our findings. We see that it does not follow from our result for $N = 1$ that $\mathbb{E}[k^{11}] = \bar{G}$ for $N > 1$, since there is now more than one pore for which an initial conductance value is drawn. Instead, in Figures 12.16(a) and 12.16(b) we see that as N increases, the spread of the permeability distribution decreases and the expected permeability approaches a constant, which we call $\bar{k}^{11}_{N\to\infty}$. We interpret this limit, $\bar{k}^{11}_{N\to\infty}$, as the approximate (since we do not study cells larger than $N = 100$) mean-permeability of an infinitely large non-periodic network.

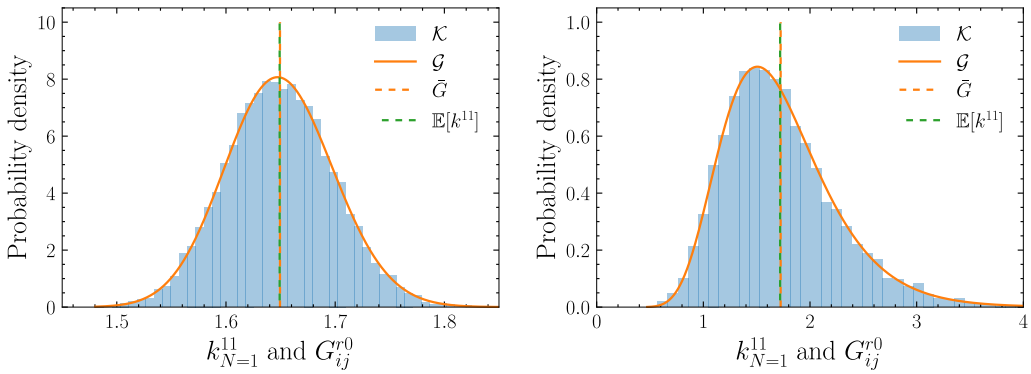

(a) (b)

Figure 12.15: Graphs showing the pdf, g, of the initial conductance distribution, $\mathcal{G}$, and the resulting permeability distribution, $\mathcal{K}$. The parameters are $\mu = 0.5$, $S = 10,000$, and $N = 1$. The pdf of $\mathcal{G}$ is shown in a solid orange line. Samples of $\mathcal{K}$ are shown with blue bars. The mean of $\mathcal{G}$, $\bar{G}$, which is equal to the permeability of the mean network, $\bar{k}_4$, is shown in a dashed orange line. The expected value of the samples of $\mathcal{K}$, $\mathbb{E}[k^{11}]$, is shown in a dashed green line. (a) The narrower case, $\sigma = 0.03$. (b) The wider case, $\sigma = 0.3$.

Finite cell error

Firstly, note, from Figures 12.16(c) and 12.16(d), that the mean permeability of a cell of size N, $\mathbb{E}[k^{11}]$, becomes an increasingly accurate approximation of the mean permeability of the non-periodic network, $\bar{k}^{11}_{N\to\infty}$, as N increases (compare blue dots to dashed blue line). This is true for all σ, so that we find that the convergence occurs at approximately the same rate for all initial conductance distributions considered (see Figure 12.16(c) for a typical narrower case, and Figure 12.16(c) for a wider one). Indeed, we find that the difference between the mean permeability of the cell of size N, $\mathbb{E}[k^{11}]$, and the mean permeability of the non-periodic random network, $\bar{k}^{11}_{N\to\infty}$ (as a fraction of $\bar{k}^{11}_{N\to\infty}$), satisfies

$$E^k_{\mathrm{c}} = \frac{\left|\mathbb{E}[k^{11}] - \bar{k}^{11}_{N\to\infty}\right|}{\bar{k}^{11}_{N\to\infty}} \approx \beta N^{-1}, \tag{12.33}$$

where β depends on σ. This explains the limit, $\mathbb{E}[k^{11}] \to \bar{k}^{11}_{N\to\infty}$ as $N \to \infty$, that we observe. We interpret this quantity, E^k_{c}, which we plot in Figure 12.17, as the error that we make to the mean permeability (note the superscript, k) when we replace the random network with a finite cell (note the subscript, c) of size N. The implication of (12.33) is that, as the size of the cell grows, this error decreases like N^{-1}. For example, when $\sigma = 0.3$, averaging samples of a size $N = 9$ cell leads us to overestimate the mean permeability of the infinitely-large non-periodic random network by approximately 0.5% (see the dashed green line in Figure 12.17(b)). Even a cell of size just $N = 4$ leads to an overestimate of only approximately 1.1% (see the dashed orange line in Figure 12.17(b)). This result suggests that the multiscale system that we derived

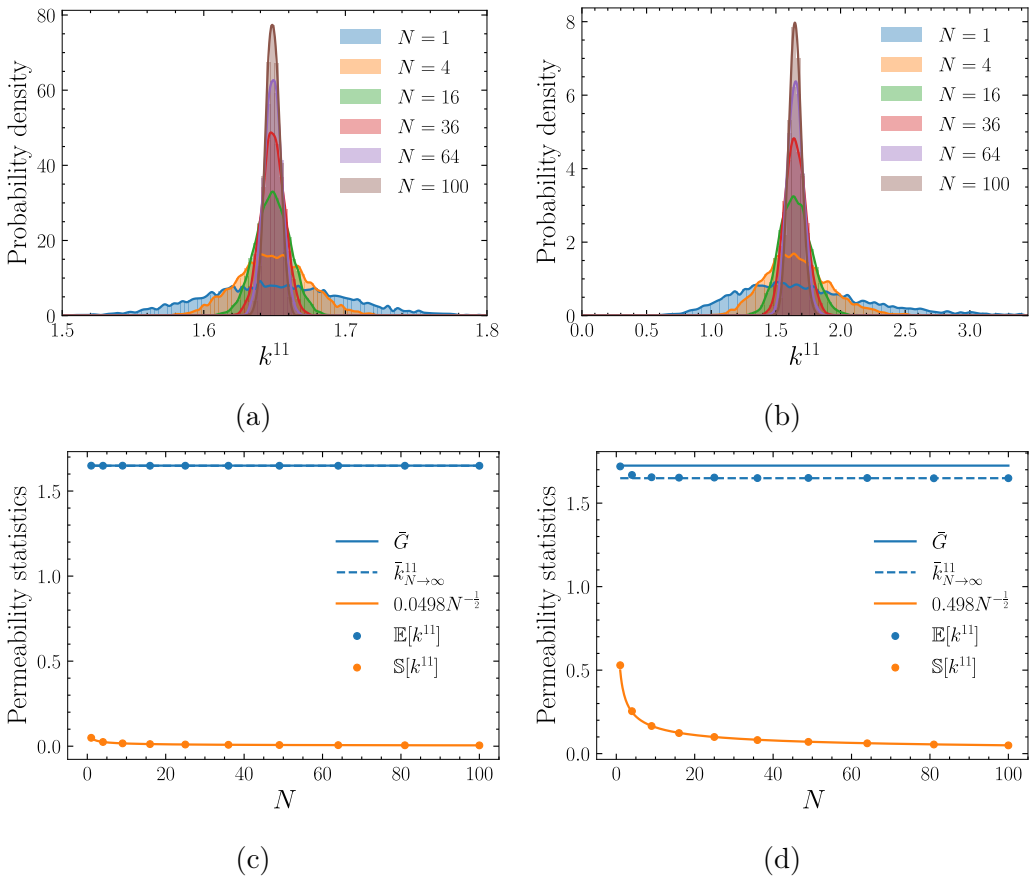

Figure 12.16: Graphs showing how the distribution of samples of the permeability, k^{11}, varies with the cell size, N, in a four-regular network. The parameters are $\mu = 0.5$, $S = 10,000$ and $\sigma = 0.03$ (left) or $\sigma = 0.3$ (right). (a) The case $\sigma = 0.03$. Coloured bars show a histogram of the distribution, $\mathcal{K}$, of the permeability, k^{11}, for various N. Correspondingly coloured lines interpolate the histogram at bar midpoints, to show an approximate pdf of $\mathcal{K}$. (b) A similar plot to (a), but using $\sigma = 0.3$. (c) The mean (blue dots) and standard deviation (orange dots) of the permeability distribution, $\mathbb{E}[k^{11}]$ and $\mathbb{S}[k^{11}]$, as functions of N, for $\sigma = 0.03$. The solid blue curve shows the mean conductance, $\bar{G}$, which is also the permeability of the mean network, $\bar{k}_4$. The dashed blue line shows the approximate mean permeability of an infinite non-periodic four-regular network, $\bar{k}^{11}_{N\to\infty}$, approximated using $N = 100$. Note that this is almost invisible to the eye, since it lies almost exactly below the solid blue line. The solid orange line shows a fit to the standard deviation, achieved by plotting in log-log space. (d) A similar plot to (c), but using $\sigma = 0.3$.

from a periodic-network system may also be able to capture the behaviour of the corresponding system defined on a non-periodic network. Furthermore, note the reduction in the computational complexity of finding the permeability of a small cell as opposed to an entire network (or even a large cell), since, as we have discussed, to find the permeability, (12.7), we solve a linear problem, (12.11), of size of the number of nodes in the cell, N.

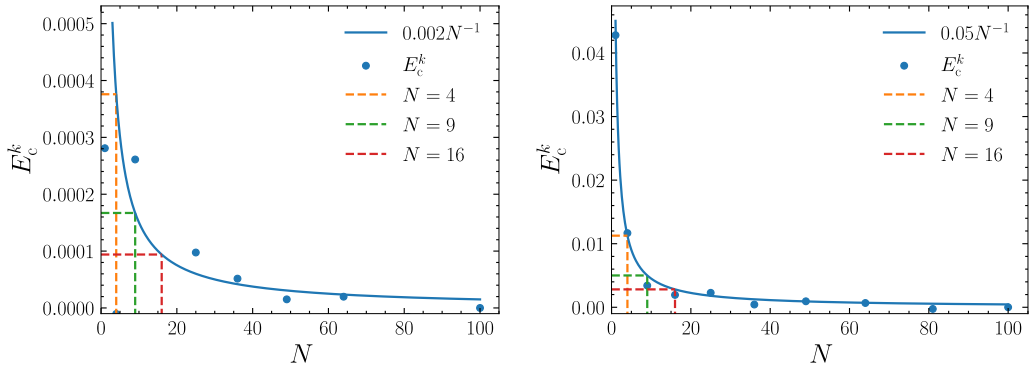

(a) (b)

Figure 12.17: Graphs showing how the finite cell error, E_c^k, varies with the cell size, N. The parameters are $\mu = 0.5$, $S = 10,000$ and $\sigma = 0.03$ (left) or $\sigma = 0.3$ (right). Blue dots show the numerical result. Solid blue lines show a fitting. The errors that result from using cells of size $N = 4$ (orange), $N = 9$ (green), and $N = 16$ (red) are approximated in coloured dashed lines. (a) The case $\sigma = 0.03$. (b) The case $\sigma = 0.3$.

Mean network error

Secondly, note that $\bar{k}^{11}_{N\to\infty}$ is smaller than the permeability of the mean network, $\bar{k}_4 = \bar{G}$, which demonstrates the nonlinear dependence of the permeability on the initial conductances. This is true for all σ, although, for wider initial conductance distributions (see Figure 12.16(d)), this difference is more pronounced, while for narrower cases (see Figure 12.16(c)) the difference is smaller (compare the blue dots with the solid blue line). Indeed, we find that the difference between the permeability of the mean network, $\bar{k}_4 = \bar{G}$, and the mean permeability of the non-periodic random network, $k^{11}_{N\to\infty}$ (as a fraction of $k^{11}_{N\to\infty}$), satisfies

$$E_n^k = \frac{\left|\bar{G} - \bar{k}^{11}_{N\to\infty}\right|}{\bar{k}^{11}_{N\to\infty}} \approx 0.52\sigma^2, \tag{12.34}$$

so that

$$\bar{k}^{11}_{N\to\infty} \to \bar{G} = e^{\mu+\frac{\sigma^2}{2}} \tag{12.35}$$

as $\sigma \to 0$. We interpret this quantity, E_n^k, which we plot in Figure 12.18, as the error we make when we replace the permeability (hence the superscript, k) of the random network with the permeability of the mean network (hence the subscript, n). The implication of (12.34) is that, as σ decreases, so that the initial conductance distribution narrows, the size of this error decreases like σ^2. For example, use of $\bar{G}$ in place of $\bar{k}^{11}_{N\to\infty}$ would lead to an underestimate of the mean permeability of the infinitely large non-periodic random network of approximately 4.4% for $\sigma = 0.3$ and approximately 0.04% for $\sigma = 0.03$ (see the green and orange dashed lines in Figure 12.18, respectively). Note that, if we are willing to accept the error for a given σ, then replacement leads to a considerable ($C_{PC} = \mathcal{O}(F(N^2)^L)$, see Section 12.1)

reduction in computational complexity, since the permeability need not be sampled and so the pre-calculation step is redundant. Instead, we assume that the mean of the permeability distribution is well approximated by the mean of the conductance distribution and solve the multiscale system once using this value.

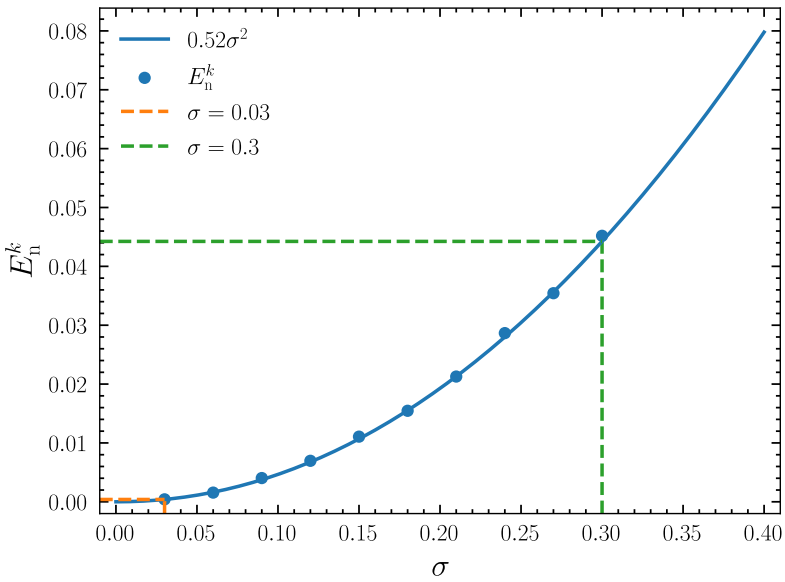

Figure 12.18: Graph showing how the mean network error, E_{n}^k, varies with the standard deviation of the initial conductance distribution, σ. Blue dots show the numerical result. Solid blue lines show a fitting. The errors that result from replacing a network consisting of cells containing initial conductances drawn from distributions with standard deviations of $\sigma = 0.03$ and $\sigma = 0.3$ with the mean network are approximated with a dashed orange and green lines, respectively.

Sampling error

Thirdly, note that in Figures 12.16(c) and 12.16(d) we see that the standard deviation of the permeability, $\mathbb{S}[k^{11}]$, decays with N like $N^{-1/2}$ (compare the orange dots with the solid orange line). This has two important implications. Firstly, we note that these standard deviations are larger than the errors caused either by replacement by small cells (see Figure 12.17) or replacement by the mean network (see Figure 12.18). We might consider either replacement acceptable, then, since we do not expect the errors in the solution resulting from either to exceed the error caused by a random sample. Secondly, the slow decay of the standard deviation with N, along with the rapid convergence of the mean with N, has further implications when the goal is to evaluate the permeability for a non-periodic network. As we have established, the cell problem, (12.11), is a linear problem with a computational complexity of at least $\mathcal{O}(N^2)$ [180]. Since the permeability formula, (12.7), depends on the solution of the cell problem, W_i^1, the complexity associated with pre-calculation of the permeability is itself greater

than $\mathcal{O}(N^2)$ and in particular is greater than $\mathcal{O}(N^{-1/2})$, which we have shown to be the convergence rate of the standard deviation. Thus, it is computationally advantageous to average over many realisations of a relatively small cell as opposed to averaging over fewer realisations of a large cell. As one further remark, note that the permeability distribution for the $N = 1$ cell in the narrower case, $\sigma = 0.03$, is approximately the distribution for the $N = 100$ cell in the wider case, $\sigma = 0.3$. One interpretation is that a factor of 10 increase in the standard deviation of the underlying conductance distribution therefore has a factor of 100 effect on the size of the cell required for network homogenisation.

12.3.2.2 Adhesivity

Next, in Figure 12.19, we display a similar (see Figure 12.16) assessment of the adhesivity distribution, $\mathcal{J}$, for narrower (left) and wider (right) initial conductance distributions, $\mathcal{G}$. We see that the qualitative behaviour of the statistics of the adhesivity is similar to that of the permeability (in Figure 12.16). That is, as N increases, the variance of the adhesivity also decreases and its expected value approaches a constant, $\bar{j}^1_{N\to\infty}$ say. In analogy with $\bar{k}^{11}_{N\to\infty}$, $\bar{j}^1_{N\to\infty}$ may be interpreted as the approximate mean-adhesivity of an infinitely large non-periodic random network.

Blocked pore distribution

Unlike the permeability, however, observing Figure 12.19(a) we see that when $\mathcal{G}$ is narrower, the resulting adhesivity distribution is a set of distinct peaks with zero probability-density between them, at any given cell size, N. To explain this phenomenon, we begin by noting that

$$j^1 = -\frac{1}{l^1 l^2}\sum_{i=1}^{N}\sum_{j=1}^{N}\sum_{\boldsymbol{r}\in\boldsymbol{\mathcal{R}}} G^{\boldsymbol{r}}_{ij}(W^1_j + r^1 l^1 - W^1_i)A^{-\boldsymbol{r}}_{ji}H^{-r^1}_{ji} \tag{12.36}$$

$$= -\frac{1}{l^1 l^2}\sum_{i=1}^{N}\sum_{j=1}^{N}\sum_{\boldsymbol{r}\in\boldsymbol{\mathcal{R}}} G^{\boldsymbol{r}}_{ij}\Delta^{-r^1}_{ji}A^{-\boldsymbol{r}}_{ji}H^{-r^1}_{ji} \tag{12.37}$$

$$\approx -\frac{1}{l^1 l^2}\sum_{i=1}^{N}\sum_{j=1}^{N}\sum_{\boldsymbol{r}\in\boldsymbol{\mathcal{R}}} \mathbb{E}[G^{\boldsymbol{r}}_{ij}\Delta^{-r^1}_{ji}]A^{-\boldsymbol{r}}_{ji}H^{-r^1}_{ji} \tag{12.38}$$

$$\approx -\frac{1}{l^1 l^2}\sum_{i=1}^{N}\sum_{j=1}^{N}\sum_{\boldsymbol{r}\in\boldsymbol{\mathcal{R}}} \mathbb{E}[G^{\boldsymbol{r}}_{ij}]\mathbb{E}[\Delta^{-r^1}_{ji}]A^{-\boldsymbol{r}}_{ji}H^{-r^1}_{ji} \tag{12.39}$$

$$= -\frac{\bar{G}}{l^1 l^2}\sum_{i=1}^{N}\sum_{j=1}^{N}\sum_{\boldsymbol{r}\in\boldsymbol{\mathcal{R}}} \mathbb{E}[\Delta^{-r^1}_{ji}]A^{-\boldsymbol{r}}_{ji}H^{-r^1}_{ji}. \tag{12.40}$$

The first equation is the definition of j^1, (12.9), and the second is the definition of the pore pressure drop, $\Delta^{r^1}_{ij}$, (11.132). The third uses that, for narrow enough conductance distributions, such that $\sigma \ll 1$, values of the conductance, and therefore the pore pressure drop, lie close to their expectation (compare the values of $G^{\boldsymbol{r}}_{ij}$ and

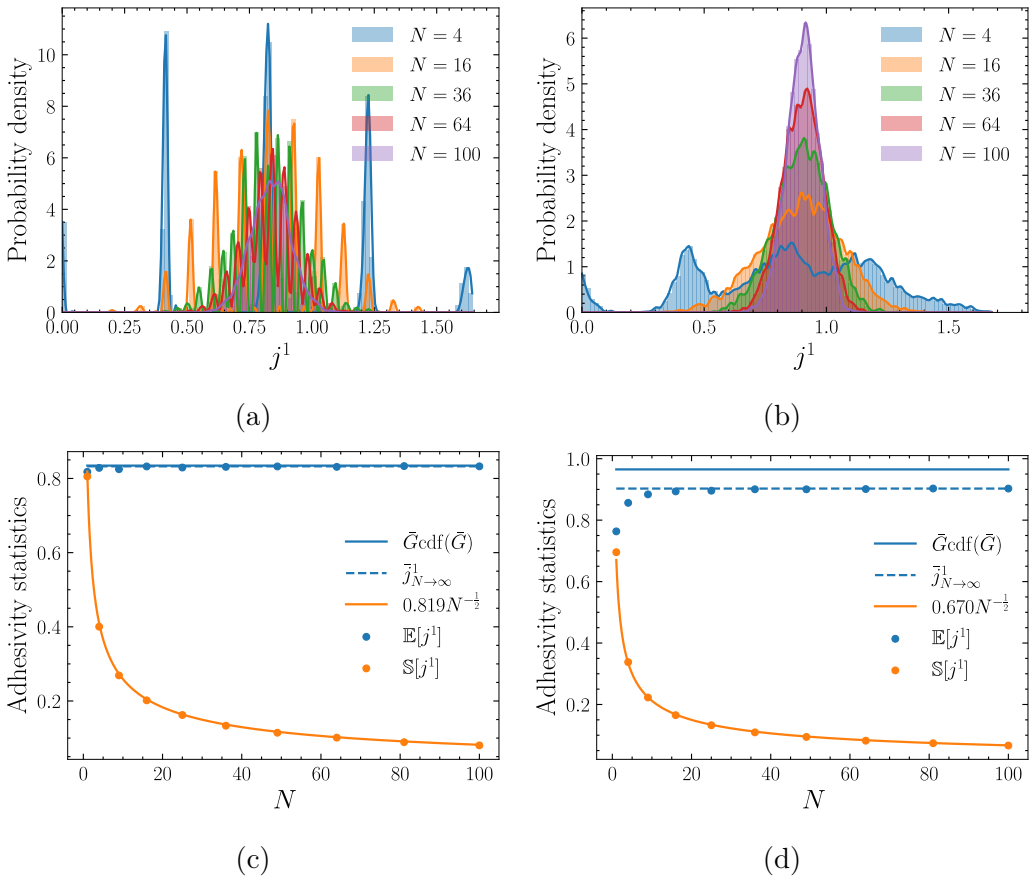

Figure 12.19: Graphs showing how the distribution of samples of the adhesivity, j^1, varies with the cell size, N, in a four-regular network. The parameters are $\mu = 0.5$, $S = 10,000$ and $\sigma = 0.03$ (left) or $\sigma = 0.3$ (right). (a) The case $\sigma = 0.03$. Coloured bars show a histogram of the distribution, $\mathcal{J}$, of the adhesivity, j^1, for various N. Correspondingly coloured lines interpolate the histogram at bar midpoints, to show an approximate PDF of $\mathcal{J}$. (b) A similar plot to (a), but using $\sigma = 0.3$. (c) The mean (blue dots) and standard deviation (orange dots) of the adhesivity distribution, $\mathbb{E}[j^1]$ and $\mathbb{S}[j^1]$, as functions of N, for $\sigma = 0.03$. The solid blue curve shows the adhesivity of the mean four-regular network, $\bar{j}_4 = \bar{G}\text{cdf}(\bar{G})$ (as we will show). The dashed blue line shows the approximate mean adhesivity of an infinite non-periodic four-regular network, $\bar{j}^1_{N\to\infty}$, approximated using $N = 100$. Note that this is almost invisible to the eye, since it lies almost exactly below the solid blue line. The solid orange line shows a fit to the standard deviation, achieved by plotting in log-log space. (d) A similar plot to (c), but using $\sigma = 0.3$.

$\Delta^{r^1}_{ij}$ for small f in Figure 12.6 with those in 12.2). Note that the fourth equation holds despite the dependence of the directional pressure drop, $\Delta^{r^1}_{ij}$, on the conductance, since $\sigma \ll 1$.

Next, we note that

$$\mathbb{E}[\Delta^{r^1}_{ij}] = \cos\theta^{\boldsymbol{r}}_{ij}, \tag{12.41}$$

where $\theta_{ij}^{\boldsymbol{r}}$ is the angle that the pore $ij\boldsymbol{r}$ makes with the direction of macroscale pressure gradient (x^1 in the present case). To see this, note that the pore pressure drop is maximal in pores that are parallel to the direction of the pressure gradient, x^1, since flow down these pores contributes solely to the macroscale behaviour. It decreases smoothly as the angle the pore makes with the macroscale flow direction increases. On pores that are transverse to the flow (see Figure 12.13), the pore pressure drop is zero, since flow through these pores does not contribute to flow in the x^1 direction.

Choosing edges in the four-regular cell, without loss of generality, to be aligned exactly parallel and perpendicular to the x^1 direction (and therefore to the flow, see Figure 12.13), it follows, by substituting (12.40) into (12.40), that

$$j^1 \approx -\frac{\bar{G}}{l^1 l^2} \sum_{i=1}^{N} \sum_{j=1}^{N} \sum_{\boldsymbol{r}\in\boldsymbol{\mathcal{R}}} \cos\theta_{ij}^{\boldsymbol{r}} A_{ji}^{-\boldsymbol{r}} H_{ji}^{-r^1}. \tag{12.42}$$

$$= \bar{G}\frac{b^{1\|}}{l^1 l^2}. \tag{12.43}$$

The second equation, (12.43), is a result of the fact that $\cos\theta_{ij}^{\boldsymbol{r}} \neq 0$ only for edges parallel to the flow, so that the sum counts the number of edges parallel to the x^1 direction that block per unit area in the cell, and $b^{1\|}/l^1 l^2$ represents this quantity per unit cell-area. We therefore define

$$\tilde{j}^1 = \bar{G}\frac{b^{1\|}}{l^1 l^2}, \tag{12.44}$$

which we call the approximate-adhesivity, since $j^1 \approx \tilde{j}^1$ by (12.43). The number of blocked pores, $b^{1\|}$, is a random variable drawn from a distribution, $\mathcal{B}^{\|}$ say. From (12.44) we see that the behaviour of the approximate adhesivity, $\tilde{j}^1$, and thus the structure of the adhesivity, $j^1 \sim \mathcal{J}$, is given by the structure of the blocked pore distribution, $b^{1\|} \sim \mathcal{B}^{\|}$, and our aim is to find this. To this end, we recall that (12.28) and (12.29), together with (12.30), imply that when particles with concentration $c^{\max}$ pass through pore $ij\boldsymbol{r}$, it remains unblocked if $c^{\max}G_{ij}^{\boldsymbol{r}} < G_{ij}^{\boldsymbol{r}0}$, but blocks if $c^{\max}G_{ij}^{\boldsymbol{r}} > G_{ij}^{\boldsymbol{r}0}$. Moreover, note that initial conductances, $G_{ij}^{\boldsymbol{r}0}$, are drawn independently and so edges are either blocked or unblocked independently. It follows that the event that pore $ij\boldsymbol{r}$ blocks, $E_{ij}^{\boldsymbol{r}}$, is a two-outcome random variable, and thus a Bernoulli trial with parameter $p = \mathbb{P}[E_{ij}^{\boldsymbol{r}}] = \mathrm{cdf}(c^{\max}\bar{G})$ (see (12.31)), so that

$$E_{ij}^{\boldsymbol{r}} \sim \mathrm{Ber}(\mathrm{cdf}(c^{\max}\bar{G})). \tag{12.45}$$

Since there are $2N$ unique edges in the four-regular cell, and thus N edges parallel to the flow, it follows that the random variable $b^{1\|}$, which is the total number of these that are blocked by the concentration $c^{\max}$, follows a Binomial distribution with parameters $n = N$, and $p = \mathrm{cdf}(c^{\max}\bar{G})$, so that

$$b^{1\|} \sim \mathrm{Bin}\left(N, \mathrm{cdf}\left(c^{\max}\bar{G}\right)\right) \tag{12.46}$$

$$\approx \mathrm{Norm}\left(N\mathrm{cdf}\left(c^{\max}G\right), N\mathrm{cdf}\left(c^{\max}\bar{G}\right)\left(1-\mathrm{cdf}\left(c^{\max}\bar{G}\right)\right)\right). \tag{12.47}$$

The approximation (12.47) follows from the fact that the normal distribution with parameters $\mu = np$ and $\sigma = \sqrt{np(1-p)}$, $\text{Norm}(np, np(1-p))$, provides a good approximation of the binomial distribution with parameters n and p, $\text{Bin}(n,p)$, if n is large enough or if $p \approx 1/2$ [181]. In our case, $n = N$ and $p = \text{cdf}(c^{\max}\bar{G})$, and we have chosen example initial conductance distributions for which $\text{cdf}(\bar{G}) \approx 1/2$, so that this approximation holds.

We plot samples of the distribution of $b^{1\|}$ for narrower (left) and wider (right) initial conductance distributions in Figures 12.20(a) and 12.20(b) (coloured bars) in the case $c^{\max} = 1$. We see that the samples agree well with both the probability-mass function of the binomial distribution (correspondingly coloured dots) in (12.46) and the probability density function of the normal distribution (correspondingly coloured solid lines) in (12.47). In Figure 12.20(c), meanwhile, we illustrate the mean and standard deviation of $b^{1\|}$. Note that these are approximated well by $N/2$ and $\sqrt{N}/2$ for narrow enough conductance distributions, since $\text{cdf}(\bar{G}) \approx 1/2$ for $\sigma \ll 1$, for example $\sigma = \sigma_N = 0.03$. In Figure 12.20(d), we see that this proxy for the mean of $b^{1\|}$ is less useful for wider conductance distributions, for example $\sigma = \sigma_{\text{W}} = 0.3$, for which $\text{cdf}(\bar{G})$ deviates more extremely from 1/2. The standard-deviation approximation remains useful.

Combining (12.44) with (12.46) and (12.47), we see that

$$\tilde{j}^1 \sim \frac{\bar{G}}{N}\text{Bin}\left(N, \text{cdf}\left(c^{\max}\bar{G}\right)\right) \tag{12.48}$$

$$\approx \frac{\bar{G}}{N}\text{Norm}\left(N\text{cdf}\left(c^{\max}\bar{G}\right), N\text{cdf}\left(c^{\max}\bar{G}\right)\left(1 - \text{cdf}\left(c^{\max}\bar{G}\right)\right)\right), \tag{12.49}$$

where we have used that $l^0 = l^1 = \sqrt{N}$. We have found that the random variable, $\tilde{j}^1$, which we call the approximate adhesivity, follows a scaled binomial distribution, as a result of the fact that the number of edges that are blocked in the cell, $b^{1\|}$, follows a binomial distribution, (12.46). The behaviour of $\tilde{j}^1$ is approximately equal to that of the adhesivity, j^1, due to (12.43), which explains the quasi-discrete behaviour of the adhesivity, illustrated, for example, in Figure 12.19(a).

Some other plots of the adhesivity distribution, $\mathcal{J}$, for particular cell sizes, N, are shown in Figure 12.21, for narrower (left) and wider (right) initial conductance distributions, $\mathcal{G}$. We see that peaks of j^1 (solid blue lines) are distributed near to peaks of $\tilde{j}^1$ (dashed orange lines) (see (12.48)). These are located at values that are $\bar{G}/(l^1 l^2)$ away from each other, due to (12.44). Each location corresponds to the adhesivity that results from blocking a specific number of pores. For example, the first peak corresponds to the case where no pores block, the second to one pore being blocked, and so on. There are $N+1$ such peaks since there are N unique flow-parallel pores in a four-regular cell (plus one peak for the no blocking case). The height of each peak is dictated by the probability that the corresponding number of pores is blocked, given by the distribution of $b^{1\|}$, $\mathcal{B}^{\|}$. The width of each peak depends on the width of $\mathcal{G}$. For example, in Figures 12.21(a,c,e), we see that when $\mathcal{G}$ is narrower, the peaks of j^1 are tight around peaks of the binomial distribution, $\tilde{j}^1$, in (12.48). On the other hand, when $\mathcal{G}$ is wider, as is illustrated in Figures 12.21(b,d,f), the binomial

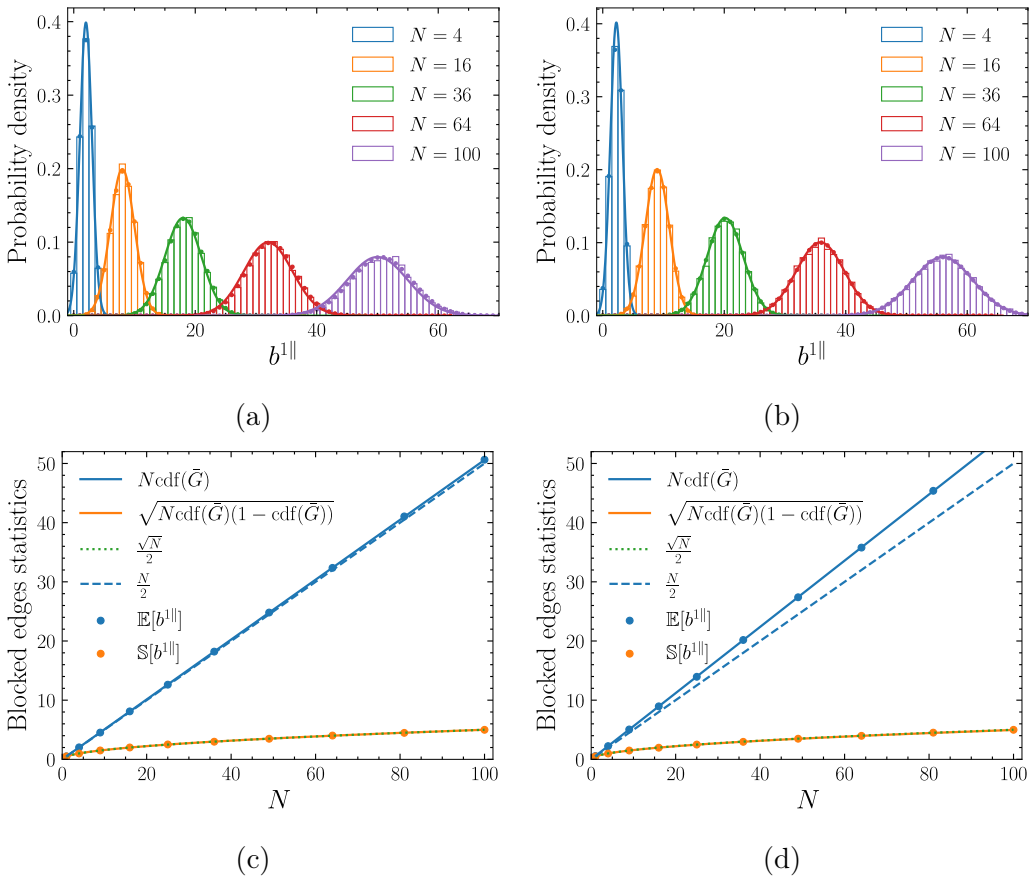

Figure 12.20: Graphs showing how the distribution of samples of the number of blocked flow-parallel pores, $b^{1\|}$, varies with the cell size, N, in a four-regular network. The parameters are $\mu = 0.5$, $S = 10,000$ and $\sigma = 0.03$ (left) or $\sigma = 0.3$ (right). (a) The case $\sigma = 0.03$. Coloured bars show a histogram of samples of the distribution of blocked flow-parallel pores, $\mathcal{B}^{\|}$, for various N. The binomial distribution that this approximates is plotted with correspondingly coloured dots for each N. The normal distribution that this approximates is plotted with correspondingly coloured solid curves for each N. (b) A similar plot to (a), but using $\sigma = 0.3$. (c) The mean (blue dots) and standard deviation (orange dots) of the blocked flow-parallel pore distribution, $\mathbb{E}[b^{1\|}]$ and $\mathbb{S}[b^{1\|}]$, as functions of N, for $\sigma = 0.03$. The solid blue line shows the mean of the corresponding binomial distribution, $np = N\mathrm{cdf}(\bar{G})$. The dashed line shows an approximation of the mean, $N/2$, which holds since we chose $\bar{G} \approx 1/2$. The solid orange line shows the standard deviation of the corresponding binomial distribution, $(np(1-p))^{1/2} = (N\mathrm{cdf}(\bar{G})(1-\mathrm{cdf}(\bar{G})))^{1/2}$. The dotted green line shows an approximation of the standard deviation, $\sqrt{N}/2$, which holds since we chose $\bar{G} \approx 1/2$. (d) A similar plot to (c), but using $\sigma = 0.3$.

structure of j^1 is mostly lost, due to the increased spread in pore pressure drops, Δ_{ij}^{r1}, caused by the increased width of initial conductances, $G_{ij}^{\boldsymbol{r}0}$, via the cell problem, (12.11). Despite the loss of overall binomial structure, the upper and lower limits of the approximate-adhesivity distribution, $\tilde{j}^1$, remain useful to bound the overall width

of $\mathcal{J}$. Indeed, as can be seen in Figure 12.21, values of j^1 always lie between 0, which occurs when no edges block, and the maximal value of $\tilde{j}^1$, $\bar{G}$, which occurs when N edges (the number of edges parallel to the x^1 direction) block.

Finite cell error

In further analogy with the permeability (see Figures 12.16(c) and 12.16(d)), in Figures 12.19(c) and 12.19(d), we firstly see that the mean adhesivity of the cell of size N, $\mathbb{E}[j^1]$, becomes an increasingly accurate approximation of the mean adhesivity of the non-periodic network, $\bar{j}^1_{N\to\infty}$, as N increases. As with the permeability, the convergence occurs at approximately the same rate for all initial conductance distributions considered. Indeed, we find that the difference between the mean adhesivity of the cell of size N, $\mathbb{E}[j^1]$, and the mean adhesivity of the non-periodic random network, $\bar{j}^1_{N\to\infty}$ (as a fraction of $\bar{j}^1_{N\to\infty}$), satisfies

$$E^j_{\mathrm{c}} = \frac{|\mathbb{E}[j^1] - \bar{j}^1_{N\to\infty}|}{\bar{j}^1_{N\to\infty}} \approx \beta N^{-1}, \tag{12.50}$$

where β depends on σ. Consequently, $\mathbb{E}[j^1] \to \bar{j}^1_{N\to\infty}$ as $N \to \infty$. We interpret E^j_{c}, which we plot in Figure 12.22, as the error that we make in the adhesivity parameter (note the superscript, j) when we replace the random network with a cell (note the subscript, c) of size N. Comparing (12.50) to (12.33), we see that, as the size of the cell, N, grows, this error decreases like N^{-1}, just as the corresponding permeability error does. For the adhesivity, when $\sigma = 0.3$, averaging of samples of a cell of size $N = 9$ leads to an underestimate of the mean adhesivity of the infinitely-large non-periodic random network of approximately 2% (see the dashed green line in Figure 12.22(b)), while a cell of size $N = 4$ leads to an underestimate of only approximately 4.2% (see the dashed orange line in Figure 12.22(b)). Note that, although the adhesivity error for a given cell size is larger than the corresponding permeability error (by comparing Figures 12.17 and 12.22), these adhesivity errors are still modest. This result suggests that the multiscale system may be able to capture the behaviour of the corresponding system defined on a non-periodic network, despite containing a reaction term (via the adhesivity) as well as an advection term (via the permeability) (see (12.3)). The computational complexity of the adhesivity, (12.9), is approximately equal to that of the permeability, (12.7), since they rely on solution of the same cell problem, (12.11). It follows that this result, (12.50), offers considerable reduction in the complexity of solving the effective system even when it contains a reaction term, by replacing the network with a smaller cell.

Mean network error

Secondly, in Figure 12.20, we note that $\bar{j}^1_{N\to\infty}$ is close to (but larger than) $\bar{G}\mathrm{cdf}(c^{\max}\bar{G})$ (with $c^{\max} = 1$). To understand this, note that one important application of the approximate-adhesivity distribution, $\tilde{j}^1$, which is distributed as in (12.48), is that it can be used to approximate the mean of the adhesivity distribution, $\mathbb{E}[j^1]$. Since

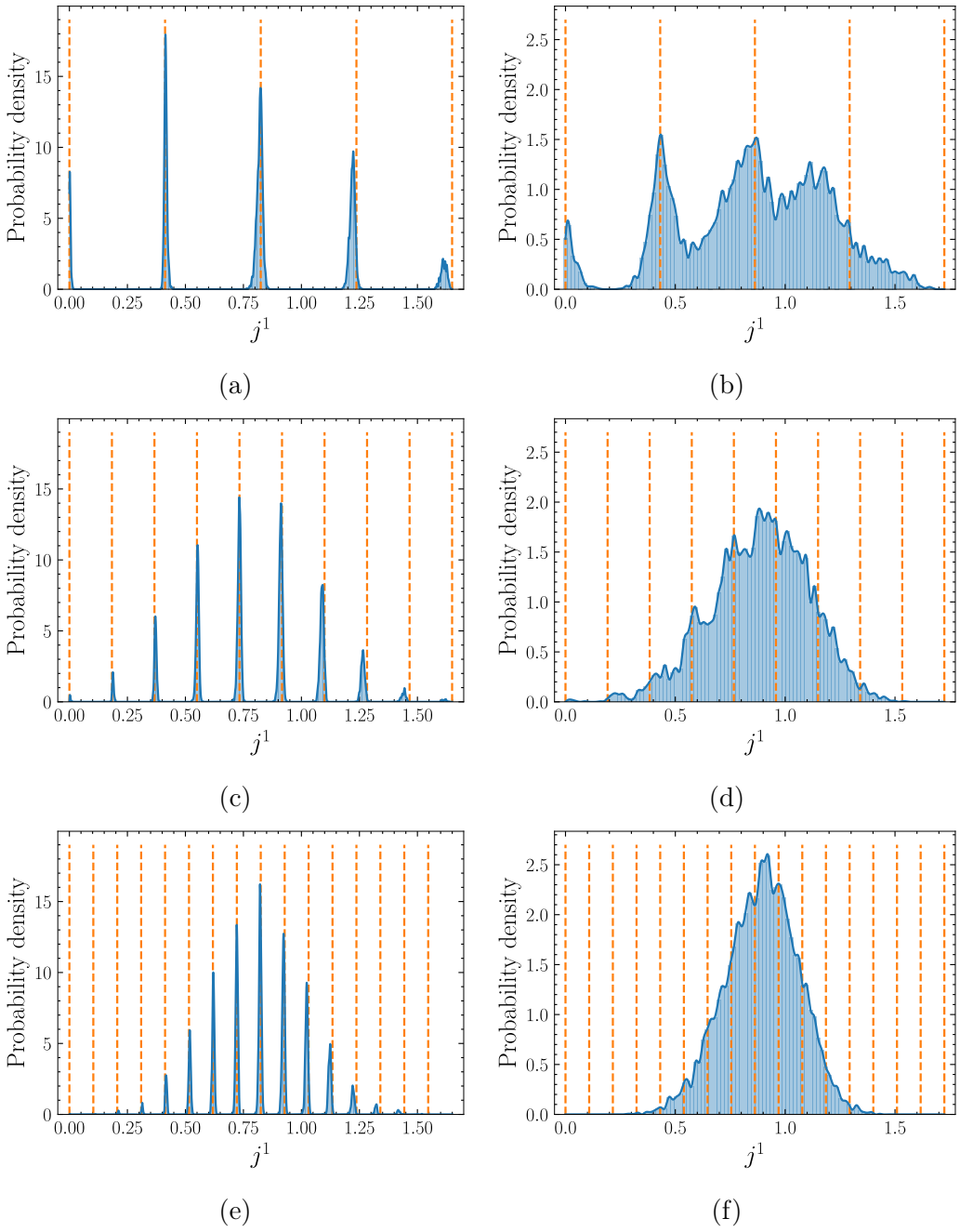

Figure 12.21: Graphs showing the distribution of samples of the adhesivity, j^1, in a four-regular network. The parameters are $\mu = 0.5$, $S = 10,000$ and $\sigma = 0.03$ (left) or $\sigma = 0.3$ (right). Coloured bars show a histogram of the distribution, $\mathcal{J}$, of the adhesivity, j^1. Correspondingly coloured lines interpolate the histogram at bar midpoints, to show an approximate pdf of $\mathcal{J}$. Dashed orange lines show the discrete locations at which probability in the distribution of the approximate adhesivity, $\tilde{j}^1$, is found. (a) $N = 4$ and $\sigma = 0.03$. (b) $N = 4$ and $\sigma = 0.3$. (c) $N = 9$ and $\sigma = 0.03$. (d) $N = 9$ and $\sigma = 0.3$. (e) $N = 16$ and $\sigma = 0.03$. (f) $N = 16$ and $\sigma = 0.3$.

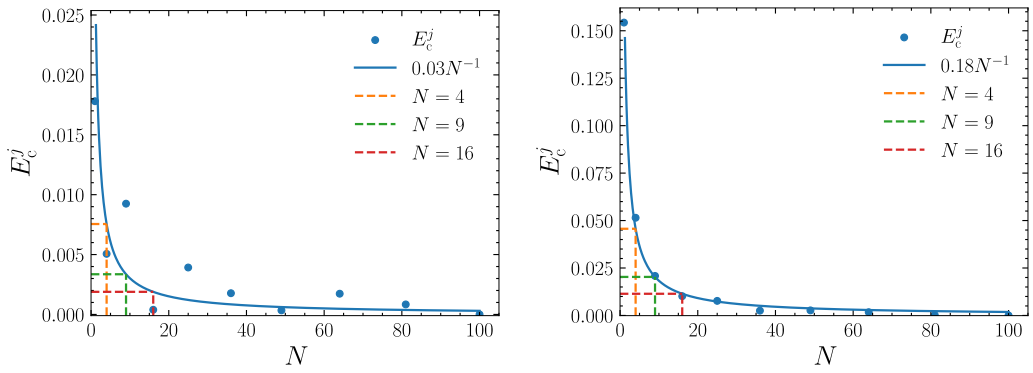

(a) (b)

Figure 12.22: Graphs showing how the finite cell error, E_c^j, varies with the cell size, N. The parameters are $\mu = 0.5$, $S = 10,000$ and $\sigma = 0.03$ (left) or $\sigma = 0.3$ (right). Blue dots show the numerical result. Solid blue lines show a fitting. The errors that result from using cells of size $N = 4$ (orange), $N = 9$ (green), and $N = 16$ (red) are approximated in coloured dashed lines. (a) The case $\sigma = 0.03$. (b) The case $\sigma = 0.3$.

the expected value of a random variable that follows a binomial distribution with parameters n and p is np, it follows from (12.48) that

$$\mathbb{E}[\tilde{j}^1] = \bar{G}\text{cdf}(\bar{G}), \tag{12.51}$$

and consequently that

$$\mathbb{E}[j^1] \approx e^{\mu+\frac{\sigma^2}{2}}\text{cdf}\left(e^{\mu+\frac{\sigma^2}{2}}\right), \tag{12.52}$$

where we have used the approximation (12.43)and the definition of $\bar{G}$. One immediate consequence is that the adhesivity of the mean network is given by $\bar{j}_4 = \bar{G}\text{cdf}(\bar{G})$ (when $c^{\max} = 1$). To see why, note that, in the mean network, the adhesivity is $\bar{G}$, since $\text{cdf}(\bar{G}) = 1$ because all edges have a conductance equal to the mean. The value $0 \leq \text{cdf}(c^{\max}\bar{G}) \leq 1$ is a scaling that accounts for the fact that, in more general networks, not all edges block because edge conductances are distributed about the mean. For wider initial conductance distributions (see Figure 12.19(d)), the difference between $\bar{j}^1_{N\to\infty}$ and $\bar{G}\text{cdf}(\bar{G})$ is more pronounced, while for narrower cases (see Figure 12.19(c)) the difference is smaller. Indeed, we find that the difference between the scaled adhesivity of the mean network, $\bar{j}_4 = \bar{G}\text{cdf}(\bar{G})$, and the mean adhesivity of the non-periodic random network, $\bar{j}^1_{N\to\infty}$ (as a fraction of $\bar{j}^1_{N\to\infty}$), satisfies

$$E_n^j = \frac{\left|\bar{G}\text{cdf}(\bar{G}) - \bar{j}^1_{N\to\infty}\right|}{\bar{j}^1_{N\to\infty}} \approx 0.45\sigma^{\frac{3}{2}}, \tag{12.53}$$

(in the case $c^{\max} = 1$), so that

$$\bar{j}^1_{N\to\infty} \to \bar{G}\text{cdf}(\bar{G}) = e^{\mu+\frac{\sigma^2}{2}}\left(\frac{1}{2}\left(1 + \text{erf}\left(\frac{\log(e^{\mu+\frac{\sigma^2}{2}}) - \mu}{\sigma\sqrt{2}}\right)\right)\right) \tag{12.54}$$

as $\sigma \to 0$, where we have used the formula for the cumulative-density function of a log-normal distribution, and the definition of $\bar{G}$. We interpret this quantity, E_{n}^{j}, which we plot in Figure 12.23, as the error we make when we replace the adhesivity (hence the superscript, j) of the random network with the scaled adhesivity associated with the mean network (hence the subscript, n). The implication of (12.53) is that, as σ decreases, so that the initial conductance distribution narrows, the size of this error decreases like $\sigma^{3/2}$. Note that this decay is not as fast as that of the permeability in (12.34), which is $\mathcal{O}(\sigma^2)$. However, use of $\bar{G}\mathrm{cdf}(\bar{G})$ in place of $\bar{j}^1|_{N\to\infty}$ would lead to an error in the mean adhesivity of the infinitely-large non-periodic random network of approximately 7.4% for $\sigma = 0.3$ and approximately 0.25% for $\sigma = 0.03$ (see green and orange dashed lines in Figure 12.23), compared to 4.4% and 0.04% for the permeability (compare to the green and orange dashed lines in Figure 12.18). As for the permeability (see (12.35)), (12.54) provides an estimate for the mean adhesivity that only depends on the statistics of the initial conductance distribution, μ and σ. As such, if we accept the associated error, E_{n}^{j}, using (12.54) avoids the need for sampling of the adhesivity, (12.9), and consequently the need for solution of the cell problem, (12.11). The result is a significant reduction of the computational complexity associated with solution of the effective system.

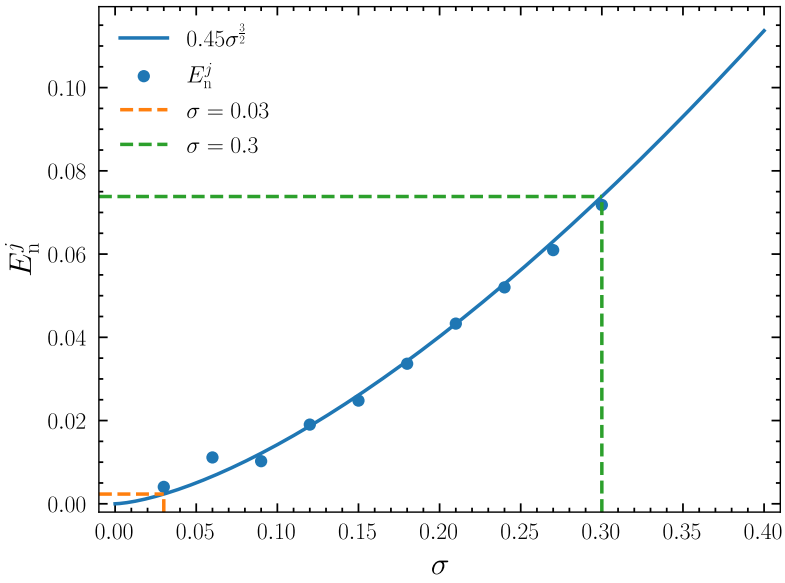

Figure 12.23: Graph showing how the mean network error, E_{n}^{j}, varies with the standard deviation of the initial conductance distribution, σ. Blue dots show the numerical result. Solid blue lines show a fitting. The errors that result from replacing a network consisting of cells containing initial conductances drawn from distributions with standard deviations of $\sigma = 0.03$ and $\sigma = 0.3$ with the mean network are approximated with a dashed orange and green lines, respectively.

Sampling error

Thirdly, note that, in Figures 12.19(c) and 12.19(d), the standard deviation of the adhesivity, $\mathbb{S}[j^1]$, decays with N like $N^{-1/2}$, as did the standard deviation of the permeability, $\mathbb{S}[k^{11}]$ (compare to Figures 12.16(c) and 12.16(d)). Thus, our arguments extend readily to cases of non-zero adhesivity. Firstly, that is, we might accept the errors associated with replacement of $\mathbb{E}[j^1]$ with either $\bar{j}^1_{N\to\infty}$ or $\bar{G}\mathrm{cdf}(c^{\max}\bar{G})$, in (12.50) and (12.53), since these are smaller than the average sample error. Secondly, as with the permeability, the $\mathcal{O}(N^{-1/2})$ decay of the standard deviation of the adhesivity indicates that it is better to average over many realisations of a relatively small unit cell than to average over just a few realisations of a large unit cell.

12.3.3 Six-regular structure

Four-regular networks are commonly used, partly because they are easy to visualise and program. However, they are not an accurate characterisation of the random networks that represent the microscale of porous material, even when the conductances of their pores are distributed randomly. The average degree of porous media networks is often larger than four, and is usually around six. Even when edges have the same resistance per unit length, this difference in average degree has a significant impact on effective properties, such as permeability and adhesivity. To demonstrate this, we next consider a six-regular network, in which each node is connected to exactly six other nodes in a regular lattice.

To construct a six-regular network, we first consider the basic cell illustrated in Figure 12.24. The lengths of its sides are $L^1 = s$ and $L^2 = \sqrt{3}s$, where s is a scale factor chosen to maintain unit node density, to aid comparison of the effective properties with those of the four-regular network. There are two nodes in the basic cell, at positions $(0, 0)$ and $(s/2, (\sqrt{3}s)/2$, and it follows that $s^2 = 2/\sqrt{3}$. We draw initial conductances from the same log-normal distributions as before, but scale the results so that the pore resistance per unit length is the same as in the four-regular network ($\approx 1/1.72$). Cells of size $N = 2n^2$ for $n \in \{1, 2, \ldots 9, 10\}$ are then constructed by repeating n copies of the basic cell in the x^1 and x^2 directions (see Figure 12.24).

12.3.3.1 Permeability

We plot samples of the permeability distribution, $\mathcal{K}$, and their statistics, $\mathbb{E}[k^{11}]$ and $\mathbb{S}[k^{11}]$ in Figure 12.25 (similarly to the four-regular case in Figure 12.16). Our plots in Figures 12.25(b) and 12.25(d) agree well (up to the randomness caused by sampling) with those in [80] (Figure 4). Qualitatively, we see that behaviour of $\mathcal{K}$ is similar to that in the four-regular network. As the cell size increases, the permeability distribution tightens around a value that is close to the permeability, $\bar{k}_6$ say, of the mean network, which is a six-regular network in which all pores have the mean conductance per unit length, $\bar{G}$. However, as expected, we see that the permeability of the six-regular networks is much larger than that of the four-regular networks, owed to the larger average degree. We find that $\bar{k}_6 \approx 2.66$, which is substantially larger than

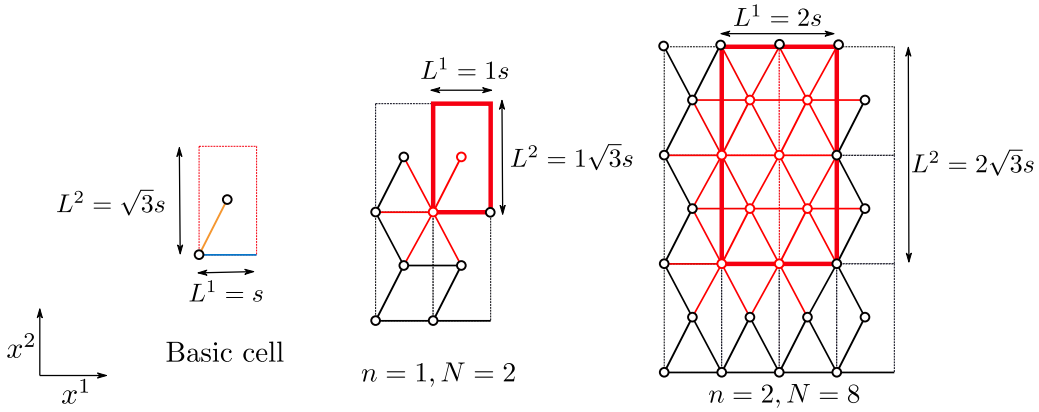

Figure 12.24: Diagram of the basic construction cell and six-regular cells of sizes $N = 2$ and $N = 8$ ($N = 2n^2$ for $n = 1$ and $n = 2$) inside larger networks. For each N, nodes and edges that are part of the cell are coloured red, and the cell is highlighted with a red box. The dimensions of the cell are set to be $L^1 = ns$ and $L^2 = \sqrt{3}ns$ for $s^2 = 2/\sqrt{3}$, so that the node density, ϱ, satisfies $\varrho = 1$ in a cell of any size, N. Consequently, the length of each pore $ij\boldsymbol{r}$ is $L^{\boldsymbol{r}}_{ij} = ns$. We arbitrarily choose the x^1 direction to be from left to right. Thus, horizontal edges, like the blue edge in the basic cell, are parallel to the pressure gradient, and thus the flow. We call these flow-parallel edges. Diagonal edges, like the orange edge in the basic cell, are at an angle $\theta^{\boldsymbol{r}}_{ij} = \pi/3$ to the flow, so that $\cos(\theta^{\boldsymbol{r}}_{ij}) = 1/2$. We call these flow-diagonal edges.

$\bar{k}_4 \approx 1.72$. The distribution of the permeability in the smallest cell, $k^{11}_{N=2}$, is no longer the same as the initial conductance distribution, $\mathcal{G}$, and has a larger mean, because in a six-regular configuration there are three unique edges (rather than one in the four-regular case) to conduct flow.

Finite cell error

Observing Figures 12.25(c) and 12.25(d), we see that as N increases, the average permeability of the cell, $\mathbb{E}[k^{11}]$ (blue dots) approaches the approximate average permeability of the entire network, $\bar{k}^{11}_{N\to\infty}$ (dashed blue line). Thus, as before, the error in the permeability that we make when we replace an infinitely large network with a cell of finite size N, E^k_{c}, decreases with N. The behaviour of this function is similar to that in the four-regular case, so we do not repeat our analysis here. The implication, however, is that this error is always relatively small. Even use of the smallest cell, $N = 2$, only produces an overestimation of $E^k_{\mathrm{c}} \approx 3\%$ when $\sigma = 0.3$. This is larger than a similarly sized cell in the four-regular case, but still modest.

Mean network error

Secondly, comparing the dashed blue line with the solid blue line in Figures 12.25(c) and 12.25(d), we see that $\bar{k}^{11}_{N\to\infty}$ is not equal to $\bar{k}_6$. That is, because permeability is a function of the conductances, as well as structure, the error we make when we

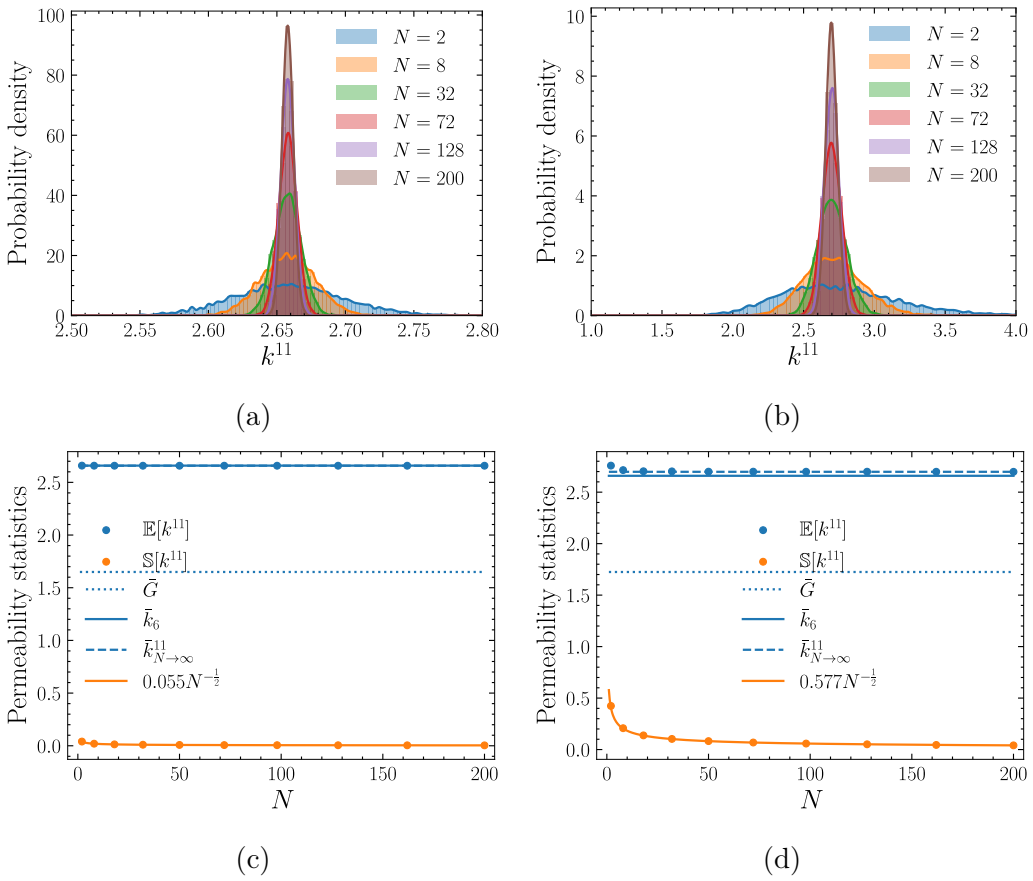

Figure 12.25: Graphs showing how the distribution of samples of the permeability, k^{11}, varies with the cell size, N, in a six-regular network. The parameters are $\mu = 0.5$, $S = 10,000$ and $\sigma = 0.03$ (left) or $\sigma = 0.3$ (right). (a) The case $\sigma = 0.03$. Coloured bars show a histogram of the distribution, $\mathcal{K}$, of the permeability, k^{11}, for various N. Correspondingly coloured lines interpolate the histogram at bar midpoints, to show an approximate PDF of $\mathcal{K}$. (b) A similar plot to (a), but using $\sigma = 0.3$. (c) The mean (blue dots) and standard deviation (orange dots) of the permeability distribution, $\mathbb{E}[k^{11}]$ and $\mathbb{S}[k^{11}]$, as functions of N, for $\sigma = 0.03$. The solid blue curve shows the permeability of the mean six-regular network, $\bar{k}_6$. The dashed blue line shows the approximate mean permeability of an infinite non-periodic six-regular network, $\bar{k}^{11}_{N\to\infty}$, approximated using $N = 200$. Note that this is almost invisible to the eye, since it lies almost exactly below the solid blue line. The solid orange line shows a fit to the standard deviation, achieved by plotting in log-log space. The dotted blue line shows the mean conductance $\bar{G}$, which is also the permeability of the mean four-regular network, $\bar{k}_4$. (d) A similar plot to (c), but using $\sigma = 0.3$.

replace the random network with the mean network, E^k_{n}, is non-zero. However, as in the four-regular case, this error is small, and decreases proportionally to the variance of the conductance distribution, σ^2. As such, in Figure 12.25(c), for example, we see that when $\sigma \ll 1$, this error is infinitesimal.

Sampling error

Thirdly, in Figures 12.25(c) and 12.25(d), we see that the standard deviation of the permeability (see orange dots) decreases like $N^{-1/2}$ (see orange lines), which is the same rate as in the four-regular scenario. It remains computationally advantageous to sample a small cell many times, if the goal is to obtain the average permeability of a large network.

12.3.3.2 Adhesivity

Next, in Figure 12.26, we plot samples of the adhesivity distribution, $\mathcal{J}$, for the six-regular network (similarly to the four-regular case in Figure 12.19). As with the permeability, the adhesivity of the six-regular network is also larger than that of the four-regular network, because there are more pores per cell with the potential to become blocked. Qualitatively, the behaviour of the distribution is similar to that in the four-regular case. As the cell size increases, the adhesivity distribution narrows and the value $j^{11}_{N\to\infty}$ becomes more likely. As before, for each cell size, the adhesivity is distributed between a discrete set of values. These are different from those observed in the four-regular case.

Blocked pore distribution

To predict the values that the adhesivity takes, we analyse the probability distribution for the number of pores that are blocked in the cell. The procedure is similar to before. We begin by noting that

$$j^1 = -\frac{1}{l^1 l^2}\sum_{i=1}^{N}\sum_{j=1}^{N}\sum_{\boldsymbol{r}\in\boldsymbol{\mathcal{R}}} G^{\boldsymbol{r}}_{ij}(W^1_j + r^1 l^1 - W^1_i)A^{-\boldsymbol{r}}_{ji}H^{-r^1}_{ji} \tag{12.55}$$

$$\approx -\frac{\bar{G}}{l^1 l^2}\sum_{i=1}^{N}\sum_{j=1}^{N}\sum_{\boldsymbol{r}\in\boldsymbol{\mathcal{R}}} \mathbb{E}[\Delta^{-r^1}_{ji}]A^{-\boldsymbol{r}}_{ji}H^{-r^1}_{ji} \tag{12.56}$$

$$= -\frac{\bar{G}}{l^1 l^2}\sum_{i=1}^{N}\sum_{j=1}^{N}\sum_{\boldsymbol{r}\in\boldsymbol{\mathcal{R}}} \cos\theta^{\boldsymbol{r}}_{ij}A^{-\boldsymbol{r}}_{ji}H^{-r^1}_{ji}. \tag{12.57}$$

$$= \frac{\bar{G}}{l^1 l^2}(b^{1\parallel} + \frac{1}{2}b^{1\angle}), \tag{12.58}$$

where we have used the relationship between the pore pressure drop and the angle that the pore makes with the flow direction, (12.41). That is, this time there are two types of pore in the network: flow-parallel pores and flow-diagonal pores, see Figure 12.24. As before, the expected pressure drop in pores $ij\boldsymbol{r}$ that are parallel to the flow is $\Delta^{-r^1}_{ji} = \cos(0) = 1$. The expected pressure drop in pores $ij\boldsymbol{r}$ that are diagonal to the flow is $\Delta^{-r^1}_{ji} = \cos(\pi/3) = 1/2$. We define b^1 to be the number of pores that are blocked in the cell, drawn from the distribution $\mathcal{B}$. Of these, $b^{1\parallel}$ is the number of

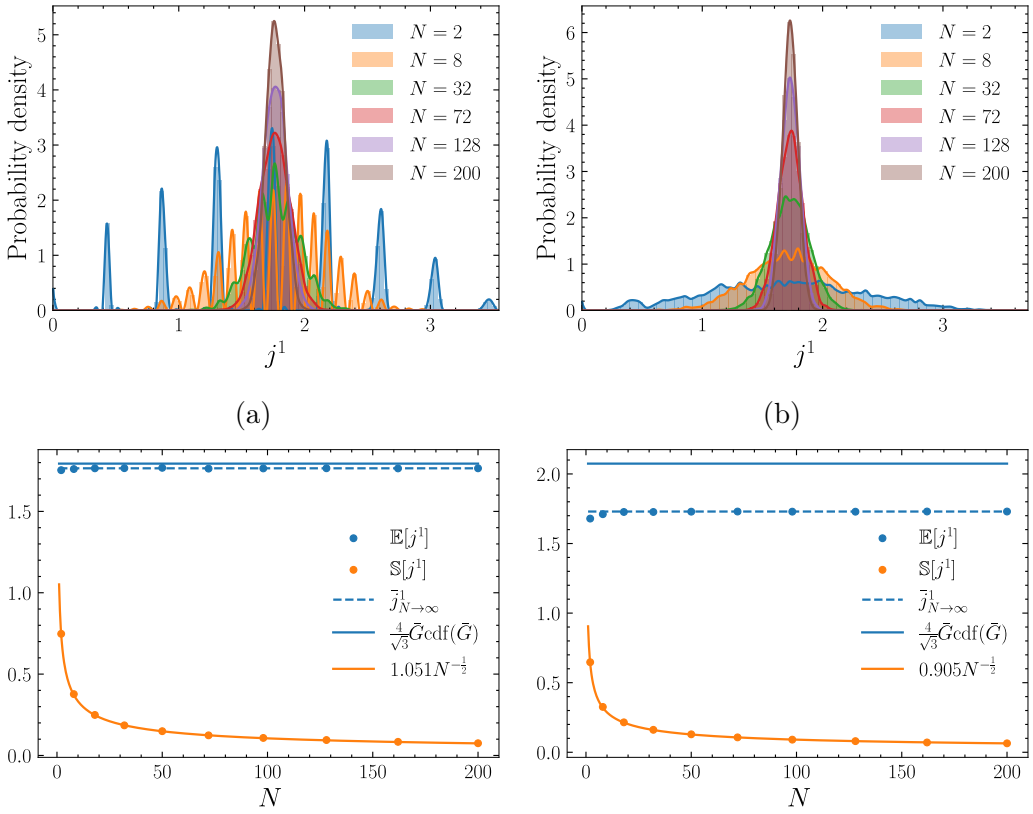

Figure 12.26: Graphs showing how the distribution of samples of the adhesivity, j^1, varies with the cell size, N, in a six-regular network. The parameters are $\mu = 0.5$, $S = 10,000$ and $\sigma = 0.03$ (left) or $\sigma = 0.3$ (right). (a) The case $\sigma = 0.03$. Coloured bars show a histogram of the distribution, $\mathcal{J}$, of the adhesivity, j^1, for various N. Correspondingly coloured lines interpolate the histogram at bar midpoints, to show an approximate pdf of $\mathcal{J}$. (b) A similar plot to (a), but using $\sigma = 0.3$. (c) The mean (blue dots) and standard deviation (orange dots) of the adhesivity distribution, $\mathbb{E}[j^1]$ and $\mathbb{S}[j^1]$, as functions of N, for $\sigma = 0.03$. The solid blue curve shows the adhesivity of the mean six-regular network, $\bar{j}_6 = (4/\sqrt{3})\bar{G}\mathrm{cdf}(\bar{G})$ (as we will show). The dashed blue line shows the approximate mean adhesivity of an infinite non-periodic six-regular network, $\bar{j}^1_{N\to\infty}$, approximated using $N = 200$. Note that this is almost invisible to the eye, since it lies almost exactly below the solid blue line. The solid orange line shows a fit to the standard deviation, achieved by plotting in log-log space. (d) A similar plot to (c), but using $\sigma = 0.3$.

blocked flow-parallel pores, with distribution $\mathcal{B}^{\parallel}$, while $b^{1\angle}$ is the number of blocked flow-diagonal pores, with distribution $\mathcal{B}^{\angle}$. Therefore, we define

$$\tilde{j}^1 = \frac{\bar{G}}{l^1 l^2}(b^{1\parallel} + \frac{1}{2}b^{1\angle}), \tag{12.59}$$

and call this the approximate adhesivity for the six-regular network, since we have shown that $j^1 \approx \tilde{j}^1$ in (12.58). To evaluate the approximate adhesivity, $\tilde{j}^1$, we must analyse the structure of the distributions for blocked pores, $\mathcal{B}$, $\mathcal{B}^{\parallel}$, and $\mathcal{B}^{\angle}$, as before.

Proceeding similarly to the four-regular case, we note that the event that pore $ij\boldsymbol{r}$ blocks due to the concentration $c^{\max}$ is a Bernoulli trial with probability $p = \text{cdf}(c^{\max}\bar{G})$, as in (12.45). This time, there are $3N$ unique edges in the cell (see Figure 12.24). It follows that the number of pores that block due to the concentration $c^{\max}$, b^1, should be drawn from a binomial distribution with parameters $n = 3N$ and $p = \text{cdf}(c^{\max}\bar{G})$, so that

$$b^1 \sim \text{Bin}(3N, \text{cdf}(c^{\max}\bar{G})) \tag{12.60}$$

$$\approx \text{Norm}(3N\text{cdf}(c^{\max}\bar{G}), 3N\text{cdf}(c^{\max}\bar{G})(1 - \text{cdf}(c^{\max}\bar{G}))). \tag{12.61}$$

We plot samples of $\mathcal{B}$ in Figure 12.27, and compare these to the theoretical distributions that we have derived in (12.60) and (12.61). We see that the distributions match as expected, and that the normal approximation (12.61) is almost exact, since $p = \text{cdf}(c^{\max}\bar{G}) \approx 1/2$, as in the four-regular case.

One of every three unique edges in the six-regular network is flow-parallel, with the other two being flow-diagonal (see Figure 12.24). It follows that we expect the number of flow-parallel pores that are blocked to satisfy

$$b^{1\parallel} \sim \text{Bin}(N, \text{cdf}(c^{\max}\bar{G})) \tag{12.62}$$

$$\approx \text{Norm}(N\text{cdf}(c^{\max}\bar{G}), N\text{cdf}(c^{\max}\bar{G})(1 - \text{cdf}(c^{\max}\bar{G}))), \tag{12.63}$$

and the number of flow-diagonal pores that are blocked to satisfy

$$b^{1\angle} \sim \text{Bin}(2N, \text{cdf}(c^{\max}\bar{G})) \tag{12.64}$$

$$\approx \text{Norm}(2N\text{cdf}(c^{\max}\bar{G}), 2N\text{cdf}(c^{\max}\bar{G})(1 - \text{cdf}(c^{\max}\bar{G}))). \tag{12.65}$$

Note that the theoretical distribution of blocked flow-parallel pores, (12.62), is identical to that in the four-regular case, (12.46). This helps to explain why we see a substantially larger adhesivity in the six-regular network (see the dashed blue lines in Figure 12.26) than in the four-regular network (compare to the dashed blue lines in Figure 12.19). The same average number of flow-parallel pores block, $np = N\text{cdf}(c^{\max}\bar{G})$, but, on average, $np = 2N\text{cdf}(c^{\max}\bar{G})$ flow-diagonal pores also block, which contributes to the adhesivity of the network, since these have non-zero pore pressure drop in the flow direction, $\Delta_{ij}^{r^1} = 1/2$. We plot samples of $\mathcal{B}^{1\parallel}$ and $\mathcal{B}^{1\angle}$ in Figure 12.28. As we expect, samples are distributed binomially subject to (12.62) and (12.64), with any small difference due to slight undersampling. The accuracy of the normal approximations, (12.62) and (12.64), increases with the cell size, N, as we would expect.

We plot samples of j^1 (blue lines), and the values at which peaks in the distribution $\tilde{j}^1$ occur (orange lines) in Figure 12.29 (compare with the four-regular case in Figure 12.21(d)). We see that j^1 is indeed well approximated by the distribution of $\tilde{j}^1$, as we predicted in (12.58). From (12.59), we see that $\tilde{j}^1$ is dictated by the distributions of $b^{1\parallel}$ and $b^{1\angle}$, (12.62) and (12.64), and so we see that distinct peaks of j^1 occur close

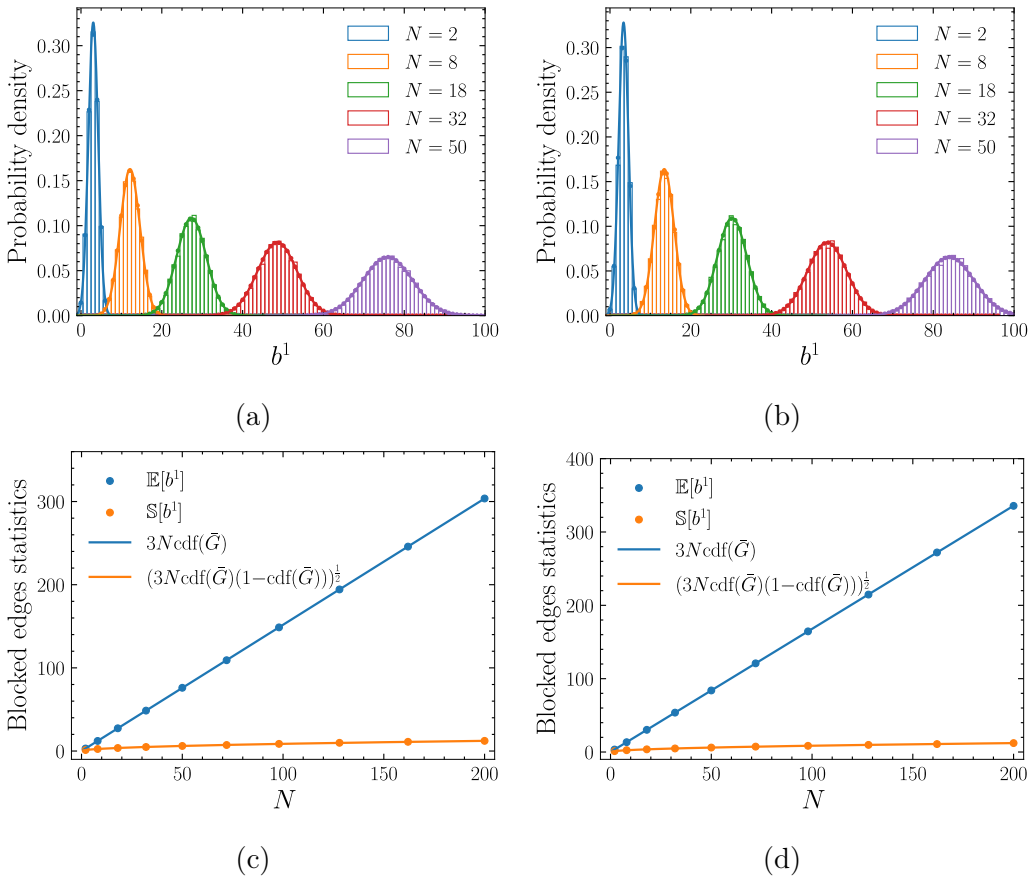

Figure 12.27: Graphs showing how the distribution of samples of the number of blocked pores, b^1, varies with the cell size, N, in a six-regular network. The parameters are $\mu = 0.5$, $S = 10,000$ and $\sigma = 0.03$ (left) or $\sigma = 0.3$ (right). (a) The case $\sigma = 0.03$. Coloured bars show a histogram of samples of the distribution of blocked pores, $\mathcal{B}$, for various N. The corresponding binomial distribution is plotted with correspondingly coloured dots for each N. The corresponding normal distribution is plotted with correspondingly coloured solid lines for each N. (b) A similar plot to (a), but using $\sigma = 0.3$. (c) The mean (blue dots) and standard deviation (orange dots) of the blocked pore distribution, $\mathbb{E}[b^1]$ and $\mathbb{S}[b^1]$, as functions of N, for $\sigma = 0.03$. The blue line shows the mean of the corresponding binomial distribution, $np = 3N\mathrm{cdf}(\bar{G})$. The orange line shows the standard deviation of the corresponding binomial distribution, $(np(1-p))^{1/2} = (3N\mathrm{cdf}(\bar{G})(1-\mathrm{cdf}(\bar{G})))^{1/2}$. (d) A similar plot to (c), but using $\sigma = 0.3$.

to discrete values that correspond to different numbers of edges being blocked. This time these values are $\bar{G}/\sqrt{3}N$ apart, since this is the adhesivity that corresponds to a single flow-diagonal pore being blocked. Here, and throughout, the factor of $\sqrt{3}$ emerges from the scaling of l^1 and l^2 to aid comparison with the four-regular case. As before, the widths of the spikes in j^1 are proportional to the standard deviation, σ, of the conductance distribution, $\mathcal{G}$. As a result, when σ is larger, for example $\sigma = 0.3$ in Figures 12.29(b) and 12.29(d), discrete structure is lost, because the contribution

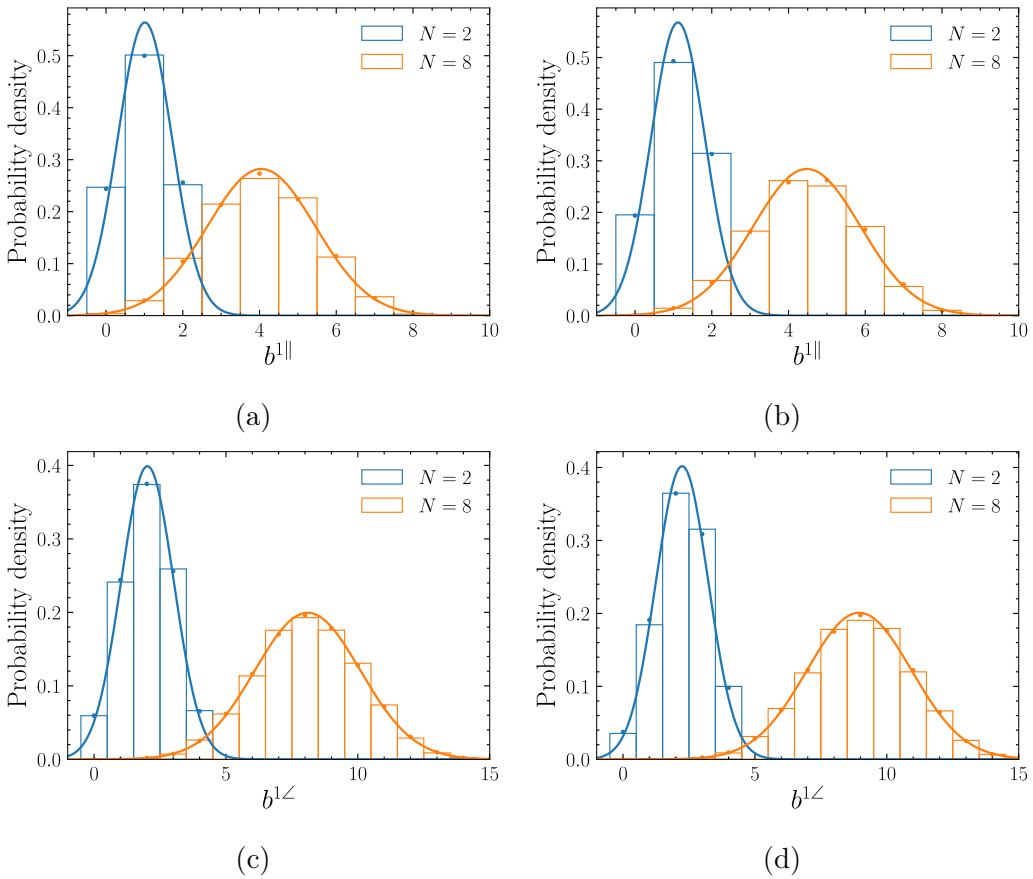

Figure 12.28: Graphs showing the distributions of samples of the number of blocked flow-parallel (top) and flow-diagonal (bottom) pores, $b^{1\parallel}$ and $b^{1\angle}$, for various cell sizes, N, in a six-regular network. The parameters are $\mu = 0.5$, $S = 10,000$ and $\sigma = 0.03$ (left) or $\sigma = 0.3$ (right). The cell sizes are $N = 2$ and $N = 8$. Coloured bars show a histogram of samples of the distribution. The corresponding binomial distribution is plotted with correspondingly coloured dots. The corresponding normal distribution is plotted with correspondingly coloured solid lines. (a) The case $\sigma = 0.03$ for the distribution of $\mathcal{B}^{\parallel}$. (b) The case $\sigma = 0.3$ for the distribution of $\mathcal{B}^{\parallel}$. (c) The case $\sigma = 0.03$ for the distribution of $\mathcal{B}^{\angle}$. (d) The case $\sigma = 0.3$ for the distribution of $\mathcal{B}^{\angle}$.

to the adhesivity from one particular number of pores being blocked merges with that of another. The width of the overall distribution is bounded by the values that correspond to the cases where no pores and all pores block, respectively.

Finite cell error

Returning to the plots of the adhesivity distribution in Figure 12.26, in Figures 12.26(c) and 12.26(d), we see that as N increases, the average adhesivity of the cell, $\mathbb{E}[j^1]$ (blue dots) approaches the approximate average adhesivity of the network, $\bar{j}^1_{N\to\infty}$ (dashed blue line). Thus, as with the permeability, the adhesivity error that we make when we replace a large network with a smaller cell of size N, E^j_{c}, decreases

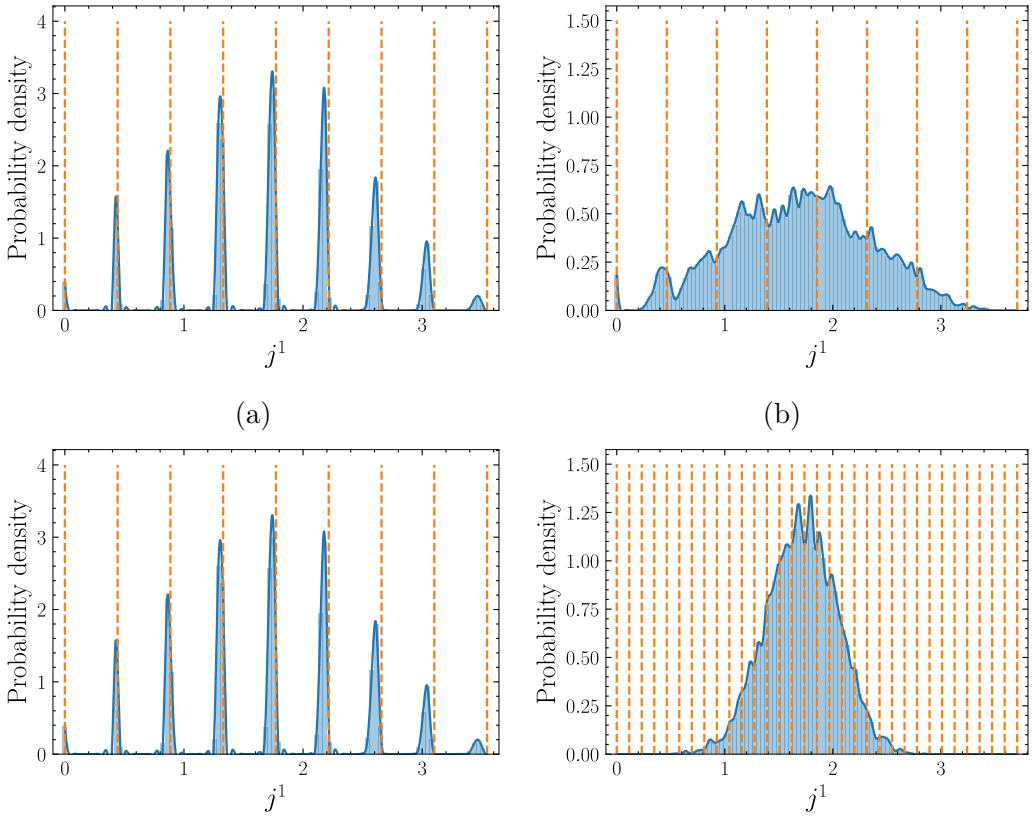

Figure 12.29: Graphs showing the distribution of samples of the adhesivity, j^1, in a six-regular network. The parameters are $\mu = 0.5$, $S = 10,000$ and $\sigma = 0.03$ (left) or $\sigma = 0.3$ (right). Coloured bars show a histogram of the distribution, $\mathcal{J}$, of the adhesivity, j^1. Correspondingly coloured lines interpolate the histogram at bar midpoints, to show an approximate pdf of $\mathcal{J}$. Dashed orange lines show the discrete locations at which probability in the distribution of the approximate adhesivity, $\tilde{j}^1$, is found. (a) $N = 2$ and $\sigma = 0.03$. (b) $N = 2$ and $\sigma = 0.3$. (c) $N = 8$ and $\sigma = 0.03$. (d) $N = 8$ and $\sigma = 0.3$.

with N. For example, in Figure 12.26(d), we see that the blue dots lie on the dashed blue line for cell sizes $N \geq 18$, which demonstrates that relatively small cells capture the behaviour of the adhesivity of six-regular networks, even when the underlying conductance distribution, $\mathcal{G}$, is relatively wide.

Mean network error

As usual, the nonlinearity of the adhesivity formula, (12.9), means that the adhesivity of six-regular networks with random conductances is not equal to that of the mean six-regular network. In fact, when the conductance distribution is wider, comparing the dashed blue line with the solid blue line in Figure 12.26(d), we see that the mean network error, E^j_{n}, that we would make if we used $\bar{j}_6$ in place of $\bar{j}^{11}_{N\to\infty}$, is large

(compared with the equivalent in a four-regular network, for example). For example, this error is around 23% for $\sigma = 0.3$, which is considerably larger than the mean network error associated with the permeability, E_{n}^{k}. On the other hand, when the conductance distribution is more narrow, we see that the error is much smaller. In Figure 12.26(c), we see that when $\sigma = 0.03$, $E_{\mathrm{n}}^{j} \approx 5\%$. The behaviour of E_{n}^{j} with σ is similar to that in the four-regular case, and thus we do not conduct a more detailed analysis here.

Sampling error

Lastly, in Figures 12.26(c) and 12.26(d), we see that the standard deviation of the adhesivity (see orange dots) decreases like that of the permeability, proportionally to $N^{-1/2}$ (see orange lines), so that the disadvantages of larger sampling errors associated with the use of smaller cells are favourable over the disadvantages of larger computational costs associated with using larger cells.

12.3.4 Six-irregular structure

Next, we assess the impact of random connectivity on the effective properties of the network. Our results so far suggest that networks with higher average degree have larger permeability and adhesivity, even when the conductivities of their pores are drawn from the same distribution. We are interested in how well regularly structured networks characterise the effective properties of networks with random structure, since regular networks are computationally cheaper to construct. We focus on six-irregular networks. These have an average degree of six, but individual nodes may be connected to fewer or more than six other nodes.

To construct a cell of this network, an example of which is shown in Figure 12.30, we draw the x^1 and x^2 coordinates of N points from a uniform distribution, and place nodes at these points. We then use a Delaunay triangulation to connect these nodes. We choose the dimensions of each cell to be $L^1 = \sqrt{N}$ and $L^2 = \sqrt{N}$, to preserve unit density, and choose a fixed resistance per unit length (1/1.72, to make comparison with the other two structures simple), so that pore conductances are inversely proportional to the distance between nodes (see the thicknesses of edges in Figure 12.30, which are proportional to their conductance. Shorter edges are thicker and thus have larger conductance). The average degree of the resulting cell is six, which is a property of the Delaunay triangulation method [182].

12.3.4.1 Permeability

We plot samples of the permeability distribution for the six-irregular case in Figure 12.31 (similarly to Figure 12.25). These figures agree well (up to the randomness caused by sampling) with those presented in [80] (Figure 5). The first thing we note is that the qualitative behaviour of $\mathcal{K}$ is relatively similar to that in the four-regular and six-regular cases, despite the fact that the underlying conductance distribution, $\mathcal{G}$, is no longer log-normal. Despite this, in Figure 12.31(a), we see that the distribution has

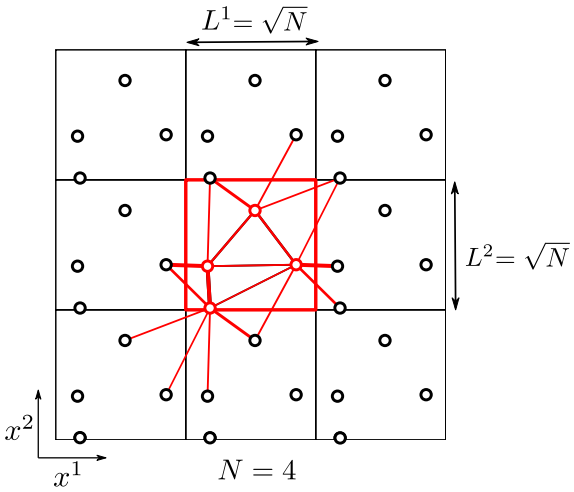

Figure 12.30: Diagram of a cell with size $N = 4$ in a six-irregular network. Nodes and edges that are part of the cell are coloured red, and the cell is highlighted with a red box. The dimensions of the cell are set to be $L^1 = \sqrt{N}$ and $L^2 = \sqrt{N}$ so that the node density, ϱ, satisfies $\varrho = 1$ in a cell of any size, N. Node positions are drawn uniformly, and edge lengths are drawn from the distribution that results from node positions and the triangulation. Edge thicknesses are proportional to their inverse lengths, so that shorter edges are thicker.

multiple peaks when the cell size is relatively small. This is particularly noticeable in the case $N = 4$ (blue line), for example. These peaks are real and are due to variance in the ratio of inter- and intra-cell pores when N is smaller, as opposed to being caused by undersampling. This variance is not present in regular structures (see Figure 12.25, for example), since the number of pores that cross cell boundaries does not vary from sample to sample.

Finite cell error

Similarly to regular networks, as N increases, in Figure 12.31(a) we see that the permeability approaches a uni-modal distribution. This implies that the error caused by replacing a large network with a finite cell of size N, E_c^k, decreases as N increases. We confirm this by comparing the blue dots with the dashed blue line in Figure 12.31(b). We see that the convergence of $\mathbb{E}[k^{11}]$ to $k^{11}_{N\to\infty}$ is much slower here than in the regular networks, because of the variance in the number of inter-cell edges. Even so, the average permeability of a cell with around $N = 36$ nodes is similar to that of a much larger network.

Mean network error

Importantly, comparing the dashed and solid blue lines in Figure 12.31(b), we see that the average permeability of the six-irregular network is close to that of the mean

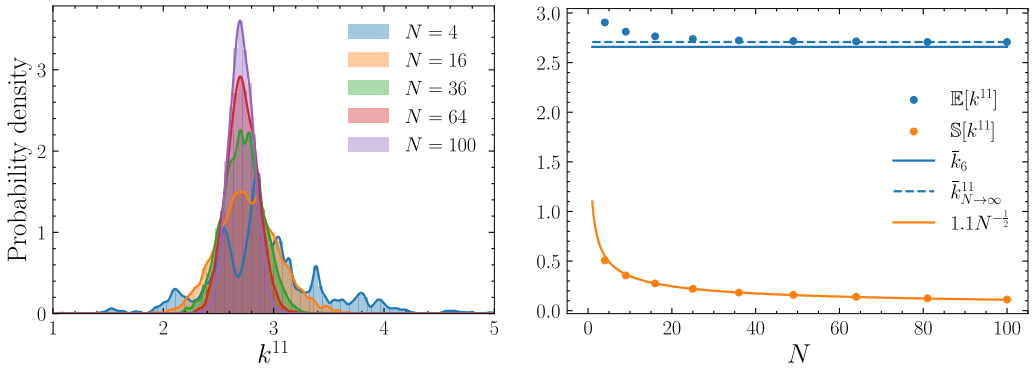

(a) (b)

Figure 12.31: Graphs showing how the distribution of samples of the permeability, k^{11}, varies with the cell size, N, in a six-irregular network. The number of samples is $S = 10,000$. (a) Coloured bars show a histogram of the distribution, $\mathcal{K}$, of the permeability, k^{11}, for various N. Correspondingly coloured lines interpolate the histogram at bar midpoints, to show an approximate pdf of $\mathcal{K}$. (b) The mean (blue dots) and standard deviation (orange dots) of the permeability distribution, $\mathbb{E}[k^{11}]$ and $\mathbb{S}[k^{11}]$, as functions of N, for $\sigma = 0.03$. The solid blue curve shows the permeability of the mean six-regular network, $\bar{k}_6$. The dashed blue line shows the approximate mean permeability of an infinite non-periodic six-irregular network, $\bar{k}^{11}_{N\to\infty}$, approximated using $N = 100$. The solid orange line shows a fit to the standard deviation, achieved by plotting in log-log space.

six-regular network. As we hypothesised, the average degree of nodes in the cell plays an important (perhaps more important than the conductance distribution) in determining the permeability of the network. That the exact number of nodes that each node connects to is different in six-regular and six-irregular networks appears to have little effect, so that replacing the six-irregular network with the mean six-regular network leads to small errors, E^k_{n}. One implication is the potential for decreased computational cost of simulation, since regular structures can be significantly cheaper to program than irregular ones.

Sampling error

In Figure 12.31(b), we see that, despite the multiple peaks for smaller values of N, the standard deviation of the permeability of six-irregular networks decreases like $N^{-1/2}$. Thus, even though, in general, much larger cells are required for representation of large irregular than is the case for regular ones, it is still advantageous to average over many samples of small cells as opposed to few samples of large ones.

12.3.4.2 Adhesivity

Lastly, we analyse the adhesivity of six-irregular networks. We plot samples in Figure 12.32. The first thing we note is that the adhesivity distribution, $\mathcal{J}$, does not

focus around discrete values, as it does for regular networks with small conductance variance. This is because of the increase in the width of the initial conductance distribution, $\mathcal{G}$, which is caused by the variability in pore lengths that result from the uniform distribution of junction locations. For example, we see that the six-irregular adhesivity distribution resembles the regular case $\sigma = 0.3$ in Figure (12.26(b)) much more than the case $\sigma = 0.03$ in Figure (12.26(a)).

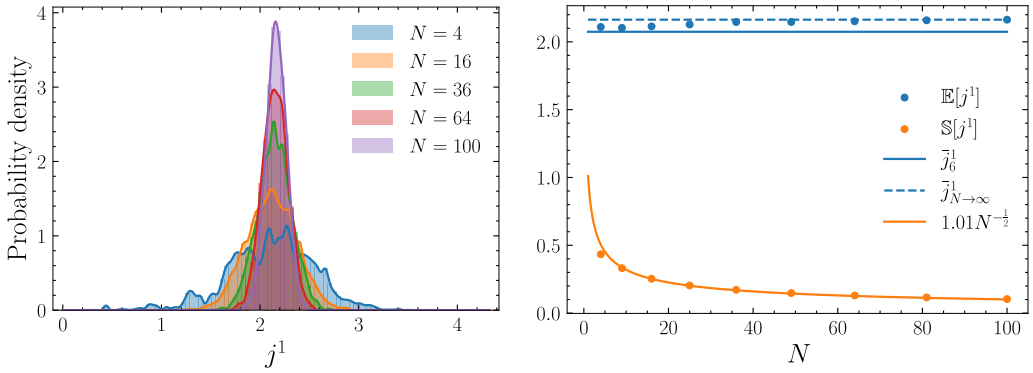

(a) (b)

Figure 12.32: Graphs showing how the distribution of samples of the adhesivity, j^1, varies with the cell size, N, in a six-irregular network. The number of samples is $S = 10,000$. (a) Coloured bars show a histogram of the distribution, $\mathcal{J}$, of the adhesivity, j^1, for various N. Correspondingly coloured lines interpolate the histogram at bar midpoints, to show an approximate pdf of $\mathcal{J}$. (b) The mean (blue dots) and standard deviation (orange dots) of the adhesivity distribution, $\mathbb{E}[j^1]$ and $\mathbb{S}[j^1]$, as functions of N. The solid blue curve shows the adhesivity of the mean six-regular network, $\bar{j}_6 = (4/\sqrt{3})\bar{G}\text{cdf}(\bar{G})$. The dashed blue line shows the approximate mean adhesivity of an infinite non-periodic six-irregular network, $\bar{j}^1_{N\to\infty}$, approximated using $N = 100$. The solid orange line shows a fit to the standard deviation, achieved by plotting in log-log space.

Blocked pore distribution

The loss of the discrete adhesivity structure observed in regular networks is not related to a change in the behaviour of the distribution that governs the number of pores that are blocked, $b^1 \sim \mathcal{B}$. To show this, we plot samples (coloured bars) of this distribution in Figure 12.33(a), and compare these with the distribution of blocked pores in the six regular case (coloured dots and lines). We see that (see Figure 12.33(b)), for any given cell size, N, the average number of blocked pores is considerably larger than that in the six-regular case. This suggests a skew in the conductance distribution that encourages more initial conductances to lie below the threshold conductance, due to more long pores. That is, the mean lies further to the left of the median in the six-irregular construction than it does in the log-normal distribution associated with the six-regular construction. This helps to explain why the mean adhesivity of

a six-irregular network (see the dashed blue line in Figure 12.32(b) is considerably larger than that of a six-regular network (compare with the dashed blue line in Figure 12.26(b).

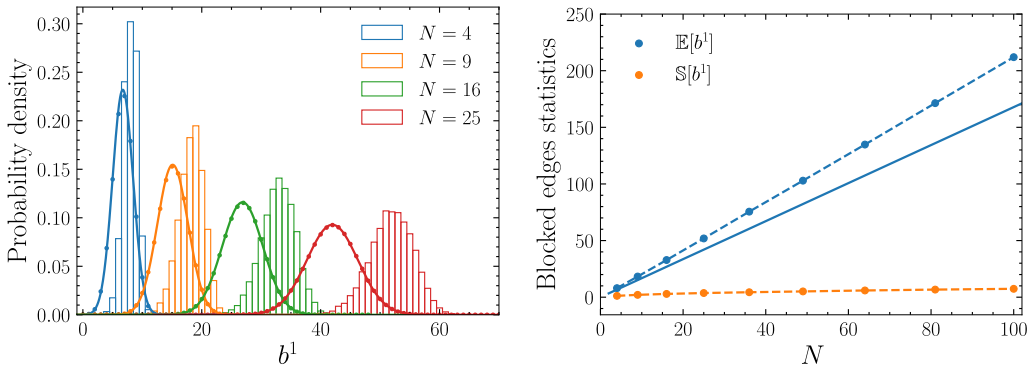

(a) (b)

Figure 12.33: Graphs showing how the distribution of samples of the number of blocked pores, b^1, varies with the cell size, N, in a six-irregular network. The number of samples is $S = 10,000$. (a) Coloured bars show a histogram of samples of the distribution of blocked pores, $\mathcal{B}$, for various N. The corresponding binomial distribution for a six-regular network is plotted with correspondingly coloured dots for each N. The corresponding normal distribution for a six-regular network is plotted with correspondingly coloured solid lines for each N. (b) The mean (blue dots) and standard deviation (orange dots) of the blocked pore distribution, $\mathbb{E}[b^1]$ and $\mathbb{S}[b^1]$, as functions of N, for $\sigma = 0.03$. The solid blue line shows the mean of the corresponding binomial distribution for a six-regular network, $np = 3N\text{cdf}(\bar{G})$. The dashed blue and orange lines show interpolations of the correspondingly coloured dots, to aid the eye.

Finite cell error

The finite cell error for adhesivity, E_{c}^j, converges to zero relatively slowly with N (see the blue dots and dashed blue line in Figure 12.32(b)). A cell of size $N \approx 49$ is required to capture the adhesivity of larger irregular networks correctly. This is larger than for the six-regular networks. This is unsurprising, noting the larger variance in the conductance distribution caused by the variance in pore lengths.

Mean network error

Comparing the blue solid line to the blue dashed line in Figure 12.32(b), we note that the error in the adhesivity that we would make if we replaced the six-irregular network with the mean six-regular network is relatively small ($E_{\text{n}}^j \approx 5\%$), especially considering that their conductances are drawn from distributions with different statistics.

Sampling error

Unlike the permeability, the standard deviation of the adhesivity of six-irregular networks is more similar to that of six-regular ones, since the relative proportion of intra- and inter-cell pores is irrelevant in determining the adhesivity. Even though a cell of $N \approx 49$ is required to capture the adhesivity of a large network with low error, it remains computationally advantageous to accept the increased cost incurred by repeated sampling of this relatively small cell.

12.3.5 Structure comparison

In this section we have analysed samples of the permeability and adhesivity of four-regular, six-regular, and six-irregular structures. We summarise our findings by comparing the means and standard deviations of these samples, $\mathbb{E}[k^{11}]$ and $\mathbb{S}[k^{11}]$, which we plot together in Figure 12.34.

Finite cell error

In [80], the authors find that, as the size of the cell increases, the average permeability of all three networks approaches a fixed value. Our results agree. In Figure 12.34(a), we see that as N increases, $\mathbb{E}[k^{11}]$ (see the coloured markers) approaches $k^{11}_{N\to\infty}$ (see the dashed lines of corresponding colour), which can be thought of as the average permeability of a large network with the corresponding structure. The implication is that, in purely advective macroscale systems, in which particles do not interact with pores and cause changes to the structure of the microscale network, cells of sizes as small as $N \approx 25$ can be used to pre-calculate the permeability parameter of the system, even when the network is irregular. In Figure 12.34(c), we see that samples of the adhesivity behave similarly, so that $\mathbb{E}[j^1]$ (see the coloured markers) approaches $j^1_{N\to\infty}$ (see the dashed lines of corresponding colour) as N increases. This means that our conclusion can be extended to advection–reaction systems, in which particles do interact with pores in the underlying network. Convergence of the adhesivity is slightly slower than that of the permeability and so slightly larger cells, say $N \approx 49$ (at worst, when the network is irregular), are required for advection–reaction systems than those required for advection only. Nevertheless, pre-calculation of the parameters is possible even when the network is dynamic, which decreases the computational expense of solution of multiscale advection–reaction systems by orders of magnitude.

Mean network error

The relatively small differences in the dashed and solid lines in Figures 12.34(a) indicates that the permeability of networks is approximated well by a network with the same average degree and the mean conductance in every pore. Comparing the equivalent lines in 12.34(c), we see this approximation is significantly worse for the adhesivity. One implication is that, in purely advective systems on static networks, using the statistics of the underlying conductance distribution to calculate the permeability will not lead to large errors in the solution. Using the conductance statistics

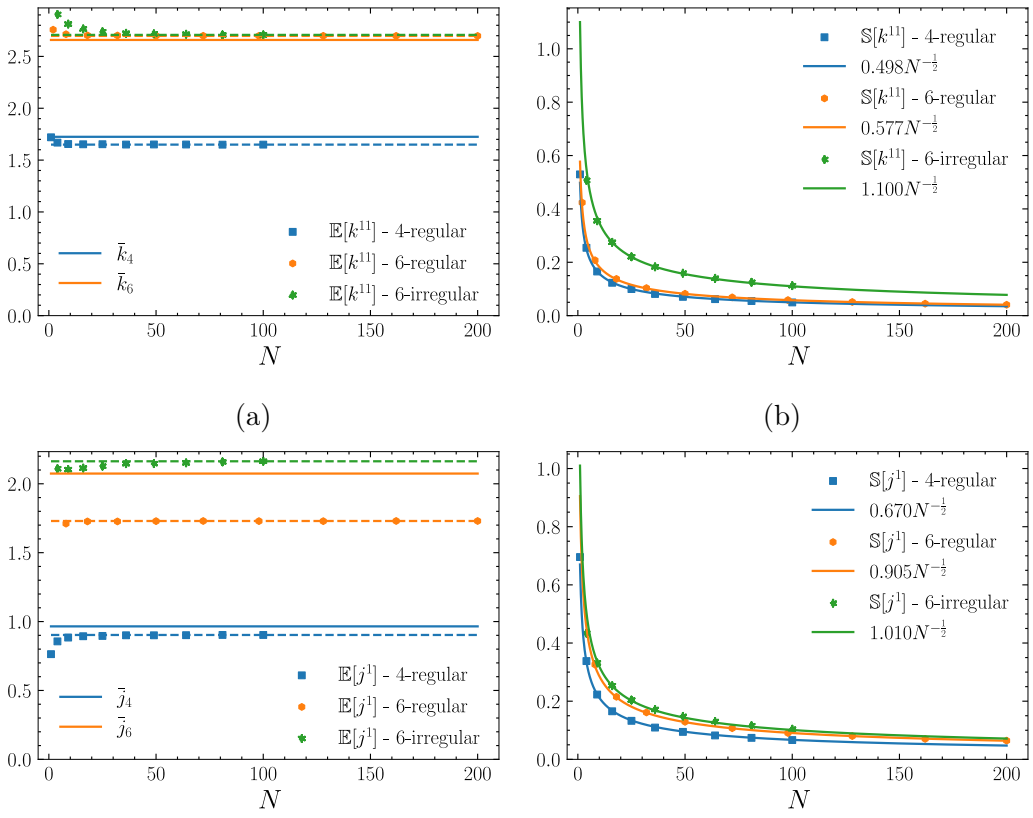

Figure 12.34: Graphs showing how the mean (left) and standard deviation (right) of samples of the permeability (top), k^{11}, and adhesivity (bottom), j^1, vary with the cell size, N. The parameters are $S = 10,000$ and $\mu = 0.3$. The four-regular, six-regular, and six-irregular cases are shown with blue, orange, and green correspondingly shaped markers. (a) The mean of the permeability distribution, $\mathbb{E}[k^{11}]$, as a function of the cell size, N. The limit $\bar{k}^{11}_{N\to\infty}$ is shown for each case in a correspondingly coloured dashed line. The permeabilities of the mean four-regular and six-regular networks, $\bar{k}_4$ and $\bar{k}_6$, are shown in blue and orange solid lines, respectively. (b) The standard deviation of the permeability distribution, $\mathbb{S}[k^{11}]$, as a function of the cell size, N. The solid lines of corresponding colour show fits achieved by plotting in log-log space. (c) A similar plot as (a), but for the mean of the adhesivity distribution, $\mathbb{E}[j^1]$. (d) A similar plot as (b), but for the standard deviation of the adhesivity distribution, $\mathbb{S}[j^1]$.

to calculate the adhesivity in advection–reaction equations on dynamics networks will lead to much larger errors in the effective solution.

Sampling error

Comparing Figures 12.34(a) and 12.34(c), we see that the standard deviations of the permeability and adhesivity samples, $\mathbb{S}[k^{11}]$ and $\mathbb{S}[j^1]$, are roughly the same size for

a given structure (compare lines of the same colour), and, moreover, they behave in the same way as functions of N (decreasing like $N^{-1/2}$). Since pre-calculation of the adhesivity, using (12.9), has the same computational cost as that of the permeability, (12.7), the conclusion that is computationally advantageous to sample the smallest cell possible multiple times, rather than sampling a larger cell fewer times, extends to systems on networks with dynamic structure.

Chapter 13

Conclusions for the multiscale model

In Part III, Chapters 10–12, we motivated, derived, and solved a novel multiscale model for filtration. This strikes a useful compromise between computationally expensive network models that accurately capture microscale effects, and macroscale models that ignore microscale information but are usually computationally cheaper.

13.1 Summary

13.1.1 Motivation for the model

In Chapter 10, we began by introducing multiscale models as a candidate framework for filtration simulations. In particular, in Section 10.1, we highlighted the multiscale nature of the filtration process. Particle and pore interactions on the microscale dictate flow and particle concentration behaviour on the macroscale. This dependence results in computational feasibility problems for network models in which the entire pore space is resolved.

Multiscale models were introduced as a potential alternative in Section 10.2. Examples that consider a continuum microscale are common. Those that model the microscale as a network are less common, but network homogenisation methods have been used to derive the effective permeability, most notably in [80].

In Section 10.3, we motivated a novel multiscale model that accounts for the deposition of particles, as well as their transport. This causes changes to the structure of the network, which manifests in a second effective parameter, the adhesivity, in addition to the permeability in [80].

13.1.2 Derivation of the model

In Chapter 11, we derived the multiscale model. In particular, in Section 11.1, we began by adapting the microscale model that we derived and solved in Part II into a system defined on a repeated cell, representative of the overall microscale, which forms a periodic network with initial conditions corresponding to mono-dispersed and log-normally poly-dispersed pore sizes and thus conductances. Nondimensionalising,

we found that the microscale model depends on three dimensionless parameter groups: α (the adherence parameter); β (the particle size parameter); and ε (the ratio of the cell length to the network length).

In Section 11.2, we outlined the process of network homogenisation. Considering periodic node and edge indices as position references that are independent of the macroscale position reference, asymptotically expanding quantities defined at nodes and edges, and seeking solutions at the correct asymptotic order, we explained how to average the network model to obtain an effective model, the solution of which approaches that of the network model asymptotically in the small cell limit $\varepsilon \to 0$.

In Sections 11.3 and 11.4, we averaged our periodic network model, firstly in a quasi-one-dimensional setting, and secondly in the case where the network is embedded in space of arbitrary dimension. We homogenised:

- a linear algebraic equation describing fluid mass conservation in nodes. The result is a continuous partial differential equation that describes the spatial independence of the flow rate;
- a definition of the average microscale velocity. The result is the Darcy equation, a partial differential equation describing the proportionality between the effective flow rate and pressure gradient, via the effective permeability;
- an ordinary differential equation describing the conservation of the mass of particles as they are transported and deposited within the microscale geometry. The result is an advection–reaction equation for the effective particle concentration. The advection and reaction rates are dictated by the effective permeability and adhesivity, which average the effects of microscale transport and deposition;
- an ordinary differential equation describing pore volume conservation, and thus conductance changes as deposition occurs. The result is a partial differential equation that relates microscale conductance to macroscale variables.

As such, our multiscale model for filtration is a system of continuous partial differential equations that govern the evolution of effective variables through the continuum geometry of the macroscale. The parameters of the system, the effective permeability and adhesivity, depend on the dynamic structure of the discrete network microscale. This is updated via solution of a coupled linear problem that is the size of the number of nodes in the cell.

13.1.3 Solution of the model

In Chapter 12, we found numerical solutions of our multiscale model. To this end, in Section 12.1, we started by averaging over flow-transverse directions, to permit quasi-one-dimensional solutions. We then outlined a numerical solution scheme, and suggested a simplifying step that involves pre-calculation of potential conductances and resulting permeability and adhesivity values. This decreases the computational expense of the solution considerably.

We used this method, in Section 12.2, to compute solutions on a four-regular periodic network. Firstly, we considered the deterministic initial network case, in which all edge conductances are equal, which corresponds to mono-dispersed pores. We found that a single simulation of the multiscale model approaches that of the network model as $\varepsilon \to 0$, as expected. Secondly, we discussed a random network case, in which conductances are drawn from a log-normal distribution, corresponding to poly-dispersed initial pore sizes. Individual simulations qualitatively agree with the network model, but not quantitatively, since each initialisation is generally unique. We hypothesised that the statistics of ensemble solutions of the two models should agree.

To show this, in Section 12.3, we computed sampled distributions of the permeability and adhesivity by repeatedly solving the multiscale model. We analysed these distributions for three networks structures: a four-regular network with log-normally distributed initial conductances; a six-regular network with initial conductances drawn from an equivalent log-normal distribution; a six-irregular network, with initial conductances drawn from a distribution related to the length of edges between nodes with uniformly distributed positions. For each structure, we computed the sampled mean and standard deviation of the permeability and adhesivity, and compared these with the corresponding parameters of: a large network with identical structure; the mean network (a network with the same coordination number with each edge conductance equal to the mean conductance). We reached three key conclusions:

- The 'finite cell error' (the difference between the permeability or adhesivity of a large network and that of a smaller cell) decreases like N^{-1} as N increases (where N is the number of nodes in the cell). Therefore, the cell becomes increasingly 'representative' of the entire network as its size increases, but the cell need not be too large before it represents the network well. Since the pre-calculation step is $\mathcal{O}(N^2)$, this fact drastically reduces the computational complexity of the multiscale solution, which is already significantly cheaper than solution of the underlying network model. Only slightly larger cells are needed for the adhesivity than for the permeability, which implies that network homogenisation is a useful method for dynamic network models, as well as the static ones discussed in [80];

- The 'mean network error' (the difference between the permeability or adhesivity of the mean network and that of a smaller representative cell) decreases like σ^2 as σ decreases (where σ is the standard deviation of the underlying conductance distribution). As such, the random network is increasingly well approximated by the mean network as the conductance distribution narrows. For certain structures and sufficiently narrow conductance distributions, the permeability and adhesivity of the mean network may be used in place of the mean of the distributions from repeated sampling, decreasing computational complexity further;

- The 'sampling error' (the difference between the permeability or adhesivity from a particular run and the mean of a suitably large sample) decreases with $N^{-1/2}$

as N increases. Since the cost of calculation of the permeability or adhesivity is $\mathcal{O}(N^2)$, this means that more repeats using a smaller, 'less representative' cell is a computationally advantageous strategy compared to fewer repeats using a larger, 'more representative' cell, on average.

Additionally, we found that, as the coordination number of the underlying network increases, its average permeability and adhesivity increases. Consequently, users of network and multiscale models should ensure that the coordination number of the chosen network is sufficiently close to that of the porous material of interest.

In summary, results for the advective system on the static networks discussed in [80] extend to our advection–reaction system on dynamic networks with the same initial structure. That is: Network homogenisation leads to an effective system that matches the behaviour of the network system in the limit where many cells constitute the network; The effective properties of large networks are approximated well by pre-calculating the statistics of small cells, which reduces computational complexity; Repeatedly sampling the smallest feasible cells is computationally advantageous. However, reaction terms lead to the need for a slightly larger repeating cell.

13.2 Further work

There are several potential avenues for further research.

13.2.1 Additional particle and pore interactions

In general, we used a relatively simple model for the filter microscale, to aid simple demonstration of the key aspects of our novel multiscale framework. The derivation and inclusion of more complex network dynamics, which more accurately represent the complex particle–pore interactions that occur physically, would be relatively straightforward and yet useful. Indeed, one advantage of this framework is its generality: we made no assumptions regarding the connectivity; dimension; size distributions; or initial and boundary conditions on the underlying microscale. Decisions regarding these were purely illustrative.

13.2.2 Multiscale and microscale solution comparison

One next step might be to find the temporally varying velocity and particle concentration distributions that follow from the permeability and adhesivity distributions established in Section 12.3. These should show, for example, that the solution of the multiscale model on a randomly generated network does indeed agree statistically with the equivalent network model in the limit $\varepsilon \to 0$, as we conjectured in Subsection 12.2.2. It might be interesting to compare these results across different structures, for example, the three discussed in Section 12.3. The permeability and adhesivity behaviour, which we discussed at length, gives us a good clue that increasing the coordination number increases the average velocity and the reaction rate in the advection–reaction equation, so that particles are transported and captured more

rapidly, resulting in a concentration profile that drops more quickly as the wave of particles traverses the filter.

13.2.3 Industrially relevant properties

Our model lends itself to the calculation of properties of industrial interest. In [80], Chapman *et al.* discuss the ease with which the tortuosity of a filter is calculated when its microscale is reduced to a network. This measure of geometric complexity is one of the key parameters for the determination of a material's transport properties. The authors go on to show a correlation between tortuosity and permeability. It would be interesting to use our model to extend this analysis to networks with dynamic connectivity, and to establish the relationship between tortuosity and adhesivity, for example.

13.2.4 Optimisation and porosity gradients

As we demonstrated in Part II, network models permit simple derivation of secondary filter properties of industrial interest, such as the particle retention efficiency and total throughput. Future work should exploit the relative computational tractability of this model for the calculation of these properties, without loss of accuracy. It would be relatively straightforward, for example, to establish the dependence of these properties on the parameters of the underlying conductance distribution, since repeated calculation is feasibly quick. This highlights the potential for optimisation routines that rely on parameter sweeps or cost function descents. One experiment might propose a spatially graded mean for the conductance distribution (which is possible, since we asymptotically expanded each pore conductance, to permit macroscale variation), and then find the gradient parameter that maximises the total throughput given a threshold requirement for the particle retention efficiency, thus finding the optimal microscale configuration for process performance. Conclusions regarding the desirable porosity gradients could then be compared to those in [77] and [78], for example.

13.2.5 Network representation and experimental data

Industrial data would be a useful addition at both the initial and final stages of this framework. As we discussed in the context of network models, data on real porous media samples would lead to the derivation of initial networks corresponding to real membrane samples. The results of experiments on the same samples could be used for solution comparison, allowing for free parameter tuning, again made possible by the computational tractability of our multiscale method. Our conclusions could then be used to quantitatively understand real filtration materials, and aid their design.

Chapter 14

Conclusion

In this chapter, we draw this thesis to a conclusion by summarising our key motivations and ideas, and highlighting three key areas for further research. Specific conclusions for Parts I, II, and III can be found in Chapters 5, 9, and 13, respectively.

14.1 Motivation

In Chapter 1, we established that filtration is an increasingly important industrial process for which mathematical models can be broadly separated into three categories:

- Macroscale models, which are computationally cheap but sometimes inaccurate because they ignore microscale information;
- Microscale models, which are usually more accurate but more computationally expensive;
- Multiscale models, which provide a useful balance between the other two approaches, although the continuum microscale models that they encompass can still be expensive, or else over-idealise the true geometry.

This motivated the study of three novel models, which broadly fit into each of these three categories.

14.2 Summary

We motivated, derived, and solved these three models in Parts I, II, and III, respectively.

14.2.1 Macroscale model: A size structured model for filtration

In Part I, we explored a novel framework that allows for the continuous monitoring of the size distributions of particles in the feed and pores in the filter. The parameters

of most other macroscale systems are estimated by empirical measurements. In our model, the functions that determine the permeability and reactivity of the filter are found dynamically as part of the solution scheme. They depend on the relationship between the particle and pore size distributions, which change subject to models for physical and chemical phenomena. As a result, our solutions behave intuitively, and we found various ways of saving computational expense, via asymptotic methods.

14.2.2 Microscale model: A network model for filtration

In Part II, we derived and analysed a novel microscale model for filtration. This serves as a simple example of a framework in which the pore clogging due to particle capture is modelled as changes to the connectivity of a network and decrease in the particle concentration in a continuum fluid. Our model is useful to predict important effective properties of filters, such as the particle retention efficiency and process termination time. Despite this, our network model suffers from the same problem as many others: the quality of microscale resolution means that simulation of areas large enough to characterise the filter as a whole is computationally infeasible, which motivates the study of an alternative framework.

14.2.3 Multiscale model: A multiscale model for filtration

In Part III, we explored a multiscale model for filtration. We used network homogenisation to systematically average the microscale model from Part II in such a way that the two models agree in a physically relevant asymptotic limit. The result is a set of equations that govern the macroscale properties of the filter. However, as in Part I, the parameters of this system are solved as part of the model. This time, these depend on the interactions between particles and pores via the connectivity of the microscale geometry, as well as the size distribution of pores. Unlike in traditional multiscale models, the microscale is a network as opposed to a continuum, which decreases the computational complexity of solution whilst still including connectivity information. This allows for the systematic study of the effect of a random microscale on the statistical properties of the parameters of the effective system, via repetition of solution that is infeasible for the more expensive microscale model in Part II.

14.3 Further work

Avenues for further research can be broadly summarised into three key themes: incorporation of additional physical and chemical effects; inclusion and calculation of additional industrially relevant filter properties; and use of experimental data, especially for optimisation.

14.3.1 Additional physical and chemical effects

In this thesis, in general, we have focused on the use of simple models governing particle–pore interactions to demonstrate the general behaviour of our models. There is therefore much scope for the derivation and use of more detailed laws that more accurately take into account physical and chemical microscale phenomena. A more detailed description of the pore size that results from deposition of a particular particle would be simple to incorporate in our size structured framework, for example, via a more complex transformation function. We only discussed blocking and deposition as clogging mechanisms, and ignored partial surface blocking and caking effects introduced in Chapter 1. We ignored diffusive effects in general, although we established, in Chapter 1, that microfiltration generally occurs at low flow rates. In our network model, diffusion would result in terms containing the concentration difference on edges (as opposed to the pressure difference), and it would be interesting to analyse the diffusivity parameter that would emerge in the multiscale model, similarly to the permeability and adhesivity.

14.3.2 Industrially relevant properties

Our focus was on derivation and solution of models for the evolution of primary filter characteristics, such as the flow rate and particle concentration. It would be relatively straightforward, and of significant industrial interest, to derive and analyse secondary quantities from these, such as retention and energy efficiency, and operating time.

14.3.3 Experimental data and optimisation

Empirical data would be a useful addition to any of our models. Firstly, initial state information would increase solution accuracy. In the size structured model, use of the size distributions of actual feeds or membranes would be easily incorporated. Our chosen distributions were for illustrative purposes only. In the network and multiscale models, statistical information about the size distribution and coordination number of specific porous media would be incorporated by tuning the parameters of the initial pore conductance distribution and parametrisation of an algorithm for random network structure generation, respectively. Secondly, solution data would allow for validity checks of our models. Further, systematic analysis of the difference between the mathematical and empirical solutions could allow for parameter tuning, made possible by the small numbers of free parameters in our systems, and their computational tractability. The combination of correct initial conditions and well tuned parameters would render our models suitable for simulation of real filtration experiments, decreasing financial expense and industrial waste. Future research would also explore the possibility of parameter sweeps for the cost function descents involved in the computational optimisation of filter performance metrics.

These avenues for future work would hopefully lead to filters with increased retention efficiency and throughput potential with decreased energy demands, which were targets that we set out in the introduction of this thesis.

Appendix A

Appendix: A multiscale model for filtration

In this appendix, we prove the algebraic results necessary for the network homogenisation of our network model. We begin with the results we use in the quasi-one-dimensional setting, and then prove the similar (if more notationally complex) results that we use in the D-dimensional derivation.

Before we begin, we define the following two operations, which are utilised extensively in the subsequent sections.

Operation 1. A re-indexing $i \leftrightarrow j$ followed by use of $G^{\boldsymbol{r}}_{ji} = G^{-\boldsymbol{r}}_{ij}$. We refer to this equality as *the symmetry of conductance*, which holds due to the periodicity of the network, so that these objects describe the conductance of the same link.

Operation 2. A re-indexing $\boldsymbol{r} \leftrightarrow -\boldsymbol{s}$, followed by use of the fact that summing over $-\boldsymbol{s}$ is equivalent to summing over $\boldsymbol{s}$, since, if $-\boldsymbol{s} \in \boldsymbol{\mathcal{R}}$, then $\boldsymbol{s} \in \boldsymbol{\mathcal{R}}$, followed by a re-indexing $\boldsymbol{s} \to \boldsymbol{r}$.

A.1 Algebraic results in one dimension

A.1.1 Relation of basic matrices

In this subsection, we show that

$$\boldsymbol{A}^{(s)}\mathbf{1} = \mathbf{0}, \quad \mathbf{1}^\top \boldsymbol{B}^{(s)}\mathbf{1} = \mathbf{0}, \quad \boldsymbol{D}^{(s)}\mathbf{1} = \mathbf{0}, \quad \boldsymbol{F}^{(s)}\mathbf{1} = \mathbf{0}, \tag{A.1}$$

and that

$$\mathbf{1}^\top \boldsymbol{D}^{(s)} = \frac{\partial}{\partial x}\Big(\mathbf{1}^\top \boldsymbol{B}^{(s)}\Big), \tag{A.2}$$

$$\mathbf{1}^\top \boldsymbol{E}^{(s)}\mathbf{1} = \frac{\partial}{\partial x}\Big(\mathbf{1}^\top \boldsymbol{C}^{(s)}\mathbf{1}\Big). \tag{A.3}$$

To show the results in (A.1), firstly, we have

$$\left(\boldsymbol{A}^{(s)}\mathbf{1}\right)_i = \sum_{j=1}^{N}\sum_{r\in\mathcal{R}}\left(G_{ij}^{r(s)} - \delta_{ij}\sum_{k=1}^{N}G_{ik}^{r(s)}\right) \tag{A.4}$$

$$= \sum_{j=1}^{N}\sum_{r\in\mathcal{R}}G_{ij}^{r(s)} - \sum_{j=1}^{N}\sum_{r\in\mathcal{R}}G_{ij}^{r(s)} \tag{A.5}$$

$$= 0. \tag{A.6}$$

Secondly, we have

$$\mathbf{1}^\top\boldsymbol{B}^{(s)}\mathbf{1} = \sum_{i=1}^{N}\sum_{j=1}^{N}\sum_{r\in\mathcal{R}}\left(G_{ij}^{r(s)}(X_j + rl) - \delta_{ij}X_i\sum_{k=1}^{N}G_{ik}^{r(s)}\right) \tag{A.7}$$

$$= \sum_{i=1}^{N}\sum_{j=1}^{N}\sum_{r\in\mathcal{R}}G_{ij}^{r(s)}(X_j + rl) - \sum_{i=1}^{N}\sum_{j=1}^{N}\sum_{r\in\mathcal{R}}G_{ij}^{r(s)}X_i \tag{A.8}$$

$$= \sum_{i=1}^{N}\sum_{j=1}^{N}\sum_{r\in\mathcal{R}}G_{ij}^{r(s)}(X_j + rl) - \sum_{i=1}^{N}\sum_{j=1}^{N}\sum_{r\in\mathcal{R}}G_{ij}^{-r(s)}X_j \tag{A.9}$$

$$= \sum_{i=1}^{N}\sum_{j=1}^{N}\sum_{r\in\mathcal{R}}G_{ij}^{r(s)}(X_j + rl) - \sum_{i=1}^{N}\sum_{j=1}^{N}\sum_{r\in\mathcal{R}}G_{ij}^{r(s)}X_j \tag{A.10}$$

$$= l\sum_{i=1}^{N}\sum_{j=1}^{N}\sum_{r\in\mathcal{R}}G_{ij}^{r(s)}r \tag{A.11}$$

$$= -l\sum_{i=1}^{N}\sum_{j=1}^{N}\sum_{r\in\mathcal{R}}G_{ij}^{r(s)}r \tag{A.12}$$

$$= 0, \tag{A.13}$$

where the second equation uses δ_{ij} followed by a re-indexing $k \to j$, the third uses Operation 1 on the second term, the fourth uses Operation 2 on the second term, and the sixth uses that if $r \in \mathcal{R}$ then $-r \in \mathcal{R}$. Thirdly, we have

$$\left(\boldsymbol{D}^{(s)}\mathbf{1}\right)_i = \sum_{j=1}^{N}\sum_{r\in\mathcal{R}}\left(\frac{\partial G_{ij}^{r(s)}}{\partial x}M_{ij}^{r} - \delta_{ij}\sum_{k=1}^{N}\frac{\partial G_{ik}^{r(s)}}{\partial x}M_{ik}^{r}\right) \tag{A.14}$$

$$= \sum_{j=1}^{N}\sum_{r\in\mathcal{R}}\frac{\partial G_{ij}^{r(s)}}{\partial x}M_{ij}^{r} - \sum_{j=1}^{N}\sum_{r\in\mathcal{R}}\frac{\partial G_{ij}^{r(s)}}{\partial x}M_{ij}^{r} \tag{A.15}$$

$$= 0. \tag{A.16}$$

Lastly, we have

$$\left(\boldsymbol{F}^{(s)}\mathbf{1}\right)_i = \frac{1}{2}\sum_{j=1}^{N}\sum_{r\in\mathcal{R}}\left(\frac{\partial^2 G_{ij}^{r(s)}}{\partial x^2}(M_{ij}^r)^2 - \delta_{ij}\sum_{k=1}^{N}\frac{\partial^2 G_{ik}^{r(s)}}{\partial x^2}(M_{ik}^r)^2\right) \tag{A.17}$$

$$= \frac{1}{2}\left(\sum_{j=1}^{N}\sum_{r\in\mathcal{R}}\frac{\partial^2 G_{ij}^{r(s)}}{\partial x^2}(M_{ij}^r)^2 - \sum_{j=1}^{N}\sum_{r\in\mathcal{R}}\frac{\partial^2 G_{ij}^{r(s)}}{\partial x^2}(M_{ij}^r)^2\right) \tag{A.18}$$

$$= 0. \tag{A.19}$$

We next show the result given by (A.2). On one hand,

$$\frac{\partial}{\partial x}\left(\mathbf{1}^\top \boldsymbol{B}^{(s)}\right)_j = \frac{\partial}{\partial x}\left(\sum_{i=1}^{N}\sum_{r\in\mathcal{R}}\left(G_{ij}^{r(s)}(X_j + rl) - \delta_{ij}X_i\sum_{k=1}^{N}G_{ik}^{r(s)}\right)\right) \tag{A.20}$$

$$= \sum_{i=1}^{N}\sum_{r\in\mathcal{R}}\left(\frac{\partial G_{ij}^{r(s)}}{\partial x}(X_j + rl) - \delta_{ij}X_i\sum_{k=1}^{N}\frac{\partial G_{ik}^{r(s)}}{\partial x}\right) \tag{A.21}$$

$$= \sum_{i=1}^{N}\sum_{r\in\mathcal{R}}\frac{\partial G_{ij}^{r(s)}}{\partial x}(X_j + rl) - \sum_{i=1}^{N}\sum_{r\in\mathcal{R}}\frac{\partial G_{ji}^{r(s)}}{\partial x}X_j \tag{A.22}$$

$$= \sum_{i=1}^{N}\sum_{r\in\mathcal{R}}\frac{\partial G_{ij}^{r(s)}}{\partial x}(X_j + rl) - \sum_{i=1}^{N}\sum_{r\in\mathcal{R}}\frac{\partial G_{ij}^{-r(s)}}{\partial x}X_j \tag{A.23}$$

$$= \sum_{i=1}^{N}\sum_{r\in\mathcal{R}}\frac{\partial G_{ij}^{r(s)}}{\partial x}(X_j + rl) - \sum_{i=1}^{N}\sum_{r\in\mathcal{R}}\frac{\partial G_{ij}^{r(s)}}{\partial x}X_j \tag{A.24}$$

$$= \sum_{i=1}^{N}\sum_{r\in\mathcal{R}}\frac{\partial G_{ij}^{r(s)}}{\partial x}rl, \tag{A.25}$$

where the third equation uses δ_{ij} followed by a re-indexing $k \to i$, the fourth uses the symmetry of conductance, and the fifth uses Operation 2 on the second term. On the other hand,

$$\left(\mathbf{1}^\top \boldsymbol{D}^{(s)}\right)_j = \sum_{i=1}^{N}\sum_{r\in\mathcal{R}}\left(\frac{\partial G_{ij}^{r(s)}}{\partial x}M_{ij}^r - \delta_{ij}\sum_{k=1}^{N}\frac{\partial G_{ik}^{r(s)}}{\partial x}M_{ik}^r\right) \tag{A.26}$$

$$= \sum_{i=1}^{N}\sum_{r\in\mathcal{R}}\frac{\partial G_{ij}^{r(s)}}{\partial x}M_{ij}^r - \sum_{i=1}^{N}\sum_{r\in\mathcal{R}}\frac{\partial G_{ji}^{r(s)}}{\partial x}M_{ji}^r \tag{A.27}$$

$$= \sum_{i=1}^{N}\sum_{r\in\mathcal{R}}\frac{\partial G_{ij}^{r(s)}}{\partial x}M_{ij}^r - \sum_{i=1}^{N}\sum_{r\in\mathcal{R}}\frac{\partial G_{ij}^{-\boldsymbol{r}(s)}}{\partial x}M_{ji}^r \tag{A.28}$$

$$= \sum_{i=1}^{N}\sum_{r\in\mathcal{R}}\frac{\partial G_{ij}^{r(s)}}{\partial x}\left(M_{ij}^r - M_{ji}^{-r}\right) \tag{A.29}$$

$$= \sum_{i=1}^{N}\sum_{r\in\mathcal{R}}\frac{\partial G_{ij}^{r(s)}}{\partial x}rl, \tag{A.30}$$

where the second equation uses δ_{ij} followed by a re-indexing $k \to i$, the third uses the symmetry of conductance, the fourth uses Operation 2 on the second term, and the fifth uses the definition of the midpoint (11.23). We lastly show the result given by (A.3). On one hand,

$$\frac{\partial}{\partial x}\Big(\mathbf{1}^\top \boldsymbol{C}^{(s)}\mathbf{1}\Big) = \frac{\partial}{\partial x}\left(\frac{1}{2}\sum_{i=1}^{N}\sum_{j=1}^{N}\sum_{r\in\mathcal{R}}\left(G_{ij}^{r(s)}(X_j + rl)^2 - \delta_{ij}X_i^2\sum_{k=1}^{N}G_{ik}^{r(s)}\right)\right) \tag{A.31}$$

$$= \frac{1}{2}\sum_{i=1}^{N}\sum_{j=1}^{N}\sum_{r\in\mathcal{R}}\left(\frac{\partial G_{ij}^{r(s)}}{\partial x}(X_j + rl)^2 - \delta_{ij}X_i^2\sum_{k=1}^{N}\frac{\partial G_{ik}^{r(s)}}{\partial x}\right) \tag{A.32}$$

$$= \frac{1}{2}\Bigg(\sum_{i=1}^{N}\sum_{j=1}^{N}\sum_{r\in\mathcal{R}}\Bigg(\frac{\partial G_{ij}^{r(s)}}{\partial x}(X_j + rl)^2 - \sum_{i=1}^{N}\sum_{j=1}^{N}\sum_{r\in\mathcal{R}}\frac{\partial G_{ij}^{r(s)}}{\partial x}X_i^2\Bigg)\Bigg) \tag{A.33}$$

$$= \frac{1}{2}\Bigg(\sum_{i=1}^{N}\sum_{j=1}^{N}\sum_{r\in\mathcal{R}}\Bigg(\frac{\partial G_{ij}^{r(s)}}{\partial x}(X_j + rl)^2 - \sum_{i=1}^{N}\sum_{j=1}^{N}\sum_{r\in\mathcal{R}}\frac{\partial G_{ij}^{-r(s)}}{\partial x}X_jX_j\Bigg)\Bigg) \tag{A.34}$$

$$= \frac{1}{2}\Bigg(\sum_{i=1}^{N}\sum_{j=1}^{N}\sum_{r\in\mathcal{R}}\Bigg(\frac{\partial G_{ij}^{r(s)}}{\partial x}(X_j + rl)^2 - \sum_{i=1}^{N}\sum_{j=1}^{N}\sum_{r\in\mathcal{R}}\frac{\partial G_{ij}^{r(s)}}{\partial x}X_jX_j\Bigg)\Bigg) \tag{A.35}$$

$$= \frac{1}{2}\sum_{i=1}^{N}\sum_{j=1}^{N}\sum_{r\in\mathcal{R}}\frac{\partial G_{ij}^{r(s)}}{\partial x}(X_jrl + X_jrl + r^2l^2), \tag{A.36}$$

where the third equation uses δ_{ij} followed by a re-indexing $k \to j$, the fourth uses Operation 1 on the second term, and the fifth uses Operation 2 on the second term.

On the other hand,

$$\mathbf{1}^\top \boldsymbol{E}^{(s)}\mathbf{1} = \sum_{i=1}^{N}\sum_{j=1}^{N}\sum_{r\in\mathcal{R}}\left(\frac{\partial G_{ij}^{r(s)}}{\partial x}M_{ij}^{r}(X_j+rl) - \delta_{ij}X_i\sum_{k=1}^{N}\frac{\partial G_{ik}^{r(s)}}{\partial x}M_{ik}^{r}\right) \tag{A.37}$$

$$= \sum_{i=1}^{N}\sum_{j=1}^{N}\sum_{r\in\mathcal{R}}\frac{\partial G_{ij}^{r(s)}}{\partial x}M_{ij}^{r}(X_j+rl) - \sum_{i=1}^{N}\sum_{j=1}^{N}\sum_{r\in\mathcal{R}}\frac{\partial G_{ij}^{r(s)}}{\partial x}M_{ij}^{r}X_i \tag{A.38}$$

$$= \sum_{i=1}^{N}\sum_{j=1}^{N}\sum_{r\in\mathcal{R}}\frac{\partial G_{ij}^{r(s)}}{\partial x}M_{ij}^{r}(X_j+rl) - \sum_{i=1}^{N}\sum_{j=1}^{N}\sum_{r\in\mathcal{R}}\frac{\partial G_{ij}^{-r(s)}}{\partial x}M_{ji}^{r}X_j \tag{A.39}$$

$$= \sum_{i=1}^{N}\sum_{j=1}^{N}\sum_{r\in\mathcal{R}}\frac{\partial G_{ij}^{r(s)}}{\partial x}M_{ij}^{r}(X_j+rl) - \sum_{i=1}^{N}\sum_{j=1}^{N}\sum_{r\in\mathcal{R}}\frac{\partial G_{ij}^{r(s)}}{\partial x}M_{ji}^{-r}X_j \tag{A.40}$$

$$= \frac{1}{2}\sum_{i=1}^{N}\sum_{j=1}^{N}\sum_{r\in\mathcal{R}}\frac{\partial G_{ij}^{r(s)}}{\partial x}\Big(X_jrl + X_jrl + r^2l^2 + X_jrl + X_irl\Big) \tag{A.41}$$

$$= \frac{\partial}{\partial x}\Big(\mathbf{1}^\top\boldsymbol{C}^{(s)}\mathbf{1}\Big) + \frac{1}{2}\sum_{i=1}^{N}\sum_{j=1}^{N}\sum_{r\in\mathcal{R}}\frac{\partial G_{ij}^{r(s)}}{\partial x}X_jrl + \frac{1}{2}\sum_{i=1}^{N}\sum_{j=1}^{N}\sum_{r\in\mathcal{R}}\frac{\partial G_{ij}^{r(s)}}{\partial x}X_irl, \tag{A.42}$$

$$= \frac{\partial}{\partial x}\Big(\mathbf{1}^\top\boldsymbol{C}^{(s)}\mathbf{1}\Big) + \frac{1}{2}\sum_{i=1}^{N}\sum_{j=1}^{N}\sum_{r\in\mathcal{R}}\frac{\partial G_{ij}^{r(s)}}{\partial x}X_jrl + \frac{1}{2}\sum_{i=1}^{N}\sum_{j=1}^{N}\sum_{r\in\mathcal{R}}\frac{\partial G_{ij}^{-r(s)}}{\partial x}X_jrl, \tag{A.43}$$

$$= 0, \tag{A.44}$$

where the second equation uses δ_{ij} followed by a re-indexing $k \to j$, the third uses Operation 1 on the second term, the fourth uses Operation 2 on the second term, the fifth uses the definition of the midpoint (11.23), the seventh uses Operation 1 on the third term, and the eighth uses Operation 2 on the third term.

A.1.2 Simplification of permeability terms

In this subsection, we simplify the terms in the permeability scalar $k^{(0)}$. Firstly, we show that

$$\mathbf{1}^\top\boldsymbol{B}^{(0)}\boldsymbol{W} = -l\sum_{i=1}^{N}\sum_{j=1}^{N}\sum_{r\in\mathcal{R}}rG_{ij}^{r(0)}W_i. \tag{A.45}$$

We have

$$\mathbf{1}^\top \boldsymbol{B}^{(0)}\boldsymbol{W} = \sum_{i=1}^{N}\sum_{j=1}^{N}\sum_{r\in\mathcal{R}}\left(G_{ij}^{r(0)}(X_j + rl) - \delta_{ij}X_i\sum_{k=1}^{N}G_{ik}^{r(0)}\right)W_j \tag{A.46}$$

$$= \sum_{i=1}^{N}\sum_{j=1}^{N}\sum_{r\in\mathcal{R}}G_{ij}^{r(0)}W_j(X_j + rl) - \sum_{i=1}^{N}\sum_{j=1}^{N}\sum_{r\in\mathcal{R}}G_{ij}^{r(0)}W_iX_i \tag{A.47}$$

$$= \sum_{i=1}^{N}\sum_{j=1}^{N}\sum_{r\in\mathcal{R}}G_{ij}^{-r(0)}W_i(X_i + rl) - \sum_{i=1}^{N}\sum_{j=1}^{N}\sum_{r\in\mathcal{R}}G_{ij}^{r(0)}W_iX_i \tag{A.48}$$

$$= \sum_{i=1}^{N}\sum_{j=1}^{N}\sum_{r\in\mathcal{R}}G_{ij}^{r(0)}W_i(X_i + (-r)l) - \sum_{i=1}^{N}\sum_{j=1}^{N}\sum_{r\in\mathcal{R}}G_{ij}^{r(0)}W_iX_i \tag{A.49}$$

$$= -l\sum_{i=1}^{N}\sum_{j=1}^{N}\sum_{r\in\mathcal{R}}rG_{ij}^{r(0)}W_i. \tag{A.50}$$

The first equation uses δ_{ij} followed by a re-indexing $k \to j$, the third uses Operation 1 on the first sum, and the fourth uses Operation 2 on the first term.

Secondly, we prove that

$$\mathbf{1}^\top \boldsymbol{C}^{(0)}\mathbf{1} = -\frac{1}{2}\sum_{i=1}^{N}\sum_{j=1}^{N}\sum_{r\in\mathcal{R}}G_{ij}^{r(0)}\Big(2X_irl - r^2l^2\Big). \tag{A.51}$$

We have

$$\mathbf{1}^\top \boldsymbol{C}^{(0)}\mathbf{1} = \frac{1}{2}\sum_{r\in\mathcal{R}}\left(G_{ij}^{r(0)}(X_j + rl)^2 - \delta_{ij}X_i^2\sum_{k=1}^{N}G_{ik}^{r(0)}\right) \tag{A.52}$$

$$= \frac{1}{2}\Bigg(\sum_{i=1}^{N}\sum_{j=1}^{N}\sum_{r\in\mathcal{R}}G_{ij}^{r(0)}X_j^2 + \sum_{i=1}^{N}\sum_{j=1}^{N}\sum_{r\in\mathcal{R}}G_{ij}^{r(0)}2X_jrl + \tag{A.53}$$

$$\sum_{i=1}^{N}\sum_{j=1}^{N}\sum_{r\in\mathcal{R}}G_{ij}^{r(0)}r^2l^2 - \sum_{i=1}^{N}\sum_{j=1}^{N}\sum_{r\in\mathcal{R}}G_{ij}^{r(0)}X_i^2\Bigg)$$

$$= \frac{1}{2}\Bigg(\sum_{i=1}^{N}\sum_{j=1}^{N}\sum_{r\in\mathcal{R}}G_{ij}^{-r(0)}X_i^2 + \sum_{i=1}^{N}\sum_{j=1}^{N}\sum_{r\in\mathcal{R}}G_{ij}^{-r(0)}2X_irl + \tag{A.54}$$

$$\sum_{i=1}^{N}\sum_{j=1}^{N}\sum_{r\in\mathcal{R}}G_{ij}^{r(0)}r^2l^2 - \sum_{i=1}^{N}\sum_{j=1}^{N}\sum_{r\in\mathcal{R}}G_{ij}^{r(0)}X_i^2\Bigg)$$

$$= -\frac{1}{2}\sum_{i=1}^{N}\sum_{j=1}^{N}\sum_{r\in\mathcal{R}}G_{ij}^{r(0)}\Big(2X_irl - r^2l^2\Big). \tag{A.55}$$

The second equation uses δ_{ij} followed by a re-indexing $k \to j$ in the final term, the third uses Operation 1 on the first and second terms, and the third uses Operation 2 on the first and second terms, so that the first and last terms cancel.

A.1.3 Independence of node location and permeability equality

We show that the permeability tensor is independent of the node locations, to show that

$$k^{(0)} = \sigma^{(0)}. \tag{A.56}$$

We begin by simplifying $k^{(0)}$. We have

$$k^{(0)} = \frac{1}{2}\sum_{i=1}^{N}\sum_{j=1}^{N}\sum_{r\in\mathcal{R}} rG_{ij}^{r(0)}\Big(W_j - W_i + X_j + rl - X_i\Big) \tag{A.57}$$

$$= \frac{1}{2}\Bigg(\sum_{i=1}^{N}\sum_{j=1}^{N}\sum_{r\in\mathcal{R}} rG_{ij}^{r(0)}\Big(W_j + X_j + rl\Big) - \sum_{i=1}^{N}\sum_{j=1}^{N}\sum_{r\in\mathcal{R}} rG_{ij}^{r(0)}\Big(W_i + X_i\Big)\Bigg) \tag{A.58}$$

$$= \frac{1}{2}\Bigg(\sum_{i=1}^{N}\sum_{j=1}^{N}\sum_{r\in\mathcal{R}} rG_{ij}^{-r(0)}\Big(W_i + X_i + rl\Big) - \sum_{i=1}^{N}\sum_{j=1}^{N}\sum_{r\in\mathcal{R}} rG_{ij}^{r(0)}\Big(W_i + X_i\Big)\Bigg) \tag{A.59}$$

$$= \frac{1}{2}\Bigg(\sum_{i=1}^{N}\sum_{j=1}^{N}\sum_{r\in\mathcal{R}} (-r)G_{ij}^{r(0)}\Big(W_i + X_i + (-r)l\Big) - \sum_{i=1}^{N}\sum_{j=1}^{N}\sum_{r\in\mathcal{R}} rG_{ij}^{r(0)}\Big(W_i + X_i\Big)\Bigg) \tag{A.60}$$

$$= -\sum_{i=1}^{N}\sum_{j=1}^{N}\sum_{r\in\mathcal{R}} rG_{ij}^{r(0)}\Big(W_i + X_i - \frac{rl}{2}\Big), \tag{A.61}$$

where the first equation uses the definition of the permeability, (11.68), the third uses Operation 1 on the first term, and the fourth uses Operation 2 on the first term. We simplify $\sigma^{(0)}$ similarly. Indeed, using the simplified forms of the permeability terms, $\mathbf{1}^\top \boldsymbol{B}^{(0)}\boldsymbol{W}$ and $\mathbf{1}^\top \boldsymbol{C}^{(0)}\mathbf{1}$, (A.45) and (A.51), we have

$$\sigma^{(0)} = \frac{1}{l}\Big(\mathbf{1}^\top \boldsymbol{B}^{(0)}\boldsymbol{W} + \mathbf{1}^\top \boldsymbol{C}^{(0)}\mathbf{1}\Big) \tag{A.62}$$

$$= -\frac{1}{2l}\sum_{i=1}^{N}\sum_{j=1}^{N}\sum_{r\in\mathcal{R}} G_{ij}^{r(0)}\Big(2lrW_i + 2X_i rl - (rl)^2\Big) \tag{A.63}$$

$$= -\sum_{i=1}^{N}\sum_{j=1}^{N}\sum_{r\in\mathcal{R}} rG_{ij}^{r(0)}\Big(W_i + X_i - \frac{rl}{2}\Big) \tag{A.64}$$

$$= k^{(0)}, \tag{A.65}$$

where the last equation uses the simplified definition of $k^{(0)}$, (A.61).

We will show that $k^{(0)}$, and therefore $\sigma^{(0)}$, is independent of X_a^b. Using the simplified definition of $k^{(0)}$, (A.61), we have

$$\frac{\partial k^{(0)}}{\partial X_a^b} = \frac{\partial}{\partial X_a^b}\Big(-\sum_{i=1}^{N}\sum_{j=1}^{N}\sum_{r\in\mathcal{R}} r G_{ij}^{r(0)}\Big(W_i + X_i - \frac{rl}{2}\Big)\Big) \tag{A.66}$$

$$= -\sum_{i=1}^{N}\sum_{j=1}^{N}\sum_{r\in\mathcal{R}} r G_{ij}^{r(0)}\Big(\frac{\partial W_i}{\partial X_a^b} + \delta_{ia}\delta^{nb}\Big). \tag{A.67}$$

Now, we note that

$$\Big(\boldsymbol{A}^{(0)}\frac{\partial \boldsymbol{W}}{\partial X_a^b}\Big)_i = \Big(\frac{\partial}{\partial X_a^b}(\boldsymbol{A}^{(0)}\boldsymbol{W})\Big)_i \tag{A.68}$$

$$= \Big(\frac{\partial}{\partial X_a^b}(-\boldsymbol{B}^{(0)}\mathbf{1})\Big)_i \tag{A.69}$$

$$= -\frac{\partial}{\partial X_a^b}\left(\sum_{j=1}^{N}\sum_{r\in\mathcal{R}}\Big(G_{ij}^{r(0)}(X_j + rl) - \delta_{ij}X_i\sum_{k=1}^{N}G_{ik}^{r(0)}\Big)\right) \tag{A.70}$$

$$= -\frac{\partial}{\partial X_a^b}\left(\sum_{j=1}^{N}\sum_{r\in\mathcal{R}} G_{ij}^{r(0)}(X_j + rl) - \sum_{j=1}^{N}\sum_{r\in\mathcal{R}} G_{ij}^{r(0)}X_i\right) \tag{A.71}$$

$$= -\left(\sum_{j=1}^{N}\sum_{r\in\mathcal{R}} G_{ij}^{r(0)}\delta_{ja}\delta^{nb} - \sum_{j=1}^{N}\sum_{r\in\mathcal{R}} G_{ij}^{r(0)}\delta_{ia}\delta^{nb}\right) \tag{A.72}$$

$$= -\left(\sum_{r\in\mathcal{R}}\Big(G_{ia}^{r(0)} - \delta_{ia}\sum_{k=1}^{N}G_{ik}^{r(0)}\Big)\right)\delta^{nb} \tag{A.73}$$

$$= -A_{ia}^{(0)}\delta^{nb} \tag{A.74}$$

$$= -\Big(\boldsymbol{A}^{(0)}\boldsymbol{e}_a\delta^{nb}\Big)_i, \tag{A.75}$$

where the first equation uses the cell problem, (11.52). Therefore

$$\boldsymbol{A}^{(0)}\Big(\frac{\partial \boldsymbol{W}}{\partial X_a^b} + \boldsymbol{e}_a\delta^{nb}\Big) = \mathbf{0}, \tag{A.76}$$

and so, using that $\boldsymbol{A}^{(0)}\mathbf{1} = \mathbf{0}$ from (11.43), we arrive at

$$\frac{\partial \boldsymbol{W}}{\partial X_a^b} = \alpha\mathbf{1} - \boldsymbol{e}_a\delta^{nb}, \tag{A.77}$$

so that

$$\frac{\partial W_i}{\partial X_a^b} = \alpha - \delta_{ia}\delta^{nb}, \tag{A.78}$$

for some function $\alpha(x,t)$ that is independent of the microscale. Substituting this result, (A.78), into the equation for the derivative of $k^{(0)}$, (A.67), we find that

$$\frac{\partial k^{(0)}}{\partial X_a^b} = -\sum_{i=1}^{N}\sum_{j=1}^{N}\sum_{r\in\mathcal{R}} r G_{ij}^{r(0)}\Big(\frac{\partial W_i}{\partial X_a^b} + \delta_{ia}\delta^{nb}\Big) \tag{A.79}$$

$$= -\sum_{i=1}^{N}\sum_{j=1}^{N}\sum_{r\in\mathcal{R}} r G_{ij}^{r(0)}\alpha \tag{A.80}$$

$$= -\sum_{i=1}^{N}\sum_{j=1}^{N}\sum_{r\in\mathcal{R}} (-r) G_{ij}^{r(0)}\alpha \tag{A.81}$$

$$= \sum_{i=1}^{N}\sum_{j=1}^{N}\sum_{r\in\mathcal{R}} r G_{ij}^{r(0)}\alpha \tag{A.82}$$

$$= -\frac{\partial k^{(0)}}{\partial X_a^b}, \tag{A.83}$$

where the third equation uses Operation 1 followed by Operation 2. We have therefore shown that

$$\frac{\partial k^{(0)}}{\partial X_a^b} = 0, \tag{A.84}$$

and therefore that

$$\frac{\partial}{\partial X_a^b}\left(\frac{1}{l}\Big(\mathbf{1}^\top \boldsymbol{B}^{(0)}\boldsymbol{W} + \mathbf{1}^\top \boldsymbol{C}^{(0)}\mathbf{1}\Big)\right) = \frac{\partial \sigma^{(0)}}{\partial X_a^b} \tag{A.85}$$

$$= \frac{\partial k^{(0)}}{\partial X_a^b} \tag{A.86}$$

$$= 0, \tag{A.87}$$

where the first equation uses the definition of $\sigma^{(0)}$. So $k^{(0)}$ and $\sigma^{(0)}$, and therefore $\boldsymbol{B}^{(0)}$ and $\boldsymbol{C}^{(0)}$, are independent of X_a^b, which permits the choice $X_a^b = 0$ in the original definitions of the latter two, (11.38) and (11.39), allowing us to re-write these as

$$B_{ij}^{(0)} = \sum_{r\in\mathcal{R}} G_{ij}^{r(0)} r l, \tag{A.88}$$

$$C_{ij}^{(0)} = \frac{1}{2}\sum_{r\in\mathcal{R}} G_{ij}^{r(0)} r^2 l^2. \tag{A.89}$$

This completes our proof.

Using these more simple definitions, we also note that $\boldsymbol{B}^{(0)}$ is skew-symmetric so that

$$\Big(\boldsymbol{B}^{(0)}\Big)^\top = -\boldsymbol{B}^{(0)}, \tag{A.90}$$

and $\boldsymbol{C}^{(0)}$ is symmetric so that

$$\left(\boldsymbol{C}^{(0)}\right)^{\top} = \boldsymbol{C}^{(0)}, \tag{A.91}$$

since, using Operation 2,

$$\begin{aligned} B_{ji}^{(0)} &= \sum_{r\in\mathcal{R}} G_{ji}^{r(0)} rl && \text{(A.92)}\\ &= \sum_{r\in\mathcal{R}} G_{ij}^{-r(0)} rl && \text{(A.93)}\\ &= \sum_{r\in\mathcal{R}} G_{ij}^{r(0)} (-r) l && \text{(A.94)}\\ &= -\sum_{r\in\mathcal{R}} G_{ij}^{r(0)} rl && \text{(A.95)}\\ &= -B_{ij}^{(0)}, && \text{(A.96)} \end{aligned}$$

and

$$\begin{aligned} C_{ji}^{(0)} &= \frac{1}{2}\sum_{r\in\mathcal{R}} G_{ji}^{r(0)} r^2 l^2 && \text{(A.97)}\\ &= \frac{1}{2}\sum_{r\in\mathcal{R}} G_{ij}^{-r(0)} r^2 l^2 && \text{(A.98)}\\ &= \frac{1}{2}\sum_{r\in\mathcal{R}} G_{ij}^{r(0)} (-r) l (-r) l && \text{(A.99)}\\ &= \frac{1}{2}\sum_{r\in\mathcal{R}} G_{ij}^{r(0)} r^2 l^2 && \text{(A.100)}\\ &= C_{ij}^{(0)}. && \text{(A.101)} \end{aligned}$$

A.1.4 Intra-cell particle conservation

In this subsection, we show that $\mathbf{1}^\top \boldsymbol{S}^{(0)} = \mathbf{0}^\top$ and $\boldsymbol{S}^{(0)}\mathbf{1} = \mathbf{0}$. We first show that $\boldsymbol{S}^{(0)}\mathbf{1} = \mathbf{0}$. We have

$$\left(\boldsymbol{S}^{(0)}\mathbf{1}\right)_i = \sum_{j=1}^{N}\sum_{r\in\mathcal{R}}\Big(G_{ij}^{r(0)}(W_j - W_i + X_j + rl - X_i)H_{ji}^{-r(0)} + \tag{A.102}$$

$$\delta_{ij}\sum_{k=1}^{N} G_{ik}^{r(0)}(W_k - W_i + X_k + rl - X_i)H_{ik}^{r(0)}\Big)$$

$$= \sum_{j=1}^{N}\sum_{r\in\mathcal{R}}\Big(G_{ij}^{r(0)}(W_j - W_i + X_j + rl - X_i) \tag{A.103}$$

$$= \sum_{j=1}^{N}\sum_{r\in\mathcal{R}}\Big(G_{ij}^{r(0)} - \delta_{ij}\sum_{k=1}^{N} G_{ik}^{r(0)}\Big)W_j + \tag{A.104}$$

$$\sum_{j=1}^{N}\sum_{r\in\mathcal{R}}\Big(G_{ij}^{r(0)}(X_j + rl) - \delta_{ij}\sum_{k=1}^{N} G_{ik}^{r(0)}X_i\Big)$$

$$= (\boldsymbol{A}^{(0)}\boldsymbol{W})_i + (\boldsymbol{B}^{(0)}\mathbf{1})_i \tag{A.105}$$

$$= 0. \tag{A.106}$$

The first equation uses the definition of $\boldsymbol{S}^{(0)}$, (11.77), the second uses δ_{ij} followed by the Heaviside identity, (11.74), and the fifth uses the cell problem,

Next, we show that $\mathbf{1}^\top \boldsymbol{S}^{(0)} = \mathbf{0}^\top$. We have

$$\left(\mathbf{1}^\top \boldsymbol{S}^{(0)}\right)_j = \sum_{i=1}^{N}\sum_{r\in\mathcal{R}}\Big(G_{ij}^{r(0)}(W_j - W_i + X_j + rl - X_i)H_{ji}^{-r(0)} + \delta_{ij}\sum_{k=1}^{N} G_{ik}^{r(0)}(W_k - W_i + X_k + rl - X_i)H_{ik}^{r(0)}\Big) \tag{A.107}$$

$$= \sum_{i=1}^{N}\sum_{r\in\mathcal{R}}\Big(G_{ij}^{r(0)}(W_j - W_i + X_j + rl - X_i)H_{ji}^{-r(0)} + \sum_{i=1}^{N}\sum_{r\in\mathcal{R}} G_{ji}^{r(0)}(W_i - W_j + X_i + rl - X_j)H_{ji}^{r(0)}\Big) \tag{A.108}$$

$$= \sum_{i=1}^{N}\sum_{r\in\mathcal{R}}\Big(G_{ij}^{r(0)}(W_j - W_i + X_j + rl - X_i)H_{ji}^{-r(0)} - \sum_{i=1}^{N}\sum_{r\in\mathcal{R}} G_{ji}^{r(0)}(W_j - W_i + X_j - rl - X_i)H_{ji}^{r(0)}\Big) \tag{A.109}$$

$$= \sum_{i=1}^{N}\sum_{r\in\mathcal{R}}\Big(G_{ij}^{r(0)}(W_j - W_i + X_j + rl - X_i)H_{ji}^{-r(0)} - \sum_{i=1}^{N}\sum_{r\in\mathcal{R}} G_{ij}^{r(0)}(W_j - W_i + X_j + rl - X_i)H_{ji}^{-r(0)}\Big) \tag{A.110}$$

$$= 0. \tag{A.111}$$

The second equation uses δ_{ij} followed by a re-indexing $k \to i$ in the second term, the third uses a factorisation of -1 in the second term to achieve like-terms, and the fourth uses the symmetry of conductance in the second term followed by Operation 2 on the second term.

A.1.5 Interpretation of advective terms

In this subsection we show that the coefficient in the advective term of equation for conservation of particles, (11.92), is related to the permeability by

$$\mathbf{1}^\top \boldsymbol{K}^{(0)}\mathbf{1} = lk^{(0)} = l\sigma^{(0)}. \tag{A.112}$$

We have

$$\mathbf{1}^\top \boldsymbol{K}^{(0)}\mathbf{1} = \sum_{i=1}^{N}\sum_{j=1}^{N}\sum_{r\in\mathcal{R}} G_{ij}^{r(0)}(W_j - W_i + X_j + rl - X_i)(X_j + rl)H_{ji}^{-r(0)} + \tag{A.113}$$
$$\sum_{i=1}^{N}\sum_{j=1}^{N}\sum_{r\in\mathcal{R}} G_{ij}^{r(0)}(W_j - W_i + X_j + rl - X_i)X_i H_{ij}^{r(0)}$$
$$= \sum_{i=1}^{N}\sum_{j=1}^{N}\sum_{r\in\mathcal{R}} G_{ij}^{r(0)}(W_j - W_i + X_j + rl - X_i)(X_j + rl)H_{ji}^{-r(0)} + \tag{A.114}$$
$$\sum_{i=1}^{N}\sum_{j=1}^{N}\sum_{r\in\mathcal{R}} G_{ij}^{-\boldsymbol{r}(0)}(W_i - W_j + X_i + rl - X_j)X_j H_{ji}^{r(0)}$$
$$= \sum_{i=1}^{N}\sum_{j=1}^{N}\sum_{r\in\mathcal{R}} G_{ij}^{r(0)}(W_j - W_i + X_j + rl - X_i)(X_j + rl)H_{ji}^{-r(0)} + \tag{A.115}$$
$$\sum_{i=1}^{N}\sum_{j=1}^{N}\sum_{r\in\mathcal{R}} G_{ij}^{r(0)}(W_i - W_j + X_i - rl - X_j)X_j H_{ji}^{-r(0)}$$
$$= \sum_{i=1}^{N}\sum_{j=1}^{N}\sum_{r\in\mathcal{R}} G_{ij}^{r(0)}(W_j - W_i + X_j + rl - X_i)rlH_{ji}^{-r(0)}, \tag{A.116}$$

where the first equation uses an expansion of the definition of $K_{ij}^{(0)}$, (11.83), the second uses Operation 1 on the second term, and the third uses Operation 2 on the second term. Defining

$$\Lambda_{ij}^{r(0)} = G_{ij}^{r(0)}(W_j - W_i + X_j + rl - X_i)rl, \tag{A.117}$$

and noting that $\Lambda_{ji}^{-r(0)} = \Lambda_{ij}^{r(0)}$, it follows that

$$\mathbf{1}^\top \boldsymbol{K}^{(0)}\mathbf{1} = \frac{1}{2}\sum_{i=1}^{N}\sum_{j=1}^{N}\sum_{r\in\mathcal{R}} \Lambda_{ij}^{r(0)}H_{ji}^{-r(0)} + \frac{1}{2}\sum_{j=1}^{N}\sum_{i=1}^{N}\sum_{r\in\mathcal{R}} \Lambda_{ji}^{r(0)}H_{ij}^{-r(0)} \tag{A.118}$$
$$= \frac{1}{2}\sum_{i=1}^{N}\sum_{j=1}^{N}\sum_{-r} \Lambda_{ij}^{r(0)}H_{ji}^{-r(0)} + \frac{1}{2}\sum_{i=1}^{N}\sum_{j=1}^{N}\sum_{r\in\mathcal{R}} \Lambda_{ij}^{-r(0)}H_{ij}^{-r(0)} \tag{A.119}$$
$$= \frac{1}{2}\sum_{i=1}^{N}\sum_{j=1}^{N}\sum_{r\in\mathcal{R}} \Lambda_{ij}^{r(0)} \tag{A.120}$$
$$= \frac{1}{2}\sum_{i=1}^{N}\sum_{j=1}^{N}\sum_{r\in\mathcal{R}} G_{ij}^{r(0)}(W_j - W_i + X_j + rl - X_i)rl \tag{A.121}$$
$$= lk^{(0)}, \tag{A.122}$$

where the first equation uses a splitting of terms followed by a re-labelling $i \leftrightarrow j$ in the second term, the second uses the symmetry of $\Lambda_{ij}^{r(0)}$, the third uses Operation 2 on

the second term followed by the Heaviside function identity, (11.74), the fourth uses the definition of $\Lambda_{ij}^{r(0)}$, (A.117), and the fifth uses the definition of the permeability, (11.68).

A.2 Algebraic results in D dimensions

In this section, we prove the algebraic results necessary for network homogenisation in D dimensions.

A.2.1 Relation of basic matrices

In this subsection, we show that

$$\boldsymbol{A}^{(s)}\mathbf{1} = \mathbf{0}, \quad \mathbf{1}^\top \boldsymbol{B}^{m(s)}\mathbf{1} = \mathbf{0}, \quad \boldsymbol{D}^{m(s)}\mathbf{1} = \mathbf{0}, \quad \boldsymbol{F}^{mn(s)}\mathbf{1} = \mathbf{0}, \tag{A.123}$$

and that

$$\mathbf{1}^\top \boldsymbol{D}^{m(s)} = \frac{\partial}{\partial x^m}\Big(\mathbf{1}^\top \boldsymbol{B}^{m(s)}\Big), \tag{A.124}$$

$$\mathbf{1}^\top \boldsymbol{E}^{mn(s)}\mathbf{1} = \frac{\partial}{\partial x^m}\Big(\mathbf{1}^\top \boldsymbol{C}^{mn(s)}\mathbf{1}\Big) + \frac{1}{2}\sum_{i=1}^{N}\sum_{j=1}^{N}\sum_{\boldsymbol{r}\in\boldsymbol{\mathcal{R}}} \frac{\partial G_{ij}^{\boldsymbol{r}(s)}}{\partial x^m}(r^n l^n X_i^m - r^m l^m X_i^n). \tag{A.125}$$

To show the results in (A.123), firstly, we have

$$\Big(\boldsymbol{A}^{(s)}\mathbf{1}\Big)_i = \sum_{j=1}^{N}\sum_{\boldsymbol{r}\in\boldsymbol{\mathcal{R}}}\Big(G_{ij}^{\boldsymbol{r}(s)} - \delta_{ij}\sum_{k=1}^{N} G_{ik}^{\boldsymbol{r}(s)}\Big) \tag{A.126}$$

$$= \sum_{j=1}^{N}\sum_{\boldsymbol{r}\in\boldsymbol{\mathcal{R}}} G_{ij}^{\boldsymbol{r}(s)} - \sum_{j=1}^{N}\sum_{\boldsymbol{r}\in\boldsymbol{\mathcal{R}}} G_{ij}^{\boldsymbol{r}(s)} \tag{A.127}$$

$$= 0. \tag{A.128}$$

Secondly, we have

$$\mathbf{1}^\top \boldsymbol{B}^{m(s)}\mathbf{1} = \sum_{i=1}^{N}\sum_{j=1}^{N}\sum_{\boldsymbol{r}\in\boldsymbol{\mathcal{R}}}\left(G_{ij}^{\boldsymbol{r}(s)}(X_j^m + r^m l^m) - \delta_{ij}X_i^m\sum_{k=1}^{N}G_{ik}^{\boldsymbol{r}(s)}\right) \tag{A.129}$$

$$= \sum_{i=1}^{N}\sum_{j=1}^{N}\sum_{\boldsymbol{r}\in\boldsymbol{\mathcal{R}}}G_{ij}^{\boldsymbol{r}(s)}(X_j^m + r^m l^m) - \sum_{i=1}^{N}\sum_{j=1}^{N}\sum_{\boldsymbol{r}\in\boldsymbol{\mathcal{R}}}G_{ij}^{\boldsymbol{r}(s)}X_i^m \tag{A.130}$$

$$= \sum_{i=1}^{N}\sum_{j=1}^{N}\sum_{\boldsymbol{r}\in\boldsymbol{\mathcal{R}}}G_{ij}^{\boldsymbol{r}(s)}(X_j^m + r^m l^m) - \sum_{i=1}^{N}\sum_{j=1}^{N}\sum_{\boldsymbol{r}\in\boldsymbol{\mathcal{R}}}G_{ij}^{-\boldsymbol{r}(s)}X_j^m \tag{A.131}$$

$$= \sum_{i=1}^{N}\sum_{j=1}^{N}\sum_{\boldsymbol{r}\in\boldsymbol{\mathcal{R}}}G_{ij}^{\boldsymbol{r}(s)}(X_j^m + r^m l^m) - \sum_{i=1}^{N}\sum_{j=1}^{N}\sum_{\boldsymbol{r}\in\boldsymbol{\mathcal{R}}}G_{ij}^{\boldsymbol{r}(s)}X_j^m \tag{A.132}$$

$$= l^m\sum_{i=1}^{N}\sum_{j=1}^{N}\sum_{\boldsymbol{r}\in\boldsymbol{\mathcal{R}}}G_{ij}^{\boldsymbol{r}(s)}r^m \tag{A.133}$$

$$= -l^m\sum_{i=1}^{N}\sum_{j=1}^{N}\sum_{\boldsymbol{r}\in\boldsymbol{\mathcal{R}}}G_{ij}^{\boldsymbol{r}(s)}r^m \tag{A.134}$$

$$= 0, \tag{A.135}$$

where the second equation uses δ_{ij} followed by a re-indexing $k \to j$, the third uses Operation 1 on the second term, the fourth uses Operation 2 on the second term, and the sixth uses that if $r^m \in \mathcal{R}$ then $-r^m \in \mathcal{R}$. Thirdly, we have

$$\left(\boldsymbol{D}^{m(s)}\mathbf{1}\right)_i = \sum_{j=1}^{N}\sum_{\boldsymbol{r}\in\boldsymbol{\mathcal{R}}}\left(\frac{\partial G_{ij}^{\boldsymbol{r}(s)}}{\partial x^m}M_{ij}^{\boldsymbol{r}m} - \delta_{ij}\sum_{k=1}^{N}\frac{\partial G_{ik}^{\boldsymbol{r}(s)}}{\partial x^m}M_{ik}^{\boldsymbol{r}m}\right) \tag{A.136}$$

$$= \sum_{j=1}^{N}\sum_{\boldsymbol{r}\in\boldsymbol{\mathcal{R}}}\frac{\partial G_{ij}^{\boldsymbol{r}(s)}}{\partial x^m}M_{ij}^{\boldsymbol{r}m} - \sum_{j=1}^{N}\sum_{\boldsymbol{r}\in\boldsymbol{\mathcal{R}}}\frac{\partial G_{ij}^{\boldsymbol{r}(s)}}{\partial x^m}M_{ij}^{\boldsymbol{r}m} \tag{A.137}$$

$$= 0. \tag{A.138}$$

Lastly, we have

$$\left(\boldsymbol{F}^{mn(s)}\mathbf{1}\right)_i = \frac{1}{2}\sum_{j=1}^{N}\sum_{\boldsymbol{r}\in\boldsymbol{\mathcal{R}}}\left(\frac{\partial^2 G_{ij}^{\boldsymbol{r}(s)}}{\partial x^m\partial x^n}M_{ij}^{\boldsymbol{r}m}M_{ij}^{\boldsymbol{r}n} - \delta_{ij}\sum_{k=1}^{N}\frac{\partial^2 G_{ik}^{\boldsymbol{r}(s)}}{\partial x^m\partial x^n}M_{ik}^{\boldsymbol{r}m}M_{ik}^{\boldsymbol{r}n}\right) \tag{A.139}$$

$$= \frac{1}{2}\left(\sum_{j=1}^{N}\sum_{\boldsymbol{r}\in\boldsymbol{\mathcal{R}}}\frac{\partial^2 G_{ij}^{\boldsymbol{r}(s)}}{\partial x^m\partial x^n}M_{ij}^{\boldsymbol{r}m}M_{ij}^{\boldsymbol{r}n} - \sum_{j=1}^{N}\sum_{\boldsymbol{r}\in\boldsymbol{\mathcal{R}}}\frac{\partial^2 G_{ij}^{\boldsymbol{r}(s)}}{\partial x^m\partial x^n}M_{ij}^{\boldsymbol{r}m}M_{ij}^{\boldsymbol{r}n}\right) \tag{A.140}$$

$$= 0. \tag{A.141}$$

We next show the result given by (A.124). On one hand,

$$\frac{\partial}{\partial x^m}\left(\mathbf{1}^\top \boldsymbol{B}^{m(s)}\right)_j = \frac{\partial}{\partial x^m}\left(\sum_{i=1}^{N}\sum_{\boldsymbol{r}\in\boldsymbol{\mathcal{R}}}\left(G_{ij}^{\boldsymbol{r}(s)}(X_j^m + r^m l^m) - \delta_{ij}X_i^m\sum_{k=1}^{N}G_{ik}^{\boldsymbol{r}(s)}\right)\right) \tag{A.142}$$

$$= \sum_{i=1}^{N}\sum_{\boldsymbol{r}\in\boldsymbol{\mathcal{R}}}\left(\frac{\partial G_{ij}^{\boldsymbol{r}(s)}}{\partial x^m}(X_j^m + r^m l^m) - \delta_{ij}X_i^m\sum_{k=1}^{N}\frac{\partial G_{ik}^{\boldsymbol{r}(s)}}{\partial x^m}\right) \tag{A.143}$$

$$= \sum_{i=1}^{N}\sum_{\boldsymbol{r}\in\boldsymbol{\mathcal{R}}}\frac{\partial G_{ij}^{\boldsymbol{r}(s)}}{\partial x^m}(X_j^m + r^m l^m) - \sum_{i=1}^{N}\sum_{\boldsymbol{r}\in\boldsymbol{\mathcal{R}}}\frac{\partial G_{ji}^{\boldsymbol{r}(s)}}{\partial x^m}X_j^m \tag{A.144}$$

$$= \sum_{i=1}^{N}\sum_{\boldsymbol{r}\in\boldsymbol{\mathcal{R}}}\frac{\partial G_{ij}^{\boldsymbol{r}(s)}}{\partial x^m}(X_j^m + r^m l^m) - \sum_{i=1}^{N}\sum_{\boldsymbol{r}\in\boldsymbol{\mathcal{R}}}\frac{\partial G_{ij}^{-\boldsymbol{r}(s)}}{\partial x^m}X_j^m \tag{A.145}$$

$$= \sum_{i=1}^{N}\sum_{\boldsymbol{r}\in\boldsymbol{\mathcal{R}}}\frac{\partial G_{ij}^{\boldsymbol{r}(s)}}{\partial x^m}(X_j^m + r^m l^m) - \sum_{i=1}^{N}\sum_{\boldsymbol{r}\in\boldsymbol{\mathcal{R}}}\frac{\partial G_{ij}^{\boldsymbol{r}(s)}}{\partial x^m}X_j^m \tag{A.146}$$

$$= \sum_{i=1}^{N}\sum_{\boldsymbol{r}\in\boldsymbol{\mathcal{R}}}\frac{\partial G_{ij}^{\boldsymbol{r}(s)}}{\partial x^m}r^m l^m, \tag{A.147}$$

where the third equation uses δ_{ij} followed by a re-indexing $k \to i$, the fourth the symmetry of conductance, and the fifth uses Operation 2 on the second term. On the other hand,

$$\left(\mathbf{1}^\top \boldsymbol{D}^{m(s)}\right)_j = \sum_{i=1}^{N}\sum_{\boldsymbol{r}\in\boldsymbol{\mathcal{R}}}\left(\frac{\partial G_{ij}^{\boldsymbol{r}(s)}}{\partial x^m}M_{ij}^{\boldsymbol{r}m} - \delta_{ij}\sum_{k=1}^{N}\frac{\partial G_{ik}^{\boldsymbol{r}(s)}}{\partial x^m}M_{ik}^{\boldsymbol{r}m}\right) \tag{A.148}$$

$$= \sum_{i=1}^{N}\sum_{\boldsymbol{r}\in\boldsymbol{\mathcal{R}}}\frac{\partial G_{ij}^{\boldsymbol{r}(s)}}{\partial x^m}M_{ij}^{\boldsymbol{r}m} - \sum_{i=1}^{N}\sum_{\boldsymbol{r}\in\boldsymbol{\mathcal{R}}}\frac{\partial G_{ji}^{\boldsymbol{r}(s)}}{\partial x^m}M_{ji}^{\boldsymbol{r}m} \tag{A.149}$$

$$= \sum_{i=1}^{N}\sum_{\boldsymbol{r}\in\boldsymbol{\mathcal{R}}}\frac{\partial G_{ij}^{\boldsymbol{r}(s)}}{\partial x^m}M_{ij}^{\boldsymbol{r}m} - \sum_{i=1}^{N}\sum_{\boldsymbol{r}\in\boldsymbol{\mathcal{R}}}\frac{\partial G_{ij}^{-\boldsymbol{r}(s)}}{\partial x^m}M_{ji}^{\boldsymbol{r}m} \tag{A.150}$$

$$= \sum_{i=1}^{N}\sum_{\boldsymbol{r}\in\boldsymbol{\mathcal{R}}}\frac{\partial G_{ij}^{\boldsymbol{r}(s)}}{\partial x^m}\left(M_{ij}^{\boldsymbol{r}m} - M_{ji}^{-\boldsymbol{r}m}\right) \tag{A.151}$$

$$= \sum_{i=1}^{N}\sum_{\boldsymbol{r}\in\boldsymbol{\mathcal{R}}}\frac{\partial G_{ij}^{\boldsymbol{r}(s)}}{\partial x^m}r^m l^m, \tag{A.152}$$

where the second equation uses δ_{ij} followed by a re-indexing $k \to i$, the third uses the symmetry of conductance, the fourth uses Operation 2 on the second term, and the fifth uses the definition of the midpoint (11.23). We lastly show the result given

by (A.126). On one hand,

$$\frac{\partial}{\partial x^m}\Big(\mathbf{1}^\top \boldsymbol{C}^{mn(s)}\mathbf{1}\Big) = \frac{\partial}{\partial x^m}\Bigg(\frac{1}{2}\sum_{i=1}^{N}\sum_{j=1}^{N}\sum_{\boldsymbol{r}\in\boldsymbol{\mathcal{R}}}\Bigg(G_{ij}^{\boldsymbol{r}(s)}(X_j^m + r^m l^m)(X_j^n + r^n l^n) - \tag{A.153}$$

$$\delta_{ij} X_i^m X_i^n \sum_{k=1}^{N} G_{ik}^{\boldsymbol{r}(s)}\Bigg)\Bigg)$$

$$= \frac{1}{2}\sum_{i=1}^{N}\sum_{j=1}^{N}\sum_{\boldsymbol{r}\in\boldsymbol{\mathcal{R}}}\Bigg(\frac{\partial G_{ij}^{\boldsymbol{r}(s)}}{\partial x^m}(X_j^m + r^m l^m)(X_j^n + r^n l^n) - \tag{A.154}$$

$$\delta_{ij} X_i^m X_i^n \sum_{k=1}^{N} \frac{\partial G_{ik}^{\boldsymbol{r}(s)}}{\partial x^m}\Bigg)$$

$$= \frac{1}{2}\Bigg(\sum_{i=1}^{N}\sum_{j=1}^{N}\sum_{\boldsymbol{r}\in\boldsymbol{\mathcal{R}}}\Bigg(\frac{\partial G_{ij}^{\boldsymbol{r}(s)}}{\partial x^m}(X_j^m + r^m l^m)(X_j^n + r^n l^n) - \tag{A.155}$$

$$\sum_{i=1}^{N}\sum_{j=1}^{N}\sum_{\boldsymbol{r}\in\boldsymbol{\mathcal{R}}}\frac{\partial G_{ij}^{\boldsymbol{r}(s)}}{\partial x^m} X_i^m X_i^n\Bigg)\Bigg)$$

$$= \frac{1}{2}\Bigg(\sum_{i=1}^{N}\sum_{j=1}^{N}\sum_{\boldsymbol{r}\in\boldsymbol{\mathcal{R}}}\Bigg(\frac{\partial G_{ij}^{\boldsymbol{r}(s)}}{\partial x^m}(X_j^m + r^m l^m)(X_j^n + r^n l^n) - \tag{A.156}$$

$$\sum_{i=1}^{N}\sum_{j=1}^{N}\sum_{\boldsymbol{r}\in\boldsymbol{\mathcal{R}}}\frac{\partial G_{ij}^{-\boldsymbol{r}(s)}}{\partial x^m} X_j^m X_j^n\Bigg)\Bigg)$$

$$= \frac{1}{2}\Bigg(\sum_{i=1}^{N}\sum_{j=1}^{N}\sum_{\boldsymbol{r}\in\boldsymbol{\mathcal{R}}}\Bigg(\frac{\partial G_{ij}^{\boldsymbol{r}(s)}}{\partial x^m}(X_j^m + r^m l^m)(X_j^n + r^n l^n) - \tag{A.157}$$

$$\sum_{i=1}^{N}\sum_{j=1}^{N}\sum_{\boldsymbol{r}\in\boldsymbol{\mathcal{R}}}\frac{\partial G_{ij}^{\boldsymbol{r}(s)}}{\partial x^m} X_j^m X_j^n\Bigg)\Bigg)$$

$$= \frac{1}{2}\sum_{i=1}^{N}\sum_{j=1}^{N}\sum_{\boldsymbol{r}\in\boldsymbol{\mathcal{R}}}\frac{\partial G_{ij}^{\boldsymbol{r}(s)}}{\partial x^m}(X_j^m r^n l^n + X_j^n r^m l^m + r^m l^m r^n l^n), \tag{A.158}$$

where the third equation uses δ_{ij} followed by a re-indexing $k \to j$, the fourth uses Operation 1 on the second term, and the fifth uses Operation 2 on the second term.

On the other hand,

$$\mathbf{1}^\top \boldsymbol{E}^{mn(s)}\mathbf{1} = \sum_{i=1}^{N}\sum_{j=1}^{N}\sum_{\boldsymbol{r}\in\boldsymbol{\mathcal{R}}}\Big(\frac{\partial G_{ij}^{\boldsymbol{r}(s)}}{\partial x^m}M_{ij}^{\boldsymbol{r}m}(X_j^n + r^n l^n) - \delta_{ij}X_i^n\sum_{k=1}^{N}\frac{\partial G_{ik}^{\boldsymbol{r}(s)}}{\partial x^m}M_{ik}^{\boldsymbol{r}m}\Big) \tag{A.159}$$

$$= \sum_{i=1}^{N}\sum_{j=1}^{N}\sum_{\boldsymbol{r}\in\boldsymbol{\mathcal{R}}}\frac{\partial G_{ij}^{\boldsymbol{r}(s)}}{\partial x^m}M_{ij}^{\boldsymbol{r}m}(X_j^n + r^n l^n) - \sum_{i=1}^{N}\sum_{j=1}^{N}\sum_{\boldsymbol{r}\in\boldsymbol{\mathcal{R}}}\frac{\partial G_{ij}^{\boldsymbol{r}(s)}}{\partial x^m}M_{ij}^{\boldsymbol{r}m}X_i^n \tag{A.160}$$

$$= \sum_{i=1}^{N}\sum_{j=1}^{N}\sum_{\boldsymbol{r}\in\boldsymbol{\mathcal{R}}}\frac{\partial G_{ij}^{\boldsymbol{r}(s)}}{\partial x^m}M_{ij}^{\boldsymbol{r}m}(X_j^n + r^n l^n) - \sum_{i=1}^{N}\sum_{j=1}^{N}\sum_{\boldsymbol{r}\in\boldsymbol{\mathcal{R}}}\frac{\partial G_{ij}^{-\boldsymbol{r}(s)}}{\partial x^m}M_{ji}^{\boldsymbol{r}m}X_j^n \tag{A.161}$$

$$= \sum_{i=1}^{N}\sum_{j=1}^{N}\sum_{\boldsymbol{r}\in\boldsymbol{\mathcal{R}}}\frac{\partial G_{ij}^{\boldsymbol{r}(s)}}{\partial x^m}M_{ij}^{\boldsymbol{r}m}(X_j^n + r^n l^n) - \sum_{i=1}^{N}\sum_{j=1}^{N}\sum_{\boldsymbol{r}\in\boldsymbol{\mathcal{R}}}\frac{\partial G_{ij}^{\boldsymbol{r}(s)}}{\partial x^m}M_{ji}^{-\boldsymbol{r}m}X_j^n \tag{A.162}$$

$$= \frac{1}{2}\sum_{i=1}^{N}\sum_{j=1}^{N}\sum_{\boldsymbol{r}\in\boldsymbol{\mathcal{R}}}\frac{\partial G_{ij}^{\boldsymbol{r}(s)}}{\partial x^m}\Big(X_j^m r^n l^n + X_j^n r^m l^m + r^m l^m r^n l^n + X_j^n r^m l^m + X_i^m r^n l^n\Big) \tag{A.163}$$

$$= \frac{\partial}{\partial x^m}\Big(\mathbf{1}^\top \boldsymbol{C}^{mn(s)}\mathbf{1}\Big) + \frac{1}{2}\sum_{i=1}^{N}\sum_{j=1}^{N}\sum_{\boldsymbol{r}\in\boldsymbol{\mathcal{R}}}\frac{\partial G_{ij}^{\boldsymbol{r}(s)}}{\partial x^m}\Big(X_j^n r^m l^m + X_i^m r^n l^n\Big), \tag{A.164}$$

where the second equation uses δ_{ij} followed by a re-indexing $k \to j$, the third uses Operation 1 on the second term, the fourth uses Operation 2 on the second term, and the fifth uses the definition of the midpoint, (11.23).

A.2.2 Simplification of permeability terms

In this subsection, we simplify the terms in the permeability tensor, $\boldsymbol{k}^{(0)}$. Firstly, we show that

$$\mathbf{1}^\top \boldsymbol{B}^{m(0)} \boldsymbol{W}^n = -l^m \sum_{i=1}^{N} \sum_{j=1}^{N} \sum_{\boldsymbol{r}\in\boldsymbol{\mathcal{R}}} r^m G_{ij}^{\boldsymbol{r}(0)} W_i^n. \tag{A.165}$$

We have

$$\mathbf{1}^\top \boldsymbol{B}^{m(0)} \boldsymbol{W}^n = \sum_{i=1}^{N} \sum_{j=1}^{N} \sum_{\boldsymbol{r}\in\boldsymbol{\mathcal{R}}} \left(G_{ij}^{\boldsymbol{r}(0)} (X_j^m + r^m l^m) - \delta_{ij} X_i^m \sum_{k=1}^{N} G_{ik}^{\boldsymbol{r}(0)} \right) W_j^n \tag{A.166}$$

$$= \sum_{i=1}^{N} \sum_{j=1}^{N} \sum_{\boldsymbol{r}\in\boldsymbol{\mathcal{R}}} G_{ij}^{\boldsymbol{r}(0)} W_j^n (X_j^m + r^m l^m) - \tag{A.167}$$

$$\sum_{i=1}^{N} \sum_{j=1}^{N} \sum_{\boldsymbol{r}\in\boldsymbol{\mathcal{R}}} G_{ij}^{\boldsymbol{r}(0)} W_i^n X_i^m$$

$$= \sum_{i=1}^{N} \sum_{j=1}^{N} \sum_{\boldsymbol{r}\in\boldsymbol{\mathcal{R}}} G_{ij}^{-\boldsymbol{r}(0)} W_i^n (X_i^m + r^m l^m) - \tag{A.168}$$

$$\sum_{i=1}^{N} \sum_{j=1}^{N} \sum_{\boldsymbol{r}\in\boldsymbol{\mathcal{R}}} G_{ij}^{\boldsymbol{r}(0)} W_i^n X_i^m$$

$$= \sum_{i=1}^{N} \sum_{j=1}^{N} \sum_{\boldsymbol{r}\in\boldsymbol{\mathcal{R}}} G_{ij}^{\boldsymbol{r}(0)} W_i^n (X_i^m + (-r^m) l^m) - \tag{A.169}$$

$$\sum_{i=1}^{N} \sum_{j=1}^{N} \sum_{\boldsymbol{r}\in\boldsymbol{\mathcal{R}}} G_{ij}^{\boldsymbol{r}(0)} W_i^n X_i^m$$

$$= -l^m \sum_{i=1}^{N} \sum_{j=1}^{N} \sum_{\boldsymbol{r}\in\boldsymbol{\mathcal{R}}} r^m G_{ij}^{\boldsymbol{r}(0)} W_i^n. \tag{A.170}$$

The first equation uses δ_{ij} followed by a re-indexing $k \to j$, the third uses Operation 1 on the first sum, and the fourth uses Operation 2 on the first term. Since the above was calculated without loss of generality in m and n, it trivially follows that

$$\mathbf{1}^\top \boldsymbol{B}^{n(0)} \boldsymbol{W}^m = -l^n \sum_{i=1}^{N} \sum_{j=1}^{N} \sum_{\boldsymbol{r}\in\boldsymbol{\mathcal{R}}} r^n G_{ij}^{\boldsymbol{r}(0)} W_i^m. \tag{A.171}$$

Secondly, we prove that

$$\mathbf{1}^\top \boldsymbol{C}^{mn(0)} \mathbf{1} = -\frac{1}{2} \sum_{i=1}^{N} \sum_{j=1}^{N} \sum_{\boldsymbol{r}\in\boldsymbol{\mathcal{R}}} G_{ij}^{\boldsymbol{r}(0)} \Big(X_i^m r^n l^n + X_i^n r^m l^m - r^m l^m r^n l^n \Big). \tag{A.172}$$

We have

$$\mathbf{1}^\top \boldsymbol{C}^{mn(0)}\mathbf{1} = \frac{1}{2}\sum_{\boldsymbol{r}\in\boldsymbol{\mathcal{R}}}\left(G_{ij}^{\boldsymbol{r}(0)}(X_j^m + r^m l^m)(X_j^n + r^n l^n) - \delta_{ij}X_i^m X_i^n \sum_{k=1}^{N} G_{ik}^{\boldsymbol{r}(0)}\right) \tag{A.173}$$

$$= \frac{1}{2}\Bigg(\sum_{i=1}^{N}\sum_{j=1}^{N}\sum_{\boldsymbol{r}\in\boldsymbol{\mathcal{R}}} G_{ij}^{\boldsymbol{r}(0)} X_j^m X_j^n + \tag{A.174}$$

$$\sum_{i=1}^{N}\sum_{j=1}^{N}\sum_{\boldsymbol{r}\in\boldsymbol{\mathcal{R}}} G_{ij}^{\boldsymbol{r}(0)}\Big(X_j^m r^n l^n + X_j^n r^m l^m\Big) +$$

$$\sum_{i=1}^{N}\sum_{j=1}^{N}\sum_{\boldsymbol{r}\in\boldsymbol{\mathcal{R}}} G_{ij}^{\boldsymbol{r}(0)} r^m l^m r^n l^n - \sum_{i=1}^{N}\sum_{j=1}^{N}\sum_{\boldsymbol{r}\in\boldsymbol{\mathcal{R}}} G_{ij}^{\boldsymbol{r}(0)} X_i^m X_i^n\Bigg)$$

$$= \frac{1}{2}\Bigg(\sum_{i=1}^{N}\sum_{j=1}^{N}\sum_{\boldsymbol{r}\in\boldsymbol{\mathcal{R}}} G_{ij}^{-\boldsymbol{r}(0)} X_i^m X_i^n + \tag{A.175}$$

$$\sum_{i=1}^{N}\sum_{j=1}^{N}\sum_{\boldsymbol{r}\in\boldsymbol{\mathcal{R}}} G_{ij}^{-\boldsymbol{r}(0)}\Big(X_i^m r^n l^n + X_i^n r^m l^m\Big) +$$

$$\sum_{i=1}^{N}\sum_{j=1}^{N}\sum_{\boldsymbol{r}\in\boldsymbol{\mathcal{R}}} G_{ij}^{\boldsymbol{r}(0)} r^m l^m r^n l^n - \sum_{i=1}^{N}\sum_{j=1}^{N}\sum_{\boldsymbol{r}\in\boldsymbol{\mathcal{R}}} G_{ij}^{\boldsymbol{r}(0)} X_i^m X_i^n\Bigg)$$

$$= -\frac{1}{2}\sum_{i=1}^{N}\sum_{j=1}^{N}\sum_{\boldsymbol{r}\in\boldsymbol{\mathcal{R}}} G_{ij}^{\boldsymbol{r}(0)}\Big(X_i^m r^n l^n + X_i^n r^m l^m - r^m l^m r^n l^n\Big). \tag{A.176}$$

The second equation uses δ_{ij} followed by a re-indexing $k \to j$ in the final term, the third uses Operation 1 on the first and second terms, and the third uses Operation 2 on the first and second terms, so that the first and last terms cancel.

A.2.3 Cancellation of fluid conservation terms

In this subsection, we show that

$$G_{ij}^{\boldsymbol{r}(0)}(r^n l^n X_i^m - r^m l^m X_i^n) + \mathbf{1}^\top \boldsymbol{B}^{m(0)}\boldsymbol{W}^n - \mathbf{1}^\top \boldsymbol{B}^{n(0)}\boldsymbol{W}^m = 0. \tag{A.177}$$

First note, using the cell problem, (11.123), that

$$0 = (\boldsymbol{A}^{(0)}\boldsymbol{W}^m)_i + (\boldsymbol{B}^{m(0)}\mathbf{1})_i \tag{A.178}$$

$$= \sum_{j=1}^{N}\sum_{\boldsymbol{r}\in\boldsymbol{\mathcal{R}}}\left(G_{ij}^{\boldsymbol{r}(0)}(W_j^m + X_j^m + r^m l^m) - \delta_{ij}(W_i^m + X_i^m)\sum_{k=1}^{N} G_{ik}^{\boldsymbol{r}(0)}\right) \tag{A.179}$$

$$= \sum_{j=1}^{N}\sum_{\boldsymbol{r}\in\boldsymbol{\mathcal{R}}} G_{ij}^{\boldsymbol{r}(0)}\Big(y_j^m - y_i^m + r^m l^m\Big), \tag{A.180}$$

where we have defined $\boldsymbol{y}^m$ by $y_i^m = X_i^m + W_i^m$, so that

$$\sum_{j=1}^{N} \sum_{\boldsymbol{r}\in\boldsymbol{\mathcal{R}}} G_{ij}^{\boldsymbol{r}(0)} r^m l^m = \sum_{j=1}^{N} \sum_{\boldsymbol{r}\in\boldsymbol{\mathcal{R}}} G_{ij}^{\boldsymbol{r}(0)} \Big(y_i^m - y_j^m \Big). \tag{A.181}$$

Since we have formulated the cell problem independently of X_a^b in (A.181), the fluid conservation problem itself is independent of X_a^b, and it follows that

$$\sum_{i=1}^{N} \sum_{j=1}^{N} \sum_{\boldsymbol{r}\in\boldsymbol{\mathcal{R}}} G_{ij}^{\boldsymbol{r}(0)} (r^n l^n X_i^m - r^m l^m X_i^n) + \mathbf{1}^\top \boldsymbol{B}^{m(0)} \boldsymbol{W}^n - \mathbf{1}^\top \boldsymbol{B}^{n(0)} \boldsymbol{W}^m = \tag{A.182}$$

$$\sum_{i=1}^{N} \sum_{j=1}^{N} \sum_{\boldsymbol{r}\in\boldsymbol{\mathcal{R}}} G_{ij}^{\boldsymbol{r}(0)} \Big(r^n l^n y_i^m - r^m l^m y_i^n \Big) = \tag{A.183}$$

$$\sum_{i=1}^{N} \Bigg(y_i^m \Big(\sum_{j=1}^{N} \sum_{\boldsymbol{r}\in\boldsymbol{\mathcal{R}}} G_{ij}^{\boldsymbol{r}(0)} r^n l^n \Big) - y_i^n \Big(\sum_{j=1}^{N} \sum_{\boldsymbol{r}\in\boldsymbol{\mathcal{R}}} G_{ij}^{\boldsymbol{r}(0)} r^m l^m \Big) \Bigg) = \tag{A.184}$$

$$\sum_{i=1}^{N} \Bigg(y_i^m \Big(\sum_{j=1}^{N} \sum_{\boldsymbol{r}\in\boldsymbol{\mathcal{R}}} G_{ij}^{\boldsymbol{r}(0)} (y_i^n - y_j^n) \Big) - y_i^n \Big(\sum_{j=1}^{N} \sum_{\boldsymbol{r}\in\boldsymbol{\mathcal{R}}} G_{ij}^{\boldsymbol{r}(0)} (y_i^m - y_j^m) \Big) \Bigg) = \tag{A.185}$$

$$\sum_{i=1}^{N} \sum_{j=1}^{N} \sum_{\boldsymbol{r}\in\boldsymbol{\mathcal{R}}} G_{ij}^{\boldsymbol{r}(0)} \Big(y_i^n y_j^m - y_i^m y_j^n \Big) = 0. \tag{A.186}$$

The first equation uses the simplification of the permeability terms, that is, that $\mathbf{1}^\top \boldsymbol{B}^{m(0)} \boldsymbol{W}^n$ and $\mathbf{1}^\top \boldsymbol{B}^{n(0)} \boldsymbol{W}^m$ can also be written independently of X_a^b, which we showed in Appendix (A.2.2) through (A.165) and (A.171), the third uses the reformulation of the cell problem, (A.181), and the fourth uses a splitting of the sum, followed by Operation 1 on the second term, followed by Operation 2 on the second term.

A.2.4 Independence of node location and permeability equality

We show that the permeability matrix is independent of the node locations, and, consequently, that

$$k^{mn(0)} = \sigma^{mn(0)}. \tag{A.187}$$

We begin by simplifying $k^{mn(0)}$. We have

$$k^{mn(0)} = \frac{l^m}{2\prod_{a=1}^{D} l^a} \sum_{i=1}^{N}\sum_{j=1}^{N}\sum_{\boldsymbol{r}\in\boldsymbol{\mathcal{R}}} r^m G_{ij}^{\boldsymbol{r}(0)} \Big(W_j^n - W_i^n + X_j^n + r^n l^n - X_i^n \Big) \tag{A.188}$$

$$= \frac{l^m}{2\prod_{a=1}^{D} l^a} \Bigg(\sum_{i=1}^{N}\sum_{j=1}^{N}\sum_{\boldsymbol{r}\in\boldsymbol{\mathcal{R}}} r^m G_{ij}^{\boldsymbol{r}(0)} \Big(W_j^n + X_j^n + r^n l^n \Big) - \tag{A.189}$$

$$\sum_{i=1}^{N}\sum_{j=1}^{N}\sum_{\boldsymbol{r}\in\boldsymbol{\mathcal{R}}} r^m G_{ij}^{\boldsymbol{r}(0)} \Big(W_i^n + X_i^n \Big) \Bigg)$$

$$= \frac{l^m}{2\prod_{a=1}^{D} l^a} \Bigg(\sum_{i=1}^{N}\sum_{j=1}^{N}\sum_{\boldsymbol{r}\in\boldsymbol{\mathcal{R}}} r^m G_{ij}^{-\boldsymbol{r}(0)} \Big(W_i^n + X_i^n + r^n l^n \Big) - \tag{A.190}$$

$$\sum_{i=1}^{N}\sum_{j=1}^{N}\sum_{\boldsymbol{r}\in\boldsymbol{\mathcal{R}}} r^m G_{ij}^{\boldsymbol{r}(0)} \Big(W_i^n + X_i^n \Big) \Bigg)$$

$$= \frac{l^m}{2\prod_{a=1}^{D} l^a} \Bigg(\sum_{i=1}^{N}\sum_{j=1}^{N}\sum_{\boldsymbol{r}\in\boldsymbol{\mathcal{R}}} (-r^m) G_{ij}^{\boldsymbol{r}(0)} \Big(W_i^n + X_i^n + (-r^n) l^n \Big) - \tag{A.191}$$

$$\sum_{i=1}^{N}\sum_{j=1}^{N}\sum_{\boldsymbol{r}\in\boldsymbol{\mathcal{R}}} r^m G_{ij}^{\boldsymbol{r}(0)} \Big(W_i^n + X_i^n \Big) \Bigg)$$

$$= -\frac{l^m}{2\prod_{a=1}^{D} l^a} \sum_{i=1}^{N}\sum_{j=1}^{N}\sum_{\boldsymbol{r}\in\boldsymbol{\mathcal{R}}} r^m G_{ij}^{\boldsymbol{r}(0)} \Big(W_i^n + X_i^n - \frac{r^n l^n}{2} \Big), \tag{A.192}$$

where the first equation uses the definition of the permeability, (11.137), the third uses Operation 1 on the first term, and the fourth uses Operation 2 on the first term. We simplify $\sigma^{mn(0)}$ similarly. Indeed, using the simplified forms of the permeability terms $\mathbf{1}^\top \boldsymbol{B}^{m(0)} \boldsymbol{W}^n$ and $\mathbf{1}^\top \boldsymbol{B}^{n(0)} \boldsymbol{W}^m$, (A.165) and (A.171), we have

$$\sigma^{mn(0)} = \frac{1}{\prod_m l^m} \Big(\frac{1}{2} \mathbf{1}^\top \boldsymbol{B}^{m(0)} \boldsymbol{W}^n + \frac{1}{2} \mathbf{1}^\top \boldsymbol{B}^{n(0)} \boldsymbol{W}^m + \mathbf{1}^\top \boldsymbol{C}^{mn(0)} \mathbf{1} \Big) \tag{A.193}$$

$$= -\frac{1}{2\prod_m l^m} \sum_{i=1}^{N}\sum_{j=1}^{N}\sum_{\boldsymbol{r}\in\boldsymbol{\mathcal{R}}} G_{ij}^{\boldsymbol{r}(0)} \Big(l^m r^m W_i^n + l^n r^n W_i^m \tag{A.194}$$

$$+ X_i^m r^n l^n + X_i^n r^m l^m - r^m l^m r^n l^n \Big).$$

We note that for diagonal elements, that is, the case $n = m$, the result follows

simply, since

$$\sigma^{mm(0)} = \frac{1}{\prod_m l^m}\Big(\mathbf{1}^\top \boldsymbol{B}^{m(0)}\boldsymbol{W}^m + \mathbf{1}^\top \boldsymbol{C}^{mm(0)}\mathbf{1}\Big) \tag{A.195}$$

$$= -\frac{1}{2\prod_m l^m}\sum_{i=1}^{N}\sum_{j=1}^{N}\sum_{\boldsymbol{r}\in\boldsymbol{\mathcal{R}}} G_{ij}^{\boldsymbol{r}(0)}\Big(2l^m r^m W_i^m + 2X_i^m r^m l^m - (r^m l^m)^2\Big) \tag{A.196}$$

$$= -\frac{l^m}{\prod_m l^m}\sum_{i=1}^{N}\sum_{j=1}^{N}\sum_{\boldsymbol{r}\in\boldsymbol{\mathcal{R}}} r^m G_{ij}^{\boldsymbol{r}(0)}\Big(W_i^m + X_i^m - \frac{r^m l^m}{2}\Big) \tag{A.197}$$

$$= k^{mm(0)}, \tag{A.198}$$

where the first equation uses the simplified definition of $k^{mm(0)}$, (A.194), and the second uses the simplified definition of $k^{mm(0)}$, (A.192). For off-diagonal elements, and thus in general, we have the case $n \neq m$, and from (A.194) it instead follows that

$$\sigma^{mn(0)} = -\frac{1}{2\prod_m l^m}\sum_{i=1}^{N}\sum_{j=1}^{N}\sum_{\boldsymbol{r}\in\boldsymbol{\mathcal{R}}} G_{ij}^{\boldsymbol{r}(0)}\Big(l^m r^m W_i^n + l^n r^n W_i^m + \tag{A.199}$$

$$X_i^m r^n l^n + X_i^n r^m l^m - r^m l^m r^n l^n\Big)$$

$$= -\frac{1}{2\prod_m l^m}\Bigg(l^m\sum_{i=1}^{N}\sum_{j=1}^{N}\sum_{\boldsymbol{r}\in\boldsymbol{\mathcal{R}}} r^m G_{ij}^{\boldsymbol{r}(0)}\Big(W_i^n + X_i^n - \frac{r^n l^n}{2}\Big) + \tag{A.200}$$

$$l^n\sum_{i=1}^{N}\sum_{j=1}^{N}\sum_{\boldsymbol{r}\in\boldsymbol{\mathcal{R}}} r^n G_{ij}^{\boldsymbol{r}(0)}\Big(W_i^m + X_i^m - \frac{r^m l^m}{2}\Big)\Bigg)$$

$$= \frac{1}{2}(k^{mn(0)} + k^{nm(0)}), \tag{A.201}$$

where the last equation uses the simplification of $k^{mn(0)}$, (A.192), once more. It remains, therefore, to show that $k^{nm(0)} = k^{mn(0)}$ for $n \neq m$.

To this end, we will show that $k^{mn(0)}$, and therefore $\sigma^{mn(0)}$, is independent of X_a^b. Using the simplified definition of $k^{mn(0)}$, (A.192), we have

$$\frac{\partial k^{mn(0)}}{\partial X_a^b} = \frac{\partial}{\partial X_a^b}\Bigg(-\frac{l^m}{\prod_m l^m}\sum_{i=1}^{N}\sum_{j=1}^{N}\sum_{\boldsymbol{r}\in\boldsymbol{\mathcal{R}}} r^m G_{ij}^{\boldsymbol{r}(0)}\Big(W_i^n + X_i^n - \frac{r^n l^n}{2}\Big)\Bigg) \tag{A.202}$$

$$= -\frac{l^m}{\prod_m l^m}\sum_{i=1}^{N}\sum_{j=1}^{N}\sum_{\boldsymbol{r}\in\boldsymbol{\mathcal{R}}} r^m G_{ij}^{\boldsymbol{r}(0)}\Big(\frac{\partial W_i^n}{\partial X_a^b} + \delta_{ia}\delta^{nb}\Big). \tag{A.203}$$

Now, we note that

$$\Big(\boldsymbol{A}^{(0)}\frac{\partial \boldsymbol{W}^n}{\partial X_a^b}\Big)_i = \Big(\frac{\partial}{\partial X_a^b}(\boldsymbol{A}^{(0)}\boldsymbol{W}^n)\Big)_i \tag{A.204}$$

$$= \Big(\frac{\partial}{\partial X_a^b}(-\boldsymbol{B}^{n(0)}\mathbf{1})\Big)_i \tag{A.205}$$

$$= -\frac{\partial}{\partial X_a^b}\left(\sum_{j=1}^{N}\sum_{\boldsymbol{r}\in\boldsymbol{\mathcal{R}}}\Big(G_{ij}^{\boldsymbol{r}(0)}(X_j^n + r^n l^n) - \delta_{ij}X_i^n\sum_{k=1}^{N}G_{ik}^{\boldsymbol{r}(0)}\Big)\right) \tag{A.206}$$

$$= -\frac{\partial}{\partial X_a^b}\left(\sum_{j=1}^{N}\sum_{\boldsymbol{r}\in\boldsymbol{\mathcal{R}}}G_{ij}^{\boldsymbol{r}(0)}(X_j^n + r^n l^n) - \sum_{j=1}^{N}\sum_{\boldsymbol{r}\in\boldsymbol{\mathcal{R}}}G_{ij}^{\boldsymbol{r}(0)}X_i^n\right) \tag{A.207}$$

$$= -\left(\sum_{j=1}^{N}\sum_{\boldsymbol{r}\in\boldsymbol{\mathcal{R}}}G_{ij}^{\boldsymbol{r}(0)}\delta_{ja}\delta^{nb} - \sum_{j=1}^{N}\sum_{\boldsymbol{r}\in\boldsymbol{\mathcal{R}}}G_{ij}^{\boldsymbol{r}(0)}\delta_{ia}\delta^{nb}\right) \tag{A.208}$$

$$= -\left(\sum_{\boldsymbol{r}\in\boldsymbol{\mathcal{R}}}\Big(G_{ia}^{\boldsymbol{r}(0)} - \delta_{ia}\sum_{k=1}^{N}G_{ik}^{\boldsymbol{r}(0)}\Big)\right)\delta^{nb} \tag{A.209}$$

$$= -A_{ia}^{(0)}\delta^{nb} \tag{A.210}$$

$$= -\Big(\boldsymbol{A}^{(0)}\boldsymbol{e}_a\delta^{nb}\Big)_i, \tag{A.211}$$

where the first equation uses the cell problem, (11.123). Therefore

$$\boldsymbol{A}^{(0)}\Big(\frac{\partial \boldsymbol{W}^n}{\partial X_a^b} + \boldsymbol{e}_a\delta^{nb}\Big) = \mathbf{0}, \tag{A.212}$$

and so, using that $\boldsymbol{A}^{(0)}\mathbf{1} = \mathbf{0}$ from (11.115), we arrive at

$$\frac{\partial \boldsymbol{W}^n}{\partial X_a^b} = \alpha\mathbf{1} - \boldsymbol{e}_a\delta^{nb}, \tag{A.213}$$

so that

$$\frac{\partial W_i^n}{\partial X_a^b} = \alpha - \delta_{ia}\delta^{nb}, \tag{A.214}$$

for some function $\alpha(x,t)$ that is independent of the microscale. Substituting this

result, (A.214), into the equation for the derivative of $k^{mn(0)}$, (A.203), we find that

$$\frac{\partial k^{mn(0)}}{\partial X_a^b} = -\frac{l^m}{\prod_m l^m}\sum_{i=1}^{N}\sum_{j=1}^{N}\sum_{\boldsymbol{r}\in\boldsymbol{\mathcal{R}}} r^m G_{ij}^{\boldsymbol{r}(0)}\Big(\frac{\partial W_i^n}{\partial X_a^b} + \delta_{ia}\delta^{nb}\Big) \tag{A.215}$$

$$= -\frac{l^m}{\prod_m l^m}\sum_{i=1}^{N}\sum_{j=1}^{N}\sum_{\boldsymbol{r}\in\boldsymbol{\mathcal{R}}} r^m G_{ij}^{\boldsymbol{r}(0)}\alpha \tag{A.216}$$

$$= -\frac{l^m}{\prod_m l^m}\sum_{i=1}^{N}\sum_{j=1}^{N}\sum_{\boldsymbol{r}\in\boldsymbol{\mathcal{R}}} (-r^m) G_{ij}^{\boldsymbol{r}(0)}\alpha \tag{A.217}$$

$$= \frac{l^m}{\prod_m l^m}\sum_{i=1}^{N}\sum_{j=1}^{N}\sum_{\boldsymbol{r}\in\boldsymbol{\mathcal{R}}} r^m G_{ij}^{\boldsymbol{r}(0)}\alpha \tag{A.218}$$

$$= -\frac{\partial k^{mn(0)}}{\partial X_a^b}, \tag{A.219}$$

where the third equation uses Operation 1 followed by Operation 2. We have therefore shown that

$$\frac{\partial k^{mn(0)}}{\partial X_a^b} = 0. \tag{A.220}$$

Since this was proved for general m and n, it trivially follows that

$$\frac{\partial k^{nm(0)}}{\partial X_a^b} = 0, \tag{A.221}$$

and therefore that

$$\frac{\partial}{\partial X_a^b}\bigg(\frac{1}{\prod_m l^m}\Big(\frac{1}{2}\mathbf{1}^\top \boldsymbol{B}^{m(0)}\boldsymbol{W}^n + \frac{1}{2}\mathbf{1}^\top \boldsymbol{B}^{n(0)}\boldsymbol{W}^m + \mathbf{1}^\top \boldsymbol{C}^{mn(0)}\mathbf{1}\Big)\bigg) = \tag{A.222}$$

$$\frac{\partial \sigma^{mn(0)}}{\partial X_a^b} = \tag{A.223}$$

$$\frac{1}{2}\frac{\partial}{\partial X_a^b}(k^{mn(0)} + k^{nm(0)}) = 0, \tag{A.224}$$

where the first equation uses the definition of $\sigma^{mn(0)}$, (11.129), and the second uses the relationship between $\sigma^{mn(0)}$ and $k^{mn(0)}$, (A.201). So $k^{mn(0)}$ and $\sigma^{mn(0)}$, and therefore $\boldsymbol{B}^{m(0)}$ and $\boldsymbol{C}^{mn(0)}$, are independent of X_a^b, which permits the choice $X_a^b = 0$ in the original definitions of the latter two, (11.110) and (11.111), allowing us to re-write these as

$$B_{ij}^{m(0)} = \sum_{\boldsymbol{r}\in\boldsymbol{\mathcal{R}}} G_{ij}^{\boldsymbol{r}(0)} r^m l^m, \tag{A.225}$$

$$C_{ij}^{mn(0)} = \frac{1}{2}\sum_{\boldsymbol{r}\in\boldsymbol{\mathcal{R}}} G_{ij}^{\boldsymbol{r}(0)} r^m l^m r^n l^n. \tag{A.226}$$

Using these more simple definitions, we note that $\boldsymbol{B}^{m(0)}$ is skew-symmetric in the lower indices, so that

$$\left(\boldsymbol{B}^{m(0)}\right)^{\top} = -\boldsymbol{B}^{m(0)} \tag{A.227}$$

and $\boldsymbol{C}^{mn(0)}$ is symmetric in the lower indices, so that

$$\left(\boldsymbol{C}^{mn(0)}\right)^{\top} = \boldsymbol{C}^{mn(0)}, \tag{A.228}$$

since, using Operation 2, we have that

$$\begin{aligned}
B_{ji}^{m(0)} &= \sum_{\boldsymbol{r}\in\boldsymbol{\mathcal{R}}} G_{ji}^{\boldsymbol{r}(0)} r^m l^m && \text{(A.229)}\\
&= \sum_{\boldsymbol{r}\in\boldsymbol{\mathcal{R}}} G_{ij}^{-\boldsymbol{r}(0)} r^m l^m && \text{(A.230)}\\
&= \sum_{\boldsymbol{r}\in\boldsymbol{\mathcal{R}}} G_{ij}^{\boldsymbol{r}(0)} (-r^m) l^m && \text{(A.231)}\\
&= -\sum_{\boldsymbol{r}\in\boldsymbol{\mathcal{R}}} G_{ij}^{\boldsymbol{r}(0)} r^m l^m && \text{(A.232)}\\
&= -B_{ij}^{m(0)}, && \text{(A.233)}
\end{aligned}$$

and that

$$\begin{aligned}
C_{ji}^{mn(0)} &= \frac{1}{2}\sum_{\boldsymbol{r}\in\boldsymbol{\mathcal{R}}} G_{ji}^{\boldsymbol{r}(0)} r^m l^m r^n l^n && \text{(A.234)}\\
&= \frac{1}{2}\sum_{\boldsymbol{r}\in\boldsymbol{\mathcal{R}}} G_{ij}^{-\boldsymbol{r}(0)} r^m l^m r^n l^n && \text{(A.235)}\\
&= \frac{1}{2}\sum_{\boldsymbol{r}\in\boldsymbol{\mathcal{R}}} G_{ij}^{\boldsymbol{r}(0)} (-r^m) l^m (-r^n) l^n && \text{(A.236)}\\
&= \frac{1}{2}\sum_{\boldsymbol{r}\in\boldsymbol{\mathcal{R}}} G_{ij}^{\boldsymbol{r}(0)} r^m l^m r^n l^n && \text{(A.237)}\\
&= C_{ij}^{mn(0)}. && \text{(A.238)}
\end{aligned}$$

As a result, we have symmetry in the upper indices of the permeability terms, such that

$$\begin{aligned}
(\boldsymbol{W}^n)^{\top}\boldsymbol{B}^{m(0)}\mathbf{1} &= \left((\boldsymbol{B}^{m(0)}\mathbf{1})^{\top}\boldsymbol{W}^n\right)^{\top} && \text{(A.239)}\\
&= (\boldsymbol{B}^{m(0)}\mathbf{1})^{\top}\boldsymbol{W}^n && \text{(A.240)}\\
&= (-\boldsymbol{A}^{(0)}\boldsymbol{W}^m)^{\top}\boldsymbol{W}^n && \text{(A.241)}\\
&= -(\boldsymbol{W}^m)^{\top}\boldsymbol{A}^{(0)}\boldsymbol{W}^n && \text{(A.242)}\\
&= (\boldsymbol{W}^m)^{\top}\boldsymbol{B}^{n(0)}\mathbf{1}. && \text{(A.243)}
\end{aligned}$$

Now, choosing $X_a^b = 0$ in the simplified definition of $k^{mn(0)}$, (A.192), we have

$$k^{mn(0)} - k^{nm(0)} = -\frac{l^m}{\prod_m l^m} \sum_{i=1}^{N} \sum_{j=1}^{N} \sum_{\boldsymbol{r}\in\boldsymbol{\mathcal{R}}} r^m G_{ij}^{\boldsymbol{r}(0)} \Big(W_i^n - \frac{r^n l^n}{2} \Big) + \tag{A.244}$$

$$\frac{l^n}{\prod_n l^n} \sum_{i=1}^{N} \sum_{j=1}^{N} \sum_{\boldsymbol{r}\in\boldsymbol{\mathcal{R}}} r^n G_{ij}^{\boldsymbol{r}(0)} \Big(W_i^m - \frac{r^m l^m}{2} \Big)$$

$$= -\frac{1}{\prod_m l^m} \Bigg(\sum_{i=1}^{N} \sum_{j=1}^{N} \sum_{\boldsymbol{r}\in\boldsymbol{\mathcal{R}}} G_{ij}^{\boldsymbol{r}(0)} \Big(l^m r^m W_i^n - l^n r^n W_i^m \Big) \Bigg) \tag{A.245}$$

$$= -\frac{1}{\prod_m l^m} \Big((\boldsymbol{W}^n)^\top \boldsymbol{B}^{m(0)} \mathbf{1} - (\boldsymbol{W}^m)^\top \boldsymbol{B}^{n(0)} \mathbf{1} \Big) \tag{A.246}$$

$$= 0, \tag{A.247}$$

where we have used this the symmetry, (A.243), in the last equation. Therefore, using (A.201), we arrive at

$$\sigma^{mn(0)} = \frac{1}{2}(k^{mn(0)} + k^{nm(0)}) = k^{mn(0)}. \tag{A.248}$$

A.2.5 Intra-cell particle conservation

In this subsection, we show that $\mathbf{1}^\top \boldsymbol{S}^{m(0)} = \mathbf{0}^\top$ and $\boldsymbol{S}^{m(0)}\mathbf{1} = \mathbf{0}$.

We first show that $\boldsymbol{S}^{m(0)}\mathbf{1} = \mathbf{0}$. We have

$$\Big(\boldsymbol{S}^{m(0)} \mathbf{1} \Big)_i = \sum_{j=1}^{N} \sum_{\boldsymbol{r}\in\boldsymbol{\mathcal{R}}} \Big(G_{ij}^{\boldsymbol{r}(0)} (W_j^m - W_i^m + X_j^m + r^m l^m - X_i^m) H_{ji}^{-\boldsymbol{r}(0)} + \tag{A.249}$$

$$\delta_{ij} \sum_{k=1}^{N} G_{ik}^{\boldsymbol{r}(0)} (W_k^m - W_i^m + X_k^m + r^m l^m - X_i^m) H_{ik}^{\boldsymbol{r}(0)} \Big)$$

$$= \sum_{j=1}^{N} \sum_{\boldsymbol{r}\in\boldsymbol{\mathcal{R}}} \Big(G_{ij}^{\boldsymbol{r}(0)} (W_j^m - W_i^m + X_j^m + r^m l^m - X_i^m) \tag{A.250}$$

$$= \sum_{j=1}^{N} \sum_{\boldsymbol{r}\in\boldsymbol{\mathcal{R}}} \Big(G_{ij}^{\boldsymbol{r}(0)} - \delta_{ij} \sum_{k=1}^{N} G_{ik}^{\boldsymbol{r}(0)} \Big) W_j^m + \tag{A.251}$$

$$\sum_{j=1}^{N} \sum_{\boldsymbol{r}\in\boldsymbol{\mathcal{R}}} \Big(G_{ij}^{\boldsymbol{r}(0)} (X_j^m + r^m l^m) - \delta_{ij} \sum_{k=1}^{N} G_{ik}^{\boldsymbol{r}(0)} X_i^m \Big)$$

$$= (\boldsymbol{A}^{(0)} \boldsymbol{W}^m)_i + (\boldsymbol{B}^{m(0)} \mathbf{1})_i \tag{A.252}$$

$$= 0. \tag{A.253}$$

The first equation uses the definition of $\boldsymbol{S}^{m(0)}$, (11.146), the second uses δ_{ij} followed by the Heaviside function identity, (11.143), and the fifth uses the cell problem (11.123).

Next, we show that $\mathbf{1}^\top \boldsymbol{S}^{m(0)} = \mathbf{0}^\top$. We have

$$\left(\mathbf{1}^\top \boldsymbol{S}^{m(0)}\right)_j = \sum_{i=1}^{N} \sum_{\boldsymbol{r}\in\boldsymbol{\mathcal{R}}} \Big(G_{ij}^{\boldsymbol{r}(0)} (W_j^m - W_i^m + X_j^m + r^m l^m - X_i^m) H_{ji}^{-\boldsymbol{r}(0)} + \tag{A.254}$$

$$\delta_{ij} \sum_{k=1}^{N} G_{ik}^{\boldsymbol{r}(0)} (w_k^m - W_i^m + X_k^m + r^m l^m - X_i^m) H_{ik}^{\boldsymbol{r}(0)} \Big)$$

$$= \sum_{i=1}^{N} \sum_{\boldsymbol{r}\in\boldsymbol{\mathcal{R}}} \Big(G_{ij}^{\boldsymbol{r}(0)} (W_j^m - W_i^m + X_j^m + r^m l^m - X_i^m) H_{ji}^{-\boldsymbol{r}(0)} + \tag{A.255}$$

$$\sum_{i=1}^{N} \sum_{\boldsymbol{r}\in\boldsymbol{\mathcal{R}}} G_{ji}^{\boldsymbol{r}(0)} (W_i^m - W_j^m + X_i^m + r^m l^m - X_j^m) H_{ji}^{\boldsymbol{r}(0)} \Big)$$

$$= \sum_{i=1}^{N} \sum_{\boldsymbol{r}\in\boldsymbol{\mathcal{R}}} \Big(G_{ij}^{\boldsymbol{r}(0)} (W_j^m - W_i^m + X_j^m + r^m l^m - X_i^m) H_{ji}^{-\boldsymbol{r}(0)} - \tag{A.256}$$

$$\sum_{i=1}^{N} \sum_{\boldsymbol{r}\in\boldsymbol{\mathcal{R}}} G_{ji}^{\boldsymbol{r}(0)} (W_j^m - W_i^m + X_j^m - r^m l^m - X_i^m) H_{ji}^{\boldsymbol{r}(0)} \Big)$$

$$= \sum_{i=1}^{N} \sum_{\boldsymbol{r}\in\boldsymbol{\mathcal{R}}} \Big(G_{ij}^{\boldsymbol{r}(0)} (W_j^m - W_i^m + X_j^m + r^m l^m - X_i^m) H_{ji}^{-\boldsymbol{r}(0)} - \tag{A.257}$$

$$\sum_{i=1}^{N} \sum_{\boldsymbol{r}\in\boldsymbol{\mathcal{R}}} G_{ij}^{\boldsymbol{r}(0)} (W_j^m - W_i^m + X_j^m + r^m l^m - X_i^m) H_{ji}^{-\boldsymbol{r}(0)} \Big)$$

$$= 0. \tag{A.258}$$

The second equation uses δ_{ij} followed by a re-indexing $k \to i$ in the second term, the third uses a factorisation of -1 in the second term to achieve like-terms, and the fourth uses the symmetry of conductance in the second term followed by Operation 2 on the second term.

A.2.6 Interpretation of advective terms

In this subsection we show that the coefficient in the advective term of the particle-conservation equation, (11.160), is related to the permeability by

$$\mathbf{1}^\top \boldsymbol{K}^{mn(0)} \mathbf{1} = \prod_{a=1}^{D} l^a k^{mn(0)} = \prod_{a=1}^{D} l^a \sigma^{mn(0)}. \tag{A.259}$$

We have

$$\mathbf{1}^\top \boldsymbol{K}^{mn(0)}\mathbf{1} = \tag{A.260}$$

$$\sum_{i=1}^{N}\sum_{j=1}^{N}\sum_{\boldsymbol{r}\in\boldsymbol{\mathcal{R}}} G_{ij}^{\boldsymbol{r}(0)}(W_j^m - W_i^m + X_j^m + r^m l^m - X_i^m)(X_j^n + r^n l^n)H_{ji}^{-\boldsymbol{r}(0)} +$$

$$\sum_{i=1}^{N}\sum_{j=1}^{N}\sum_{\boldsymbol{r}\in\boldsymbol{\mathcal{R}}} G_{ij}^{\boldsymbol{r}(0)}(W_j^m - W_i^m + X_j^m + r^m l^m - X_i^m)X_i^n H_{ij}^{\boldsymbol{r}(0)} = \tag{A.261}$$

$$\sum_{i=1}^{N}\sum_{j=1}^{N}\sum_{\boldsymbol{r}\in\boldsymbol{\mathcal{R}}} G_{ij}^{\boldsymbol{r}(0)}(W_j^m - W_i^m + X_j^m + r^m l^m - X_i^m)(X_j^n + r^n l^n)H_{ji}^{-\boldsymbol{r}(0)} +$$

$$\sum_{i=1}^{N}\sum_{j=1}^{N}\sum_{\boldsymbol{r}\in\boldsymbol{\mathcal{R}}} G_{ij}^{-\boldsymbol{r}(0)}(W_i^m - W_j^m + X_i^m + r^m l^m - X_j^m)X_j^n H_{ji}^{\boldsymbol{r}(0)} = \tag{A.262}$$

$$\sum_{i=1}^{N}\sum_{j=1}^{N}\sum_{\boldsymbol{r}\in\boldsymbol{\mathcal{R}}} G_{ij}^{\boldsymbol{r}(0)}(W_j^m - W_i^m + X_j^m + r^m l^m - X_i^m)(X_j^n + r^n l^n)H_{ji}^{-\boldsymbol{r}(0)} +$$

$$\sum_{i=1}^{N}\sum_{j=1}^{N}\sum_{\boldsymbol{r}\in\boldsymbol{\mathcal{R}}} G_{ij}^{\boldsymbol{r}(0)}(W_i^m - W_j^m + X_i^m - r^m l^m - X_j^m)X_j^n H_{ji}^{-\boldsymbol{r}(0)} = \tag{A.263}$$

$$\sum_{i=1}^{N}\sum_{j=1}^{N}\sum_{\boldsymbol{r}\in\boldsymbol{\mathcal{R}}} G_{ij}^{\boldsymbol{r}(0)}(W_j^m - W_i^m + X_j^m + r^m l^m - X_i^m)r^n l^n H_{ji}^{-\boldsymbol{r}(0)},$$

where the first equation uses an expansion of the definition of $K_{ij}^{mn(0)}$, (11.151), the second uses Operation 1 on the second term, and the third uses Operation 2 on the second term. Defining

$$\Lambda_{ij}^{\boldsymbol{r}mn(0)} = G_{ij}^{\boldsymbol{r}(0)}(W_j^m - W_i^m + X_j^m + r^m l^m - X_i^m)r^n l^n, \tag{A.264}$$

and noting that $\Lambda_{ji}^{-\boldsymbol{r}mn(0)} = \Lambda_{ij}^{\boldsymbol{r}mn(0)}$, it follows that

$$\mathbf{1}^\top \boldsymbol{K}^{mn(0)}\mathbf{1} = \frac{1}{2}\sum_{i=1}^{N}\sum_{j=1}^{N}\sum_{\boldsymbol{r}\in\boldsymbol{\mathcal{R}}} \Lambda_{ij}^{\boldsymbol{r}mn(0)} H_{ji}^{-\boldsymbol{r}(0)} + \frac{1}{2}\sum_{j=1}^{N}\sum_{i=1}^{N}\sum_{\boldsymbol{r}\in\boldsymbol{\mathcal{R}}} \Lambda_{ji}^{\boldsymbol{r}mn(0)} H_{ij}^{-\boldsymbol{r}(0)} \tag{A.265}$$

$$= \frac{1}{2}\sum_{i=1}^{N}\sum_{j=1}^{N}\sum_{-\boldsymbol{r}} \Lambda_{ij}^{\boldsymbol{r}mn(0)} H_{ji}^{-\boldsymbol{r}(0)} + \frac{1}{2}\sum_{i=1}^{N}\sum_{j=1}^{N}\sum_{\boldsymbol{r}\in\boldsymbol{\mathcal{R}}} \Lambda_{ij}^{-\boldsymbol{r}mn(0)} H_{ij}^{-\boldsymbol{r}(0)} \tag{A.266}$$

$$= \frac{1}{2}\sum_{i=1}^{N}\sum_{j=1}^{N}\sum_{\boldsymbol{r}\in\boldsymbol{\mathcal{R}}} \Lambda_{ij}^{\boldsymbol{r}mn(0)} \tag{A.267}$$

$$= \frac{1}{2}\sum_{i=1}^{N}\sum_{j=1}^{N}\sum_{\boldsymbol{r}\in\boldsymbol{\mathcal{R}}} G_{ij}^{\boldsymbol{r}(0)}(W_j^m - W_i^m + X_j^m + r^m l^m - X_i^m) r^n l^n \tag{A.268}$$

$$= \prod_{a=1}^{D} l^a k^{nm(0)} \tag{A.269}$$

$$= \prod_{a=1}^{D} l^a k^{mn(0)}, \tag{A.270}$$

where the first equation uses a splitting of terms followed by a re-labelling $i \leftrightarrow j$ in the second term, the second uses the symmetry of $\Lambda_{ij}^{\boldsymbol{r}mn(0)}$, the third uses Operation 2 on the second term followed by the Heaviside function identity, (11.143), the fourth uses the definition of $\Lambda_{ij}^{\boldsymbol{r}mn(0)}$, (A.264), the fifth uses the definition of the permeability tensor, (11.137), and the sixth uses the symmetry of the permeability matrix, (A.247).

A.3 Darcy velocity

In this appendix, we show that our definitions of the Darcy velocity, (11.58) and (11.130), are the correct choice, using an alternative but equivalent formulation. As an illustrative example, consider the $m = 1$ case in two dimensions. Intuitively, the net flux per unit area out of a reference cell into cells with a right-facing component is

$$\hat{u}^1 = \frac{1}{l^2}\sum_{i=1}^{N}\sum_{j=1}^{N}\sum_{\boldsymbol{r}\in\boldsymbol{\mathcal{R}}_+^1} Q_{ij}^{\boldsymbol{r}}, \tag{A.271}$$

where $\boldsymbol{\mathcal{R}}_+^1 = \{\boldsymbol{r} \in \boldsymbol{\mathcal{R}} \,|\, r^1 = 1\}$ is the set of references for cell positions immediately to the right of a cell, and l^2 is the vertical length, so that $l^1 l^2$ represents the cross-

sectional area in the two-dimensional case. Now, we observe that

$$\hat{u}^1 = \frac{1}{2l^2}\left(\sum_{i=1}^{N}\sum_{j=1}^{N}\sum_{\boldsymbol{r}\in\boldsymbol{\mathcal{R}}^1_+} r^1 Q^{\boldsymbol{r}}_{ij} + \sum_{i=1}^{N}\sum_{j=1}^{N}\sum_{\boldsymbol{r}\in\boldsymbol{\mathcal{R}}^1_+} r^1 Q^{\boldsymbol{r}}_{ji}\right) \tag{A.272}$$

$$= \frac{1}{2l^2}\left(\sum_{i=1}^{N}\sum_{j=1}^{N}\sum_{\boldsymbol{r}\in\boldsymbol{\mathcal{R}}^1_+} r^1 Q^{\boldsymbol{r}}_{ij} - \sum_{i=1}^{N}\sum_{j=1}^{N}\sum_{\boldsymbol{r}\in\boldsymbol{\mathcal{R}}^1_+} r^1 Q^{-\boldsymbol{r}}_{ij}\right) \tag{A.273}$$

$$= \frac{1}{2l^2}\left(\sum_{i=1}^{N}\sum_{j=1}^{N}\sum_{\boldsymbol{r}\in\boldsymbol{\mathcal{R}}^1_+} r^1 Q^{\boldsymbol{r}}_{ij} + \sum_{i=1}^{N}\sum_{j=1}^{N}\sum_{\boldsymbol{r}\in\boldsymbol{\mathcal{R}}^1_-} r^1 Q^{\boldsymbol{r}}_{ij}\right) \tag{A.274}$$

$$= u^1, \tag{A.275}$$

where $\boldsymbol{\mathcal{R}}^m_- = \{\boldsymbol{r} \in \boldsymbol{\mathcal{R}} \,|\, r^m = -1\}$ denotes the set of positions of cells immediately to the left of the reference cell. The first equation is a relabelling $i \leftrightarrow j$ in the second term, and the second equation uses $Q^{\boldsymbol{r}}_{ij} = Q^{-\boldsymbol{r}}_{ji}$ in the second term. The final equation is our original definition of the Darcy velocity, (11.58) and (11.130). So the flux through the cell is equal to half of the flux out of the cell to all other cells, due to the periodicity of the network.

Bibliography

[1] K. Sutherland and G. Chase, "Filters and filtration handbook," *Elsevier*, 2011.

[2] M. J. Matteson and C. Orr, "Filtration: Principles and practices. 2," *Penn Well Publishing Corp.*, 1998.

[3] M. Yurtsever, "Are nonwoven fabrics used in foods made of cellulose or plastic? Cellulose/plastic separation by using Schweizer's reagent and analysis based on a sample of tea bags," *Process Safety and Environmental Protection*, vol. 151, pp. 188–194, 2021.

[4] M. Eulitz, I. Kölling-Speer, K. Speer, *et al.*, "Effect of the water feeding onto the brew and the filter cake using a household coffee maker," *22nd International Conference on Coffee Science: Association Scientifique Internationale du Café*, pp. 492–495, 2008.

[5] J. Wu, M. Cao, D. Tong, Z. Finkelstein, and E. M. Hoek, "A critical review of point-of-use drinking water treatment in the United States," *Nature Partner Journals: Clean Water*, vol. 4, no. 1, p. 40, 2021.

[6] I. Ray and K. R. Smith, "Towards safe drinking water and clean cooking for all," *The Lancet Global Health*, vol. 9, no. 3, pp. 361–365, 2021.

[7] C.-S. Wang, "Electrostatic forces in fibrous filters–a review," *Powder Technology*, vol. 118, no. 1-2, pp. 166–170, 2001.

[8] S. Hube *et al.*, "Direct membrane filtration for wastewater treatment and resource recovery: A review," *Science of the Total Environment*, vol. 710, p. 136 375, 2020.

[9] A. Adin and M. Elimelech, "Particle filtration for wastewater irrigation," *Journal of Irrigation and Drainage Engineering*, vol. 115, no. 3, pp. 474–487, 1989.

[10] L. A. Ikner, C. P. Gerba, and K. R. Bright, "Concentration and recovery of viruses from water: A comprehensive review," *Food and Environmental Virology*, vol. 4, pp. 41–67, 2012.

[11] J. Cashdollar and L. Wymer, "Methods for primary concentration of viruses from water samples: A review and meta-analysis of recent studies," *Journal of Applied Microbiology*, vol. 115, no. 1, pp. 1–11, 2013.

[12] R. Frith and W. Scott, "Control of solids contamination in hydraulic systems–an overview," *Wear*, vol. 165, no. 1, pp. 69–74, 1993.

[13] P. Máchal *et al.*, "Design and verification of additional filtration for the application of ecological transmission and hydraulic fluids in tractors," *Acta Universitatis Agriculturae et Silviculturae Mendelianae Brunensis*, vol. 61, no. 5, pp. 1305–1311, 2013.

[14] A. Jaworek, A. Krupa, and T. Czech, "Modern electrostatic devices and methods for exhaust gas cleaning: A brief review," *Journal of Electrostatics*, vol. 65, no. 3, pp. 133–155, 2007.

[15] B. Guan, R. Zhan, H. Lin, and Z. Huang, "Review of the state-of-the-art of exhaust particulate filter technology in internal combustion engines," *Journal of Environmental Management*, vol. 154, pp. 225–258, 2015.

[16] V. Masson-Delmotte *et al.*, "IPCC, 2018: Global warming of 1.5C. An IPCC special report on the impacts of global warming of 1.5C above pre-industrial levels and related global greenhouse gas emission pathways, in the context of strengthening the global response to the threat of climate change, sustainable development, and efforts to eradicate poverty," *World Meteorological Organization*, 2018.

[17] S. Manabe and R. T. Wetherald, "Thermal equilibrium of the atmosphere with a given distribution of relative humidity," *Journal of Atmospheric Science*, 1967.

[18] I. M. Held and B. J. Soden, "Robust responses of the hydrological cycle to global warming," *Journal of Climate*, vol. 19, no. 21, pp. 5686–5699, 2006.

[19] M. Z. Jacobson, "Review of solutions to global warming, air pollution, and energy security," *Energy and Environmental Science*, vol. 2, no. 2, pp. 148–173, 2009.

[20] T. Barker, P. Ekins, N. Johnstone, and T. Barker, "Global warming and energy demand," *Routledge*, 1995.

[21] A. Kumar *et al.*, "Direct air capture of CO2 by physisorbent materials," *Angewandte Chemie International Edition*, vol. 54, no. 48, pp. 14 372–14 377, 2015.

[22] M. Chen, F. Soyekwo, Q. Zhang, C. Hu, A. Zhu, and Q. Liu, "Graphene oxide nanosheets to improve permeability and selectivity of PIM-1 membrane for carbon dioxide separation," *Journal of Industrial and Engineering Chemistry*, vol. 63, pp. 296–302, 2018.

[23] R. G. Taylor *et al.*, "Ground water and climate change," *Nature Climate Change*, vol. 3, no. 4, pp. 322–329, 2013.

[24] M. T. Van Vliet *et al.*, "Global water scarcity including surface water quality and expansions of clean water technologies," *Environmental Research Letters*, vol. 16, no. 2, pp. 20–24, 2021.

[25] I. M. Fund, "World economic outlook update 2022: Rising caseloads, a disrupted recovery, and higher inflation," *IMF Global Reports*, 2022.

[26] D. Hinrichsen and H. Tacio, "The coming freshwater crisis is already here: The linkages between population and water," *Woodrow Wilson International Center for Scholars*, pp. 1–26, 2002.

[27] B. Malmqvist and S. Rundle, "Threats to the running water ecosystems of the world," *Environmental Conservation*, vol. 29, no. 2, pp. 134–153, 2002.

[28] R. Kant, "Textile dyeing industry an environmental hazard," *Scientific Research: Open Access*, 2011.

[29] M. Wu and S. Janssen, "Dosed without prescription: A framework for preventing pharmaceutical contamination of our nation's drinking water," *American Chemical Society*, 2011.

[30] F. Macedonio, E. Drioli, A. A. Gusev, A. Bardow, R. Semiat, and M. Kurihara, "Efficient technologies for worldwide clean water supply," *Chemical Engineering and Processing: Process Intensification*, vol. 51, pp. 2–17, 2012.

[31] J. Brainard, N. Jones, I. Lake, L. Hooper, and P. R. Hunter, "Facemasks and similar barriers to prevent respiratory illness such as COVID-19: A rapid systematic review," *MedRxiv*, 2020.

[32] A. Gouel-Cheron, C. Couffignal, Y. Elmaleh, E. Kantor, and P. Montravers, "Preliminary observations of anaesthesia ventilators used for prolonged mechanical ventilation in intensive care unit patients during the COVID-19 pandemic," *Anaesthesia Critical Care and Pain Medicine*, vol. 39, no. 3, pp. 371–372, 2020.

[33] L. H. Kwong *et al.*, "Review of the breathability and filtration efficiency of common household materials for face masks," *American Chemical Society*, vol. 15, no. 4, pp. 5904–5924, 2021.

[34] A. IPCC, "IPCC Fifth Assessment Report-Synthesis Report," *IPPC Rome, Italy*, 2014.

[35] F. Owa, "Water pollution: Sources, effects, control and management," *Mediterranean Journal of Social Sciences*, vol. 4, no. 8, p. 65, 2013.

[36] UNICEF *et al.*, "The state of food security and nutrition in the world 2022," 2022.

[37] T. Lang and M. Heasman, "Food wars: The global battle for mouths, minds and markets," 2015.

[38] D. M. Morens and A. S. Fauci, "Emerging pandemic diseases: How we got to COVID-19," *Cell*, vol. 182, no. 5, pp. 1077–1092, 2020.

[39] *UK Statutory Instruments: National emission ceilings regulations 2018*, `www.legislation.gov.uk`, Accessed: 2023-03-01.

[40] C. Mitchell and P. Connor, "Renewable energy policy in the UK 1990–2003," *Energy Policy*, vol. 32, no. 17, pp. 1935–1947, 2004.

[41] V. K. Vijayan, H. Paramesh, S. S. Salvi, and A. A. K. Dalal, "Enhancing indoor air quality–the air filter advantage," *Lung India: Indian Chest Society*, vol. 32, no. 5, p. 473, 2015.

[42] A. Gadgil, "Drinking water in developing countries," *Annual Review of Energy and the Environment*, vol. 23, no. 1, pp. 253–286, 1998.

[43] H. Ma, C. Burger, B. S. Hsiao, and B. Chu, "Ultra-fine cellulose nanofibers: New nano-scale materials for water purification," *Journal of Materials Chemistry*, vol. 21, no. 21, pp. 7507–7510, 2011.

[44] C. H. Koo, A. W. Mohammad, *et al.*, "Recycling of oleochemical wastewater for boiler feed water using reverse osmosis membranes–a case study," *Desalination*, vol. 271, no. 1-3, pp. 178–186, 2011.

[45] S. Salvi and A. Paranjape, "Study of transformer oil filtration machine," *International Research Journal of Engineering and Technology*, pp. 2471–2474, 2017.

[46] R. D. Hudgens and R. D. Hercamp, "Filtration of coolants for heavy duty engines," *Society of Automobile Engineers: Technical Papers*, 1988.

[47] S. Ebnesajjad, "Expanded PTFE applications handbook: Technology, manufacturing and applications," *William Andrew*, 2016.

[48] S. Ebnesajjad, "Expanded PTFE applications handbook: Properties, characteristics, and applications of expanded PTFE (ePTFE) products," *Elsevier*, pp. 163–170, 2017.

[49] S. Ebnesajjad, "Introduction to fluoropolymers," *Elsevier*, pp. 55–71, 2017.

[50] *W.L. Gore & Associates, Inc.* `www.wlgore.com`, Accessed: 2023-01-30.

[51] I. M. Griffiths, A. Kumar, and P. S. Stewart, "A combined network model for membrane fouling," *Journal of Colloid and Interface Science*, vol. 432, pp. 10–18, 2014.

[52] B. F. Ruth, "Studies in filtration III. Derivation of general filtration equations," *Industrial and Engineering Chemistry*, vol. 27, no. 6, pp. 708–723, 1935.

[53] P. Sanaei, G. Richardson, T. Witelski, and L. Cummings, "Flow and fouling in a pleated membrane filter," *Journal of Fluid Mechanics*, vol. 795, pp. 36–59, 2016.

[54] J. C. Chen, Q. Li, and M. Elimelech, "In situ monitoring techniques for concentration polarization and fouling phenomena in membrane filtration," *Advances in Colloid and Interface Science*, vol. 107, no. 2-3, pp. 83–108, 2004.

[55] C. M. Bondy and C. Santeufemio, "Analysis of fouling within microporous membranes in biopharmaceutical applications using latex microsphere suspensions," *Journal of Membrane Science*, vol. 349, no. 1-2, pp. 12–24, 2010.

[56] M. Ferrando, A. Rozek, M. Zator, F. Lopez, and C. Gudell, "An approach to membrane fouling characterization by confocal scanning laser microscopy," *Journal of Membrane Science*, vol. 250, no. 1-2, pp. 283–293, 2005.

[57] H. Li, A. G. Fane, H. G. Coster, and S. Vigneswaran, "Direct observation of particle deposition on the membrane surface during crossflow microfiltration," *Journal of Membrane Science*, vol. 149, no. 1, pp. 83–97, 1998.

[58] J. Altmann and S. Ripperger, "Particle deposition and layer formation at the crossflow microfiltration," *Journal of Membrane Science*, vol. 124, no. 1, pp. 119–128, 1997.

[59] M. Hamachi and M. Mietton-Peuchot, "Experimental investigations of cake characteristics in crossflow microfiltration," *Chemical Engineering Science*, vol. 54, no. 18, pp. 4023–4030, 1999.

[60] A. P. Mairal, A. R. Greenberg, W. B. Krantz, and L. J. Bond, "Real-time measurement of inorganic fouling of RO desalination membranes using ultrasonic time-domain reflectometry," *Journal of Membrane Science*, vol. 159, no. 1-2, pp. 185–196, 1999.

[61] L.-H. Cheng, Y.-C. Yang, J. Chen, Y.-H. Lin, and S.-H. Wang, "A new view of membrane fouling with 3D ultrasonic imaging techniques: Taking the canola oil with phospholipids for example," *Journal of Membrane Science*, vol. 372, no. 1-2, pp. 134–144, 2011.

[62] T. C. Chilcott, M. Chan, L. Gaedt, T. Nantawisarakul, A. G. Fane, and H. G. L. Coster, "Electrical impedance spectroscopy characterisation of conducting membranes: I. Theory," *Journal of Membrane Science*, vol. 195, no. 2, pp. 153–167, 2002.

[63] T. C. Chilcott, M. Chan, L. Gaedt, T. Nantawisarakul, A. G. Fane, and H. G. L. Coster, "Electrical impedance spectroscopy characterisation of conducting membranes: II. Experimental," *Journal of Membrane Science*, vol. 195, no. 2, pp. 169–180, 2002.

[64] T. Abichou, C. H. Benson, and T. B. Edil, "Network model for hydraulic conductivity of sand-bentonite mixtures," *Canadian Geotechnical Journal*, vol. 41, no. 4, pp. 698–712, 2004.

[65] R. Chan and V. Chen, "Characterization of protein fouling on membranes: Opportunities and challenges," *Journal of Membrane Science*, vol. 242, no. 1-2, pp. 169–188, 2004.

[66] R. Lohmann *et al.*, "Are fluoropolymers really of low concern for human and environmental health and separate from other PFAS?" *Environmental Science & Technology*, vol. 54, no. 20, pp. 12 820–12 828, 2020.

[67] P. Hermans and H. Bredée, "Zur kenntnis der filtrationsgesetze (the laws of filtration)," *Recueil des Travaux Chimiques des Pays-Bas*, vol. 54, no. 9, pp. 680–700, 1935.

[68] T. Iwasaki, J. J. Slade, and W. E. Stanley, "Some notes on sand filtration (with discussion)," *American Water Works Association*, vol. 29, no. 10, pp. 1591–1602, 1937.

[69] C. Ison and K. Ives, "Removal mechanisms in deep bed filtration," *Chemical Engineering Science*, vol. 24, no. 4, pp. 717–729, 1969.

[70] V. Jegatheesan and S. Vigneswaran, "Deep bed filtration: Mathematical models and observations," *Critical Reviews in Environmental Science and Technology*, vol. 35, no. 6, pp. 515–569, 2005.

[71] M. Rahimi, S. Madaeni, M. Abolhasani, and A. A. Alsairafi, "CFD and experimental studies of fouling of a microfiltration membrane," *Chemical Engineering and Processing: Process Intensification*, vol. 48, no. 9, pp. 1405–1413, 2009.

[72] N. A. Marrufo-Hernández, M. Hernández-Guerrero, J. M. Nápoles-Duarte, J. P. Palomares-Báez, and M. A. Chávez-Rojo, "Prediction of the filtrate particle size distribution from the pore size distribution in membrane filtration: Numerical correlations from computer simulations," *American Institute of Physics: Advances*, vol. 8, no. 3, pp. 35–38, 2018.

[73] A. Fouladitajar, F. Z. Ashtiani, A. Okhovat, and B. Dabir, "Membrane fouling in microfiltration of oil-in-water emulsions; a comparison between constant pressure blocking laws and genetic programming (GP) model," *Desalination*, vol. 329, pp. 41–49, 2013.

[74] Q.-F. Liu and S.-H. Kim, "Evaluation of membrane fouling models based on bench-scale experiments: A comparison between constant flowrate blocking laws and artificial neural network (ANNs) model," *Journal of Membrane Science*, vol. 310, no. 1-2, pp. 393–401, 2008.

[75] Q. Xiong, T. G. Baychev, and A. P. Jivkov, "Review of pore network modelling of porous media: Experimental characterisations, network constructions and applications to reactive transport," *Journal of Contaminant Hydrology*, vol. 192, pp. 101–117, 2016.

[76] M. Bruna and S. J. Chapman, "Diffusion in spatially varying porous media," *SIAM Journal on Applied Mathematics*, vol. 75, no. 4, pp. 1648–1674, 2015.

[77] M. P. Dalwadi, I. M. Griffiths, and M. Bruna, "Understanding how porosity gradients can make a better filter using homogenization theory," *Proceedings of the Royal Society A: Mathematical, Physical and Engineering Sciences*, vol. 471, no. 2182, p. 20 150 464, 2015.

[78] M. P. Dalwadi, M. Bruna, and I. M. Griffiths, "A multiscale method to calculate filter blockage," *Journal of Fluid Mechanics*, vol. 809, pp. 264–289, 2016.

[79] S. J. Chapman and A. Shabala, "Effective transport properties of lattices," *SIAM Journal on Applied Mathematics*, vol. 77, no. 5, pp. 1631–1652, 2017.

[80] S. J. Chapman and Z. M. Wilmott, "Homogenization of flow through periodic networks," *SIAM Journal on Applied Mathematics*, vol. 81, no. 3, pp. 1034–1051, 2021.

[81] C. M. Rooney, C. P. Please, and S. D. Howison, "Homogenisation applied to thermal radiation in porous media," *European Journal of Applied Mathematics*, vol. 32, no. 5, pp. 784–805, 2021.

[82] G. Printsypar, M. Bruna, and I. M. Griffiths, "The influence of porous-medium microstructure on filtration," *Journal of Fluid Mechanics*, vol. 861, pp. 484–516, 2019.

[83] O. Iliev, Z. Lakdawala, and G. Printsypar, "On a multiscale approach for filter efficiency simulations," *Computers and Mathematics with Applications*, vol. 67, no. 12, pp. 2171–2184, 2014.

[84] S. Y. Yang, I. Ryu, H. Y. Kim, J. K. Kim, S. K. Jang, and T. P. Russell, "Nanoporous membranes with ultrahigh selectivity and flux for the filtration of viruses," *Advanced Materials*, vol. 18, no. 6, pp. 709–712, 2006.

[85] C. Keith, "Particle size studies on tobacco smoke," *Contributions to Tobacco and Nicotine Research*, vol. 11, no. 3, pp. 123–131, 1982.

[86] S. Bensaid, D. L. Marchisio, and D. Fino, "Numerical simulation of soot filtration and combustion within diesel particulate filters," *Chemical Engineering Science*, vol. 65, no. 1, pp. 357–363, 2010.

[87] Y.-S. Chen, S.-S. Hsiau, J. Smid, J.-F. Wu, and S.-M. Ma, "Removal of dust particles from fuel gas using a moving granular bed filter," *Fuel*, vol. 182, pp. 174–187, 2016.

[88] H. Wand, G. Vacca, P. Kuschk, M. Krüger, and M. Kästner, "Removal of bacteria by filtration in planted and non-planted sand columns," *Water Research*, vol. 41, no. 1, pp. 159–167, 2007.

[89] Z. Zhu *et al.*, "Multistage recovery process of seaweed pigments: Investigation of ultrasound assisted extraction and ultra-filtration performances," *Food and Bioproducts Processing*, vol. 104, pp. 40–47, 2017.

[90] C. Tien and B. V. Ramarao, "Granular filtration of aerosols and hydrosols," *Butterworth–Heinemann*, 2013.

[91] C. Davies, "Filtration of aerosols," *Journal of Aerosol Science*, vol. 14, no. 2, pp. 147–161, 1983.

[92] B. A. Zeydabadi, D. Mowla, M. Shariat, and J. F. Kalajahi, "Zinc recovery from blast furnace flue dust," *Hydrometallurgy*, vol. 47, no. 1, pp. 113–125, 1997.

[93] A. Stephen, K. Anupama, G. Orukaimani, and S. Prasad, "A new microsieving technique in pollen analysis," *Journal of Palaeosciences*, vol. 57, no. 1-3, pp. 551–557, 2008.

[94] Y.-J. Wang *et al.*, "Comparison of mercury removal characteristic between fabric filter and electrostatic precipitators of coal-fired power plants," *Journal of Fuel Chemistry and Technology*, vol. 36, no. 1, pp. 23–29, 2008.

[95] E. A. Ogbuoji, A. M. Zaky, and I. C. Escobar, "Advanced research and development of face masks and respirators pre and post the coronavirus disease 2019 (COVID-19) pandemic: A critical review," *Polymers*, vol. 13, no. 12, p. 1998, 2021.

[96] M. H. Chua *et al.*, "Face masks in the new COVID-19 normal: Materials, testing, and perspectives," *National Library of Medicine*, 2020.

[97] S. Cabanillas-Barea *et al.*, "Effects of using the surgical mask and FFP2 during the 6-minute walking test. A randomized controlled trial," *International Journal of Environmental Research and Public Health*, vol. 18, no. 23, p. 12 420, 2021.

[98] R. Aditya, "A review of general and modern methods of air purification," *Journal of Thermal Engineering*, vol. 5, no. 2, pp. 22–28, 2018.

[99] K. Katsouyanni, "Ambient air pollution and health," *British Medical Bulletin*, vol. 68, no. 1, pp. 143–156, 2003.

[100] S. Gustafsson and A. Mihranyan, "Strategies for tailoring the pore-size distribution of virus retention filter papers," *American Chemical Society: Applied materials and Interfaces*, vol. 8, no. 22, pp. 13 759–13 767, 2016.

[101] J. Kitagawa, S. Asami, K. Uehara, and T. Hijikata, "Improvement of pore size distribution of wall flow type diesel particulate filter," Society of Automobile Engineers: Technical Papers, Tech. Rep., 1992.

[102] S. K. Bowry, "Nano-controlled membrane spinning technology: Regulation of pore size, distribution and morphology of a new polysulfone dialysis membrane," *Contributions to Nephrology*, vol. 137, pp. 85–94, 2002.

[103] K. H. Wong, M. Hernández-Guerrero, A. M. Granville, T. P. Davis, C. Barner-Kowollik, and M. H. Stenzel, "Water-assisted formation of honeycomb structured porous films," *Journal of Porous Materials*, vol. 13, no. 3, pp. 213–223, 2006.

[104] M. Hernández-Guerrero and M. H. Stenzel, "Honeycomb structured polymer films via breath figures," *Polymer Chemistry*, vol. 3, no. 3, pp. 563–577, 2012.

[105] E. Iritani, "A review on modeling of pore-blocking behaviors of membranes during pressurized membrane filtration," *Drying Technology*, vol. 31, no. 2, pp. 146–162, 2013.

[106] J. Chang, S. Vigneswaran, J. Kandasamy, and L. Tsai, "Effect of pore size and particle size distribution on granular bed filtration and microfiltration," *Separation Science and Technology*, vol. 43, no. 7, pp. 1771–1784, 2008.

[107] I. M. Griffiths, I. Mitevski, I. Vujkovac, M. R. Illingworth, and P. S. Stewart, "The role of tortuosity in filtration efficiency: A general network model for filtration," *Journal of Membrane Science*, vol. 598, p. 117 664, 2020.

[108] J. Kassotis, J. Shmidt, L. T. Hodgins, and H. P. Gregor, "Modelling of the pore size distribution of ultrafiltration membranes," *Journal of Membrane Science*, vol. 22, no. 1, pp. 61–76, 1985.

[109] G. G. Stokes, "On the theories of the internal friction of fluids in motion, and of the equilibrium and motion of elastic solids," *Transactions of the Cambridge Philosophical Society*, vol. 8, pp. 287–341, 1845.

[110] G. Alon and A. Adin, "Mathematical modeling of particle size distribution in secondary effluent filtration," *Water Environment Research*, vol. 66, no. 6, pp. 836–841, 1994.

[111] C. R. O'Melia and W. Ali, "The role of retained particles in deep bed filtration," *Ninth International Conference on Water Pollution Research*, pp. 167–182, 1979.

[112] J. Kozeny, "Uber kapillare leitung der wasser in boden (on the capillary conduction of water in soil)," *Royal Academy of Science Proceedings: Class I*, vol. 136, pp. 271–306, 1927.

[113] P. C. Carman, "Fluid flow through granular beds," *Transactions of the Institution of Chemical Engineers*, vol. 15, pp. 150–166, 1937.

[114] P. C. Carman, "Flow of gases through porous media," *Academic Press*, 1956.

[115] N. Wei, X. Peng, and Z. Xu, "Understanding water permeation in graphene oxide membranes," *Americal Chemical Society: Applied Materials and Interfaces*, vol. 6, no. 8, pp. 5877–5883, 2014.

[116] A. S. Kim and E. M. Hoek, "Cake structure in dead-end membrane filtration: Monte Carlo simulations," *Environmental Engineering Science*, vol. 19, no. 6, pp. 373–386, 2002.

[117] B. J. Sung and A. Yethiraj, "Permeation of a hard sphere fluid into a quenched matrix," *Journal of Chemical Physics*, vol. 126, no. 3, p. 034 704, 2007.

[118] J. F. Salinas and H. Dominguez, "Studies of diffusion coefficients in disordered porous matrices confined in a slit-pore," *Molecular Physics*, vol. 105, no. 10, pp. 1419–1431, 2007.

[119] F. Brauer, P. Van den Driessche, J. Wu, and L. J. Allen, "Mathematical epidemiology," *Springer*, vol. 1945, 2008.

[120] A. G. McKendrick, "Applications of mathematics to medical problems," *Proceedings of the Edinburgh Mathematical Society*, vol. 44, pp. 98–130, 1926.

[121] H. von Foerster, "Some remarks on changing populations," *The Kinetics of Cellular Proliferation*, pp. 382–407, 1959.

[122] J. A. Trangenstein, "Numerical solution of hyperbolic partial differential equations," *Cambridge University Press*, 2009.

[123] P. Sanaei and L. J. Cummings, "Membrane filtration with multiple fouling mechanisms," *Physical Review Fluids*, vol. 4, no. 12, p. 124 301, 2019.

[124] P. Sanaei and L. J. Cummings, "Membrane filtration with complex branching pore morphology," *Physical Review Fluids*, vol. 3, no. 9, p. 094 305, 2018.

[125] D. Fong, L. Cummings, S. Chapman, and P. Sanaei, "On the performance of multilayered membrane filters," *Journal of Engineering Mathematics*, vol. 127, pp. 1–25, 2021.

[126] S. Aytas, M. Yurtlu, and R. Donat, "Adsorption characteristic of Uranium (VI) ion onto thermally activated bentonite," *Journal of Hazardous Materials*, vol. 172, no. 2-3, pp. 667–674, 2009.

[127] A. Ghassemi and A. Pak, "Pore scale study of permeability and tortuosity for flow through particulate media using lattice boltzmann method," *International Journal for Numerical and Analytical Methods in Geomechanics*, vol. 35, no. 8, pp. 886–901, 2011.

[128] M. Kohler, G. Curtis, D. Kent, and J. Davis, "Experimental investigation and modeling of Uranium (VI) transport under variable chemical conditions," *Water Resources Research*, vol. 32, no. 12, pp. 3539–3551, 1996.

[129] S.-G. Li, F. Ruan, and D. McLaughlin, "A space-time accurate method for solving solute transport problems," *Water Resources Research*, vol. 28, no. 9, pp. 2297–2306, 1992.

[130] X. Ren, S. Wang, S. Yang, and J. Li, "Influence of contact time, pH, soil humic/fulvic acids, ionic strength and temperature on sorption of Uranium (VI) onto mx-80 bentonite," *Journal of Radioanalytical and Nuclear Chemistry*, vol. 283, no. 1, pp. 253–259, 2010.

[131] I. Griffiths and P. Stewart, "A hybrid discrete–continuum framework for modelling filtration," *Journal of Membrane Science*, vol. 647, p. 120 258, 2022.

[132] B. Gu, L. Kondic, and L. J. Cummings, "A graphical representation of membrane filtration," *SIAM Journal on Applied Mathematics*, vol. 82, no. 3, pp. 950–975, 2022.

[133] B. Gu, L. Kondic, and L. J. Cummings, "Network-based membrane filters: Influence of network and pore size variability on filtration performance," *Journal of Membrane Science*, vol. 657, p. 120 668, 2022.

[134] M. J. Blunt *et al.*, "Pore-scale imaging and modelling," *Advances in Water Resources*, vol. 51, pp. 197–216, 2013.

[135] R. A. Ketcham and W. D. Carlson, "Acquisition, optimization and interpretation of X-ray computed tomographic imagery: Applications to the geosciences," *Computers and Geosciences*, vol. 27, no. 4, pp. 381–400, 2001.

[136] L. M. Keller, L. Holzer, R. Wepf, P. Gasser, B. Münch, and P. Marschall, "On the application of focused ion beam nanotomography in characterizing the 3D pore space geometry of Opalinus clay," *Physics and Chemistry of the Earth*, vol. 36, no. 17-18, pp. 1539–1544, 2011.

[137] L. Tomutsa, D. Silin, and V. Radmilovic, "Analysis of chalk petrophysical properties by means of submicron-scale pore imaging and modeling," *Society of Petroleum Engineers: Reservoir Evaluation and Engineering*, vol. 10, no. 03, pp. 285–293, 2007.

[138] M. E. Curtis, "Structural characterization of gas shales on the micro-and nano-scales," *Canadian Unconventional Resources and International Petroleum Conference*, 2010.

[139] H. J. Lemmens, A. R. Butcher, and W. S. K. Botha, "FIB/SEM and automated mineralogy for core and cuttings analysis," *Society of Petroleum Engineers: Russian Oil and Gas Conference and Exhibition*, 2010.

[140] B. Blümich, F. Casanova, and S. Appelt, "NMR at low magnetic fields," *Chemical Physics Letters*, vol. 477, no. 4-6, pp. 231–240, 2009.

[141] P. T. Callaghan, "Principles of nuclear magnetic resonance microscopy," *Oxford University Press*, 1993.

[142] H. Giesche, "Mercury porosimetry: A general (practical) overview," *Particles and Particle Systems Characterization*, vol. 23, no. 1, pp. 9–19, 2006.

[143] C. A. Leon, "New perspectives in mercury porosimetry," *Advances in Colloid and Interface Science*, vol. 76, pp. 341–372, 1998.

[144] J. Rouquerol *et al.*, "The characterization of macroporous solids: An overview of the methodology," *Microporous and Mesoporous Materials*, vol. 154, pp. 2–6, 2012.

[145] M. Thommes, "Physical adsorption characterization of nanoporous materials," *Chemie Ingenieur Technik*, vol. 82, no. 7, pp. 1059–1073, 2010.

[146] M. Piri and M. J. Blunt, "Three-dimensional mixed-wet random pore-scale network modeling of two- and three-phase flow in porous media. I. Model description," *Physical Review E*, vol. 71, no. 2, p. 026 301, 2005.

[147] C. A. Baldwin, A. J. Sederman, M. D. Mantle, P. Alexander, and L. F. Gladden, "Determination and characterization of the structure of a pore space from 3D volume images," *Journal of Colloid and Interface Science*, vol. 181, no. 1, pp. 79–92, 1996.

[148] Z. R. Liang, C. P. Fernandes, F. S. Magnani, and P. C. Philippi, "A reconstruction technique for three-dimensional porous media using image analysis and Fourier transforms," *Journal of Petroleum Science and Engineering*, vol. 21, no. 3-4, pp. 273–283, 1998.

[149] W. B. Lindquist, S.-M. Lee, D. A. Coker, K. W. Jones, and P. Spanne, "Medial axis analysis of void structure in three-dimensional tomographic images of porous media," *Journal of Geophysical Research: Solid Earth*, vol. 101, no. B4, pp. 8297–8310, 1996.

[150] W. B. Lindquist, A. Venkatarangan, J. Dunsmuir, and T.-F. Wong, "Pore and throat size distributions measured from synchrotron X-ray tomographic images of Fontainebleau sandstones," *Journal of Geophysical Research: Solid Earth*, vol. 105, no. B9, pp. 21 509–21 527, 2000.

[151] S. L. Bryant and M. J. Blunt, "Prediction of relative permeability in simple porous media," *Physical Review A*, vol. 46, no. 4, p. 2004, 1992.

[152] S. L. Bryant, P. R. King, and D. W. Mellor, "Network model evaluation of permeability and spatial correlation in a real random sphere packing," *Transport in Porous Media*, vol. 11, pp. 53–70, 1993.

[153] S. L. Bryant, D. W. Mellor, and C. A. Cade, "Physically representative network models of transport in porous media," *American Institute of Chemical Engineers*, vol. 39, no. 3, pp. 387–396, 1993.

[154] S. Bakke and P.-E. Øren, "3-D pore-scale modelling of sandstones and flow simulations in the pore networks," *Society of Petroleum Engineers*, vol. 2, no. 02, pp. 136–149, 1997.

[155] P.-E. Øren, S. Bakke, and O. J. Arntzen, "Extending predictive capabilities to network models," *Society of Petroleum Engineers*, vol. 3, no. 04, pp. 324–336, 1998.

[156] P. Adler and J.-F. Thovert, "Real porous media: Local geometry and macroscopic properties," 1998.

[157] A. Roberts and S. Torquato, "Chord-distribution functions of three-dimensional random media: Approximate first-passage times of Gaussian processes," *Physical Review E*, vol. 59, no. 5, p. 4953, 1999.

[158] C. L. Y. Yeong and S. Torquato, "Reconstructing random media," *Physical Review E*, vol. 57, no. 1, p. 495, 1998.

[159] H. Okabe and M. J. Blunt, "Prediction of permeability for porous media reconstructed using multiple-point statistics," *Physical Review E*, vol. 70, no. 6, p. 066 135, 2004.

[160] I. Fatt, "The network model of porous media," *Transactions of the American Institute of Mining*, vol. 207, no. 01, pp. 144–181, 1956.

[161] S. Kirchhoff, "On the passage of an electric current through a plane, especially a circular one," *Annals of Physics*, vol. 140, no. 4, pp. 497–514, 1845.

[162] H. D. Young, R. A. Freedman, T. R. Sandin, and A. L. Ford, "University physics," *Addison–Wesley*, vol. 9, 1996.

[163] E. Giné, G. R. Grimmett, L. Saloff-Coste, and G. Grimmett, "Percolation and disordered systems," *Lectures on Probability Theory and Statistics: Ecole d'Eté de Probabilités de Saint-Flour*, pp. 153–300, 1997.

[164] Y. Mehmani, T. Sun, M. T. Balhoff, P. Eichhubl, and S. L. Bryant, "Multiblock pore-scale modeling and upscaling of reactive transport: Application to carbon sequestration," *Transport in Porous Media*, vol. 95, pp. 305–326, 2012.

[165] M. J. Blunt, M. D. Jackson, M. Piri, and P. H. Valvatne, "Detailed physics, predictive capabilities and macroscopic consequences for pore-network models of multiphase flow," *Advances in Water Resources*, vol. 25, no. 8-12, pp. 1069–1089, 2002.

[166] X. Lopez, P. H. Valvatne, and M. J. Blunt, "Predictive network modeling of single-phase non-newtonian flow in porous media," *Journal of Colloid and Interface Science*, vol. 264, no. 1, pp. 256–265, 2003.

[167] A. V. Ryazanov, M. I. J. Van Dijke, and K. S. Sorbie, "Two-phase pore-network modelling: Existence of oil layers during water invasion," *Transport in Porous Media*, vol. 80, pp. 79–99, 2009.

[168] A. G. Yiotis, I. N. Tsimpanogiannis, A. K. Stubos, and Y. C. Yortsos, "Pore-network study of the characteristic periods in the drying of porous materials," *Journal of Colloid and Interface Science*, vol. 297, no. 2, pp. 738–748, 2006.

[169] J. Meyers and A. Liapis, "Network modeling of the convective flow and diffusion of molecules adsorbing in monoliths and in porous particles packed in a chromatographic column," *Journal of Chromatography A*, vol. 852, no. 1, pp. 3–23, 1999.

[170] A. P. Jivkov and Q. Xiong, "A network model for diffusion in media with partially resolvable pore space characteristics," *Transport in Porous Media*, vol. 105, pp. 83–104, 2014.

[171] J. A. E. Andersson, J. Gillis, G. Horn, J. B. Rawlings, and M. Diehl, "CasADi – A software framework for nonlinear optimization and optimal control," *Mathematical Programming Computation*, 2018.

[172] U. Hornung, "Homogenization and porous media," *Springer Science & Business Media*, vol. 6, 1997.

[173] E. Sanchez-Palencia, "Homogenization in mechanics. A survey of solved and open problems," *Rendiconti del Seminario Matematico Universita e Politecnico di Torino*, vol. 44, no. 1, pp. 1–45, 1986.

[174] C. Conca, "Numerical results on the homogenization of Stokes and Navier-Stokes equations modeling a class of problems from fluid mechanics," *Computer Methods in Applied Mechanics and Engineering*, vol. 53, no. 3, pp. 223–258, 1985.

[175] J.-L. Auriault and P. Adler, "Taylor dispersion in porous media: Analysis by multiple scale expansions," *Advances in Water Resources*, vol. 18, no. 4, pp. 217–226, 1995.

[176] J.-P. Bouchaud and A. Georges, "Anomalous diffusion in disordered media: Statistical mechanisms, models and physical applications," *Physics reports*, vol. 195, no. 4-5, pp. 127–293, 1990.

[177] S. Havlin and D. Ben-Avraham, "Diffusion in disordered media," *Advances in Physics*, vol. 36, no. 6, pp. 695–798, 1987.

[178] O. Braun and C. Sholl, "Diffusion in generalized lattice-gas models," *Physical Review B*, vol. 58, no. 22, p. 14 870, 1998.

[179] Z. Koza, "General technique of calculating the drift velocity and diffusion coefficient in arbitrary periodic systems," *Journal of Physics A: Mathematical and General*, vol. 32, no. 44, p. 7637, 1999.

[180] G. Strang, "Introduction to Linear Algebra," *Wellesley–Cambridge Press*, vol. 3, 1993.

[181] M. Schader and F. Schmid, "Two rules of thumb for the approximation of the binomial distribution by the normal distribution," *The American Statistician*, vol. 43, no. 1, pp. 23–24, 1989.

[182] J. Meijering, "Interface area, edge length, and number of vertices in crystal aggregates with random nucleation," *Philips Research Reports*, vol. 8, pp. 270–290, 1953.